ACTA PHYSICA ACADEMIAE SCIENTIARUM HUNGARICAE

TOMUS XLIX

FASCICULI 1—3

AKADÉMIAI KIADÓ, BUDAPEST

1980

ACTA PHYS. HUNG.

APAHAQ 49 (1—3) 1—318 (1980)

ACTA PHYSICA

ACADEMIAE SCIENTIARUM HUNGARICAE

SZERKESZTI

KOVÁCS ISTVÁN

Az *Acta Physica* angol, német, francia vagy orosz nyelven közöl értekezéseket. Évente két kötetben, kötetenként 4—4 füzetben jelenik meg. Kéziratok a szerkesztőség címére (1521 Budapest XI., Budafoki út 8.) küldendők.

Megrendelhető a belföld számára az Akadémiai Kiadónál (1363 Budapest Pf. 24. Bankszámla 215-11488), a külföld számára pedig a ,,Kultúra" Külkereskedelmi Vállalatnál (1389 Budapest 62, P.O.B. 149. Bankszámla 217-10990) vagy annak külföldi képviseleteinél.

The *Acta Physica* publish papers on physics in English, German, French or Russian in issues making up two volumes per year. Distributor: "Kultura" Foreign Trading Company (1389 Budapest 62, P.O. Box 149) or its representatives abroad.

Die *Acta Physica* veröffentlichen Abhandlungen aus dem Bereich der Physik in deutscher, englischer, französischer oder russischer Sprache, in Heften, die jährlich zwei Bände bilden.

Bestellbar bei »Kultura« Außenhandelsunternehmen (1389 Budapest 62, Postfach 149) oder seinen Auslandsvertretungen.

Les *Acta Physica* publient des travaux du domaine de la physique en français, anglais, allemand ou russe, en fascicules qui forment deux volumes par an.

On peut s'abonner à l'Entreprise du Commerce Extérieur «Kultura» (1389 Budapest 62, P.O.B. 149) ou chez représentants à l'étranger.

«*Acta Physica*» публикуют трактаты из области физических наук на русском, немецком, английском и французском языках.

«*Acta Physica*» выходят отдельными выпусками, составляющими два тома в год.

Заказы принимает предприятие по внешней торговле **«Kultura» (1389 Budapest 62, P.O.B. 149)** или его заграничные представительства.

ACTA PHYSICA

ACADEMIAE SCIENTIARUM HUNGARICAE

ADIUVANTIBUS

R. GÁSPÁR, K. NAGY, L. PÁL, A. SZALAY, I. TARJÁN

REDIGIT

I. KOVÁCS

TOMUS XLIX

AKADÉMIAI KIADÓ, BUDAPEST
1980

ACTA PHYS. HUNG.

INDEX

Tomus 49

GENERAL PHYSICS

NUCLEAR PHYSICS

ATOMIC AND MOLECULAR PHYSICS

PHYSICS OF CONDENSED MATTER

VACUUM PHYSICS

ACTA PHYSICA

ACADEMIAE SCIENTIARUM HUNGARICAE

ADIUVANTIBUS

R. GÁSPÁR, K. NAGY, L. PÁL, A. SZALAY, I. TARJÁN

REDIGIT

I. KOVÁCS

TOMUS XLIX

FASCICULI 1—3

AKADÉMIAI KIADÓ, BUDAPEST
1980

The Hungarian-Austrian Vacuum Conference (Győr, Hungary, October 22—25, 1979) was organized by the Sections for Vacuum Physics and the Physics of Thin Films of Roland Eötvös Physical Society and by the Österreichische Gesellschaft für Vakuumtechnik, in co-operation with

— the Hungarian National Committee of IUVSTA
— the Regional Group of the Roland Eötvös Physical Society in Győr
— the Coordinating Committee of Vacuum Physics and Physics of Thin Films of the Hungarian Federation of Technical and Scientific Societies (MTESZ).

Organizing and Program
Committee

Hungary:
Prof. J. Antal
Chairman

Dr. P. B. Barna
Chairman of the Program Committee

E. Barla
Dr. J. Erdélyi
Dr. L. Füstöss
Dr. G. Gergely
Dr. J. Gyulai

Dr. J. Kispéter
S. Tisza
Dr. L. Tolnai
Mrs. E. Nagy

Austria:
Prof. F. Viehböck
Chairman

Dr. F. Grasenick
Prof. E. Hörl

This issue contains the (texts of) invited papers, short contributions and posters presented at the Conference and submitted to the Program Committee before January 31, 1980. For papers not submitted by the above date, the original abstracts are published.

The issue was closed and submitted to the Editor of Acta Physica Hungarica the same date by the Conference Program Committee. The material was compiled and prepared for publication by Dr. G. Gergely.

PROCEEDINGS OF THE VACUUM CONFERENCE

Győr, 22—25 October, 1979

Organized by

EÖTVÖS LORÁND FIZIKAI TÁRSULAT, BUDAPEST

and

ÖSTERREICHISCHE GESELLSCHAFT FÜR VAKUUMTECHNIK,
WIEN

INDEX

PHYSICS OF CONDENSED MATTER

NUCLEAR PHYSICS

VACUUM PHYSICS

Acta Physica Academiae Scientiarum Hungaricae, Tomus 49 (1–3), pp. 7–22 (1980)

INVITED PAPERS

DÜNNE ORGANISCHE SCHICHTEN

Von

M. Auwärter

INSTITUT FÜR ANGEWANDTE PHYSIK, UNIVERSITÄT TÜBINGEN, TÜBINGEN, BRD

Unter Dünnen Schichten versteht man meistens anorganische materielle Zustände, bei denen das Verhältnis

$$\frac{\text{Volumenatome}}{\text{Oberflächenatome}} < 10^4 \text{ ist.}$$

Es gibt eine Fülle organischer Schichten, welche diese Definition ebenfalls erfüllen.

Bei allen Dünnen Schichten beeinflusst die freie Oberflächenenergie das physikalische Verhalten.

Die Biologen haben schon lange festgestellt, dass die Farben vieler Tiere durch Dünne Schichten entstehen. Die Natur benützt ausser der Brechung alle physikalischen Möglichkeiten zu ihrer Erzeugung. Dafür werden Beispiele angeführt.

Organische langkettige Stoffe wie z.B. Paraffine sind durch hydrophile und hydrophobe Enden begrenzt. Sie haben auf einer Wasseroberfläche ähnliche Strukturen, wie die Lipide in der Membran einer biologischen Zelle. Da ihre Schichtdicke 10 nm beträgt, sind sie ebenfalls unter die Dünnen Schichten einzuordnen. Ihr Aufbau und ihre Wirkungsweise werden beschrieben.

Von besonderer Bedeutung ist die Photosynthese, von der erwartet wird, dass eine Wasserstofftechnologie entwickelt werden kann, welche das Energieproblem langfristig lösen könnte.

Auf einen schwerwiegenden Negativeffekt wird hingewiesen, der durch Dünne organische Schichten auf Wasserflächen entstehen kann.

Der Versuch, möglichst viele und sehr verschiedenartige organische dünne Schichten zu beschreiben, ist für den Physiker besonders reizvoll. Dass beim vorliegenden Referat spezifische biologische Probleme vernachlässigt werden müssen, liegt an der ungenügenden Fachkenntnis des Referenten.

Dünne, fast ausschliesslich anorganische Schichten werden seit rund 40 Jahren in physikalischen Laboratorien mit grossem Aufwand an apparativen Mitteln erforscht und entwickelt. Ihre Produktion füllt heute Fabriken.

Die Natur aber schafft über Regelsysteme, die in vielen ihrer Einzelheiten immer noch ungeklärt sind, eine Mannigfaltigkeit aus organischen Substanzen.

Die zunehmende Zusammenarbeit zwischen Biologen, Medizinern, Physikern und Chemikern führt bereits zu einer Fülle neuer Erkenntnisse, die sich in einem Übermass an Veröffentlichungen dokumentieren. Physikalische Forschungsmittel wie das Elektronenmikroskop, das Rasterelektronenmikroskop und die verschiedenen Oberflächenanalysengeräte haben ermöglicht, Eigenschaften der Grenzflächen und die an ihnen ablaufenden Erscheinungen besser verstehen zu können. Sicher werden bei einem vertieften Verständnis der energetischen Abläufe eine Menge an Anregungen auch für nichtbiologische Prozesse zu erwarten sein.

Ein wesentlicher Unterschied zwischen dem Verhalten anorganischer und organischer Reaktionspartner ist die Geschwindigkeit der Bildung einer Verbindung. Organische Reaktionen laufen fast immer viel langsamer ab als anorganische.

Wenn es üblich geworden ist, allein künstlich erzeugten »dünnen Schichten« aus nahezu ausschliesslich anorganischen Substanzen diese Bezeichnung zu reservieren, dann liegt dafür keine sinnvolle Begründung vor. Alle Arten von Schichtsystemen unterliegen physikalischen Gesetzmässigkeiten, die ihre Eigenschaften mitbestimmen. Dies gilt auch für solche, die aus lebender Materie bestehen. Es ist deshalb vernünftig, eine erweiterte Definition zu geben.

Der Begriff »Dünne Schichten« umfasse alle materiellen Zustände, die sich in Abgrenzung zum Festkörper oder einer Flüssigkeit durch ihre Dünne und ihre dabei flächenhafte Ausdehnung unterscheiden. Eine quantitative Aussage lässt sich durch das Verhältnis

$$\frac{\text{Volumenatome}}{\text{Oberflächenatome}} < 10^4$$

machen.

Damit aber sind charakteristische Eigenschaften mit einem solchen System gekoppelt. Es grenzt mit seinen Oberflächen immer an stofflich fremde Phasen, wobei das Volumen im Gegensatz zum Festkörper beeinflusst wird. Dies gilt auch für dünne Schichten unter Hochvakuumbedingungen. Bei 10^{-7} Pa ist eine reine Oberfläche nach 10^{-3} Sekunden mit 10^{12} Atomen bedeckt, die wegen ihrer Oberflächenbeweglichkeit solche Plätze besetzen, bei denen die freie Oberflächenenergie ein Minimum wird. Diese bevorzugten Plätze aber ändern sich infolge der Gitterschwingungen ständig.

In einem Mehrphasensystem haben die an der Oberfläche des Festkörpers liegenden Atome, Ionen oder Moleküle weniger umgebende Nachbarn als im Inneren und deshalb eine nicht vollständige Valenzabsättigung.

Die Energie eines beliebigen Gesamtsystems ist

$$G = NG^0 + fG^s ,$$

wo N die Zahl der Atome des Festkörpers, G^0 die Energie eines seiner Atome, G^s die freie Oberflächenenergie σ pro Flächeneinheit und f das Oberflächenareal bedeuten.

Im Gleichgewichtszustand ist G bestrebt, sich auf ein Minimum einzustellen. Dies ist beim Festkörper nur über eine Reduktion von G^s möglich.

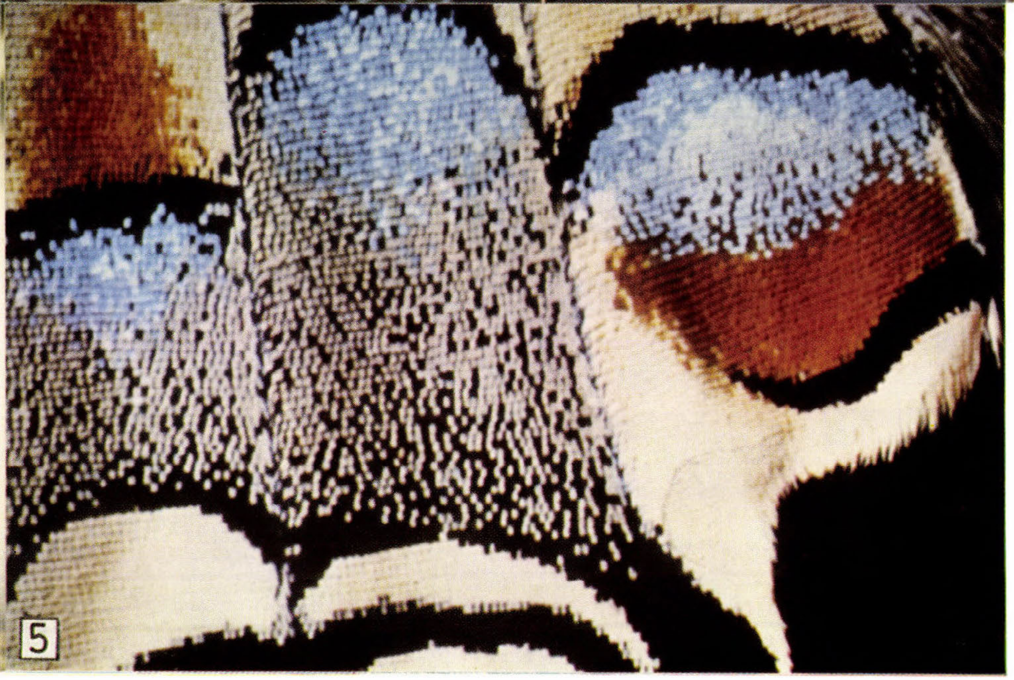

Abb. 2. Das Weibchen des braunen Kolibris (SELAPHORUS RUFUS). Die Färbung des Gefieders entsteht hauptsächlich durch Interferenzeffekte [4].

Abb. 3. Das Männchen der rotköpfigen Spielart des Goldsamadines (ERYTHRURA GOULDIAE), dessen Färbung durch Absorption und Interferenz entsteht [5].

Abb. 4. Der Schwalbenschwanz [6]

Abb. 5. 15-fache Vergrösserung eines Ausschnittes der Flügeldecke des Schwalbenschwanzes mit dachziegelartiger Anordnung der Schuppen, in denen Interferenzen die Farben erzeugen [6].

Abb. 6. Der nordamerikanische Puppenräuber (CALOSOMA SCRUTATOR), dessen Farben durch Interferenz und Beugung entstehen [7].

Da σ immer positiv ist, werden in Grenzschichten zwischen verschiedenen Phasen die Valenzkräfte miteinander so wechselwirken, dass die freie Oberflächenenergie verkleinert wird. Bestehen die Phasen aus Flüssigkeiten oder anderen leicht deformierbaren Körpern wie z. B. Gelen, dann werden sich die Grenzflächen im Gegensatz zu Festkörpern geometrisch nach kleineren f ändern. Die günstigste Geometrie wäre die Kugel. Im Interface zwischen den starren Festkörpern treten komplexe und erhebliche Spannungen auf [1] (Abbildung 1a und b.)

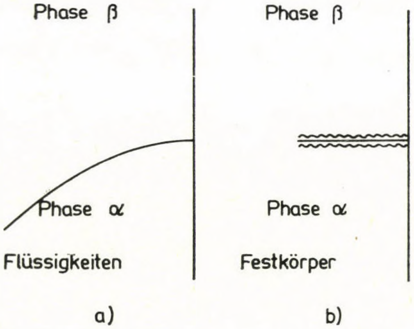

Abb. 1. a) Zwei flüssige Phasen α und β, deren Grenzfläche wegen ihrer unterschiedlichen Oberflächenspannungen gekrümmt ist; b) zwei Festkörper. Im Interface treten wegen der verschiedenen freien Oberflächenenergien Spannungen auf.

Biologische Systeme werden wegen des oft hohen Wassergehalts ein(energetisch günstige geometrische Form annehmen.

Es ist üblich, σ bei Flüssigkeiten mit Oberflächenspannung, bei Festkörpen mit freier Oberflächenenergie zu benennen.

Die Grösse der freien Oberflächenenergie ist für Elemente und Verbindungen ausserordentlich verschieden. Der besonders niedrige Wert für σ bei organischen Substanzen gegenüber Metallen und Oxiden ist besonders auffallend. Die dadurch bedingte niedrige energetische Wechselwirkung macht sich z. B. beim Begehen frisch geölter oder gewachster Fussböden oft unangenehm bemerkbar.

Als Beispiel des Einflusses von σ diene die Legierung Pt-Ag. Sie hat an ihrer Oberfläche eine durch Diffusion entstandene einatomare Schicht aus Ag, weil $\sigma_{Ag} < \sigma_{Pt}$. Diese Veränderung in der Zusammensetzung der Festkörperoberfläche tritt auch dann ein, wenn Ag nur als Verunreinigung im Pt enthalten ist.

Es wäre zu untersuchen, ob die an Blättern und Früchten vieler Pflanzen beobachteten wasserabstossenden dünnen Oberflächenschichten ebenfalls durch die freie Oberflächenenergie bedingt sind. Auf der zellfreien, die Pflanze vor Austrocknung schützenden Aussenschicht, der Kutikula, bildet sich eine amorphe Wachsschicht. Dadurch werden auf solchen Blättern und Früchten

Tabelle I

Werte der freien Oberflächenenergie σ für Metalle, anorganische und organische Verbindungen

Substanz	σ (10^3 Joule/m^2)	Temperatur (K)
W	2900	2000
Pt	2340	1520
Ni (110)	1900	1490
Ni (100)	1821	1490
Au	1410	1300
Ag	1140	1180
MgO	1200	298
NaCl	227	298
Wasser	72,75	293
Polyvinylchlorid	39	293
Polystyrol	33	293
Polyäthylen	31	293
Polytetrafluoräthylen (Teflon)	18,5	293

kontaminierte schädliche Verunreinigungen wie z. B. Aerosole durch Regen leichter abgewaschen als von wachsfreien Pflanzen. Besonders wichtig ist ein erhöhter Schutz vor Verstopfung der für den Gasaustausch unentbehrlichen Spältöffnungen.

Zur Untersuchung dieser dünnen Wachsschichten benützte **Rentschler** [2] die elektronenmikroskopische Präparationsmethode der Gefrierätzung nach **Moor** und **Mühlethaler** [3] als einzig brauchbare.

Erstaunlich ist die Fähigkeit der Natur, ausser der Brechung Farben mit allen anderen der Physik bekannten Methoden zu erzeugen, wobei organische dünne Schichten selbst oder indirekt Träger sind. Das Referat schliesst nicht Überlegungen ein, wie die Farben bei Pflanzen und Tieren *genetisch* entstanden sind und auch nicht über ihren Zweck ausser in Fällen, bei denen die spezifische Physik die entscheidende Rolle spielt.

Absorption, Reflexion, Streuung, Interferenz und Beugung, Doppelbrechung und Polarisation sind die Mittel, welche die Natur an Oberflächen und dünnen Schichten anwendet, um Farbeffekte zu gewinnen. Einige Bilder sollen den Eindruck der Vielgestaltigkeit vermitteln.

Abb. 2 zeigt das Weibchen des braunen Kolibris (SELAPHORUS RUFUS), dessen Färbung hauptsächlich durch Interferenzeffekte entsteht [4].

Abb. 3 zeigt das Männchen der rotköpfigen Spielart des Goldsamadine (ERYTHRURA GOULDIAE), einen Prachtfink aus dem Norden Australiens, dessen Farben durch Absorption und Interferenz bedingt sind [5].

Der Schwalbenschwanz und ein ~ 15-fach vergrösserter Ausschnitt aus der Flügeldecke dieses schönen Schmetterlings sind in der Abbildung 4 bzw. 5 zu sehen. Die dachziegelartige Anordnung der Schuppen, in denen Interferenzen die Farbe erzeugen, ist deutlich zu sehen [6].

Der nordamerikanische Puppenräuber (Abb. 6) (CALOSOMA SCRUTATOR) ist ein naher Verwandter des europäischen Laufkäfers Goldschmied. Seine Färbung entsteht durch Interferenz und Beugung [7].

Körperfarben entstehen durch selektive Absorption an Stoffen, die entweder in geschlossener Form vorliegen oder in der farblosen Matrix einer dünnen Schicht körnig verteilt sind. Die so eingelagerten Partikel bezeichnet die Biologie mit Pigment. Solche Körperfarben allein verursachen die Färbung der Blüten und Früchte von Pflanzen und ihr Blattgrün. Auch bei Tieren findet man sie häufig. Farben dieser Art zeigen keine Änderung ihres Spektrums bei verschiedenen Einfallswinkeln.

Relativ selten findet man die meist matte Färbung durch den *Tyndalleffekt*. Er entsteht beim Durchgang von Licht durch optisch inhomogene Medien, d. h. wenn die Brechzahl durch Fremdkörper oder Dichteschwankungen in eng begrenzten Bereichen variiert. Die Grösse der Fremdkörper liegt bei Bruchteilen der Wellenlängen des eingestrahlten Lichtes. Die Intensität des gestreuten Lichtes ist proportional der Zahl der streuenden Teilchen in der Volumeneinheit, dem Quadrat ihres Volumens und umgekehrt proportional der vierten Potenz der Wellenlänge λ. Dass auch in dünnen Schichten intensive Streufarben entstehen, wurde experimentell durch thermische Ausscheidung atomar in einer $\lambda/4$ starken Matrix aus MgF_2 verteilten Goldes nachgewiesen. Dabei war es möglich, eine Streuintensität zu erreichen, die der eines 1 cm dicken Rubinglases entspricht. Ein Beispiel für den Tyndalleffekt sind die Farben von Libellen.

Sehr häufig findet man bei Insekten, Muscheln, Kopffüsslern, Fischen und beim Gefieder der Vögel *Interferenzerscheinungen* an dünnen Schichten, die ebenso wie die Beugung charakteristische Farben ergeben. Der Schwerpunkt ihres Spektrums ändert sich mit steigendem Einfallswinkel nach kürzeren Wellen. Der Biologe bezeichnet diese Erscheinung mit Schillerfarbe. Vielleicht dient sie dazu, Feinde zu irritieren und abzuschrecken.

Interferenz entsteht dann, wenn sich kohärente und linear polarisierte Wellen mit gemeinsamen Schwingsebenen überlagern.

An jeder Grenzfläche zwischen verschiedenen absorptionsarmen Medien wird die reflektierte Amplitude des senkrecht einfallenden Lichtes durch den Fresnelkoeffizienten

$$r = \frac{n_0 - n_1}{n_0 + n_1}$$

bestimmt, wo n_0 und n_1 die Brechzahlen der Medien 1 und 2 sind. Ist $n_1 > n_0$, dann entsteht ein Phasensprung von $\lambda/2$, nicht jedoch, wenn $n_1 < n_0$ ist.

Eine dünne Schicht besitzt zwei Grenzflächen, an denen Wellenzüge reflektiert werden und sich überlagern. Ein schönes Beispiel zeigt eine Seifenblase, bei der für eine Phasendifferenz von $\lambda/2n$, wo n die Brechzahl der Seifenlamelle ist, völlige Auslöschung des einfallenden Lichtes entsteht.

Ein Mehrschichtsystem mit abwechselnd hohen und niedrigen Brechzahlen kann bei geeigneter Anordnung zu hochreflektierenden Spiegeln mit über 99, 90% Reflexionsvermögen führen. Die dafür notwendige Schichtzahl bei Brechzahlen von 1,45 und 2,4 liegt bei 50. Solche Spiegel mit geringstem Absorptionsvermögen sind Vorbedingung für die Erzeugung hoher Intensitäten bei den optischen Resonatoren von Lasern.

Den Strahlengang in einer Mehrfachschicht zeigt schematisch Abb. 7. Die den p_n zugeordneten Amplituden werden durch die Formeln für p_1, p_2, p_3 und p_n Schichten wiedergegeben [8]. (Abb. 8).

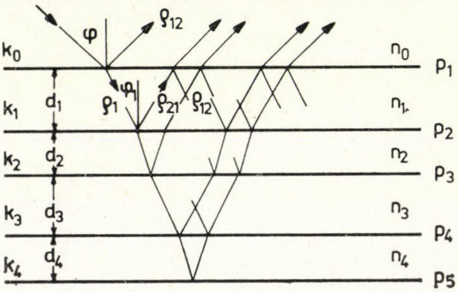

Abb. 7. Strahlengang in einer 4-fachschicht
$n_0 = 1{,}0$ Luft, $n_1 = n_3 = 1{,}38$ Mg F$_2$, $n_2 = n_4 = 2{,}30$ Al$_2$O$_3$, k = Schichten, p = Grenzschichten

$$\mathbf{r}_1 = \frac{\varrho_{21} + \varrho_{10} \cdot e^{-i\alpha_1}}{1 - \varrho_{12}\varrho_{10}\, e^{-i\alpha_1}};$$

$$r_{21} = \frac{\varrho_{32} + \mathbf{r}_1 \cdot e^{-i\alpha_2}}{1 - \varrho_{23}\, \mathbf{r}_1 \cdot e^{-i\alpha_2}};$$

$$r_{321} = \frac{\varrho_{43} + r_{21} \cdot e^{-i\alpha_3}}{1 - \varrho_{34}\, r_{21} \cdot e^{-i\alpha_3}};$$

$$\cdots\cdots\cdots\cdots\cdots\cdots$$

$$r_{p,p-1\ldots 2,1} = \frac{\varrho_{p+1,p} + r_{p-1}, \ldots 2{,}1\, e^{-i\alpha p}}{1 - \varrho_{p,p+1}\, r_{p-1,p-2}\, 2{,}1 \cdot e^{-i\alpha p}};$$

$$\varrho_{k,k+1} = -\varrho_{k+1,k};$$

$$\alpha_k = \frac{4\pi}{\varkappa} \cdot n_k \cdot c_k \cdot d_k; \quad c_k = \cos \varphi_k;$$

Abb. 8. Die Formeln für das Reflexionsvermögen eines Vielschichtsystems

Abb. 9 gibt ein System von 8 Schichten aus anorganischen Substanzen mit

$$n_0 = 1{,}0\ (\text{Luft}),\ n_1 = 1{,}38\ (\text{MgF}_2),\ n_2 = 2{,}30\ (\text{Al}_2\text{O}_3)$$

in alternierender Folge der Brechzahlen n_1 und n_2 wieder und Abb. 10 zeigt die zugehörigen Kurven der Reflexion für 6 und 8 Schichten. Die Abszisse wird, um Symmetrie zu erhalten, mit λ/λ_0 aufgetragen, wo λ_0 die Phasendifferenz $\lambda_0/2n$ und λ die von ihr abweichenden Wellenlängen bedeuten [9].

Die Natur bildet soche Stapelsysteme in verschiedener Weise aus. Abb. 11 zeigt schematisch ein Teilstück einer Entenfeder mit Mehrfachschichten aus Melaninstäbschen *M* in der dorsalen Rinde ***dR*** und Abb. 12 ihre Anordnung in der Feder [10].

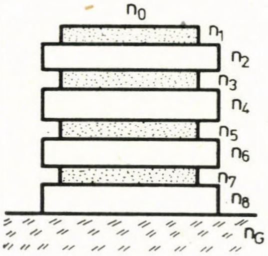

Abb. 9. Schematischer Aufbau eines Systems mit 8 Schichten. $n_0 = 1{,}0$ Luft; $n_1 = n_3 = n_5 = n_7$; $n_2 = n_4 = n_6 = n_8$; $n_G = 1{,}54$ Glas

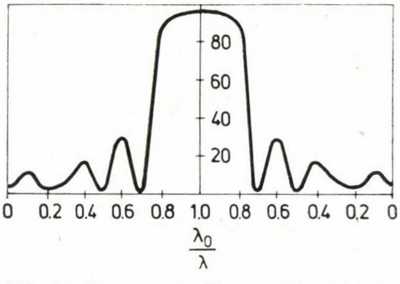

Abb. 10. Kurve zum System der Abb. 9

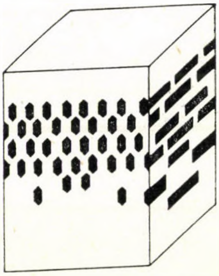

Abb. 11. Schematische Anordnung von dünnen Melaninschichten

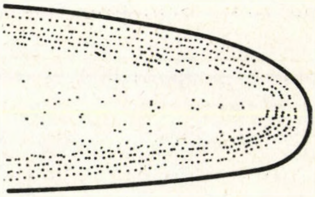

Abb. 12. Die Verteilung von dünnen Melaninschichten in der dorsalen Rinde einer Entenfeder

Pulker und Steinbbecht untersuchen die Kutikula der Puppe des Schmetterlings EUPLOEA aus der Familie der DANAIDEA. Sie haben freundlicherweise aus ihrer noch unveröffentlichten Arbeit in einem Ausschnitt ein Bild der Schichtstruktur der Kutikula zur Verfügung gestellt. Es ist bewundernswert, mit welcher Präzision die Natur Mehrfachschichten aus alternierend angeordneten nieder- und hochbrechenden Substanzen aufbaut (Abb. 13).

Solche hochreflektierenden Strukturen findet man in den Augen von Kopffüsslern und Muscheln mit diskreten Schichten oder Platten aus Guanin (eine Purinbase $C_5H_5N_5O$) mit der Brechzahl $n_G = 1{,}83$ und dem niedrigbrechenden Cytoplasma ($n_c = 1{,}34$).

Abbildung 14 zeigt sehr schematisch den Aufbau des Auges der Kammuschel. Das einfallende Licht durchtritt eine Sammellinse und wird dann durch den Reflektor auf die Retina konzentriert. Da seine Dicke $6 \cdot 10^3$ nm beträgt, besteht er aus ~ 50 Einzelschichten [11].

Seltener treten bei Tieren an dafür geeigneten Strukturen Farben durch *Beugung* auf. Beugung des Lichtes entsteht immer dann, wenn es an seiner freien Ausbreitung z. B. durch eine Blende gehindert wird. Langwelliges Licht wird stärker abgelenkt alz kurzwelliges. Weisses Licht wird deshalb spektral zerlegt. Besonders eindrücklich ist dies an einem Beugungsgitter der Fall. Dabei tritt bei der Wellenlänge λ ein Maximum an Intensität bei

$$d \cdot \sin \alpha = \mathrm{m} \cdot \lambda$$

auf, wo d der Gitterabstand, α der Beugungswinkel und m eine ganze Zahl bedeutet. $(0, \pm 1, \pm 2, \ldots)$.

Farben durch Beugung zeigen Rippenquallen (CTEMOPHORES) und die Seemaus (APHRODITE ACULEATA), ein Meereswurm, der zu den Vielborstern gehört. An seiner Körperseite trägt er lange Borsten und in Längsrichtung verlaufende Chitin-Fibrillen.

Ein klassisches Beugungsgitter zeigen Käfer der Gattung SERICA aus der Familie der SCARABAIDEA auf ihren Flügeldecken. In Richtung der Körperachse sind auf ihnen Kerben der Strichzahl 8000–10 000 pro cm zu

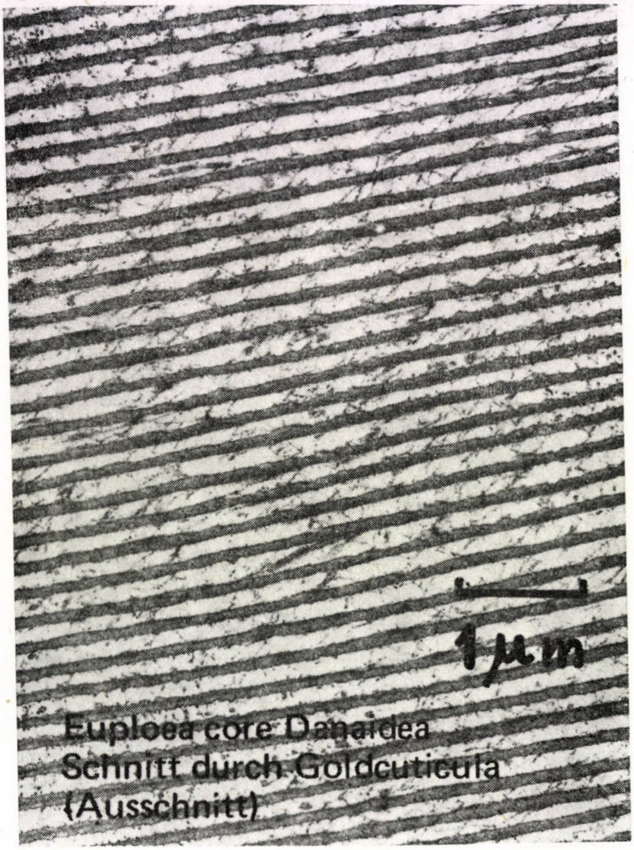

Abb. 13. Schnitt durch die Kutikula der Schmetterlingspuppe EUPLOEA aus der Familie DANAIDEA. Die elektronenmikroskopische Aufnahme wurde von den Herren Dozenten R. A. Steinbrecht vom Institut für Verhaltensphysiologie des MPI und H. K. Pulker, Balzers AG, freundlicherweise zur Verfügung gestellt.

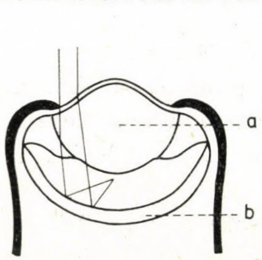

Abb. 14. Schema des Auges der Kammuschel mit Linse (a) und Reflektor (b) nach M. F. Land

zählen. Hochwertige Gitterstrichmaschinen erlauben höchstens 2 bis 3 mal mehr Striche pro cm unterzubringen.

Natürlich ist die Ursache für das, was eben mit Interferenz und Beugung bezeichnet wurde, physikalisch dieselbe, nämlich die Überlagerung von interferenzfähigen Wellenzügen. Alle Arten der PLUSIOTIS, die zu der bereits erwähnten Familie SCARABAEIDEA gehören, sind besonders farbige Käfer. Sie haben ausser einem reflexionserzeugenden Vielfachschichtsystem noch eine dünne Chitinschicht in der äusseren Kutikula, die bis zu 70% Harnsäure (2, 6, 8-trihydroxypurin) enthält. Diese $1{,}8 \cdot 10^3$ nm dicke Schicht ist richtungsorientiert. Bedingt durch Orientierung und Doppelbrechung der Härnsaure entstehen alle möglichen physikalischen Effekte wie *zirkularpolarisiertes Licht* und *optische Aktivität*. Der Drehwinkel ist der Schichtdicke proportional und wellenlängenabhängig. Diese äussere Schicht entspricht einem perfekten $\lambda/2$ Plättchen, Ursache für das zirkular polarisierte Licht. Die aus der Optik bekannten Experimente zeigen, diesmal *nicht* durch Interferenz bedingt, intensive Farben.

Agnes Pockels [12] beobachtete 1891 das eigenartige Verhalten von Kampfermolekülen, die sich aus der Grenzfläche zwischen dem Kristall und Wasser auf der Flüssigkeitsoberfläche ausbreiten.

Sind die Kräfte zwischen den Molekülen eines Lösungsmittels und denen einer gelösten Substanz kleiner als die zwischen den Molekülen des Lösungsmittels, dann werden sich nach dem Gibbschen Satz die Moleküle der gelösten Substanz an der Oberfläche des Lösungsmittels ansammeln. Da dafür eine kleinere Arbeit nötig ist, als für die Moleküle des Lösungsmittels, wird die Oberflächenspannung des Lösungsmittels verkleinert. Stoffgruppen dieses Verhaltens sind Kohlenwasserstoffe mit langen Ketten und einem polaren Ende. Sie heissen kapillaraktive Substanzen. Der Gibbsche Satz lässt durch Messung der Änderung der Oberflächenspannung in Abhängigkeit der Konzentration die Substanzmenge feststellen. Langmuir [13] konstruierte für solche Messungen die nach ihm benannte Waage. Eines der damit gewonnenen Ergebnisse ergab, dass alle paraffinischen Stoffe mit gestreckten Kohlenwasserstoffketten pro Molekül und unabhängig von der Länge einen Platzbedarf von 0,2 nm^2 benötigen. Daraus folgt, dass bei einer Schicht dichtester Packung alle Moleküle parallel zueinander und senkrecht auf der Oberfläche des Lösungsmittels stehen müssen. Die Kraft zwischen dem hydrophilen Ende der Kette und den Oberflächenmolekülen des Lösungsmittels ist kleiner als die Bindung der Moleküle des Lösungsmittels zueinander.

Wird eine solche organische monomolekulare Schicht in das Lösungsmittel Wasser gedrückt, dann faltet sie sich zu einer bimolekularen Schicht, in der ihre hydrophoben Enden gegeneinander und die hydrophilen Enden wieder nach dem Lösungsmittel gerichtet sind. An solchen Schichten wurde übrigens von Langmuir und Blodgett Reflexionsverminderung beobachtet.

Eine Faltung von Phospholipidmolekülen mit ihren amphipolaren Eigenschaften zeigt Abb. 15. Die so künstlich hergestellte Doppelschicht hat eine Ähnlichkeit mit den Membranen biologischer Zellen [14].

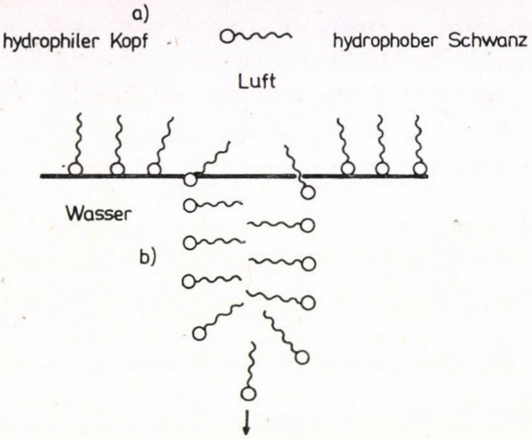

Abb. 15. Phospholipidmolekül (a) und Bildung einer Phospholipidmembran (b) nach M. Höfer

Unter einer solchen Zelle versteht man einen Bereich aus kernhaltigem Zytoplasma, der durch eine ihn umhüllende Membran gegenüber der Umgebung abgegrenzt ist. Innerhalb dieses Bereiches liegt bei den meisten Zellarten der Zellkern und verschiedene Organellen, die wieder von Membranen umgeben sind. Ihre Dicke ist ~ 10 nm. Sie gehören demnach gemäss der gemachten Definition zu den dünnen Schichten.

Die Zelle ist der Elementarorganismus des Lebens und die Zentrale der Energiekonversion über die Photosynthese. Durch ihre Membranen erfolgt der Stoffaustausch zwischen der Umgebung und dem Inneren der Zelle über verschiedenartige Wege.

Der Bau einer Einheitsmembran ist in Abb. 16 sehr schematisch dargestellt [15]. Die hydrophilen Köpfe der Moleküle der bimolekularen Lipidschicht sind nach aussen orientiert. Sie werden auf beiden Seiten mit unterschiedlichen Proteinschichten bedeckt. Ausserdem, nicht in der Abbildung eingezeichnet, durchdringen Poren die Membran und Proteinmoleküle mit ihren hydrophilen Enden durchstossen die Lipidschichten oder sie sind mit den hydrophoben Enden in diese eingebaut.

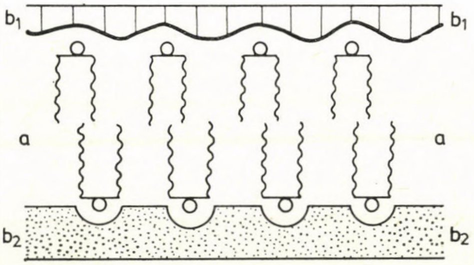

Abb. 16. Modell der Einheitsmembran mit bimolekularer Lipidschicht (a) bedeckt mit assymmetrischen Proteinschichten (b_1) und (b_2)

Die tierischen und pflanzlichen Zellen enthalten ein Röhrensystem, dessen Wandungen aus Einheitsmembranen bestehen und die Zellmembran mit der Kernmembran verbinden. Dieses endoplasmatische Retikulum genannte System erfüllt Aufgaben des Stoffwechsels.

Der Feinbau der Mitochondrien, ein meistens langgestrecktes Zellorganell mit einer Länge von 10^3 nm und einem Durchmesser von 10^2 nm ist relativ gut bekannt. Abbildung 17 [16] zeigt, wieder sehr schematisch, ihren Aufbau. Von den zwei Membransystemen hat die innere Membran Falten und röhrenförmige Gebilde. Sie besteht aus hydratisierten Protein- und fettartigen Lipoidschichten. Die Mitochondrien sind die Träger der Atmungsfermente. Durch Oxydation der Nährstoffe wird Energie gewonnen, die hauptsächlich für die Synthese von Adenosintriphosphat, einer beim Stoffwechsel und der Photosynthese besonders wichtigen Substanz, verwendet wird. Ihr grosser Anteil an der Zellmasse bis zu 25% lässt ihre Bedeutung für die Existenz der Zelle ahnen.

Ein anderes Zellorganell ist der Golgi-Apparat. Erbesteht aus übereinander geschichteten flachen, wieder mit Membranen umhüllten Räumen. Sie dienen dazu, Stoffe, die im zytoplasmatischen Raum durch eine Überproduktion schädlich werden, aufzunehmen, zu isolieren und aus der Zelle zu entfernen (Abb. 18).

Die kaum fassbare Bedeutung der biologischen Membranen und ihre Funktionen sollte mit dieser kurzen und fragmentarischen Darstellung gezeigt werden.

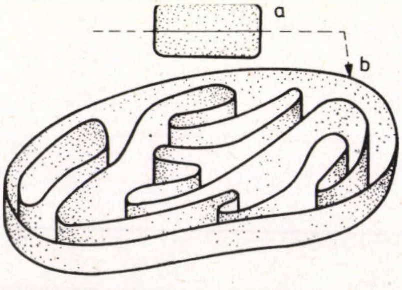

Abb. 17. Mitochondrium (a) und das Schnittbild (b) mit schematisch gezeichneter Doppelmembran (nach J. PFEIFFER [15])

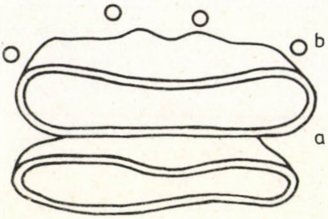

Abb. 18. Schematischer Schnitt durch den Golgi-Apparat mit Golgi-Zisterne (a) und Golgi-Vesikel (b) (Nach G. VOGEL und H. ANGERMANN)

Beim Stofftransport durch die Zellmembran werden Moleküle einer Substanz von einem Kompartiment in ein anderes übergeführt. Dabei kann Energie aus dem Stoffwechsel benötigt werden. Der Vorgang heisst dann aktiver Transport im Gegensatz zum spontan ablaufenden, dem passiven Transport.

Die Diffusion durch die Membran ist *eine* Art des Stofftransports. Da die Membran wegen ihrer bimolekularen Lipidstruktur für hydrophile Substanzen, also auch für das lebenswichtige Wasser, eine Barriere bildet, wird angenommen, dass sich in der Membran Poren befinden, die sich für einen gesteuerten Durchgang von Wassermolekülen und seinen Ionen eignen.

Ausserdem wird neben den oft durch katalytische Reaktionen bedingten Vorgängen ein Stofftransport durch Trägermoleküle angenommen. Diese mit Carrier bezeichneten Proteinmoleküle, sind bereits erwähnt worden. Sie durchdringen die Lipoidschicht und ermöglichen über eine Komplexbildung mit den zu transportierenden Substanzen auf noch nicht geklärte Weise den Stoffübergang.

Um ihre Funktionen erfüllen zu können, sind die Nervenzellen, im Gegensatz zu nahezu allen in grober Näherung kugelförmigen Körperzellen, stark verästelt. Sie können deshalb aus grösseren Bezirken aufgenommene Impulse an die operativen Stellen weiterleiten. Dabei aber wird gegenüber anderen Zellen mehr Energie verbraucht, die nur durch erhöhten Stoffwechsel über die extrem grossflächige Membran geliefert werden kann.

Auch Muskelzellen haben infolge ihrer langgestreckten Form grosse Membranoberflächen. Für ihre durch Nervenimpulse ausgelösten raschen und starken Formänderungen wird erhöht Energie benötigt. Sie wird wieder über den Stofftransport durch die vergrösserte Membran zugeführt.

Es wurde bereits auf die fundamentale Bedeutung der biologischen Zellen grüner Pflanzen als Zentralen der Energiekonversion über die Photosynthese hingewiesen.

Die Chloroplasten (Abb. 19) sind Zellorganellen, die frei im Zellplasma existieren und ein pigmentbesetztes Membransystem enthalten, das Thylakoid. In ihm sitzen die Grana in Stapelform, wieder ein System aus Protein- und Lipoidschichten. In die Lipoidschicht sind die für die Photosynthese wirksamen Pigmente aus Chlorophyll und Cartinoid eingebaut [17]. An ihnen erfolgt über die Einstrahlung der Sonnenenergie die sehr komplexe Reaktion

$$6\ CO_2 + 6\ H_2O + h\nu \rightarrow C_6H_{12}O_6 + 6\ O_2,$$

also die Bildung von Zucker und freiem Sauerstoff. Über eine weitere Reaktionskette wird Zucker in Eiweiss, Stärke und Cellulose, die Nahrung der Tiere und Bakterien, übergeführt.

Die Leistung der Photosynthese ist immens. Im Jahr werden von ihr $1{,}7 \cdot 10^{11}$ Tonnen Trockensubstanz mit einem Energieinhalt von $3 \cdot 10^{21}$ Joule gebildet.

Die so gewonnene Energie wird von der Natur fast ausschliesslich zum erneuten Aufbau von Pflanzen genützt. Es wäre deshalb interessant, die Reaktionskette der Photosynthese dort abzubrechen, wo die Energie, statt zum Aufbau der Pflanzen, zur freien Verfügung des Menschen gewonnen werden könnte. Diese Aufgabenstellung ist heute eine der grossartigsten der Forschung. Sie wird in vielen Instituten intensiv bearbeitet [18].

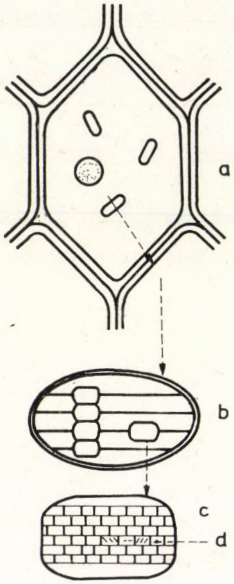

Abb. 19. Photosynthese
Pflanzenzelle mit Chloroplasten (a) Stromalamelle (b) und Grana mit Lipoidschichten (c) in die Chlorophyll und Carotinoid (d) eingelagert sind.
(nach G. Vogel und H. Angermann)

Ein anderer Weg wird von Kuhn und seinen Mitarbeitern [19] als mögliche Lösung vorgeschlagen und bereits in grossartigen experimentellen Teilschritten verfolgt. Für die Überlassung von auch nicht veröffentlichten Manuskripten sei Prof. Kuhn gedankt.

Sie versuchen, den Prozess der Energiekonversion der Sonnenenergie in chemische Energie so nachzuahmen, dass mit künstlich erzeugten dünnen Schichten der Vorgang der Dissoziation des Wassers durch eingestrahlte Lichtquanten erzielt wird und so freier Wasserstoff gewonnen werden kann. Dazu muss man das Grundprinzip des Elektronenkreislaufes, wie er in der Pflanze staffindet, an solchen künstlichen Membranen realisieren. Die dünnen

Schichten selbst werden mit der gleichen Methode erzeugt, wie sie bereits bei der Herstellung einer bipolaren Lipidschicht beschrieben wurde. An ihrer Stelle werden Schichten aus dafür geeigneten Farbstoffmolekülen verwendet.

Sollte es auf dem einen oder anderen Weg gelingen, freien Wasserstoff zu gewinnen, dann wäre das Energieproblem für immer lösbar.

Dünne organische Schichten sind elegante Studienobjekte vielseitiger Art. Es war deshalb zu erwarten, dass die Chemie diese Art eines materiellen Zustandes für die Lösung reaktionskinetischer Probleme übernommen hat.

Die Methoden der Verdampfung und Zerstäubung von Metallen bei gleichzeitiger Kondensation einer organischen Substanz unter Hochvakuum und als dünne Schicht öffnen der Chemie Möglichkeiten zu neuartigen Synthesen.

Metallatome besonders der Übergangsmetalle haben im Festkörper eine starke Wechselwirkung. Die Energie des freien Metallatoms aber ist grösser. Deshalb ist zu erwarten, dass sein Einbau in eine anorganische oder organische Substanz als *isoliertes* Atom zu Reaktionen führt, die auch bei tiefen Temperaturen ablaufen. In den letzten Jahren haben solche Untersuchungen bei organischen Synthesen wesentliche Erfolge erbracht, so dass von einer neuen Chemie gesprochen wird.

Eine Zusammenfassung apparativer und experimenteller Ergebnisse anlässlich eines 1974 stattgefundenen Symposiums geben einen ersten Überblick [20].

Wie bereits beschrieben, entsteht nahezu vollständig der freie Sauerstoff als Folgeprodukt der Photosynthese, wobei wie erwähnt Laubbäume und besonders die Algen Hauptproduzenten sind. Der Verbrauch an Sauerstoff wird durch die Verbrennung der fossilen Vorräte so gesteigert, dass in entwickelten Ländern die Sauerstoffbilanz negativ geworden ist. Die Zerstörung der Regenwälder der tropischen Zonen durch Raubbau und Zersiedlung wird in unverantwortlicher Weise gesteigert.

Dünne organische Schichten z. B. aus Ölen haben die Eigenheit, wegen der meist geringen Löslichkeit und kleinen Oberflächenspannung gegenüber Wasser, Gewässer mit einer dünnen Schicht, die einmolekular sein kann, zu bedecken. Dies ist meistens in Küstennähe des Meeres der Fall. Damit wird der in einem Gleichgewicht stehende Stoffaustausch zwischen Algen, Wasser und Atmosphäre belastet. Dies aber führt zu einer Gefährdung der Meeresflora und Fauna mit all den vorausschaubaren Negativeffekten. Was die Natur mit einer Vielfalt von dünnen Schichten zu lebenstragenden Systemen entwickelte, zerstört der Mensch wieder durch von ihm verursachte dünne Schichten. So erwächst für Biologen, Chemiker, Physiker und Ingenieure die Aufgabe, auf die für den nicht Fachorientierten schwierig überschaubaren Gefahren aufmerksam zu machen und selbst mitzuwirken, ihnen zu begegnen.

LITERATUR

1. G. A. Somorjai, Science, **201**, Nr. 4355, 489, 1978.
   F. Garcia—Moliner, Surface Science, Vol. 1, IAEA—SMR Wien, 3, 1975.
   S. Anderson, Surface Science, Vol. 1, IAEA—SMR Wien, 77, 1975.
2. I. Rentschler, Microscopica Acta, **82,** 47, 1979.
   I. Rentschler, Planta, **117,** 153, 1974.
   I. Rentschler, Cytobiologie, **3,** 172, 1971.
3. H. Moor, in Ergebnisse der Hochvakuumtechnik und der Physik dünner Schichten, herausgegeben von M. Auwärter, Wiss. Verlagsges. MbH. Stuttgart, 1971.
4. E. Porter, Knauers Tierreich in Farben, Vögel, Farbtafel 102.
5. L. Goetz, Knauers Tierreich in Farben, Vögel, Farbtafel 217.
6. O. Danesch, Silva-Verlag, Zürich, S. 11, 1968; O. Danesch, Silva-Verlag, Zürich, S. 10, 1968.
7. A. B. Klots, Knauers Tierreich in Farben, Insekten, Farbtafel 37.
8. R. Haefer, in Ergebnisse der Hochvakuumtechnik und der dünnen Schichten, herausgegeben von M. Auwärter, Wiss. Verlagsges. MbH. Stuttgart, S. 123, 1957.
9. P. W. Baumeister, in Sommerkurs über Moderne Methoden der Zeichnung optischer Kurven, The Institute of Optics, University of Rochester, 1963.
10. D. L. Fox, Animal Biochromes and Structural Colours, Cambridge University Press, Cambridge, 1953. (umfangreiches Literaturverzeichnis)
    C. G. Bernhard, G. Gemme and A. R. Møller, Quarterly Reviews of Biophysics, **1,** 89, 1968.
    H. Durrer und W. Villiger, Zsch. Zellforschung, **109**, 407, 1970.
    E. Rutschke, Zsch. Zellforschung, **73**, 432, 1966.
    W. J. Schmidt und H. Ruska, Zsch. Zellforschung, **57,** 1, 1962.
    S. Caveney, Proc. Roy. Soc. London, B. **178,** 205, 1971.
    E. J. Denton and M. F. Land, Proc. Roy. Soc. London, A. **178,** 43, 1970.
    A. C. Neville and S. Caveney, Biological Reviews, **44,** 531, 1969.
    W. Lippert und K. Gentil, Zsch. Morph. Okol. Tiere, **48,** 115, 1959.
    T. F. Anderson and A. G. Richards, J. Appl. Phys., **13,** 748, 1942.
    C. Mason, Phys. Chem. **30,** 383, 1926; **31,** 321, 1927; **31,** 1856, 1927.
11. Michael F. Land, Scientific American, **239,** Nr. 6, 88, 1978.
    M. F. Land, Progress in Biophysics and Molecular Biology, **33,** 77, 1972.
    M. F. Land, J. Exp. Biol., **45,** 433, 1966; J. Physiol., **197,** 138, 1965.
12. Agnes Pockels, Nature, 439, 1891.
13. I. Langmuir, J. Amer. Chem. Soc., **39,** 1848, 1917.
14. M. Häfer, Verlag Chemie GmbH, Weinheim, 1977.
15. M. Häfer, ibid.
    J. Pfeiffer, Die lebende Zelle, Verlag RoRoRo, 1977.
    A. L. Lehninger, Biogenetik, Georg Thieme Verlag, Stuttgart, 1974.
    G. Vogel und H. Angermann, Atlas zur Biologie, Band **1,** 1967, Band **2,** 1968, Deutscher Taschenbuch Verlag GmbH und Co. KG, München, 1967.
    A. G. Lee, Endeavour, **34,** 67, 1975.
    H. U. Schulze und H. Staudinger, Naturwissenschaften, **62,** 331, 1975.
    E. Bamberg, R. Benz, P. Länger und G. Stark, Chemie in unserer Zeit, **8,** Nr. 2, 1974.
16. G. Vogel und H. Angermann, Atlas zur Biologie, Band **1,** 17, 1967.
17. L. Lehninger, Biogenetik, Kapitel: Photosynthesen und Chloroplast, S. 106—129, Georg Thieme Verlag, Stuttgart, 1974. G. Vogel und H. Angermann, Atlas zur Biologie 2. Deutscher Taschenbuchverlag GmbH, Co. KG. München, 1968.
18. P. Böger, Naturwissenschaften, **65,** 407, 1978.
19. H. Kuhn, Journal of Photochemistry, **10,** 111, 1979.
    D. Möbius, Berichte der Bunsengesellschaft für Physikalische Chemie, **82,** 848, 1978.
    E. E. Polymeropoulos, D. Möbius and H. Kuhn, J. Chem. Phys., **68,** 3918, 1978.
20. New Synthetic Methods Vol. 3, Herausgeber: H. W. Kohlschütter und Mitarbeiter, Verlag Chemie GmbH, Weinheim, 1975.

Acta Physica Academiae Scientiarum Hungaricae, Tomus 49 (1—3), pp, 23—38 (1980)

METASTABLE STATES IN GASES WITH LIVES OVER 24 HOURS

By

DJ. A. BOŠAN, M. M. PEJOVIĆ

FACULTY OF ELECTRONIC ENGINEERING, NIŠ, YUGOSLAVIA

and

M. V. VUJOVIĆ

BORIS KIDRICH INSTITUTE OF NUCLEAR SCIENCES, BEOGRAD, YUGOSLAVIA

These investigations were conducted in order to study the behaviour and lifetime of metastables in various vapours and gases including noble gases as well as H_2 and N_2. Metastables were detected by time delay measurements of electrical breakdown in gases (this being caused by secondary emission from the deexcitation of metastables at the cathode.) It was confirmed that metastable states at pressures smaller than 1 bar deexcite exponentially with a half-life of 50 min and under certain conditions even an order of magnitude longer. The decrease of lifetime with the increase of pressure was also confirmed. A sharp dependence of the concentration of metastables on electrode temperatures was discovered. Transport phenomena of metastables through several meter long glass tubes were observed as well as deexcitation by illumination. New data were obtained on the dependence of breakdown time delays and correspondingly on concentrations of metastables on the type and pressure of the gas filling, shapes and materials of electrodes, overvoltages, gas flow rates, temperatures, etc.

1. Introduction

Atoms and molecules may pass, by means of absorption of energy, into two kinds of excited states:

— excited states, in the narrower sense, from which they decay to lower energy states by electric dipole radiation (further referred to as excited states) and

— metastable states from which selection rules forbid electric dipole transitions (further referred to as metastables). Metastables may deexcite electromagnetically via mechanisms to which these selection rules do not apply, such as electric quadrupole or magnetic dipole radiation.

However, these radiative deexcitations are far less probable than the electric dipole ones. Such deexcitations take place theoretically in an absolute vacuum and practically under cosmic space conditions. Under real earthly conditions deexcitations are mostly done by other mechanisms.

Metastables deexcite nonradiatively in collisions with electrons, atoms and molecules in a gas or in collisions with solids such as vessel walls or electrodes. These deexcitations are far more probable and take place under normal experimental conditions.

Taking into account phenomena studied in this paper the most important metastable deexcitation mechanism is the secondary emission of cathode electrons.

2. Metastable life in gases according to literature

Lifetimes of excited states of atoms decaying via electric dipole radiation are according to DELCROIX and his coworkers [1] in the range from 10^{-10} to 10^{-2} s.

Metastables have a longer radiative life which, according to literature, mostly has values between 10^{-4} and 10^{5} s. SMIRNOV [2] cites the data on considerably longer lifetimes. ALLEN [3] gives a characteristic example of a long lifetime of hydrogen metastables which is $3.5 \cdot 10^{14}$ s. This is the well-known 21 cm radiation in radioastronomy.

Conclusions on the metastable state lifetimes in this paper are based on measurements of collective effects related to electric breakdown in gases in the period after the current through the gas is switched off (afterglow period). Measured were time spans after which the gas in a diode completely returns to the stationary state defined by the temperature and the intensities of light, radioactive, cosmic and other radiations. That is the period of time for which the recombination of ions and deexcitation of excited and metastable states take place up to the degree when they cannot considerably influence the breakdown and other macroscopic electrical characteristics of a gas. In this paper this is referred to as the "total recovery time" τ_r.

The total gas recovery time τ_r after the breakdown has been investigated extensively under various conditions and the obtained values were, as a rule, between 10^{-10} and 1 s.

MCCANN and CLARK [4] find that after the breakdown at large gaps in air τ_r is about 14 ms. STRIGEL [5], HAGENGUTH [6, 7] and many other investigators who, because of the fundamental character of this problem for electroenergetics, did investigations for the largest world companies of electrical engineering, obtain results of the same order of magnitude. From the BUTKEVICH's monography [8] it can be seen that after breakdown in power lines up to 500 kV deionization times were measured to be below 1 s. After POLAK [9], MALKIN [10] and others the measured times τ_r in plasma physics were also far below 1 s and are mostly between 10^{-6} and 10^{-3} s.

Similar results were obtained in investigations of the a. c. electric arc (SISOJAN, [11]), and also of various afterglow phenomena [12] and other specific investigations carried out by BOUCIQUÉ and his coworkers [13], HERTZ [14], JABLONSKIJ and JANKIN [15], etc.

In the same range were also the τ_r values obtained in measurements of eletric charcteristics of gas filled electron tubes described by KAGANOV [16],

Philips Data Handbook [17, 18], **Fogeljson** and coworkers [19], **Knoll** and **Eichmeier** [20], **Brandt** and **Tihomirov** [21], etc.

The longest total recovery times were obtained by the method of time delay measurement of electrical breakdown in gases. Prior to the experiments described in this paper the obtained values of τ_r were less than 10 min. (**Büge**, [22]). The same method, improved and used by **Bošan** and coworkers ([23] etc.) showed that $\tau_r > 24$ h.

3. Time delay of electrical breakdown in gases

Electrical breakdown in gases does not take place instantly upon applying a definitive voltage to the electrode, but after a corresponding delay. The first investigations in this field were reported by **Jaumann** in 1895 [24] and **Warburg** in 1896 and 1897 [25, 26]. The first measurements were carried out so that there was only one measurement of time delay of electrical breakdown in a gas (t_d) under definite conditions. Thus, nothing could be observed concerning the stochastic characteristics of the phenomenon. A clear picture of this phenomenon was given by **Zuber** in 1925 [27] showing that t_d values are subjected to statistical fluctuations and have a definite distribution. Very detailed investigations of these phenomena were done by **Strigel** [5, 28], **Hagenguth** [6, 7] and many other authors because of the importance of this problem in electroenergetics. In 1949 **Wijsman** [29] published a detailed analysis of the breakdown probabilities in gases. Many authors dealing with the problems of breakdown time delays referred to this paper. An extensive paper with modern electronic data handling was published by **Tagashira** and **Sakamoto** in 1969 [30]. A detailed survey of this problem with the latest results of investigations from the point of view of connection of these phenomena with metastables was given by **Bošan** in 1975 [23] and the latest situation is included in the monography by **Meek** and **Craggs** [31].

From the cited literature it can be seen that the problem of electrical breakdown time delays in gases was mostly treated under conditions when the value of t_d was between 10^{-6} and 1 s. This time may, of course, have much larger values. The time t_d, under other given conditions, despends on the voltage applied to diode U_w. When the voltage U_w in decreasing tends to the static breakdown voltage U_s, the t_d values tend to infinity. **Llewellyn-Jones** [32] gives a theoretical analysis of time delays in hydrogen with $U_s = 350$ V. In the case when U_w is only 0,1 V that is 0,03 % smaller than U_s, one obtains $t_d = 10^{300}$ s, having no practical significance. However, from this, one can see that the static breakdown voltage is very sharply defined owing to the knowledge of breakdown probability and delay processes.

4. Conditions under which time delays of electrical breakdown t_d were measured

As already mentioned, the values of t_d can have large fluctuations. However, the mean values of data obtained by measurements under identical conditions depend on various experimental parameters, but before all on the overvoltage $\left(\frac{U_w-U_s}{U_s}\cdot 100\%\right)$. The smaller the t_d value, the more important it is to have its exact definition. On the other hand for large t_d the measurement problem is simpler, so that with the increase of t_d values the need of a precise definition disappears. According to the definition given by TAMM [28] the time delay of the electrical breakdown is the time elapsed from the moment when the applied voltage reaches the value of static breakdown voltage, to the moment when it starts to decrease due to the breakdown across the diode.

Regarding that longer time delays, such as those between 10^{-2} and 10^3 s, were investigated by the authors of this paper, the definition for practical reasons would be [23]: t_d is the time which passes from the moment of applying an operating voltage U_w (where $U_w > U_s$) to the diode, up to the moment when the current across the diode reaches the value of 10 μA. Since the saturation value of the current across the diode is above 1 mA, this definition did not affect the exactness of the measurements.

As already known (PENNING, [33], MEEK and CRAGGS, [34] etc) the time delay t_d includes two parts:

— the first is the "statistical time delay" t_s or the delay of the initiation of the breakdown. That is the time which passes from the moment when voltage U_w is applied to the diode up to the beginning of the discharge development, i. e. up to the appearance of the electron which initiates the breakdown in the gas,

— the second is the "formative time" t_f. That is the time of the current increase from zero (more exactly from the values which are usually between 10^{-19} and 10^{-8} A) up to about 10 μA. Thus $t_d = t_s + t_f$.

The statistical time delay has a stochastic character, and as shown by LAUE [35], the values of t_s obtained in measurements meet the requirements of the following equation: $\log N_t/N_0 = -kt$, where N_t is the number of the measured time delays with values larger than t, N_0 is the total number of the measured values, t the obtained values of t_d, k is a constant.

Although LAUE's mathematical treatment of this problem had to be corrected to some extent so far, it has not lost its fundamental significance.

Part of the measurement data in this paper has been processed statistically and was in good agreement with classical LAUE's diagrams or "lauegrams" [23]. The latest processing aspects of these data are given in the mentioned MEEK—CRAGGS monography [31].

From each group of data obtained in measurements described here arithmetic mean values were used for further processing. Such a choice was made because it was shown that the same results were obtained as when the most probable or some other characteristic values are used from each data group.

The measurement conditions were always such that the time t_f was negligibly small with regard to t_s:

$$t_f \ll t_s;\ t_d \approx t_s\ .$$

Therefore from now on we shall mention only the t_d values.

The formative time is also of a stochastic character with a definite distribution. Since under operating conditions t_f was many orders of magnitude smaller than t_s, it was not necessary to consider it.

All investigations of electrical breakdown in gases, described in this paper, were carried out under conditions excluding the possibility of the appearance of thermoelectron, autoelectron (field-) and photoelectron emission.

All measurements of t_d values were done on electrodes at room temperature except one that was done on specially prepared electrodes. Analysing RICHARDSON—DUSHMAN's expression (DUSHMAN [36], SLIVKOV [37]) one can conclude that under operating conditions thermoelectron emission was practically excluded, and theoretically completely negligible.

Autoelectron emission, which is realized by tunnel-effect mechanism, occurs in strong electric fields which are not used here. Analysing the problem by Fowler-Nordheim's equation it can be concluded that autoelectron emission in these experiments could be disregarded (LOEB [38], STEENBECK [39], BRODSKIJ [40] etc).

To eliminate the photoelectron emission, tubes were protected from the light.

The tubes were also held far from the radiation sources of radiowaves of all frequencies, as well as from X-ray radiation.

From all said it comes out that in diodes, in which after long passive time metastable states disappeared, the appearance of electrons causing the breakdown might arise only under the action of environmental radioactive or cosmic radiation.

5. Survey of investigations

The described investigations originate from the research done by BOŠAN [23] in Electronics Industry (Elektronska industrija, former Zavodi RR), Nis (Yugoslavia) on the development of surge arresters. The investigations were done on diodes filled with He, Ne, Ar, Kr, Xe, H_2, N_2, Cl_2, Hg, water vapour and air as well as with many mixtures of the mentioned gases and vapours. The pressure range was between 1.3 mbar and 1.013 bar. Electrodes were made of Al, Fe, Cu, Mo, Ba, W, Au, Hg and Pb. The bulbs were made of glass or iron with corresponding insulators. Measurements were carried out with various sizes and shapes of electrodes and bulbs with different overvoltages, with d. c. and a. c. voltages at frequencies between 50 Hz and 15 kHz. In addition to measurement on diodes in darkness, some measurements were also done with diodes under various kinds of natural and artificial illumination or irradiation by radioactive sources. Investigated were also systems of diodes interconnected with glass or metal tubings, etc. Besides measurements with cold electrodes, some were also done with electrodes heated up to 673 K.

The diodes were hermetically sealed, however, measurements were done also with gases flowing through the diode at various rates in the mentioned pressure range.

Many t_d dependences on different parameters observed were such as:

- overvoltage;
- radiation of various kinds;
- voltage, frequency;
- electrode gap;
- pressure and gas flow rate;
- electrode material;
- "passive time" of diode τ (memory curve) and
- combination of these and other parameters.

These measurements were reported by Bošan [41, 42, 23, 43] and Bošan and Pejović [44, 45, 46, 47, 48]. Data on these investigations are cited because they are in a good agreement with the statement on the metastable state lifetime.

5.1. Memory curves

The most important results of these experiments include the "memory curves" of diodes. That is a functional dependence of the breakdown time delay t_d on the "passive time" τ of the diode. Cycles t_c of such measurements are shown in Fig. 1. One measurement of t_d is carried out during one cycle. As Fig. 1 shows each cycle consists of a "passive" and an "active" part.

A passive time τ is a constant period of time between two measurements during which diode voltage equals zero. An active time t_a is a period of time during which the diode is under voltage. It consists of two parts: the breakdown time delay t_d and the constant period t_i during which current i flows through the diode. Therefore:

$$t_c = \tau + t_a ,$$

$$t_a = t_d + t_i .$$

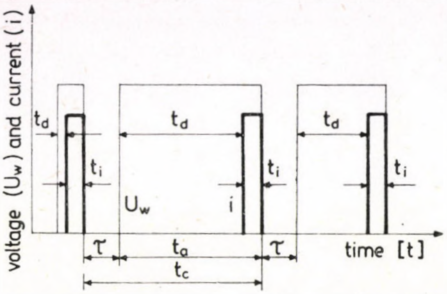

Fig. 1. Applied voltage (U_w) and diode current (i) versus time (t) diagram

In all measurements t_i was held at 1 s. This was sufficient to establish saturation concentrations of ions, excited states and metastables in the diode. The increase of t_i is irrelevant for the measurement results. As can be seen, times τ and t_i are constant in the cycle, and only time t_d varies because of the stochastic character of the phenomenon. In measuring the memory curves ($t_d = f(\tau)$), time τ had various and predetermined values, while all other conditions of measurement were the same. For each value of τ there have been made at least one hundred measurements of t_d and the corresponding arithmetic mean value has been found. Measurements were done according to the schematic diagram in Fig. 2.

A typical memory curve is given in Fig. 3, curve 1. Time τ had a value ranging from 3 s up to 7 days. As can be seen, breakdown delay depends largely on the period of time τ. The curve reaches saturation after a period which is certainly longer than 24 h. Clearly, the diode "memorizes" that there was a breakdown through it before the voltage is switched on.

As was shown by **Bošan** in 1956 [41] and later [23, 42—44] and by **Bošan** and **Pejović** [45, 46, 47, 48] such curves were obtained for all noble gases, as well as for H_2 and N_2.

Most of these curves were obtained with spherical iron electrodes, 1 cm in diameter and with an 1 to 5 mm electrode gap. Pressures were above the

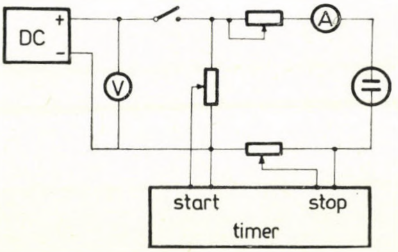

Fig. 2. Schematic diagram of measurements

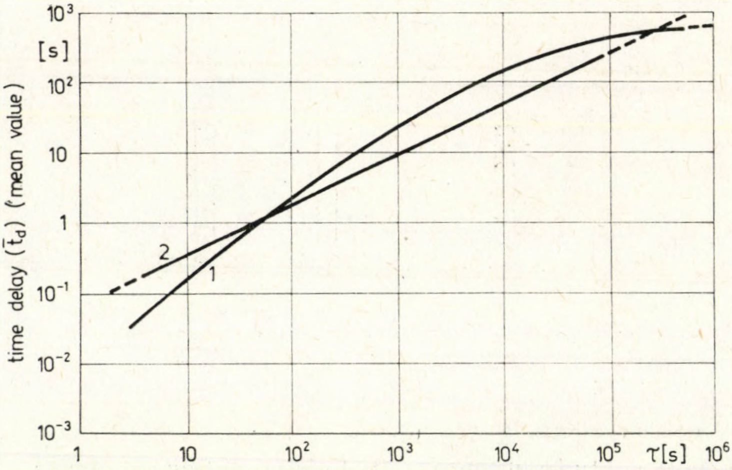

Fig. 3. Mean value of time delay ($\bar{t}_d$) as a function of passive time (τ)

values which correspond to the minima on Paschen's curves. A possible informal explanation of this phenomenon is the hypothesis on the presence of long-lived metastable states of atoms or molecules in the gas.

5.2 Check of the hypothesis on the long-lived metastable states

To obtain the final explanation of the prolonged diode "memory" it was necessary to establish whether the phenomenon was due to the gas, to bulb or to electrodes.

To answer the question whether the long diode memory was due to the bulb, two diodes were made differing only in bulb volumes the ratio of which was 1 : 40 (Bošan, [23]). The electrodes were of spherically shaped iron, 1 cm in diameter, 1.3 mm spaced. The tubes were nitrogen filled under 4 mbar pressure. Measured were memory curves on these two diodes and it was found that over the wide range of τ values time delays in the small diode were longer than in the big one. That points to the part metastables play in initiating the electrical breakdown.

The investigations done by Sadeghi and Pebay-Peyroula [49], and Martišovitš et al [50] showed the decrease of metastables concentration towards the vessel walls, i. e. their more intensive deexcitation on the walls than inside the gas. Since the larger tube has small bulb and electrode surface per unit gas volume, deexcitation will be smaller, metastable lifetime longer, and concentration higher. That means that one may expect a higher breakdown probability in the larger tube, that is, shorter time t_d, what was experimentally confirmed.

A further crucial confirmation that the cause of the long memory times originates from the gas, is obtained by measurement of t_d in the diode with gas streaming under various conditions (Bošan, [23, 43]). It was also shown that the cause of the breakdown, originating from the gas stream by electrical discharge or by heating the electrode, is transported through the gas and that it may be detected by measuring t_d values. As shown in our laboratory the initiators of the electrical breakdown in the described diode were transported by a very slow gas stream through the many meter long glass tubes. Such a phenomenon can be explained by the existence of the long-lived metastables.

The same conclusions on metastables result from the measurement of t_d on the diodes with controlled heating. Various polarities and combinations of voltages show that with the increase of temperature, due to the increase of metastable concentration, time delay decreases (Bošan [23, 43], Bošan and Pejović, [45]).

The most interesting results from this series of experiments were given by the following combination of conditions. Metastables, generated by the heated electrode, were transported by the gas stream to the diode where they were detected by the measurement of t_d. The action was cancelled illuminating the gas stream by certain light rays. That gives the possibility for an exact identification of the kind of metastable states.

In principle, it is possible to look for an explanation for the long memory in solid state phenomena supposing the phenomenon originates from the metal electrode, i. e. from the solid state properties of electrode material. To check such a supposition we made a mercury electrode diode (similar to mercury switches) filled with hydrogen under low pressure. The memory curve was measured in the range of τ from 5 up to 60 s (Bošan, [23]). In that range the curves did not show any tendency towards saturation, meaning that the liquid mercury electrode behaves identically to the solid metal electrode. It is interesting to mention that certain results of the breakdown delay measurements with mercury electrodes were obtained by Pedersen [51] in 1923.

We may also suppose a hypothesis that the described phenomena are due to the Paetow-Malter's effect. To check that supposition a diode was made with iron bulb in which the free surface of insulating parts was reduced to a minimum and placed far away from the discharge place. Iron electrodes were spherical.

Measurements of memory curves were done with H_2, N_2 and air, with and without gas flow at atmospheric pressure. In part of the measurements the bulb was at anode potential, and during the passive diode time there was a voltage between the cathode and the anode-bulb system which was slightly lower than the static breakdown voltage. Under all mentioned conditions the standard memory curves (Bošan, [23]) pointed out that the role of Paetow-Malter's effect was excluded.

Memory curves were also measured in a diode filled with water vapour in which the total pressure was equal to the pressure of the saturated water vapour at 20 °C. Measurements were made in the range of τ from 1 to 60 s and also under these conditions the diode showed typical memory phenomena differing only in t_d which was slightly shorter than in other gases.

In the chlorine streaming diode under atmospheric pressure t_d was measured for the case when $\tau = 5$ s. The t_d values were in the range of at least 1 : 10000 which is much higher than in other gases. Due to great difficulties in the work with chlorine, memory curve was not measured.

Pejović, Bošan and Stoiljković [48] investigated the electrode gap influence on the breakdown time delay in a diode with spherical iron electrodes. The diode was filled with nitrogen under 3 mbar pressure. Measurements showed that the curve has a maximum at a definite electrode gap.

The investigations done by Haydon, Folkard and Williams [61, 65, 70, 71, 72, etc] and Molnar [73, 74] showed a definite dependence of the mentioned secondary emission coefficient on the electrode gap. A comparison of our results with those cited in these papers is in progress.

The following conclusions can be drawn from the cited experiments:

1. The long diode memory is neither due to the electrode or bulb materials nor is a surface phenomenon related to them.
2. The electrode material has a definite quantitative influence on the t_d values in terms of the material work function, but does not influence the process quality.
3. Experiments with various gases under different conditions show that the memory is in the gas.
4. Experiments done on diodes with non-excited streaming gas, as well as in a flow of gas previously excited by an auxiliary heated electrode or electric discharge, show that the carriers of the memory in the gas are metastable states.
5. In the experiment in which the deexcitation of the metastable states by illumination was detected it was shown that the gas is the link between the whole complex of the described phenomena.
6. In these measurements the electrical breakdown time delay in gases (t_d) was used as a method of qualitative metastable states detection.

6. On the role of metastables in electrical breakdown in gases

Metastable states play an important role in the electrical breakdown of gases, in the case of the high time delay values. Engstrom and Huxford [52] showed that the diffusion of argon metastable atoms towards the cathode and the consecutive secondary electron emission is the source of breakdown at high t_d values. **Loeb** [38] considers their contribution to be an important pioneering investigation.

An analysis of the t_d value distribution faciliated the separation of the number of the secondary electrons released on the cathode by the positive ions and argon metastable atoms. It was shown that at relatively low pressures in breakdown mechanisms and Townsend discharges an important role is played by metastable atoms diffusing and ionizing the gas or impurities in it and releasing electrons from the cathode.

Newton [53] made an analysis of the transition phenomena of the breakdown in Townsend discharge. It was shown that electromagnetic radiation, ions and metastables, each on its own part, influence the second Townsend coefficient. On the curve of the discharge formation we can separate three phases, each with its own saturation value. The first part is initiated by the action of electrons and photons 10^{-8} s after the process started, the second part by the action af ions 10^{-6} s later, and the third part is caused by the action of the diffused metastables on the cathode 10^{-3} s after the process started.

The influence of the long-lived metastables on the operation of counters filled with argon or argon-CO_2 mixtures was studied by **Colli** and **Facchini** [54]. An analysis of the influence of metastables on the ionization precesses in nitrogen is given by **Haydon** and **Williams** [55] and other authors. As shown by various authors (**Haydon** [61], **Haydon** and **Williams** [62]) the secondary electron emission from the cathode caused by the impact of metastable molecules N_2 ($A^3\,\Sigma_u^+$) plays the most important role in the process of the molecular nitrogen ionization. As shown by **Janča** [63] the radiative lifetime of these states is 12 s.

Experiments have shown (**Razevig**, **Sokolova** [64], **Molnar** [73]) that the coefficient of the secondary emission from the cathode surface in an impact of the metastable atoms or molecules of some gases is close to or even larger than the coefficient of the secondary emission caused by the positive ion impact. Thus, for example, in argon filled diodes with tungsten electrodes the coefficient of the secondary emission for metastables is 0.023, and for positive ions 0.022. For argon filled diodes with molybdenum electrodes the corresponding coefficients for metastables and ions are 0.071 and 0.065, respectively [64].

Extensive investigations in the field of gas discharge associated with the secondary electron emission from the cathode are presented by **Haydon**, **Williams** and **Folkard** [61, 65, 66, 70, 71, 72]. These authors used copper and gold electrodes in hydrogen and nitrogen, as well as other arrangements. The papers also describe the fundamental role of molecules N_2 ($A^3\Sigma_u^+$).

As shown by **Borst** [67], at low energies in nitrogen, the states $A^3\Sigma_u^+$, $a^1\,\Pi_g$ and $E^3\Sigma_g^+$, with energies 6.12, 8.55 and 11.82 eV, respectively are important (Vidaud and Engel [75]). Molecules in these states are not able to ionize the gas, but can cause secondary electron emission from the cathode [61, 68]. The radiative lifetime of $a^1 \Pi_g$ state is $15 \cdot 10^{-6}$ s (Reits [69]).

As mentioned before the radiative lifetime of the nitrogen metastable state $A^3\Sigma_u^+$ is some ten seconds. The real life of those and other metastable states, because of the nonradiative deexcitation, should even be considerably shorter.

However, the investigations described in this paper suggest that either the data from the literature are not exact enough or that there are some other states with considerably longer lifetimes. Because of the character of investigations the question does not arise whether metastable states are transferred from one molecule to another, what is very likely, but is of no significance in this case.

7. Conclusion

It was definitely shown that measuring the electrical breakdown time delay metastable states in a gas filled diode may be detected more than 24 h after the interruption of the current in all previously mentioned gases.

The memory curves prove that the metastable concentration decreases in the diodes in exponential manner.

The metastable concentration in gases under favourable conditions may reach high values. Thus, for example, the metastable concentration of helium immediately after the discharge is stopped may reach the value of about 10^{13} cm^{-3} at total concentration of helium atoms of 10^{17} cm^{-3} and exceeds the electron concentration that is 10^{11} up to 10^{12} cm^{-3} (Smirnov [2]). Even higher metastable concentrations may be reached in nitrogen (10^{14} cm^{-3}).

As mentioned before, the most frequently used metastable detection method is the absorption of light of a definite wavelength. That is the method which can be used in high metastable concentrations. The light rays used for this purpose are obtained by interference filters. The metastable of He 2^3S is investigated by the 388.9 nm wavelength light, and He 2^1S by 501.6 nm, etc. According to Bolden et al [58] this is the way to determine metastable concentrations above $5 \cdot 10^6$ cm^{-3}.

In the case of smaller concentrations it is more effective to detect electrons produced by the secondary emission caused by metastable interaction with metal surface (Martišovitš and Košinar [56]). According to the latest data (Lancaster and Nygaard [57]) this method may be 10^8 times more sensitive than the optical methods.

In order to obtain tentative data on the half-lives of metastable states under the described conditions we made two suppositions:

Firstly, that at pressures between 1.3 and 40 mbar, the metastable concentration immediately after the interruption of the discharge in the diode is $N_0 = 10^{13}$ cm^{-3} (JANČA [63]).

Secondly, that by the measurement method of t_d it is possible to detect metastable states at a concentration $N = 10^4$ cm^{-3} (LUKASHEV and CHISTYAKOV [76]).

From the formula $N = N_0 \exp\left(-\frac{0.7\,t}{T}\right)$, for $t = 24$ h, the half-lifetime of the detected states T is about 50 min (BOŠAN and PEJOVIĆ [45]).

Even having these conclusions and data in mind the newly obtained memory curve is very surprising. That is curve 2 in Fig. 3. It refers to helium at 1.3 mbar pressure. As can be seen, the curve up to $\tau = 24$ h does not show a saturation tendency. This indicates the existence of at least one order of magnitude longer metastable lifetimes than in previous cases. Such a tendency was in principle expected from the papers published so far.

In nonradiative deexcitation mechanism the mean metastable lifetime depends also on the gas pressure. PIKE [59] measured the mean metastable lifetime $\bar{\tau}$ of neon and found that for the state $^3P_2$

$$\bar{\tau} = \frac{2 \cdot 10^{-3}}{P},$$

where P is the pressure.

MOY and coworkers [60] also published a paper on measurements with helium from which it can be seen that in the range from zero to about 40 mbar, the lifetime of the excited states decreases with the increase of pressure. Similar results were obtained by other authors, thus curve 2 (Fig. 3) is a confirmation of a similar trend on the new order of magnitude of metastable lifetime.

Metastable lifetimes are cited in many papers. However, very often they do not state explicitly which lifetime is in question: whether it is a radiative, nonradiative, mean or half-lifetime of an exponential destruction process (decay). In the literature the lifetime often refers to the period after which the metastable concentration decreases to the level below which detection cannot be done by the method applied. In those cases the plotted destruction curves cross the abscissa without indicating the exponential character of the process.

The reason that under the real experimental conditions, at pressures from 1 to 1000 mbar, long-lived metastable states have not been detected so far, probably lies in the insufficient sensitivity of methods applied. Owing to this it will be interesting to repeat some classical experiments in the light of the described results.

Acknowledgements

It is a pleasure for us to have the opportunity to express our deep gratitude to our friends and coworkers for their precious help in achieving these results:
— to Mr. DJ. KRMPOTIĆ (University of Belgrade, Faculty of Natural Sciences) whose analyses and advice have stimulated the investigations for more than two decades;
— to Mr. M. M. POPOVIĆ and Mr. S. S. POPOVIĆ (Institute of Physics, Belgrade) for the inspiring advice and help in the most critical phases of the electronic tubes development;
— to Mr. B. DIMITRIJEVIĆ (Faculty of Electronic Engineering, Niš) for the help in designing and working out of the electronic equipment;
— to Mr. T. STOJKOVIĆ, Miss M. LUKIĆ and Mr. V. STEFANOVIĆ (Electronics Industry, Niš) for the help rendered for many decades, in the production of equipment, performance of experiments and data processing.

These investigations were in part supported by the Research Council of Serbia.

REFERENCES

1. J. L. DELCROIX, C. M. FERREIRA and A. RICARD, Proc. 11th Int. Conf. on Phenomena in Ionized Gases, Prague, Sept. 1973 Invited Papers, p. 301, Ed. L. Pekárek, L. Láska, Ceskoslovenska Akad. Ved. Ustav. Fiz.
2. B. M. SMIRNOV, Ioni i vozbuždennie atomi v plazme, Atomizdat, Moskva, 1974.
3. C. W. ALLEN, Astrophysical Quantities, Univ. of London, The Athlone Press, 1973.
4. G. D. MCCANN and J. J. CLARK, Trans. of the Amer. Inst. of E. E., **62**, 45, 1943.
5. R. STRIGEL, Elektrische Stossfestigkeit, Springer, Berlin, 1939.
6. J. H. HAGENGUTH, Trans. Amer. Inst. E. E., **56**, 67, 1937.
7. J. H. HAGENGUTH, Trans. Amer. Inst. E. E., **60**, 803, 1941.
8. G. V. BUTKEVICH, Dugovie processi pri kommutacii elektriceskih cepej, Energija, Moskva, 1973.
9. L. S. POLAK, Ocerki fiziki i himii nizkotemperaturnoj plazmi, Nauka, Moskva, 1971.
10. O. A. MALKIN, Impulsnij tok i relaksacija v gaze, Atomizdat, Moskva, 1974.
11. G. A. SISOJAN, Elektriceskaja duga v elektriceskoj peci, Metalurgija, Moskva, 1974.
12. Various authors, Proc. 9th Int. Conf. on Phenomena in Ionized Gases, Bucharest, Sept. 1969. Contributed papers, No: 14, 15, 16, 17 and 19. Ed. G. Musa, I. Ghica et al, Editura Acad.
13. R. BOUCIQUÉ, W. BRUYNOOGHE and P. MORTIER, Proc. 9th Int. Conf. on Phenomena in Ionized Gases, Bucharest, Sept. 1969. Contributed papers, p. 264, Ed. G. Musa, I. Ghica et al, Editura Acad.
14. W. HERTZ, Proc. 9th Int. Conf. on Phenomena in Ionized Gases, Bucharest, Sept. 1969. Contributed papers, p. 296, Ed. G. Musa, I. Ghica et al, Editura Acad.
15. F. M. JABLONSKIJ and G. M. JANKIN, Dekatroni, Energija, Moskva, 1967.
16. I. L. KAGANOV, Ionnie pribori, Energija, Moskva, 1972.
17. Philips Data Handbook, Electron tubes, Part 7, Gas-filled tubes, Febr. 1974 and Aug. 1975.
18. Philips Data Handbook, Electron tubes, Geiger-Mueller Tubes, Part 6, July 1975.
19. T. B. FOGELJSON, L. N. BREUSOVA and L. N. VAGIN, Impulsnie vodorodnie tiratroni, Sovjetskoe radio, Moskva, 1974.
20. M. KNOLL and J. EICHMEIER, Technische Elektronik, B. II, Stromsteuernde und elektronenoptische Entladungsgeräte, Springer, 1966.
21. A. A. BRANDT and JU. V. TIHOMIROV, Plazmennie umnožiteli častoti, Nauka, Moskva, 1974.
22. M. BÜGE, Archiv für Elektrotechnik, **19**, 480, 1928.
23. DJ. A. BOŠAN, Investigation of Physical Phenomena during an Electrical Breakdown in Gases in Metal Electrode Tubes, Doctoral Thesis, University of Belgrade, Faculty of Natural Sciences, Beograd, Yugoslavia, (in Serbo-croat), 1975/1976.
24. G. JAUMANN, Ann. Chem. Phys., (Wiedemann'sche Annalen), **55**, 656, 1895.
25. E. WARBURG, Ann. Chem. Phys. (Wiedemann'sche Annalen), **59**, 9, 1, 1896.
26. E. WARBURG, Ann. Chem. Phys. (Wiedemann'sche Annalen), **62**, 11, 385, 1897.
27. K. ZUBER, Ann d. Phys., **76**, 231, 1925.
28. R. STRIGEL, Wissenschaftliche Veröffentlichungen aus den Siemens Werken, **11**, 2, 52, 1932.
29. R. A. WIJSMAN, Phys. Rev., **75**, 833, 1949.
30. H. TAGASHIRA and S. SAKAMOTO, J. Phys. D: Appl. Phys., **2**, 1193, 1969.

31. J. M. Meek and J. D. Craggs, Electrical Breakdown of Gases, John Wiley, 1978.
32. F. Llewellyn-Jones, Ionization Avalanches and Breakdown, Chapman and Hall, Methuen and Co., 1967.
33. F. M. Penning, Electrical Discharges in Gases, Philips' Technical Library, 1957.
34. J. M. Meek and J. D. Craggs, Electrical Breakdown of Gases, Clarendon Press, 1953.
35. M. von Laue, Annalen der Physik, **76**, 261, 1925.
36. S. Dushman, Scientific Foundations of Vacuum Technique, John Wiley, New York, 1949.
37. I. N. Slivkov, V. I. Mihailov, N. I. Sidorov and A. I. Nastjuha, Električeskij proboj i razrjad v vakuume, Atomizdat, Moskva, 1966.
38. L. B. Loeb, Basic Processes of Gaseous Electronics, Univ. of California Press, Berkeley, 1961.
39. M. Steenbeck, Wissenschaftliche Veröffentlichungen aus den Siemens Werken, **8**, 3, 94, 1930.
40. A. M. Brodskij and Ju. Ja. Gurević, Teorija elektronnoj emisii iz metallov, Nauka, Moskva 1973.
41. Dj. A. Bošan, Development of Surge Arresters, Technical report, Zavodi RR, Niš, Yugoslavia, No. TD—PO 2, (in Serbo-croat), 1956.
42. Dj. A. Bošan, 1st Symp. on Phys. of Ionized Gases, Beograd, Yugoslavia, (in Serbo-croat), 1962.
43. Dj. A. Bošan, Proc. 5th Int. Conf. on Gas Discharges, Liverpool, Sept. 1978, IEE Conference Publication Number 165, p. 273.
44. Dj. A. Bošan and M. M. Pejović, Proc. 14th Yugoslav Symp. on Electronic Components and Materials, Ljubljana, Yugoslavia, Oct. 1978, (Zbornik referatov simpzija o elektronskih sastavnih delih in materialih — SD 78), Publ: Elektrotehniska zveza Slovenije, Ljubljana, Yugoslavia, p. 147.
45. Dj. A. Bošan and M. M. Pejović, J. Phys. D: Appl. Phys., **12**, 1699, 1979.
46. M.M. Pejović and Dj. A. Bošan, 23rd Yugoslav Conf. for Electronics, Telecommunication, Automatics and Nuclear Engineering, Maribor, Yugoslavia, (in Serbo-croat), p. I. 403, 1979.
47. M. M. Pejović, Dj. A. Bošan and Dj. M. Krmpotić, Beiträge aus der Plasmaphysik, Vol. 21. No. 1.
48. M. M. Pejović, Dj. A. Bošan and B. Stoiljkovic, Elektrotechnika (Beograd), No. 2, p. 260, 1980.
49. N. Sadeghi and J. C. Pebay-Peyroula, Proc. 11th Int. Conf. on Phenomena in Ionized Gases, Prague, Sept. 1973, Contributed papers, p. 65, Ed. I. Stoll, J. Datlov et al., Ceskoslovenska Akad. Ved. Ustav. Fiz.
50. V. Martišovitš, I. Košinar, P. Tarábek and Š. Veis, Proc. 12th Int. Conf. on Phenomena in Ionized Gases, Eindhoven, 1976, Contributed papers, p. 59, Ed. J. G. A. Hölscher, D. C. Schram, North-Holland Publ. Comp. Amsterdam, 1976.
51. P. O. Pedersen, Ann. d. Phys., **71**, 317, 1923.
52. R. W. Engstrom and W. S. Huxford, Phys. Rev., **58**, 67, 1940.
53. R. R. Newton, Phys. Rev., **73**, 6, 1948.
54. L. Colli and U. Facchini, Phys. Rev., **88**, 987, 1952.
55. S. C. Haydon and O. M. Williams, Proc. 12th Int. Conf. on Phenomena in Ionized Gases, Eindhoven 1976, Contributed papers p. 43, Ed. J. G. A. Hölscher, D. C. Schram, North Holland Publ. Comp. Amsterdam, 1976.
56. V. Martišovitš and I. Košinár, Proc. 11th Int. Conf. on Phenomena in Ionized Gases, Prague, Sept. 1973, Contributed papers, p. 485, Ed. I. Stoll, J. Datlov et al., Ceskoslovenska Akad Ved. Ustav Fiz.
57. B. M. Lancaster and K. J. Nygaard, Proc. 12th Int. Conf. on Phenomena in Ionized Gases, Eindhoven, 1976, Contributed papers, p. 91, Ed. J. G. A. Hölscher, D. C. Schram, North Holland Publ. Comp. Amsterdam 1976.
58. R. C. Bolden, R. S. Hemsworth, M. J. Shaw and N. D. Twiddy, Proc. 9th Int. Conf. on Phenomena in Ionized Gases, Bucharest, Sept. 1969 Contributed papers, p. 27, Ed. G. Musa, I. Ghica et al, Editura Acad.
59. E. W. Pike, Phys. Rev., **49**, 513, 1936.
60. J. P. Moy, J. C. Gauthier and J. P. Geindre, Proc. 12th Int. Conf. on Phenomena in Ionized Gases, Eindhoven 1976, Contributed papers, p. 16, Ed. J. G. A. Hölscher, D. C. Schram, North Holland Publ. Comp. Amsterdam, 1976.
61. S. C. Haydon, Proc. US-Japan Seminar on Gas Breakdown and its Fundamental Processes (Japan), 95, 1972.
62. S. C. Haydon and O. M. Williams, J. Phys. D: Appl. Phys., **9**, 523, 1975.
63. J. Janča, Scr. Fac. Sci. Nat. UJEP Brunensis Physica, **2**, 75, 1972.

64. D. V. Razevig and M. V. Sokolova, Rasčot nacalnih i razrjadnih napraženij gazovih promežutkov, Energija, Moskva, 1977.
65. S. C. Haydon and O. M. Williams, J. Phys. D: Appl. Phys., **5**, L79, 1972.
66. S. C. Haydon and O. M. Williams, J. Phys. B: Atom. Molec. Phys., **6**, 1866, 1973.
67. W. L. Borst, Phys. Rev. A, **5**, 648, 1972.
68. S. C. Haydon and A. I. McIntosh, Proc. 4th Int. Conf. on Gas Discharges, Swansea, Sept. 1976, p. 184, IEE Conference Publication Number 143.
69. B. J. Reits, J. Appl. Phys., **48**, 3697, 1977.
70. M. A. Folkard and S. C. Haydon, J. Phys. B: Atom. Molec. Phys., **6**, 214, 1973.
71. S. C. Haydon and O. M. Williams, J. Phys. B: Atom. Molec. Phys., **6**, 227, 1973.
72. S. C. Haydon and O. M. Williams, J. Phys. D: Appl. Phys., **9**, 523, 1976.
73. J. P. Molnar, Phys. Rev., **83**, 940, 1951.
74. J. P. Molnar, Phys. Rev., **83**, 933, 1951.
75. P. H. Vidaud and A. von Engel, Proc. Roy. Soc., A, **313**, 531, 1969.
76. A. A. Lukashev and P. N. Chistyakov, Proc. 9th Int. Conf. on Phenomena in Ionized Gases, Bucharest, Sept. 1969. Contributed papers, p. 18, Ed. G. Musa, I. Ghica et al, Editura Acad.

Acta Physica Academiae Scientiarum Hungaricae, Tomus 49 (1—3), pp. 39—53 (1980)

X-RAYS INDUCED BY LIGHT IONS

By

H. Paul

INSTITUTE FOR PHYSICS, JOHANNES KEPLER UNIVERSITY
LINZ, A-4040 LINZ/AUHOF, AUSTRIA

The main processes involved in energy loss of charged particles are briefly considered and compared to inner shell ionization. Some applications of particle induced X-ray emission are mentioned. The higher order corrections to the PWBA and SCA theories for the ionization cross section are briefly sketched and compared to each other.

Selected K-shell cross section data (from the compilation by Gardner and Gray, and from some recent publications) for projectiles from protons to oxygen ions on various targets are compared to each other and to theories. It is found that almost all the data lie between 60% above and 60% below the corrected PWBA theory by Brandt et al, but that there are also systematic discrepancies between theory and experiments where the reduced velocity variable ξ has about the values 0.2, 0.3, and 0.6. Possible reasons for these discrepancies are given. The SCA theory, as corrected by Laegsgaard et al, has a rather limited range of validity, but within this range, it agrees better with the data than the PWBA theory.

1. Introduction

It may be useful first to consider what happens to a beam of light ions (e. g. 1 MeV protons) as it hits a solid. Let us assume that there will be about 1 ionizing collision per atomic target layer and that each ionizing collision produces, as in a gas, an energy loss of about 30 eV. Then we expect a range of about 3×10^4 atomic layers or $6 \mu m$ (assuming an average layer spacing of 0.2 nm, as for Cu). Indeed, the range of 1 MeV protons in Cu is 7 μm [1]. It follows that 1 MeV protons are useful to investigate thin films or near-surface layers.

Actually, the stopping is not constant as we have assumed but reaches a maximum at about 100 keV [1]. At this energy, the proton velocity is just twice the Bohr velocity, v_0. Hence it seems plausible that the stopping power has its maximum where the proton velocity is close to the orbital velocity of outer target electrons.

Compared to those ionizing collisions which affect mainly the outermost electrons, K-shell ionization is a very rare process. Indeed, since the K-shell ionization cross section for 1 MeV protons on Cu is 17b, the probability to produce 1 K-shell hole throughout the range, given by the cross section times the number of target atoms per unit surface, is less than 10^{-3}. Nevertheless this process is easily detected via the subsequent X-radiation.

In analogy to the stopping power, we may expect the maximum K-shell ionization where the projectile velocity v_1 matches the orbital velocity of target K-shell electrons, v_{2K}, To express this expectation also in terms of energy, we introduce the variable η_K [2]:

$$\eta_K = \frac{v_1^2}{v_{2K}^2} = \frac{m}{M_1} \cdot \frac{E_1}{Z_{2K}^2 R} = \frac{\Theta_K}{4} \frac{T_m}{I_K}, \tag{1}$$

where $Z_{2K} = Z_2 - 0.3$ corrects for inner shielding, Θ_K $(0.6 \lesssim \Theta_K \lesssim 1)$ for outer shielding. $R = 13.6$ eV is the Rydberg energy, $T_m = 4mE_1/M_1$ is the maximum possible energy transfer to a free electron (mass m) at rest, E_1 is the incident projectile energy, M_1 the projectile mass, I_K the experimental K-ionization energy. The indices 1 and 2 refer to projectile and target, respectively.

In these terms, the maximum cross section is expected where $\eta_K \approx 1$ or where $T_m \approx 4I_K$. On the other hand, a collision with an electron which is free except that its binding energy must be overcome, could never lead to ionization if $T_m < I_K$. Or conversely, it is only the binding that makes ionizing collisions in the low energy region possible [2]. Hence we expect the low energy cross section to increase strongly with increasing η_K and to decrease strongly with increasing Z_2. This behaviour of the cross section is clearly seen, e. g. in the figures given by Basbas et al [3].

2. Applications

The measurement of particle induced X-ray emission (PIXE) is well suited to determine the concentration of many elements simultaneously in small samples, with ppm sensitivity. Many applications have been described in the first conference on this subject [4], and more recently in [5].

PIXE measurements may also be used to determine the depth profile of a foreign element in bulk material, due to the strong variation of the cross section with energy. If one assumes, e. g., that the foreign atoms occupy a layer of thickness *b* at a mean depth *a*, with a concentration *c*, then these three parameters may be determined by measuring the X-ray yield of the sample at three different energies, if the yield for a thick layer of the pure foreign material is also known [6]. This method, although not as generally applicable as Rutherford backscattering, should be useful for elements of similar *Z*, for low-*Z* foreign material in high-*Z* bulk, and for foreign material of low concentration. Another recent application of this method has been published by Vegh et al [7].

3. Theoretical description

Clearly, the quantitative application of PIXE requires either calibration measurements on known samples, or a knowledge of the cross sections. Empirical relations could be used here [8], but it is also of interest to see how well the cross sections are described by theoretical approaches. In the following, we restrict the discussion to K-shell ionization by light ions ($Z_1 < 0.3\, Z_2$).

Two basic approaches have recently been used with considerable success: the semi-classical approximation (SCA) [9] and the Plane-Wave-Born-Approximation (PWBA) [2]. It has been shown that both approaches must lead to identical results if the same electron wave functions are used [10]. The SCA approach can be easily visualized: the projectile passes the target atom at a distance b from the nucleus, flying in a straight line at constant speed, and it ionizes the K-shell through its rapidly varying electric field. Integrating over all impact parameters b yields the total cross section, σ_K.

Both approaches correspond to first order perturbation; the cross section obtained is therefore proportional to Z_1^2 and depends on the projectile energy only through v_1 [11].

It is useful to know which impact parameter b contributes most to the total σ_K, for a given v_1. Here again, the simplest classical argument leads to a correct result: the collision time (of the oder b/v_1) should be comparable to the period of revolution, $1/\omega_K$. Hence the largest contribution comes from $b = v_1/\omega_K = r_{ad}$, where r_{ad} is the so-called "adiabatic distance" [9]:

$$r_{ad} = v_1/\omega_K = \hbar v_1/I_K\,. \tag{2}$$

In terms of r_{ad}, we may define a reduced velocity ξ which bears a simple relation to η_K:

$$\xi = r_{ad}/a_{2K} = (2/\Theta_K)\sqrt{\eta_K}\,, \tag{3}$$

where $a_{2K} = a_0/Z_{2K}$ is the screened hydrogenic K-shell radius. When properly normalized, σ_K is a universal function of ξ [3]. Although the basic features of the cross section are well described by both theories, a detailed comparison with experiments shows the necessity of additional corrections:

a. Increased binding. At low v_1, where $\xi \ll 1$, the projectile passes well within the target K-shell radius, thus increasing the binding energy I_K and decreasing σ_K. The simplest way to correct for this effect [12] is to replace Z_{2K}^2 by $(Z_{2K} + Z_1)^2$, thus decreasing η_K in Eq. [1].

b. Polarisation [3]. At higher values v_1, the projectile may be thought of as passing outside the K-shell, deforming the wave function in such a way as to decrease I_K (since the electron is, on the average, farther away from the nucleus). This increases σ_K.

c. Relativity. Most calculations use (non-relativistic) hydrogenic wave functions. This cannot be correct for high-Z_2 targets (and even for medium Z_2 if the innermost part of the atom is probed by slow projectiles). Strongly bound electrons move fast; this increases T_m (due to the relativistic mass increase) and hence η_K. **Brandt** and **Lapicki** [13] have recently shown how this can be easily incorporated into the PWBA calculation.

d. Coulomb deflection. For low v_1, the projectile can no more be assumed to move at constant speed in a straight line. The Coulomb force both deflects the projectile and slows it down, thus decreasing η_K.

All these effects have been incorporated into the PWBA theory [3, 13]. The binding, relativity and Coulomb corrections are also contained in the formulation of the SCA theory given by **Laegsgaard** et al [12]. Because of the simple binding correction (see above), the latter is only good for small projectile velocities ($\xi < 0.25$).

Since the Coulomb correction is much different from unity wherever the relativity correction is [14] and since these two corrections tend to cancel each other, it is not easy to separate them by experiment.

There is, however, another theoretical approach which sheds light on the binding/polarization correction. **Ford** et al [15] have calculated K-shell ionization by protons using second order perturbation theory for cases where both relativity and Coulomb corrections are not important. Comparing their second order to their first order result should give the same binding/polari-

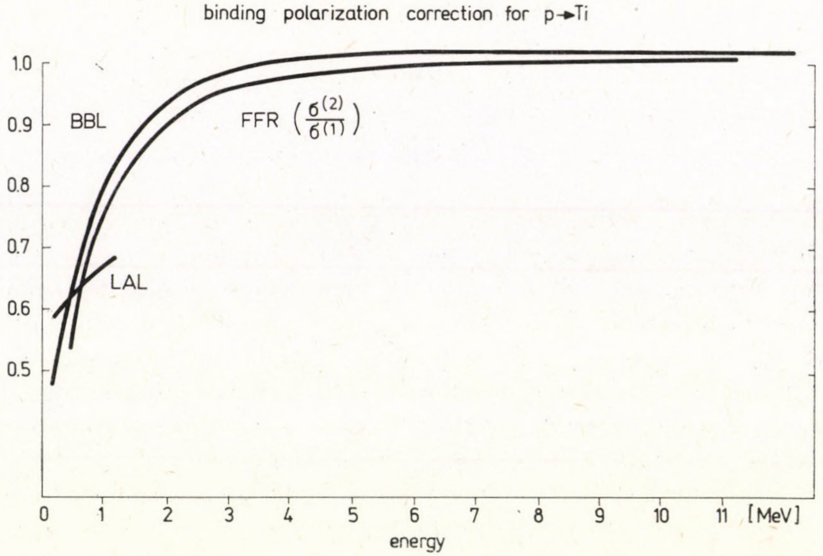

Fig. 1. The binding/polarization correction for protons on Ti according to three different theoretical approaches: BBL [3], FFR [15], and LAL [12]

zation correction as is obtained by comparing the corrected to the uncorrected PWBA cross section. Fig. 1 shows that there is indeed fairly good agreement between the two approaches. The SCA curve (labelled LAL) behaves quite differently, it is remarkable that it does not agree with the PWBA curve (labelled BBL) in the limit of vanishing energy (where it should be best).

4. Comparison of experimental and theoretical ionization cross-sections

Since the compilation of K-shell ionization cross sections was recently published by Gardner and Gray [16], we have been trying to use the large amount of information from Table I of that compilation to compare the experimental data both with each other and with the theories, using a computer program. First results have been presented before [17].

More recently, we have augmented the data base by new published data, and we have changed the program to normalize the data through division by the PWBA theory with all corrections. Ideally, then, all the normalized cross section data should be close to unity; in practice, we find almost all the data in the range (0.4, 1.6) and the great majority within (0.8, 1.2) i. e. the overall agreement with the corrected PWBA theory (for many different $Z_1 - Z_2$ combinations) is good, although some experiments may have excessive errors. By way of example, we present here a few representative graphs; the full comparison will be published elsewhere [20].

Fig. 2 shows relative cross sections for protons on Ne. The different symbols refer to different measurements identified by codes. Of this code, the first letter gives the type of measurement (X for X-ray, A or I for Auger); the second letter gives the type of target (G for gas, N for thin solids, K for a thick solid); the remaining symbols define the publication (see Table I). Before plotting, the experimental X-ray or Auger data have been converted to ionization cross sections using the table of fluorescence coefficients by Krause [18]. Fig. 2 shows rather large discrepancies between different experiments at low energy.

Fig. 3 (p on Cu) shows good agreement between many different authors, and a few experimental discrepancies. Fig. 4 (p on Au) shows that the high energy points now agree rather well with the corrected PWBA theory, due to the inclusion of the relativity correction [13], but that the theory is too high for low energies. The corrected SCA theory is also plotted as a line (×−×−× in the region $\xi < 0.25$, and +−+−+ in the region $\xi > 0.25$); it follows the data very well.

In Fig. 5, cross section data are plotted for protons ($E_1 \leq 15$ MeV) on five different targets (${}_{47}$Ag — ${}_{51}$Sb), versus the reduced velocity variable ξ. Although the various corrections are not only functions of ξ, an approximately universal behaviour is seen at low energy: the points bend down sharply at $\xi \approx 0.2$. The high points (p $\rightarrow {}_{49}$In) are due to KL76. Fig. 6 (p on Ag) shows that the low energy bend is found by three different groups: BR78, LA79, and BE79. This is somewhat in contradiction to BRANDT and LAPICKI [13] who state that only ANHOLT's data [14] are not in agreement with their theory. The reason for these different findings may be the somewhat different data base.

Table I

References for experimental data

AK74	R. AKSELSSON and T. B. JOHANSSON, Z. Physik, **266,** 245, 1974.
AN78	R. ANHOLT, Phys. Rev., **A17,** 983, 1978.
BE73	R. C. BEARSE, J. A. CLOSE, J. J. MALANIFY and C. J. Umbarger, Phys. Rev., **A7,** 126, 1973.
BE78	A. BERINDE, C. DEBERTH, I. NEAMU, C. PROTOP, N. SCINTEI, V. ZORAN, M. DOST, and S. RÖHL, J. Phys., **B11,** 2875, 1978.
BE79	O. BENKA and M. GERETSCHLÄGER, J. Phys. B. **13,** 3223, 1980.
BD78	T. BADICA, C. CIORTEA, A. PETROVICI and I. POPESCU, Rev. Roum. Phys., **23,** 1019, 1978.
BR78	C. BAUER, R. MANN and W. RUDOLPH, Z. Physik, **A287,** 27, 1978.
GR76A	T. J. GRAY, P. RICHARD, R. L. KAUFFMAN, T. C. HOLLOWAY, R. K. GARDNER, G. M. LIGHT, J. GUERTIN, Phys. Rev., **A13,** 1344, 1976.
HO75A	F. HOPKINS, R. BRENN, A. R. WHITTEMORE, J. KARP and S. K. BHATTACHERJEE, Phys. Rev., **A11,** 916, 1975.
HO75B	F. HOPKINS, R. BRENN, A. R. WHITTEMORE, N. CUE and V. DUTKIEWICZ, Phys. Rev., **A11,** 1482, 1975.
KA77	M. KAMIYA, K. ISHII, K. SERA, S. MORITA and H. TAWARA, Phys. Rev., **A16,** 2295, 1977.
KB76	N. KOBAYASHI, N. MADEA, H. HORI and M. SAKAISAKA, J. Phys. Soc. Japan, **40,** 1421, 1976.
KH75	N. A. KHELIL and T. J. GRAY, Phys. Rev., **A11,** 893, 1975.
KL76	E. KOLTAY, D. BERENYI, I. KISS, S. RICZ, G. HOCK and J. BASCO, Z. Physik, **A278,** 299, 1976.
LA76	A. LANGENBERG and J. VAN ECK, J. Phys., **B9,** 2421, 1976.
LA79	E. LAEGSGAARD, E. U. ANDERSEN and F. HOGEDAL, Nucl. Instr. & Meth., **169,** 293, 1980.
LE75	R. LEAR and T. J. GRAY, Phys. Rev., **A8,** 2469, 1973.
LI73	R. B. LIEBERT, T. ZABEL, D. MILJANIC, H. LARSON, V. VALKOVIC and G. C. PHILLIPS, Phys. Rev., **A8,** 2336, 1973.
LO79B	J. S. LOPES, A. P. JESUS and S. C. RAMOS, Nucl. Instr. & Meth., **169,** 311, 1980.
MD77A	F. D. MCDANIEL, J. L. DUGGAN, P. D. MILLER and G. D. ALTON, Phys. Rev., **A15,** 846, 1977.
MI76	M. MILAZZO and G. RICCOBONO, Phys. Rev., **A13,** 578, 1976.
MK76	R. H. MCKNIGHT and R. G. RAINS, Phys. Rev., **A14,** 1388, 1976.
PE79	M. PONCET and Ch. ENGELMANN, Nucl. Instt. & Meth., **159,** 455, 1979.
RN76	R. R. RANDALL, J. A. BEDNAR, B. CURNUTTE and C. L. COCKE, Phys. Rev., **A13,** 204, 1976.
RS76	MD. RASHIDUZZAMAN KHAN, D. CRUMPTON and P. E. FRANCOIS, J. Phys., **B9,** 455, 1976.
SO76	C. G. SOARES, R. D. LEAR, J. T. SANDERS and H. A. VAN RINSVELT, Phys. Rev., **A13,** 953, 1976.
ST75	N. STOLTERFOHT and D. SCHNEIDER, Phys. Rev., **A11,** 721, 1975.
TR77	J. TRICOMI et al, Phys. Rev., **A15,** 2269, 1977.
WL76	S. R. WILSON, F. D. MCDANIEL, J. R. ROWE and J. L. DUGGAN, Phys. Rev., **A16,** 903, 1977.
WO74	C. W. WOODS, R. L. KAUFFMAN, K. A. JAMISON, C. L. COCKE and P. RICHARD, J. Phys. **B7,** L474, 1974.
WO76	C. W. WOODS, R. L. KAUFFMAN, K. A. JAMISON, N. STOLTERFOHT and P. RICHARD, Phys. Rev., **A13,** 1358, 1976.

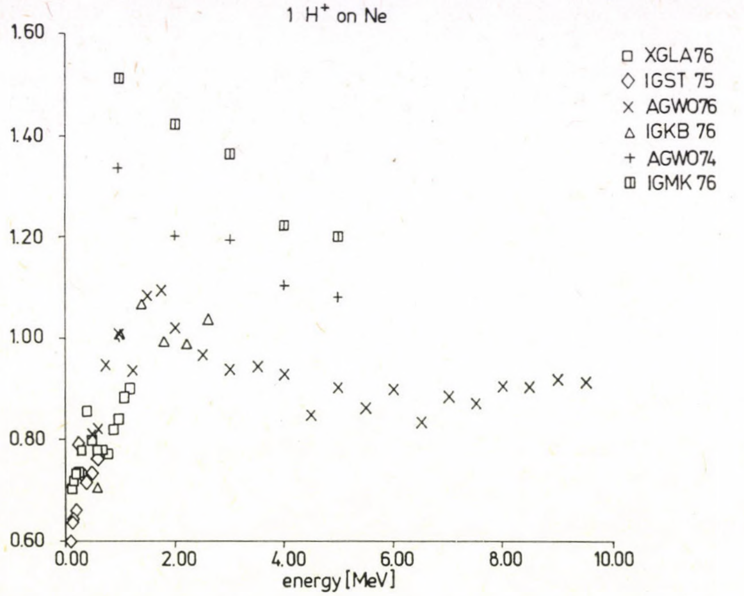

Fig. 2. Experimental K-shell ionization cross section for protons on Ne versus projectile energy, divided by the fully corrected PWBA theory [3, 13]. The different symbols correspond to different references (see Table I), the first two letters define the type of measurement and the type of target (see text)

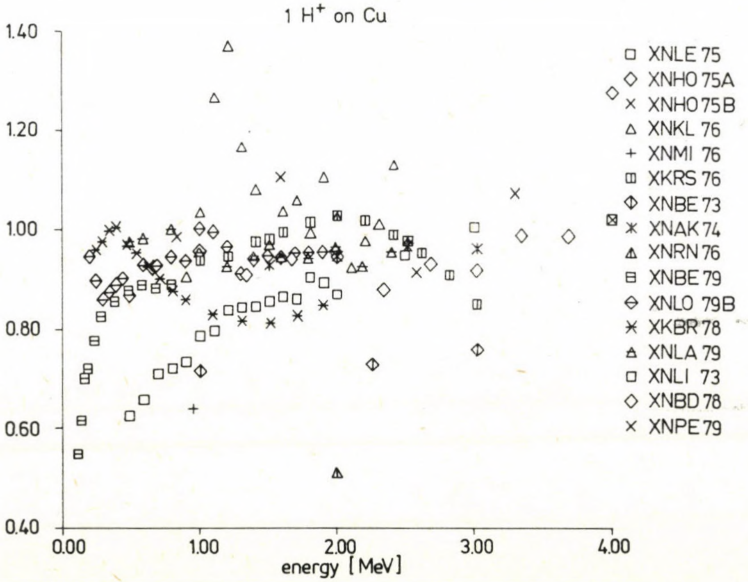

Fig. 3. Like Fig. 2, for protons on Cu. Note that a few symbols have been used twice

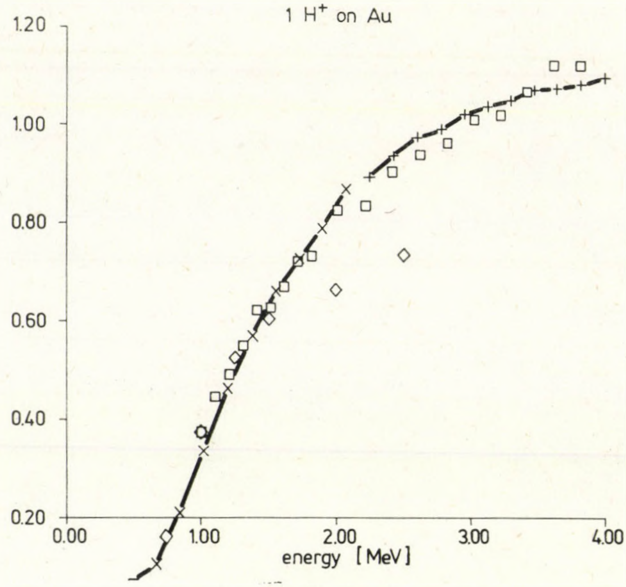

Fig. 4. Like Fig. 2, for protons on Au. The (normalized) SCA-theory [12] is plotted here as a line (x–x–x for 1 > 0.25, +—+—+ for $\xi > 0.25$). It fits the data at low energies much better than the PWBA theory. Data are due to KA77 (squares) and AN78 (diamonds)

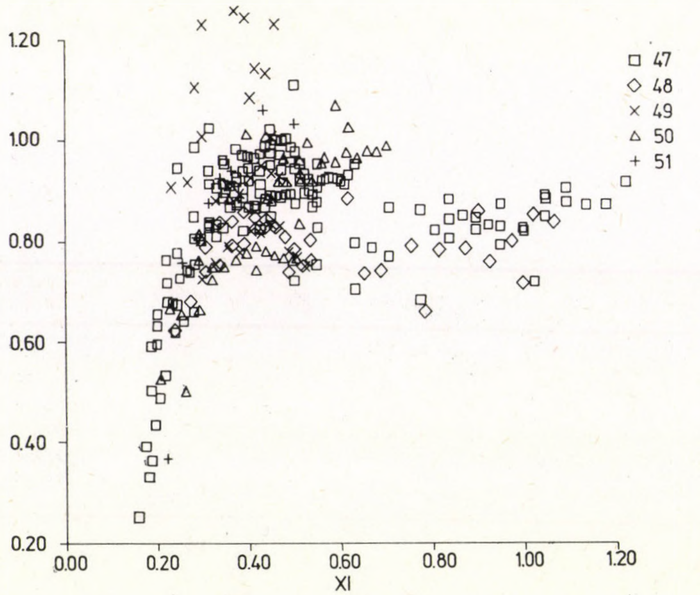

Fig. 5. Experimental K-shell ionization cross sections, normalized as in Fig. 2, plotted versus the reduced velocity ξ (Eq. 3), for protons on Ag, Cd, In, Sn, and Sb. The different symbols correspond to different target atomic numbers, as shown. Note the low energy bend at $\xi \sim 0.2$

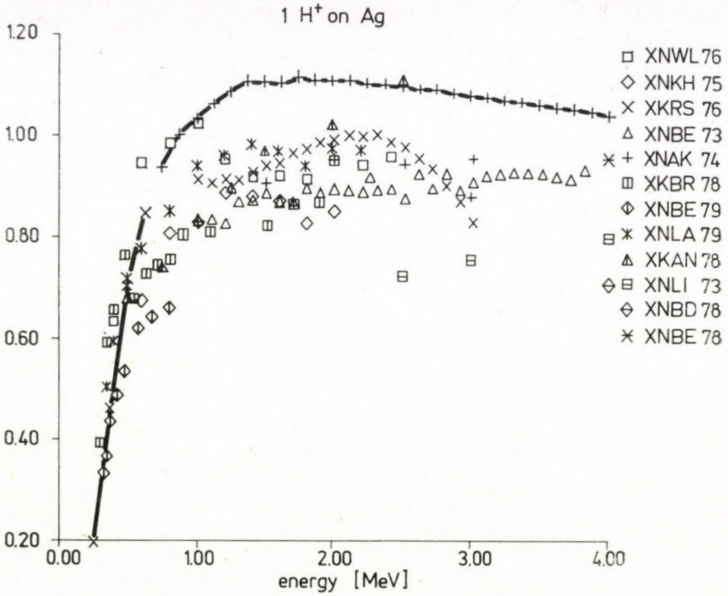

Fig. 6. Like Fig. 4, for protons on Ag

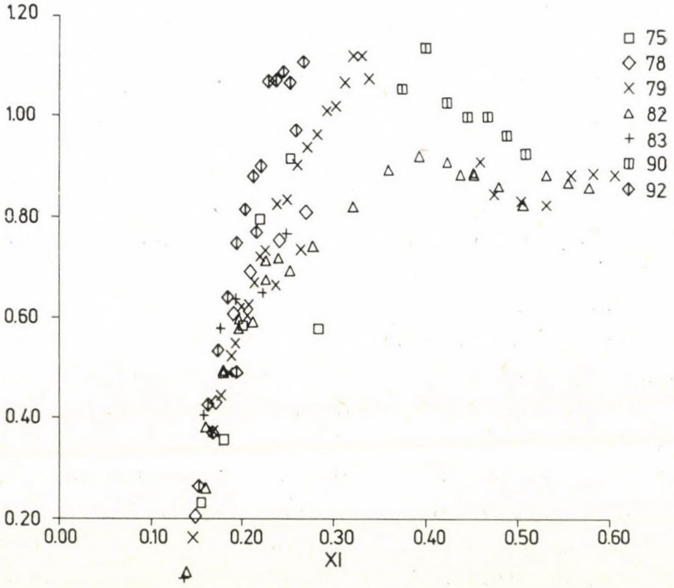

Fig. 7. Like Fig. 5, for protons on heavy targets

Fig. 7 (protons on heavy targets: $_{75}$Re — $_{92}$U, $E_1 < 13$ MeV) shows the same general behaviour. The low energy bend is again found by three groups: KA77, AN78, and LA79.

Fig. 8 (alphas on targets from $_{22}$Ti to $_{30}$Zn, $E_1 < 10$ MeV) shows very many points within (0.8, 1.2), a few high points (KL76) and a few low points (SO76). Here, the bend at $\xi \sim 0.2$ is only based on measurements by one group (BE79).

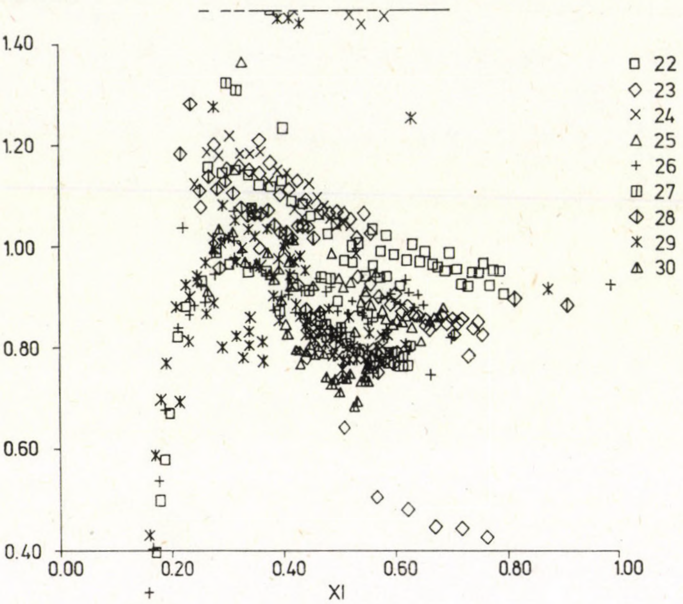

Fig. 8. Like Fig. 5, for alphas on targets from Ti to Zn

There may also be an indication of a maximum at $\xi \sim 0.3$. Fig. 9 (alphas on heavy targets, $E_1 < 60$ MeV) shows the same general behaviour; the low energy points are here only due to AN78.

The remaining figures refer to slightly heavier projectiles. Figs. 10 and 11 (^{14}N projectiles on targets from $_{20}$Ca to $_{51}$Sb, $E < 36$ MeV) show a new feature: a pronounced minimum at $\xi \sim 0.6$. Whereas Fig. 10 contains almost only data by MD77A, Fig. 11 has data by four different groups: MD77A, BR78, GR76A, TR77.

Fig. 12 (^{16}O on $_{26}$Fe to $_{35}$Br, $E < 91$ MeV) shows the same minimum less clearly due to the somewhat discrepant data. Fig 13 (^{16}O on $_{37}$Rb to $_{62}$Sm, $E < 56$ MeV) may again show the maximum at $\xi \sim 0.3$, though not very clearly. Fig. 14 (^{16}O on $_{67}$Ho to $_{92}$U, $E < 56$ MeV) shows the bend at $\xi \sim 0.2$ and the maximum at $\xi \sim 0.3$.

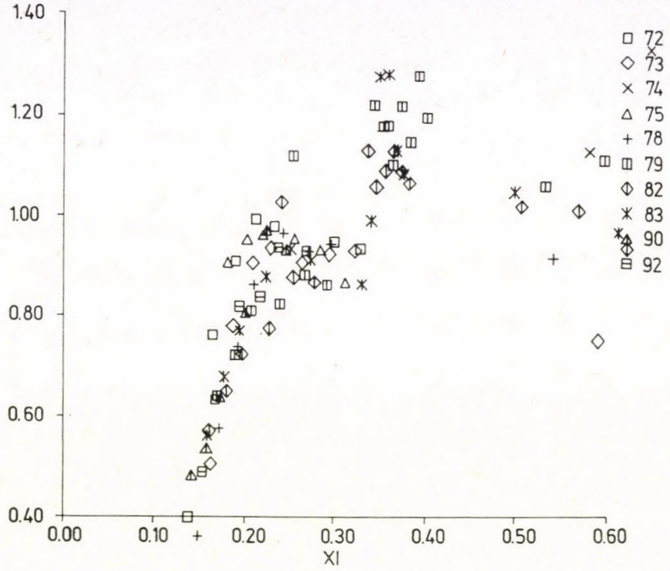

Fig. 9. Like Fig. 5, for alphas on heavy targets

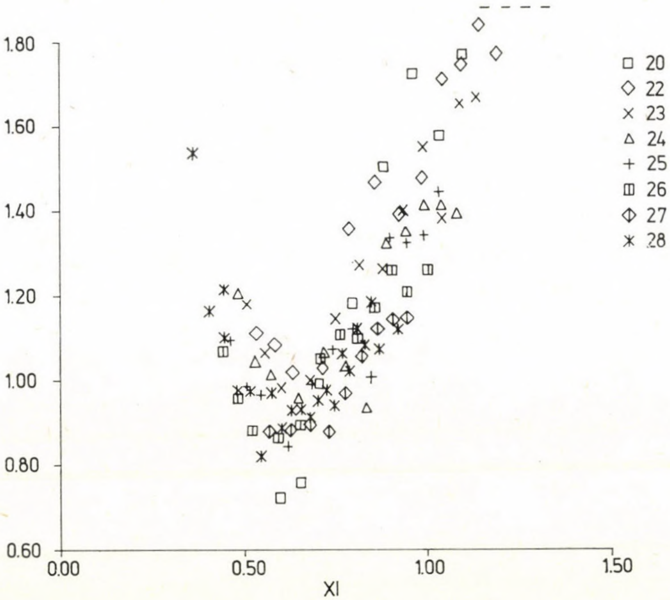

Fig. 10. Like Fig. 5, for ^{14}N projectiles on targets from Ca to Ni. Note the minimum at $\xi \sim 0.6$

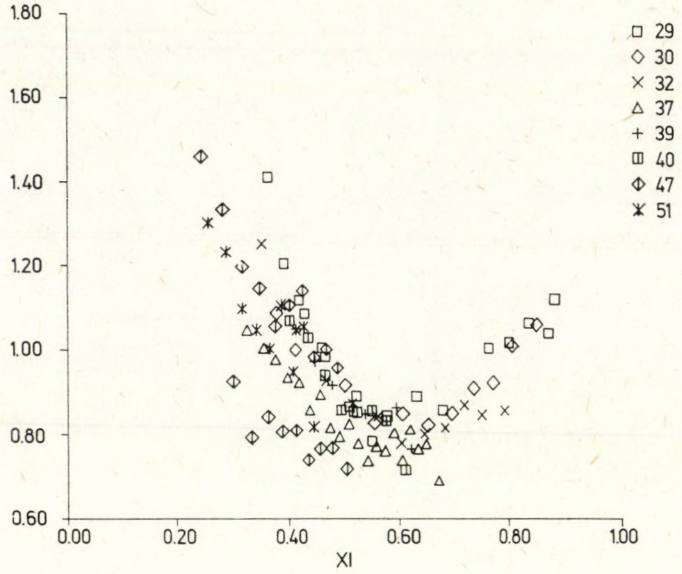

Fig. 11. Like Fig. 5, for ^{14}N projectiles on targets from Cu to Sb

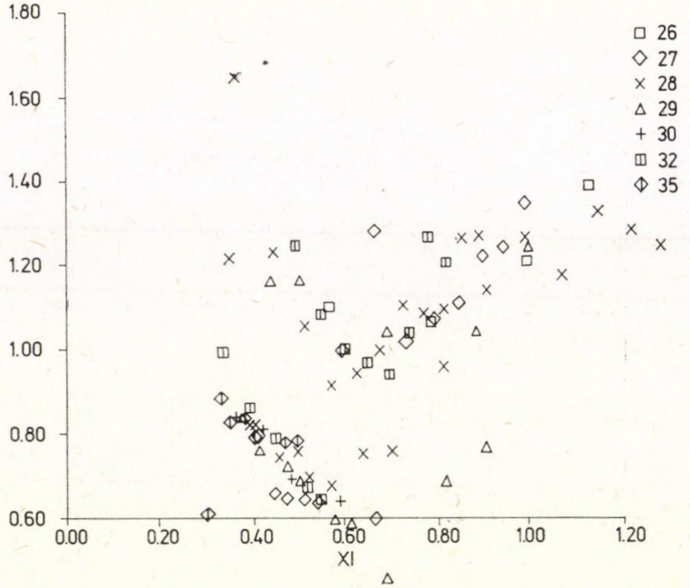

Fig. 12. Like Fig. 5, for ^{16}O projectiles on targets from Fe to Br. A possible minimum at $\xi \sim 0.6$ is barely perceptible due to somewhat discrepant data

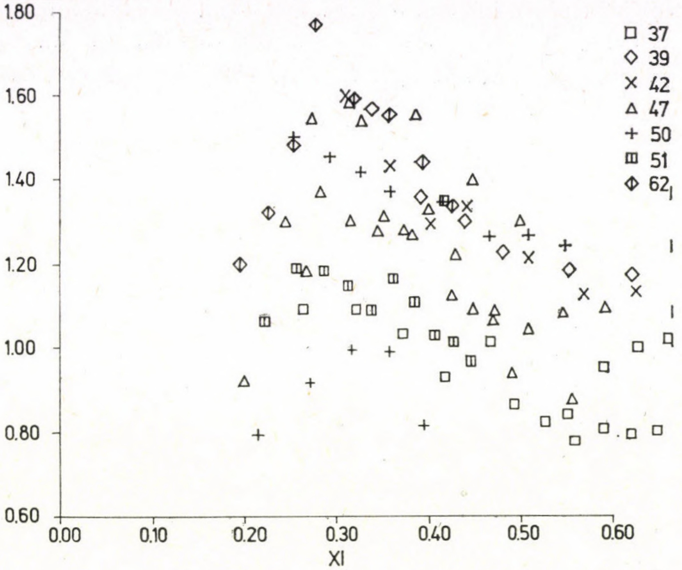

Fig. 13. Like Fig. 5, for ^{16}O projectiles on targets from Rb to Sm

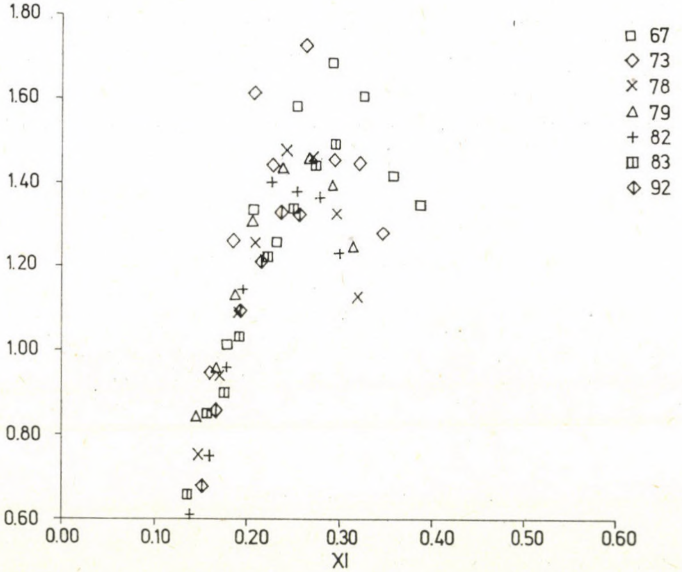

Fig. 14. Like Fig. 5, for ^{16}O projectiles on targets from Ho to U. Note the maximum at $\xi \sim 0.3$

In retrospect, it can be noted that not only the bend at $\xi \sim 0.2$ but also the features at $\xi \sim 0.3$ and $\xi \sim 0.6$ can be seen (or guessed) from the Figures for protons and alphas, but that they are less pronounced there than for the heavier projectiles.

5. Discussion

Although these remaining discrepancies between the corrected PWBA theory due to BRANDT et al [3, 13] and experiments are not very large, it would be interesting to find reasons. Clearly, this will not be possible from our comparisons alone, but will require theoretical insight also.

Concerning the bend at $\xi \sim 0.2$, we may assume, following the work of KOCBACH [19] and ANHOLT [14], that BRANDT's [3, 13] Coulomb correction factor is not as different from unity as it should be.

Since electron capture by the projectile is not included in the theories used, the question arises whether the maximum at $\xi \sim 0.3$ could be due to this effect. Taking ^{16}O projectiles as an example, one would indeed expect the maximum of K-capture to occur around $E_1 = 26$ MeV (where v_1 equals the velocity of projectile K-electrons). But the corresponding values of ξ would then lie between $\xi = 0.17$ (for U) and $\xi = 0.53$ (for Rb), whereas the maximum is empirically found at a fixed value ξ.

Finally, one may ask whether the features at $\xi = 0.3$ and 0.6 are due to not quite satisfactory theoretical corrections. Here the binding correction would be the most likely candidate since it becomes more important with increasing Z_1. For ^{14}N projectiles, e. g. it amounts to about 0.16 for $\xi = 0.6$, whereas the other corrections are close to unity. Hence, the deviations may well be due to the binding correction.

The corrected SCA theory is not within its range of validity ($\xi < 0.25$) on most graphs. Where it is valid, however, it follows the data better than the PWBA theory.

6. Acknowledgements

I should like to thank Prof. BASBAS, DUGGAN and McDANIEL for their interest and help that made it possible for me to produce the figures by means of a computer program written during several stays at North Texas State University. The help of Prof. MACKEY, who wrote the Plot Package program, was also essential. Finally, this work would have been impossible without the help of Prof. GRAY who provided me his tables in the form of punched cards.

REFERENCES

1. H. H. ANDERSEN and J. F. ZIEGLER, Hydrogen Stopping Powers and Ranges in all Elements, Pergamon Press, New York, 1977.
2. E. MERZBACHER and H. W. LEWIS, in: Encyclopedia of Physics, S. Flügge, ed. Springer, Berlin, **34**, 166 ff, 1958.

3. G. Basbas, W. Brandt and Laubert, Phys. Rev., **A17,** 1655, 1978.
4. Intern. Conf. on Particle induced X-ray Emission and its Analytical Applications, Lund (Sweden) 1976; Nucl. Instr. & Meth. 142, 1977.
5. 1978 Conf. Appl. small Accelerators in Res. and Ind., Denton TX, 1978; IEEE Trans. Nucl. Sc. NS-26, No. 1, part 2, 1979.
6. O. Benka, M. Geretschläger and A. Kropf, Nucl. Instr. & Meth., **149,** 441, 1978.
7. J. Vegh et al, Nucl. Instr. & Meth., **153,** 553, 1978.
8. S. A. E. Johansson and T. B. Johansson, Nucl. Instr. & Meth., **137,** 473, 1976.
9. J. M. Hansteen, in: Adv. Atomic and Molec. Phys., ed. by D. R. Bates and B. Bederson, Acad. Press, New York, **11,** 299 ff. 1975.
10. D. H. Madison and E. Merzbacher, in: Atomic Inner Shell Processes, ed. by B. Crasemann, Academic Press, New York, 1975, Vol. 1,1.
11. G. Basbas, Proc. 4th Conf. Sci. and Ind. Appl. of Small Accelerators, Denton TX, 1976; IEEE, New York, 1977, 142.
12. E. Laegsgaard, J. U. Andersen and M. Lund, in: 10th Int. Conf. Phys. Electronic Atomic Coll. (Paris), G. Watel, ed., North-Holland Publ. Co., Amsterdam, 1978, p. 353.
13. W. Brandt and G. Lapicki, Phys. Rev., **A20,** 465, 1979.
14. R. Anholt, Phys. Rev., **A17,** 983, 1978.
15. A. L. Ford, E. Fitchard and J. F. Reading, Phys. Rev., **A16,** 133, 1977.
16. R. K. Gardner and T. J. Gray, At. Data Nucl. Data Tables **21,** 515, 1978.
17. H. Paul, Nucl. Instr. & Meth., **169,** 249, 1980.
18. M. O. Krause, J. Phys. Chem. Ref. Data **8,** 307, 1979.
19. L. Kocbach, Phys. Norv., **8,** 187, 1976.
20. H. Paul, At. Data Nucl. Data Tables, in print.

Acta Physica Academiae Scientiarum Hungaricae, Tomus 49 (1—3), pp. 55—66 (1980)

RECENT DEVELOPMENT IN AND BY RUTHERFORD BACKSCATTERING STUDIES

By

J. GYULAI

CENTRAL RESEARCH INSTITUTE FOR PHYSICS, HUNGARIAN ACADEMY OF SCIENCES
H-1525 BUDAPEST, HUNGARY

Backscattering spectrometry (BS) developed recently in two directions. 1. Better understanding of channelling opened up the area of surface and defect studies, 2. optimalized experimental conditions led to better "chemical", depth and lateral resolution.

BS helps TEM[1] as a non-destructive preliminary tool and helps SIMS[2] and Auger (sputter) profiling with an absolute depth and concentration scale, as well as with a check of artefacts connected with sputtering.

The understanding of different interactions between materials and particles or photons gives information on the physical state of these materials. In many cases structural composition characterization is possible. The goal of these investigations is to prepare "tailored" structures. Accelerated ions became important from all three phases of tailoring, i.e. doping (implantation), machining (sputtering), and analysis (Fig. 1).

In this review, recent developments are summarized, when information comes from the scattering of MeV light ions in solids. These solids may be amorphous or crystalline, and the information is mainly about chemical composition and structure of surface layers, down to some microns.

The term Rutherford backscattering (RBS or RIBS, "I" for ion) according to the majority of users does not include particle channelling in crystalline targets. In this paper Backscattering Spectrometry (BS) will be used as a general term [1].

BS still does not include Particle Induced X-Ray Excitation (PIXE) and Particle Induced Nuclear Reactions (PINR), though the three techniques are closely related to each other. They are complementary in a sense that, if resolution or sensitivity of one of these methods fails for a particular case, the others may be still adaptable. Technically this is very convenient, because all three methods are based on the same equipment apart from special detectors.

---

[1] TEM: Transmission Electron Microscopy

[2] SIMS: Secondary Ion Mass Spectrometry

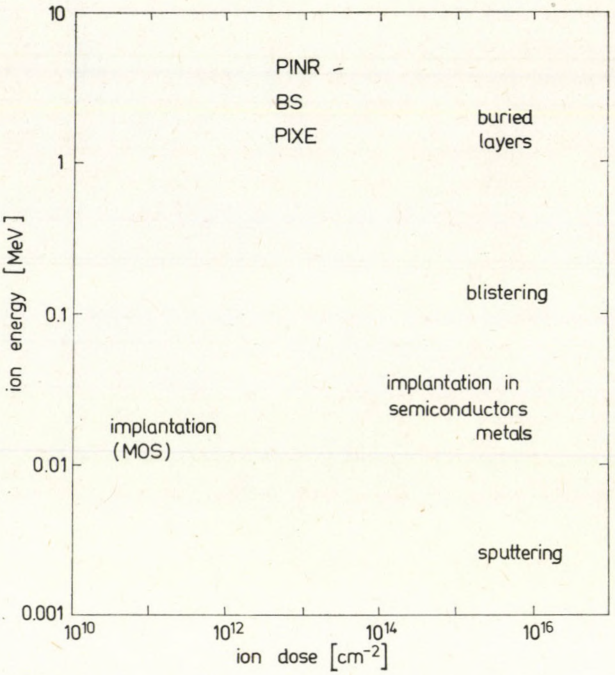

Fig. 1. Different uses of ions

Quantities measured in BS analysis

A BS measurement can be characterized by different quantities and features, i. e.

1) energy losses (kinematic and stopping);
2) angular scan;
3) flux peaking (anomalous yield);
4) critical angle;
5) shadow cones of atoms;
6) minimum yield;
7) dechannelling;
8) direct backscattering from the first atomic row or from lattice defects.

There are still more parameters, such as energy straggling, influence of multiple scattering, but these are presently treated as parasitic effects, no structural information was extracted from measurements of these quantities.

Another important issue is to optimize

1) the type of particle (H^+, He^+ ,. . ., C^+, N^+),
2) its acceleration energy,

3) scattering geometry,

4) beam spot size

to each problem, though most results were obtained with 1—2 MeV He$^+$ at 165° scattering and with a beam size of some tenth of a mm.

In this review, first some recent and characteristic examples will be given, how to extract information from the measured quantities and, later, some cases will illustrate the use of optimalized experimental conditions.

Energy losses were the first quantities analyzed in BS, to get depth-dependent chemical composition. After detailed discussions and criticisms, these days most data required by quantitative analysis seem convincing [1].

For crystalline solids, further characteristics of BS measurement are important.

Angular scan is still one of the most informative measurements in BS. It can be taken at any energy window of the backscattered particles, therefore, it may represent different chemical elements at different depths in the solid. Characteristic are the half-width and the relative depth of the valley. This latter, when taken at an energy right behind the so-called surface peak, is called the minimum yield ($\chi_{\min}$). The half-width was used e. g. by Merz et al [2]

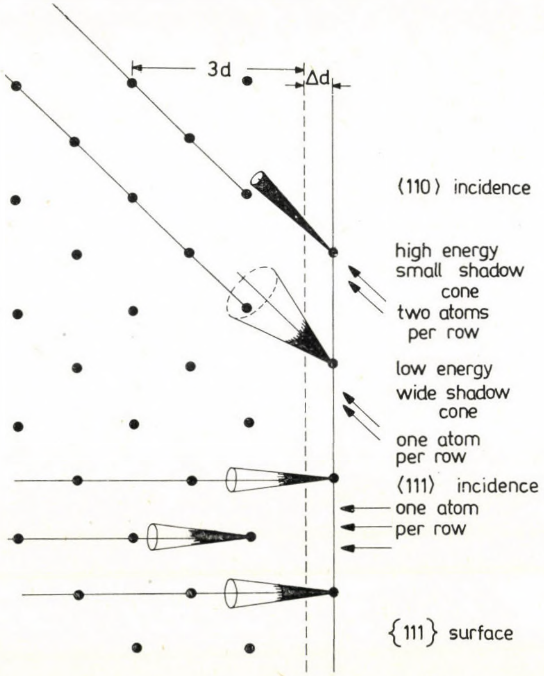

Fig. 2. Measurement of surface relaxation by BS. Nonrectangular incidence brings the information (after [4])

to determine lattice location of implanted Bi in GaP. Comparison of the three half-widths showed that the Bi sits on phosphorus sites.

The angular scan is extremely important, when interstitials are on special lattice positions. The Coulomb potential in the channels steering the incoming particles may focus the beam, say, along the median axis of the channel. If impurity atoms sit preferentially there, the backscattered yield will increase for ions running in the axis and hitting those atoms *(flux peaking)*.

The *critical angle* is a quantity describing the condition for the travelling ions to stay in the channel. This angle goes inversely with $\sqrt{E}$, i. e. decreases with energy. This feature was used to detect "highly oriented" silicon crystallites (polycrystalline Si) on silicon single crystal [3], because for a lower energy good channelling was found, while higher energy BS detected the surface as "amorphou ".

This technique is related to results analyzing the shadow cones. A remarkable example is that of DAVIES et al [4], who have measured the surface relaxation of platinum crystals. It can be seen in Fig. 2 that if relaxation occurred, the lattice constant were modified by Δd for the first atomic layer. A non-rectangular, though channelled backscattering analysis taken at higher beam energies will see twice as much "surface" atoms, than a lower energy BS analysis or the one at normal incidence does.

This is one of the experiments, which clearly demonstrates the power of the BS, as it really "sees" individual atoms.

The next quantities, as the *minimum yield* and *dechannelling* are key to defect identification. Defects in single crystals may cause

1) direct backscattering;
2) enhanced dechannelling;
3) enhanced minimum yield.

Fig. 3 shows the first observation of orientation dependence of epitaxial regrowth in disordered implanted layers [5]. The 1.5 MeV analysis feels crystal quality both by minimum yield (at approx. 1.1 MeV) of the aligned spectra and by dechannelling (slope of the curves). The best crystal regrows if $<110>$ substrates were used. The problem of regrowth was investigated in detail for silicon self-implanted layers by CSEPREGI et al [6]. Fig. 4 shows the dependence of regrowth rate of Si on crystal orientation, while Fig. 5 displays the corresponding Arrhenius plots for Si and Ge. The equal slope indicates the same vacancy-type regrowth mechanism.

Amorphization by self-implantation and a low temperature heat treatment for regrowth helped to improve the crystalline quality of silicon on sapphire substrate (SOS). In this case an inverted amorphization was made by high energy channelled implant [7] leaving the surface of the silicon undamaged. The 560 °C heat treatment was enough to produce an epitaxial

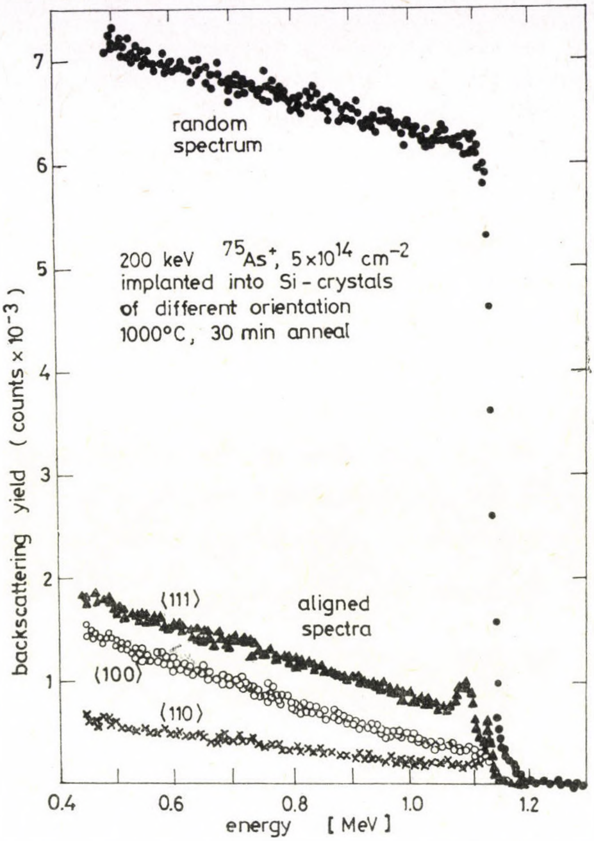

Fig. 3. Orientation dependence of epitaxial regrowth for As-implanted silicon (implantation at room temperature). Note different minimum yields and dechannelling.

regrowth from this surface layer down to the interface, where most of the defects were located before (Fig. 6). Both structural and electrical characteristics of this sandwich improved by an order of magnitude [8].

The influence of dislocations on dechannelling was calculated by Quéré [9] and measured first on Al bombarded with Zn by Foti et al (Fig. 7, [10]). In accordance with Quéré's model, dislocations do not cause direct backscattering, but the dechannelling due to them has an E-dependence.

BS picture of misfit dislocations lying 460 nm deep, produced by thermal oxidation of phosphorus-implanted layers in silicon, was detected by Tseng et al ([11], Fig. 8). The step in the channelled spectrum is caused by the decrease in "transparency" of the channel (Fig. 9).

Stacking faults, on the other hand, increase the minimum yield, but dechannelling is independent of bombarding energy [12].

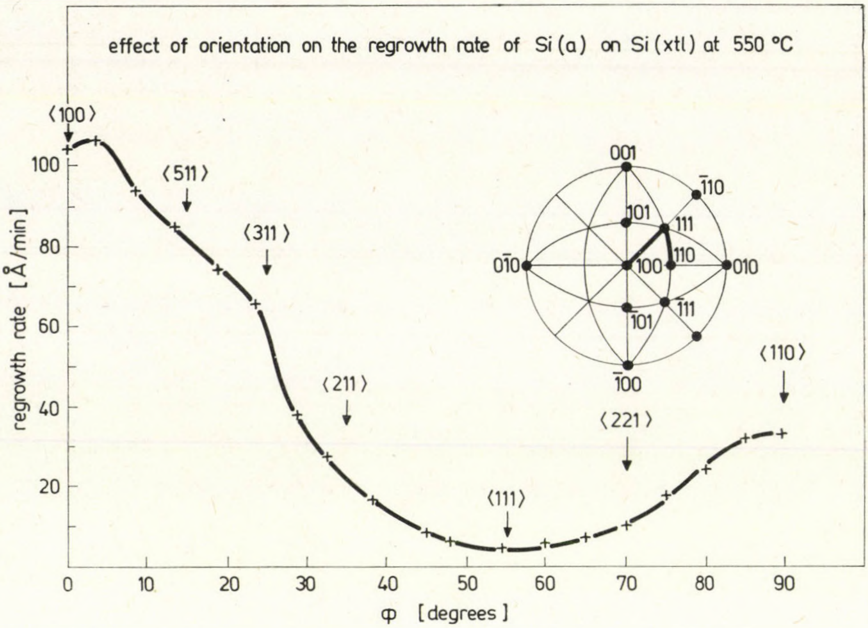

Fig. 4. Regrowth of amorphous (a) layers on Si-samples of different orientation, self-implanted at liquid N_2 temperature (after [6])

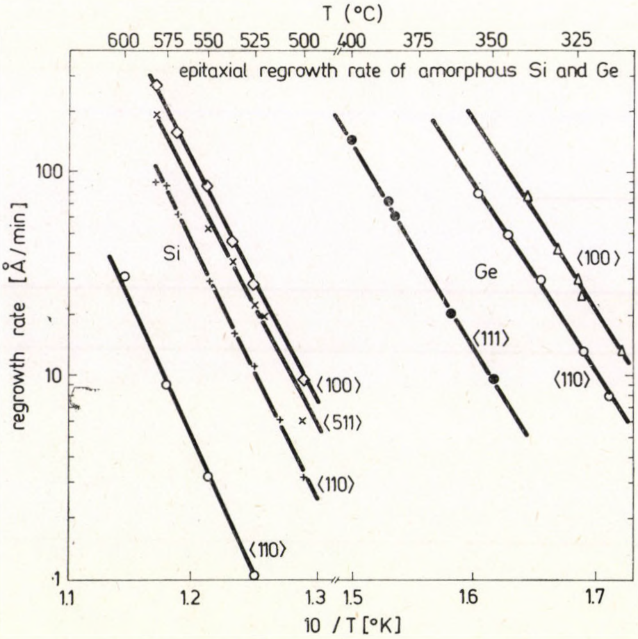

Fig. 5. Arrhenius plots of epitaxial regrowth rate of amorphous layers on self-implanted Si (after [6])

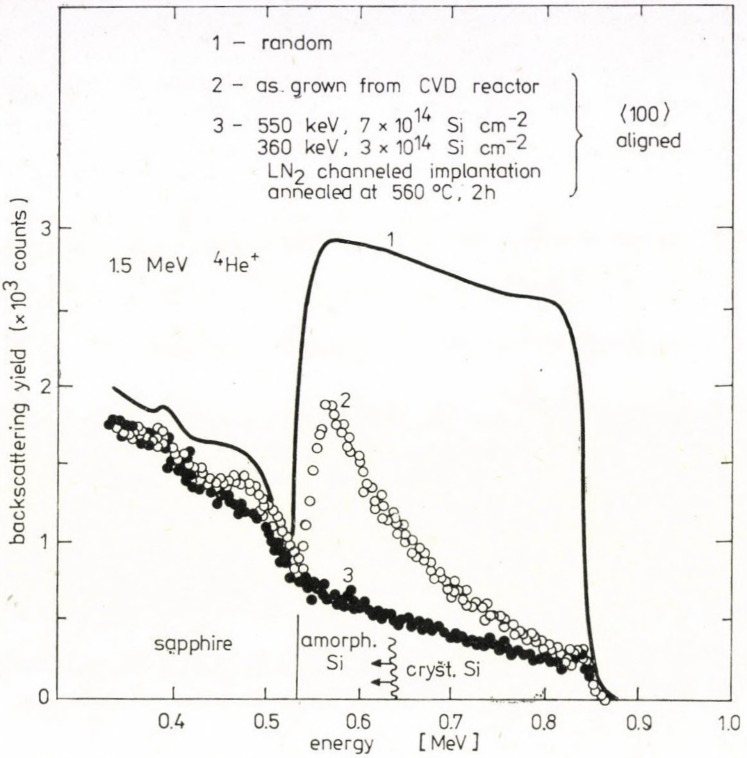

Fig. 6. Regrowth of silicon on sapphire after a channelled, low temperature self-implantation. Regrowth front moves downwards from undamaged surface layer. Note improved dechannelling, i.e. improved crystal quality

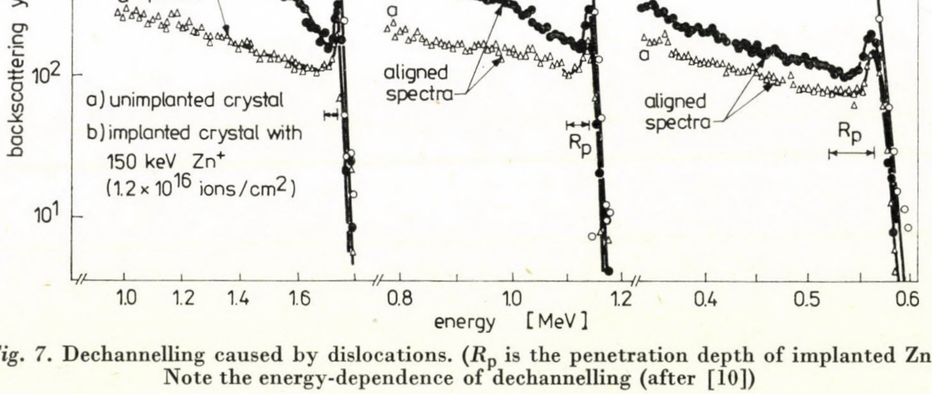

Fig. 7. Dechannelling caused by dislocations. (R_p is the penetration depth of implanted Zn). Note the energy-dependence of dechannelling (after [10])

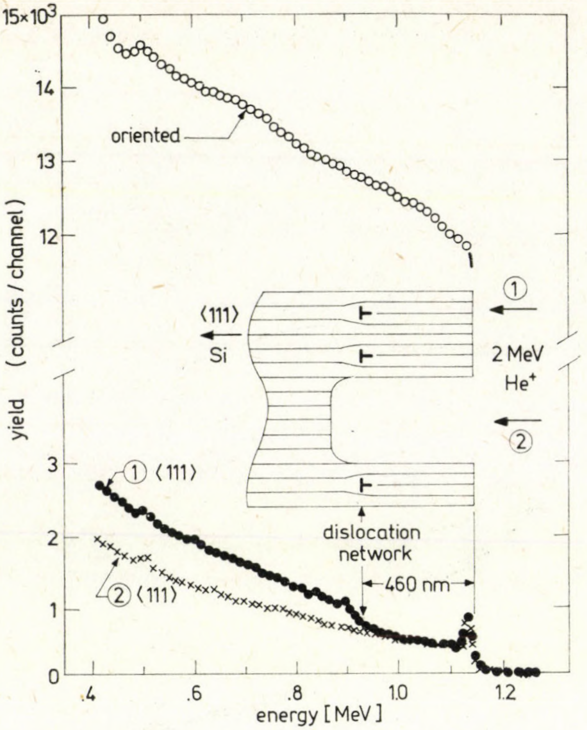

Fig. 8. **BS spectrum influenced by misfit dislocations. The structure was produced by thermal oxidation of a high-dose phosphorus-implanted Si**

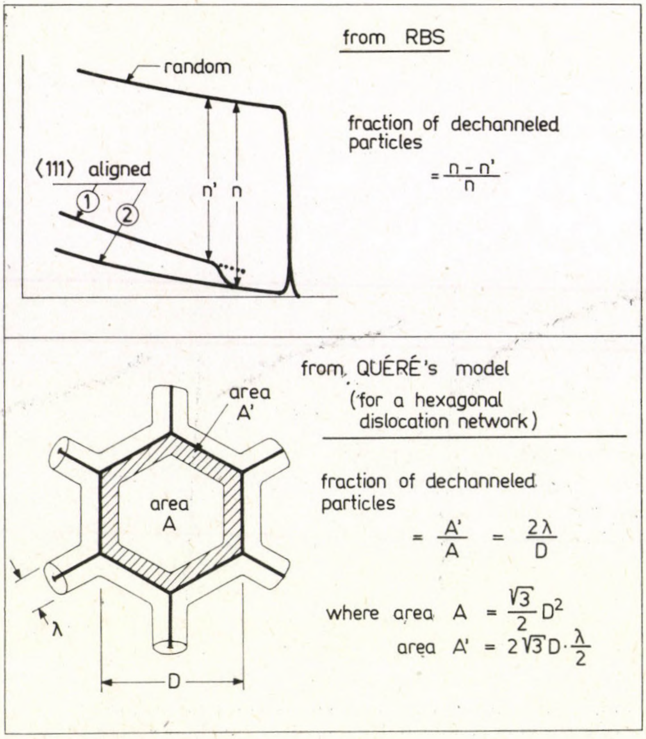

Fig. 9. **Explanation of Fig. 8 by the decrease of "transparency" of the channel in the presence of hexagonal dislocation network proven also by TEM**

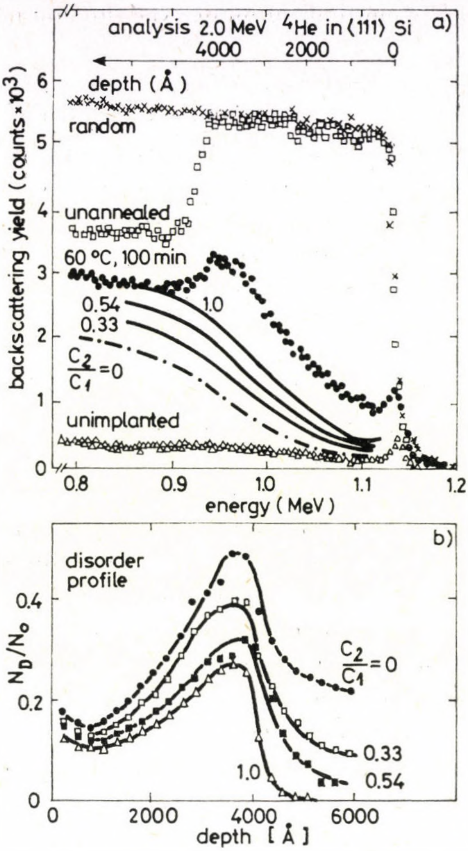

Fig. 10. Extraction of information from BS on twinned regions in silicon (after [13])

Twins manifest themselves through relatively good <511> channelling, as this is the direction of twin-growth in diamond lattice. Distribution of twins was deduced from BS spectra by PRONKO et al (Fig. 10 [13]).

The question is at hand, what can BS do for practical analysis? Of course, transmission electron microscopy (TEM) is the method to detect individual defects. However, TEM needs laborious sample preparation and it is destructive. BS gives in a relatively short time an overview about the depth distribution and nature of defects. Its non-destructiveness may also be important.

There are other analytical methods, which need help from BS. The SIMS and Auger profiling may be subject to artefacts due to selective sputtering. The BS, being based on first principles, is a natural tool to check sputtering.

Results by optimalization of experimental conditions

The choice of the proper *bombarding particle* may increase the sensitivity of BS. DEARNALEY et al [14] analyzed carbon substrates with sputtered-on heavy metals from a Tokamak wall. It turned out that a 3 MeV $^{14}N^+$ BS analysis is an absolute and the most sensitive method for this type of problems: sub-monolayer coverage of a light substrate. The total number of heavy metal atoms involved in the analysis was about 10^9.

An example for *optimum energy* is the 3.05 MeV resonant scattering of He^+ ions on oxygen atoms [15, 16]. A BS analysis at this energy has an almost 20-fold increase in sensitivity for oxygen. Composition of "native" oxides, say, on GaP can be studied this way (Fig. 11, [17]). By stepwise changing the acceleration energy, the depth distribution of oxygen can be measured. This technique can be applied, in general, for analytical applications of resonant nuclear reactions, say, of $(p\gamma)$, $(p\alpha)$, (dp) type.

Optimum geometry may increase depth resolution. WILLIAMS [18] proposed a glancing angle geometry for both beam-in and beam-out case improving depth resolution to about 2 nm. In this case channelling studies are not possible (at least not axial channelling). In a version by MEZEY et al [19] and WILLIAMS [20], only the detector was tilted to glancing angles. This way channelled incidence is possible with all benefits and the depth resolution is still good, about 4 nm. Fig. 12 shows a comparison of "regular" BS (top) and "tilted-detector" BS (bottom) on an antimony-implanted sample. The extended depth scale for the latter case gives better distribution of displaced Si-atoms.

Focussing of the analyzing beam "microbeam" is also a challenging area, especially in a world keen on microelectronics. Focussing is rather simple

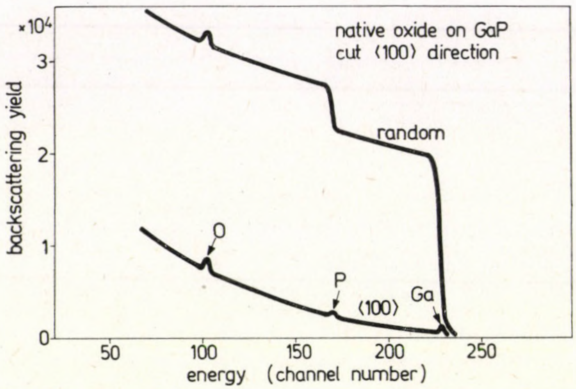

Fig. 11. Native oxide on GaP. Peaks marked with arrow show the three elements in the surface layer. Comparison of areas gives chemical composition

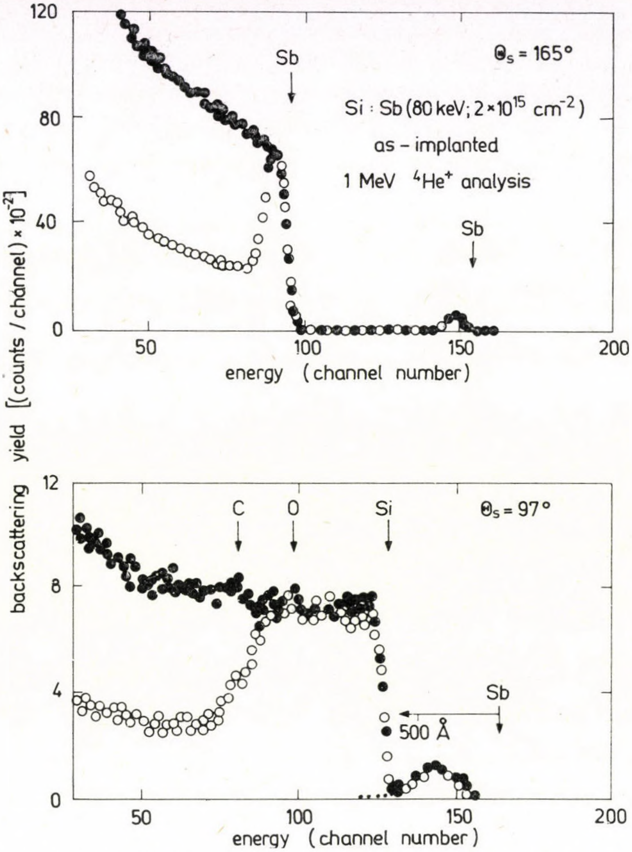

Fig. 12. Comparison of "regular" BS and "tilted-detector" geometry. Note the expansion of the depth scale and enhanced sensitivity to surface impurities (C and O).

to 10—15μm, but 1—2 μm is possible, e. g. [21]. As ion beam exposure of lithography resist layers is a field of growing interest, microbeam facilities may also get a push from that side.

In summary, BS made a remarkable progress in the field of defect and surface studies through the better understanding of the channelling effect. Optimalized experimental conditions led to improved "chemical", depth and lateral resolution. The built-in calibration of both concentration and depth scales is very useful to help sensitive, but less quantitative methods, as SIMS and Auger profiling.

REFERENCES

1. W.-K. Chu, J. W. Mayer and N. A. Nicolet, Backscattering Spectrometry, Academic Press, N. Y. 1978.
2. J. L. Merz, D. W. Mingay, W. M. Augustinyak and L. C. Feldman, Ion Implantation in Semiconductors Eds. I. Ruge and J. Graul, Springer, Berlin, 1971, p. 182.

3. L. Csepregi, W.-K. Chu, H. Müller, J. W. Mayer and T. W. Sigmon, Rad. Effects, **28**, 227, 1976.
4. J. A. Davies, O. T. Jackson, J. B. Mitchell, P. R. Norton and R. L. Tapping, Nucl. Instr. Meth., **132**, 609, 1976.
5. H. Müller, W.-K. Chu, J. Gyulai, J. W. Mayer, T. W. Sigmon and T. R. Cass, Appl. Phys. Letters, **26**, 292, 1975.
6. E. g. L. Csepregi, J. W. Mayer and T. W. Sigmon, Appl. Phys. Letters, **29**, 93, 1976.
7. S. S. Lau, S. Matteson, J. W. Mayer, P. Revesz, J. Gyulai, J. Roth, T. W. Sigmon and T. R. Cass, Appl. Phys. Letters, **34**, 76, 1979.
8. M. E. Roulet, P. Schwob, I. Golecki and M. A. Nicolet, Electronic Lett., **15**, 527, 1979.
9. Y. Quéré, J. Nucl. Mater., **53**, 262, 1974.
10. G. Foti, S. T. Picraux, S. U. Campisano, E. Rimini and R. A. Kant, Ion Implantation in Semiconductors (Eds. F. Chernow, J. A. Borders, D. K. Brice) Plenum, 1972, p. 247.
11. W. F. Tseng, J. Gyulai, S. S. Lau, J. Roth, T. Koji, and J. W. Mayer, Nucl. Instr. Meth., **149**, 615, 1978.
12. S. U. Campisano, G. Foti, E. Rimini and S. T. Picraux, Nucl. Instr. Meth., **149**, 615, 1978.
13. P. P. Pronko, M. D. Rechtin, G. Foti, L. Csepregi, E. F. Kennedy and J. W. Mayer, Ion Implantation in Semiconductors, Eds. F. Chernow, J. A. Borders, D. K. Brice, Plenum, N.Y., 1972, p. 503.
14. G. Dearnaley, G. M. McCracken, J. F. Turner and J. Vince, Nucl. Instr. Meth., **149**, 253, 1978.
15. L. Keszthelyi, I. Demeter, G. Mezey, Z. Szőkefalvi-Nagy and L. Varga, Int. Conf. on Ion Implantation, Rossendorf, 1972, ZfK—236, p. 111.
16. G. Mezey, J. Gyulai, T. Nagy, E. Kotai and A. Manuba, Proc. Int. Conf. on Ion Beam Analysis (Eds. O. Meyer, G. Linker, F. Kappeler) Plenum, N. Y. 1976, p. 303.
17. G. Mezey, T. Nagy, J. Gyulai, E. Kotai, T. Lohner and M. Somogyi, Thin Solid Films, **43**, L23, 1977.
18. J. S. Williams, Nucl. Instr. Meth., **126**, 205, 1975.
19. G. Mezey, E. Kotai, T. Lohner, T. Nagy, J. Gyulai, and A. Manuaba, Nucl. Instr. Meth., **149**, 253, 1978.
20. J. S. Williams, Nucl. Instr. Meth., **149**, 207, 1978.
21. C. R. Allen, G. Dearnaley and N. E. W. Hartley, Proc. Int. Conf. on Ion Beam Analysis (Eds. O. Meyer, G. Linker, F. Kappeler) Plenum, N. Y., 1976, p. 901.

Acta Physica Academiae Scientiarum Hungaricae, Tomus 49 (1—3), p. 67 (1980)

PHYSICS AND TECHNOLOGY OF VACUUM IN FUSION EXPERIMENTS

By

W. P. POSCHENRIEDER

MAX PLANCK INSTITUTE FOR PLASMA PHYSICS, ASSOCIATION EURATOM-IPP
8046 GARCHING, FRG

Abstract

The generation of proper vacuum conditions in a fusion reactor with magnetic confinement represents a challenging task for vacuum technology. Starting from rather elementary physical considerations a certain frame of specifications for the vacuum outline of a reactor as envisaged today will be derived. But uncertainties originating from still incomplete knowledge of important details in plasma behaviour — e. g. plasma confinement of Helium —render it impossible to gain all necessary data. The vacuum technology of a plasma experiment — typical for present day machines — will be discussed briefly and compared with a somewhat deliberately selected reactor design to show the enormous increase in complexity, caused, last but not least, by the handling of tritium in the vacuum system, and by the neutron activation of structural vacuum components.

LITERATURE RELEVANT TO THIS SUBJECT

D. PFIRSCH, Physikalische Blätter, **32,** 651, 1976.
H. W. DRAWIN, Physikalische Blätter, **35,** 119 and 150, 1979.
W. POSCHENRIEDER, Proceedings of V Congresso Italiano Del Vuoto, Perugia, AIV, Milan, 199, 1975.
F. ENGELMANN and A. NOCENTINI, Comments on Plasma Phys. and Controlled Nucl. Fusion (in publication)
INTOR, Draft Final Report, IAEA, Vienna, EUR FU BRU IXII (501/79) EDV 80
L. A. ARTSIMOVICH, Controlled Thermonuclear Reactions, Gordon and Breach Science Publishers, New York, 1964.
A number of papers are also found in:
Proceedings 6th Intern. Vac. Congr. Jap. Journ. Appl. Phys. Supplement 2, Part 1 217—239, 1974.
Proceedings 7th Intern. Vac. Congr. Dobrozemsky et al. Publishers, Vienna, Austria, Section 1.16, 1977.

A paper with similar scope as presented at the Conference is intended for publication in J. Vac. Sci. Technol.

Acta Physica Academiae Scientiarum Hungaricae, Tomus 49 (1—3), p. 69 (1980)

ATOMIC SCATTERING FROM SINGLE CRYSTAL SURFACES

By

H. WILSCH

PHYSICAL INSTITUTE, UNIVERSITY OF ERLANGEN—NÜRNBERG, D-8520 ERLANGEN, FRG

Abstract

Scattering of neutral atoms and molecules with thermal energy from single crystal surfaces has born out in the last years many interesting results. Especially if diffraction is observed, important details of the gas atom—crystal surface interaction potential become experimentally accessible and permit generalized quantitative knowledge on physisorption. Atomic scattering also allows the investigation of thermal properties of surface atoms and of structural problems of the topmost surface layer. Examples of atomic scattering results from ionic crystals, semiconductors, and metal surfaces with ordered absorbates are discussed.

REFERENCES

H. WILSCH, in Topics in Surface Chemistry, Ed. E. Kay and P. S. Bagus, Plenum Publishing Corporation, New York, 1978, p. 135.

H. HOINKES, Habilitationsschrift, Erlagen 1980; Rev Mod. Phys., **52**, issue 4, 1980.

H. FRANK, H. HOINKES and H. WILSCH, Surface Sci., **63**, 121, 1977.

H. HOINKES, H. NAHR and H. WILSCH, Surface Sci., **33**, 516, 1972.

H. FRANK, H. HOINKES and H. WILSCH, Surface Sci., **64**, 362, 1977.

M. J. CARDILLO and G. E. BECKER, Phys. Rev. Lett., **42**, 508, 1979.

K. H. RIEDER and T. ENGEL, Phys. Rev. Lett., **43**, 373, 1979.

Acta Physica Academiae Scientiarum Hungaricae, Tomus 49 (1—3), pp. 71—73 (1980)

ELECTRON AND PHOTON STIMULATED DESORPTION — ESTABLISHED FACTS AND RECENT DEVELOPMENTS

By

D. Menzel

INSTITUTE FOR SOLID STATE PHYSICS, PHYSICS DEPARTMENT OF TU MÜNCHEN
D-8046 GARCHING, FRG

Extended Abstract

Electron Stimulated Desorption (ESD), the liberation of ions and neutrals from adsorption layers by bombardment with slow electrons, has been studied in detail for the last 15 years (for a review of older work see [1] and the literature given therein). Up to recently, most findings were explained in terms of the Redhead—Menzel—Gomer (RMG) mechanism, which assumes a primary valence excitation with cross section comparable to those of excitation and ionization of corresponding isolated molecules, followed by de-exciting recapture processes of the outgoing desorbing particle for which the probability is generally high for metal surfaces (most investigations so far were done on such surfaces) but strongly variable depending on the type and strength of the bond. This mechanism explains many observed characteristics, for instance the generally low cross sections, their strong variation between different adsorption states of the same particle on the same surface and, in particular, the isotope effect which can be extremely high (e. g. a factor of 150 for H/D on W(100) [2]). Brenig [3] has given a quantum mechanical version of this mechanism. Last year Knotek and Feibelman [4] have proposed another mechanism for ionic surfaces (where RMG would not be expected to work): core level ionization followed by Auger decay. For maximum valence oxides where the metal ions do not retain any valence electrons and the latter all reside on the O^{2-} ions, the first step is supposed to be mainly ionization of high lying metal core electrons and the second step interatomic Auger decay which transfer up to three electrons from O^{2-} to the metal ions. The proof consists in strong secondary thresholds for O^+ desorption found at the *metal* core energies (besides a weak one at the 0(2s) energy). We have shown [5] that such secondary thresholds can also be found for O/W(100) for an adsorption state which can be assumed to be oxidic. More importantly, we have shown more recently [6] that *adsorbate* core excitation of covalently bound CO on W leads to ion desorption as evidenced by secondary thresholds. The explanation is also Auger decay of primary core excitations which leads to charge accumulation in the bonding region and to "Coulombic explosion" [7] of the adsorbate complex.

Photon Induced Desorption (PSD), the corresponding process induced by primary photoexcitation [8], is a controversial subject, as it has not been completely clear in many instances whether the observed effects are due to thermal processes (for neutral desorption at low energies) or, where this is no problem (for ion desorption at high photon energies) whether the effects are due to ESD by secondary or photoelectrons [9] or to real primary photoeffects. The proof for the latter was possible for CO/W(100) [6]. For oxides and similar surfaces, KNOTEK has shown that his mechanism also works with photons [10]; it should be usable for a very surface-specific type of EXAFS [11]. This possibility as well as another application has been envisaged also for adsorbate core excitation [6].

On the side of applications, ESD had been used to monitor the concentrations of particular surface species (for examples see [1]), and to deduce structural information [12]. In recent years, the application of ESDIAD (Electron Stimulated Desorption Ion Angular Distributions [13]) for the elucidation of geometrical information on the adsorbate has become more widespread. As an example, we have deduced recently from such measurements that part of the molecular CO layer on W(100) is oriented nonvertically on the surface [14]. Somewhat similar results on CO/Mo(100) have been interpreted very differently, namely as expression of the vibrational distribution of the adsorbate [15]. The contribution of the latter, as well as of other effects, to the angular widths of ESDIAD peaks is not yet completely clear at present [16].

For practical purposes, the extremely strong dependence of ESD and PSD cross section on surface conditions and the strong changes often induced by very small amounts of impurities are most noteworthy, albeit in a negative sense, as they make a prediction of the ESD and PSD properties of a practical surface virtually impossible. These characteristics are understandable in terms of both the RMG and the KF (or other Auger) mechanisms and can be attributed to the contributions of minority species in ESD and PSD.

REFERENCES

1. D. MENZEL, Surface Sci., **47**, 370, 1975.
2. W. JELEND and D. MENZEL, Chem. Phys. Lett., **21**, 178, 1973.
3. W. BRENIG, Proc. 7th IVC and 3rd ICSS, Vienna, 1977, p. 719.
4. M. L. KNOTEK and P. J. FEIBELMAN, Phys. Rev. Lett., **40**, 964, 1978.
   P. J. FEIBELMAN and M. L. KNOTEK, Phys. Rev., B **18**, 6571, 1978.
5. W. KIRSCHNER, D. MENZEL and P. STAIB, Surface Sci., **87**, L 267, 1979.
6. R. FRANCHY and D. MENZEL, Phys. Rev. Lett., **43**, 865, 1979.
7. See, e. g. T. A. CARLSON and M. O. KRAUSE, J. Chem. Phys., **56**, 3206, 1972.
8. See, e. g. D. LICHTMAN and Y. SHAPIRA, CRC. Crit. Rev. Solid State Met. Sci., **7**, 167, 1978.

9. R. Franchy and D. Menzel, Proc. 7th IVC and 3rd ICSS, Vienna, 1977, p. 1209.
10. M. L. Knotek, V. O. Jones and V. Rehn, Phys. Rev. Lett., **43,** 300, 1979.
11. M. L. Knotek, private communication.
12. R. Jaeger and D. Menzel, Surface Sci., **63,** 232, 1977.
13. J. J. Czyzewski, T. E. Madey and J. T. Yates, Jr., Phys. Rev. Lett., **32,** 777, 1974. T. E. Madey, Surface Sci., **79,** 575, 1979 and references therein.
14. R. Jaeger and D. Menzel, Surface Sci., **93,** 71, 1980.
15. H. Niehus, Surface Sci., in press.
16. R. Jaeger, W. Riedl and D. Menzel, to be published.

Note added in proof: The proposition mentioned above that PSD via core ionization could be used for a very surface-specific EXAFS measurement has very recently been realized for O^+ from O/Mo (100) where it was possible to determine the Mo—Mo distance in the surface (R. Jaeger et al., submitted to Phys. Rev. Lett.).

Acta Physica Academiae Scientiarum Hungaricae, Tomus 49 (1—3), p. 75 (1980)

COMPLEX INVESTIGATION ON Fe (111) AND Cr Ni STAINLESS STEEL (100) SURFACES BY SURFACE ANALYSIS METHODS

By

F. STORBECK

TECHNICAL UNIVERSITY DRESDEN, PHYSICS SECTION, DRESDEN, GDR

Abstract

Results of the investigation of initial states of the oxidation of stainless steel by the methods

- LEED (Low Energy Electron Diffraction)
- AES (Auger Electron Spectroscopy)
- SIMS (Secondary Ion Mass Spectroscopy)
- WFC (Work Function Change)
- ELS (Energy Loss Spectroscopy)

are discussed. The complex use of these methods gives exact information about the structure of the surface layers.

By the same methods the structure of the $p(1\times 1)$ sulphur layer formed on the Fe (111) surface by sulphur segregation during annealing of the monocrystal has been investigated. The comparison of the experimental and theoretical LEED data allows the estimation of the position of the sulphur atoms on the iron (111) surface. The advantage of the combination of different methods in the field of surface science has been demonstrated.

REFERENCES

W. ARABCZYK, H.-J. MÜSSIG and F. STORBECK, phys. stat. sol. (a) **55,** 437, 1979.
W. ARABCZYK and H.-J. MÜSSIG, Thin Solid Films, **34,** 103, 1976.
F. STORBECK, Kristall und Technik, **13,** 331, 1978.
F. STORBECK, Kristall und Technik, **11,** 969, 1976.
B. ADOLPHI and H.-J. MÜSSIG, Kristall und Technik, **133,** 317, 1978.

Acta Physica Academiae Scientiarum Hungaricae, Tomus 49 (1—3), pp. 77—85 (1980)

SURFACE CHEMICAL PHENOMENA INFLUENCING THE GROWTH OF THIN FILMS

By

P. B. Barna, Á. Barna

RESEARCH INSTITUTE FOR TECHNICAL PHYSICS, HUNGARIAN ACADEMY OF SCIENCES
H-1325 BUDAPEST, HUNGARY

and

Z. Paál

INSTITUTE OF ISOTOPES, HUNGARIAN ACADEMY OF SCIENCES,
H-1525 BUDAPEST, HUNGARY

The formation of thin films is discussed by considering the surface chemical interactions taking place between the very active surface of the developing film and the foreign species impinging. The surface structure — steps, kinks, etc. — which represent the sites of films growth are also extremely sensitive to impinging impurities by breaking bonds, developing bonds of precursor state and by contributing to the formation of stable compounds.

The foreign species codeposited in these ways can be built into the lattice or accumulated onto the surface of the growing crystals or amorphous grains developing a surface covering layer.

The formation of vacuum deposited thin films involves the build-up of these films via incorporation of impinging adatoms. This atom-by-atom process takes place on the free surface of the developing film. The structure of this surface is reorganized from time to time during the film formation and it is very open to every influence of the environment. That is the reason why the experiments revealed a high sensitivity of structure, structural changes and properties of the films on the nature and impinging rate of impurity species coming either from the residual gases or from the evaporation sources (targets). Recent results of the chemical analysis carried out by electron beam microprobe, Auger, SIMS or by RBS proved that most of the thin films are more or less contaminated [1—4]. Oxygen and carbon are usually detected in them and the quantity of these contaminants is generally correlated to the different properties of the films.

The superconducting behaviour of Al films is ascribed to the oxide layer covering the grain boundaries [5]. The validity of this hypothesis has been proved by phase contrast imaging of these types of films in the TEM [6]. Alexander and Hoffmann [7] have found a correlation between the average intrinsic stress in vapour deposited Ni films and the concentration of oxygen. Müller et al [8] presented an example how carbon built in can stabilize the structure of Bi films during a heat treatment. The stabilization of amorphous Ge and Si films by incorporated oxygen is also well known [9, 10].

The in situ electronmicroscopic study of the formation of In films carried out by Pócza et al [11] and by Barna [12] discovered that both carbon and oxygen contaminants are accumulated onto the surface of the growing crystals. A layer of these impurities or their compounds covering completely the surface of the growing crystals can develop and stop their growth. Film formation proceeds by new nucleation and growth on the surface of these covered crystals at this growth stage.

The list of these examples could be continued. But instead of this we have to conclude that in spite of the large number of experimental results our knowledge on the mechanisms how these impurity species are deposited and participate in the build up process and in which way they influence the structure, is very limited. To understand these phenomena two problems should be analysed:

1. The adsorption and in given circumstances also the formation of impurity species condensed on the growing film surface;
2. The participation of impurity species in the atom-by-atom building process of the film structure and/or their influence on this process.

A large amount of information and ideas to understand the phenomena mentioned in point 1. are offered by the very detailed and sometimes sophisticated surface studies carried out on static surfaces in the last decade. Some of these can be mentioned also here only to illustrate the large variety of surface chemical interactions studied until now.

A model of a heterogeneous solid surface depicting different possible surface sites considered by the surface scientists [13] is shown in Fig. 1. Active sites represented mainly by geometrical configurations are the monoatomic steps, kinks, step adatoms and terrace vacancies. The very detailed LEED studies discovered the large variety of these configurations which can develop on the different crystallographic faces. This is the reason why the different faces should be characterized by different microchemical activity. It is now also well known that the chemical processes taking place on crystals are

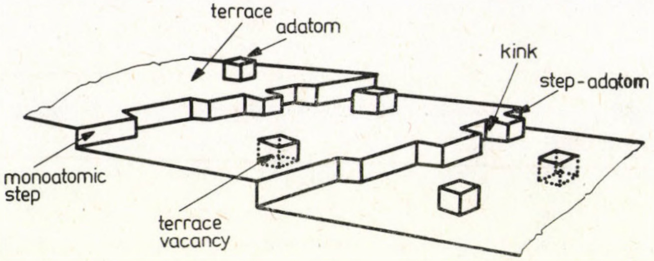

Fig. 1. Model of a heterogeneous solid surface. The different surface sites are characterized by their number of nearest neighbours.

determined both by the kind of materials and by the orientation and actual structure of the crystal faces.

Experiments by Chesters and Somorjai [14] on gold crystal proved the rate of oxidation to be independent of the orientation of the crystal face. These "surface oxides" proved to be very stable. Whereas the crystal faces of different Miller indices showed different adsorption characteristics of hydrocarbons.

The oxygen uptake curves of the (100), (110) and (111) faces of Al crystal measured by Flodström and Martinsson [15] are shown in Fig. 2. The differences in the uptake rates on the different faces can be seen clearly. The LEED studies revealed these adsorbed oxygen layers to be amorphous on (110) and (100) faces, whereas they exhibit a regular structure on the (111) face.

The list of examples can be continued by mentioning the observations that atoms on the steps and kinks are extremely active in splitting chemical bonds of high binding energy such as H—H, C—H and C—C, etc. [13]. Kinks proved to be active in C—C bond breaking, whereas the other two types of bonds may split on steps too [16]. That is why e. g. Somorjai has attributed most of catalytic activities to the existence of such steps. Carbon-containing molecules arriving from the gas phase may form a carbonaceous overlayer which can be ordered or disordered as proved by LEED. Different types of overlayers may exhibit different catalytic activities.

Carbon may also form three dimensional structures on metal catalysts. Fryer and Paál [17] have found spiral graphite whiskers formed on Pt black surface from 1-hexane. The growth of carbon whiskers on Ni surface has been observed by Baker et al [18]. The deposition of columnar and laminar forms

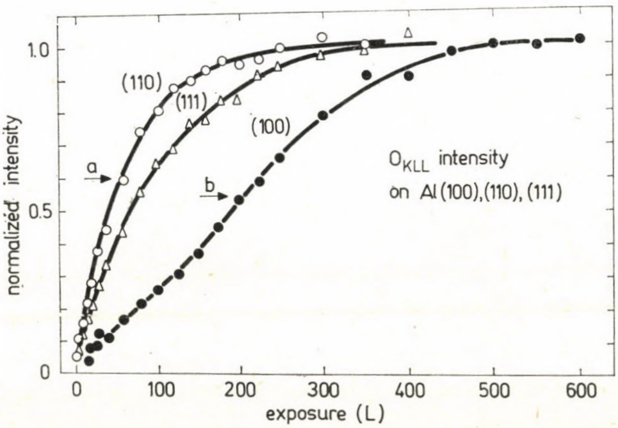

Fig. 2. Intensity change for the O_{KLL} peak on the (100), (110), and (111) crystal faces as a function of oxygen exposure. The disappearence of the LEED pattern from the (110) and (100) faces is indicated by arrows, a and b, respectively [15].

of carbon on polycrystalline Ni foils has been described by Baird [19]. The carbon produced from CO, propane or butadiene may tear off small metal particles from the Ni layer grains. These small particles are built into the three dimensional carbon "fiber" and stimulate its further growth [18].

Another contaminant important for changes of metal catalysts is hydrogen. Baird et al [20] proved that heating platinum black in hydrogen causes sintering at temperatures as low as 500—700 K. Apparently, hydrogen enters the metal lattice and produces its recrystallization. The activation of hydrogen may occur also on steps. The reconstruction of Pt single crystal surfaces under hydrogen adsorption has been also observed. Special attention should be drawn to the fact that monoatomic steps became twice as high under the effect of adsorbed hydrogen as shown by Maire and co-workers [21].

Impurity atoms situated on the surfaces of crystals can influence their behaviour. When crystals of platinum black containing silicon in the range of a few tenths of per cent are heated near to 1200 K, a gradual sintering is observed by in situ electron microscopy (Fig. 3).

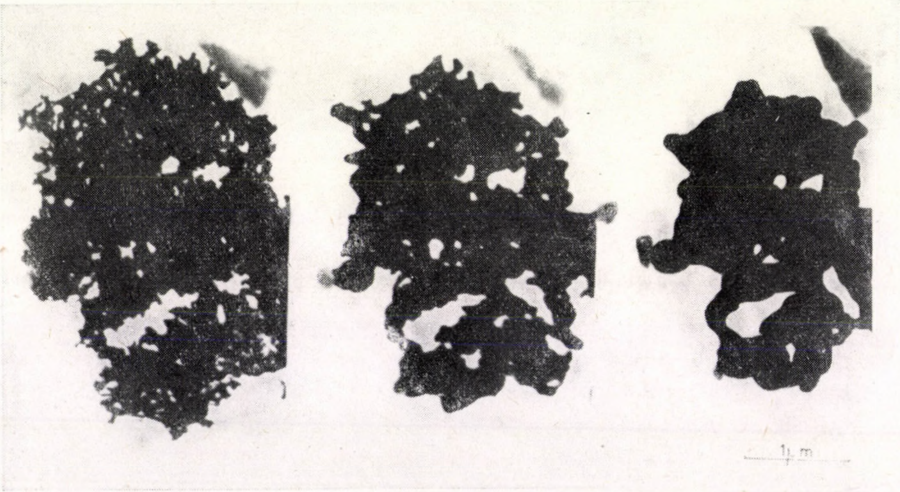

Fig. 3. Gradual sintering of the crystals of platinum black containing Si during a heat treatment at 1200 K

Oxygen adlayers or oxide layers can alter seriously the surface tension of small crystals. This may result in the crystallization of small droplets [22] or in transforming small faceted crystals into globular ones. This oxide layer can hinder the coalescence of contacting grains [23], can change the wetting of substrate and promote the mobility of crystals on the substrate [24]. Platinum particles are "flat" on oxide substrates without oxygen. In the presence of oxygen wetting does not take place and the subsequent breaking up of the particles increases the dispersion [25]. This phenomenon may be extremely important for industrial catalysis. Its importance cannot be denied from the point of view of film formation since it is not indifferent whether the film adheres well to its support or tends to form small globules instead.

Interrupting here the list of examples we may conclude the following:

- Surfaces exhibit special chemical properties correlated to their specific atomic structures.
- Surface studies applying the newest sophisticated methods accumulated already a very important resource of knowledge in this respect, however, our present understanding of these phenomena is very limited.
- From the point of view of film formation, the surface atomic structures (e. g. steps, kinks, etc.) represent the sites of further film growth, they are also extremely sensitive to impinging impurities.
- The very intensive surface studies in progress may add more and more to our knowledge and understanding of real surface structures and the chemical phenomena taking place on them. In this way thin film physics people may search for this kind of information to be applied for the description of their specific systems.

Now we have to come back to our first problem and give some ideas about the phenomena by which the codeposition of impurity species can take place.

First of all it can be understood that the building up process of thin films produces the active elements of surface structure shown in Fig. 1 continuously, both in the case of crystalline and amorphous films. As a consequence of this the first steps of all surface interactions correlating to these active sites take place during the preparation of the films. Phenomena to be considered in this respect are summarized in Table I.

The next point is to give ideas how these impurity species adsorbed can participate in and/or influence the building up process of the atomic systems of thin films. For this purpose we summarize the basic growth processes of thin film formation according to REICHA and BARNA [23], in Table II.

Process A takes place on the substrate surface and is determined mainly by its properties.

Process B represents the growth of grains (growth of crystals or an amorphous network). That process exists practically during the whole period of film preparation. Consequently, the influence of surface interactions should have the strongest influence on this process.

Process C is usually a very short one existing mainly in the case of liquid like coalescence. It is controlled by the orientation and surface conditions of the contacting crystals as well as by the substrate-grain interface energy. Surface properties of contacting surfaces (orientation, coverage) are developed during the grain growth process before coalescence.

Table I

Surface interactions contributing to the participation of impurity species in the building up of films

Phenomena	Species	Sources of species
condensation	e. g. metal, carbon	evaporation source; targets; heated parts of the system
bonding in precursor state	atoms and molecules of gases and vapours	environment; desorption
breaking bonds, formation of fragments to be condensed	molecules of gases and vapours	environment, desorption
formation of stable compounds	atoms or molecules: impinging or bonded in precursor state and fragments	evaporation source; targets; heated parts; environment; desorption

Table II

Basic growth processes of thin film formation

Process	takes place
A Nucleation	at the beginning of the condensation and later on the empty substrate surface developing at the contraction during the liquid-like coalescence
B Building up of the structure by an atom-by-atom process — growth of crystal — building up of amorphous network	in the individual grains following the nucleation and liquid-like coalescence in islands and in continuous films — the growth of film perpendicular to the substrate
C Coalescence — liquid-like (contraction) — growth	when the individual crystals/grains become contacted
D Recrystallization, lateral growth of grains	in islands; in continuous films

The lateral growth of grains in the islands or continuous films is influenced by the properties of grain boundaries (low or large angle grain boundary and coverage) developed during the grain growth.

This analysis indicates that the grain growth (crystal lattice or amorphous network) is the process most sensitive to impurities.

Some experimental results on crystalline films will be mentioned in the following to get ideas on the contribution of impurity species in the growth mechanism of atomic structures in films:

— Development of a stable layer of impurities or their compounds covering the surface of crystals partly or completely [11, 12, 23]. These show clearly that some impurity species can be accumulated onto the surface during the growth of these crystals.

— Bunches of growth steps can develop on the surfaces of Al single crystals of thin films in the presence of oxygen [23, 26].

— Crystals of different orientations have different growth morphologies [26].

Based on these results we make some proposals concerning some possible mechanisms [23, 26]:

— Impurity species are bonded in a precursor state at the active sites of surface structures but they can be mobile too.

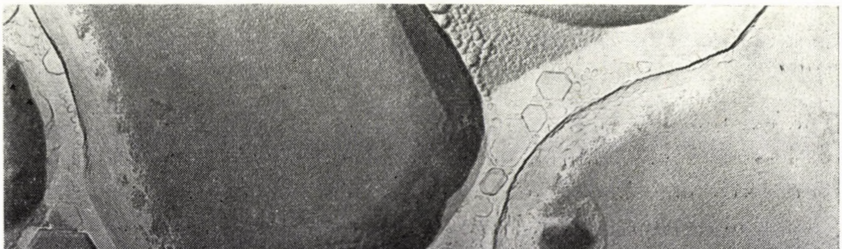

Fig. 4. Al crystal grown epitaxially on mica at 820 K substrate temperature. The edges between (111) planes are destroyed by the developed oxide layer.

— These impurity species can be replaced by the impinging film adatoms.

— Impurity species can be drawn with the moving growth steps in this way and their concentration along the steps increases.

— Reaching a critical concentration, the stable phase of impurities (their compounds) can be nucleated at the active sites of steps.

— A two or three dimensional phase of impurities (compounds) can be developed by the adatoms because the edge of this new phase can be very active for binding the impurity species.

Reicha and Barna [23] explained the formation of bunches of steps and different types of hillocks in Al films in the presence of oxygen, by considering these mechanisms.

The crystal shown in Fig. 4 taken by Reicha and Barna [23] presents an example to illustrate the effect [15] of the different oxygen uptake rates of different crystal faces of Al on the growth morphology. It is clearly shown that the edges between (111) planes are destroyed. The covering layer developed here hindered the growth in this area. The edges between (111) and (100) faces are very sharp.

Conclusion

The existence of active sites on the surface of developing films is — more or less — a precondition of further film growth and at the same time represents extremely active sites where surface chemical processes can take place, i. e. where film growth may be stopped. The separation of these two opposite effects requires further careful considerations and studies as well as a very intensive collaboration of scientists working in surface science and thin film physics.

REFERENCES

1. R. E. Thomas and G. A. Haas, J. Appl. Phys., **43**, 4900, 1972.
2. J. M. Morabito, Thin Solid Films, **19**, 21, 1973.
3. R. E. Thomas and G. A. Haas, J. Appl. Phys., **46**, 963, 1975.
4. G. Nocerino and K. E. Singer, Thin Solid Films, **57**, 343, 1979.
5. P. Tiemann, G. Heim and W. Buckel, Solid State Communication, **27**, 1131, 1979.
6. R. B. Pettit and J. Silcox, J. Appl. Phys., **45**, 2858, 1976.
7. P. M. Alexander and R. W. Hoffman, J. Vac. Sci. Sci. Technol., **13**, 96, 1976.
8. H. Müller, U. Heinevetter, N. Kaiser and C. Gloede, Kristall und Technik, **12**, 695, 1977.
9. S. C. Moss, P. Flinn and L. O. Bauer, Phil. Mag., **27**, 441, 1973.
10. Á. Barna, P. B. Barna, G. Radnóczi, H. Sugawara and P. Thomas, Proc. Conf. on Excitation of Amorphous Solids, (Ed. G. Lucowsky, F. L. Galeener), American Institute of Physics, New York, 1976. p. 199.
11. J. F. Pócza, Á. Barna, I. Pozsgai and G. Radnóczi, Japanese J. Appl. Phys., Suppl. 2, Part 1. 525, 1974.
12. P. B. Barna, Formation Processes of Thin Films Observed by In Situ Electron Microscopy, Ph. D. Thesis, Budapest, 1964.

13. G. A. Somorjai, Advances in Catalysis, (Ed. D. D. Eley, H. Pines and P. B. Weisz), Academic Press, London, 1977. p. 1.
14. M. A. Chesters and G. A. Somorjai, Surface Sci., **52,** 21. 1975.
15. C. W. B. Martinson and S. A. Flodström, Surface Sci., **80,** 306, 1979.
16. D. W. Blakely and G. A. Somorjai, J. Catal., **42,** 181, 1976.
17. J. R. Fryer and Z. Paál, Carbon, **11,** 665, 1973.
18. R. T. K. Baker, M. A. Barber, P. S. Harris, F. S. Feates and R. J. Waite, J. Catal., **26,** 51, 1972.
19. T. Baird, Carbon, **15,** 379, 1977.
20. T. Baird, Z. Paál and S. J. Thomson, J. Chem. Soc., Faraday Trans., I., **69,** 50, 1973; **69,** 1237, 1973.
21. G. Maire, P. Bernhardt, P. Légaré and G. Lindauer, Proc. 7th Int. Vacuum Congr. and 3rd Int. Conf. on Solid Surf., (Ed. R. Dobrozemsky, F. Rüdenauer, F. P. Viehböck and A. Breth), Vienna, 1977. Vol. I. p. 861.
22. Á. Barna, P. B. Barna and J. F. Pócza, J. Vac. Sci. Technol., **6,** 472, 1968.
23. F. M. Reicha and P. B. Barna, this Conference, p. 237.
24. S. Wong, M. Flytzani-Stephanopoulos, M. Chen, T. E. Hutchinson and L. D. Schmidt, J. Vac. Sci. Technol., **14,** 452, 1977.
25. D. W. Blakely and G. A. Somorjai, Surface Sci., **65,** 419, 1977.
26. Á. Barna, P. B. Barna, G. Radnóczi, F. M. Reicha and L. Tóth, Phys. stat. sol., (a) **55,** 427, 1979.

Acta Physica Academiae Scientiarum Hungaricae, Tomus 49 (1—3), pp. 87—91 (1980)

SHORT CONTRIBUTIONS AND POSTERS

SURFACE PHYSICS

SOME PROBLEMS OF QUANTITATIVE AES IN FRACTOGRAPHY

By

G. Gergely

RESEARCH INSTITUTE FOR TECHNICAL PHYSICS, HUNGARIAN ACADEMY OF SCIENCES
H-1325 BUDAPEST, HUNGARY

In general the quantitative Auger electron spectroscopic analysis of metal fracture surfaces is based on elemental sensitivity factors of the components, segregated impurities or second phases. In metallurgical AES studies mostly the PHI Auger Handbook is used, the relative sensitivities being determined on atomic clean metal and semiconductor surfaces, or insulating compounds (e.g. MgO, KCl, CdS, GaP). In the literature, many contradictory data are communicated. In the analysis of segregated films, however (C, S, P etc.), the contribution of backscattering from the fractured metal might be important.

Some problems of fracture analysis on steel and tungsten are discussed, considering the backscattering correction, escape depth and excitation cross sections as well.

The use of elemental sensitivity factors in Auger electron spectroscopy is a widely applied practical approximation [1—6]. A resonable accuracy of surface analysis can be achieved in many cases, under some conditions:

— the energy of Auger peaks (escape depth of Auger electron) is not very different;

— the backscattering excitation can be neglected for elements situated in the neighbourhood in the periodic table;

— Auger emission is produced by atomic transitions (i. e. not KVV or LVV transitions in insulators);

— roughness of the surface can be neglected.

In the analysis of segregated impurities below the monolayer thickness range, considerable discrepancies may occur. Apparently anomalous values or relative sensitivity factors of some segregated (e. g. S) elements have been described in the literature (e. g. [4]).

In the literature of quantitative AES using elemental sensitivity factors, little attention has been paid hitherto to backscattering excitation. After the fundamental works of **Gallon** and coworkers [7], recently **Jablonski** [8] showed the great importance of the backscattering.

In this paper some problems of quantitative AES of segregated impurities on fracture surfaces are discussed. **McMahon** and coworkers published a great number of works on AES studies of steel facture surfaces (e. g. [9]).

Recently, the author and coworkers reported on AES study of tool steel [10], whereas Menyhárd reported on tungsten [11].

In this work analysis is based on the newly published method of Marchut and McMahon [12], improving their accuracy with considering the effect of backscattering excitation. Marchut and McMahon derived some simple equations for the case of two component alloys with X_1 and $X_2 = 1-X_1$ surface composition; associated with I_1 and I_2 Auger peak intensities:

$$\frac{I_1}{I_2} = \frac{P_1}{P_2} \cdot \frac{X_1}{1-X_1} \; \frac{1-k_2}{1-k_1}\,, \tag{1}$$

In Eq. (1) P_1 and P_2 are the Auger yields,

$$k_i = \exp\left(-\frac{L}{0{,}74\,L_i}\right);$$

L is the lattice spacing, L_i denotes the escape depth of Auger electrons. The factor 0.74 in k_1 comes from the 42° collecting angle of the CMA.

In a similar way Marchut derived a simple expression for the case of a surface impurity (I_i) with coverage Θ on a substrate with Auger emission intensity I_1:

$$\frac{I_2}{I_1} = \frac{P_2 \Theta}{P_1\left(\frac{1}{1-k_1} - \Theta\right)} \tag{2}$$

It will be shown in this paper that P_1 and P_2 can be derived from the elemental sensitivity factors, taking into account the backscattering excitation [r_B] comparing the Auger peak heights of two homogeneous samples:

$$\frac{I_1}{I_2} = \frac{P_1}{P_2} \frac{r_{B1}}{r_{B2}} \frac{1-k_2}{1-k_1}\,. \tag{3}$$

Eq. (3) however corresponds to the Auger spectra presented in the PHI Handbook [1]. The ratio P_1/P_2 can be determined for any pair of elements, provided reliable data are available for the escape depth L_i and the backscattering excitation factors. In our Eqs. (1—3) L_i/L denotes the number of atomic layers crossed by escaping Auger electrons. Our analysis is based on the recently published data of LeHéricy [5]. On the other hand, real values of the backscattering factor are rather problematic. Besides of some early experimental data of Smith [7], Goto [13], Vrakking [14] below $E_p = 1{,}5$ keV excitation energy, Jablonski's recent calculations gave considerably higher values. Recently, the backscattering spectra of various elements have been measured in our laboratory [15].

The backscattering coeffients — not identical with the Auger excitation backscattering factors — found in our recent work showed similarity with Everhart's [16] and McAfee's data [17], available unfortunately only below $Z = 32$. For higher Z values, saturation character was observed [16], as found also by Smith [7] on r_B. For this reason, in some cases r_B values where derived by extrapolating Gallon's experimental data [7]. Some results are summarized in Fig. 1 exhibiting also calculated data of Jablonski, for $E_p/E_i = 10$.

It is reasonable to assume that the (Auger excitation) backscattering factor r_B should be proportional to the backscattering coefficient r of the surface. Fitting the experimental r values with Jablonski's data, they are conform below $Z = 26$, but above iron, deviation is increasing with Z. Jablonski made his calculation up to $Z = 46$ (Pd) only for some elements. Supposing the proportionality, in our analysis, the reduced r_B curve was applied. In Fig. 1 experimental points available [7, 14] are also indicated.

The parameters used in our analysis and results are summarized in Table I. The Auger yield ratios are referred to the 703 eV peak of iron [4] for $E_p = 3$ keV excitation energy. The Auger excitation cross sections σ are taken from Vrakking and Mayer [18], but for 3 keV.

$\sigma(E)$ was calculated according to Vrakking for σ_K and Gryzinski [7] for σ_L. In principle, the P_i Auger yield values should be proportional to σ. In a similar

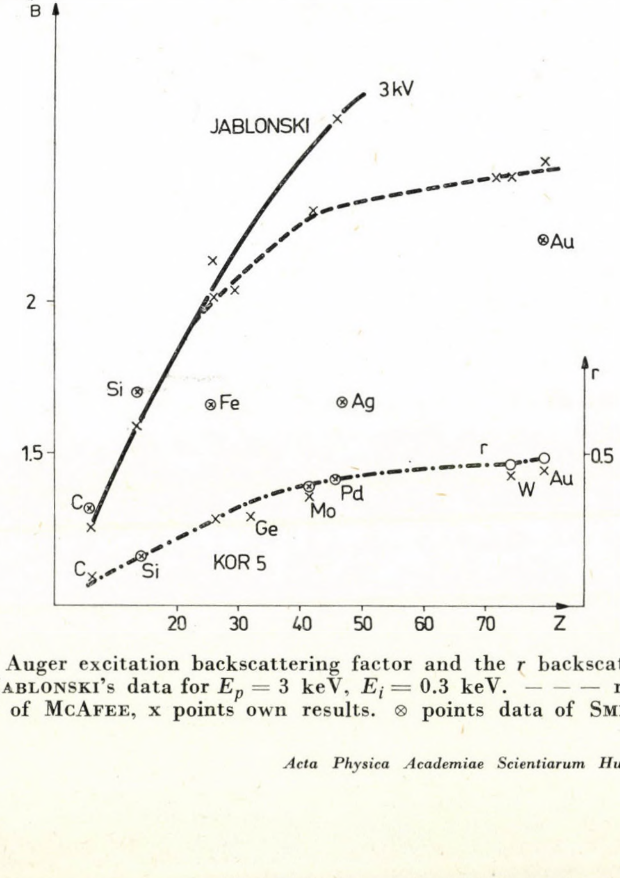

Fig. 1. The r_B Auger excitation backscattering factor and the r backscattering coefficient versus Z —— Jablonski's data for $E_p = 3$ keV, $E_i = 0.3$ keV. — — — reduced r_B curve. —·—·— r, curve of McAfee, x points own results. ⊗ points data of Smith and Gallon

Table I

Numerical values of parameters for AES

Element (compound)	Z	α/α_{Fe} Palmberg	r_{Bi}	L_i/L	σ x10^{-19} cm^2	P_{Fe}/P_i
C	6	2.08	1.21	3.2	0.43	1.1
Si	14	0,58	1.55	1.8	2.1	0.25
P(GaP)	15/23	0.39	1.75	2	1.9	0.208
S(CdS)	16/32	0.35	1.85	2.3	1.6	0.216
K(KCl)	19	0.28	1.64	3.1		0.19
Fe	26	1	1.61	5	0.3	1
W	74	3.04	2.1	2.85		2.43

way, P_i is proportional approximately to the elemental sensitivity factor, neglecting the effect of backscattering. Let us compare data in Table I with experimental calibration data, published in the literature. For this reason, the Auger signal or coverage has to be compared with them. Introducing the backscattering excitation into Eqs. (2):

$$\frac{I_2}{I_1} = \frac{P_2}{P_1} \frac{r_{B21}}{r_{B1}} \frac{\Theta}{\left(\frac{1}{1-k_1} - \Theta\right)} . \tag{4}$$

r_{B1} denotes the backscattering factor of the substrate, whereas r_{B21} denotes the excitation of segregated impurity by the substrate, taking into account the excitation energies. Knowing parameters P_i and r_{B1} Eq. (4) can be used for evaluating Auger spectra of thin surface layers, segregated on grain boundary fractures.

For two impurities with intensities I_2 and I_3 and coverages Θ_2 and Θ_3

$$\frac{I_3}{I_1} = \frac{P_3}{P_1} \cdot \frac{r_{B31}}{r_{B1}} \frac{\Theta_3}{\left(\frac{1}{1-k_1} - \Theta_2 - \Theta_3\right)} . \tag{5}$$

Unfortunately, very few reliable calibration data are available in the literature.

In AES fractography of steel alloys, S, P, and Sb are the most interesting segregating impurities, producing temper embrittlement. For P, Sb and Sn, calibration standards have been studied by MARCHUT [13]. Calculating I_2/I_1 for $\Theta = 0{,}1$ phosphorus with Eq. (4) gives 0.54, instead of 0.30 found by MARCHUT. The discrepancy can be explained by the inadequacy of $\alpha = 0.55$ elemental sensitivity factor of P, determined on GaP. GaP is a semiconductor crystal of high perfection, possibly providing a higher mean free path (escape depth) of Auger electrons, as given by the 'immaterial'' standard curve. It should be emphasized that in LeHéricy's recent paper experimental points are widely scattered around the standard curve. The discrepancy of the α of phosphorus also occurs, comparing its σ excitation cross section with that of Si. The author is not aware of reliable calibration data of S on Fe, but α and σ of S are similar to those of P. Regarding the case of potassium on tungsten, quantitative data are given by Thomas and Haas [19]. For $\Theta = 0.5$ Eq. (4) gives 6.1, instead of 2.5 [19]. The ratio of elemental sensitivity factors of K and W makes 27. Even with our corrections in Table I, this ratio is 12.8. The discrepancy can be resolved again by the high escape depth of Auger electrons in KCl, a highly perfect insulator crystal, as found by Battye and coworkers [20] on alkali halide crystals. Summarizing the results of this analysis, the evaluation of Auger spectra obtained on fracture surfaces needs extreme care. In case of segregated P or S, or K on W (surface diffusion, as found by Menyhárd), the simple use of elemental sensitivity factors is hardly justified.

Acknowledgement

Author is expressing his sincere thanks to Professor McMahon for kindly sending his preprint, quoted in this paper.

REFERENCES

1. P. W. Palmberg, G. E. Riach, R. E. Weber and N. C. MacDonald, Handbook of Auger electron spectroscopy, Physical Electronics, 1973.
2. C. C. Chang, Surface Sci., **48,** 9, 1975.
3. J. M. Morabito, Surface Sci. **49,** 318, 1975.
4. F. Pons, J. LeHéricy, and J. P. Langeron, J. Microsc. Spectroscop. Electron, **2,** 49, 1977; Surface Sci., **69,** 565, 547, 1977.
5. J. LeHéricy, Spectrométrie Auger, 19—23 mars 1979. Les Arcs, Le vide, les couches minces, Numéro spécial, mars 1979, 307.
6. W. Färber, J. Vac. Sci. Technol., **15,** 1139, 1978.
7. T. E. Gallon, J. Phys. D. (Appl. Phys.), **5,** 822, 1972,
   D. M. Smith and T. E. Gallon, J. Phys. D. (Appl. Phys.), **7,** 151, 1974.
8. A. Jablonski, Surface Sci., **74,** 621, 1978.
9. H. Ohtani, H. C. Feng, C. J. McMahon Jr, and R. A. Mulford, Met. Trans., **7A,** 87, 1133, 1976;
   T. Ogura, C. J. McMahon, Jr. H. C. Feng and V. Vitek, Acta Met., **26,** 1317, 1978.
10. K. Romhányi, Zs. Szász-Csih, G. Gergely, M. Menyhárd, Kristall und Technik **4,** 471, 1980.
11. M. Menyhárd, Proc. Conf. Surface Analysis 79, Karlovy Vary, 1979. Ed.: D. Stulik, Skoda, Plzen, 38, 1979.
12. L. Marchut and C. J. McMahon, Jr., Electron and Positron Spectroscopies in Materials Science and Engineering, ed. O. Buck et al., Academic Press, 1979. p. 183.
13. K. Goto, K. Ishikawa, T. Koshikawa and R. Shimizu, Surface Sci., **47,** 477, 1975.
14. J. J. Vrakking and F. Meyer, Surface Sci., **47,** 50, 1975.
15. G. Gergely, B. Gruzza and M. Menyhárd, Acta Phys. Hung. **48,** 337, 1980.
16. T. E. Everhart, J. Appl. Phys., **31,** 1483, 1960.
17. W. S. McAfee, J. Appl. Phys., **47,** 1179, 1976.
18. J. J. Vrakking and F. Meyer, Phys. Rev., **A9,** 1932, 1974.
19. S. Thomas and T. W. Haas, J. Vac. Sci. Technol., **10,** 218, 1973.
20. F. L. Battye, J. Liesegang, R. C. G. Leckey and J. G. Jenkin, Phys. Rev., **B13,** 2646, 1976.

Acta Physica Academiae Scientiarum Hungaricae, Tomus 49 (1—3), p. 93 (1980)

XPS-INVESTIGATIONS OF ELECTRODE SURFACES

By

M. F. Ebel

INSTITUTE FOR TECHNICAL PHYSICS, TECHNICAL UNIVERSITY OF VIENNA, AUSTRIA

and

E. Pungor

INSTITUTE FOR GENERAL AND ANALYTICAL CHEMISTRY, TECHNICAL UNIVERSITY
H-1521 BUDAPEST, HUNGARY

Abstract

XPS (X-ray photoelectron spectroscopy) provides information on the surface in a depth of some atoms. This technique has been applied to investigate different kinds of ion-selective electrodes. Preparation of the materials, evaluation of the experimental results and a comparison of physical and chemical behaviour is given.

Acta Physica Academiae Scientiarum Hungaricae, Tomus 49 (1—3), p. 95 (1980)

THE DETERMINATION OF CONCENTRATION MAPS AT SOLID SURFACES FROM DIGITAL SECONDARY ION MICROGRAPHS

By

W. STEIGER and F. G. RÜDENAUER

SGAE, A-1082 VIENNA, AUSTRIA

Abstract

The contrast in secondary ion micrographs of topographically structured surfaces is modified by artifacts (i. e. intensity modulations, not produced by local elemental concentration variations). Elimination of artifact contrast is performed by a quantitative correction procedure applied in each pixel of the digitized ion micrographs. Thus, elemental maps may be produced where the contrast is determined by elemental concentration only. The correction procedure is performed on a PDP-11 minicomputer and requires an average of 0.2 s per pixel. A fast 1-parameter LTE-algorithm is used as a correction routine.

Acta Physica Academiae Scientiarum Hungaricae, Tomus 49 (1—3), p. 97 (1980)

MICROANALYSIS OF SOLIDS WITH A QUADRUPOLE-ION MICROPROBE

By

F. G. RÜDENAUER, W. STEIGER
SGAE, A-1082 VIENNA, AUSTRIA

and

U. KRAUS
LEYBOLD-HERAEUS, COLOGNE, FRG

Abstract

A new scanning ion microprobe is described which uses a quadrupole mass filter for secondary ion mass analysis. Smallest primary spot size is 5 μ, maximum current density for O^+ is 40 mA/cm^2. Applications include the isotopic analysis of Ni, Cr, Fe in small steel grains for burnup determination of nuclear fuel elements, the analysis of corrosion spots on 30 μ Cu wires and the micro-analysis on integrated circuits.

Acta Physica Academiae Scientiarum Hungaricae, Tomus 49 (1—3), p. 99 (1980)

SURFACE SPECTROSCOPY USING AN ATOMIC BEAM OF NEUTRAL ATOMS OF VERY LOW ENERGY

By

E. SEMERAD and E. M. HÖRL

SGAE, RESEARCH CENTER SEIBERSDORF, A-2444 SEIBERSDORF, AUSTRIA

Abstract

By scattering of Ne-atoms of very low energy ($E_{\mathrm{kin}} \sim 2.4$ meV) from the (001) face of a LiF crystal information on the dynamics of gas-surface interactions can be obtained. Structures in the intensity distributions of the specular, of the $(\bar{1}\bar{1})$ and (11) beam caused by bound state resonances are observed. Measurements of the temperature dependence of the specular reflected intensity are reported. From these data a surface Debye temperature for LiF is derived. The application of an appropriate Debye model and corrections due to the finite size of the impinging atoms are discussed. The determination of energy and momentum changes during the scattering process by time of flight measurements should enable us to study the annihilation and creation of surface phonons. At surface tenperatures of $T \sim 100$ K elastic scattering is dominant, but a background of diffuse scattered atoms exists.

Acta Physica Academiae Scientiarum Hungaricae, Tomus 49 (1—3), p. 101 (1980)

CRITICAL INVESTIGATIONS OF THE SECONDARY ION EMISSION OF PURE METALS USING THE PSEUDO-ATOM METHOD

By

J. ANTAL, S. KUGLER and B. ZSIGMOND

INSTITUTE OF PHYSICS, TECHNICAL UNIVERSITY, H-1521 BUDAPEST, HUNGARY

Abstract

The secondary ion emission of 25 metals was investigated by means of one dimensional pseudo-atom model. The computed ionisation probabilities were compared with experimental results which were in the range of 10^{-2}—10^{-6}. The reliability of the input data (work function, Fermi energy, free electron number) was investigated. Varying input data within the experimental limits published the agreement between theoretical and experimental values of the probability of the secondary ion emission was better than one order of magnitude for all metals investigated.

Acta Physica Academiae Scientiarum Hungaricae, Tomus 49 (1—3), pp. 103 (1980)

COMPUTER SIMULATED INVESTIGATIONS ON QUASI-THERMODYNAMICAL DESCRIPTION OF SPUTTERED BEAMS

By

J. ANTAL, L. OROSZ and S. KUGLER

INSTITUTE OF PHYSICS, TECHNICAL UNIVERSITY, H-1521 BUDAPEST, HUNGARY

Abstract

A particle beam source of the energy distribution $f(E) = E(E + E_b)^{-3}$ was simulated (E_b the surface binding energy, emission was described by exponential time distribution) hitting a linear oscillator by given frequency and mass. The means of x^2 of the oscillator were computed.

Acta Physica Academiae Scientiarum Hungaricae, Tomus 49 (1—3), pp. 105—115 (1980)

SECONDARY ION EMISSION OF HOMOGENEOUS ALLOYS

By

M. Riedel

DEPARTMENT OF PHYSICAL CHEMISTRY AND RADIOLOGY, ROLAND EÖTVÖS UNIVERSITY
H-1088 BUDAPEST, HUNGARY

and

J. Antal, S. Kugler

INSTITUTE OF PHYSICS, TECHNICAL UNIVERSITY, H-1521 BUDAPEST, HUNGARY

The secondary ion emission of dilute and concentrated alloys was studied on the basis of the one-dimensional pseudo-atom emission model [5]. The original model was extended to alloys. The computed relative ionization probabilities were compared with experimental results and agreement better than one order of magnitude was found for most alloys.

Introduction

The quantitative and qualitative description of the secondary ion emission of alloys including highly concentrated alloys and that of their components prove to become very interesting theoretically as well as experimentally. Recently, the secondary ion emission due to metals containing only one component has been studied theoretically, and several models have been elaborated [1—7]. A few attempts were made to apply some of these models for dilute many-component alloys [8—16]. Several authors have recently compared experimental results on concentrated alloys with extended versions of the LTE model (Rüdenauer [17], Rodriguez [18], Riedel [19, 20]), of the ASI model (Narusawa [21] and [18—20]) and with some other simple models (Pivin [22], Jiricek [23]), but there is no proper model worked out for concentrated alloys. In this paper, we are going to describe the secondary ion emission of concentrated alloys using the pseudo-atom model [5] and to make a comparison between theoretical and experimental results collected from the literature.

It is well-known that the secondary ion yield depends also on the spatial distribution of different atoms in the bulk. This is the reason why we studied as the simplest case, homogeneous alloys only. The elements from the first row of transition metals easily form homogeneous alloys [24], they have great practical significance and experimental data are known only concerning their alloys.

Table I shows the binary systems investigated. These can be divided into two important groups: Fe- and Ni-based alloys.

Table I

Investigated alloys

Atomic number	Component (1)	Component (2)						
		V	Cr	Mn	Fe	Co	Ni	Cu
23	V				×			
24	Cr				×		×	
25	Mn				×			
26	Fe	×	×	×		×	×	
27	Co				×		×	
28	Ni			×	×	×		×
29	Cu						×	

Theoretical

For pure metals, the probability of a secondary ion emission R^+ can be calculated by the one-dimensional pseudo-atom emission model, which can be written in the following form [5]:

$$R^+ = \left(\frac{1-\beta}{1+\beta}\right)^2, \tag{1}$$

where

$$\beta = \sqrt{\frac{2E_i - \Phi}{E_F + 2E_i \exp(-\lambda r_0)}}\,. \tag{2}$$

E_i is the first ionization energy of the emitted atoms, Φ is the work function, E_F is the Fermi energy and

$$\lambda^2 = 4\pi e^2 N(E_F)\,, \tag{3}$$

$$r_0 = \left(\frac{3}{4\pi\varrho}\right)^{1/3}. \tag{4}$$

$N(F_F)$ is the density of states of electrons at the Fermi energy and ϱ is the atomic density in the bulk.

In the case of alloys Φ, E_F (and λ) depend on the composition which can be expressed by the concentration (c) of one of the components. If E_{ix} means the first ionization energy of the atom, we get

$$R^+(c) = \left(\frac{1-\beta_x(c)}{1+\beta_x(c)}\right)^2, \tag{5}$$

where

$$\beta_x(c) = \sqrt{\frac{2\,E_{ix} - \Phi(c)}{E_F(c) + 2E_{ix}\exp\left(-\lambda(c)\,r_{0x}\right)}} \tag{6}$$

and

$$r_{0x} = \left(\frac{3}{4\pi\varrho}\right)^{1/3}. \tag{7}$$

According to RÜDENAUER's assumption [17], $\Phi\,(c)$ can be approximated by a linear form. Recent experimental data and theoretical calculations confirm its validity in case of several alloys [25—27]. So we used the work functions for alloys as follows:

$$\Phi(c) = c\Phi_1 + (1 - c)\,\Phi_2. \tag{8}$$

The Fermi energy of the bulk was approximated as:

$$E_F(c) - \frac{\hbar^2}{2m}(3\pi^2)^{2/3}\left[n(c)\right]^{2/3}, \tag{9}$$

where

$$n(c) = v_1\,\varrho_1 c + v_2\,\varrho_2(1 - c)\,. \tag{10}$$

v_1, v_2, ϱ_1, ϱ_2 are the valencies and atomic densities of the two components, respectively [41].

Calculations

For calculating the probability of secondary ion emission according to formula (5), the necessary experimental data are: atomic densities, ionization energies, free electron numbers and work functions. The first two of them are well-known, the published data are accurate and correct [28, 29]. The valency of a single atom can be found but this value is not, in all cases, equal to the "free" electron number in metal [30]. There are no reliable data for the latter in the literature. In our calculation we considered the free electron number to be 2 as a most probable value.

There are further doubts concerning the work function of metals. A number of different measured values are available. Therefore, we have calculated the probability of secondary ion emission for every component with the preferred value of the work function [31, 32] and have repeated the calculation with its minimum and maximum value (see Table II). $R^+\,(c)$ has been calculated in the range of 0—100% concentration in 10% steps for each

Table II

Data collected from the literature (see [42])

Element	Ionization energy (eV)	Work function, eV			Atomic density $10^{22}/cm^3$
		preferred	maximum	minimum	
V	6.74	4.21	4.42	3.80	7.12
Cr	6.76	4.54	4.68	3.72	8.33
Mn	7.43	3.97	4.25	3.77	7.93
Fe	7.90	4.40	4.80	3.92	8.49
Co	7.86	4.70	4.09	4.98	8.97
Ni	7.63	4.90	5.34	4.02	9.14
Cu	7.72	4.53	5.26	3.85	8.46

Table III

Probability of secondary ion emission calculated by Eq. (5) concerning dilute alloys (x 10^{-3})

Matrix	Components						
	V	Cr	Mn	Fe	Co	Ni	Cu
V	3.2			0.14			
Cr		7.9		1.5		2.6	
Mn			1.3	0.41			
Fe	7.2	7.6	3.1	1.5	1.7	2.5	
Co				2.7	3.0	4.1	
Ni		12.3		3.4	3.8	5.1	4.3
Cu						2.8	2.2

combination of the preferred, maximum and minimum value of Φ_1 and Φ_2. In the following we are using the values calculated by preferred work functions. The dependence of R^+_{rel} on the work function is indicated in Figs. 1—8 by bars for 3 different concentrations.

Considering the infinitesimally dilute alloys (see Table III) first it seems that the calculated absolute value of probability of secondary ion emission varies in the range of 10^{-2}—10^{-4} in this case. According to the present model when Fe is the solute, the probability depends on the matrix, while in the case of Ni and Co the dependence is not so significant. The calculated probability of element emitted from its own matrix in a dilute alloy does not depend, of course, on the solute of very low concentration, because the above-mentioned approximations are used.

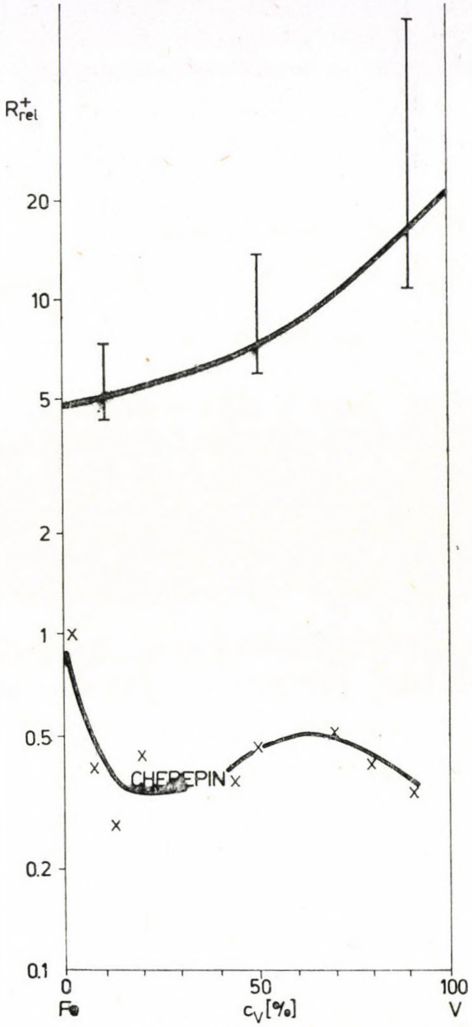

Fig. 1. Relative probabilities of secondary ion emission for Fe-V alloys (Fe is M_1). (Calculated values are denoted by the upper thick line). Experimental data: CHEREPIN [33]

Since all the experimental data published so far for concentrated alloys present only relative ion yields or yields in arbitrary units, the relative ionization probability of both components (R_1^+, R_2^+) in the concentrated alloys is calculated

$$R^+_{\mathrm{rel}}(c) = \frac{R^+_{\mathrm{Me2}}(c)}{R^+_{\mathrm{Me1}}(1-c)} \tag{11}$$

which is used for a comparison with the experimental results.

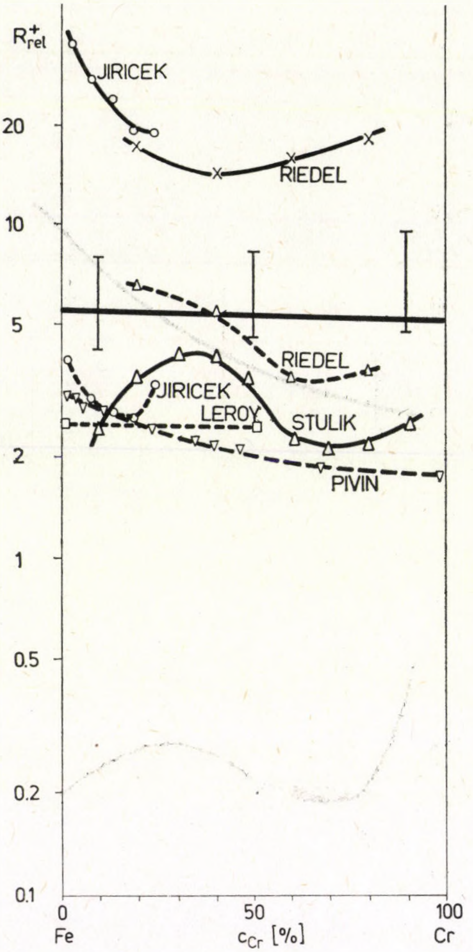

Fig. 2. Measured and calculated relative probabilities for Fe-Cr. Experimental data: JIRICEK [23], RIEDEL [20], LEROY [34], PIVIN [22], STULIK [36]

The computed results and their spread (due to the different values of the work function) are shown (thick full lines) in Figs. 1—8. As function of the concentration, the calculated relative probabilities do not change too much and they generally are of the order of 1.

Discussion

Experimental data for secondary ion emission of concentrated alloys have been collected from the literature. The thin full and dotted lines of Figs. 1—8 are the averages of experimental data for clean and oxidized surfaces,

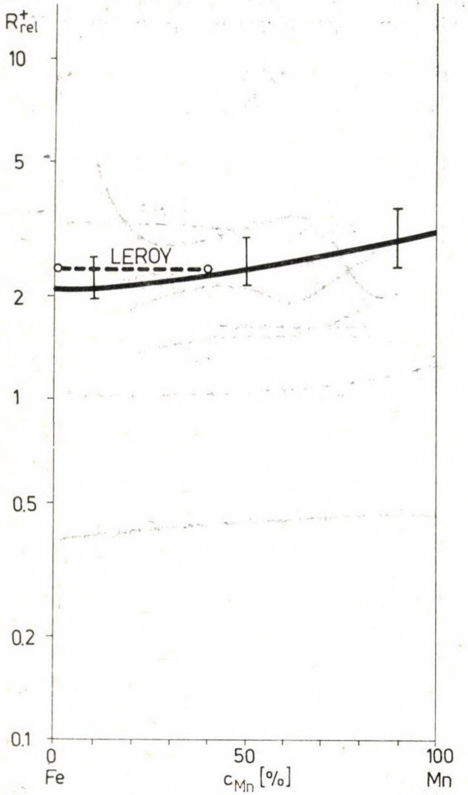

Fig. 3. Calculated and measured (LEROY [34]) relative probabilities for Fe-Mn

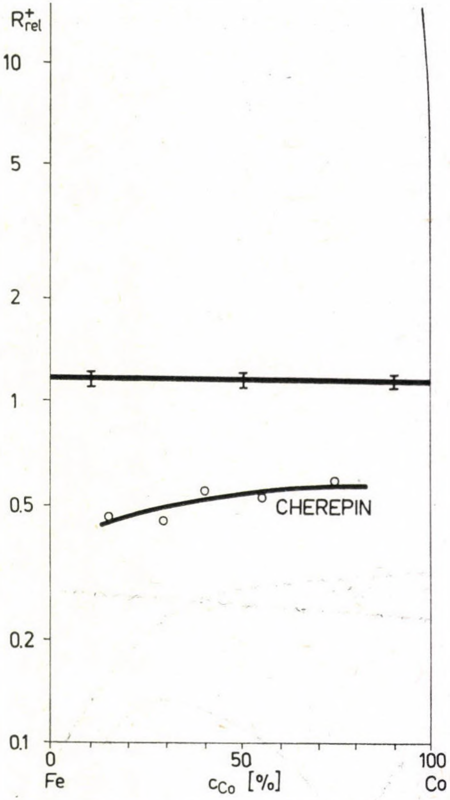

Fig. 4. Calculated and measured (CHEREPIN [33]) relative probabilities for Fe-Co

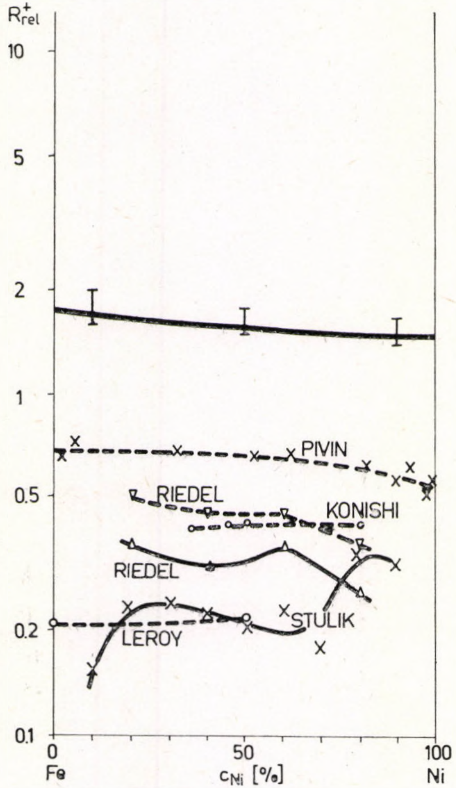

Fig. 5. Measured and calculated relative probabilities for Fe-Ni. Experimental data: LEROY [34], PIVIN [22], RIEDEL [20], KONISHI [35], STULIK [36]

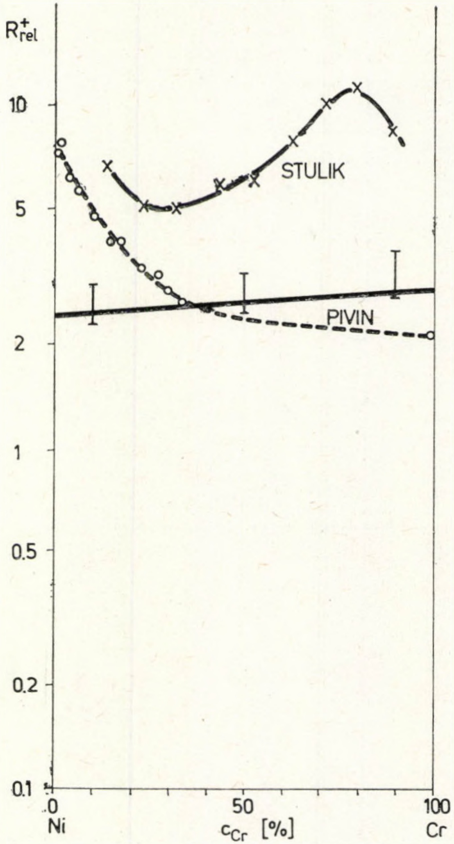

Fig. 6. Calculated and measured relative probabilities for Ni-Cr (STULIK [36], PIVIN [22])

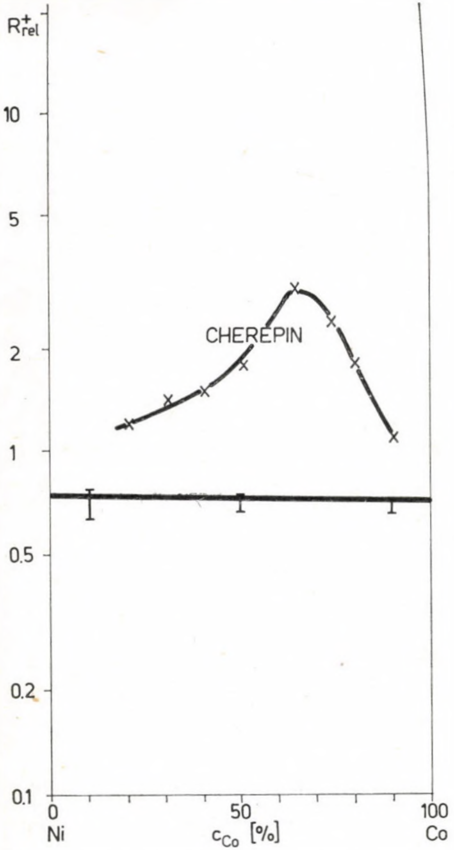

Fig. 7. Calculated and measured (Cherepin [33]) relative probabilities for Ni-Co

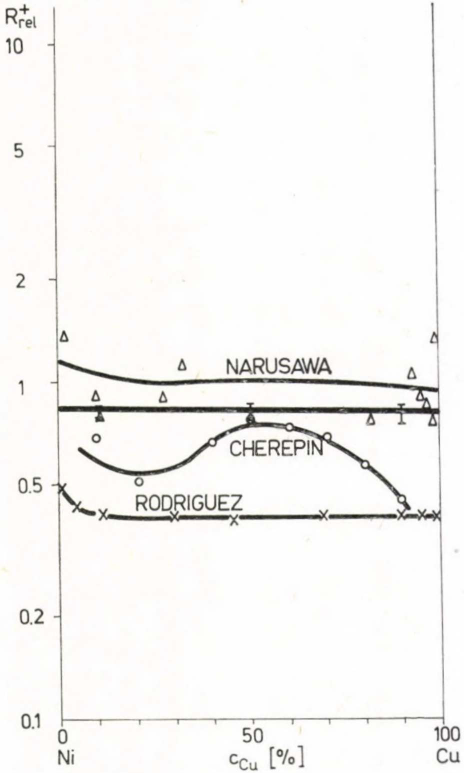

Fig. 8. Measured and calculated relative probabilities for Ni-Cu. Experimental data: Narusawa [21], Cherepin [33], Rodriguez [18]

respectively. The most important parameters of the measurements collected are shown in Table IV. The comparison of the calculated and experimental curves shows that the pseudo-atom model provides good results for Fe—Mn, Fe—Co, Ni—Cu, but the deviation between the theoretical and measured results is larger than one order of magnitude for clean Fe—V. The shapes of curves are, however, rather different in some cases (Fe—Co, Fe—Mn). But we have to mention here that the data measured by different authors are rather scattered as shown in the Figures.

Table IV

Most important parameters of measured data

Author	Pressure (Pa)	Bombarding ion	Current density αA/cm²
Cherepin [33]	10^{-4}	5 KV Ar^+	1000
Leroy [34]	10^{-2}*	O^+	100
Rodriguez [18]	10^{-7}	11 KV Ar^+	1500
Jiricek [23]	—	O^+, Ar^+	—
Riedel [19, 20]	10^{-4}	4 KV Kr^+	2 and 15
Narusawa [21]	10^{-7}	1,5 KV Xe^+	25
Konishi [35]	10^{-3}	12 KV Ar^+	500
Stulik [36]	10^{-4}	3 KV Xe^+	—
Pivin [22]	10^{-3}*	O^+	300

* in oxygen

Even if the correlation is not always good enough, it is remarkable, however, that as far as we know this is the only model at present in which no fitting parameter is needed. The pseudo-atom model in this rough one-dimensional approximation may be rather sensitive to the density of the valence electrons and to the work function. In any case, one should develop a more elaborate model for concentrated alloys and should get more reliable values of the mentioned input data.

The relative degree of ionization is frequently used for analysis by SIMS. One usually assumes that they are more reliable than the absolute values owing to standard errors occurring in the experiments [9, 19]. On the other hand, it is remarkable that the variation of sputtering yield can cause further deviation depending on the concentration within one order of magnitude [37—40].

Acknowledgements

The authors express their thanks to B. Zsigmond for his help in collecting some of the quoted references.

REFERENCES

1. C. A. ANDERSEN and J. R. HINTHORNE, Science, **175,** 853, 1972.
2. Z. JURELA, Int. J. Mass Spectrom. Ion Phys., **12,** 33, 1973.
3. J. M. SCHROEER, Surface Sci., **36,** 485, 1973.
4. Z. ŠROUBEK, Surface Sci., **44,** 47, 1974.
5. J. ANTAL, Phys. Lett., **55A,** 493, 1976.
6. J. ANTAL, VII. Int. Conf. on Atomic Collisions in Solids (Moscow) Publ. House of State Univ. Moscow, **2,** 296, 1977.
7. G. BLAISE, Radiat. Eff., **18,** 235, 1973).
8. P. JOYES, J. Phys. (Paris), **29,** 774, 1968.
9. D. H. SMITH and H. W. CHRISTIE, Int. J. Mass Spectrom. Ion Phys., **26,** 61, 1978.
10. J. M. SCHOEER, J. Vac. Sci. Technol., **14,** 343, 1977.
11. R. SHIMIZU, T. ISHITANI, T. KONDO and H. TAMURA, Anal. Chem., **47,** 1020, 1975.
12. J. SCHELTEN, Z. Naturforsch., **23A,** 109, 1967.
13. G. BLAISE and G. SLODZIAN, J. Phys. (Paris), **35,** 237, 1974,
14. H. E. BESKE, Z. Naturforsch., **22A,** 459, 1967.
15. F. G. RÜDENAUER and W. STEIGERT, Vacuum, **26,** 537, 1976.
16. W. H. GRIES and F. G. RÜDENAUER, Int. J. Mass Spectrom. Ion Phys., **18,** 111, 1975.
17. F. G. RÜDENAUER, W. STEIGER and R. PORTENSCHLAG, Microchim. Acta Suppl., **5,** 421, 1974.
18. H. RODRIGUEZ-MURCIA and H. E. BESKE, Ber. Kernforsch., Jülich No. Jül. 1292, 1976.
19. M. RIEDEL, Thesis for "Candidate of Sciences" Degree, Budapest, 1978. (Hungarian Academy of Sciences.)
20. M. RIEDEL, T. NENADOVIĆ and B. PEROVIĆ, Acta Chim. Acad. Sci. Hung., **97,** 187, 1978.
21. T. NARUSAWA, T. SATAKE and S. KOMIJA, J. Vac. Sci. Technol., **13,** 414, 1976.
22. J. C. PIVIN, C. ROQUES-CARMES and G. SLODZIAN, Int. J. Mass Spectrom. Ion Phys., **26,** 219, 1978.
23. P. JIRICEK, Z. HULEK, J. KRAL, M. SETVAK and G. CHADZITASKOS, Int. Conf. on Ion Beam Modification of Materials, Budapest, Ed: Centr. Ins. Phys. Hung. Acad. Sci. Budapest, 1978.
24. M. HANSEN, Constitution of Binary Alloys, McGraw Hill Co., New York, 1958.
25. R. E. DAVIDSON and S. C. FAIN, J. Vac. Sci. Technol., **13,** 209, 1976.
26. S. C. FAIN and J. M. McDONALD, Phys. Rev. B., **13,** 1853, 1976.
27. S. C. FAIN and J. M. McDONALD, Phys. Rev. B., **9,** 5099, 1974.
28. American Institute of Physics Handbook, ed. by D. E. Gray, 3rd Ed., McGraw-Hill Co., 1972.
29. Handbook of Chemistry and Physics, ed. by Hodgman, CRP Co., Cleveland, 1974.
30. L. S. DARKEN and R. W. GURRY, Physical Chemistry of Metals, McGraw Hill Co., London, 1953.
31. V. S. FOMENKO and I. A. PODCHERNYAYEVA, Emissionnüe i adsorbcionnüe svoystva veschestv i materialov, Atomizdat, Moscow, 1975.
32. H. B. MICHAELSON, J. Appl. Phys., **48,** 4729, 1977.
33. V. T. CHEREPIN and M. A. VASILYEV, Vtorichno ionno-ionnaya emissiya, Naukova Dumka, Kiev, 1975.
34. V. LEROY, J.-P. SERVAIS and L. HABRAKEN, CRM Rep. Liège, No 35. 69, 1973.
35. F. KONISHI, K. KUSAO, Y. YOSHIAOKA and N. NAKAMURA, US-Japan Joint Seminar, Hawaii, 1975, Central Res. Lab. Matsushita Electric Industries Co. Kadoma, Osaka, Japan.
36. P. STULIK, J. SUBA and A. STOPKA, Proc. Conf. Surface Analysis 79., Karlovy Vary, 1979. Ed. P. Stulik, Skoda, Plsen.
37. J. M. POATE, W. L. BROWN, R. HOMER, W. M. AUGUSTINIAK, W. M. MAYER, K. N. TU and F. W. VAN DER WEG, Nucl. Instr. Meth., **139,** 345, 1976.
38. W. FÄBER, G. BETS and P. BRAUN, Nucl. Instr. Meth., **132,** 351, 1976.
39. M. RIEDEL, T. NENADOVIĆ and B. PEROVIĆ, Acta. Chim. Acad. Sci. Hung., **97,** 177, 1978.
40. P. SIGMUND, Phys. Rev., **184,** 383, 1969.
41. M. RIEDEL, J. ANTAL and S. KUGLER, Proc. XXII. Hung. Spectr. Cong., Salgótarján, 1979. p. 171. Ed. Gépipari Tudományos Egyesület, Budapest, 1979.
42. J. ANTAL and S. KUGLER, Acta Phys. Hung., **49,** No. 4, to be published.

Acta Physica Academiae Scientiarum Hungaricae, Tomus 49 (1—3), p. 117 (1980)

ELECTRON ENERGY LOSS SPECTROSCOPY

By

P. BRAUN, G. BETZ and M. ARIAS

INSTITUTE FOR GENERAL PHYSICS, TECHNICAL UNIVERSITY OF VIENNA, VIENNA, AUSTRIA*

Abstract

Determining electron energy losses is of great interest for basic studies of interaction of low energetic electrons with solid surfaces as well as for the interpretation of Auger electron spectra. The primary energies within the range of 100—2000 eV are realizable in commercial Auger electron spectrometers and, therefore, it is possible to measure structures based on electron energy loss processes, i. e. surface and volume-plasmon excitation simultaneously to Auger electron spectroscopy. The applicability of this method is demonstrated on Al and Al-oxide as well as on Ti and Ti-oxide. Consequently, statements on concentration gradients were possible by choosing the primary energy and thereby the information depth.

---

* Address: Institut für Allgemeine Physik der Technischen Universität Wien, 1040 Wien, Österreich

Acta Physica Academiae Scientiarum Hungaricae, Tomus 49 (1—3), pp. 119—125 (1980)

OBERFLÄCHENANREICHERUNG BEIM ZERSTÄUBEN MIT VERSCHIEDENEN IONENENERGIEN

Von

M. Opitz, G. Betz und P. Braun

INSTITUT FÜR ALLGEMEINE PHYSIK, TECHNISCHE UNIVERSITÄT WIEN, WIEN, ÖSTERREICH

Unter Verwendung der Augerelektronen-Spektrometrie wurde an Hand binärer Legierungen durch Ionenbombardment induzierte Oberflächenanreicherung nachgewiesen. Wenn die Massenzahlen der Komponenten nicht sehr unterschiedlich sind, wird im allgemeinen die Komponente mit dem niedrigeren Zerstäubungskoeffizienten an der Oberfläche angereichert. Dies konnte an 13 verschiedenen binären Legierungssystemen demonstriert werden. Die verwendeten Ionen sind Ne^+, Ar^+ und Xe^+ mit 0.5, 2 und 5 keV Energie. Es konnte bei allen Legierungen gezeigt werden, dass mit steigender Ionenenergie die leichtere Komponente verstärkt an der Oberfläche angereichert wird. Dieser Effekt ist unabhängig von der verwendeten Ionenart und ist im Energiebereich von 0.5 bis 2 keV stärker ausgeprägt als zwischen 2 und 5 keV.

1. Problemstellung

Bei allen Methoden zur Analyse von Festkörperoberflächen spielt der Zerstäubungsprozess eine wichtige Rolle. Einerseits werden die zerstäubten Teilchen selbst zur Analyse der Oberfläche herangezogen wie in der Sekundärionenmassenspektrometrie (SIMS), anderseits wird das Zerstäuben in der Augerelektronen-Spektrometrie (AES), Ionenstreuung (ISS), und in der Photoelektronen-Spektrometrie (XPS, UPS) als wichtiges Hilfsmittel zur Probenreinigung, zum Entfernen von Kontaminationsschichten und im allgemeinen zum definierten Abtragen von Schichten zur Messung der chemischen Zusammensetzung als Funktion der Tiefe bei dünnen Schichten verwendet.

Im allgemeinen ist zu erwarten, dass beim Zerstäuben von Legierungen und Verbindungen eine oder mehrere Komponenten an der Oberfläche angereichert werden. Auf Grund der verschiedenen partiellen Zerstäubungsausbeuten der einzelnen Komponenten wird eine Oberfläche geänderter Zusammensetzung entstehen.

Beim Zerstäuben von Mehrstoffsystemen betrachtet man den Gleichgewichtszustand, in dem die Zusammensetzung des abgetragenen Materials gleich der Zusammensetzung des Festkörpers ist. Bei einphasigen Legierungen oder Verbindungen stellt sich nach Abtragen einer Schicht, deren Dicke vergleichbar mit der Eindringtiefe der Primärionen ist, die neue Gleichgewichts-Oberflächenzusammensetzung ein. Danach bleibt bei weiterem Abtragen die Oberfläche mit ungeänderter Zusammensetzung erhalten [1]. Bei mehrphasigen Legierungen, in denen die Komponenten in Form einzelner Kristallite vorliegen, kann die Zeit zum Erreichen des Gleichgewichts wesentlich länger sein, da topographische Änderungen an der Oberfläche wichtig werden [1]. So können zum Beispiel Kristallite mit hohem Zerstäubungskoeffizient rascher abgetragen und ihre Konzentration an der Oberfläche so lange verringert werden, bis die Atome im selben Verhältnis die Oberfläche verlassen, in dem sie im Festkörper vorliegen.

2. Experimentelles

Die Messungen der Oberflächenanreicherung wurden in einem mit einem Zylinderanalysator ausgestatteten kommerziellen Augerelektronen Spektrometer von Physical Electronics durchgeführt. Die Primärenergie der Elektronen lag bei 2 keV bzw. bei 3 keV — je nach untersuchtem Legierungssystem. Der Strahlstrom wurde auf 30 μA konstant gehalten. Der Durchmesser des Elektronenstrahls auf der Probe betrug etwa 200μm. Die Modulationsamplitude betrug für alle Messungen 4 eV_{SS}, die Durchlaufgeschwindigkeit 2 eV/s bei einer Zeitkonstanten von 100 ms. Der Restgasdruck war besser als 6.10^{-8} Pa. Beim Zerstäuben betrug der Edelgaspartialdruck 7.10^{-3} Pa. Die Probenoberflächen wurden jeweils mit Neon, Argon und Xenon bei senkrechtem Einfall zerstäubt. Die verwendeten Ionenenergien betrugen 0.5, 2 und 5 keV, die Ionenstromdichte an der Probenoberfläche lag bei etwa 30 μA/cm^2. Der Durchmesser des Ionenstrahls auf der Probe war etwa 4 mm. Der Ionenstrahl wurde mittels eines Faradaykäfigs so justiert, dass die simultan analysierte Probenstelle in der Mitte des Zerstäubungskraters lag.

3. Ergebnisse

In der vorliegenden Arbeit wurden die in Tab. I angeführten Proben untersucht. Dabei wurde das Signalverhältnis zweier charakteristischer Augerübergänge während des Zerstäubens aufgenommen. Das Verhältnis der für die jeweiligen Elemente charakteristischen Augerübergänge ist ein Mass für die Oberflächenzusammensetzung der untersuchten Legierung. Zerstäubt wurde mit Neon, Argon und Xenon bei Energien von 0.5, 2 und 5 keV.

Es erwies sich, dass bei allen untersuchten Legierungssystemen mit steigender Ionenenergie entweder keine Änderung erfolgte oder eine geringe Vermehrung der leichteren Komponente an der Oberfläche erfolgte. Dieser Effekt konnte mit allen verwendeten Ionenarten festgestellt werden und ist unabhängig davon, welche Komponente beim selektiven Zerstäuben angerei-

Tabelle I

Daten der Proben

System A—B	Probennummer	at% A	at% B	Anzahl der Phasen	Herstellung
Ag—Au	3	20.0	80.0	1	ÖGUSSA
	4	41.0	59.0	1	ÖGUSSA
	6	78.0	12.0	1	ÖGUSSA
Au—Cu	3	56.3	43.7	1	ÖGUSSA
	5	40.0	60.0	1	ÖGUSSA
	6	20.0	80.0	1	ÖGUSSA
Ag—Pd	3	20.0	80.0	1	ÖGUSSA
	4	35.0	65.0	1	ÖGUSSA
	5	50.0	50.0	1	ÖGUSSA
	6	65.0	35.0	1	ÖGUSSA
	7	80.0	20.0	1	ÖGUSSA
Cu—Pd	3	20.0	80.0	1	ÖGUSSA
	5	35.0	65.0	1	ÖGUSSA
	7	60.0	40.0	1	ÖGUSSA
	9	90.0	10.0	1	ÖGUSSA
Au—Pd	3	75.6	24.4	1	ÖGUSSA
	5	55.7	44.3	1	ÖGUSSA
	6	44.8	55.2	1	ÖGUSSA
	7	35.1	64.9	1	ÖGUSSA
Pt—Ni	2	33.8	66.2	1	ÖGUSSA
	4	87.8	12.2	1	ÖGUSSA
Pt—Cu	2	24.6	75.4	1	ÖGUSSA
	4	74.6	25.4	1	ÖGUSSA
Fe—Cr	1	95.0	5.0	1	VEW
	2	84.1	15.9	1	VEW
	3	67.8	32.2	1	VEW
	4	52.4	47.6	1	VEW
	5	22.1	77.9	1	VEW
	6	6.5	93.5	1	VEW
Fe—Ni	1	95.2	4.8	1?	HF-Ofen
	2	90.9	9.1	2	HF-Ofen
	3	80.3	19.7	2	HF-Ofen
	4	70.0	30.0	2	HF-Ofen
	5	62.1	37.9	2	HF-Ofen
	6	52.2	47.8	2	HF-Ofen
	7	38.1	61.9	2	HF-Ofen
	8	25.0	75.0	2?	HF-Ofen
	9	9.8	90.2	2?	HF-Ofen
	10	5.2	94.8	2?	HF-Ofen
Al—Au	1	50.0	50.0	?	HF-Ofen
	2	33.3	66.7	?	HF-Ofen
Al—Ni	AlNi	25.0	75.0	1	HF-Ofen
Al—Fe	AlFe	50.0	50.0	1	HF-Ofen
Al—Cr	AlCr	33.3	66.7	1	HF-Ofen

chert wird. Ebenso konnte keine Abhängigkeit dieses Effektes von der Konzentration der Legierungskomponente gefunden werden. Ausserdem konnte festgestellt werden, dass die Änderungen in der Oberflächenzusammensetzung zwischen 0.5 und 2 keV Ionenenergie wesentlich stärker ausgeprägt waren als zwischen 2 keV und 5 keV Ionenenergie.

In den Abb. 1 und 2 ist der Verlauf der Augerpeakhöhenverhältnisse in Abhängigkeit von der Ionenenergie anhand einiger typischer Proben dargestellt. Der auf der Ordinate mit einem Dreieck (▲) markierte Wert entspricht der Volumenzusammensetzung des Festkörpers.

Wie erwähnt, ist das Verhältnis der partiellen Zerstäubungsausbeuten S_L/S_S für eine Ionenenergie von 500 eV grösser als für 2 keV, wobei L die leichtere Komponente ist. Dies konnte bei allen untersuchten Legierungssystemen und — mit Ausnahme zweier Proben — mit allen verwendeten Gasen (Ne, Ar und Xe) verifiziert werden. In Abb. 3 ist über dem Massenverhältnis der leichteren zur schwereren Komponente $0 \leq M_L/M_S \leq 1$ das Verhältnis von S_L/S_S bei 500 eV zu dem bei 2 keV aufgetragen; Abb. 4 und 5 stellen die entsprechenden Diagramme für Argon bzw. Xenon dar. Bei denjenigen Elementen, bei denen zwei Augerübergänge ausgewertet wurden, wurde jeweils der Mittelwert zur Bildung der Verhältnisse S_L/S_S herangezogen. Durch die lineare Regression ergaben sich die in den Abb. 3—5 eingezeich-

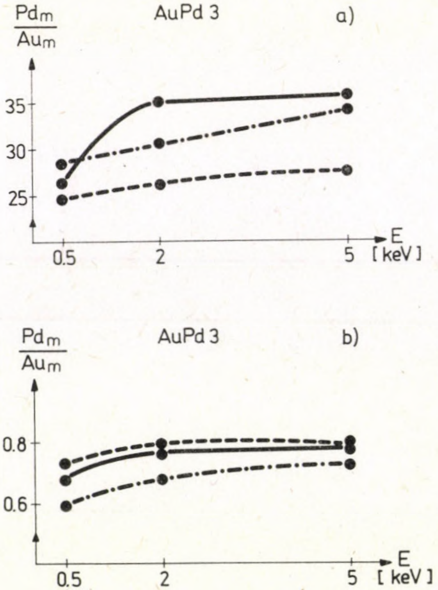

Abb. 1. Verhältnis der gemessenen Augersignale Pd_m (326/330 eV)/Au_m(2024 eV) (a) und Pd_m (326/330eV)/Au_m(69eV) (b) als Funktion der Primärionenenergie für Neon (— —), Argon (— · — · —) und Xenon (——)

neten Geraden. Wie die Analyse zeigt, erfolgt die vermehrte Anreicherung der leichteren Komponente mit steigender Ionenenergie nahezu unabhängig von der Konzentration der Komponenten in der Legierung.

Eine der Ursachen für die Anreicherung ist offenbar der Knock-in-Effekt, der bei höheren Ionenenergien gegenüber niedrigeren stärker ausgeprägt sein dürfte. Dabei werden durch den Beschuss mit Ionen mit Energien

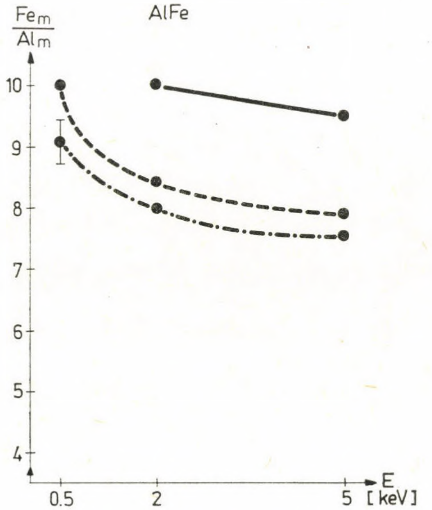

Abb. 2. Verhältnis der gemessenen Augersignale Fe_m (703 eV)/Al_m(1396 eV) als Funktion der Primärionenenergie für Neon (— —), Argon (— · — · —) und Xenon (——)

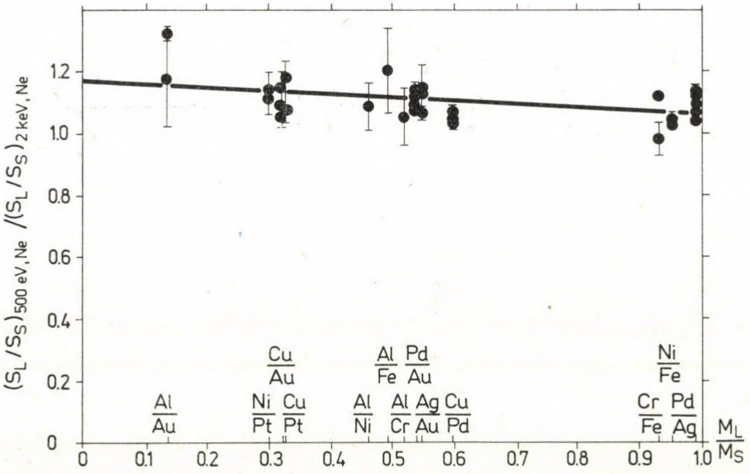

Abb. 3. Änderung des Verhältnisses der partiellen Zerstäubungskoeffizienten S_L/S_S bei Beschuss mit Neonionen von 500 eV und 2k eV in Abhängigkeit vom Massenverhältnis der Legierungspartner

von mehreren keV die schwereren Atome bevorzugt in den Festkörper bis in eine Tiefe eingeschossen, die grösser als die Austrittstiefe der Augerelektronen sein kann [1]. Dabei ist es von untergeordneter Bedeutung, in welcher Konzentration die schwereren Atome vorliegen. Eine weitere Ursache für die Änderung der Oberflächenanreicherung liegt im unterschiedlichen Konzentrationsverlauf in der geänderten Oberflächenschicht als Folge der unterschiedlichen Stosskaskaden bei verschiedenen Primärionenenergien.

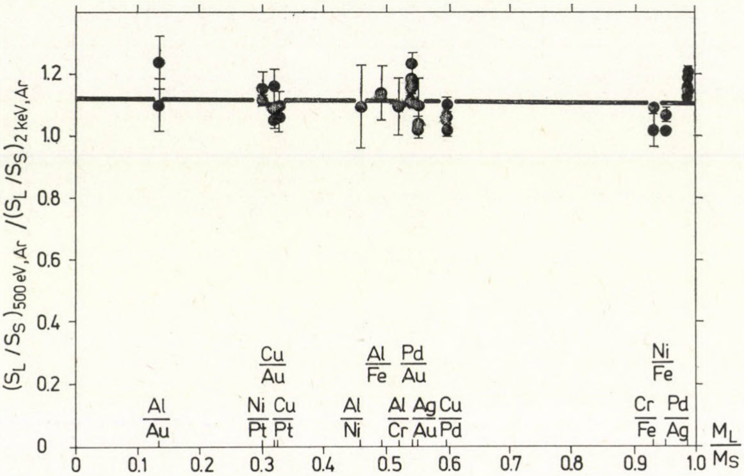

Abb. 4. Änderung des Verhältnisses der partiellen Zerstäubungskoeffizienten S_L/S_S bei Beschuss mit Argonionen von 500 eV und 2 keV in Abhängigkeit vom Massenverhältnis der Legierungspartner

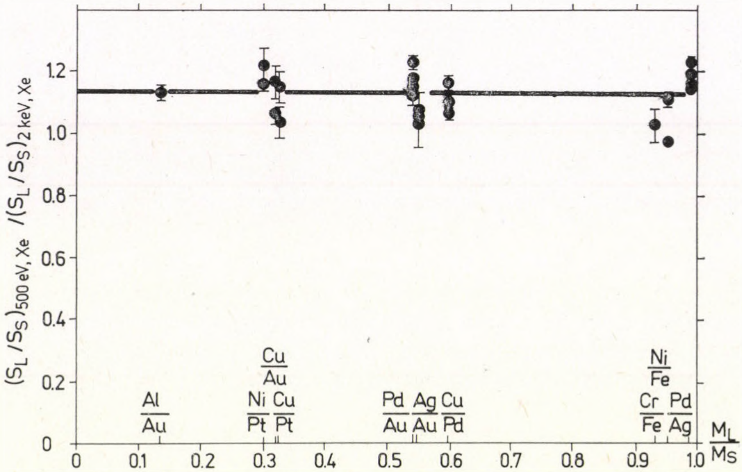

Abb. 5. Änderung des Verhältnisses der partiellen Zerstäubungskoeffizienten S_L/S_S bei Beschuss mit Xenonionen von 500 eV und 2k eV in Abhängigkeit vom Massenverhältnis der Legierungspartner

Tabelle II

Experimentelle Ergebnisse

System A—B	Anreicherung an der Oberfläche von	S_A/S_B (bei 2 keV Ar)	Mit steigender Ionenenergie Zunahme an der Oberfläche von
Ag—Au	Au	1.7 [2]	Ag
Au—Cu	—	1.0 [2]	Cu
Ag—Pd	Pd	2.2—2.7 [3]	Pd
Cu—Pd	Pd	1.5 [3]	Cu
Au—Pd	Pd	1.0—1.4 [3]	Pd
Cu—Pt	Pt	1.6—3.0 [4]	Cu
Ni—Pt	Pt	1.5—1.9 [4]	Ni
Fe—Cr	(Cr)	1.0—1.3 [5]	Cr
Fe—Ni	—	1.0 [5]	Fe
Al—Au	Au	(5.3) [5]	Al
Al—Ni	Ni	1.4 [5]	Al
Al—Fe	Fe	2.2 [5]	Al
Al—Cr	Cr	3.2 [5]	Al

4. Zusammenfassung

Die Oberflächenanreicherung beim Zerstäuben von Zweistoffsystemen in Abhängigkeit von der Ionenenergie und der Masse der Primärionen war Gegenstand von Untersuchungen an Proben aus 13 verschiedenen Binärsystemen. Obwohl im Bereich der verwendeten Ionenenergien von 0.5 bis 5 keV die Änderungen der Oberflächenanreicherung bei Beschuss mit dem Primärionen Ne, Ar und Xe relativ gering sind und oft innerhalb der Messgenauigkeit der Augeranalyse liegen, kann doch generell eine Anreicherung der leichteren Komponente mit steigender Ionenenergie festgestellt werden. Dieser Effekt hängt nicht von der Zusammensetzung der Legierung ab und ist auch von der Grösse des Massenunterschiedes der Legierungspartner unabhängig.

LITERATUR

1. G. K. Wehner in Methods of Surface Analysis, Ed.: A. W. Czanderna; Elsevier, New York, 1975.
2. W. Färber, Dissertation, Wien, 1975.
3. G. Betz, J. Marton and P. Braun, Nucl. Instr. Meth., **168**, 541, 1980.
4. G. Betz, Surf. Sci., **92**, 283, 1980.
5. M. Opitz, Dissertation, Wien, 1979.

Acta Physica Academiae Scientiarum Hungaricae, Tomus 49 (1—3), pp. 127—132 (1980)

ON THE FRACTURE OF DOPED TUNGSTEN

By

A. KELE and M. MENYHÁRD

RESEARCH INSTITUTE FOR TECHNICAL PHYSICS, HUNGARIAN ACADEMY OF SCIENCES
H-1325 BUDAPEST, HUNGARY

The fracture surface of industrial tungsten wires containing potassium second phases were investigated by AES. The average size and number of potassium second phases were determined by TEM. Potassium was the main component of the fracture surface and its amount varied on the differently heat treated wires. Utilizing the TEM results the average surface concentration was estimated supposing that the fracture is independent of the potassium second phases. The measured value was higher showing that the fracture path is partly determined by the potassium second phases.

The high surface concentration of the potassium was explained by surface diffusion.

Introduction

It is widely accepted that both grain boundary segregations and second phases play a dominant role in the mechanical behaviour of metals. The detection of second phases with electron microprobe is rather difficult (or even impossible), if the dimensions of the second phases are very small. In a previous work [1] it was shown that the chemical nature of the second phases responsible for the fracture can be determined by the highly surface sensitive AES. In [1] all conclusions were based on two assumptions a) the potassium atoms diffuse from the three dimensional second phases onto the free surface and form there a quasi-two-dimensional layer, b) the size and the form of the potassium second phases are the "well accepted" ones [2]. In this paper the validity of these assumptions will be investigated.

Experimental

The tungsten samples were fractured in situ in a Auger electron spectroscope. The background pressure was lower than 10^{-8} Pa. The Auger spectra were recorded by a usual cylindrical mirror analyser (RIBER OPC 103). The beam current was generally about 1 μA with a diameter of 60 μm, $E_p =$ 3 kV.

The samples were fractured at various temperatures in the range of 100—300 K. During the Auger measurements the temperature of the sample holder could be varied from 100 K to 500 K. It was also possible to warm up the sample to room temperature in a short time (2—5 min).

The following tungsten samples were investigated:

a) sintered rod, and wires with diameters of 0.9 and 0.3 mm in "as received" state;

b) wires with diameter of 0.3 mm after various kinds of heat treatment (see Table I).

Table I

Annealing parameters of wires with a diameter of 0.3 mm

Sample	Annealing	
	temperature (K)	time (sec)
A	1300	300
B	2100	2400
C	3000	100

The samples were fractured perpendicular to their axis. As the "as received" wires were too ductile to fracture them in this way at room temperature, they were fractured below the ductile—brittle transition temperature. The heat treated wires and the sintered rod could be easily fractured at room temperature perpendicular to their axis, although in many cases also these samples were fractured at lower temperatures in order to limit the surface diffusion of potassium.

Results

If the samples were fractured at higher temperatures (i. e. above 220 K), the Auger signal of the potassium was constant during the measurement. On the other hand, if the samples were fractured at low enough temperatures, the surface concentration of the potassium was definitely smaller 10 minutes after the fracture (i. e. at the moment, when the first Auger spectrum could be recorded) than the corresponding "constant" signal coming from samples fractured at higher temperatures. Furthermore after low temperature fracture the Auger signal was not at all constant but it increased slowly. If, after a short measuring time (15—20 min) the fracture surface was heated up to 250 K, the surface concentration of potassium increased in a relatively short time to a constant value, which was roughly equal to the surface concentration of the wires fractured at room temperature. In Table II the "constant" surface concentrations of potassium in various states are summarized. All these data are connected with fractures at temperatures higher than 250 K.

Table II

Potassium concentration ranges on the fracture surface of tungsten samples

Sample	Potassium concentration ranges in monolayer units
Sintered rod	1.4–2.0
0,9 wire	1.9–2.7
0,3 mm wire "as received"	1.6–2.4
A	0.9–1.2
B	0.3–0.7
C	0.2–0.4

Discussion

During fracture, potassium second phases are opened up, i. e. they become connected to the free surface investigated by AES. In [1], it was suggested that at room temperatures the potassium diffuses from the inclusion opened by the fracture along the surface. In this way the surface concentration of potassium will depend, of course, on the size and form of the potassium second phases.

The size and shape of the potassium second phases varies drastically during swaging, drawing and annealing. According to the electronmicrographs the potassium second phases in the "as received" wires are elongated parallel to the axis of the wires and their length amounts to some μms. According to Fig. 1, after a slight heat treatment these elongated second phases are partially broken off and form shorter elongated parts and/or bubbles. In sample B (Fig. 2) and C there are only bubbles. In these samples the potassium Auger signal decreased as the annealing proceeded. This is in very good agreement with the Auger results and supports the belief that the fracturing path is going through the potassium second phases.

In [1] the surface diffusion data available were discussed. It was shown that the surface diffusion is generally fast enough to explain our results. In the following an experimental verification of the diffusion model will be given. The most important experimental fact supporting the diffusion model is the slow increase of the potassium signal after fracture.

At 250 K even some minutes are enough to deplete the inclusions and thus the potassium Auger signal during the AES investigation must remain constant, as observed. But at 100 K the depletion time will be longer due to the reduced diffusivity, and therefore the potassium Auger signal will increase during the measurement. Really, in the first spectrum recorded about 10 minu-

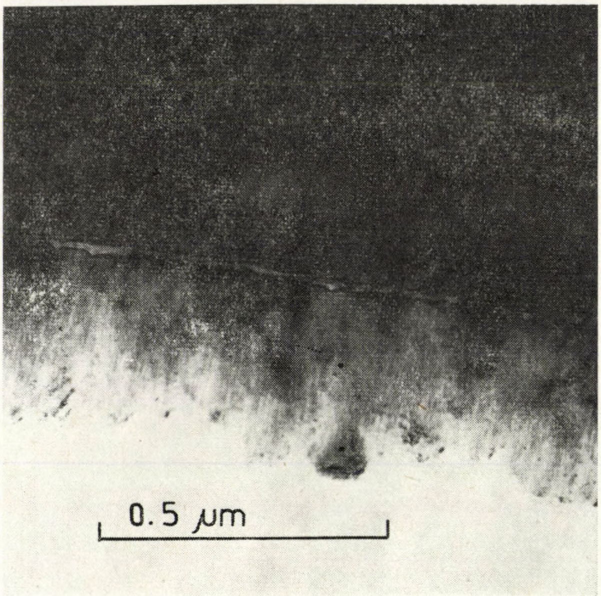

Fig. 1. Longitudinal micrograph of sample A, illustrating the bubbles and elongated rods characteristic for the partially annealed states of severely drawn doped tungsten

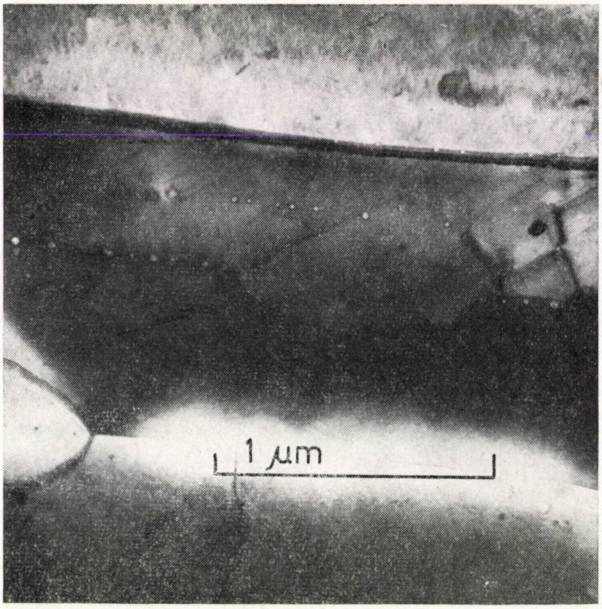

Fig. 2. Longitudinal micrograph of sample B, illustrating the bubble rows in a well annealed state

tes after the 100 K fracture the potassium Auger signal amounted only 20—40% of the Auger signal of similar samples fractured at 250 K.

Let us turn now to a more serious question: Does the total amount of the potassium detected on the surface originate from three-dimensional second phases? In principle the amount originating from three-dimensional second phases can be determined by measuring the depleting time at various temperatures. The depletion time (t_R) of bubbles with a radius of R is defined by the equation:

$$R^3 = \alpha d \cdot D_0 \cdot e^{-\frac{E}{kT}} \cdot t_R , \tag{1}$$

where d is the average thickness of the potassium surface layer, α is a constant, the value of which can be determined by the solution of the diffusion equation, D_0 and E are the unknown preexponential factor and the activation energy of the surface diffusion, respectively. The main problem is that at higher temperatures t_R is rather small and thus we have not enough measured data for fitting.

In sintered rods and in thicker wires the second phases are roughly as much larger as the diameter of the specimen [2]. According to Eq. (1), the depletion time increases very much as R increases. At any given temperature the ratio of the depletion times for the bubbles in sintered rods and in wires of 0.3. mm radius is:

$$\frac{t_{R(\mathrm{wire})}}{t_{R'(\mathrm{rod})}} = \left(\frac{R_{(\mathrm{wire})}}{R_{(\mathrm{rod})}}\right)^3 \tag{2}$$

and thus e. g. at 100 K the depletion time for a bubble in the sintered rod will be extremely large. The potassium surface concentration on the fractured surface of sintered rods (as given in Table II) is, however, higher than for the wires with a diameter of 0.3 mm. If the sintered rod was fractured at 100 K, the potassium surface concentration amounted to 25% of that after high temperature fracture. This ratio is similar to that found in the case of thin wires. This means, however, that Eq. (2) is not valid for this case; i. e. in the sintered rod only part of the potassium originates from the three-dimensional potassium second phases. The other part of potassium must be on the surface already at the very moment of the fracture.

We must conclude, therefore, that in sintered rods two kinds of potassium exist. One kind forms three-dimensional second phases, while the other builds quasi-two-dimensional second phases. This conclusion is in good agreement with the suggestion [3] that in sintered rods two kinds of potassium exist namely "active" and "non-active", if one supposes that in the sintered bodies some part of the potassium forms small bubbles, while the other part is absorbed on the surface of large voids.

Conclusions

It was experimentally verified that potassium diffusion takes place after the fracture. Comparing the potassium Auger signal on sintered rods and thin wires, we have shown that at least in sintered rods the potassium exists in two forms: in the first case potassium forms three-dimensional second phases and in the second one, it is present as an (absorbed?) layer.

Acknowledgement

It is a pleasure to acknowledge the valuable discussions with Drs. I. Gaál and G. Gergely.

REFERENCES

1. M. Menyhárd, Proceeding of "Surface Analysis 79" (Karlovy Vary 1979 ed. D. Stulik) p. 38/1.
2. D. B. Snow, Met. Trans., A7, 783, 1976.
3. L. Schreiner, 8. Plansee Seminar (Reutte, 1974).

Acta Physica Academiae Scientiarum Hungaricae, Tomus 49 (1—3), pp. 133—140 (1980)

ENERGY DISPERSIVE X-RAY MICROANALYSIS OF PHOSPHOSILICATE GLASSES (PSG)

By

A. L. Tóth

RESEARCH INSTITUTE FOR TECHNICAL PHYSICS, HUNGARIAN ACADEMY OF SCIENCES
H-1325 BUDAPEST, HUNGARY

and

J. É. Puskás

INDUSTRIAL RESEARCH INSTITUTE FOR ELECTRONICS
H-1393 BUDAPEST, HUNGARY

EDS peak height ratio method has been used for chemical microanalysis of PSG samples in a scanning electron microscope. We have applied a no-standard inverse ZAF-type correction procedure to calculate working curves as a function of beam energy and take-off angle. With the obtained correction procedure the EDS measurement is fast, precise and accurate compared with other physical techniques. Using this method a proportional relationship has been verified between the PH_3/SiH_4 ratio of the CVD process and the P concentration of the deposited PSG layer.

Introduction

Chemical vapour deposited (CVD) phosphosilicate glasses (PSG) are widely used in the semiconductor technology. They can be used as diffusion source, gate oxide in MOS devices and as insulating and passivating layer in MOS, bipolar and discrete devices [1]. The mechanical, electrical and chemical properties of PSG layers are directly related to the phosphorus concentration of the films. If the P concentration is too high, it reacts with moisture to form phosphoric acid [2]. This acid degrades the metallization layer being above or under the PSG film. On the other hand, the higher the P concentration the easier to "flow" the glass during fabrication. In the case of polysilicon gate process when PSG is deposited onto the polysilicon layer, very sharp edges occur, and the metallization layer evaporated above the PSG steps may crack (Fig. 1). If the PSG having sufficient P concentration is annealed at high temperature, the glass "flows" [3]. The obtained smooth steps can be covered with metal without any cracking (Fig. 2). Owing to the facts mentioned above the phosphosilicate glass has an optimal P content, and therefore it is important to control the P concentration of the product.

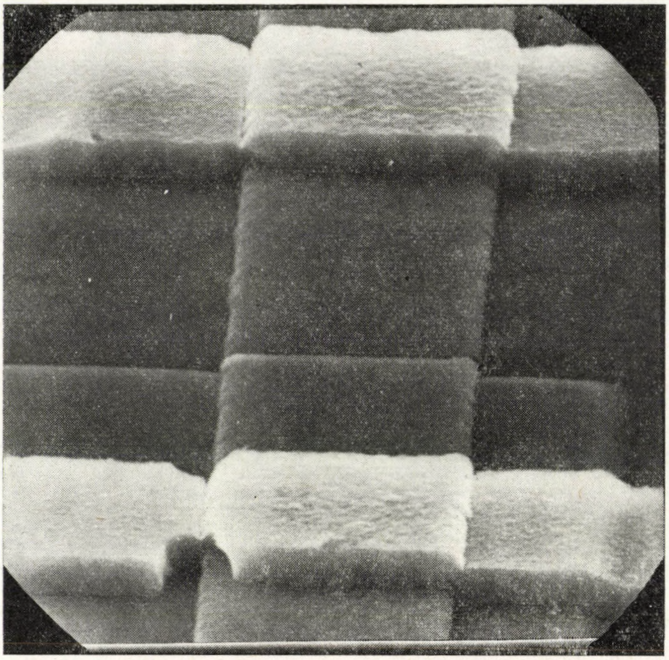

Fig. 1. PSG without flowing

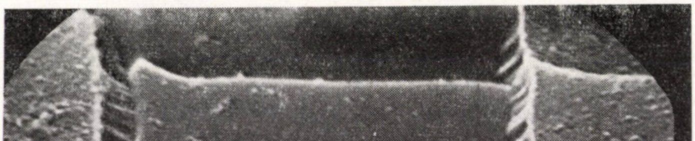

Fig. 2. PSG with flowing

Analytical methods

Inter-production testing during the CVD process requires quick, simple and cheap analytical methods. There are suitable methods, for instance the etching technique in P-etch at room temperature [4] and the sheet resistivity method, when after high temperature annealing and etching the sheet resistivity of the single crystal is measured with four point probe [5]. Both of these methods have severe disadvantages, because they require a relatively large quantity of material and calibration procedure, besides they are destructive. Some methods applied to calibration procedure are listed in Table I.

Table I

Analytical methods used for PSG P determination

Method	Locality	Depth of analysis	Time	Specimen	Standard	Destructivity	Ref.
Wet chemical analysis	cm	—	hour	solution	yes	yes	[11]
Neutron activation analysis (nAA)	cm	—	week	solution	yes	yes	[7–10]
Proton induced X-ray techn. (PIXE)	mm	μm	min	special	no	no	[14]
X-ray fluorescence method (XRF)	cm	μm	min	wafer	yes	no	[15]
Infrared spectr. (IRS)	cm	—	min	wafer	yes	no	[12–13]
Rutherford backscattering analysis (RBS)	mm	μm	hour	wafer	no	no	[14]
Wavelength dispersive X-ray microanalysis (WDS)	μm	μm	hour	device	yes	no	[4, 6, 7]
Energy dispersive X-ray microanalysis (EDX)	μm	μm	min	device	yes	no	[7]
EDS P/Si intensity ratio method	μm	μm	min	device	no	no	[7]

The P/Si ratio method

Taking into consideration the analytical volume, speed and non-destructivity the EDS P/Si method seems to be the best. Thin layers of PSG can be analysed within minutes by calculating the intensity ratio of P and Si peak heights of EDS spectrum, using a working curve to obtain concentrations. In a previous work [7] the working curve was measured using wet chemical and WDS analysis for a given E_0 beam energy and X-ray take-off angle.

As the depth of analysis is a function of E_0, too many curves would be needed for practical measurements. This problem can be overcome by exploiting the theory of correction procedures of conventional electron probe microanalysis to calculate working curves.

From the definition of the relative intensities as they are used in EDS and WDS calculations the ratio of P and Si peak heights can be expressed [16]:

$$K(P)=\frac{I_\mathrm{P}(\mathrm{P})-I_\mathrm{B}(\mathrm{P})}{I_\mathrm{P}^\mathrm{std}(\mathrm{P})-I_\mathrm{B}^\mathrm{std}(\mathrm{P})}\,;\quad K(\mathrm{Si})=\frac{I_\mathrm{P}(\mathrm{Si})-I_\mathrm{B}(\mathrm{Si})}{I_\mathrm{P}^\mathrm{std}(\mathrm{Si})-I_\mathrm{B}^\mathrm{std}(\mathrm{Si})}$$

$$\frac{K(\mathrm{P})}{K(\mathrm{Si})}=\left[\frac{I_\mathrm{P}^\mathrm{std}(\mathrm{Si})-I_\mathrm{B}^\mathrm{std}(\mathrm{Si})}{I_\mathrm{P}^\mathrm{std}(\mathrm{P})-I_\mathrm{B}^\mathrm{std}(\mathrm{P})}\right]\cdot\frac{I_\mathrm{P}(\mathrm{P})-I_\mathrm{B}(\mathrm{P})}{I_\mathrm{P}(\mathrm{Si})I_\mathrm{B}(\mathrm{Si})}=\left[\quad\right]\cdot\frac{I_\mathrm{P}(\mathrm{P})/I_\mathrm{R}(\mathrm{Si})-I_\mathrm{B}(\mathrm{P})/I_\mathrm{P}(\mathrm{Si})}{1-I_\mathrm{B}(\mathrm{Si})/I_\mathrm{P}(\mathrm{Si})}$$

$$\frac{I_\mathrm{P}(\mathrm{P})}{I_\mathrm{P}(\mathrm{Si})}=\left[\quad\right]\cdot\frac{k(\mathrm{P})}{k(\mathrm{Si})}\left(1-\frac{I_\mathrm{B}(\mathrm{Si})}{I_\mathrm{P}(\mathrm{Si})}\right)+\frac{I_\mathrm{B}(\mathrm{P})}{I_\mathrm{P}(\mathrm{Si})}=A\cdot\frac{B}{C}(1-D)+E\,.$$

The term A, that is the ratio of net intensities from the pure elements can be evaluated by a program [17] developed for no-standard EDS using MAGIC-IV [18] expressions. A is a function of E_0 and the instrument parameters. The relative intensities B and C are calculated using an inverse ZAF type program (FRAME) [19] as a function of E_0, X-ray take-off angle and concentrations. The relative background values D and E are measured ones. The obtained working curves are then used as quadratic polynoms. The input data are P/Si ratio and E_0, while the time of calculation is less than 10 seconds. Furthermore the whole analysis (collection, readout and correction) can be executed under computer control (Figs. 3 and 4.)

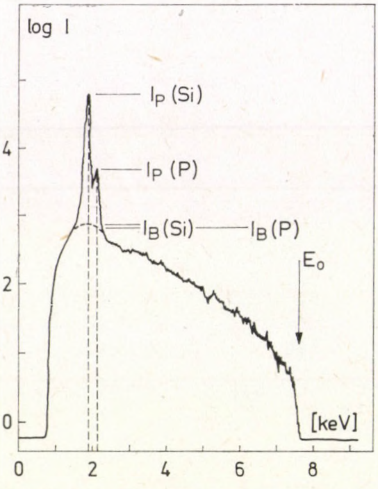

Fig. 3. EDS spectrum of a PSG sample showing the intensities used in P/Si method calculations

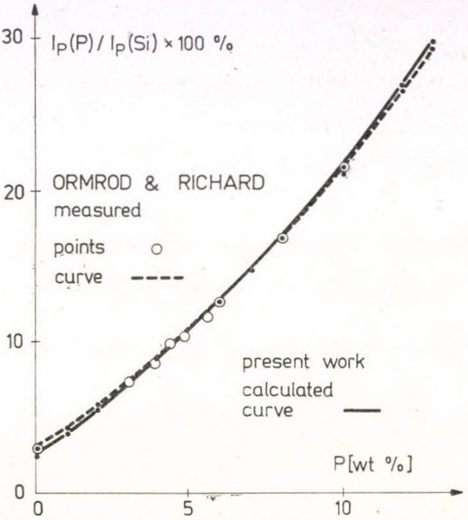

Fig. 4. Measured and calculated working curves for the same parameters (E_0, take-off angle)

Experimental setup

PSG layers were deposited by CVD process in a horizontal reactor. The gases were injected at one end of the reactor and exhausted at the other end. The wafers were placed on a quartz boat fitted to the heater unit. Silane, oxygen, phosphine and nitrogen gases were used. The chemical reaction follows the formula

$$SiH_{4(9)} + PH_{3(9)} + O_{2(9)} \xrightarrow{\triangle} \underbrace{(SiO_2)_n\,(P_2O_5)_{m(s)} + H_{2(9)}}_{PSG}.$$

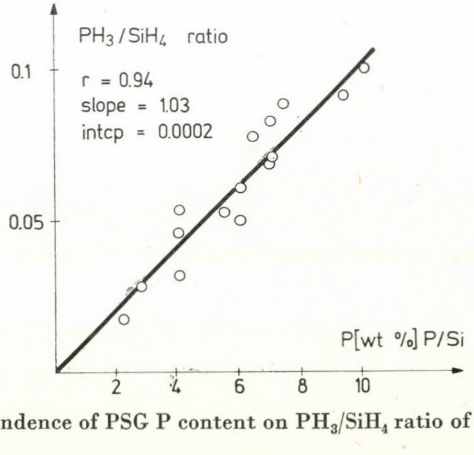

Fig. 5. Linear dependence of PSG P content on PH_3/SiH_4 ratio of CVD gas mixture

The deposition was carried out at a temperature of 723 K and at a pressure of 10^5 Pa.

The P concentration of PSG could be controlled with the amount of PH_3 in the gas mixture, while the flow rates of the other gases were kept constant.

Then the wafers were cut to four parts and the parts were analysed by different methods, i. e. etch rate tchnique, RBS, nAA and P/Si (EDS) methods.

Besides, using our new P/Si method it became possible to verify the proportional relationship between the PH_3/SiH_4 ratio and the P concentration of the deposited PSG (Fig. 5).

Comparative results and conclusions

The results of analyses measured on a large number of PSG samples using different techniques can be seen in Figs. 6—8. From the slopes and intercepts of the lines fitted to the measured points we can see that the accuracy of the P/Si method compared to the others is good. The precision of the etch rate technique is good enough, therefore this method is suitable for interproduction testing. The statistical scattering of points shows the precision of the P/Si method to be superior compared to ones of nAA and RBS measurements.

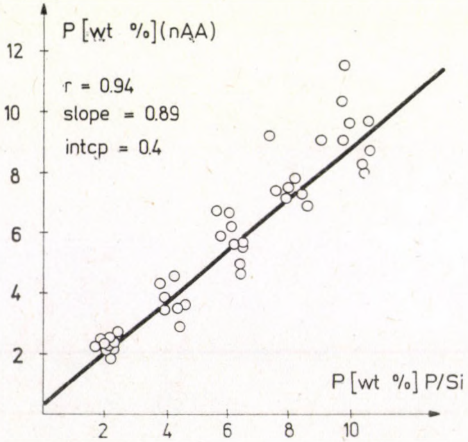

Fig. 6. Comparison of nAA and P/Si results

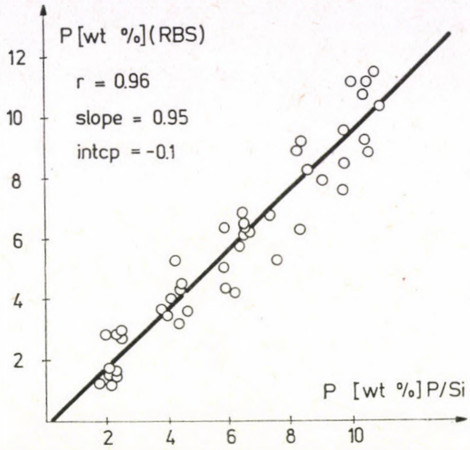

Fig. 7. Comparison of RBS and P/Si results

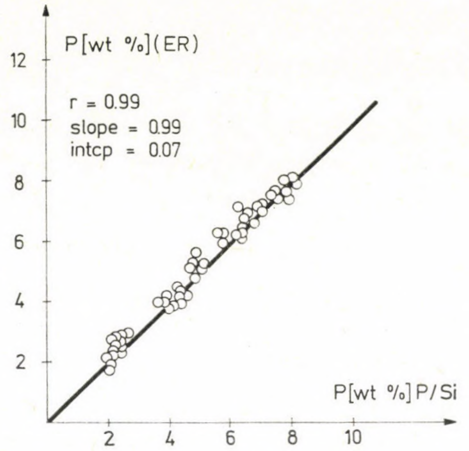

Fig. 8. Comparison of etch rate and P/SI results

Acknowledgements

The authors wish to thank Mr. E. **Kótai** for the nAA and RBS measurements and Mr. J. L. **Lábár** for discussions on correction software problems.

REFERENCES

1. G. L. **Schnable**, W. **Kern** and R. B. **Comizzoli**, J. Electrochem. Soc., **122**, 1092, 1975.
2. **Nagasima** et al, JES, **121**, 434, 1974.
3. M. **Armstrong** and A. **Tolliver**, JES, **121**, 307, 1974.
4. W. **Kern** et al, RCA Review, **37**, 3, 1976.
5. I. C. **Irwin**, Bell Syst. Techn. J., **41**, 387, 1962.

6. G. Giacomo, JES, **121**, 419, 1974.
7. S. E. Ormrod and B. P. Richards, Microelectronics, **8**, 5, 1977.
8. E. Tannenbaum, Solid State Electron., **2**, 123, 1961.
9. R. N. Ghostagore, Solid State Electron., **17**, 1065, 1974.
10. E. Kool, J. Electrochem. Soc., **111**, 1383, 1964.
11. E. H. Snow and B. E. Deal, J. Electrochem. Soc., **113**, 263, 1966.
12. A. S. Tenney and M. Ghezzo, J. Electrochem. Soc., **120**, 1276, 1973.
13. A. Czirbesz and J. Timár, HIKI Jubileumi Évkönyv 1978. (Anniversary Yearbook of Res. Inst. for Telecommunication) 23.
14. E. Kótai, to be published.
15. Pat. DuRant, NCR Microel. Div., Colorado Springs, Colorado, 1975.
16. H. Yakowitz, in "Practical Scanning Electron Microscopy" (ed. J. I. Goldstein) p. 327., Plenum N. Y., 1975.
17. J. L. Labar, to be published.
18. J. W. Colby, Adv. in X-ray Anal., **11**, 287, 1968.
19. K. F. J. Heinrich et al., NBS Techn. Note 719, 1972.

Acta Physica Academiae Scientiarum Hungaricae, Tomus 49 (1—3), p. 141 (1980)

STRUCTURE DETERMINATION OF METALLIC GLASSES WITH SIMS

By

R. Buhl

BALZERS AG, LIECHTENSTEIN

and

A. Preisinger

INSTITUTE FOR MINERALOGY, CRYSTALLOGRAPHY AND STRUCTURAL CHEMISTRY, TECHNICAL UNIVERSITY OF VIENNA, VIENNA, AUSTRIA

Abstract

During the examination of metallic glasses with static *S*econdary *I*on *M*ass *S*pectrometry (SIMS) polyatomic ions are emitted. Chemical and structural arrangements in the glasses can be deduced from these particles. Above all, it can be shown that for tempered (crystalline) glasses the same polyatomic ions occur with static SIMS. The pair distribution function was used to evaluate the X-ray diffraction spectra of the metallic glasses. The crystal structures of the tempered metallic glasses were determined from the X-ray diffraction data.

Acta Physica Academiae Scientiarum Hungaricae, Tomus 49 (1—3), pp. 143—152 (1980)

THE INTERACTION OF OXYGEN WITH THE IRON (111) SURFACE: MAINLY STUDIED BY AES

By

HANS-JOACHIM MÜSSIG and WALERIAN ARABCZYK[1]

TECHNICAL UNIVERSITY DRESDEN, PHYSICS SECTION, DEPARTMENT FOR SURFACE AND ELECTRON PHYSICS, DRESDEN, GDR

The cleaned surface was oxidized by means of pure oxygen at a pressure of 3×10^{-6}—3×10^{-3} Pa and at temperatures of 300 K, 370 K and 620 K. The Auger peaks of high energy (for oxygen at 510 eV and for iron at 703 eV) were used for the quantitative determination of the oxygen coverage on the iron surface. The experimental results on the change of oxygen coverage as a function of the dose are interpreted by means of a theoretical model and provide definite information about the bonding state of the adsorbate. In the lower energy part of the Auger spectrum there appear peak shape modifications during oxidation. These observations allow us to assume that in the process of oxidation two kinds of chemical bond are formed between oxygen and iron, which differ regarding the density of states in the valence band.

1. Introduction

It is the aim of our investigations on the iron (111) surface by means of low energy electrons to contribute to the chemical and geometrical structural analysis of the clean and of the oxygen-covered surface of a typical transition metal, in order to understand the process of chemisorption quantitatively better. The present paper deals with the adsorption kinetics of oxygen and the effect related to changes in the density of states as resulting from chemical reaction between oxygen and iron studied by Auger electron spectroscopy.

The study of adsorbed layers and surface reactions on α-iron within atomic range was introduced by PIGNOCCO, PELLISSIER, SZOSTAK, MOLIÈRE, PORTELE and LÁZNIČKA [1 to 5]. Till now, some papers [6 to 10] on single crystals have been published in which the authors mainly derived statements concerning the growth of oxide layers on the (100) surface and on the most densely packed (110) surface. On the other hand, so far only few investigations have been made on the (111) surface [11 to 14], having the lowest density of iron surface atoms, though especially this surface is important for both adsorption and surface reaction in the sense of heterogeneous catalysis.

---

[1] Present address: Politechnika Szczecińska, Instytut Technologii Chemicznej, Szczecin, Poland.

2. Experimental

The (111) surface of iron was cleaned by in situ bombardment with argon ions and subsequent heating at 620 K under ultrahigh vacuum. Fig. 1 represents the Auger electron spectrum measured by means of a cylindrical mirror analyzer, for a surface after ion bombardment. Except for small amounts of oxygen, carbon, and argon, the surface may already be regarded as clean.

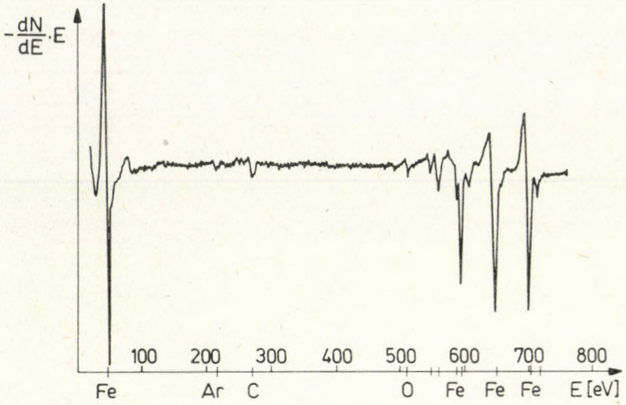

Fig. 1. Auger electron spectrum of the Fe (111) surface after bombardment with noble gas ions

By heating at 620 K, oxygen and carbon will desorb in the form of carbon monoxide, and after that argon is no longer detectable either.

The cleaned surface was oxidized by means of pure oxygen at a pressure of 3×10^{-6} Pa to 3×10^{-3} Pa and at temperatures of 300 K, 370 K and 620 K. After each oxygen exposure and pumping down to the vacuum of 10^{-8} Pa, Auger spectra were measured. In the same conditions, Auger spectra were taken on compressed pure magnetite and hematite powders. The Auger peaks of high energy (for oxygen at 510 eV and for iron at 703 eV) were used for the quantitative determination of the oxygen coverage on the iron surface, at 2,5 keV excitation energy.

3. Experimental results and discussion

3.1. *Adsorption kinetics*

In a first approximation, the oxygen coverage Θ may be determined according to the relation

$$\Theta = \tau_M \cos\alpha_0 \frac{(I_O/I_{Fe})\,(\Phi_{Fe}/\Phi_O)\,(\gamma_{Fe}/\gamma_O)}{1+(I_O/I_{Fe})\,(\Phi_{Fe}/\Phi_O)\,(\gamma_{Fe}/\gamma_O)} \tag{1}$$

if in addition to the measured signal ratio I_O/I_{Fe}, the mean escape depth τ_M of the Auger electrons — measured in monolayers —, the entrance angle α_0 of the analyzer, and the ratios of the ionization cross section Φ and the emission probabilities γ are known.

The relation $(\Phi_O/\Phi_{Fe})(\gamma_O/\gamma_{Fe}) = 3.67$ has been experimentally obtained on the compact magnetite and hematite samples. By means of this value, the mean escape depth of the Auger electrons is then obtained for the energy 703 eV of the L_3VV transition, if, e. g. the signal ratio I_O/I_{Fe} is measured on a fully developed p(1×1) — O superstructure representing a coverage of $\Theta = 1$. The numerical value is 1.05 nm.

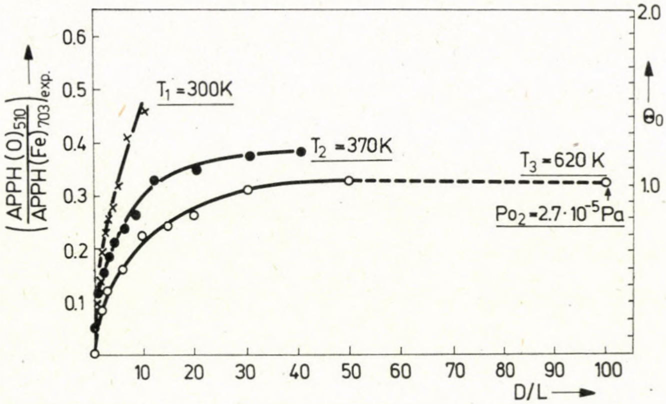

Fig. 2. Change of peak-height ratio and degree of coverage as a function of the dose for variou temperatures ($p_{O_2} = 3\times10^{-6}$ Pa)

By means of this calibration it became possible to describe the kinetics of the initial step of the oxygen adsorption on the Fe(111) surface quantitatively. Fig. 2 shows the change of the Auger peak-height ratio of oxygen and iron and the coverage, respectively, as a function of the oxygen exposure at a constant pressure of 3×10^{-6} Pa for the temperatures 300 K, 370 K and 620 K. No pressure dependency could be stated in the range of 10^{-6} Pa.

The experimental curves may be described in good agreement by a theoretical model with a physisorption precursor state, which will not be dealt with in more detail. Accordingly, adsorption takes place dissociative, not activated, and immobile at two sites. On the assumption that the physisorbed molecules very quickly achieve a state of equilibrium and the desorption rate from the state of chemisorption can be neglected we have integrated the rate equations and obtained the solution

$$\Theta + \frac{K_D}{K_1}\left(1-\frac{1}{z}\right)\left(\frac{1}{1-\Theta}-1\right) - \frac{K_D}{K_1}\,\frac{1}{z}\ln(1-\Theta) = K_A\, p_{O_2} t, \qquad (2)$$

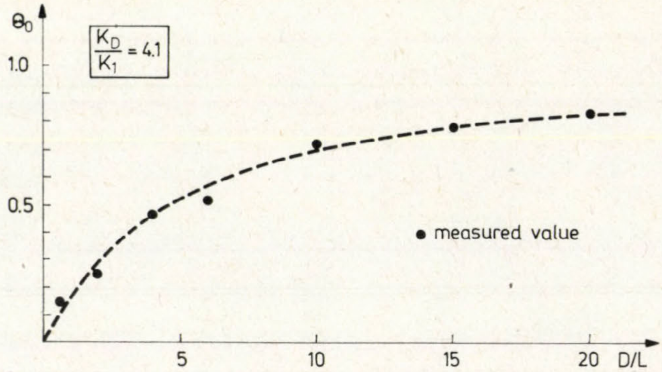

Fig. 3. Degree of coverage θ_0 of chemisorbed oxygen vs dose D ($T = 620$ K) calculated for immobile chemisorption complexes with $z = 3$

which is valid within the limits $0 \leqq \Theta < 1$. The best fitting of the theoretical function to the measured curve at 620 K can be obtained by assuming three nearest neighbours ($z = 3$) and choosing the quotient of rate constants for the desorption (K_D) and chemisorption (K_1) $K_D/K_1 = 4.1$ (Fig. 3). K_A is about 0.75×10^4 Pa^{-1}s^{-1} for the Fe(111) surface, and $p_{O_2}t$ is the oxygen dose.

3.2. Chemical changes

For the quantitative chemical analysis up to now we have only used the intensity of the Auger electron signals in the derivative mode. A possible fine structure in the peak form that refers to a splitting of core levels or re-

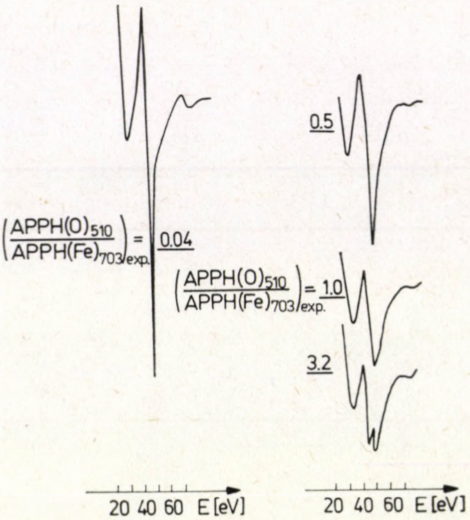

Fig. 4. Changes of Auger electron spectrum by oxidation at room temperature

flects the density of states in a bond has not been taken into account. Both effects are dominantly produced by chemical surface reactions.

In the low energy part of the Auger spectrum of pure iron (Fig. 1) there appears a peak at 47 eV corresponding to a $M_{2,3}VV$ electron transition of the Auger process. As a result of the oxidation of the iron surface at room temperature, it is observed that increasing oxygen coverage on the surface, the peak height decreases; also splitting is successively observed, as already known from literature [15 to 17], in peaks at 44 eV and 51 eV (Fig. 4). SAVTCHENKO [15] assigned the corresponding Auger electron transitions to $3p_{\mathrm{Fe}}\ 2p_{\mathrm{O}}\ 2p_{\mathrm{O}}$ and $3p_{\mathrm{Fe}}\ 3d_{\mathrm{Fe}}\ 3d_{\mathrm{Fe}}$ where the iron energy level $3p$ was shifted from 56 eV in pure iron to 58 eV in Fe_2O_3 below the Fermi level. In the valence band two maxima are found, one at 5 eV associated mainly with electrons from the $2p$ oxygen level, and the second at 1.5 eV associated with electrons from the $3d$ iron level (Fig. 5).

In Fig. 6, the peak heights at 44 eV and 51 eV in the Auger spectrum are shown, obtained on magnetite, hematite and a thin layer of oxygen on the iron surface, the Auger spectrum remaining unchanged by the further oxidation process. The comparison of the relative heights of those peaks shows that on the oxidized iron surface a thin oxide layer is formed of a composition approaching Fe_3O_4. The ratio of the peak height at 44 eV to that at 51 eV

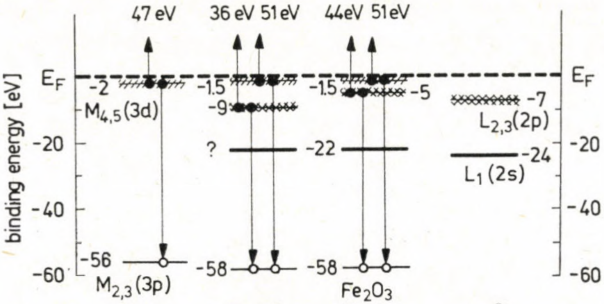

Fig. 5. Simplified schemes of energy levels

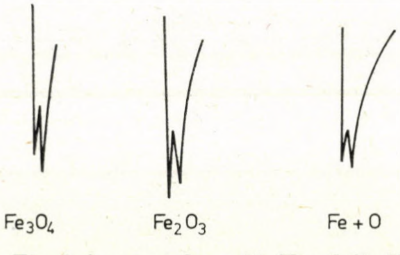

Fig. 6. Auger peaks at 44 eV and 51 eV

in hematite is higher than in magnetite. This fact confirms the contribution the cross-transition $3p_{\mathrm{Fe}}\,2p_{\mathrm{O}}\,2p_{\mathrm{O}}$ to the peak at 44 eV, because, with increasing oxygen concentration in iron oxides, the electron density increases on the $2p$ level. The probability of the Auger transitions is enhanced with these electrons contributing.

While oxidizing iron at temperatures of 370 K and 620 K, new features were observed in the Auger spectrum (Fig. 7). At a small coverage of the iron surface with oxygen, a peak is appearing at 34 eV to 36 eV. Simultaneously, at 51 eV a well defined peak is being formed that becomes clearer with progressing oxidation. As a consequence of progressing oxidation in the Auger spectrum a total decline at 47 eV peak and a simultaneous appearance of a

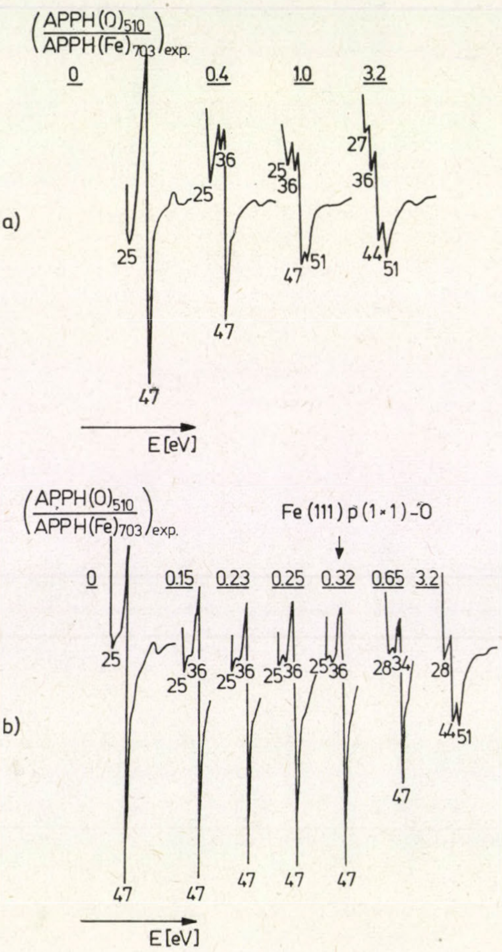

Figs. 7. Changes of Auger electron spectrum by oxygen adsorption at 370 K (a) and 620 K (b)

44 eV peak are observed while a 36 eV peak is present (see oxidation at 370 K in Fig. 7a). It proved to be practicable to determine the 36 eV peak shape during the oxidation process at 620 K (Fig. 7b), well defined at a coverage on the iron surface equal to one. 7×10^{18} atoms/m^2 correspond to the structure Fe (111) p(1×1) — O, the existence of which was stated by the method of low energy electron diffraction (LEED) [18].

Similar changes in the Auger spectrum, but in reverse order have been observed during the reduction of the iron surface oxidized at room temperature, as resulting from step by step heating (Fig. 8). By the LEED method it was stated that by heating the oxidized iron surface above 520 K, a two-dimensional structure Fe(111) $(2\sqrt{3}\times2\sqrt{3})$ — 30° — O will be formed on the surface [19]. In Fig. 9b the LEED pattern represents this superlattice at 34 eV and, for comparison, that of the clean Fe(111) surface at 30 eV is shown in Fig. 9a. The high value of the period length of this structure indicates that the diffraction pattern may not be assigned to a single substance but to a coincidence lattice of the substrate and the surface layer of FeO with the orientation (111). Thus, by means of diffusion, the most iron-rich oxide phase is developed.

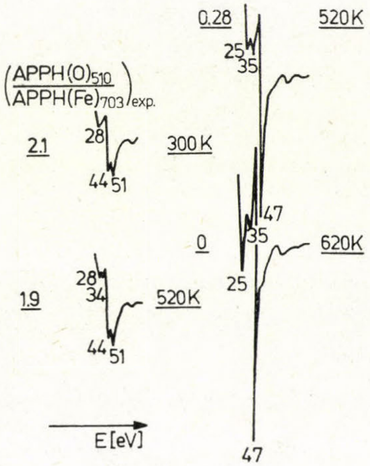

Fig. 8. Changes in the Auger electron spectrum of a sample oxidized at room temperature during a heat treatment to 620 K

The Auger spectra obtained on the iron surface after its correspondingly long oxidation within the studied range of temperatures and a pressure up to 10^{-3} Pa exhibit a similar character proving the identical chemical composition of the thin oxide surface layers.

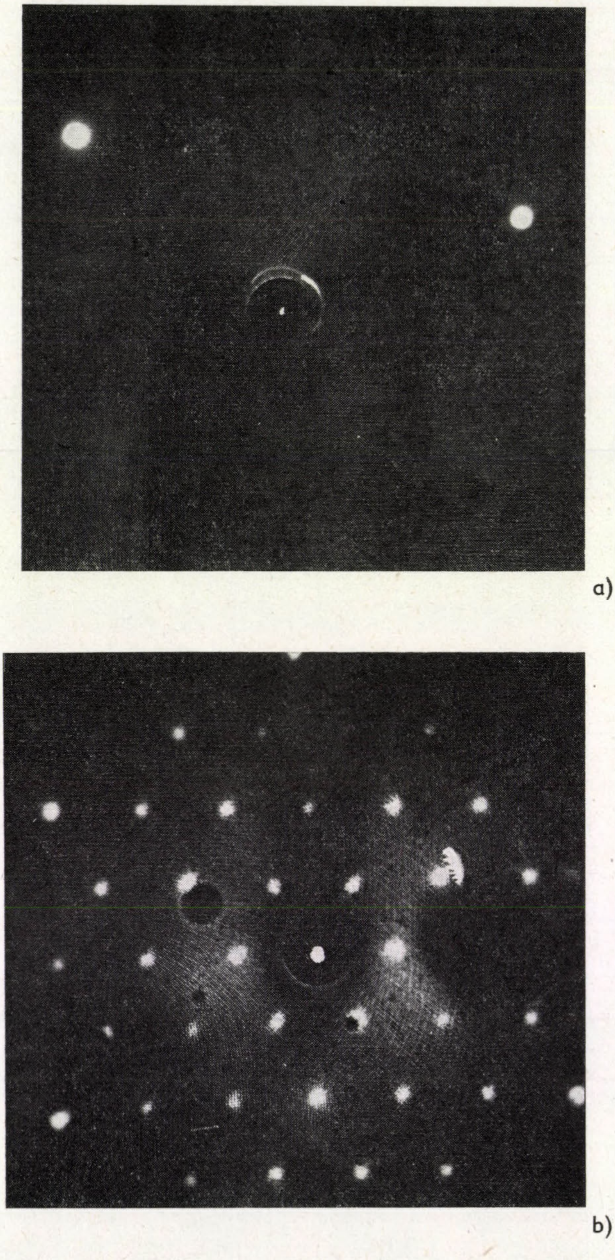

Fig. 9. LEED pattern a) of the clean Fe (111) surface ($E = 30$ eV); b) of the Fe (111) $(2\sqrt{3}\times 2\sqrt{3})-30^\circ-0$ superstructure ($E = 34$ eV)

4. Conclusions

The observations described above allow us to assume that in the process of oxidation two kinds of chemical bond of oxygen with iron are formed which differ regarding the density of states in the valence band as shown in our diagram (Fig. 5). One kind is characteristic for iron oxides, the second occurs at the first stage of oxidation and is associated with chemisorbed oxygen. In both cases, the position of maxima in the density of states related to iron was assumed to be equal which is proved by the existence, in all Auger spectra, of the 51 eV peak, corresponding to the transition $3p_{\mathrm{Fe}}3d_{\mathrm{Fe}}3d_{\mathrm{Fe}}$.

The 36 eV peak is attributed to "cross-transition" between oxygen and iron with participation of levels 3p iron and 2p chemisorbed oxygen with the maximum in the density of states located about 9 eV below the Fermi level.

As it now appears from these scattered investigations, the presence of chemisorbed oxygen on the iron surface depends on temperature and thickness of the magnetite film. At room temperature, we do not observe the peak at 36 eV in the Auger spectrum, indicating the absence of bound oxygen on the iron surface, which may be due to the fast transition of chemisorbed oxygen into oxides. This is indicated by new spots in the LEED pattern already appearing at the exposure of about 10 L oxygen.

The presence of chemisorbed oxygen is observed at higher temperatures of oxidation and reduction, respectively, when oxygen forms regular two-dimensional structures on the iron surface, also when the thin oxide layer is surely thicker than the magnitude of the escape depth of 703 eV electrons, i. e. thicker than 1.05 nm. This is proved by the 36 eV peak appearing in the Auger spectrum, when the ratio of the peak heights of oxygen to iron reaches the maximum value. From the last observation, something more may be concluded, namely that oxygen bound with iron is located at the boundary of phases:

— oxygen gas (during the measurement — the vacuum) and

— the thin oxide layer.

Finally, on the thin passive oxide layer no chemisorption of oxygen is taking place under the conditions of measurement.

REFERENCES

1. A. J. Pignocco and G. E. Pellissier, J. Electrochem. Soc., **112,** 1188, 1965.
   A. J. Pignocco and G. E. Pellissier, Surf. Sci., **7,** 261, 1967.
2. R. Szostak and K. Molière, in: Grundprobleme der Physik dünner Schichten, Ed. R. Niedermeyer and H. Meyer, Vandenhoeck and Ruprecht, Göttingen, 1966.
3. K. Molière and F. Portele, in: The Structure and Chemistry of Solid Surfaces, Ed. G. A. Somorjai, Wiley, New York 1969.
4. F. Portele, Z. Naturf., **24**a, 1268, 1969.
5. M. Láznička, Czech. J. Phys., **B19**, 1229, 1969.

6. H. Kobayashi and S. Kato, Surf. Sci., **12**, 389, 1968.
7. P. B. Sewell, D. F. Mitchell and M. Cohen, Surf. Sci., **33**, 535, 1972.
8. A. J. Melmed and J. J. Carroll, J. Vac. Sci. Technol., **10**, 164, 1973.
9. G. W. Simmons and D. J. Dwyer, Surf. Sci., **48**, 373, 1975.
10. K. O. Legg, F. P. Jona, D. W. Jepsen and P. M. Marcus, J. Phys., **C8**, L492, 1975.
11. H. Kobayashi and S. Kato, Surf. Sci., **18**, 341, 1969.
    S. Kato and H. Kobayashi, Surf. Sci., **21**, 625, 1971.
12. F. Bozso, G. Ertl, M. Grunze and M. Weiss, J. Catal., **49**, 18, 1977.
13. W. Arabczyk and H-J. Müssig, Dissertation A and B, Technische Universität Dresden. 1977.
14. F. Bozso, G. Ertl, M. Grunze and M. Weiss, Appl. Surf. Sci., **1**, 103, 1977.
    M. Grunze, F. Bozso, G. Ertl and M. Weiss, Appl. Surf. Sci., **1**, 241, 1978.
15. V. I. Savtchenko, Dokl. Akad. Nauk SSSR, **208**, 1154, 1973.
16. C. Leygraf and S. Ekelund, Surf. Sci., **40**, 609, 1973.
17. K. Ueda and R. Shimizu, Surf. Sci., **43**, 77, 1974.
18. W. Arabczyk and H.-J. Müssig, Thin Solid Films, **34**, 103, 1976.
19. W. Arabczyk and H.-J. Müssig, Exp. Tech. Phys., **23**, 475, 1975.

Acta Physica Academiae Scientiarum Hungaricae, Tomus 49 (1—3), pp. 153—158 (1980)

A COINCIDENCE-TYPE ION-ELECTRON CONVERTER DETECTOR WITH LOW BACKGROUND FOR LOW-ENERGY PROTONS

By

CHR. STRATOWA, R. DOBROZEMSKY and P. WEINZIERL

PHYSICS INSTITUTE, RESEARCH CENTER SEIBERSDORF, SGAE
A-1082, VIENNA, AUSTRIA

In the last years a series of measurements on weak-interaction in neutron decay has been performed using the coincidence detector developed by O. BENKA. A short description of this detector will be presented with special emphasis on the problem of counting low-energy protons. Special care was taken in order to ensure the detection efficiency being independent of particle energy.

1. Introduction

In the last years a series of measurements on weak-interaction in neutron decay has been performed. The essential work was the precise measurement of the energy spectrum of the recoil protons from free-neutron decay [1, 2]. For this purpose, the detecting device (developed by O. BENKA [3]) should have a very high counting efficiency for the low-energy protons ($T_{\max} = 751{,}4$ eV) under consideration. Special care had to be taken in order to ensure the detection efficiency being independent of the particle energy at the detector entrance [3, 4].

2. Requirements and layout

According to the neutron decay measurement, the detecting device has to fulfil the following requirements (see also [2, 4]):

1) to focus protons onto a converter foil (at $U_B \approx 25$kV) independent of their primary energies T at the detector entrance ($50 \text{ eV} \leq T \leq 750 \text{ eV}$);

2) to ensure a counting probability independent of the primary energy T of the protons;

3) to discriminate against counting of heavy ions (from residual gas, etc.);

4) to keep the background low (for a typical radiation-background of 1mr/h) and independent of energy setting.

On this basis, O. BENKA has developed a coincidence type ion-electron converter detector consisting of four distinguishable units [3]:

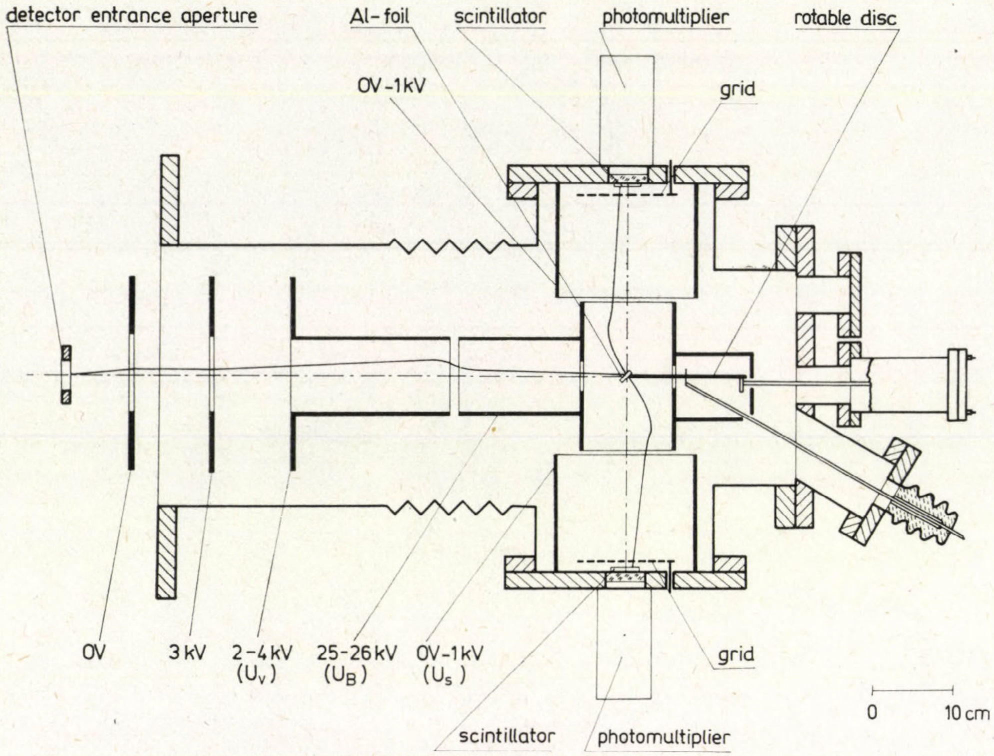

Fig. 1. Ion-electron converter detection system (all potentials given are negative with respect to ground potential).

1) Ion focusing and acceleration system
2) Ion electron converter: Al-foil
3) Electron focusing and acceleration system
4) Scintillation-detector:
   a) Scintillator, glass window, photomultiplier
   b) Pulse-discriminator and coincidence-device

The principle of this system can be seen in Fig. 1.

3. Description

The protons ($T = 50$ to 750 eV) entering the detector are accelerated by a four electrode lens to a final energy T_f of approximately 25 keV and focused onto a thin converter foil (Al-foil). In order to keep the final energy T_f independent of the primary proton energy T, the acceleration voltage U_B has to be varied accordingly: $U_B = (T_f - T)/e$.

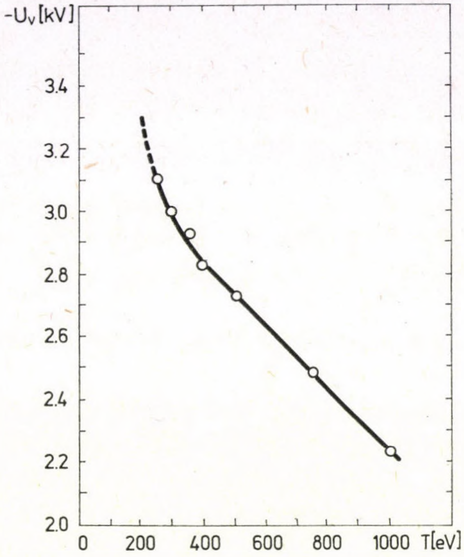

Fig. 2. Variable voltage U_v vs proton energy T (for $U_B = 25$ kV)

An optimum focusing of the protons on the converter foil was attained by varying the potential U_v of the third electrode (see Fig. 1) between -2 and -4 kV according to a calculated and experimentally tested function of the proton energy (see Fig. 2).

The accelerated protons penetrate the converter (20—40 μg/cm^2 Al-foil) which is inclined by 45° with respect to the proton flight path, and eject secondary electrons from both sides of the foil (electron yield γ at 25 kV ≈ 6.5 electrons/proton). These electrons are accelerated and focused by two cylinder-lenses onto two thin scintillator foils (NE 102 A), mounted on glass windows with a potential U_s of 0 — 1 kV applied. (To ensure a constant detection efficiency, also the impinging energies of the electrons at the scintillators have to be kept independent of the primary energy T. For this purpose, the potentials U_s of the scintillator surfaces — covered with a conducting Al-layer — are regulated accordingly). Two photomultipliers (RCA 8575) are optically coupled to these windows. Only coincident counts of the two detectors are accepted as proton events.

The thickness of the converter foil is chosen in order to stop heavier particles (e. g. residual gas ions) of comparable energies (see Fig. 3), thus preventing coincidences (mass-discrimination). To suppress background signals from secondary ions, originating from scintillator surfaces, grids at a moderate positive potential U_B with respect to the scintillator surfaces are used (see Fig. 4).

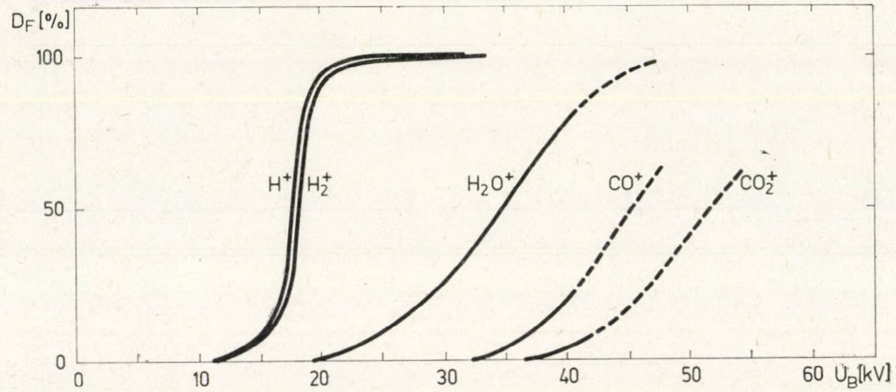

Fig. 3. Transmission D_F of a 25 μg/cm^2 Al-foil for various ions vs acceleration voltage U'

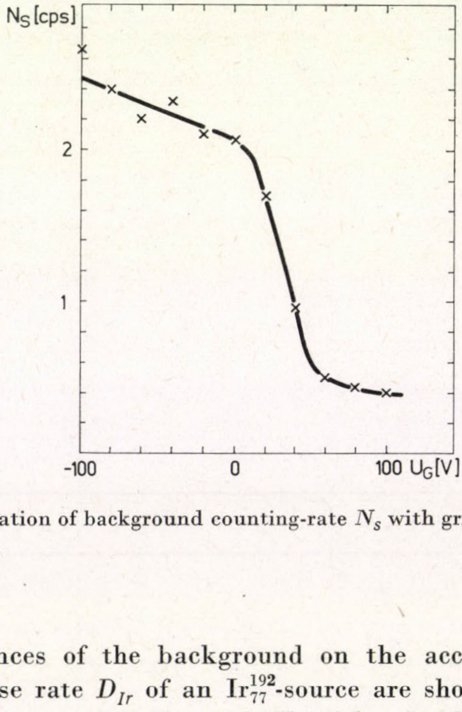

Fig. 4. Variation of background counting-rate N_s with grid voltage U_G

The dependences of the background on the acceleration voltage U_B and the gamma-dose rate D_{Ir} of an Ir_{77}^{192}-source are shown in Figs. 5 and 6. The coincidence background at $U_B = 25$ kV and 1mr/h γ-background amounted to approx. 0.1 counts/sec. The detecting device is able to measure proton counting rates of 0.1 cps to 2.10^5 cps.

To allow a variety of measurements, six foils of different sizes and thicknesses are assembled on a rotable disk (at acceleration potential) which can be moved by a rotary feedthrough.

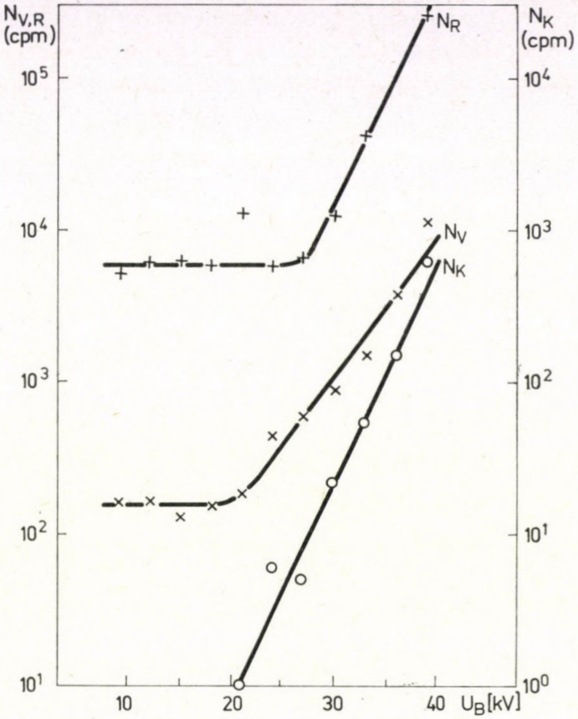

Fig. 5 Single-channel backgrounds N_V and N_R (V: scintillator seeing frontside of the foil; R: scintillator seeing back-side of the foil), and coincident background N_K as a function of accceleration voltage U_B

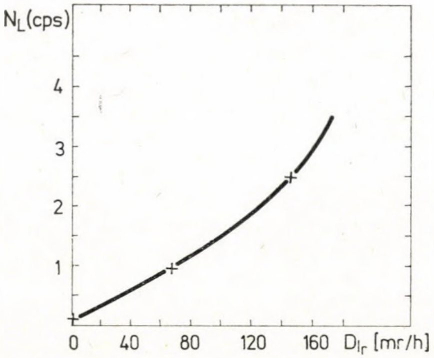

Fig. 6. Background N_L vs gamma-dose rate D_{Ir} (Ir^{192}_{77})

4. Results

By means of the detecting device described, a series of precision measurements of the energy spectrum of recoil protons following free-neutron decay has been performed, using an evacuated longitudinal beam-tube of the

ASTRA reactor. Proton spectra were measured from 150 to 750 eV, typical counting rates (at 7 MW reactor power) were 0.1 to 3 cps. Evaluating the results of the spectra measured with optimum precision, we obtained $|g_A/g_V| = 1.259 \pm 0.017$ for the ratio of the coupling constants. A more detailed description of this basic experiment can be found in [2].

REFERENCES

1. R. Dobrozemsky, E. Kerschbaum, G. Moraw, H. Paul, C. Stratowa and P. Weinzierl, Phys. Rev., **D11**, 510, 1975.
2. C. Stratowa, R. Dobrozemsky and P. Weinzierl, Phys. Rev., **D18**, 3970, 1978.
3. O. Benka, Dissertation, Univ. of Vienna, 1970 (unpublished).
4. C. Stratowa, Dissertation, Univ. of Vienna, 1977 (unpublished).

Acta Physica Academiae Scientiarum Hungaricae, Tomus 49 (1–3), pp. 159–166 (1980)

ELLIPSOMETRIC STUDY OF SEMICONDUCTOR — — METAL AND METAL – METAL OXIDE THIN FILMS SYSTEM

By

B. SZÜCS, J. ÁDÁM and P. JAKAB

TUNGSRAM RESEARCH INSTITUTE. H-1340 BUDAPEST, HUNGARY

Absorbing thin films can be characterized by a complex refractive index $\bar{n}_1 = n_1 - ik_1$. The complex refractive index raises several experimental and computational problems: the determination of the extinction coefficient k_1 requires a further, independent parameter, and a further, independent equation. For the determination of the complex refractive index and film thickness (d) on the systems Au/Si, Al/Si, NiO/Ni and thin films of Au, Al and NiO, respectively — the reflectance R was applied as new parameter. The dependence of n_1 and k_1 on d was studied using an idealized and a realistic layer model.

1. Introduction

The refractive index and thickness of non-absorbing thin films can be determined very practically by ellipsometry. Conventional ellipsometric measurements furnish the relative changes of ψ (amplitude ratio) and Δ (phase). Inserting them into the fundamental equations of ellipsometry, n_1 and d can be determined.

Absorbing thin films raise a new problem. The complex refractive index requires the determination of a new unknown quantity k_1. This can be achieved in various ways:

1. To determine every parameter merely by ellipsometry making the measurements with more angles of incidence, substrates, ambient medium, or studying film samples differing in thickness.

2. To combine ellipsometry with other methods, for determining one of the parameters (n_1, k_1 or d) with another (external) measurement, e. g. interferometry, coulometry, rate meter, etc.

The common difficulty of the methods lies in the sophisticated, long, tiresome measurements. The methods are destructive and the results are not unambiguous. A simple, unambiguous solution of the problem was found by applying the PAIK—BOCKRIS (PB) method [1]. By this method, a usual, single ellipsometric measurement provides $\bar{n}_1$ and d simultaneously. This is possible, by choosing the reflectance R as third, independent parameter, beside ψ and Δ. R can be determined with the same measurement by means of the ellipsometer. The two fundamental equations of ellipsometry are to be completed by a third independent equation of reflectance. This experimental and evaluating method is called RPD, i. e. "*r*eflectance-*p*si-*d*elta" method.

The fundamental equation of ellipsometry is:

$$\operatorname{tg} \psi \cdot e^{i\Delta} = \frac{|\bar{r}_p|}{|\bar{r}_n|} e^{i(\delta_p - \delta_n)}, \tag{1}$$

where $\bar{r}_n$ and $\bar{r}_p$, respectively, are the normal and parallel generalized Fresnel reflection coefficients of polarized light, δ_n and δ_p, respectively, denote the phase shifts of the components.

Separating the real and imaginary parts of Eq. (1) gives:

$$\operatorname{tg} \psi = f_1(n_1,\ k_1\ d), \tag{2}$$

$$\Delta = f_2(n_1, k_1, d). \tag{3}$$

A third independent equation would be given by $\bar{r}_p$ or $\bar{r}_n$, however in practice it is more advantageous to use their resultant, the reflectance R. Its equation is [1], [2], [3], [4]

$$R = |\bar{r}|^2 = |\bar{r}_p|^2 \sin^2 \alpha + |\bar{r}_n|^2 \cos^2 \alpha\,, \tag{4}$$

denoting by α the azimuth of incident light.

$$R = f_3(n_1, k_1, d). \tag{5}$$

For $\alpha = \pi/4$

$$R = \frac{1}{2}\left(|\bar{r}_p|^2 + |\bar{r}_n|^2\right). \tag{6}$$

By measuring only the relative changes of R instead of its absolute value the disturbing effects of the optical system can be eliminated.

The reflectance can be easily determined by intensity measurement.

Since

$$I_d = K I_i\, |\bar{r}|^2, \tag{7}$$

where I_d is the intensity of light reaching the detector, I_i is the intensity of light incident on the sample and K is a constant depending on the optical system

$$\frac{I_{dx} - I_{d0}}{I_{d0}} = \frac{\delta I}{I_{d0}} = \frac{2\delta\,|\bar{r}|}{|\bar{r}_0|} = 2\,\frac{|\bar{r}_x| - |\bar{r}_0|}{|\bar{r}_0|} \tag{8}$$

$$|\bar{r}_x| = |\bar{r}_0| \left(1 - \frac{\delta I}{2 I_{d0}}\right) \tag{9}$$

denoting by I_{d0} the intensity of light reflected by the clean substrate, by I_{dx} the intensity of light reflected by the thin film covered substrate, by $\bar{r}_0$ the reflection coefficient of the clean substrate, by $\bar{r}_x$ the reflection coefficient of the thin film covered substrate and by δI the intensity change due to the covering film.

The intensity was measured with the analyzer position turned by $\pi/2$ with respect to the extinction position.

Measurements were carried out by a usual manually driven ellipsometer set up, operating with the Archer method.

2. Study of stratified planar structures with an idealized and a realistic model

During the preparation and formation of thin films on substrates, considerable deviations may occur between the optical constant of ideal film substrate (Fig. 1) and real oxide film/film/interface/substrate (Fig. 2) systems, due to oxidation or the incorporation of contaminants.

Thus, in practice a real system containing surface and interface layers forms a multilayer structure. The optical parameters of multilayer systems can be calculated by the matrix method.

The effect of surface and interface layers on the optical parameters have been computed with a model, based on the matrix method.

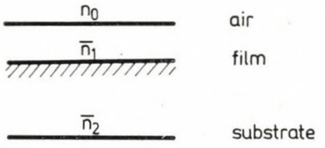

Fig. 1. Idealized (3 component) system

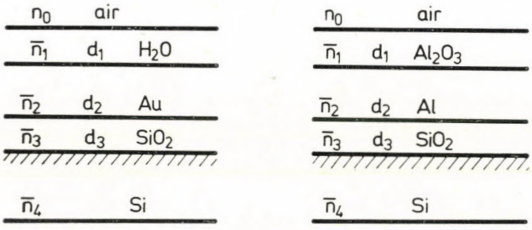

a) b)

Fig. 2. Real (5 component) system
Optical data: a. $n_1 = 1{,}33$, $n_3 = 1{,}46$, $\bar{n}_4 = 4.05 - i0.028$. Thickness values: $d_1 = 0{,}5$ nm, $d_3 = 2$ nm; b. $n_1 = 1{,}6$, $n_3 = 1{,}46$; $d_1 = 3{,}5$ nm, $d_3 = 3$ nm

Reflection and transmission effects on a boundary can be described by the equation

$$\bar{E}_i = \mathbf{S} . \bar{E}_j \tag{10}$$

according to Azzam [5], denoting by $\bar{E}_i$ and $\bar{E}_j$ the electric field on the two sides of the boundary. **S** is the scattering matrix.

The latter is formed by the product of matrices representing the effects of interface and those of the layers

$$\mathbf{S} = \mathbf{I}_{01} \mathbf{L}_1 \mathbf{I}_{12} \mathbf{L}_2 \ \ldots \ \mathbf{L}_m \mathbf{I}_{m\,(m+1)} . \tag{11}$$

The interface matrix for the i/j boundary is:

$$\mathbf{I}_{ij} = \frac{1}{\bar{t}_{ij}} \begin{bmatrix} 1 & \bar{r}_{ij} \\ \bar{r}_{ij} & 1 \end{bmatrix} ; \ (i = j - 1) \tag{12}$$

denoting by $\bar{t}_{ii}$ the transmission coefficient, and by $\bar{r}_{ij}$ the reflection coefficient.

The layer matrix for the j-th layer is

$$\mathbf{L}_j = \begin{bmatrix} e^{i\bar{\delta}_j} & 0 \\ 0 & e^{i\bar{\delta}_j} \end{bmatrix} , \tag{13}$$

with

$$\bar{\delta}_j = \frac{2\pi}{\lambda_0} d_j \cdot \bar{n}_j \cdot \cos \bar{\varphi}_j ,$$

the phase shift of incident light traversing the layer where λ_0 is the wavelength of incident light and $\bar{\varphi}_j$ is the complex angle of refraction.

The scattering matrix for an arbitrary number of layers is

$$\mathbf{S} = \begin{bmatrix} S_{11} & S_{12} \\ S_{21} & S_{22} \end{bmatrix} . \tag{14}$$

The fundamental equation of ellipsometry becomes:

$$\bar{r} = \frac{\bar{r}_p}{\bar{r}_n} = \frac{S_{21p}}{S_{11p}} \cdot \frac{S_{11n}}{S_{21n}} . \tag{15}$$

For our idealized (3 component) system (Fig. 1)

$$\mathbf{S} = \mathbf{I}_{01} \mathbf{L}_1 \mathbf{I}_{12} \tag{16}$$

and for the realistic (5 component) system

$$\mathbf{S} = \mathbf{I}_{01} \mathbf{L}_1 \mathbf{I}_{12} \mathbf{L}_2 \mathbf{I}_{23} \mathbf{L}_3 \mathbf{I}_{34} . \tag{17}$$

An ALGOL program was developed, suitable for computing the thickness and refractive index of the absorbing thin film, taking into consideration the effects of surface oxide film and the interface.

3. Experimental work

Experiments were carried out on Au and Al films, evaporated on Si substrate ($\bar{n}_2 = 4.05 - i0.028$) and NiO films grown by a thermal process on Ni substrate. The variation of the complex refractive index with film thickness was studied.

Type p Si(111) wafers (Wacker, 6 ohm cm) were used. They were etched in 98% H_2SO_4 for 10 min, rinsed in H_2O, dried and annealed in vacuum (5.10^{-5} Pa) at 573 K.

Au was evaporated from a tungsten boat, Al from a tungsten coil, using the following conditions:

substrate temperature: $T_h = 423$ K,
pressure: $p = 5.10^{-4}$ Pa,
deposition rate: $r_{\mathrm{Au}} = 0.4$ nm/s,
$r_{\mathrm{Al}} = 4$ nm/s.

Thermal growth of NiO was made at atmospheric pressure in an oxidizing furnace at 673 K. The NiO films were grown on polished (mechanical) and etched Ni substrates (Vakuumschmelze type S), baked in inert gas. The complex refractive index of the Ni substrate was determined on a great number of samples with the ellipsometer:

$$\bar{n}_2 = 1.731 - i3.26.$$

The thickness of the NiO film was controlled by the oxidation time.

Ellipsometric measurements were carried out with $\lambda = 546.1$ nm polarized light, produced by a stabilized light source. $\varphi_0 = 70°$ was chosen as angle of incidence [1], in order to provide sufficient sensitivity for the $\delta\psi$, δR and $\delta\Delta$ measurements. Considering the principal angles of incidence for Si and Ni ($\varphi_{P\mathrm{Si}} = 76.13°$, $\varphi_{P\mathrm{Ni}} = 79.9°$), ψ, Δ and R can be determined with a reasonable accuracy.

The refractive index and extinction coefficient of Au vs d film thickness are presented in Fig. 3, those of Al in Fig. 4. Curves n_r and k_r represent results calculated by the real, n_i and k_i those calculated by the idealized layer model.

In the case of Au thin film, the deviations between n_r and n_i are significant, according to Fig. 3, whereas the relative differences between k_r and k_i are much lower. For Al thin films, the difference $k_r - k_i$ becomes also sig-

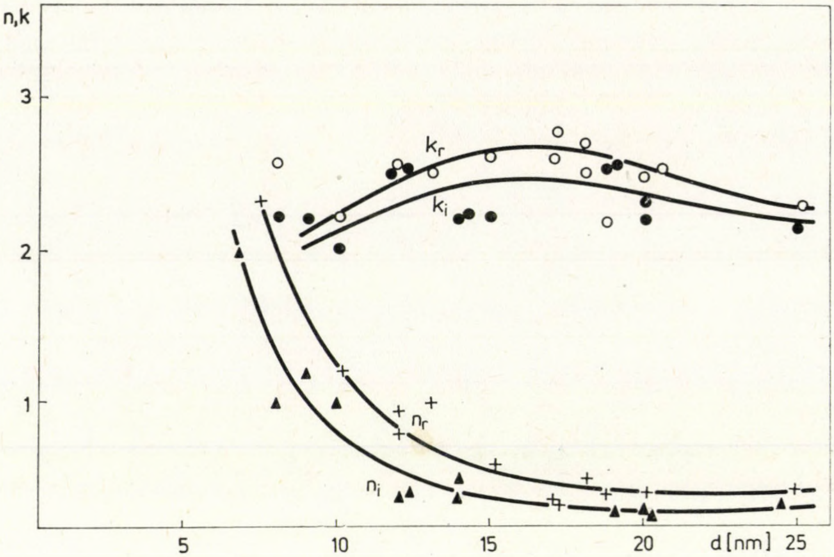

Fig. 3. Thickness dependence of the complex refractive index of Au film on Si substrate for the idealized [$\bar{n}_2 = n_i - ik_i$] and realistic [$\bar{n}_2 = n_r - ik_r$] layer models

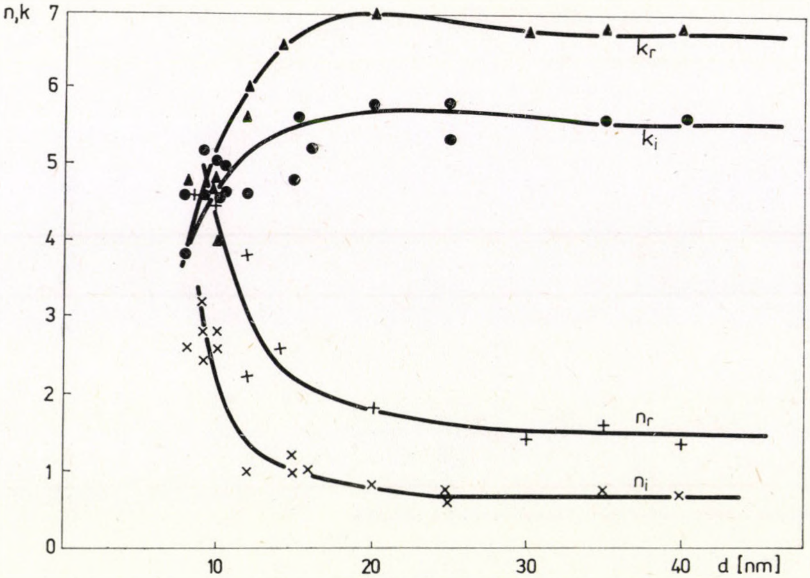

Fig. 4. Thickness dependence of the complex refractive index of Al film on Si substrate for the idealized [$\bar{n}_2 = n_i - ik_i$] and realistic [$\bar{n}_2 = n_r - ik_r$] layer models

nificant (Fig. 4). For Au and Al films, it was found that $n_r > n_i$, and $k_r > k_i$. n_1 and k_1 exhibit a strong thickness dependence in the $6 < d < 15$ nm range. Below $d < 6$ nm anomalies were noticed on our samples and layer systems. In this low d range, the application of various approximations (MAXWELL—GARNETT, STRACHAN and SIVUKHIN) did not supply reasonable results for the equivalent n_e, k_e, and d_e.

In the studies of the relations between refractive index and layer structure, the early stages of layer formation before achieving a continuous film, have been checked by electronmicroscopy (at the Research Institute for Technical Physics of the Hungarian Academy of Sciences).

Unambiguous $n_1 - d$, $k_1 - d$ relations were found on Au for $d > 8$ nm, on Al for $d > 6$ nm thickness. Films of $d_e \approx 4$ nm exhibited a granular structure. In the $d \approx 4$—6 nm range, island type structure is characteristic. For Au films above $d_e \approx 7$—8 nm, for Al above $d_e \approx 6$—7 nm, the coalescence of islands is starting. Above 10 nm, the continuous layer structure is built up. The anomalies of n_1 and k_1 can be explained by these structural transformations, and the big changes in the $6 < d < 15$ nm range as well.

The refractive index and extinction coefficient vs film thickness of NiO are presented in Fig. 5. Comparing them with results described in [8], these values are realistic. Comparing the n_r and k_r results with data published in the literature [6], [7] and taking into consideration the conditions of preparation the agreement is good.

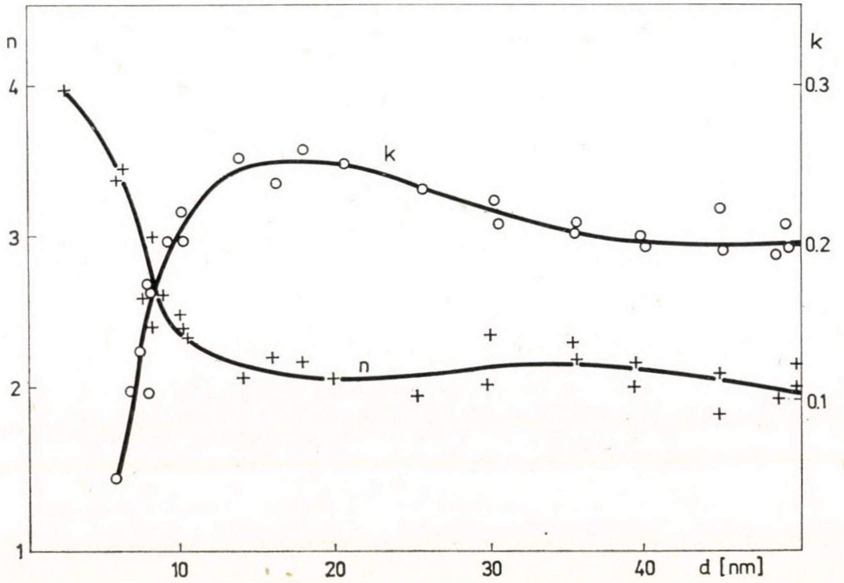

Fig. 5. Thickness dependence of the complex refractive index of NiO film prepared by thermal oxidation of Ni substrate

4. Conclusion

An experimental and computational ellipsometric method was developed for determining the refractive index and thickness of absorbing metal and metal oxide thin films. The RPD method proved to be adequate for evaporated Au and Al films, and NiO films as well, prepared by thermal oxidation.

Acknowledgements

The authors express their sincere thanks to Mr. E. BARLA, Director of the Tungsram Research Institute, for supporting their research work, to Dr. GY. GERGELY for his valuable advice in studying the structural dependence of refractive index and to Dr. B. P. BARNA (Research Institute for Technical Physics, Hungarian Academy of Sciences). for the electronmicroscopic analysis of our samples.

The authors are indebted to Mrs. M. VÁRNAI for kindly preparing the samples.

REFERENCES

1. W-K. PAIK and J. O'M. BOCKRIS, Surface Sci., **28,** 61, 1971.
2. M. BORN and E. WOLF, Principles of Optics, Pergamon Press, Oxford, 1965.
3. B. D. CAHAN, J. HORKANS and E. YEAGER, Surface Sci., **37,** 559, 1973.
4. R. C. O'HANDLEY, Surface Sci., **46,** 24, 1974.
5. R. M. A. AZZAM and N. M. BASHARA, Ellipsometry and Polarized Light, North-Holland Publ. Co., Amsterdam, 1977.
6. O. S. HEAVENS, Optical Properties of Thin Solid Films, Butterworths Sci. Publ., London, 1955.
7. L. K. CHOPRA, Thin Film Phenomena, McGraw-Hill Book Company Inc., New York, 1969.
8. K. GUPTA, J. P. MARTON and J. SHEWCHUN, J. Electrochem. Soc., **121,** 118, 1974.

Acta Physica Academiae Scientiarum Hungaricae, Tomus 49 (1—3), p. 167 (1980)

SPECTROSCOPIC ANALYSIS OF PLASMA ETCHING

By

G. VÁLYI, V. SCHILLER and I. SZABÓ

CENTRAL RESEARCH INSTITUTE FOR PHYSICS, HUNGARIAN ACADEMY OF SCIENCES
H-1525 BUDAPEST, HUNGARY

Abstract

The emission spectra of CF_4—O_2 discharges during etching of silicon and silicon dioxide are examined in order to indicate the end-point of the process. This method is used to study the mechanism of plasma etching, too. Results are explained by use of thermochemical data.

Acta Physica Academiae Scientiarum Hungaricae, Tomus 49 (1—3), pp. 169—174 (1980)

THE DETERMINATION OF Mg SURFACE ENRICHMENT IN HEAT TREATED AlMgSi ALLOYS USING THE SXES METHOD

By

L. KERTÉSZ, J. KOJNOK and A. SZÁSZ

INSTITUTE FOR SOLID STATE PHYSICS, LORÁND EÖTVÖS UNIVERSITY
H-1088 BUDAPEST, HUNGARY

Heat treatments result in Mg loss by diffusion from AlMgSi alloys. This was identified by many authors using different bulk measurements. Up to the present indirect methods have been applied to check the evaporation of Mg.

We studied this problem by soft X-ray emission spectroscopy (SXES) in the region of the $L_{2,3}$ emission peak of Al (approx. 17 nm) in a 150 nm thick layer. The heat treatment was made by electron beam, using the same beam also for the X-ray excitation, so the change of the Mg concentration in the surface layer was measured in vacuum undisturbedly.

Our results show that the Mg concentration essentially increases during the heat treatment near the surface. The bulk concentration of the Mg was 0,6 wt% and we recorded the same concentration in the initial state of the alloy on the surface too. After the heat treatment the concentration achieved a value of 70 wt% near the surface. The heat treatment was made at 480 ± 30 K.

It has been known for a long time that a prolonged heat treatment of AlMgSi alloys produces Mg enrichment on the surface [1].

In order to investigate this phenomenon resistance measurement [2], transmission electron microscopy [1], linear thermal expansion measurement [2], lattice parameter measurement [2], quadrupole mass spectrometric measurement [3], and microprobe [4] have been used.

The measurements unambiguously showed the surface enrichment or evaporation of Mg. Most of the investigations referring to this did not contain concrete data concerning the amount of Mg in the surface layer. Bulk type measurements were performed, with the exception of the measurement [4], extrapolating the Mg concentration on the surface.

In the following we summarize the main experiences of the research performed up to the present. Between the first heating and the heating cycles performed later, an essential difference was found. At the adequate temperature the process takes place in a relatively short time. The kinetics of the process can be expressed by the following relationship:

$$\frac{dc}{dt} = -M(c - c_\infty),$$

where c is the Mg concentration, c_∞ is its asymptotic value and M is a constant. Beside the effect of the diffusion processes certain oxidation processes take place. The equilibrium of the oxidation effect [5], and the evaporation [3], together with the diffusion process develop the Mg enrichment. That is why according to the measurements [4] the suitably measurable Mg enrichment develops only in the surface layer of a specimen heat-treated in air. A composite oxide structure is developing containing Mg and Al oxide [6]. The greater speed of oxidation is producing a Mg depleted zone beneath the Mg enriched surface layer.

In our present paper we attempt to determine the Mg concentration enriched in the 200 nm thick surface layer, preventing the oxidation of the specimen with heat treatment in vacuum.

Experimental equipment and conditions

For the investigation of the surface concentration of Mg we used the soft X-ray emission method (SXES). The main point of the method is that from the parameters of the characteristic soft X-ray radiation the electron density of states of the specimen can be determined. The scheme of the process is shown in Fig. 1 [7]. In our case for the relatively dilute solid solution, we performed most of our measurements on the transitions of the Al $L_{2,3}$ levels. According to the calculations of SEGALL [8] and ROOKE [9] the density of

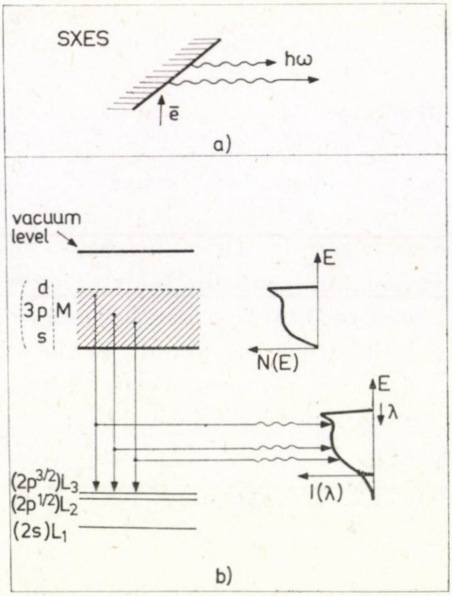

Fig. 1. The scheme of SXES process

states is given according to the relationship

$$I(E) \propto \nu^3 \, F(E) \; N(E) \, ,$$

where $I(E)$ is the X-ray intensity measured in arbitrary units, ν is the frequency of radiation, $N(E)$ is the part of the density of states involved, determined by quantum mechanical selection rules, $F(E)$ is the transition probability, and E is the energy.

On the above basis the Al $L_{2,3}$ SXES curve obtained by using the band structure calculation in [10] together with the first Brillouin zone, is shown in Fig. 2. The fine structure seen on the Al $L_{2,3}$ SXES curve, fitted at the gamma point 61.2 eV, exhibits a long wave tail with 1/2 power.

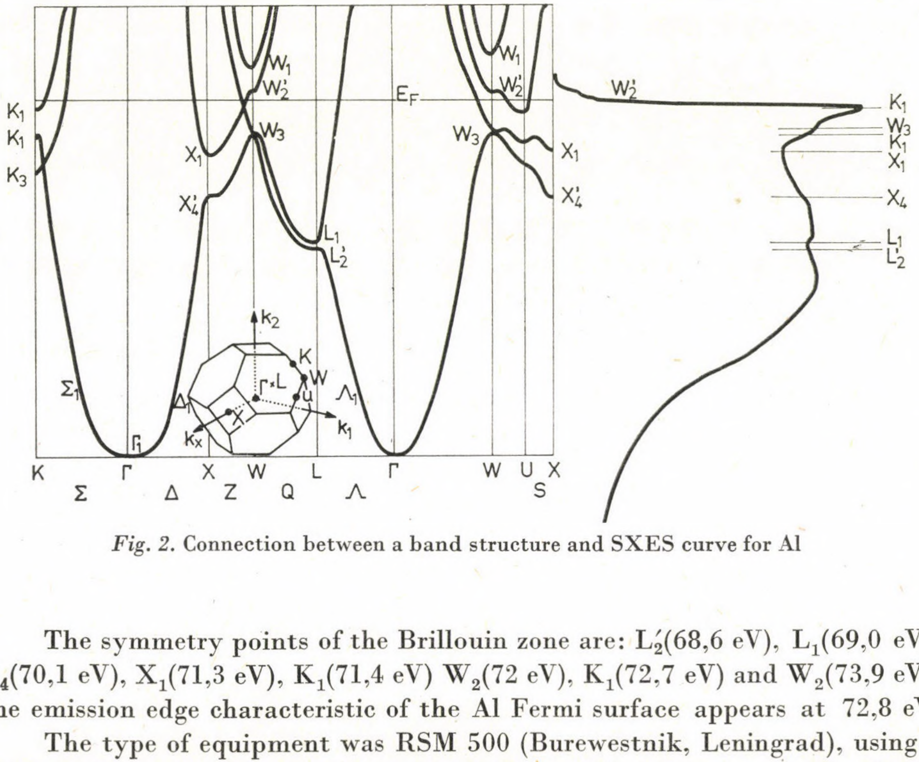

Fig. 2. Connection between a band structure and SXES curve for Al

The symmetry points of the Brillouin zone are: L_2'(68,6 eV), L_1(69,0 eV), X_4(70,1 eV), X_1(71,3 eV), K_1(71,4 eV) W_2(72 eV), K_1(72,7 eV) and W_2(73,9 eV). The emission edge characteristic of the Al Fermi surface appears at 72,8 eV.

The type of equipment was RSM 500 (Burewestnik, Leningrad), using a grating mirror, working in the 0,5—50 nm wavelength range, with photomultiplier detecting. The resolving power in the operating range was 0,07 nm (0,3 eV). The detailed description of the equipment may be found in the work of LUKIRSKII et al [11].

We performed the measurements using the transition of the Al $L_{2,3}$ levels. The specimens used were of $3 \times 10 \times 10$ mm^2, (15 mm long). The composition of the specimens was the following:

Al	matrix	
Mg	0,58 wt%	(0,65 at%)
Si	0,35 wt%	(0,34 at%)
Fe	0,14 wt%	(0,068 at%)
Cu	0,01 wt%	
Ti	0,03 wt%.	

The specimen was annealed for 45 min at 800 K in air and was quenched in water at room temperature.

The final treatment of the specimens was done "in situ" with an exciting electron beam (4 kV, 0.3 mA) in a vacuum not worse than 10^{-4} Pa. The temperature of the specimen during this heat treatment was 530 K ± 30 K, measured by the new method [12].

For the determination of the Mg concentration we used **Neddermayer**'s measurements, who has performed SXES measurements on AlMg alloys of different compositions [13].

Experimental results

As a starting point and for comparison we used the plot of AlMgSi taken after the annealing and quenching of the specimen (Fig. 3, curve a). The curve is essentially in agreement with the pure Al $L_{2,3}$ SXES curve, with the exception that the fine structure is less pronounced.

The plot shown in Fig. 3 curve b was taken after 9 min in situ heat treatment. Essential variation has not been found yet. The situation after

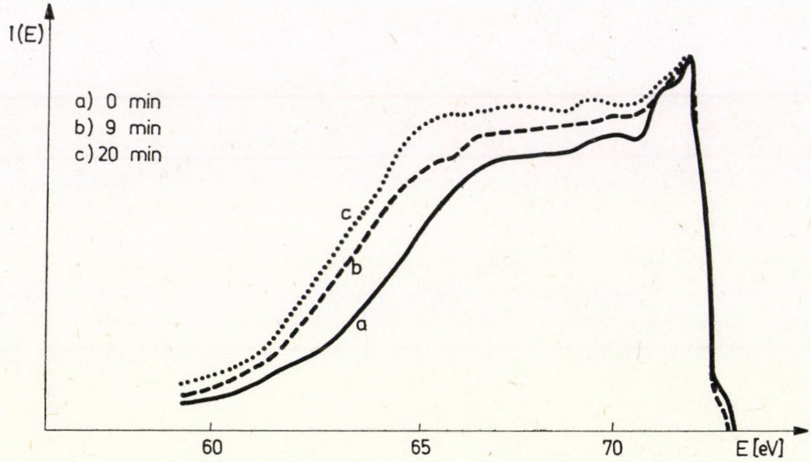

Fig. 3. SXES curves of AlMgSi alloys after annealing in vacuum. a) 0 min; b) 9 min; c) 20 min

20 min is shown by Fig. 3 curve c on which the appearance of a new local maximum can be observed at 66 eV.

With the further increase of the time of heat treatment, this peak emerges more vigorously and at the same time the maximum of the large peak below the emission edge gradually decreases. (Fig. 4 curves: a, b, c). After 80 and 90 min a new local peak appears at 63 eV (in Fig. 5 curves a, b). Curve c represents the emission spectrum after 200 min heat treatment, it does not change with further heating.

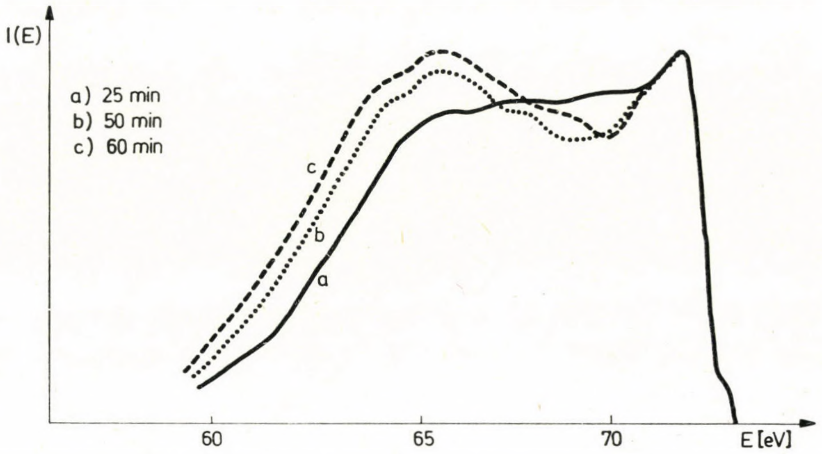

Fig. 4. SXES curves of AlMgSi alloys after annealing in vacuum a) 25 min; b) 50 min; c) 60 min

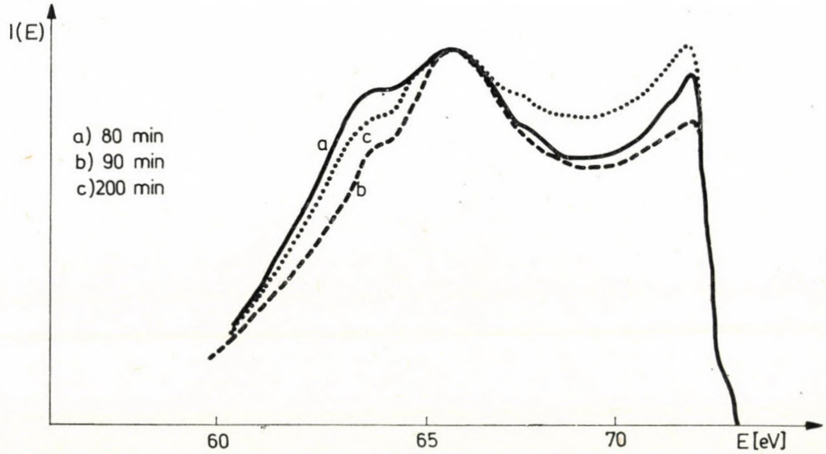

Fig. 5. SXES curves of AlMgSi alloys after annealing in vacuum. a) 80 min; b) 90 min; c) 200 min

Discussion

On the basis of NEDDERMAYER's work [13] on the various compositions of AlMg alloys, the spectra presented in Fig. 3 (curves a, b, c) correspond to 0.6 at%, 10 at% ± 5%, 20 at% ± 10% concentrations. Our experimental results in Fig. 4 (curves a, b, c) correspond to 30 at% ± 10%, 40 at% ± 10%, 50 at% ± 10% concentrations. The emission spectra in Fig. 5 (curves a, b, c) correspond to 60 at% ± 10%, 70 at% ± 10%, 40 at% ± 10% of Mg concentrations.

Thus the maximum Mg concentration in the surface layer under given conditions is 70%. It is most likely that the Mg atoms are outdiffusing from the matrix, and they evaporate from the surface during the same period.

From the measurements performed so far we can see that the enrichment of Mg concentration in the 200 nm thick surface layer significantly rearranges the density of states measured with the help of Al $L_{2,3}$.

This means that the density of states around 64 eV increases, and at the same time the density of states around the peak (72 eV) decreases significantly. These results are in adequate agreement with the modern theories (ATA, CPA) applied in the calculation of the density of states for alloys. The more detailed investigation of the problem is in progress.

In accordance with the results described above it can be ascertained that due to the effect of heat treatment for longer periods of time (90 min) at 500 K and higher temperatures, the Mg on the surface layer vigorously enriches and instead of the 24% obtained through extrapolation with the measurement [4], according to our measurements the concentration increases to 70%.

Acknowledgements

The authors wish to thank Prof. Dr. I. KOVÁCS, Dr. I. GÁL and Dr. G. TICHY for their valuable comments.

REFERENCES

1. D. K. CHATTERJEE and K. M. ENTWISTLE, J. Inst. Met., **101**, 53, 1973.
2. I. KOVÁCS, J. LENDVAI and T. UNGÁR, Mat. Sci. Eng., **21**, 169, 1975.
3. E. HIDVÉGI and E. KOVÁCS-CSETÉNYI, Mat. Sci. Eng., **27**, 39, 1977.
4. Á. CSANÁDY, V. STEFÁNIAY and D. BEKE, Mat. Sci. Eng., **38**, 55, 1979.
5. W. U. V. JENELTZER, J. Electrochem. Soc., **105**, 67, 1958.
6. Á. CSANÁDY, Conf. on Electronmicroscopy, Dresden, Jan. 23—25, p. 72, 1975.
7. D. J. SELLMAYER, Solid State Physics, **33**, 83, 1978.
8. B. SEGALL, Phys. Rev., **124**, 1797, 1961.
9. G. A. ROOKE, J. Phys. C. **1**, 767, 1968,
   J. Phys. C, **1**, 776, 1968.
10. S. P. SINGHAL and J. CALLAWAY, Phys. Rev., **16**, 1744, 1977.
11. A. P. LUKIRSKII, I. A. BRYTOV and N. I. KOMYAK: in Methods and Equipment in X-ray spectroscopy, 2. ed. Leningrad p. 2, 1967.
12. L. KERTÉSZ, A. SZÁSZ and A. A. KACNELSON: to be published.
13. H. NEDDERMAYER, in: Band Structure Spectroscopy of Metals and Alloys. Eds: D. J. Fabian and L. M. Watson, Academic Press, 1973, p. 153.

Acta Physica Academiae Scientiarum Hungaricae, Tomus 49 (1—3), p. 175 (1980)

PHOTOELECTRIC PROPERTIES OF ION-IMPLANTED SILICON

By

G. PETŐ and T. LOHNER

CENTRAL RESEARCH INSTITUTE FOR PHYSICS, HUNGARIAN ACADEMY OF SCIENCES
H-1525 BUDAPEST, HUNGARY

Abstract

The amorphous layer was formed on Si (111) surface by ion-implantation of $^{28}Si^{+}$, $^{31}P^{+}$ ions. The photoelectric properties of this amorphous layer were measured by 10,2 eV exciting photon energy and retarding field analyser. The surface contamination was checked by AES simultaneously.

The energy distribution curve of ion-implanted a-Si exhibits a very large secondary peak, structureless part towards higher energies and there is no observable edge at the high energy end of the spectrum.

The results for ion-implanted a-Si differ from the data presented in the literature for evaporated and cathode sputtered a-Si.

Acta Physica Academiae Scientiarum Hungaricae, Tomus 49 (1—3), p. 177 (1980)

CARBIDE FORMATION DUE TO Ar-ION ETCHING OF Si

By

ERICH KNY*

GRADUATE CENTER FOR MATERIALS RESEARCH
UNIVERSITY OF MISSOURI — ROLLA,
ROLLA, Mo. 65401, USA

Abstract

Hydrocarbons are among the main gaseous impurities observed in ion pumped UHV-systems. CH_4 is shown to play a crucial role in carbide formation on Si during Ar-ion etching. The carbide content of carbon free Si-samples was measured by AES during Ar-ion etching. A CH_4-content of the sputter gas of 0.9 at% corresponds to a C-content of the Si-sample of 1.2 at%, a CH_4 content of 3.7 at% corresponds to a C-content of 3.3 at%. A relationship between the C-content of a Si-surface and the CH_4-content of the Ar-gas used for Ar-ion etching can be shown. The effect of carbide formation on Si during Ar-ion etching can be attributed to ion and not to electron induced effects. To prove the formation of SiC the shape of the AES-carbon signal was compared with reference spectra of SiC and C (graphite). Mechanisms are discussed to account for the observed carbide formation on Si during Ar-ion etching. Carbide formation on Si can be avoided by working at base pressure of $4. \times 10^{-10}$ Torr or lower. This work is published elsewhere [1].

REFERENCE

1. E. KNY, J. Vac. Sci. Technol., **17**, 658, 1980.

---

* Present address: Universität Wien, Institut für Physikalische Chemie. A-1090 Wien, Austria

Acta Physica Academiae Scientiarum Hungaricae, Tomus 49 (1—3), p. 179 (1980)

THIN FILMS

ELEKTRONENMIKROSKOPISCHE STRUKTUR UND MECHANISCHE SPANNUNGEN VON SILBER- UND KUPFERAUFDAMPFSCHICHTEN UND IHRE ABHÄNGIGKEIT VON O_2-PARTIALDRUCK

Von

R. Koch und R. Abermann

INSTITUT FÜR PHYSIKALISCHE CHEMIE, A-6020 INNSBRUCK, ÖSTERREICH

Kurzfassung

Die mechanische Spannung von Ag- und Cu-Filmen wurde kontinuierlich mittels einer hochempfindlichen Biegebalkenapparatur in Abhängigkeit vom Sauerstoffdruck während der Metallaufdampfung gemessen. Mit Hilfe eines früher veröffentlichten Spannungsmodells [1] können Änderungen in den Spannungskurven eindeutig durch Strukturänderungen in den Metallfilmen erklärt werden. Die so ermittelte Schichtstruktur wurde in parallel durchgeführten elektronenmikroskopischen Untersuchungen bestätigt. Der unterschiedliche Einfluss des Sauerstoffs auf die Struktur der aufwachsenden Metallschicht lässt sich durch die unterschiedliche Stabilität der beiden Metalloxide erklären; Cu bildet bei den verwendeten O_2-Partialdrücken ein thermodynamisch stabiles Oxid, Ag jedoch nicht.

LITERATUR

1. R. Abermann, R. Kramer and J. Mäser, Thin Solid Films, **52**, 215, 1978.

Acta Physica Academiae Scientiarum Hungaricae, Tomus 49 (1—3), pp. 181—188 (1980)

FORMATION MECHANISM OF AMORPHOUS Ni-P THIN FILMS

By

T. Bagi, Z. Hegedüs

METALLURGICAL AND TECHNOLOGICAL INSTITUTE OF CSEPEL METAL WORKS TRUST
BUDAPEST, HUNGARY

E. Tóth-Kádár, I. Nagy

CENTRAL RESEARCH INSTITUTE FOR PHYSICS, HUNGARIAN ACADEMY OF SCIENCES
H-1525 BUDAPEST, HUNGARY

and

P. B. Barna

RESEARCH INSTITUTE FOR TECHNICAL PHYSICS, HUNGARIAN ACADEMY OF SCIENCES
H-1325 BUDAPEST, HUNGARY

Growth stages of amorphous Ni-P films deposited both by electrolytic and by chemical means were studied by electron microscopy. Nucleation and the growth of separated three dimensional grains have been proved.

Comparing the shape of grains with that of computed ones different mobilities of adatoms on the surface of growing grains have been found. The mobility of adatoms is promoted in the case of electrolytic deposition. The development of structural inhomogeneities ("supernetwork") can be attributed to the coalescence of grains as well as to the limited mobility of adatoms, building the amorphous structure of the grains.

Introduction

Extensive studies of amorphous films — especially of semiconductor and metallic ones — have unambiguously shown that a general characteristic of these films is a certain kind of structural inhomogeneity [1—9]. This structural inhomogeneity constitutes a quasi-periodical network, and can be visualized by means of phase contrast electronmicroscopy or by low-angle electron diffraction.

Some authors considered this network as a system of cracks [6, 7]; others [8, 9] basing their views in the first place on the investigation of amorphous Ge, amorphous Si and CoGd layers, regarded it as a region of lower density of the continuous amorphous network, a "supernetwork" [8, 9] where most of the atomic voids had accumulated. The correctness of the latter assumption was confirmed by the result of an in situ heat treatment of high purity amorphous Ge layers [3]. Thus this particular inhomogeneity in amorphous Ge layers can be heat treated. In the course of real structural rearrangement migration of the atomic voids takes place accumulating in bubbles that can be demonstrated unambiguously by means of electron microscopy. The bubbles thus formed are created principally in the original supernetwork. The rearrangement of the amorphous structure can be considered as indirect proof confirming that the supernetwork represents the region of accumulation of the atomic voids. A further justifiable assumption is — though to our knowledge no results of measurements to prove this directly have yet been published — that in the case of films having several components beside a change in density also the change in composition can be assigned to the supernetwork [9, 10].

Today it is well-known too, that the presence of structural heterogeneity and its characteristics strongly influence both the physical and chemical properties of the amorphous films (electrical conductivity in a-Ge films [11], hardness and corrosion properties of amorphous Ni-P deposited from aqueous solution [12]).

It is understandable therefore that recently increasing attention has been given not only to the determination of the real structure of amorphous films but also to the description of the formation of structural inhomogeneities. The earliest concept concerning amorphous Ge films originates from GALEENER [2], and one of the present authors developed further this model of formation of amorphous films [8]. According to this conception the formation starts with nucleation, and continues with the growth and then with the coalescence of the grains [13]. The area of the supernetwork is constituted by the regions of coalescence of grains. Thus this model takes into account the mobility of the atoms arriving at the substrate and condensing there in that case too when amorphous nuclei are formed. GUTZOV [14] and NEUMAN [15] found by thermodynamical considerations that when nuclei contain few atoms the formation of amorphous structure is more advantageous energetically. The same result was earlier obtained by GRIGOROVICI and coworkers [16] for amorphous Ge when the free energy had been calculated for different possible bond types. BARNA et al [13] simulated with a computer the change in the shape of grains growing from the solid amorphous nuclei condensed from the vapour phase. Their results represent well the effect of different supposed mobilities of adatoms on the surface of the substrate or on that of the forming amorphous grain, respectively, on the growth, the compactness and the change in shape of grains. Their results also reflect well the properties of different materials. In the case of amorphous Ge the adatoms practically cannot migrate along the periphery of the amorphous grain, thus two-dimensional grains of arm-like structure will be developed. In the case of Se and Sb films the individual adatoms should have relatively high mobility on the surface of the amorphous grains, because three dimensional cup shaped grains will grow.

Authors constructing other models for the formation of the inhomogeneous structure reflecting essentially a columnar structure, suppose that the condensing atoms are not mobile neither on the surface of the substrate nor on the surface of their developing amorphous grains [17, 18].

By computer simulation of the process they have shown that the shadow effect alone can be responsible for the columnar structure if the atoms are represented by hard spheres.

Staudinger and coworkers [7] have suggested on the basis of electrolytically prepared amorphous Ni-P films that the supernetwork is a crack network, and they assumed that it is developed according to the model of **Galeener** [2]. **Barna** et al [19] showed that during the initial period of layer formation three-dimensional grains grow up in these films deposited electrolytically and chemically.

The present authors have examined in detail the formation mechanism of the amorphous Ni-P films deposited by electrolytic and chemical means. This paper summarizes the results of the investigations.

Experimental methods

The films were prepared, in the case of chemical deposition, either on clean glass slides or on slides coated with collodium and C film, as well as on microgrids. In the case of electrolytic deposition they were deposited on an OFHC copper strip or on 100 nm thick Al film previously prepared by vacuum evaporation on microscope slides. The surface of the copper strip has been treated before preparation of the layer by chemical etching; the surface of the Al layer had been treated in NaOH and H_2SO_4 and rinsed in distilled water. In the case of chemical deposition the surface of the substrates was activated by the method known from the literature [20]. Chemical deposition took place at 90 °C. The electrolytic deposition was made from a solution containing $NiCl_2+NiSO_4$ at 75 °C, at current densities of 5 and 50 mA/cm^2.

For the purpose of TEM investigations the films were first coated with a thin layer of C (of thickness of about 10 nm), then separated from the substrate. This took place by dissolution of the colloidium or of the Al layer (the latter in 20% NaOH solution at 80 °C). From the copper foil the layer was separated in $NH_4OH+H_2O_2$.

Experimental results

Chemical deposition

Fig. 1 shows the different stages of film formation. In Fig. 1a the discrete nuclei and isolated grains grown from them can easily be seen. Nucleation of the Ni-P layer is uneven, inhomogeneous. The individual grains, proved to be amorphous by electron diffration, show a certain amount of polygonization. Their growth is not the same in the different directions. In general, growth is

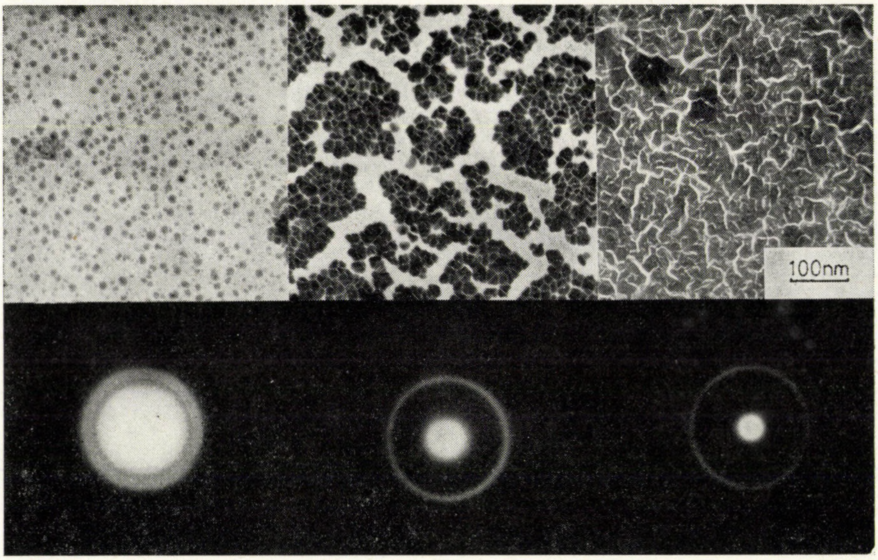

Fig. 1. Stages of the formation of a-NiP films prepared by chemical deposition

limited in the direction of the neighbouring grains, indicating thereby that the collection zone had been reduced by the neighbouring grain.

Fig. 1b shows the state of grain coalescence. It seems as if only a few contacting grains grew together by the way that their amorphous networks became connected to each other, i. e. the amorphous structure was able to become continuous. Most of the grain boundaries had sharp outlines indicating the presence of real gaps or cracks.

In the continuous films essentially three kinds of inhomogeneities are present (Fig. 1c): the coalescence zones that may be considered as reduced in density and/or in thickness; the coalescence cavities or holes formed along them [21]; the real cracks.

Electrolytic deposition

Structures characteristic of the individual stages of film growth can be seen in Fig. 2. Formation starts here also with nucleation and the growth of discrete grains (Fig. 2a). The grains present a nearly regular cup-shape form. On contact the amorphous networks developed in the grains grow together, then become continuous. However, contrast indicating the decrease of thickness or density may be observed in most coalescence zones.

In Fig. 2a where also the coalescence of some grains started, the formation of coalescence zones and cavities can be observed as well. This is similar to the process found in Sb layers [22].

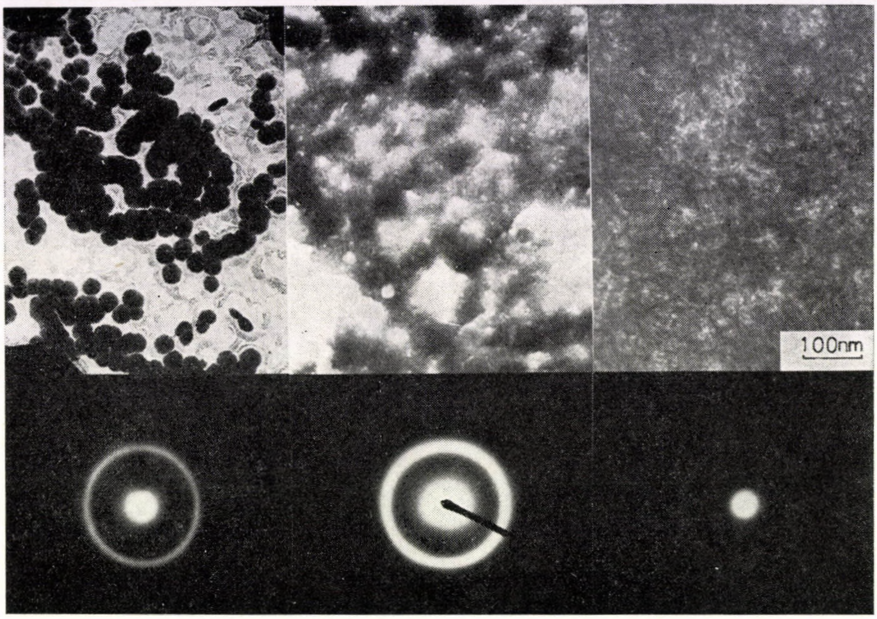

Fig. 2. Stages of the formation of a-NiP films prepared by electrolytic deposition

The already continuous layers are decorated by coalescence cavities, however, the contrast of the supernetwork representing the coalescence zones of the grains can be well distinguished, too (Fig. 2c). The cracks giving a definite, sharp outline, being so characteristic of the films formed by chemical deposition, are entirely missing here.

Conclusions

— The initial stage of formation of amorphous Ni-P films may be described in terms of nucleation, growth of three-dimensional discrete grains, then in terms of their coalescence in the case of both electrolytical and chemical deposition [23]. These results confirm the assumptions of MARTON et al [23] and STAUDINGER et al [7].

— Structure and morphology of the formed layers are determined by these processes. The inhomogeneities exhibiting the network system of lower density or thickness, the cracks and/or cavities develop during the coalescence of the amorphous grains.

— Analysis of the shape of the grains indicates that the mobility of the adatoms on the surface of the amorphous grains differs with the two methods of preparation. BARNA et al [13] have demonstrated in their computer simulation of the growth of the amorphous grains that the condition for developing

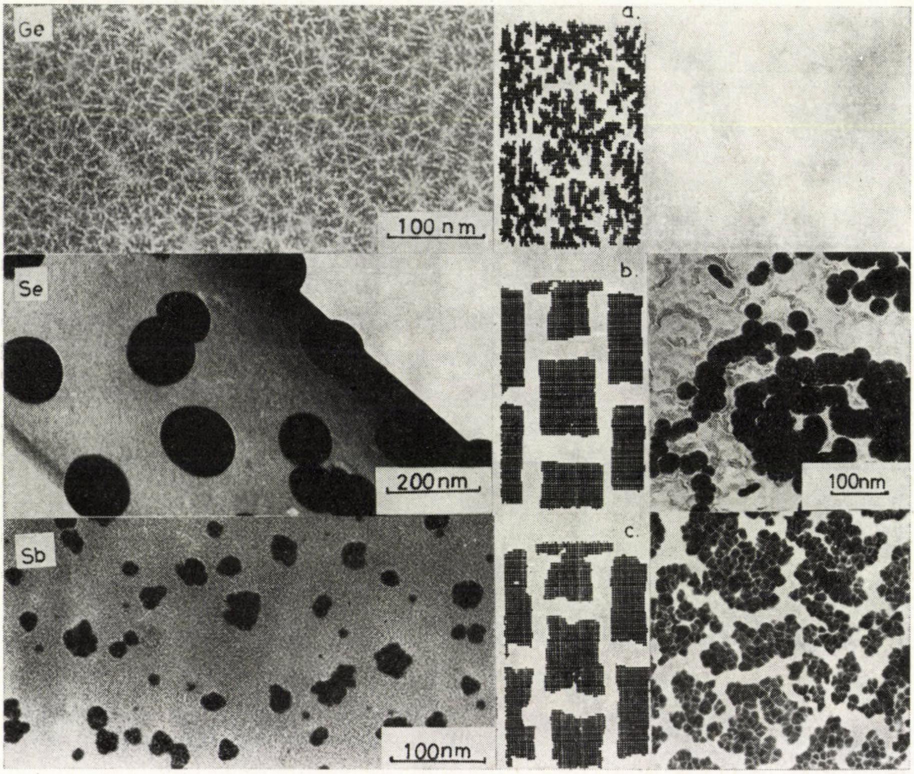

Fig. 3. The effect of adatom mobility on the shape of growing grains: Column I: grains of a-Ge (a), pure Se (b) and contaminated Sb (c) films, respectively; Column II: grains developed by computer simulation [13] by changing the mobility of adatoms; Column III: grains of a-NiP films developed by electrolytic (b); and by chemical (c) deposition

grains of regular cup-shape is the relatively high mobility of the adatoms. Thus in the case of electrolytic layer deposition one has to assume a relatively high mobility of the adatoms, whereas in the case of chemical deposition the mobility of the adatoms must be very limited. Fig. 3 shows the stage of the nucleation process of amorphous Ge, Se and Sb films in comparison with the chemical and electrolytic deposited Ni-P films and with the computer simulated ones [13] with low, high and medium adatom mobilities, respectively.

— The grains developed in the case of chemical deposition are three-dimensional although a very low mobility of the adatoms had been supposed. Based on the computer simulation [13] in that case the two-dimensional growth of indented grains should have been observed. The fact that it is not so can be explained by assuming that here "condensation" (deposition) of the adatoms constituting the film occurs only at preferred activated places, and not on the entire substrate surface. The nucleation begins at these active centres of the substrate surface and later on the places of further deposition will already be

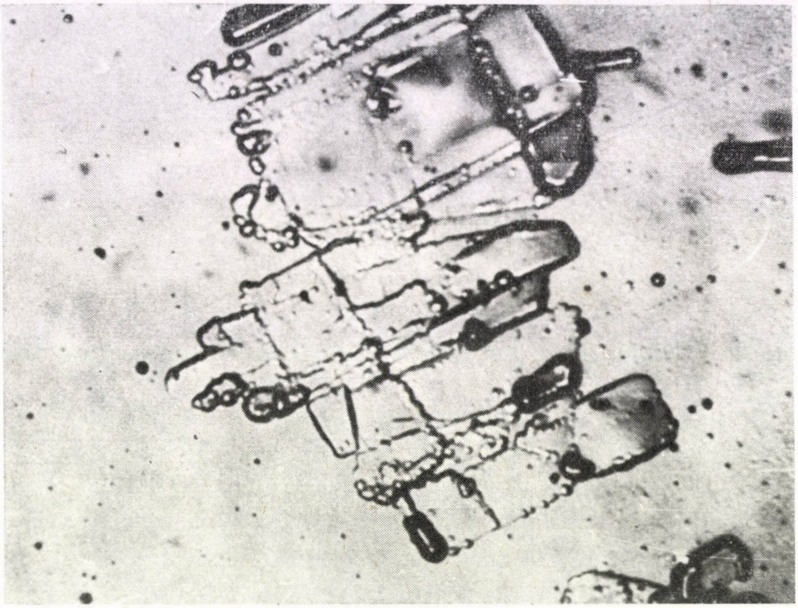

Fig. 4. Preferential nucleation of amorphous NiP on the surface of a crystalline inclusion in an amorphous CoP film

the Ni-P grains themselves. Fig. 4 shows nucleation starting on the surface of a crystalline inclusion formed in an amorphous CoP film. It can be clearly seen that the nucleation of amorphous phase begins at some preferred places of the crystal.

— The surface mobility of the adatoms controls the mechanism of grain coalescence also when preparing amorphous Ni-P films. The structure of the coalescence zone will be significantly different from the structure of grains in the case of limited mobility of the adatoms (chemical deposition), similarly, for example, to the amorphous Ge films [3]; a smaller structural difference will be created in the case of higher mobility of the adatoms (electrolytic deposition), similarly to the Sb or Se layers [22].

Acknowledgements

The authors' thanks are due to A. Barna and L. Tóth for valuable discussions.

REFERENCES

1. A. J. Shaldervan and N. G. Nakhodkin, Fizika Tverd. Tela, **11,** 3407, 1969.
2. F. L. Galeener, Phys. Rev. Lett., **27,** 1716, 1971.
3. Á. Barna, P. B. Barna, Z. Bodó, J. F. Pócza and I. Pozsgai, Proc. Fifth Int. Conf. on Amorphous and Liquid Semiconductors (Ed. J. Stuke and W. Brening), Taylor and Francis, London. 1974. Vol. 1, p. 109.

4. Á. Barna, P. B. Barna, G. Radnóczi, H. Sugawara and P. Thomas, Proc. Conf. on Structure and Excitation of Amorphous Solids (Ed. G. Lucovsky, F. L. Galeener), American Institute of Physics, New York, 1976, p. 199.
5. G. S. Cargill III., Thin Film Phenomena — Interfaces and Interactions (Ed. J. E. Baglin and J. M. Poate), The Electrochemical Society, Princeton, 1978, p. 221.
6. T. M. Donovan and K. Heinemann, Phys. Rev. Lett., **17**, 1794, 1971.
7. A. Staudinger and S. Nakahara, Thin Solid Films, **54**, 125, 1977.
8. P. B. Barna, Lecture, Conf. Amorphous Semiconductors '74, Reinhardsbrunn, 1974.
9. Á. Barna, I. Nagy, Gy. Radnóczi, P. Thomas and L. Tóth, Proc. of Amorphus Semiconductors '76 (Ed. I. Kósa-Somogyi), Akadémiai Kiadó, Budapest, 1977, p. 449.
10. T. Tarnóczi, I. Nagy, G. Mezei, T. Nagy, E. Kótai and G. Pető, 2ème Colloque International de Pulverisation Cathodique et ses Applications, Nice, 1976. V. Comp. Rendus, p. 141.
11. P. Thomas, Á. Barna, P. B. Barna and G. Radnóczi, phys. stat. sol. (a), **30**, 637, 1975.
12. K. T. Ziehlke, W. S. Dritt and C. H. Mahoney, Metal Progress, **77**, 84, 1960.
13. Á. Barna, P. B. Barna, G. Radnóczi, H. Sugawara and P. Thomas, Thin Solid Films, **48**, 163, 1978.
14. J. Gutzov and J. Avramov, J. Non-Crystalline Solids, **16**, 128, 1974.
15. H. G. Neumann, Thesis, privat communication, 1978.
16. R. Grigorovici and R. Manaila, J. Non-Cryst. Solids, **1**, 371, 1969.
17. D. Henderson, M. H. Brodsky and P. Chaudhary, Appl. Phys. Lett., **25**, 641, 1974.
18. A. G. Dirks and H. J. Leamy, Thin Solid Films, **47**, 219, 1977.
19. Á. Barna, P. B. Barna, A. Belu, A. Dévényi, G. Radnóczi, P. Thomas and L. Tóth, Abstracts, IX. Hungarian Diffraction Conference, Pécs, Hungary, 1978. p. 3.
20. G. G. Gawrilov, Chemische (stormlose) Vernicklung, Eugen Leuze Verlag, Saulgau, 1974. p. 29.
21. J. R. Lloyd and S. Nakahara, J. Vac. Sci. Technol., **14**, 655, 1977.
22. Á. Barna, P. B. Barna, G. Radnóczi and I. Rechenberg, Acta Technica Acad. Sci. Hung., **80**, 281, 1975.
23. J. P. Marton and M. Schlesinger, J. Electrochem. Soc. Electrochemical Science, **115**, 16, 1968.

Acta Physica Academiae Scientiarum Hungaricae, Tomus 49 (1—3), p. 189 (1980)

SIMULATION OF ANTIMONY THIN FILM GROWTH

By

H. MÜLLER

ACADEMY OF SCIENCES OF GDR, CENTRAL INSTITUTE FOR OPTICS AND
SPECTROSCOPY, 69 JENA, GDR

Abstract

The well-known spherulitic structure of vacuum deposited antimony films suggests a simulation with a pair of compasses. The main reason for this simulation is that no one has yet explained why the distribution of antimony clusters after the amorphous — crystalline transition is, at least in parts, organized in a regular hierarchy. Another reason, less important, for the simulation concerning the regularity is that one did not know how to explain the crystallization process.

With this purely empiric and strongly idealized method it was possible to find out a great deal of correspondence between micrographs, electron micrographs and simulated patterns both of the surface and cross-sectional structure.

The external boundaries of the spherulites are well defined by different crystallization rates and by retardation at the beginning of crystallization due to the statistical character of the coalescence.

Different assumptions about the mechanism of crystallization led to the simulation of the cross-sectional structure which is responsible for the internal boundaries of the spherulites. These internal structures are very rich in forms but always characteristic of antimony thin films.

The interaction of various models will be demonstrated by the comparison of original and simulated patterns.

Acta Physica Academiae Scientiarum Hungaricae, Tomus 49 (1–3), p. 191 (1980)

IMPULSE STIMULATED CRYSTALLIZATION IN AMORPHOUS SEMICONDUCTOR FILMS

By

G. Bajor
TECHNICAL UNIVERSITY, H-1521 BUDAPEST, HUNGARY

C. E. Wickersham
BATTELLE COLUMBUS LABORATORY, COLUMBUS, OHIO, USA

and

J. E. Greene
UNIVERSITY OF ILLINOIS, URBANA, ILLINOIS, USA

Abstract

Rapid irreversible exothermic amorphous-to-polycrystalline phase transitions have recently been reported in amorphous Ge and $In_{1-x}Ga_xSb$ films. Such transformations occur in 10^{-6} s in a local domain (with a typical diameter of 1 μm) of the film in response to an energy impulse supplied, for example, optically by a pulsed laser or mechanically by a needle tipped stylus. The crystallization front can propagate throughout the film in a cascade process with velocities of the order of several hundred cm/s if the energy released from the crystallization of one domain is sufficient to trigger the adjacent domain under the existing experimental conditions. Experimental results are presented which demonstrate that propagation of the crystalline front depends upon the sample temperature as well as its thermal history. A simple thermal transport model is also presented which expresses in functional form the parametric requirements for the propagation of impulse stimulated crystallization (ISC). All reported experimental results including the sample temperature and thermal history dependence, variations in the transformed surface topographical structure, and the critical thickness effect can be explained by this model.

Acta Physica Academiae Scientiarum Hungaricae, Tomus 49 (1—3), p. 193 (1980)

ÜBER ROTIERENDE STRAHLUNGSFILTER ZUR TRENNUNG VON TEILCHEN- UND WÄRMESTRAHLUNG BEI BEDAMPFUNGSPROZESSEN

Von

P. Golob und E. Jakopic

FORSCHUNGSZENTRUM FÜR ELEKTRONENMIKROSKOPIE, GRAZ, ÖSTERREICH

Kurzfassung

Zur strahlungsfreien Bedampfung sind seit längerem rotierende Filter bekannt [1], wobei verschiedene Ausführungsformen möglich sind, wie Scheiben, Zylinder, Trommeln. Die Optimierung solcher Anordnungen kann einerseits im Hinblick auf maximale Durchlässigkeit (grösster Dampfstrom), andererseits aber auch auf die Erzielung eines bestimmten begrenzten Geschwindigkeitsbereiches der durchgelassenen Teilchen vorgenommen werden. Die hiefür benötigten Berechnungsgrundlagen werden diskutiert.

LITERATUR

1. H. R. F. Horn, Proc. Vth Int. Congr. for Electr. Mic. Philadelphia, 1962, Vol I, A—9.

Acta Physica Academiae Scientiarum Hungaricae, Tomus 49 (1—3), p. 195 (1980)

PENNING-TYPE SPUTTERING SOURCES

By

G. KERTÉSZ and GY. VÁGÓ

INDUSTRIAL RESEARCH INSTITUTE FOR ELECTRONICS
H-1393 BUDAPEST, HUNGARY

Abstract

Sputtering plays a more and more important role among the vacuum technologies because of its advantages. The less favourable features — low rate and relatively high energy ions damaging the substrate — could have been eliminated by utilizing the Penning discharge.

The paper gives a survey of the main S-gun types. The source developed by the authors differs from the other ones in the arrangement of the magnet. There is such a magnetic field formed that the sputtering of the target surface is more homogeneous. The paper presents this source and some of the results obtained with it.

Acta Physica Academiae Scientiarum Hungaricae, Tomus 49 (1—3), p. 197 (1980)

DESCRIPTION OF GRAIN BOUNDARY-SUPPORTED INTERDIFFUSION IN THIN FILMS BY AN EFFECTIVE DIFFUSION PARAMETER

By

E. Ehrmann-Falkenau and A. Wagendristel

INSTITUTE FOR APPLIED PHYSICS, TECHNICAL UNIVERSITY OF VIENNA, VIENNA, AUSTRIA

Abstract

Short circuit diffusion along grain boundaries, interfaces and surfaces strongly support the mixing process in thin polycrystalline multilayers. For many practical considerations such a complex type of interdiffusion is sufficiently described by one single parameter, the effective diffusion coefficient. On the basis of a computer study the present paper deals with the influence of the grain boundary structure and its change during diffusion onto the mean diffusivity. An estimation of bulk diffusivities using structural data and the mean diffusivity is suggested.

Acta Physica Academiae Scientiarum Hungaricae, Tomus 49 (1—3), pp. 199—205 (1980)

MASS SPECTROMETRIC STUDY OF SEMICONDUCTOR LAYER STRUCTURES

By

D. Szigethy, G. Gergely, I. Mojzes, T. Sebestyén
RESEARCH INSTITUTE FOR TECHNICAL PHYSICS, HUNGARIAN ACADEMY OF SCIENCES
H-1325 BUDAPEST, HUNGARY

and

M. Riedel
INSTITUTE FOR PHYSICAL CHEMISTRY AND RADIOLOGY, ROLAND EÖTVÖS UNIVERSITY
H-1088 BUDAPEST, HUNGARY

The mass spectrometric study of the evaporation of As and P, respectively, during contacting of GaAs and GaP diodes was reported at the 7th International Vacuum Congress (Vienna 1977). Now new results obtained on various contact-crystal systems are presented. A laboratory SIMS system was built using a Riber QML 51 quadrupole mass spectrometer. The study of contacting processes was followed by SIMS in depth profiling of the contact-GaAs layer structures. Some SIMS studies of SiO_2 layers prepared by various methods are described.

I. Introduction

This paper is devoted to mass spectrometric studies on some semiconductor $A^{III}B^{V}$ layer structures and Si-SiO_2 systems, using the methods and equipment developed in our laboratory. The mass spectrometric study of the evaporation of volatile components during heat treatment of metallized $A^{III}B^{V}$ semiconductor layer structures was performed and described by Sebestyén and coworkers [1, 2]. Kinsbron gave new data on the dissociation of GaAs and GaAlAs covered with gold contact films [3]. Now some new results are presented on systems containing gold and silver.

II. Experimental results and discussion

The decomposition, outdiffusion and evaporation of components from metallized semiconductor surfaces were studied by a Riber QML 51 quadrupole mass spectrometer.

The contacting processes of diodes prepared from $A^{III}B^{V}$ (GaAs or GaP) crystals using various contact structures were studied in detail. Thin (100—400 nm) film of Au, AuGe, AuGeNi, AuNi, AuCr, Ag, AgSn, AgNi and InGeAg have been deposited on both faces on GaAs (100) wafers (3×3 mm^2) or on GaP (111) surfaces.

During the alloying process in the range of 300—600 °C As_2 or P_2 losses were detected by the mass spectrometer. The loss of the volatile component (Y) originates from the decomposition of the contact-crystal interface layers [1, 2]. A steep rise characteristic of the contact composition and substrate occurs at the onset of alloying.

The temperature variation of the resistance of the metal — semiconductor structure was recorded during the annealing simultaneously with the arsenic evaporation rates. According to the method described in [4] a low measuring current was applied to the specimen and the potential drop was recorded during the annealing. This voltage is proportional to the momentary resistance of the sample in the 20—200 °C temperature range as it was shown in [5]. Some characteristic $R(T)$ and $Y(T)$ curves are presented in the Figures. The study of contact system AuGeNi — GaAs has already been described in [2, 4]. The $Y(T)$ and $R(T)$ characteristics are strongly affected by the composition of the layer structures. Fig. 1 represents the R-Y-T curves for the Au—GaAs—Au system during the alloying cycle.

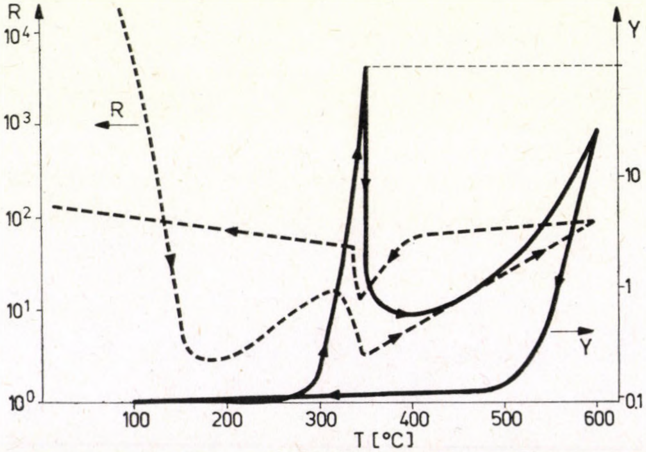

Fig. 1. Variation of R and Y (arbitrary units) with T for Au-GaAs-Au during the first annealing cycle. Heating and cooling rate 150 °C/min

Applying a second heat treatment a drastic change occurs in the R-Y-T curves due to further As_2 losses as shown in Fig. 2.

Fig. 3. represents the case of Ag—GaAs—Ag layer structures.

An interaction of an As_2 molecular beam with GaAs — metal system and same metal structures deposited on molybdenum plates was described in our recent paper [6].

Recently, mass spectrometric studies of semiconductor layer structures have been completed by SIMS studies [7, 8]. A laboratory SIMS system has been built using a Riber QML 51 mass spectrometer mounted on an UHV system built with Tungsram components, working at 10^{-7} Pa pressure range. The system operated with a PHI 04—191 ion gun, at 10^{-3}—10^{-5} Pa Ar pressure using 3—300 μA/cm^2 ion current and 0,5—5 keV. More details of the SIMS system are given in [9].

The interference microscope picture after in-depth profiling with a scanning ion beam and a copper diaphragm of 2,5 mm diameter hole, producing a steep and uniform crater is shown in Fig. 4.

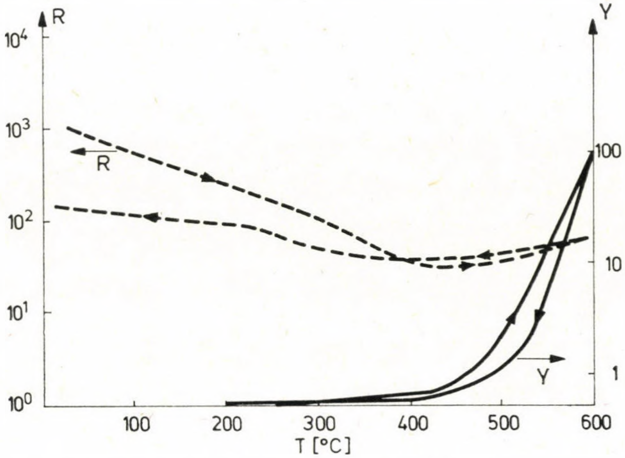

Fig. 2. Variation of *R* and *Y* (arbitrary units) with *T* for Au-GaAs-Au during the second annealing cycle. Heating and cooling rate 150 °C/min

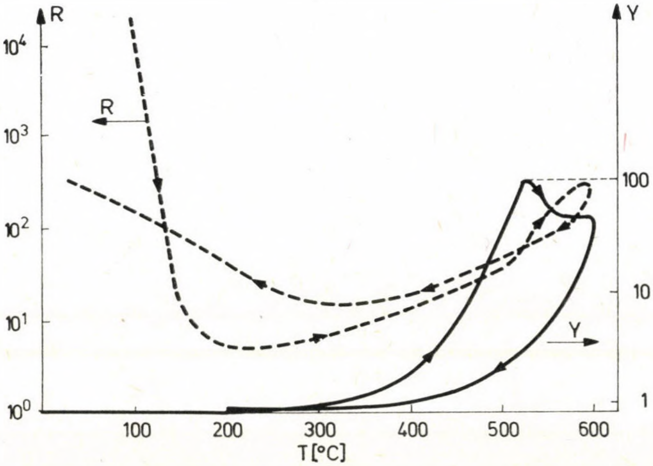

Fig. 3. Variation of *R* and *Y* (arbitrary units) with *T* for Ag-GaAs-Ag. Heating and cooling rate 150 °C/min. Alloying cycle

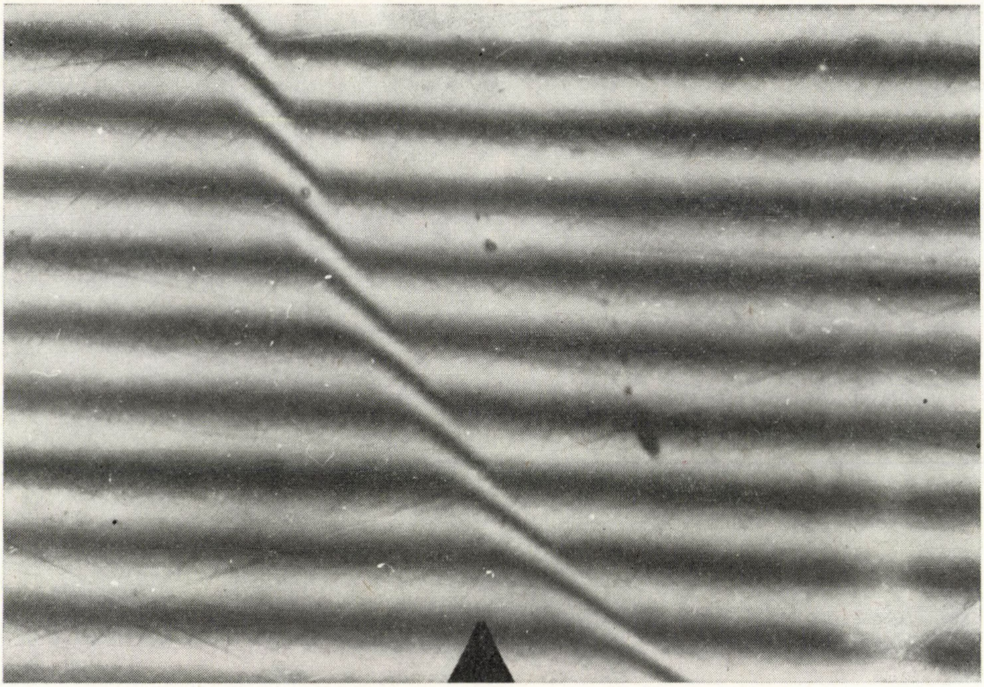

Fig. 4. Interference microscopic picture of a sputtered crater

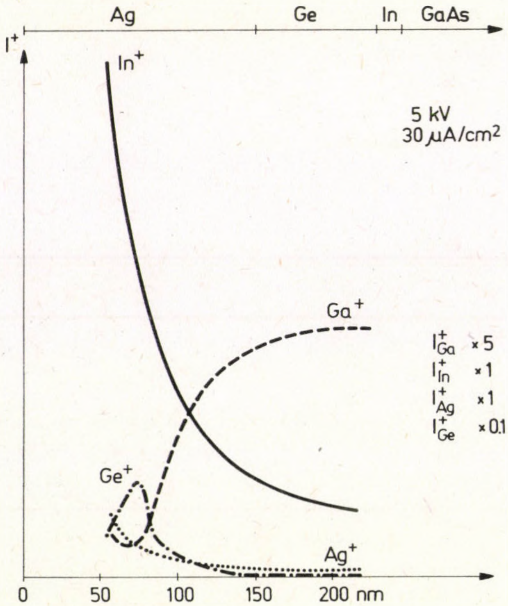

Fig. 5. In-depth profile of an Ag-Ge-In contact system evaporated on GaAs, exhibiting diffusion of the components. I_{Ge} etc. SIMS peaks in arbitrary units

Analyzing the fringes the depth of sputtering in Fig. 4 was determined as 270 nm. Sputtering rates can be determined using this method.

Some preliminary results obtained on contacted GaAs and Si—SiO_2 layer structures are presented in Figs. 5—7 and Tables I—III.

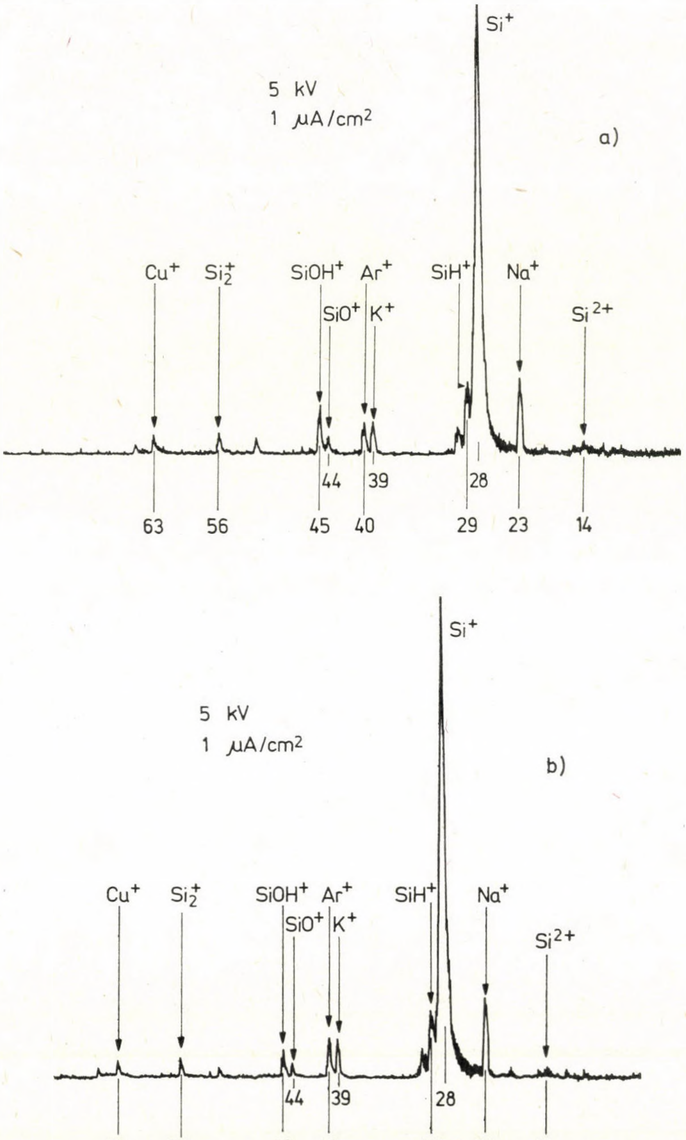

Fig. 6. SIMS spectra of two SiO_2 layer structures, prepared by different technological processes by M. NÉMETH-SALLAY. Sample a) oxidized in dry O_2; b) the same ether-treated [8]

Table I

Relative SIMS intensities of the most commonly used elements

Al^+	Si^+	Ga^+	Ge^+	In^+	Ag^+
1000	10–240	1000	10–30	100–500	5

Table II

Characteristic peaks referred to Si^+

Mass number	ion	oxidized in			
		dry O_2	wet O_2	dry O_2	wet O_2
		—	—	ether-treated	
14	Si^{2+}	0.0068	0.0079	0.0093	0.013
29	SiH^+	0.14	0.12	0.11	0.122
44	SiO^+	0.030	0.020	0.047	0.023
45	$SiOH^+$	0.093	0.038	0.049	0.040
56	Si_2^+	0.036	0.038	0.038	0.055

Table III

Characteristic peaks referred to Cu^+

Mass number	ion	oxidized in			
		dry O_2	wet O_2	dry O_2	wet O_2
		—	—	ether-treated	
14	Si^{2+}	0.20	0.19	0.39	0.30
28	Si^+	29.6	24.5	36.7	22.9
29	SiH^+	4.0	2.9	4.2	2.9
44	SiO^+	0.88	0.5	1.7	0.53
45	$SiOH^+$	2.74	0.92	1.8	0.93
56	Si_2^+	1.1	0.7	1.4	1.3

Fig. 5 represents the in-depth profile of an AgGeIn contact system evaporated on GaAs exhibiting diffusion of the components [10]. I_{Ge} etc SIMS peaks are presented in arbitrary units. As is well known, the sputtering and ion yield in SIMS studies are strongly affected by the composition of the target, conditions of sputtering on the mass spectrometer system and matching. The recorded intensities in Fig. 5 are not corrected for sputtering yield and sensitivity factors of the secondary ionization. To make a rough estimation of relative concentrations, relative secondary ion yield data taken from the literature and averaged from several authors' results [7] are given in Table I.

The Si—SiO$_2$ system was investigated by several authors. Here MAUL [10] and BÁRSONY [11] are quoted, reporting on the variation of SIMS spectra with methods of preparation of the oxide layer. In a recent paper BARNA and coworkers [12] have dealt with ether-treated SiO$_2$ layers. In our paper, some additional results are presented. In Figs. 6A and B SIMS spectra of two SiO$_2$ layer structures prepared by different technological processes, described in [12] are presented.

As found by BARNA and coworkers [12] the main effects manifest themselves in the variation of hydroxil content (observed as SiOH$^+$ ions) on SiO layers prepared by different methods. Ether-treating appreciably reduces the hydroxil content.

The copper diaphragm used for in-depth profiling supplies some kind of reference standard for the SIMS spectra, obtained on various samples.

This paper is confined to some mass spectrometric studies, illustrating their applications on semiconductor problems, associated with technology, but omitting the technological aspects. More details are given in the references quoted and will be published in other papers.

*

The authors express their sincere thanks to Mrs. M. NÉMETH-SALLAY for preparing and kindly submitting the Si—SiO$_2$ samples.

REFERENCES

1. T. SEBESTYÉN, M. MENYHARD and D. SZIGETHY, Electronics Lett., **12**, 96, 1974.
2. D. SZIGETHY, T. SEBESTYÉN, I. MOJZES and G. GERGELY in Proc. 7th International Vacuum Congress and 3rd International Conf. Solid Surfaces, Vienna, 1977, Vol. II, p. 1959.
3. E. KINSBRON, P. K. GALLAGHER and A. T. ENGLISH, Solid-State Electronics, **22**, 517, 1979.
4. I. MOJZES, phys. stat. sol. (a), **47**, K183, 1978.
5. I. MOJZES, Acta Phys. Hung., **48**, 131, 1980.
6. I. MOJZES, T. SEBESTYEN, P. B. BARNA, G. GERGELY and D. SZIGETHY, Thin Solid Films, **61**, 27, 1979.
7. M. RIEDEL and B. PEROVIĆ, Boris Kidrič Inst. Nucl. Phys. Beograd, IBK 1349, 1975.
8. K. VARGA-JOSEPOVITS and P. PAVLYÁK: A szilárdtestkutatás újabb eredményei (Recent results in solid state research, in Hungarian). Ed.: G. Gergely, Akadémiai Kiadó, Budapest, **5**, 175, 1979.
9. D. SZIGETHY and M. RIEDEL, Proc. XXII. Hung. Conf. Spectral Analysis, Salgótarján, June 1979, 191, 1979.
10. J. MAUL and K. WITTMACK, Surface Sci., **47**, 358, 1975.
11. I. BÁRSONY, D. MARTON and J. GIBER, Thin Solid Films, **51**, 275, 1978.
12. Á. BARNA, M. NÉMETH-SALLAY, I. C. SZÉP, P. I. DIDENKO, V. G. LITOVCHENKO, P. I. MARCHENKO and G. F. ROMANOVA, Thin Solid Films, **55**, 355, 1978.

Acta Physica Academiae Scientiarum Hungaricae, Tomus 49 (1—3), pp. 207—214 (1980)

STRUCTURE AND ELECTRICAL PROPERTIES OF AMORPHOUS Ge—Mo FILMS

By

A. BELU, A. DÉVÉNYI, R. MANAILA, L. MIU, C. RUSU
INSTITUTE OF PHYSICS AND MATERIALS TECHNOLOGY, BUCHAREST, ROUMANIA

and

Á. BARNA, P. B. BARNA, G. RADNÓCZI, L. TÓTH
RESEARCH INSTITUTE FOR TECHNICAL PHYSICS, HUNGARIAN ACADEMY OF SCIENCES
H-1325 BUDAPEST, HUNGARY

Coevaporated amorphous $Ge_{1-x}Mo_x$ films $(0.07 \leq x \leq 0.32)$ were investigated by means of electron microscopy, electron and X-ray diffraction and electrical measurements. Inhomogeneity in the Mo concentration has been found only in the samples of high metal content.

Mo causes drastic changes in the ED and XRD patterns of a-Ge. The experimental interference functions for $x \leq 0.22$ are well matched by those calculated on the basis of a structural model for a relaxed a-Ge random network in which the Mo atoms fill part of the empty space.

In the range 80 – 470 K both samples with $x = 0.07$ and 0.16 display activation energies ΔE 6 times less than those of a-Ge and close to $k_B T$, which is indicative of hopping on high density localized states. Below 80 K for the samples of high Mo content ΔE becomes very small suggesting the presence of metallic regions, which dominate conduction at low T.

Introduction

Cermets, consisting of a metal dispersed on atomic scale into a dielectric matrix, represent a new class of materials of technical interest, their physical properties being still hardly understood. Cermets are stable materials with controllable electrical resistivity ϱ and small thermal coefficient of the electrical resistance TCR ($\pm 5.10^{-5}\,K^{-1}$). They are good candidates for passive resistors with small TCR in microelectronics. Also, cermets with optimized profiles of the metal concentration are much explored nowadays as absorbers for solar cells. Cermets are usually obtained as thin films, by co-deposition of the components.

The system investigated in the present work represents an alteration of amorphous Ge, which is a reference material in the physics of amorphous semiconductors, by introducing a metal, thereby modifying its electrical properties and its structure. Thus, by lowering the electrical resistivity the range of conduction measurements can be extended below 10 K. Also, the relatively high Debye temperature of Mo (360 K) suggests a slow diffusion of Mo in Ge, without formation of metallic Mo islands. At higher Mo concentrations a superconducting behaviour is expected, Mo having a critical temperature T_c of 0.98 K, while Ge shows no superconductivity at normal pressure.

Preparation

$Ge_{1-x}Mo_x$ films with $0.07 \leq x \leq 0.32$ were obtained by coevaporation from two independently controlled sources, under a residual pressure of 1.10^{-4} Pa. Mo was evaporated from an electron gun while Ge from a W filament. The deposition rate was controlled by means of a calibrated photodiode. The composition parameter x was varied by changing the deposition rate of Mo. The films were deposited on fused silica substrates maintained at room temperature, on which Mo electrodes in planar configuration had been deposited. The deposition rate was 6—11 nm/min. Samples for electrical conduction, thermopower and piezoresistance measurements (thickness 80—100 nm), for electron microscopy and diffraction (thickness 30—80 nm) as well as for X-ray diffraction (thickness 0.25—0.6 μm) were deposited at the same time.

Electron microscopy

Electron micrographs of the samples Mo concentrations $x < 0.16$ show a microstructure very similar to that of pure amorphous Ge (Fig. 1) [1]. This means that a quasi-periodic density fluctuation is present in the films which causes a weak phase contrast on the micrographs. The mean period length is 10—15 nm without any remarkable change with composition. The amplitude of these fluctuations, however, becomes higher with increasing Mo content. It can be supposed that in the samples $x \geq 0.22$ fluctuations occur not only in density but also in concentration. Probably Mo-rich regions are formed without any crystalline Mo precipitation, and pointing to increasing separation tendency of two different amorphous phases with increasing metal content.

Electrical properties

Electrical resistance measurements in the wide temperature range 1,9—760 K showed a semiconducting behaviour (TCR < 0) for $x < 0.16$. The electrical properties were described by the variation of the activation energy ΔE with temperature T. The activation energies were calculated from the $\varrho(T)$ data and from the $S(T)$ (thermopower) data by a numerical differentiation program.

The samples with $x = 0.07$ and 0. 16 show activation energies of the conduction ΔE_σ smaller by a factor of $\simeq 6$ as compared to an evaporated a-Ge sample (Fig. 2). For $T > 80$ K ΔE_σ is practically equal to $k_B T$ (k_B is the Boltzmann constant) which is indicative of a hopping conduction mechanism on high density localized states [2]. These states should be attributed to Mo dispersed on an atomic scale in the a Ge matrix which seems to be a characteristic feature of the cermets [3].

The Mo concentration determines the ΔE_σ values for $T < 80$ K. For $x = 0.07$, ΔE_σ is almost coincident with k_BT while with increasing x ΔE_σ

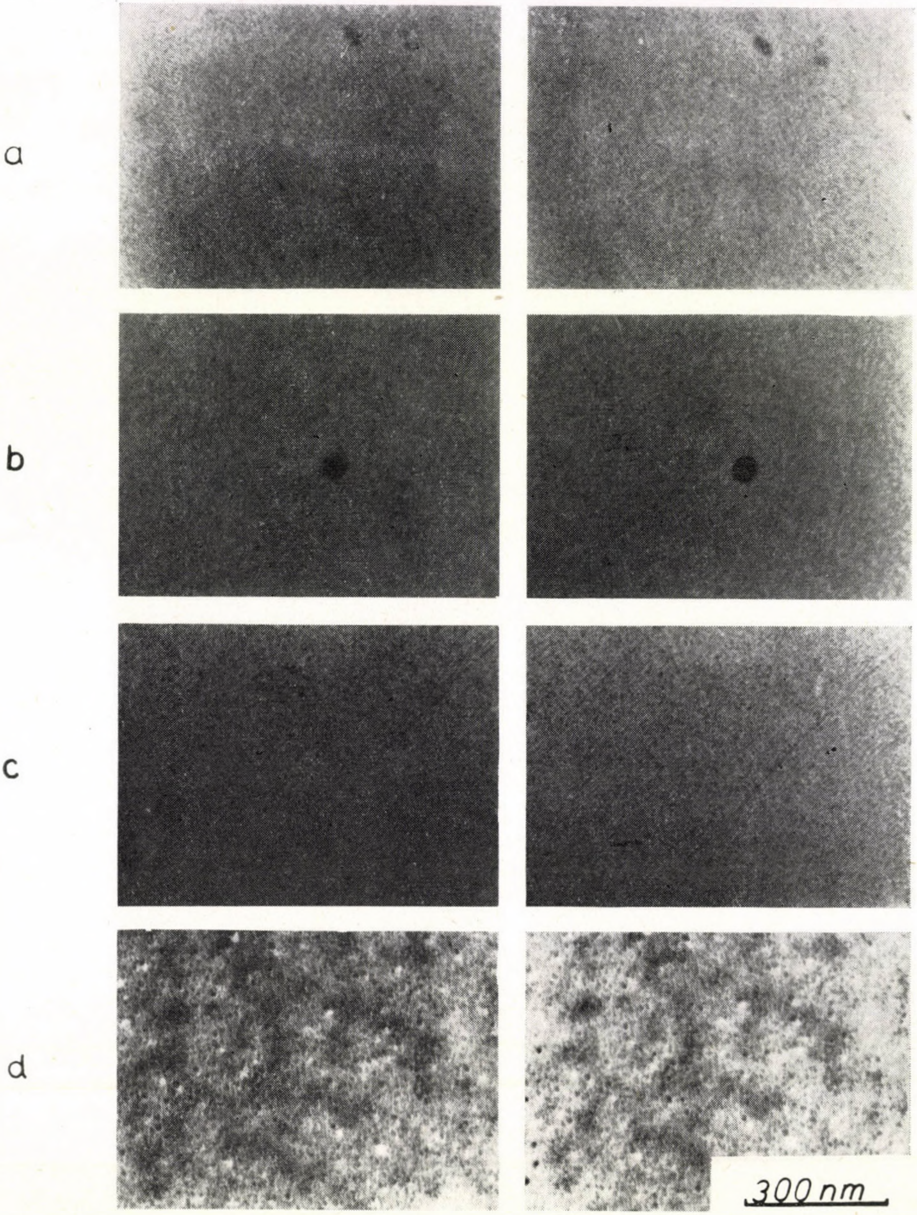

Fig. 1. Electron micrographs of the $Ge_{1-x}Mo_x$ samples. Left: focussed. Right: 100 nm underfocussed, a) $s = 0,07$; b) $x = 0,16$; c) $x = 0,22$; d) $x = 0,32$

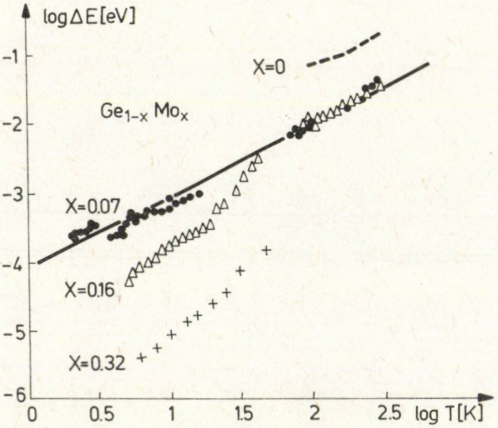

Fig. 2. Activation energy of electrical conduction. Full line: log $k_B T$

decreases below $k_B T$ (Fig. 2). This fact could be explained by the formation of "filaments" with metallic-type conductivity for $x \geq 0.16$ which take over the electrical transport at low T. These "filaments" must be related to the Mo-rich zones observed by electron microscopy for $x > 0{,}16$.

The sample with $x = 0.32$ shows a superconducting transition at $T_n = 2.9$ K, which agrees with its metallic-type conduction at very low T (TCR $\simeq 2 \cdot 10^{-3}$ K^{-1} between 3 and 6 K). Piezoresistance measurements also show the metallic character of the conduction increasing with x.

The ΔE_s thermopower activation energies are systematically lower than ΔE_σ. This fact is characteristic for other cermets too [4] and suggests different mobilites for electrons and holes in the hopping conduction.

Structure

Coevaporated $Ge_{1-x}Mo_x$ alloys $(0 \leq x \leq 0.32)$ have been found to have an amorphous structure both by electron and X-ray diffraction. A characteristic change in the electron diffraction patterns of the samples with increasing Mo-content are shown in Fig. 3. The trends of these changes are very similar to those observed by Nowak et al [5] in amorphous Ge—noble metal alloys and suggest changes in the short range order towards metallic coordination of atoms. For a more exact study the diffracted electron intensity was recorded directly and the interference function

$$F(k) = k \cdot \frac{I(k) - \langle f^2 \rangle}{\langle f \rangle^2}\,, \qquad k = 4\pi \frac{\sin \vartheta}{\lambda}$$

has been calculated. Experimental $F(k)$ functions are compared with those calculated from a model in Fig. 4.

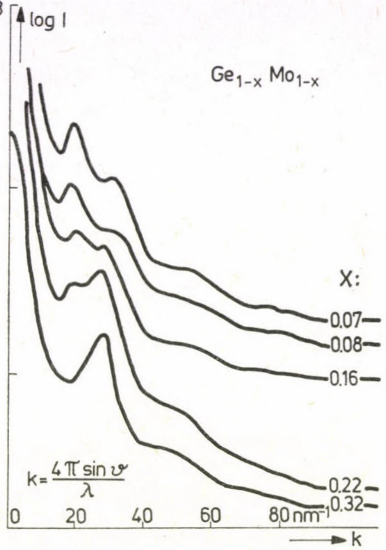

Fig. 3. Densitometric traces of electron diffraction patterns of $Ge_{1-x}Mo_x$ films

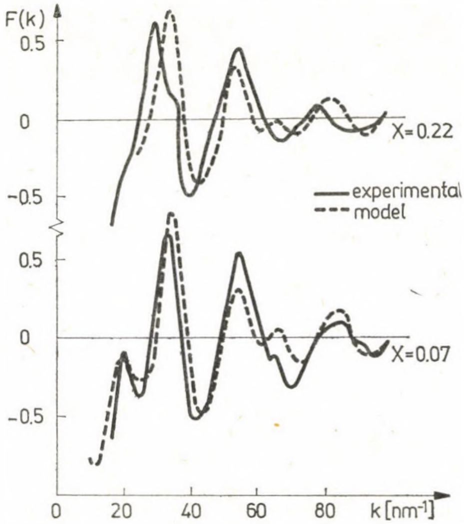

Fig. 4. Reduced interference functions $F(k)$ experimental and model calculated

Structural model for the $Ge_{1-x}Mo_x$ system

The structure of a-Ge is correctly represented by spatial models based upon local satisfaction of hybrid sp^3 bonds [6, 7]. These models satisfactorily account for the experimental atomic radial distribution (RDF) and for the diffracted intensity distribution.

A closer examination of such a model reveals much free space. On the basis of the a-Ge density ($\cong 4.92$ g $\cdot$cm^{-3}) and covalent radius of Ge atom (0.122 nm) this free space can be calculated to comprise about 70% of the total volume. A fraction of it ($\sim$ 18%) is concentrated in zones large enough to accommodate a Mo atom (metallic radius 0.139 nm). The filling of the large zones corresponds to an atomic concentration of Mo $x = 0.22$. This value is remarkably close to the threshold concentration $x = 0.16-0.22$ at which marked changes in the diffraction pattern occur. Threshold concentrations around 0.20 were also noticed in the systems a-Ge-Cu [5] and a-Si-Fe [8].

On the other hand, the Mo solubility in crystalline Ge is unmeasurably small [9] due partly to the Mo being unable to form sp^3 hybrid bonds and to enter substitutionally into the Ge lattice. In a rather crude image we can assume that during the co-deposition the a-Ge network develops preferentially, enclosing the Mo atoms.

On the basis of the above arguments the modelling of the a-Ge-Mo system has been started by placing the Mo atoms in the large free zones of a 155-atoms a-Ge model [6]. In this way one can accommodate up to 22% Mo atoms without Mo-Mo repulsive contacts.

The Mo atoms were initially placed as being tangent to 3 of the Ge atoms bordering a large free zone. On the other hand, this positioning does not correspond to the maximum interaction between Mo and Ge. We assumed for this interaction a Lennard-Jones-type potential

$$V_{\mathrm{GM}} = R^{-12} - AR^{-6},$$

where R is the interatomic distance, $A = 2R_{\mathrm{GM}}^{-6}$ and R_{GM} is the equilibrium distance between Ge and Mo (0.261 nm). The Mo positions were submitted to a minimization program for the bond energy which yielded the energetically most favourable Mo positions.

The atomic pairs distributions were obtained up to $R_{\max} = 2$ nm from the coordinates of the Ge and Mo atoms (Fig. 5). The first-order distances Mo—Ge range between 0.2 and 0.7 nm with a strong maximum at 0.261 nm (sum of the covalent Ge radius and of the metallic Mo radius). The distribution of Mo—Ge distance shows relatively sharp peaks at 0.495 and 0.630 nm too. The distribution of Mo—Mo distances displays broad maxima centred upon 0.49 and 0.75 nm which are characteristic for the topology of the "free space network" complementary to the network of the Ge atoms.

On the basis of the pairs distributions Ge—Ge, Ge—Mo and Mo—Mo the total interference function of the model $F(k)$ was computed. The pairs distributions were previously corrected for the limited size of the model and damped by a Debye-Waller-type factor in order to reduce the cut-off errors. These model interference function were computed for different x ranging between

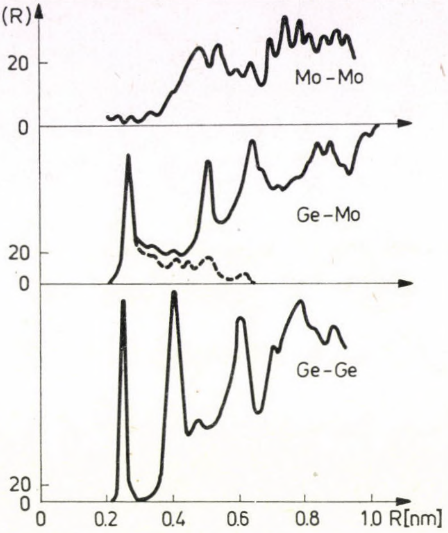

Fig. 5. Model pair density distribution (Ge-network not relaxed)

0.07 and 0.22 and checked against the experimental ones as determined from electron diffraction [1]. They account for the main changes brought about in the $F(k)$ of a-Ge by increasing the Mo concentration (Fig. 4). For example the first maximum at $k = 19{,}5\ \mathrm{nm}^{-1}$ becomes a broad shoulder for $x = 0.22$. This blurring is due to the smaller concentration of Ge—Ge pairs but also to maxima due to the Mo—Mo pairs (at $k = 9.5$ and $16.2\ \mathrm{nm}^{-1}$) and Ge—Mo pairs at $k = 15\ \mathrm{nm}^{-1}$). This change in the diffracted intensity distribution is similar to and of the same order of magnitude as that noticed in the a-Ge-Au, Cu [5], a-Ge-Fe [10] and a-Si—Fe [8] systems suggesting the similarity of these structures. Characteristic changes show up with increasing x also in the regions $k = 66$ and $82\ \mathrm{nm}^{-1}$ in agreement with the experimental $F(k)$'s.

This structural model for the a-Ge-Mo system is a rather crude description of the process of network formation during the codeposition process. A better picture will be obtained by a general relaxation computing procedure including all the interactions between the present atoms. This procedure takes into account the bond stretching and bond-bending potentials of the Ge—Ge bonds as well as a Lennard-Jones potential for the Ge—Mo bonds. It minimizes the corresponding distortion energies E_S, E_B and E_{LJ} related to the distortion of the bond lengths and angles from their equilibrium values.

Preliminary results of this relaxation show that the Ge—Mo interactions distort rather heavily the Ge—Ge distances, thereby increasing E_S while E_B is less enhanced. The effect on the computed $F(k)$ is a shift in the peak at $k = 34\ \mathrm{nm}^{-1}$ towards smaller k improving the agreement with the experiment in this region.

It is worth mentioning that the two constants which enter the Lennard-Jones potential are related to the equilibrium length of the Mo—Ge bond and to its relative strength, respectively. A correct assessment of these constants by an optimal fitting of the experimental $F(k)$'s will give a new and quite important insight into the nature of the metal-semiconductor bond in cermets. This problem is related to the total density and to the energy distribution of the localized levels in the energy gap.

The above described model should be generally valid for all amorphous tetrahedral semiconductor—metal systems with low metal solubility, provided an adjustment of the interaction parameters is made.

Acknowledgements

The authors are very much indebted to I. POZSGAI for carrying out the electron microprobe analysis on the samples.

REFERENCES

1. R. MANAILA, C. RUSU, A. DÉVÉNYI, Á. BARNA, P. B. BARNA, G. RADNÓCZI and L. TÓTH, p. S5 in Proc. 9th Hungarian Diffraction Conference, Pécs, 1978.
2. R. M. HILL, Phys. Stat. Sol. (a), **34**, 601, 1976; **35**, K29, 1976.
3. A. DÉVÉNYI, R. MANAILA and R. M. HILL, Phys. Rev. Lett., **29**, 1738, 1972.
4. A. DÉVÉNYI, R. MANAILA and C. RUSU, Thin Solid Films, **41**, 143, 1977.
5. H. J. NOWAK, H. LEITZ and W. BUCKEL, Phys. Stat. Sol. (a), **49**, 73, 1978.
6. M. POPESCU, Ph. D. Thesis, Bucharest, 1975.
7. P. STEINHARDT, R. ALBEN, M. S. DUFFY and D. E. POLK, Phys. Rev., **B18**, 6021, 1973.
8. PH. MANGIN, et al., Phil. Mag., **36**, 643, 1977.
9. M. HANSEN and K .ANDERKO, Structure of Binary Alloys, Vol. 2. Izd. Nauka, Moscow, 1962.
10. O. UEMURA, Y. SUZUKI and T. SATOW, Phys. Stat. Sol. (a), **41**, 417, 1977.

Acta Physica Academiae Scientiarum Hungaricae, Tomus 49 (1—3), p. 215 (1980)

MAGNETIC PHENOMENA IN AMORPHOUS FILMS WITH LARGE SCALE INHOMOGENEITIES

By

I. NAGY, T. TARNÓCZI, M. HOSSÓ, T. NAGY

CENTRAL RESEARCH INSTITUTE FOR PHYSICS, HUNGARIAN ACADEMY OF SCIENCES
H-1525 BUDAPEST, HUNGARY

P. B. BARNA

RESEARCH INSTITUTE FOR TECHNICAL PHYSICS, HUNGARIAN ACADEMY OF SCIENCES
H-1325 BUDAPEST, HUNGARY

and

Z. FRAIT

INSTITUTE OF PHYSICS, CZECHOSLOVAK ACADEMY OF SCIENCES, PRAGUE, ČSSR

Abstract

In the production of amorphous films, certain processes usually cause inhomogeneities which may be a variation of the density and/or chemical composition. These variations can affect essentially the physical behaviour of the materials used. The effects of the following types of inhomogeneities were investigated: 1) super network (columnar structure), 2) composition inhomogeneities in plane, 3) composition inhomogeneity in depth. The role of the super network on the macroscopic magnetic anisotropy was investigated in evaporated and sputtered Gd—Co amorphous films by magnetic, electron microscopic and backscattering methods. The domain wall motion was investigated in sputtered amorphous Gd—Co films with a compensation surface perpendicular to the film plane. Magnetic and Hall effect measurements were performed on evaporated Gd—Co films with a compensation layer due to the concentration gradient in depth. Special spin wave resonances were observed in amorphous Gd—Co films in which the concentration changes as a quadratic function of depth.

Acta Physica Academiae Scientiarum Hungaricae, Tomus 49 (1—3), pp. 217—221 (1980)

CHARACTERIZATION OF AMORPHOUS VANADIUM PENTOXIDE THIN FILMS PREPARED BY CHEMICAL VAPOUR DEPOSITION (CVD) AND VACUUM DEPOSITION

By

L. Michailovits, K. Bali, T. Szörényi and I. Hevesi

RESEARCH GROUP ON LUMINESCENCE AND SEMICONDUCTORS, HUNGARIAN
ACADEMY OF SCIENCES, SZEGED, HUNGARY

Amorphous vanadium pentoxide thin films were prepared by CVD of $VOCl_3$ with H_2O at room temperature and by vacuum deposition. The stoichiometry was estimated from quantitative EPR measurements. The amorphous to crystalline transition temperatures, 453—463 K for vacuum deposited films and 523 ± 10 K for films prepared by CVD, were determined by DTA, polarization microscopy and electrical conductivity measurements. The structural changes were monitored by electron microscopy and EPR.

Introduction

Two methods are known to obtain pure amorphous vanadium pentoxide (V_2O_5), splat-cooling [1, 2] and vacuum deposition [3—6]. Both methods involve the melting of the material. At high temperatures the melted V_2O_5 loses oxygen resulting in a non-stoichiometric oxide. The deviation from the stoichiometry depends on the temperature. An attempt to prepare amorphous V_2O_5 thin films of probably lower V^{4+} content (sub-melting-point vacuum evaporation) was reported by Colton [7].

Although relatively high temperatures are needed to obtain single crystals of good quality chemical vapour deposition proved to be a convenient method for growing crystalline vanadium oxides [8—10]. The great advantage of this method is that the stoichiometry can easily be controlled. Since the decomposition of vanadium oxychloride ($VOCl_3$) vapour with H_2O vapour is a strongly exothermic process, the reaction takes place even at room temperature according to the equation

$$2VOCl_3 + 3H_2O \rightarrow V_2O_5 + 6HCl, \tag{1}$$

which suggests that CVD at room temperature might yield non-crystalline V_2O_5 of possibly very low V^{4+} content.

In this paper we report the successful preparation of amorphous vanadium pentoxide thin films by CVD and compare the properties of the films prepared by this method and vacuum deposition.

Experimental

The starting material for vacuum deposition was V_2O_5 powder (REANAL, Hungary, purum grade). The temperature of the electrically heated molybdenum boats, as determined by an optical pyrometer, was 1670 K. The substrates were held at room temperature under high vacuum ($< 1 \times 10^{-3}$ Pa). Film thickness varied between 0.2—0.8 μm at deposition rates of 3—5 nm/s and a boat to substrate distance of 0.1 m.

To apply the CVD method $VOCl_3$ vapour (FLUKA, Switzerland) and H_2O both thermostated at 303—333 K and 295—298 K, respectively, were introduced into the quartz reaction tube by high purity N_2 or O_2 carrier gas, dried in an LN_2 cooled baffle.

Quartz and optical glass plates, polyethylene and mylar films were used as substrate materials. For electron microscopic studies the films were deposited onto platinum grids covered by a collodion and a vapour deposited SiO_x layer.

The electron micrographs were taken with a JEM 100-U (JEOL) microscope; for EPR measurements a JES—PE—1X (JEOL) X-band spectrometer was used; the IR spectra were recorded with an UNICAM SP 200 spectrophotometer. Electrical resistivity was measured by two point technique using evaporated platinum electrodes. Density data were calculated from measured weight/volume ratios. The thicknesses of the films were determined by optical interference method.

Results and discussion

Thin films prepared by both methods were originally yellow and uniform in appearance. With optical microscopy we were unable to distinguish them, but TEM pictures clearly showed that vacuum deposited samples were more homogeneous than those prepared by CVD.

Livage and his coworkers proposed a very simple method to distinguish between crystalline and amorphous V_2O_5. They pointed out that the crystalline form cannot be dissolved in water while the amorphous form readily dissolves [1, 2]. Our films easily dissolved in water yielding a yellow solution with pH $\sim$ 2. The electron microscopic studies proved unambiguously that the films were amorphous (Fig. 1a).

The density of the samples varied from 2.7 gcm^{-3} to 3.1 gcm^{-3}. The large spread is possibly due to uncertainties in weight and thickness measurements.

The variation of electrical conductivity with temperature of an initially amorphous film prepared by vacuum evaporation is shown in Fig. 2. The

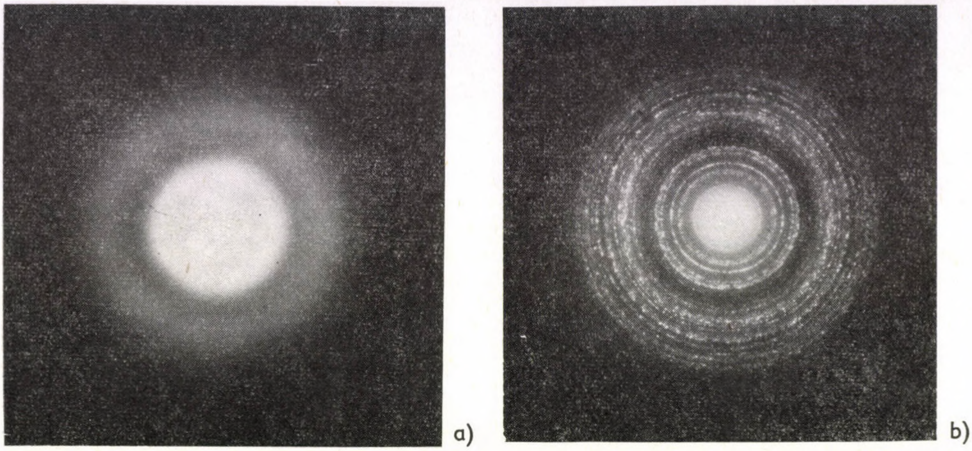

Fig. 1. Selected area electron diffraction pattern of an as-deposited film (a), and of the same film after heat treatment (b)

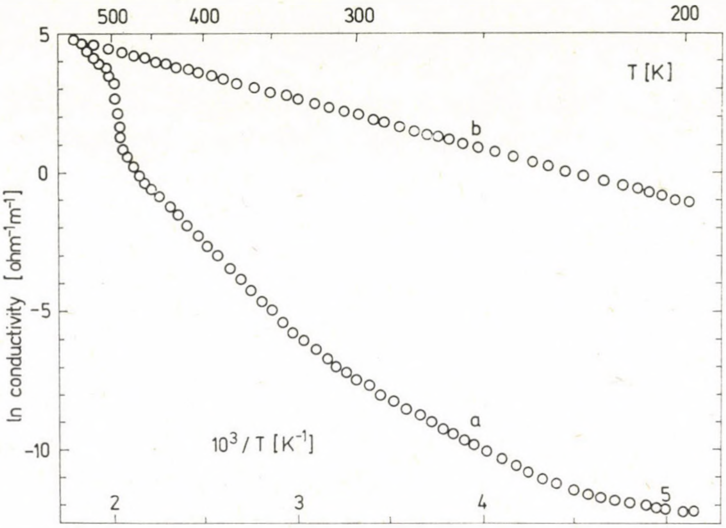

Fig. 2. Temperature dependence of the conductivity, measured on a vacuum deposited film

temperature dependence of conductivity in the amorphous phase (curve a) is consistent with the polaron model for conduction [11]. Conductivity values (measured on 7 different samples at 25 °C) ranged from 2×10^{-4} to 1×10^{-3} ohm^{-1}m^{-1} with a mean value of 6×10^{-4} ohm^{-1}m^{-1}. The high temperature activation energies were determined in the 300—450 K range. The mean value of 0.62 eV is surprisingly high as compared to data reported by ALLERSMA et al (0.29—0.39 eV) [4]. The amorphous to crystalline transition temperatures (defined by the temperature at which the conductivity suddenly increases) of the vacuum evaporated samples were found between 453 and 463 K, in agreement with our own results obtained by DTA and polarization microscopy, and those of [1, 2]. The conductivity of the crystallized material (curve b in Fig. 2) can be described by the equation

$$\sigma = \sigma_0 \exp(-E/kT) \tag{2}$$

with $E = 0.14$ eV which is close to the value reported for single crystals and polycrystalline material [3, 4]. Conductivity values of 6 $\text{ohm}^{-1}\text{m}^{-1}$ were measured at room temperature. The polycrystalline material was identified as orthorhombic V_2O_5 (ASTM 9—387) (Fig. 1b). The density of the polycrystalline films increased by 25% as compared to that of the amorphous samples.

The crystallization temperature of the CVD films was found, as determined by the same methods, 520 ± 10 K. For hydrated amorphous V_2O_5 transition temperatures between 570 and 600 K were reported [12], suggesting that the higher transition temperature observed might be due to the presence of water. Indeed, the DTA curves showed a weak endotherm signal at about 370 K. In the IR spectra two bands at 1610 and 3500 cm^{-1} could be identified beside the characteristic peaks at 650, 840 and 1015 cm^{-1}. These results proved that the films prepared by CVD contain loosely bound water.

The lineshape of the EPR spectra is of diagnostic value for distinguishing between the amorphous and crystalline forms and also for estimating the V^{4+}

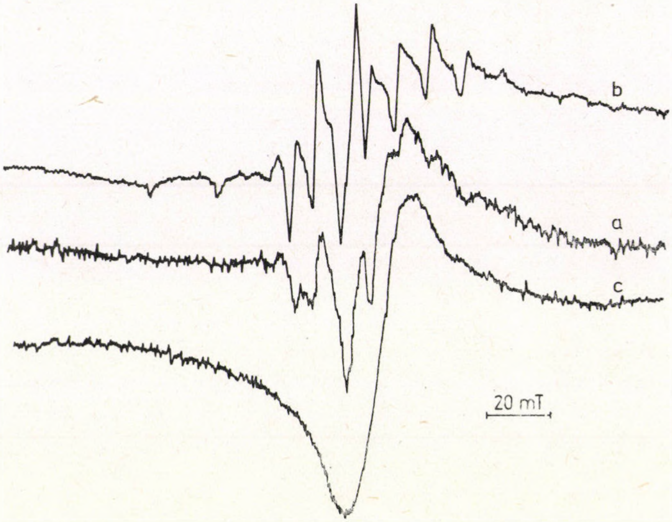

Fig. 3. EPR spectra of an as-deposited CVD film, recorded at 300 K (a) and 100 K (b); spectrum of the film after heat treatment, recorded at 300 K (c)

content. The amorphous form of low V^{4+} content exhibits a well resolved hyperfine pattern at room temperature unlike crystallized V_2O_5 [1, 2, 13]. EPR spectra of a CVD film are shown in Fig. 3. The spectra labelled with a and b are characteristic of the amorphous phase with low V^{4+} content; while the spectrum recorded after a heat treatment at 570 K for 3 hours in oxygen atmosphere (curve c) is characteristic of the crystalline phase. The room temperature EPR spectra of films prepared by vacuum deposition exhibited no hfs indicating the presence of much more V^{4+}. Quantitative EPR measurements using $CuSO_4 \cdot 5H_2O$ standard revealed that the films prepared by CVD contained only 1—2% V^{4+}, while the V^{4+} content of the films obtained by vacuum deposition was 7—8%

Summing up it may be stated that the amorphous films obtained by vacuum deposition are of very good homogeneity but exhibit large deviation from the stoichiometry; while CVD is appropriate to produce near stoichiometric amorphous vanadium pentoxide thin films.

REFERENCES

1. J. Livage and R. Collongues, Mater. Sci. and Eng., **23**, 297, 1976.
2. L. Rivoalen, A. Revcolevschi, J. Livage and R. Collongues, J. Non-Crystalline Solids, **21**, 171, 1976.
3. T. N. Kennedy, R. Hakim and J. D. Mackenzie, Mater. Res. Bull., **2**, 193, 1967.
4. T. Allersma, R. Hakim, T. N. Kennedy and J. D. Mackenzie, J. Chem. Phys., **46**, 154, 1967.
5. E. F. Ryannel', V. I. Gaman and V. M. Kaligina, Izv. VUZ Fiz., **2**, 102, 1976.
6. E. F. Ryannel', V. M. Kaligina and V. I. Gaman, Fiz. and Khim. Stekla, **2**, 109, 1976.
7. R. J. Colton, A. M. Guzman and J. W. Rabalais, J. Appl. Phys., **49**, 409, 1978.
8 H. Takei and S. Koide, J. Phys. Soc. Japan, **21**, 1010, 1966.
9. H. Takei, Japan. J. Appl. Phys., **7**, 827, 1968.
10. J. Fan and W. Paul, Vide, **150**, 232, 1970.
11. I. G. Austin and E. S. Garbett, in Electronic and Structural Properties of Amorphous Semiconductors, Academic Press, London, 1973.
12. M. Michaud, M. C. Leroy and J. Livage, Mater. Res. Bull., **11**, 1425, 1976.
13. A. Kahn, J. Livage and R. Collongues, Phys. Stat. Sol. a, **26**, 175, 1974.

Acta Physica Academiae Scientiarum Hungaricae, Tomus 49 (1—3), p. 223 (1980)

PROPERTIES OF THIN FILMS OBTAINED BY A PENNING-TYPE SPUTTERING SOURCE

By

P. GLASER, G. KERTÉSZ and GY. VÁGÓ

INDUSTRIAL RESEARCH INSTITUTE FOR ELECTRONICS
H-1393 BUDAPEST, HUNGARY

Abstract

Some physical and technical properties of pure and silicon-alloyed aluminium films obtained by using a Penning-type sputtering source ("S-gun" or "magnetron" etc.) were tested. The source has been developed in our Institute.

The following properties of the films were investigated:

a) microstructure — transmission electron microscope and electron diffraction;
b) chemical composition (Si-content) — atomabsorption;
c) specific resistance, calculated from the sheet resistivity measured with a four-point probe and from the film thickness measured with a stylus-type surface profilemeter;
d) optical reflectivity, detected with a simple, self-built instrument.

Besides aluminium also copper films were produced and investigated.

Acta Physica Academiae Scientiarum Hungaricae, Tomus 49 (1—3), p. 225 (1980)

OPTICAL TESTING OF ALUMINIUM FILMS DEPOSITED BY VACUUM-TECHNICAL METHODS

By

P. GLASER and G. BALOG

INDUSTRIAL RESEARCH INSTITUTE FOR ELECTRONICS
H-1393 BUDAPEST, HUNGARY

Abstract

Optical testing is important when a film must be processed (i. e. delineated) by photolithography. It means the measurement of the reflectivity with normal incidence white light. The reflectivity meter developed in our Institute directly indicates the reflection coefficient of any reflective film on a substrate not larger than 50 mm in dia.

The following films were investigated:

- pure aluminium evaporated from electron beam source;
- pure aluminium sputtered from a Penning-type source;
- silicon-alloyed aluminium sputtered from the same source.

The films were deposited at various rates and substrate temperatures. Deposition rate and temperature, as well as the kind of source had different effects. The silicon content of the films significantly affected their reflectivity.

Acta Physica Academiae Scientiarum Hungaricae, Tomus 49 (1—3), p. 227 (1980)

AN APPROPRIATE INSTRUMENT FOR THE OPTICAL TESTING OF REFLECTIVE FILMS

By

G. BALOG

INDUSTRIAL RESEARCH INSTITUTE FOR ELECTRONICS
H-1393 BUDAPEST, HUNGARY

Abstract

Measurement of the reflectivity with normal incidence light has a great importance especially when the layer gets in a photolithographic process (semiconductor devices, thick and thin film circuits, printed circuit boards etc.).

The reflectivity meter developed at this Institute has a tungsten lamp as light source and photovoltaic cells of 1 cm^2 made at this Institute (equivalent to BPY 63 of Siemens) as detectors. The analogue meter of the instrument directly indicates the reflection coefficient from the ratio of the light intensity in the reference and measurement pathway, respectively. The lamp is stabilized by optical/electrical feedback. The instrument is suitable for testing other reflective films if the sample can be put in the sample holder (10 . . . 50 mm dia).

Acta Physica Academiae Scientiarum Hungaricae, Tomus 49 (1—3), p. 229 (1980)

ULTRAMICROHARDNESS-TESTER FOR THIN FILMS

By

H. BANGERT, A. WAGENDRISTEL and W. ASCHINGER

INSTITUTE FOR APPLIED PHYSICS, TECHNICAL UNIVERSITY OF VIENNA, VIENNA, AUSTRIA

Abstract

A novel microhardness-tester has been designed for loads between 10^{-2} N and 5×10^{-5}N. The apparatus can be operated in any commercial scanning electron microscope without installation of additional adjusting shafts. The force is applied electromagnetically to the indenter by bending a double leaf spring and measured by means of strain gauges fixed to the springs. The equipment can be tilted in respect to the electron beam making possible the observation of the tip during indentation. The experiment thus provides information on the microhardness as well as on dynamic properties of the sample.

Acta Physica Academiae Scientiarum Hungaricae, Tomus 49 (1—3), p. 231 (1980)

ÜBER DIE ABHÄNGIGKEIT DER STRAHLUNGSABSORPTION DÜNNER SILBER-, GOLD- UND KUPFERSCHICHTEN VON DER SCHICHTSTRUKTUR

Von

H. P. Martinz, R. Kramer und R. Abermann

INSTITUT FÜR PHYSIKALISCHE CHEMIE, A-6020 INNSBRUCK, ÖSTERREICH

Kurzfassung

Wegen ihrer Bedeutung für den Bau wirkungsvoller photothermischer Wandler von Sonnenenergie ist die Absorption von Wärmestrahlung durch dünne Aufdampfschichten neuerdings von erhöhtem Interesse. In der vorliegenden Arbeit wurde einmal während der Herstellung der Aufdampfschichten die Temperaturänderung des Schichtsystems mit einem auf einen Glasträger aufgedampften Fe/Ag-Thermoelement als Funktion der Aufdampfrate gemessen. Die optischen Konstanten der untersuchten Silber-, Gold- und Kupferfilme wurden zum anderen aus der Temperaturänderung beim Ein- bzw. Abstrahlen von Wärme in Abhängigkeit der Schichtdicke punktweise ermittelt. Es wurde gefunden, dass das Absorptionsvermögen der Aufdampfschichten mit zunehmender Schichtdicke kleiner wird. Diese Abnahme des Absorptionsvermögens kann mit der Koaleszenz der Metallschicht korreliert werden.

Acta Physica Academiae Scientiarum Hungaricae, Tomus 49 (1–3), p. 233 (1980)

AN X-RAY OPTICAL STUDY OF LAYERED PHASE IN Au-Al THIN FILM COUPLES

By

A. WAGENDRISTEL, H. SCHURZ, H. BANGERT and E. EHRMANN-FALKENAU

INSTITUTE FOR APPLIED PHYSICS, TECHNICAL UNIVERSITY OF VIENNA, VIENNA, AUSTRIA

Abstract

Specular X-ray reflection originating at grazing incidence at the boundary planes of thin laminated structures interfere to give the known Kiessig fringes. The change of this interference pattern during diffusional intermixing in thin multi-layers is used for the study of phase formation in Au—Al thin film couples. Layered growth of Au_2 Al obeying a parabolic growth relation was observed in the temperature range from 560 to 80 °C. The activation energy of the process was found to be 1.05 eV.

Acta Physica Academiae Scientiarum Hungaricae, Tomus 49 (1—3), p. 235 (1980)

THE COMPOSITION OF THIN FILMS WHEN FORMED BY EVAPORATION PROCESSES UNDER HIGH VACUUM AND ULTRA HIGH VACUUM CONDITIONS

By

N. KLAUS

INSTITUTE FOR EXPERIMENTAL PHYSICS, UNIVERSITY OF VIENNA, VIENNA, AUSTRIA

Abstract

The influence of specimen preparation before and during an evaporation process has been investigated at room temperature for aluminium deposited on copper foils. The first series of specimen was prepared and analysed under UHV conditions. The second series was prepared under HV conditions, but analysed again under UHV conditions. For all targets ion etching with some 10^3 Å was used for surface cleaning. The evaporation and etching was carried out in a special UHV specimen preparation chamber. After the respective preparation the targets were transported over a UHV sluice lock to a second UHV chamber, where the target surfaces were analysed by SIMS method down to a depth of 600 Å. If preparation and aluminium deposition are done under HV conditions, the deposited layer becomes an aluminium oxide layer, while deposition under UHV conditions without surface cleaning forms a layer which consists of a pure Al layer with a strongly oxidised transition layer. Ion etching and Al deposition under UHV conditions forms a pure metal layer consisting of the evaporated material only.

Acta Physica Academiae Scientiarum Hungaricae, Tomus 49 (1—3), pp. 237—251 (1980)

ON THE MECHANISM OF HILLOCKS FORMATION IN VAPOUR DEPOSITED THIN FILMS

By

F. M. REICHA and P. B. BARNA

RESEARCH INSTITUTE FOR TECHNICAL PHYSICS, HUNGARIAN ACADEMY OF SCIENCES
H-1325 BUDAPEST, HUNGARY

Two types of growth hillocks (marked by Type I and Type II) have been identified in vapour deposited thin films. Type I develops inside the surface of large crystals, while Type II represents individual single crystals protruded over the average surface area of the film. Formation of Type I hillocks indicates the participation of foreign atoms in the film formation and their accumulation along the moving growth steps developing stable phases. Type II hillocks develop at higher growth rates in preferential crystallographic directions due either to the crystallography of crystals (e.g. Bi), or to the effect of selective uptake of foreign species on the crystallographic faces of different Miller indices developing covering layers on different surface areas controlling also the coalescence of the grains. The correlation between the partial pressure of oxygen and the formation of hillocks in Al films proved the effectivity of the last phenomenon.

1. Introduction

Most of as-prepared vapour deposited thin films exhibit so called "growth hillocks", i. e. crystallites protruding over the average surface plane of the film [1—10]. The tops of these hillocks are usually bounded by crystallographic faces and prove to be misoriented in epitaxial films (or in films exhibiting textures) [3, 4, 9].

Growth hillocks are very characteristic e. g. both of pure Al films [3, 4, 5, 9, 10] and of alloyed films [6, 7]. It is a common experience that additional hillocks can develop during the heat treatment of films [6—10].

The development of hillocks makes the films very disadvantageous in many cases of applications (e. g. in the fabrication of inter-level short-free crossovers [1] or in the preparation of front mirrors [2]).

One can conclude that the results published in literature dealing with growth hillocks are not quite sufficient to understand, control and/or prevent the formation of these hillocks. These publications do not offer any comprehensive and precise description of the morphology, crystal orientation, composition and the growth mechanism of these hillocks. The conditions of preparation of films are not well-defined either in most papers. These lead to contradictory data for the dependence of hillocks characteristics upon deposition parameters.

In this paper we are going to discuss the experimental results related to the formation of growth hillocks. Particular attention has been paid to the effect of the active components of residual gases (e. g. oxygen and water vapour) considering the results of experiments carried out on Al films. The details of these experiments have been published elsewhere [11].

2. Experimental results to be considered

2.1. *Effect of contaminations on the formation mechanism of growth hillocks (Al films)*

A very pronounced influence of residual gases on the morphology and structure of vapour deposited films can be found in the case of Al films. By increasing K_{oxygen} (the ratio of the impinging oxygen species to that of Al atoms) the surface of the films becomes rougher while the average grain size decreases. Additionally, as viewed by replica technique, the surface of the films generally exhibits typical configurations referred to as growth hillocks in the literature.

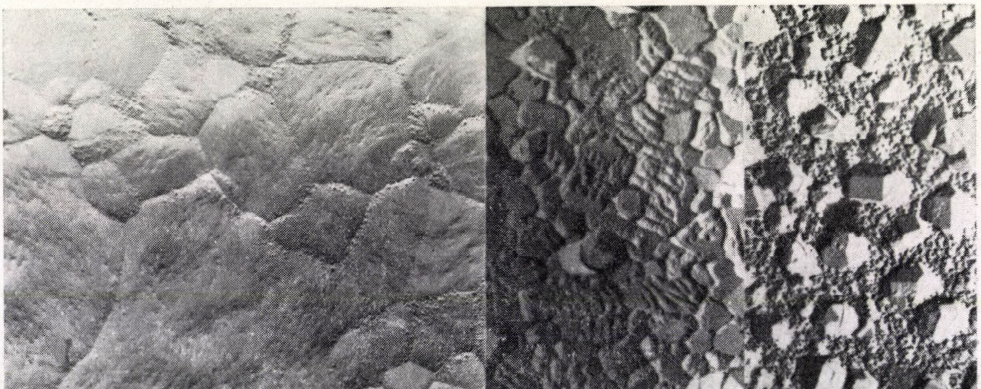

Fig. 1. Characteristic surface structures of Al films deposited at different levels of oxygen contamination. Substrate temperature: 300 °C. a) thickness 1 μm, $K_{\text{oxygen}} \sim 10^{-2}$—$10^{-3}$; b) thickness 1 μm, $K_{\text{oxygen}} \sim 10^{-1}$; c) thickness 60 nm, $K_{\text{oxygen}} \sim 1$

2.1.1. Films deposited onto amorphous substrates [11]

Characteristic structures in Fig. 1 follow each other continuously with increasing oxygen contamination level.

a) At low contamination level ($K_{\mathrm{oxygen}} \sim 10^{-2}-10^{-3}$)

The films of 1 μm thickness exhibit a predominant (111) texture orientation. These films consist of crystallites of 1—10 μm lateral sizes displaying typical surface structures of layer grown single crystals (Fig. 2). From this Figure we may observe that at given sites the growth steps of the layers are stopped. These sites are presumably nuclei (precipitates) of oxide. Bunches of growth steps supposed to be covered by oxide layer are formed around these nuclei. On the surface of large single crystals protrusions (marked by A) of flat areas and dents (marked by B) can be observed. This type of protrusions can be termed "hillocks of Type I". These are limited by bunches of steps and many of these can develop within the surface area of a large single crystal. Consequently, they have the same orientation as the basic crystal. MINKOFF and NIXON have also observed the same kind of hillock for graphite grown in iron and nickel alloys [12].

The investigation of samples of the same film in HVEM indicates that crystals of higher degree of misorientation are present according to the Bragg

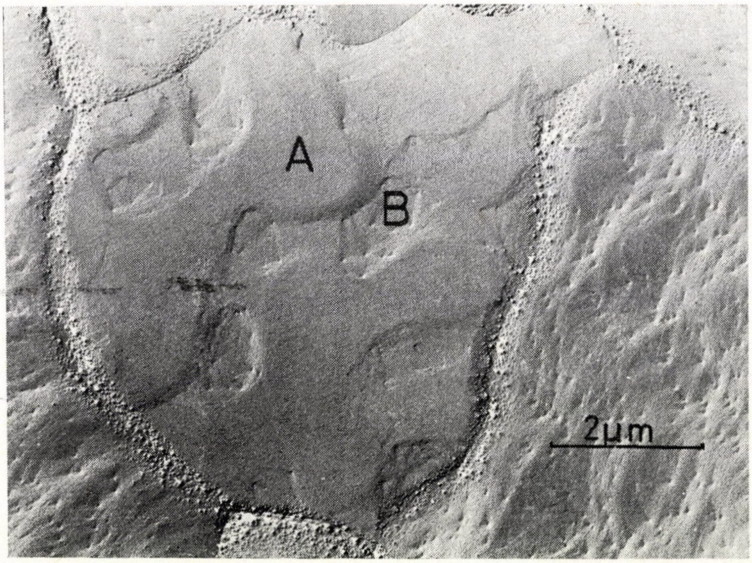

Fig. 2. Surface structure of large single crystals developed at low level of oxygen contamination (see Fig. 1a). Configurations of "Hillocks of Type I" are present.

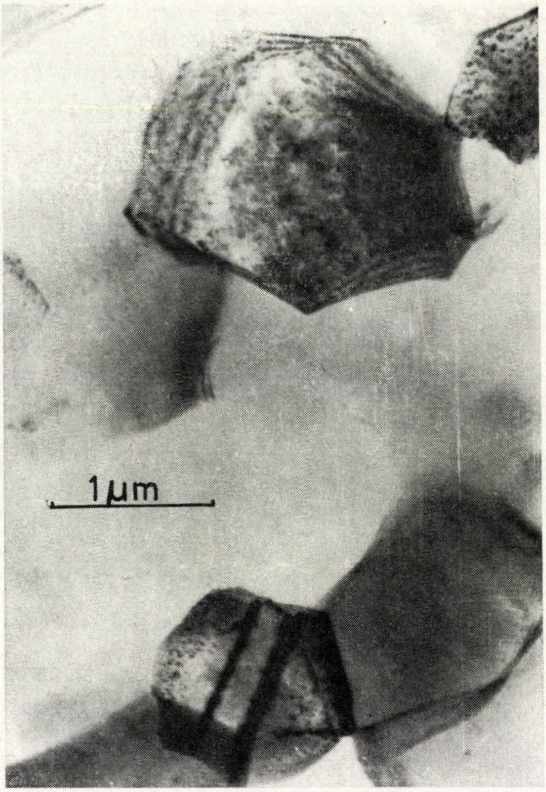

Fig. 3. HVEM image of the 1 μm thick Al film shown in Fig. 1a and Fig. 2

reflection and contrasts (Fig. 3). These crystallites are characterized by the higher concentration of defects and precipitates. The same structures are presented in HVEM micrographs of Al crystals formed in the presence of adsorbed impurities by Tochinsky [13].

b) At medium contamination level ($K_{\text{oxygen}} \sim 10^{-1}-10^{-2}$)

Films having a thickness of 1 μm exhibit grain sizes approximately equal to their thicknesses. The common characteristic of these films is a fairly rough surface and they exhibit a predominant random orientation in most cases. The electron microscopic examination of replicas shows an abnormal growth of some crystals referred to as growth hillocks in the literature. These hillocks represent single individual crystals grown over the average film surface plane (Fig. 4). The points of these protrusions are mainly composed of truncated octahedrons of well-developed faces of low Miller indices. Most of these faces are completely smooth. Their regularities are destroyed only at

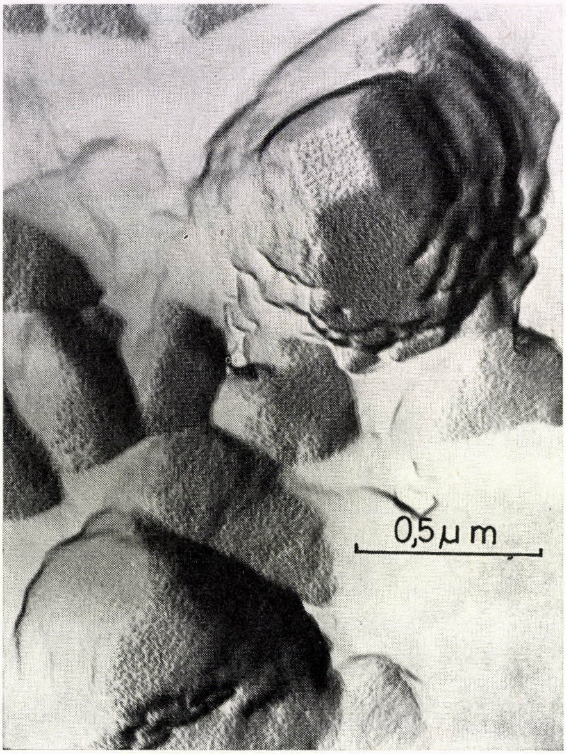

Fig. 4. Surface structure of a 1 µm thick Al film deposited at 300 °C substrate temperature and at $K_{\text{oxygen}} \sim 10^{-1}$. Protruded crystals, the so called "Hillocks of Type II" are developed.

the periphery (Fig. 4). Additionally, their lateral size nearly fits to the average grain size of the film. This type of protrusions represented by individual single crystals can be termed "hillocks of Type II".

c) At high contamination level ($K_{\text{oxygen}} \sim 1$)

Films prepared under these conditions show a very inhomogeneous structure. In films of a thickness of 60 nm it is clearly seen that most crystals are very small and overlapped while relatively large crystallites of well developed shapes protrude above the film surface (Fig. 5). Examination of these films by TED shows that they have random orientation.

The types of these protrusions are similar to that of hillocks of Type II. From Fig. 5 we can observe that the surface of these large crystals (hillocks) are not completely smooth as we have seen in the crystals at medium contamination level. These surfaces contain many dents and hillocks of Type I (marked by E). It can also be observed that some of the faces of hillocks of Type II are destroyed partly or completely as illustrated by D. Relatively

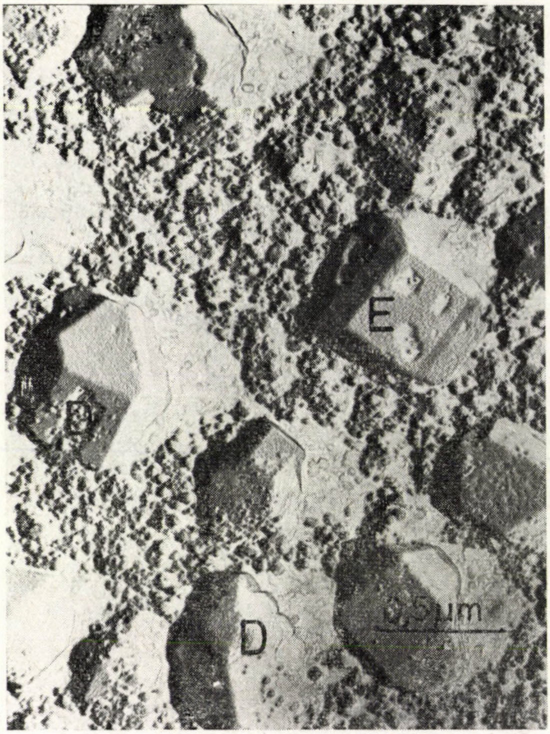

Fig. 5. Surface structure of a 60 nm thick Al film deposited at 300 °C substrate temperature and $K_{\text{oxygen}} \sim 1$. Protruded large crystals of "Hillocks of Type II" and configuration of "Hillocks of Type I" marked by "E" developed on these are shown.

long and thin protrusions like whiskers have been detected in films of higher thicknesses (150 nm) (Fig. 6).

These films present large fluctuations both in thickness and local concentration of built in oxygen [11].

*2.1.2. Al films grown epitaxially on mica**

An unambiguous correlation proved to be existing between contamination level (oxygen and water vapour) and the morphology of these films, too.

At lower contamination level (pressure of residual gases 10^{-4} Pa) using a liquid nitrogen cooling trap and at deposition rate 12 nm/s most of the crystals are grown in the orientation (111) Al//(100) mica, (e. g. crystal marked by A in Fig. 7a.) [14]. These are large and very flat crystals and some of these

---

*The authors' thanks are due to Dr. V. Stary, Institute for Vacuum Physics and Electronics, Charles University, Prague, for his kind cooperation making the films available for studying. These films were deposited onto fresh air-cleaved mica substrates at 550 °C.

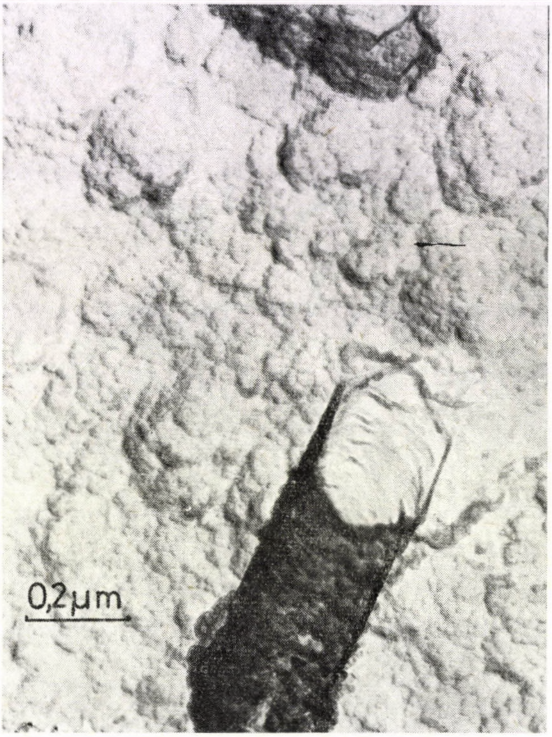

Fig. 6. Long protruded crystals, "Hillocks of Type II", developed in 150 nm thick Al film deposited at 300 °C and $K_{\text{oxygen}} \sim 1$

have facets. Their shapes are the same as given by MATTHEWS for films grown epitaxially on NaCl [15]. There are, however, crystals protruded randomly which can be considered as Type II hillocks. They have a different orientation i. e. (312) Al//(100) mica determined by SAD in films detached from mica substrate and studied in TEM (marked by B in Fig. 7). The shapes of these seem to be partially destroyed by the probably crystalline oxide coverage developed.

The crystallites of the orientation (111) Al//(100) mica seem to be coalesced without contraction while the protruding ones oriented (312) Al//(100) mica were developed mainly by liquid like coalescence (indicated by the large empty surface areas surrounding these crystals). It is remarkable that the surface of the large flat crystals oriented (111) Al//(100) mica and developed by coalescence are smooth without any detectable steps or bunches of steps on their surfaces. Because the individual crystals could have usually different heights before the coalescence as shown in Fig. 8, the smoothing of the surface of the developed large crystal has to be a very fast process.

At a higher contamination level (pressure of residual gases 5.10^{-4} Pa, without liquid nitrogen cooling trap, deposition rate 1,2 nm/s) most of the

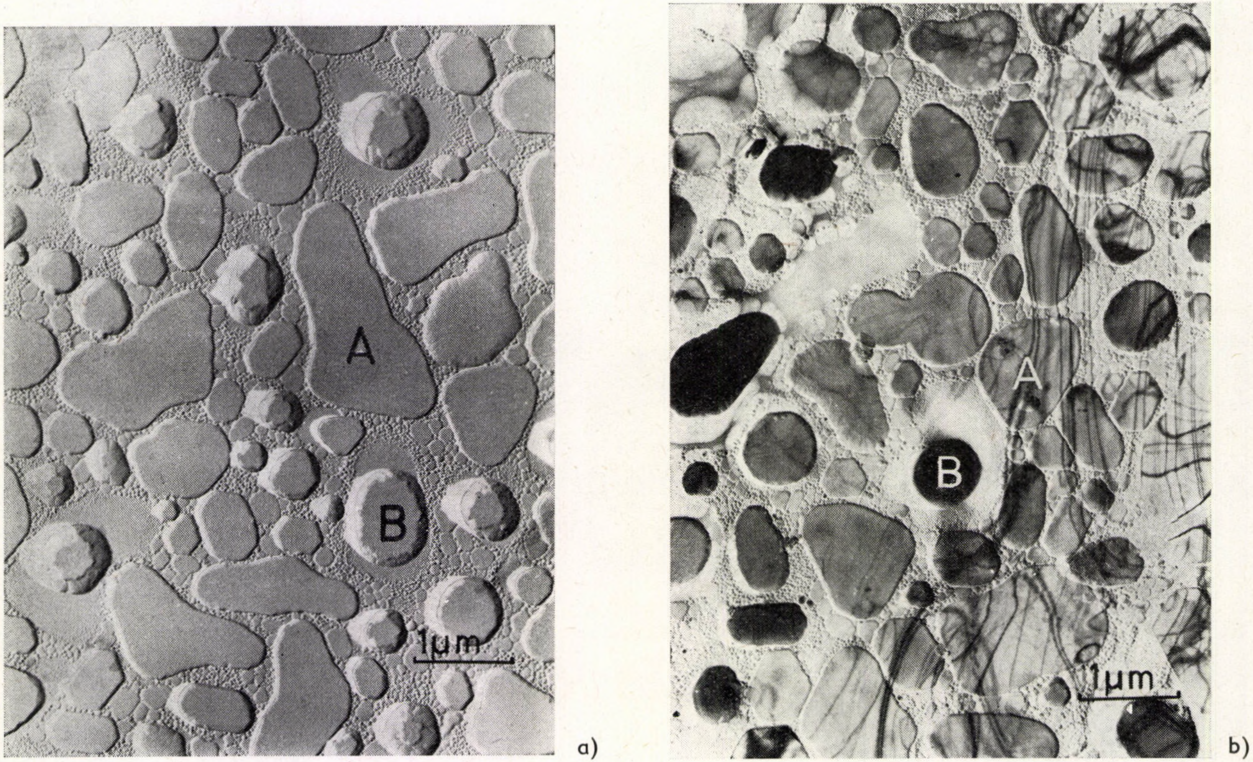

Fig. 7. Al film deposited onto mica substrate at a temperature of 550 °C, deposition rate 12 nm/s and at 10^{-4} Pa using liquid nitrogen cooling trap. a) surface replica; b) TEM image (film is supported by at hin sheet of mica and shadowed by Pt at 30°.)

crystals are grown also in the orientation of (111) Al//(100) mica but they have rather rough surfaces (Fig. 9). Bunches of steps can be identified inside the single crystals developing hillocks of Type I and dents as in the case for films grown on glass substrates. It is also shown in Fig. 9 that grain boundaries can protrude according to differences in the heights of the coalescing crystals.

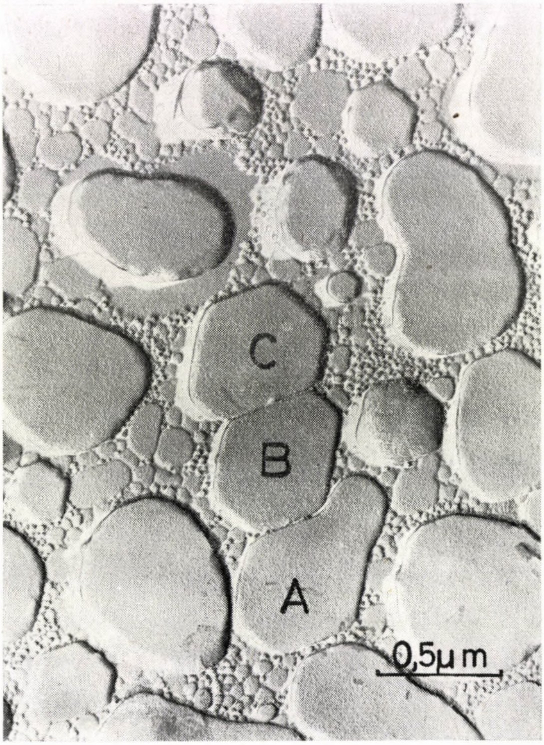

Fig. 8. Adjacent crystals of different heights developed in an Al film deposited onto mica substrate at a temperature of 550 °C, 12 nm/s and at 10^{-4} Pa (marked by A, B and C)

2.2. Growth hillocks in Bi films deposited onto glass and mica substrates [16]

Protruding crystals in continuous Bi films have been found to develop by increasing thickness both on glass and mica substrates. This type of protrusion is similer to hillocks Type II in Al films. The SAD in TEM of the shadowed samples detached from the substrate proved these crystals to be misoriented. They have C-axis perpendicular to the substrate while the C-axis of most crystals is parallel to the substrate.

3. Discussion

The analysis of the experimental results revealed both the types of hillocks and the role of impurities in the development of the various types. A pronounced effect of oxygen has been found in the case of Al films and an unambiguous correlation between the level of oxygen contamination and the types of hillocks could be determined.

3.1. Types of hillocks

Two characteristic types of hillocks have been identified:

Type I: protrusions developing inside large crystals; they have the same orientation as the basic crystals; they are bounded by surfaces covered by layers of impurities or their compounds; growth takes place on their top planes.
The growth of these hillocks is correlated to the building in and the local surface accumulation of the foreign impurity species.

Type II: Single crystals protruding over the average surface plane of the film; they are characterized by the development of low index faces bounding their points; their growth is correlated either to the difference in the growth rate at different crystallographic directions (e. g. in the case of Bi) or to impurity effects.

3.2. Formation mechanisms of growth hillocks

Impurities (residual gases or vapours) play a very important role in the development of growth hillocks. They participate in the atom-by-atom building up process. Their influence on these results also in the realization of conditions which can promote the special growth or coalescence of some crystals developing hillocks. By analysing the formation mechanisms of thin films from the point of view of impurity (gases) incorporation, we can get also direct information on both the nature of impurity uptake properties of the different crystallographic faces and the accumulation, as well as on the development of new phases or compounds important for the understanding of some phenomena of the real crystal growth. We are now also in the very propitious moment when the surface studies presented new and very importtant results both on the surface-vapour interactions and on the nature of the bonds developing between the surface layer and the adsorbed species [17, 18, 19, 20, 21] which support the ideas of hillocks formation presented in this paper.

As usual, the growth of polycrystalline thin films can be divided into the following stages [22, 23, 24]

a) Nucleation

b) Growth of nuclei developing isolated islands (single crystals or liquid/solid amorphous grains)

c) Growth of isolated islands

d) Coalescence of adjacent islands producing either liquid droplets or larger single crystals. (Liquid-like coalescence leaving bare area of substrate. Secondary nucleation in the clear area.)

e) Coalescence of adjacent single crystals developing larger islands composed of numerous crystals (growth coalescence). Development of channels and holes.

f) Filling the channels and formation of continuous film.

g) Growth of crystals in composite islands and in the continuous film: lateral growth increasing the grain size; perpendicular growth increasing the film thickness.

In addition to nucleation three basic processes can be considered as governing the film growth:

A) Development of the structure by the atom-by-atom process (growth of single crystals — layer growth; growth of liquid droplets or solid amorphous networks). These are the basic processes in growth stages b, c and g and exist also in the stages e and f.

B) Coalescence by melting or surface diffusion characterizing the growth stages d and e.

C) Recrystallization in the growth stages e and g.

The influence of residual gases on the structure and properties of films is studied in numerous experiments but the mechanisms by which their influence is realized are not well known yet. These problems are discussed by Barna et al in a paper dealing with the surface chemical interactions where the possible mechanisms which can result in the codeposition of impurity species during film formation are reviewed [17].

The environment—film interaction takes place on the developing film surface, therefore process A is influenced directly by this. Its direct influence in process B can be neglected first of all in the case of liquid-like coalescence. Process C, the recrystallization is mainly a "bulk" process, determined by the structure developed during processes A and B.

In what follows we are summarizing the phenomena related to impurities which can contribute to the development of hillocks.

i. Accumulation of impurity species can take place on the growing crystal faces by the atom-by-atom and layer growth processes, by the replacement of the impurity atoms bonded in precursor state by the impinging film adatoms and by the formation of stable phases or compounds developing

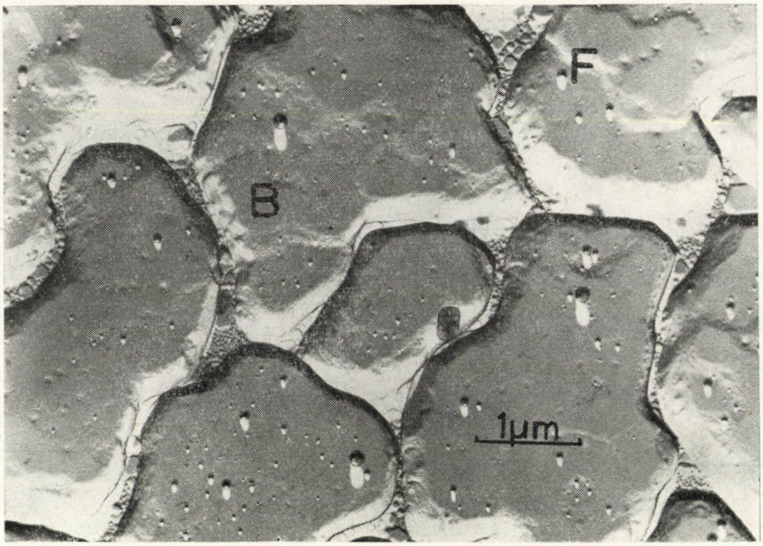

Fig. 9. Surface structure and morphology of crystals grown in Al films deposited onto mica substrate at 550 °C, deposition rate 1,2 nm/s, $5 \cdot 10^{-5}$ Pa without cooling trap. "Hillocks of Type I" (marked by B) developed inside the single crystals and protruding grain boundaries covered by oxide (marked by F) are shown.

two or three dimensional layers covering the surfaces of the growing islands partially or completely [11].

ii. The binding and arrangement or rearrangement of impurity species on the various crystallographic faces can be very different during the precursor state. The very recent results of **Martinson** et al [18], **Johansson** et al [19], **Hofmann** et al [20] and **Michel** et al [21] on Al proved that oxygen species are situated outside the surface atomic layer of the (111) face while they are arranged on the surface both in the "bridge" and "well" positions of (100) faces. For the (100) face they have found that oxygen is penetrating into the bulk and oxide phase is developing at lower coverage.

iii. According to these results the participation of oxygen species in the growth mechanism can be varied on different faces. On the (111) face they can be collected and accumulated by the layer growth mechanism mentioned in point i. [11]. On the (100) face the oxygen species can be "absorbed". It follows that oxygen species will be accumulated at edges between (111) faces by the layer growth while those drawn by the growth steps to the edges between (111) and (100) faces will be "absorbed" by the (100) face near to this edge. As a result of the selective surface accumulation of oxygen species a surface oxide layer starts to develop mainly at the corners and along the edges between (111) faces and destroy the edges themselves (Fig. 10 and Fig. 4 in [17]).

iv. This mechanism can promote the growth of hillocks of Type II (or whiskers) shown in Fig. 4 which have points of truncated octahedrons. These

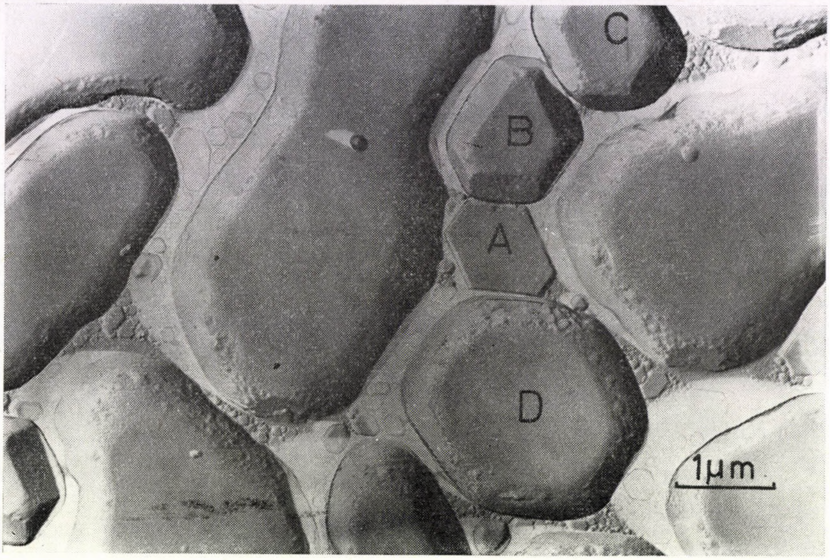

Fig. 10. Surface structure and morphology of crystals grown in Al film deposited onto mica substrate at a temperature of 550 °C, 12 nm/s and at 10^{-4} Pa. The presence of covering oxide layers is to be seen on the surfaces of crystals marked by A, B, C and D resulting in the development of new crystallographic faces. Crystal B is rotated by 60° from the position of crystals A, C and D.

hillocks are bounded namely by (100) and (111) faces as well as by edges between (111) and (100) faces.

v. A significant local concentration of foreign species (impurities or doping elements e. g. Ni, Cu) is required for the nucleation of their stable phases or compounds [25]. Layers or three dimensional segregates of the foreign species or their compounds can be formed on surface areas of growing crystals determined by the mechanisms mentioned above. New crystal faces can start to develop as illustrated in Fig. 10, namely the covering impurity layers can hinder or stop the crystal growth locally.

vi. The coalescence by adjacent crystals is controlled both by their sizes and orientation as well as by the surface covering impurity layer developed before.

4. Summary

The basic features of the formation of different types of hillocks can be summarized as follows:

a) Differences in the growth rate at the various crystallographic directions (formation of Type II hillocks, e. g.: Bi films [16]).

b) Condensation of foreign species accumulated on the surface of the growing crystals

— Development of covering layers on the surfaces of individual single crystals before coalescence. They can control the type of coalescence: liquid-like in case of pure contacting surfaces (formation of Type II hillocks) growth coalescence in the case of covered surfaces.

— Development of the coverage of growth steps resulting in the formation of bunches of steps inside large single crystals (formation of Type I hillocks).

— Selection of crystals of favoured orientation when there is a difference in the uptake properties and in the binding conditions of foreign species on the various crystallographic faces (formation of Type II hillocks).

c) Selection between liquid-like and growth coalescence by the relative orientation interface energy of contacting crystals (formation of Type II hillocks).

Acknowledgements

The authors are indebted to their Colleagues Á. Barna, G. Radnóczi and L. Tóth as well as to Dr. M. Malicskó (Laboratory for Crystal Growth, Budapest), to Dr. V. Stary. (Department for Electronics and Vacuum Physics, Charles University, Prague) and to Dr. J. Derrien (Université Aix-Marseille, II. Centre de Luminy, France) for valuable discussions. Our thanks are due to Mrs. É. Hajmásy, Mr. G. Barcza and Mrs. G. Glázer for their help in carrying out some experiments. F. M. Reicha acknowledges the support of the Hungarian Academy of Sciences, Budapest.

REFERENCES

1. P. B. Ghate, J. C. Blair and C. R. Fuller, Thin Solid Films, **45,** 69, 1977.
2. P. S. McLeod and L. D. Hartsough, J. Vac. Sci. Technol., **41,** 263, 1977.
3. F. M. d'Heurle, L. Berenbaum and R. Rosenberg, Trans. TMS—AIME, **242,** 502, 1968.
4. F. M. d'Heurle, Met. Trans., **1,** 725, 1970.
5. N. G. Dhere and T. P. Arsenio, Thin Solid Films, **30,** 267, 1975; **44,** 29, 1977.
6. A. J. Learn, Thin Solid Films, **20,** 261, 1974.
7. K. Sato, T. O. H. Matsumarus, T. Okubo and T. Nishimura, Met. Trans., **2,** 691, 1971.
8. D. S. Herman, M. A. Schuster and R. M. Gerber, J. Vac. Sci. Technol., **9,** 515, 1972.
9. A. K. Sinha and T. T. Sheng, Thin Solid Films, **48,** 117, 1978.
10. C. J. Santoro, J. Electrochem. Soc., Solid State Sci., **116,** 361, 1969.
11. Á. Barna, P. B. Barna, G. Radnóczi, F. M. Reicha and L. Tóth, phys. stat. sol., (a) **55,** 427, 1979.
12. I. Minkoff and W. C. Nixon, J. Appl. Phys., **37,** 4848, 1968.
13. E. J. Tochinsky, Krystallizatsiya i termoobrabotka tonkih plenok, Nauka i Technika, Moscow, 1976.
14. V. Stary, Czech. J. Phys., **B26,** 882, 1976; B. Smola and V. Stary, Czech. J. Phys., **B27,** 332, 1977.
15. J. W. Matthews, in: Physics of Thin Films, Vol. 4, ed. G. Hass and R. F. Thun, Academic Press, New York/London, 1967, p. 137.
16. Á. Barna, P. B. Barna, R. Fedorovich, G. Radnóczi and H. Sugawara, Thin Solid Films, **36,** 75, 1976.
17. P. B. Barna, Á. Barna and Z. Paál, this Conference, p. 77.
18. C. W. B. Martinson and S. A. Flodström, Surface Sci., **80,** 306, 1979;
    C. W. B. Martinson, S. A. Flodström, J. Rundgren and P. Western, Surface Sci., **68,** 102, 1979.

19. L. I. Johansson and J. Stöhr, Phys. Rev. Lett., **43,** 1882, 1979.
20. P. Hofmann, C. V. Muschwitz, K. Horn, K. Jacobi, A. M. Bradshaw, K. Kambe and M. Scheffler, Surface Sci., **89,** 327, 1979.
21. R. Michel, J. Castaldi, C. Allasia, C. Jourdan and J. Derrien, Surface Sci., **95,** 309, 1980.
22. Á. Barna, P. B. Barna and J. F. Pócza, J. Vac. Sci. Technol., **6,** 472, 1968.
23. K. L. Chopra, Thin Film Phenomena, McGraw-Hill, New York, 1969.
24. B. Lewis and J. C. Anderson, Nucleation and Growth of Thin Films, Academic Press, London, 1978.
25. Vijay K. Agarwala and T. Fort, Surface Sci., **54,** 60, 1976.

Acta Physica Academiae Scientiarum Hungaricae, Tomus 49 (1—3), p. 253 (1980)

EFFECT OF TRIMMING ON THE STRUCTURE OF NiCr THIN FILMS

By

M. LOMINCZY

RESEARCH INSTITUTE FOR MEASURING INSTRUMENTS, BUDAPEST, HUNGARY

P. B. BARNA and Á. BARNA

RESEARCH INSTITUTE FOR TECHNICAL PHYSICS, HUNGARIAN ACADEMY OF SCIENCES
H-1325 BUDAPEST, HUNGARY

Abstract

The exact matching of NiCr thin film resistors can be made by trimming using current pulses. The effects of current pulses — by several orders of magnitude larger than the nominal value — on the structure of the thin films were studied.

The temperature rise of the thin NiCr film during trimming was monitored by a low heat capacity and time constant thin film Pt resistance thermometer, deposited over the NiCr film and separated by a 200 μm SiO_2 insulator film. The resistance of the NiCr film changed abruptly rising its temperature above 670 K. Structural changes of the thin films deposited on a microgrid were studied in situ by a transmission electron microscope during trimming. Results of experiments are described and possible processes of resistance changes are discussed.

Acta Physica Academiae Scientiarum Hungaricae, Tomus 49 (1—3), p. 255 (1980)

INVESTIGATIONS ON NUCLEATION AND COALESCENCE IN THIN Sb-FILMS

By

N. KAISER

ACADEMY OF SCIENCES OF GDR, CENTRAL INSTITUTE FOR OPTICS AND SPECTROSCOPY, 69 JENA, GDR

Abstract

Nucleation, coalescence, and the amorphous — crystalline phase transition in thin evaporated Sb-films show the following characteristic traits:

- below a well-known substrate temperature Sb condenses in the amorphous state;
- the velocity of the transition and the film structure after the phase transition depend strongly upon the deposition conditions;
- single crystal-like orientations may occur also on amorphous substrates.

Investigations on nucleation, cluster growth and coalescence were performed to describe the phase transition under different deposition conditions such as substrate temperature and deposition rate. To obtain statistically significant results about cluster size distributions and spatial distributions of clusters electronic image analysis of electron micrographs was carried out. Measurements of the condensation coefficient by quantitative X-ray microanalysis and Rutherford backscattering technique were possible.

Some mathematical models including shape factors and fractal dimensions were tested to describe the critical degree of cluster contact at which the phase transition occurs.

Acta Physica Academiae Scientiarum Hungaricae, Tomus 49 (1—3), pp. 257—266 (1980)

EFFECT OF ALLOYING MATERIALS ON THERMAL STABILITY AND TCR-VALUE OF RESISTOR FILMS WITH Ta-BASIS

By

V. P. Kolonits and B. Zsoldos

INDUSTRIAL RESEARCH INSTITUTE FOR ELECTRONICS
H-1393 BUDAPEST, HUNGARY

The stability of pure tantalum is not high enough for high precision resistors. The stability of alloyed tantalum (TaAl) or Ta compound (TaN) films are suitable, but their temperature coefficients are relatively high. Experiments were made to prepare TaTi alloys for improving the TCR value and at the same time keeping the excellent stability. The determination of characteristic data of thermal stability from in situ measurements were carried out with computer control. A calculation method was developed to determine the parabolic rate coefficient of oxidation, the activation energy and the probable formal kinetic relationship from t, T and $R_\square$ data.

Introduction

Tantalum-nitrid (TaN) and tantalum-aluminium (TaAl) resistors with better than 0.05% stability (398 K ambient, 1000 h) can be achieved with suitable composition and suitable treatment [1] [2] [3]. These films, however, have -50 to -80×10^{-6}/K (TaN) and -80 to -110×10^{-6}/K (TaAl) temperature coefficients between 298—398 K. This negative TCR indicates chemically bound oxygen in the layer which was demonstrated by SIMS spectra [4] [5] and profile curves. The aim of this work was to inactivate the effect of this oxide in the layer.

It is known that Ti is able to take over the chemically bound oxigen from Ta [6] and simultaneously to keep its own metallic character. This is why TaN films containing Ti were produced. Comparative studies were made on TaN and TaAl layers, too. It was expected that the TCR values in consequence of this character of Ti would shift in positive direction and also the thermal stability would change advantageously, as the thermal stability of Ti is better than that of tantalum, at least above 1300 K [12].

Experimental

The production of TaN films was reported in our publications [1] [2] [4] [5]. The production of TaAl layers was reported in [3]. The alloyed layers were obtained by covering the Ta target with Al or Ti of different proportions, as shown in Fig. 1.

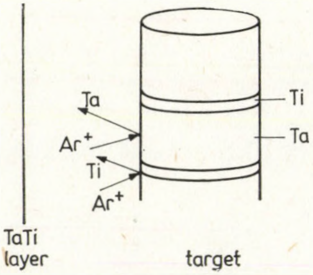

Fig. 1. Arrangement for the production of alloyed Ta films

At first with some preliminary experiments the coverage of the target with titanum was determined, resulting in a value of $0 \pm 15 \times 10^{-6}$/K TCR, then the stability of the resistors selected in this way was investigated.

The square resistance of sputtered layers was 25±5 Ohms/□ on Corning 7059 alkali-free borosilicate glass. A Ti-NiCr-Au contant layer system was applied. The resistor patterns were produced by selective photolithography. The resistance values were 1000∓100 Ohms.

To determine the kinetic characteristics of thermic oxidation within a limited time was possible only by relatively high temperature heat treatments (523—723 K). The resistance values during the heat treatments were monitored by an instrument with 0.005% accuracy, the measured values were collected with decreasing frequency and stored on magnetic tape by a compuer.

The heat treated samples naturally do not reach the temperature of the hot oven at once but after a certain time. Therefore, together with the examined samples, in the same oven and a similar sample holder, a NiCr resistor covered by 400 nm thick Si_3N_4 layer for preventig the oxidation and heat treated at 623 K temperature for 1 h was used to determine the temperature rise — time function through the change of resistance value. These measurements showed that the temperature of this sample (T) at each investigated temperature followed the function (1) where the time constant (τ) was 4±0.5 min:

$$\frac{T}{T_0} = 1 - e^{-t/\tau}. \tag{1}$$

If the thickness of the Si_3N_4 protecting layer was 200 nm, the τ values decreased to 2 min. Through this new τ value another inconsistency could be overcome at the same time, namely that at the same temperature a different oxidation rate could be computed as a function of the final temperature of the sample.

The TCR values were determined by resistance measurements at temperatures of 298 and 398 K.

The processing of experimental values

The thermal stability in its classical sense can be derived from the resistance values only in that case where the function between the thickness of through-oxidized layer, the rate of oxidation and the temperture of the reaction can be determined.

In order to convert the resistance value into layer thickness the dependence of d on R , that is the function

$$d = f(R_{\square}) \tag{2}$$

had to be known. This function has some general characteristics but it is different for each type of Ta films. The determination of this function can be carried out experimentally. For example:

$$d = \frac{2.2 \times 10^4 + \sqrt{2.2^2 \times 10^8 + 1250\, R}}{2\, R_{\square}} \tag{3}$$

is the function for TaN.

If the square resistance is above 200 Ohm/□, the small but not zero conductance of the oxidized layer adjacent to the substrate must be taken into consideration.

The decrease of the starting thickness d will be denoted by X, the rate of this decrease will be Y.

Exact information about the effective thickness change can be given only if before computing X from the value $R_{\square}$ the reversible change of resistance (TCR value) is taken into consideration. This is made by the computer, which calculates at each given time the effective data T_M from the given time constant and temperature T_0 and with the help of effective temperature and TCR values, converting the measured resistance values into room temperature.

The $Y = f(X)$ functions corrected with TCR values are shown in Fig. 2 for TaAl and in Fig. 3 for TaTi films.

The exact and in situ measurements give the opportunity to draw kinetic conclusions for the oxidation of Ta-based films. It is known that for the starting period of oxidation the following kinetic models exist for metals and also for tantalum [10—14]:

$$X = A \ln t\,, \tag{4}$$

$$\frac{1}{X} = A \ln t\,, \tag{5}$$

$$X^2 = kt\,, \tag{6}$$

$$X^3 = kt\,, \tag{7}$$

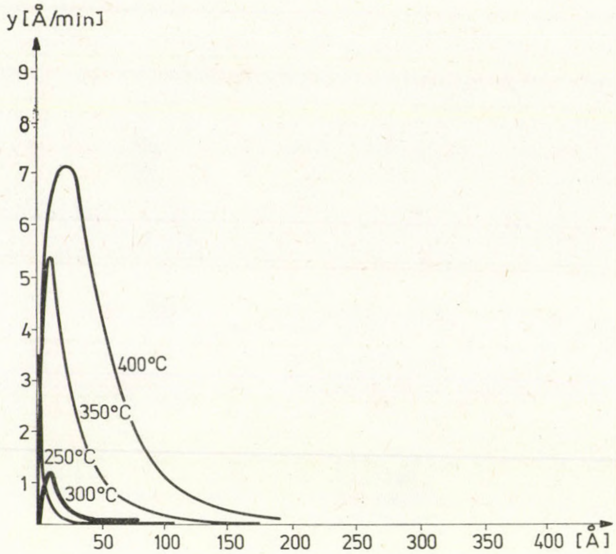

Fig. 2. The rate of oxidative decrease of metal film thickness as the function of the thickness of oxidized film and of the temperature of heat treatment in the case of TaAl

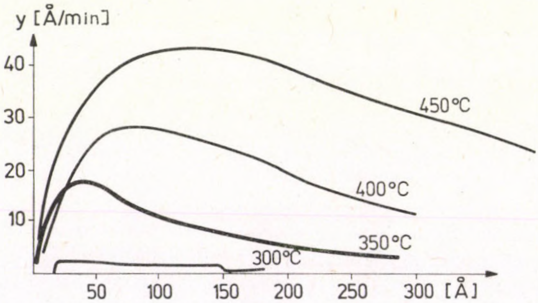

Fig. 3. The rate of oxidative decrease of metal film thickness as the function of the thickness of oxidized film and of the temperature of heat treatment in the case of TaTi

Our resistance layers are so thin that in any case the start of oxidation is characteristic. The reason for the different interpretations may be that the different authors did not take into consideration sufficiently the initial oxide thickness and the differences in heating up the samples. At the same time their methods were not so sensitive as it is possible with measuring the resistance of a layer about 150 nm thick and calculating a thickness change about 0.1 nm order of magnitude. (In most cases the determination of oxidation mechanism was carried out with weight measurement.) SIMS studies of our layers show that the thickness of the air oxide on the surface is $X = 2$ nm

[4] [5]. To draw kinetic conclusions it is considered very useful to plot either the

$$\log Y = f(\log X)$$

or (8)

$$\log Z' = \log (X + X_0)\ X$$

function.

The differential versions of the relationships (4—7) reflect the conceptions related much more to the mechanism of the oxidation process [1] [2] [4] than the time functions

$$\frac{dX}{dT} = A\, e^{-X}, \tag{9}$$

$$\frac{dX}{dt} = A\, e^{1/X}, \tag{10}$$

$$\frac{dX}{dt} = \frac{k_p}{2X}, \tag{11}$$

$$\frac{dX}{dt} = \frac{k_p}{3x^2}. \tag{12}$$

The coefficients A and k include the dependence on temperature, e. g.

$$A = A_0\, e^{-W/kT} \tag{13}$$

The shape of the function $\log X = f/\log X$ can show the mechanism of the oxidation only if we have data at least in the 2—100 nm X-range. Sometimes this is very difficult to carry out by a simple continuous heat treatment, because at 523 K or below the rate of oxidation is so slow that we have no time for the through-oxidation of that tickness.

If the available X-range is narrower the plotting of the correlations

$$Z = XY = f(X) \tag{14}$$

or

$$\log Z = \log (XY) = f(X) \tag{15}$$

is a very useful method to determine the character of oxidation and the coefficients. If the parabolic oxidation law characterized by Eq. (12) is valid, then

$$Z = X\frac{dX}{dt} = k_p \tag{16}$$

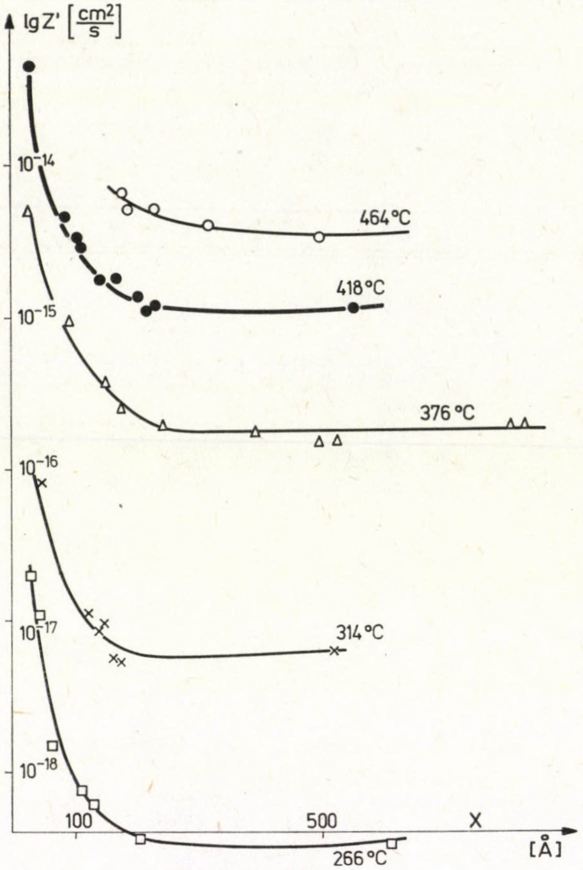

Fig. 4. Log $Z = f(X)$ correlation measured on TaN thin film resistors

that is the function is independent of X, while of one of the other three theories is valid, Z decreases with increasing X. Fig. 4 shows this for TaN films.

The Z data from Fig. 4 above 15 nm can be used to determine the parabolic rate coefficients and the activation energy of oxidative decrease of metallic layer thickness. With the help of this activation energy the Z-values obtained in the first few minutes can be re-calculated from the effective temperature T_M to the nominal temperature T_0.

Fig. 4 was already made in this way. Fig. 5 shows the log Z data belonging to effective temperatures, and Fig. 6 shows the log Z data re-calculated to T_0 nominal temperature in the case of TaAl films.

The results of in situ measurements of TaTi thin film resistors are shown in Fig. 7 ($\log Z_{T_M}$) and in Fig. 8 ($\log Z_{T_0}$). The calculation of activation energy from Z-data belonging to $X = 30$ nm can be carried out in a way shown in Fig. 9.

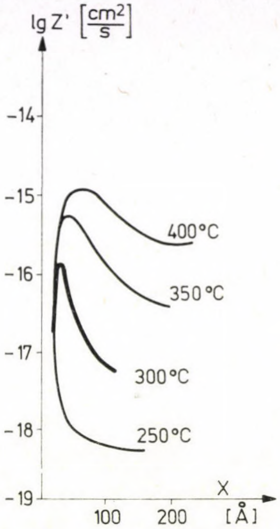

Fig. 5. The rate constant of oxidation as the function of X for TaAl thin films

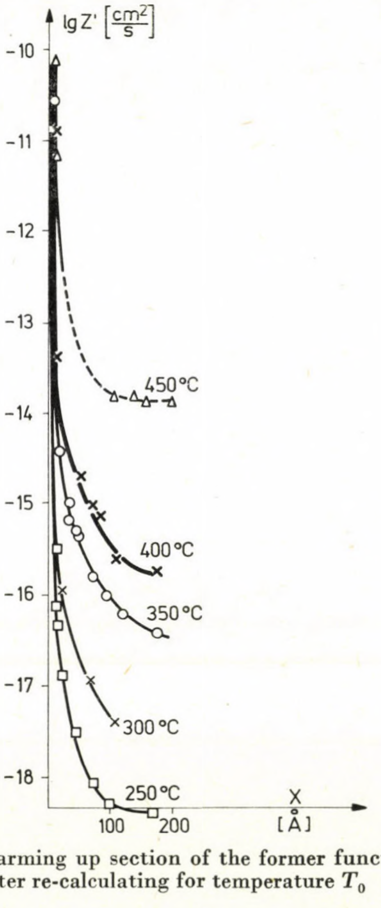

Fig. 6. The Z values in the warming up section of the former functions as the function of X after re-calculating for temperature T_0

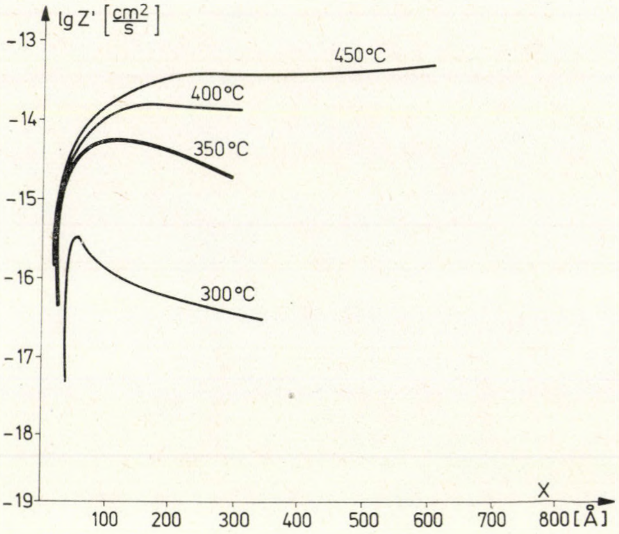

Fig. 7. Log $Z' = f(X)$ functions for TaTi films

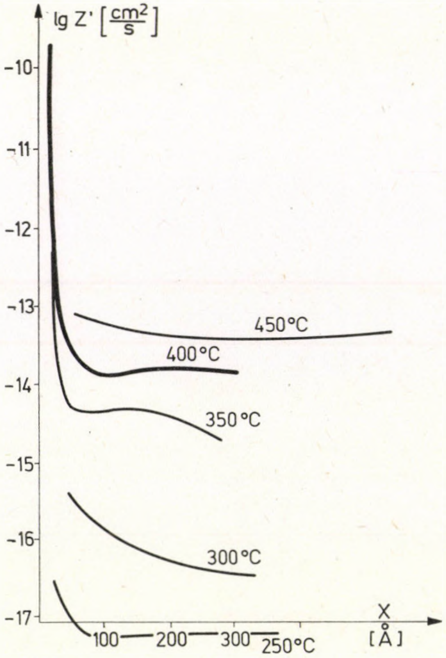

Fig 8. The data of the former functions after correction for nominal temperature T_0

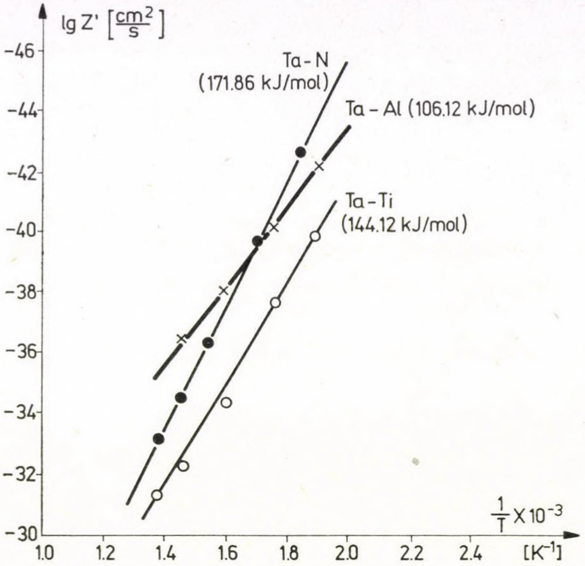

Fig. 9. Determination of activation energy for TaN, TaAl and TaTi films

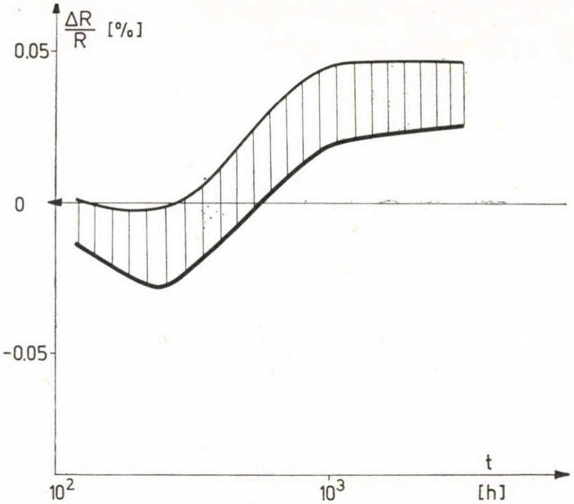

Fig. 10. Long term stability of TaTi thin film resistors

From the results it can be concluded that at higher temperatures the TaAl, at lower temperatures (below 423 K) the TaTi is more stable.

The long term stability (393 K, 1000 h) — after a suitable preliminary stabilization — was with all three films under 0.05%. This is shown for TaTi in Fig. 10.

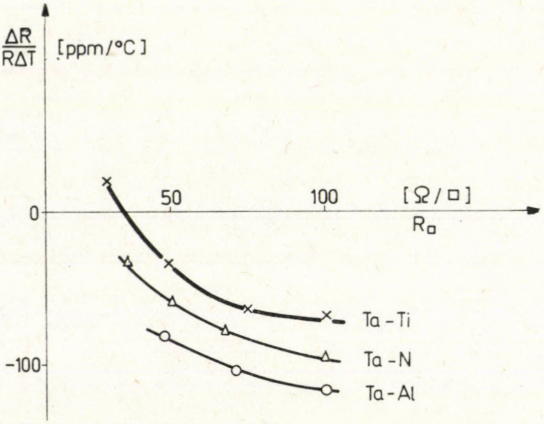

Fig. 11. Temperature coefficients of tantalum basis thin film resistors

The temperature coefficients of films manufactured under experimental conditions are the functions of layer thickness, so of R (Fig. 11). By alloying of titanium a shift towards the positive TCR direction could be reached.

TaTi films are oxidable in the same way as Ta, TaN and TaAl films, so the trimming can be carried out simply by anodic oxidation.

REFERENCES

1. P. Kolonits M. Koltai, T. Strausz HIKI Közlemények, 1978 (in Hungarian).
2. V. P. Kolonits, Tage der Wissenschaft und Technik, 1978. Karl Marx Stadt (Vortrag).
3. B. Zsoldos, Wissenschaftliche Tagung, Passive Bauelemente 11—13. Sept. 1979. Karl Marx Stadt, (Vortrag).
4. V. P. Kolonits, M. Koltai and T. Strausz, Vacuum, **27,** 635, 1977.
5. V. P. Kolonits, D. Marton and M. Koltai, Thin Solid Films, **57,** 221, 1979.
6. A. Lepselter, Bell System, **45,** 233, 1966.
7. H. Baseches, IRE Trans. Comp. Parts, CP—9, 51, 1961.
8. J. S. Fischer, Proc. Electron. Comp. Conf., N. Y. 1968, IEE p. 299.
9. R. W. Berry, P. M. Hall and M. T. Harris, Thin Film Technology, D. van Nostrand Co., Inc. Princeton, 1968.
10. E. H. Sondheimer, Adv. Phys., **1,** 1, 1951.
11. O. Kubaschewski and B. E. Hopkins, Oxidation of Metals and Alloys, Butterworth, London, 1962.
12. K. R. Lawless, Rep. Prog. Phys., **37,** 231, 1974.
13. U. R. Evans, The Corrosion and Oxidation of Metals, Edvin Arnold, London, 1960.
14. N. Caberra and N. F. Mott, Rep. Progr. Phys., **12,** 163, 1948—49.

Acta Physica Academiae Scientiarum Hungaricae, Tomus 49 (1—3), p. 267 (1980)

SUPRALEITENDE DÜNNE SCHICHTEN

Von

E. Wilfing und E. M. Hörl

ÖSTERR. FORSCHUNGSZENTRUM SEIBERSDORF, A-2444 SEIBERSDORF, ÖSTERREICH

Kurzfassung

Diese Arbeit hat sich die Herstellung und Untersuchung von dünnen, supraleitenden Schichten aus $NbSb_3$ bzw. NbN zum Ziel gesetzt. Dazu wurde eine Versuchslanlage gebaut, in der verschiedene Substrate bei hohen Temperaturen (ab 900 °C aufwärts) mittels der sg. "Fiessbettechnik" beschichtet werden. Dabei handelt es sich um ein CVD-Verfahen, in dem ein Medium (in unserem Fall Quarzsandkörnchen von 0.3—0.5 mm Durchmesser) im Gasstrom ($NbCl_5$, $SnCl_4$ bzw. N_2, reduzierendes Gas H_2, Trägergas Ar) fluidisiert und dadurch Wirbel erzeugt. Die auf diese Weise hergestellten Schichten werden auf kristallographische Struktur, chemische Zusammensetzung und supraleitende Eigenschaften hin untersucht. In Vorversuchen, die zur Klärung anlagenspezifischer Probleme dienten, wurden Nb-Schichten auf Glimmer, Quarz und rostfreiem Stahl hergestellt.

Acta Physica Academiae Scientiarum Hungaricae, Tomus 49 (1—3), pp. 269—273 (1980)

INVESTIGATION OF OXIDATION PARAMETERS OF TANTALUM-TYPE LAYERS

By

I. TRIFONOV

INDUSTRIAL RESEARCH INSTITUTE FOR ELECTRONICS
H-1393 BUDAPEST, HUNGARY

The formation rate of the oxide layers and the oxidation rate of the Ta_2N, Ta-Al, Ta-Ti layers made by reactive sputtering were investigated.

The thickness of the oxide layers was determined partly by Talystep equipment, and partly from the resistance change of tantalum type layers on account of oxidation. The formation rate and the oxidation rate were different for three types of the layers.

Tantalum-type layers are widely used in thin film microelectronics: high stability precision networks, TC compensated RC filters are made from tantalum type layers. In the manufacture of tantalum thin film capacitors it is important to know the exact anodization parameters (formation rate, oxidation rate) of different layers. In this paper the parameters of anodic oxidation of tantalum type layers were in vestigated.

Anodic oxidation of tantalum

The anodic oxide on Ta grows by the simultaneous movement of oxygen and tantalum ions through the oxide. From Faraday's Law

$$f \Delta Q = \frac{10\, F\gamma\, A \Delta d}{M}, \tag{1}$$

where f is the current efficiency factor, F is the Faraday constant, γ is the oxide density, A is the true area of the sample, d is the increment in oxide thickness produced when a charge amount ΔQ is passed through the anodizing cell. After transformation of Eq. (1)

$$\Delta d = \frac{fM}{10\, F\gamma A} \Delta Q \tag{2}$$

and adding

$$\Delta Q = Jt\,, \quad J = J_0 \exp - \left(\frac{W}{kt} \right) \exp \left(\frac{aE - bE^3}{kT} \right), \tag{3}$$

where a and b are constants, W is the migration energy and E is the field in the oxide U_{ox}/d_{ox}.

In the case of constant voltage anodization, having integrated the Eq. (2)

$$d = \int_0^{t=\infty} \frac{fM}{10\, F\gamma A} J(\tau)\, d\tau \tag{4}$$

which means $d_{ox} = \alpha U_{ox}$, where U_{ox} denotes the anodization voltage and α is the formation rate. That means that the oxide thickness depends linearly on the anodization voltage. To determine the formation rate experimentally one has to know the thickness d_s of the layer after oxidation and the remaining thickness d_m of the Ta layer (Fig. 1.)

Thicknesses d_0 and d_s can be measured directly, dt can be counted from the resistance change of the Ta layer because of oxidation.

Before oxidation

$$R_b = \frac{\varrho l}{d_0\, s}\,. \tag{5}$$

After oxidation

$$R_a = \frac{\varrho l}{d_m\, s}\,, \tag{6}$$

where l/s is the number of squares, ϱ is the resistivity of Ta layer.

Dividing (5) and (6) by each other

$$\frac{R_b}{R_a} = \frac{d_m}{d_0}\,, \quad d_m = \frac{R_b}{R_a} d_0\,,$$

The thicknesses of interest to us: d_- and d_{ox} can be written as follows:

$$d_- = d_0 - d_m = d_0 \left(1 - \frac{R_b}{R_a}\right).$$

$$d_{ox} = d_s - d_m = d_s - d_0 \frac{R_b}{R_a}\,.$$

Knowing the thicknesses d_- and d_{ox} and the anodization voltage belonging to them we can determine the formation rate:

$$\alpha = \frac{d_{ox}}{U_{ox}}$$

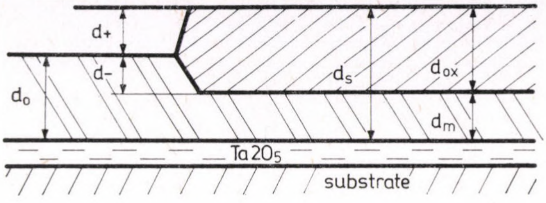

Fig. 1. Cross section of an oxidized tantalum layer

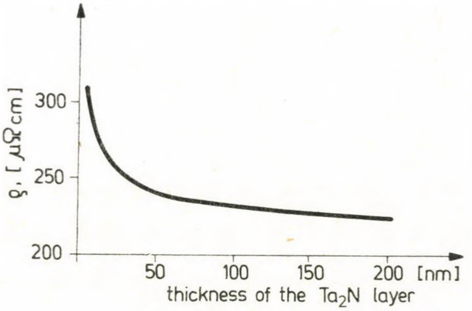

Fig. 2. Resistivity of a tantalumnitride layer versus tantalum layer thickness

and the oxidation rate:

$$\alpha_1 = \frac{d_-}{U_{\text{ox}}} \,.$$

It has to be considered that the resistivity of a sputtered layer is a function of the thickness (Fig. 2).

If the remaining thickness d_m after anodization is smaller than 50 nm, the resistance:

$$R_0 = \frac{[\varrho + \varrho(d)]\, l}{d_m\, s} \cong R_{a0} + k\varrho(d)\,,$$

where $k\varrho(d)$ is the increase of resistance because of the increasing resistivity at the substrate-Ta interface. If the remaining thickness $d_m \gg 50$ nm, the increase of resistance is negligible.

Experimental results

Three different types of tantalum layers were investigated (Ta_2N, Ta-Ti, Ta-Al). The layers were sputtered on Corning 7059 substrates covered previously by thin Ta_2O_5 films. The thickness of the layers was 300 nm. The resistivities of the Ta_2N, Ta-Al, Ta-Ti layers were of the order 250, 160, 340 cm,

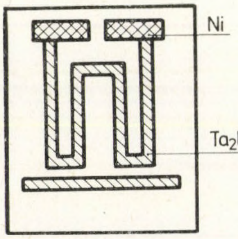

Fig. 3. Geometry of the anodized resistors

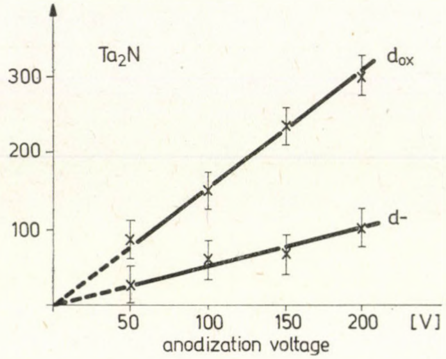

Fig. 4. Oxide thickness d_{ox} and the thickness of oxidized tantalum d versus anodization voltage for Ta_2N

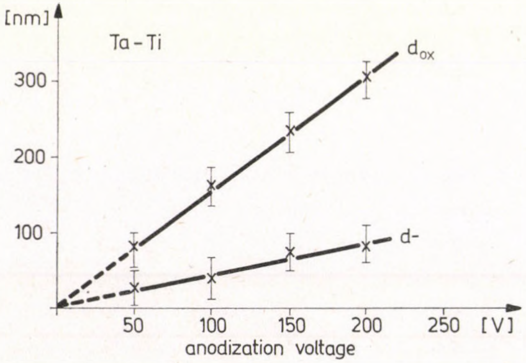

Fig. 5. Oxide thickness d_{ox} and the thickness of oxidized tantalum d versus anodization voltage for Ta-Ti

respectively. The test form is shown in Fig. 3. The anodization voltage was changing from 50 V to 250 V in 50 V steps. Thicknesses d_0 and d_s were measured by Alpha Step equipment.

In the Figs. 4, 5 and 6 we have shown the dependence of the thicknesses d_{ox} and d_- on the anodization voltage of Ta_2N, Ta-Ti, Ta-Al layers, respectively.

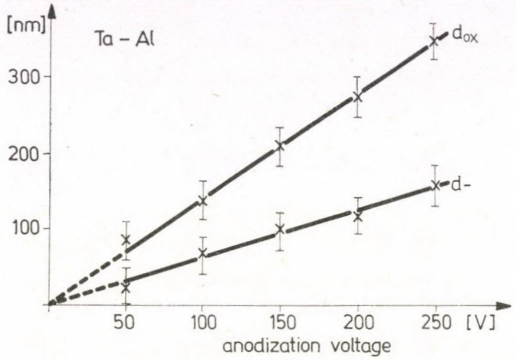

Fig. 6. Oxide thickness d_{ox} and the thickness of oxidized tantalum d versus anodization voltage for Ta-Al

The anodization parameters of tantalum type layers are:

	the formation rate	the oxidation rate
Ta_2N	1.55 nm/V ± 10%	0.51 nm/V ± 10%
Ta-Ti	1.61 nm/V ± 10%	0.54 nm/V + 10%
Ta-Al	1.41 nm/V + 10%	0.69 nm/V + 10%

REFERENCES

1. R. D. HUTTEMANN ad J. M. MORABITO, IEEE Trans. on PHP, **11**, 67, 1975.
2. W. D. WESTWOOD and N. WATERHAUSE, Tantalum Thin Films, Academic Press, London, 1975.
3. W. JUERGENS, Thin Solid Films, **16**, 359, 1973.

Acta Physica Academiae Scientiarum Hungaricae, Tomus 49 (1—3), pp. 275—279 (1980)

ELECTRICAL PROPERTIES OF SOME PHTHALOCYANINE THIN FILMS

By

W. WACŁAWEK and M. ZĄBKOWSKA

DEPARTMENT OF EXPERIMENTAL PHYSICS, PEDAGOGICAL UNIVERSITY
CZĘSTOCHOWA, POLAND

The results of the measurements of electrical conductivity, thermoelectric power as a function of temperature as well as space charge limited currents were reported for lead phthalocyanine films.

The results were compared for samples of various thicknesses and shapes as well as with these obtained for pellets. On the basis of these data the values of charge carrier mobilities were calculated.

The applicability of the band theory for lead phthalocyanine was discussed.

Introduction

The electrical and thermoelectrical properties of organic semiconductors have been attracting a great deal of interest for years.

The large family of phthalocyanines has been carefully studied because of:

- their molecular structure resembling those of many biologically active materials, e. g. chlorophyll and hemin;
- planarity of their molecules;
- their high chemical and thermal stability;
- many possibilities of various applications [1], [2].

Lead phthalocyanine is a material of particular interest because of its unusual properties.

UKEI [3]—[6] found that lead phthalocyanine films prepared in a special way could be one-dimensional conductor. HAMANN [7]—[9] observed switching phenomena on polycrystalline films of lead phthalocyanine prepared at 470K as sandwiches. YASUNAGA [10] studied the influence of oxygen on electrical and thermoelectrical properties of lead phthalocyanine single crystals and films.

Experimental

Thin film samples of lead phthalocyanine were prepared as sandwiches and surface cells by vacuum evaporation of the material at $\sim 10^{-4}$ Pa onto glass substrates. Pellet samples of the same material were prepared of powder at $\sim 10^{9}$ Pa. Gold electrodes were used.

Electrical conductivity, thermoelectric power and current-voltage characteristics as a function of temperature were measured. The measurements on pellet samples were carried out with a guard ring to exclude surface currents.

The conventional d. c. method incorporating the electrometer (type Cary 401 (USA) or Keithley 616 (USA)) was used for the measurements of electrical conductivity. The measurements were done on samples in vacuum, oxygen, hydrogen and iodine vapours.

Details of the experimental procedure were described elsewhere, e. g. in [11], [12].

Results

In spite of the same experimental conditions for different sample types the results were generally not the same. Nevertheless, similar conductivity results were obtained for films (surface cells) and pellet samples saturated with iodine vapours. For these samples the electrical conductivity value (at a temperature of 298,15 K) $\sigma_{25} \in (3;5) \cdot 10^{-2}\mathrm{Sm}^{-1}$ and the thermal activation energy for conduction $E_t \cong (0.156; 0.174)$ eV were obtained from the measurements of sample resistivity with decreasing temperature, because one could observe the electrical conductivity values to decrease and simultaneously the thermal activation energy values to increase, when temperature increases.

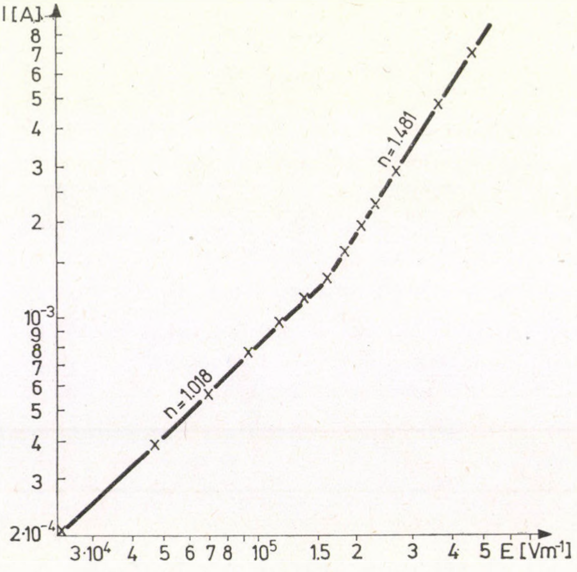

Fig. 1. **Dependence of current I on electrical field E applied to lead phthalocyanine film (sandwich cell) saturated with iodine vapours at 293,77K**

In all cases (for samples placed in different atmospheres) the thermal activation energy values for samples prepared as sandwich cells were smaller than those for others. At low electric fields all current-voltage characteristics were ohmic, hence their slopes, n, were equal to 1. For some samples (pellet samples and surface cells) in higher fields (of the order of $10^5\,\mathrm{Vm}^{-1}$) the characteristics started to be non-ohmic, but their slopes were only somewhat greater than for the low field measurements.

The same has been found in the case of lead phthalocyanine film (surface cell) saturated with iodine vapours (Fig. 1). Similar results were obtained earlier in this laboratory [11], [13] as well as by other authors e. g. [14].

For lead phthalocyanine films (sandwich cells) differences between the first and subsequent runs of current-voltage characteristics were observed: for the first run the characteristic was ohmic for higher electric fields than it was for the following runs. So, the characteristic for the second run was different from the first one, but it did not change for the third and subsequent runs regardless of the electrical field increased or decreased during the run (Fig. 2). The reproducibility of the runs was good. In case of Seebeck coefficient Q its value of the pellet samples was greater than of the films (surface cells).

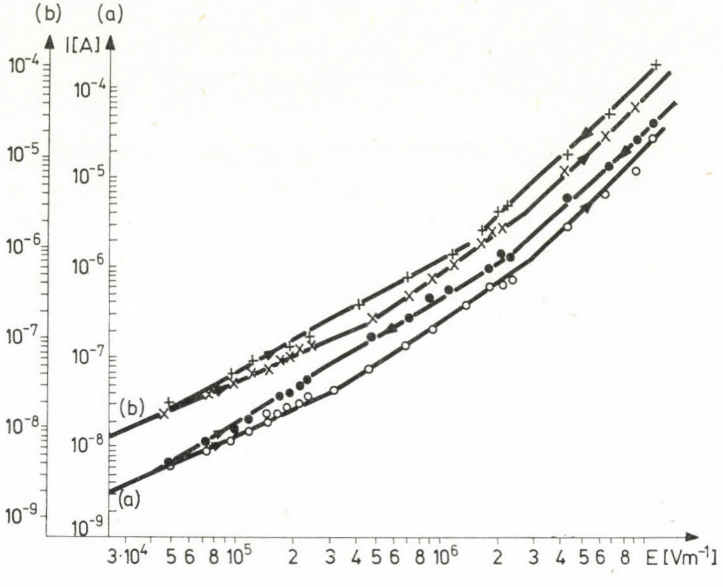

Fig. 2. Dependence of current I on electrical field E applied to lead phthalocyanine film (sandwich cell): (a) at 317,12K: o—I run, o—II and following runs: (b) at 341,24K: ×—I run, +—II and following runs

It has been established e. g. in [15], that its value for films depends on film thickness, d:

$$Q = Q_0 - \frac{\text{const}}{d}$$

due to diffusion processes.

Discussion

The electric conductivity values for lead phthalocyanine sandwich cells and pellet samples were comparable. Similar results were obtained by e. g. INOKUCHI [16] for perylene films (sandwich cells) and pellet samples. σ_{25} values obtained for surface cells were somewhat greater, among others because of surface current. These differences may be minimalized by choosing suitable sample dimensions.

If one assumes that the preexponential factor of conductivity, σ_0, is connected with the mobility of charge carriers [2], [17], the mobility values for films (surface cells) and pellet samples mostly are of the same order of magnitude and are greater by some orders of magnitude than the values obtained for films (sandwich cells).

The charge carrier mobilities obtained on the basis of space charge limited current measurements for lead phthalocyanine sandwich cells were very small (of the order of 10^{-10} $m^2 V^{-1} s^{-1}$).

For pellet samples mobility values were obtained by comparison of electrical conductivity and thermoelectric power data. In the atmospheres of hydrogen, oxygen and vacuum their values were of the order of $10^{-4} m^2 V^{-1} s^{-1}$ or $10^{-5} m^2 V^{-1} s^{-1}$, moreover they decreased with temperature [18] as it should be according to the band theory [19].

REFERENCES

1. Z. WITKIEWICZ and R. DABROWSKI, Wiad. Chem., **27**, 141, 1973.
2. H. MEIER, Organic Semiconductors. Dark- and Photoconductivity of Organic Solids, Monographs in Modern Chemistry, Verlag Chemie, Weinheim, 1974.
3. K. UKEI, Acta Cryst., **B29**, 2290, 1973.
4. K. UKEI, K. TAKAMOTO and E. KANDA, Phys. Lett., **A45**,, 345, 1973.
5. K. UKEI, Phys. Lett., **A55**, 111, 1975.
6. K. UKEI, J. Phys. Soc. Japan, **40**, 140, 1976.
7. C. HAMANN, H. J. HÖHNE, F. KERSTEN, M. MÜLLER and M. STARKE, Wiss. Zeit. Pädagog. Hochschule Dr. T. Neubauer, Erfurt/Mühlhausen, Math.-Naturwiss. Reihe, **14**, 21, 1978.
8. C. HAMANN, H. J. HÖHNE, F. KERSTEN, M. MÜLLER and M. STARKE, Electrical and Related Properties of Organic Solids, Prace Naukowe Inst. Chemii Org. Fiz. Polit. Wrocławskiej, Seria: Konferencje, **16**, 27, 1978.
9. C. HAMANN, H. J. HÖHNE, F. KERSTEN, M. MÜLLER, F. PRZYBOROWSKI and M. STARKE, Phys. Stat. Sol., **A50**, K189, 1978.

10. H. Yasunaga, K. Kojima, H. Yohida and K. Takeya, J. Phys. Soc. Japan, **37,** 1024, 1974.
11. M. Ząbkowska, Dissertation, Physics Institute, Warsaw Polytechnical University, Warsaw, 1978.
12. M. Ząbkowska and W. Wacławek, Potsdamer Forschungen, Wiss. Schriftreihe der Pädagogischen Hochschule "Karl Liebknecht", Potsdam, Reihe B — Naturwiss. Reihe, 146, 1979.
13. M. Ząbkowska and W. Wacławek, Electrical and Related Properties of Organic Solids, Prace Naukowe Inst. Chemii Org. Fiz. Polit. Wrocławskiej, Seria: Konferencje, **16,** 329, 1978.
14. G. A. Yurlova, Zh. Fiz. Khim., **45,** 1663, 1971.
15. E. A. Soa and F. Völklein, Exp. Techn. Phys., **26,** 145, 1978.
16. H. Inokuchi and H. Akamatu, Solid State Phys., **12,** 93, 1961.
17. D. D. Eley, A. S. Fawcett and M. R. Willis, Trans. Faraday Soc., **64,** 1513, 1968.
18. M. Ząbkowska and W. Wacławek, to be published.
19. M. Kryszewski and L. Brehmer, Faserforschung und Textiltechnik, Zeit. Polymerforschung, **29,** 502, 1978.

Acta Physica Academiae Scientiarum Hungaricae, Tomus 49 (1—3), p. 281 (1980)

VACUUM PHYSICS

RADIATION ENHANCED DIFFUSION AND PERMEATION OF HYDROGEN IN STAINLESS STEEL*

By

R. DOBROZEMSKY, G. SCHWARZINGER, CHR. STRATOWA and A. BRETH

PHYSICS INSTITUTE, RESEARCH CENTER SEIBERSDORF, SGAE
A-1082 VIENNA, AUSTRIA

Abstract

Measurements of the radiation enhanced diffusion and permeation of hydrogen in stainless steel type 4301 (s. s. 304) in the temperature range of 350 to 600 °C are reported. As radiation source an edge position of the ASTRA-reactor core was used (dose rate 0.1 to 0.5 W/g). The permeation as well as the diffusion coefficient were found to be considerably larger during irradiation than the thermal effects at the same temperatures (measured by ohmic heating with the reactor shut down). A detailed description of the apparatus is given together with a discussion of the results hitherto achieved.

---

* This research was supported in part by the "Fonds zur Förderung der wissenschaftlichen Forschung in Österreich", Vienna (Proj. Nr. 3423).

Acta Physica Academiae Scientiarum Hungaricae, Tomus 49 (1—3), p. 283 (1980)

QUADRUPOLE MASS SPECTROMETERS IN THE ATOMKI

By

I. BERECZ, S. BOHÁTKA, Z. DIÓS, S. JENEY, L. KISS and G. LANGER

INSTITUTE OF NUCLEAR RESEARCH OF THE HUNGARIAN ACADEMY OF SCIENCES
ATOMKI, DEBRECEN, HUNGARY

Abstract

This paper presents the line of quadrupole mass spectrometers constructed in the ATOMKI. The basic of this line is the NZ-850 which has a mass range of 1—300 a. m. u. and 7.10^{-4} A/mbar sensitivity. The Q-100U is a smaller instrument with reduced mass range (1—100 a. m. u.) but other features — like total pressure measurement, leak detector unit — make it significant. The PS-500 peak selector makes for both types possible to measure only the preselected peaks (max. 9), an opportunity of controlling certain processes.

Acta Physica Academiae Scientiarum Hungaricae, Tomus 49 (1—3), p. 285 (1980)

VAKUUMMESSUNG MIT PTC-WIDERSTAND

Von

R. Essl

FORSCHUNGSZENTRUM FÜR ELEKTRONENMIKROSKOPIE, GRAZ, ÖSTERREICH

Kurzfassung

Die Widerstandsänderung eines elektrisch geheizten PTC-Widerstandes kann zur Druckmessung herangezogen werden. Die Kleinheit des PTC-Widerstandes als Fühler im Vakuum eröffnet gegenüber herkömmlichen Druckfühlern neue Anwendungsmöglichkeiten. Mit Hilfe des Varistoreffektes ist es möglich, ohne separaten Heizwiderstand durch Selbstheizung des PTC-Widerstandes die Druckmessung zu realisieren. Dazu ist jedoch ein Wechselbetrieb Heizen — Messen erforderlich. Die Heizung erfolgt mit hoher Spannung, wodurch die Widerstandserniedrigung eine entsprechende Leistungsaufnahme ermöglicht. Die Messung erfolgt mit niedriger Spannung, sodass der Widerstand in dieser Periode nicht von der Spannung, sondern der Temperatur des Fühlers abhängt. Diese ist aber im Druckbereich von 10^{-2} bis 100 Torr wesentlich von der Wärmeabgabe an das Restgas und damit vom Druck abhängig.

Acta Physica Academiae Scientiarum Hungaricae, Tomus 49 (1—3), pp. 287—292 (1980)

SOME INTERESTING MEASUREMENTS WITH QUADRUPOLE MASS SPECTROMETERS

By

S. BOHÁTKA, I. BERECZ and G. LANGER

INSTITUTE OF NUCLEAR RESEARCH OF THE HUNGARIAN ACADEMY OF SCIENCES
ATOMKI, DEBRECEN, HUNGARY

Some measurements made with the NZ-850 type quadrupole mass spectrometer of the ATOMKI are reported. The analysis of gases in operating rooms showed 1 ppm—10^5 ppm concentration of narcotics. Purity control of gases regularly helps the radioactive pollution measurements and radio carbon dating technique at our Institute. In an other application evidence of new possibilities is given which arise from coupling the quadrupole to electron diffraction apparatus. Examples of blood gas analyses and some applications in chemical technology are also given.

Besides the development of quadrupole mass spectrometers and of complex equipment including mass spectrometers, we have also made at the ATOMKI some measurements which may be of some interest. In each case we used our NZ-850 type quadrupole [1] in the investigations.

Environmental pollution tests

In anaesthesiology, narcotics are applied in a 0.5—5% concentration (halothane, penthrane, etc.) added to a mixture of O_2 and N_2O. These materials have not only an anaesthetic effect but they are poisonous too, and their regular inhalation may cause severe lesions in the human organism. During anaesthetization the narcotic gases escape into the air and without proper exhaustion or absorption, doctors and nurses may inhale them as well. So the operating staff works under hazardous conditions day by day, which fact is confirmed by statistical data showing, unfortunately, an increased rate of injuries and even deaths. At the University Medical School of Debrecen, Department I of Surgery, air pollution is avoided with the use of disposable narcotic filters. A regeneration technique of the filters has also been worked out to considerably reduce the costs of this extremely expensive method [2].

During the course of clinical research on air pollution in the operating room, the effectiveness of filters and the efficiency of their regeneration have been quantitatively determined with the quadrupole mass spectrometer.

Air samples were carried to the mass spectrometer in rubber balloons. The fact that rubber balloons absorb narcotics fairly well caused quite a prob-

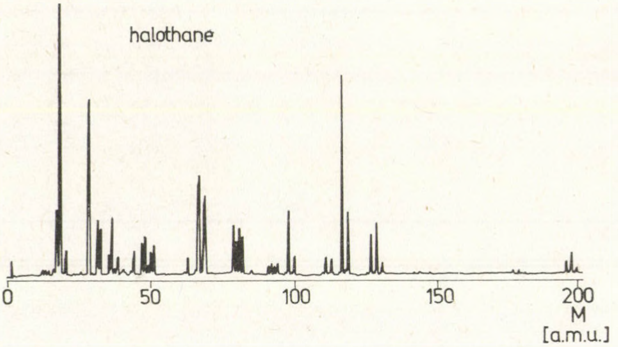

Fig. 1. Mass spectrum of halothane

lem, but we managed to exclude inaccuracies by letting the ballons soak up with the air to be tested and took samples only after the saturation of surfaces. To identify the compounds we used the peaks at 81 a. m. u. and 117 a. m. u. for penthrane and halothane, respectively. The mass spectrum of halothane — air mixture can be seen in Fig. 1. The mass spectrometer output signal was calibrated against the temperature compensated vaporiser which produced the anaesthetic gas mixtures. Filters reduce the pollution to 1% and 0.1% of the original values in the case of halothane and penthrane, respectively. They do not absorb N_2O. The efficiencies of new and regenerated filters were practically the same. Halothane and penthrane concentrations on operation spots were between 1.5—2 ppm and 6—15 ppm, which coincided with the sensitivity limit of our instrument (1.5 ppm and 6 ppm).

Contamination control

Another series of measurements has been carried out to assist the research work of our Colleagues by controlling the contamination of the materials used. Certain components of radioactive pollution (e. g. ^{85}Kr) escaping at explosion tests and from nuclear reactors are measured regularly at the Institute [3]. The activity of ^{85}Kr is measured with Geiger-Müller counters. The efficiency of counting is influenced among others by the purity of the Kr sample, so the latter is regularly checked. The amount of contaminations in the samples (Ar; Xe) was less than 0.1%. On another occasion we checked the purity of CO_2 used for radio carbon dating, in which NO (e. g. when burning collagen, 0.2—6%) and SO_2 (e. g. when burning hard coal, 0.1%) were detected. As part of the same method, CO_2 is synthetized into methane, where we checked the process of synthesis with the mass spectrometer.

The third example is related to the liquefaction of He. On one occasion the helium to be liquefied was said to have got contaminated and our task was to decide whether there was actually Ne in it or not, since Ne freezes during the liquefaction of He and its hard crystals may irreparably spoil the pistons of the compressor. In different samples we detected 0.01—1% neon: the measurement made it possible to save the equipment.

Interdisciplinary research

At the Central Research Institute of Chemistry (KKKI) in Budapest research work has been in progress for a long time in the field of molecular structures. This work is of theoretical as well as of practical value: more can be learned of the nature of materials tested, thus their behaviour in technological processes can be better understood, moreover, under favourable conditions they can be calculated in advance. The measuring technique applied is mainly gas electron diffraction. Nevertheless, several times during the evaporation of samples difficulties occur because the material does not keep its original composition at the high temperature of evaporation and it becomes uncertain on what material the electron beam scatters. This is the problem attempted to solve by the combined electron diffraction —mass spectrometric

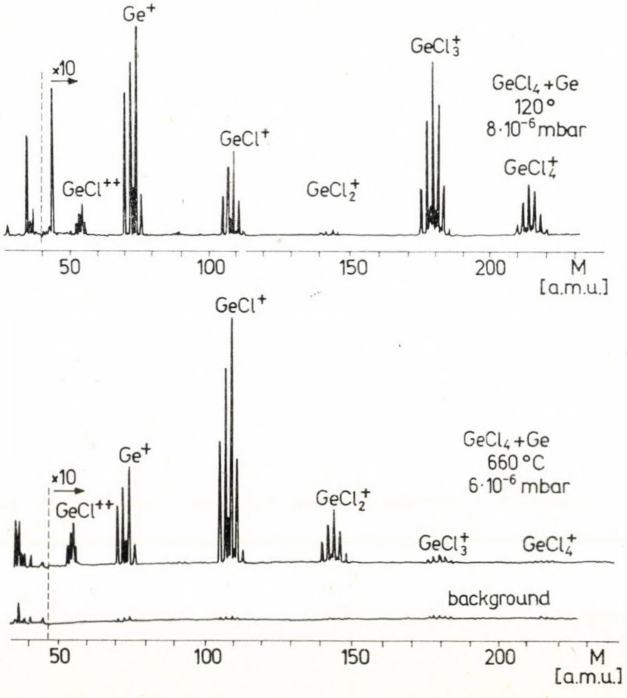

Fig. 2. Evidence of different reactivities of $GeCl_4$ at different temperatures

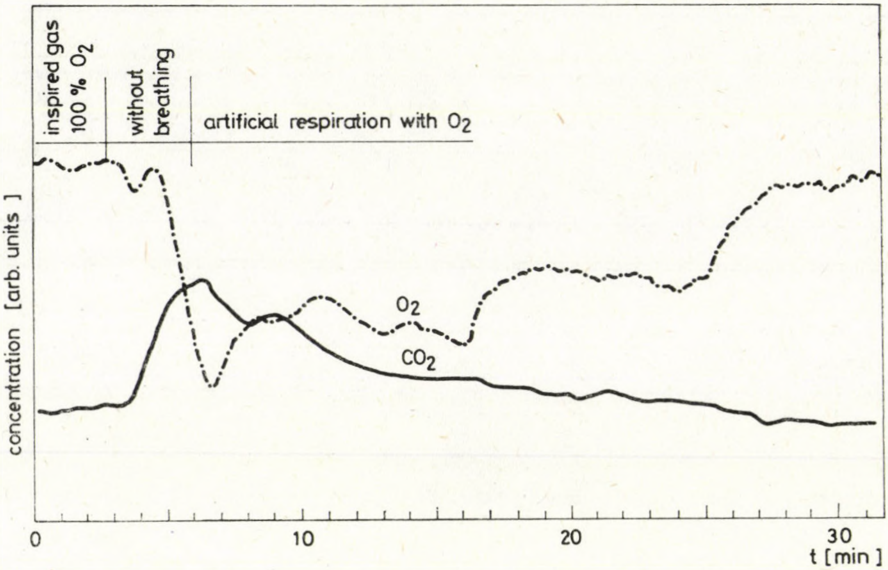

Fig. 3. Concentration changes of O_2 and CO_2 dissolved in the blood of a dog

technique [4]. With the quadrupole mass spectrometer optimal conditions of the sample evaporation and the composition of the evaporated material can be determined. In future experiments simultaneous mass spectrometric and electron diffraction measurements may also be possible. This kind of technique widens the range of application of the gas electron diffraction method to a considerable extent and increases its capacity. Fig. 2 shows how $GeCl_4$ gas, flowing over Ge sample at a high temperature, transforms into $GeCl_2$.

In cooperation with the University Medical School of Debrecen, Department II of Surgery we measured the blood gases of dogs in various experiments. For a more detailed survey on the measuring technique developed by us the reader is referred to our other paper in this issue [5]. As an example Fig. 3 shows simultaneous changes of O_2 and CO_2 dissolved in a dog's blood, when stopping its respiration and when applying artifical respiration.

Application in chemical technology

At the Department of Applied Chemistry of Kossuth Lajos University, Debrecen, research work was carried out into production processes of pesticides containing sulfur and chlorine [6]. Using the results of mass spectrometric analyses of chemical intermediates (Fig. 4), we managed to find the most favourable technological processes.

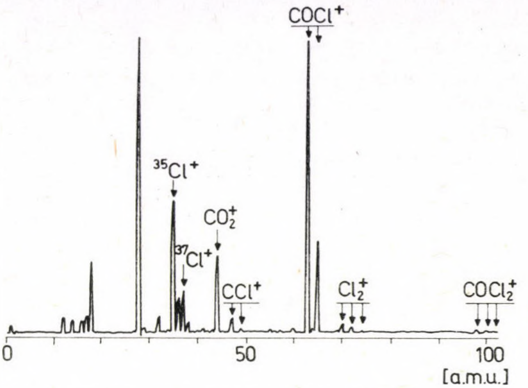

Fig. 4. Mass spectrum of $COCl_2$

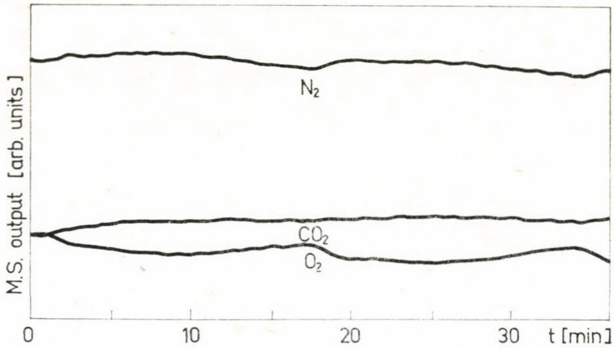

Fig. 5. Concentration changes of N_2, O_2 and CO_2 dissolved in a fermentor

In the production of antibiotics, the productivity of the microorganisms producing antibiotics depends on how sucessfully their essential conditions can be kept optimal. Microorganisms are bred in fermentors, and — beside other parameters — volatile compounds dissolved in the fermentor are also of a decisive importance from the point of view of productivity, or an outgrowth of other important phenomena. That is why the determination of the concentration of dissolved gases may become an important part of the technology. The measuring technique is in fact the same as that one developed for blood gases [5]. Our measurements made in collaboration with the BIOGAL Pharmaceutical Works have proved that the concentration of the two most important components, O_2 and CO_2, can safely be determined with the quadrupole mass spectrometer (Fig. 5). This measuring technique can be realized more easily in factory conditions than other analysers, and it offers a possibility to detect other gas components, which we intend to investigate thoroughly in the near future.

REFERENCES

1. I. Berecz, S. Bohátka, J. Gál and A. Paál, ATOMKI Közl., 19, 123, 1977 (in Hungarian).
2. É. Uray, Á. Félegyházi, J. Országh, I. Berecz, S. Bohátka and G. Langer, Orvos és technika 1977/2, 53 (in Hungarian).
3. É. Csongor, Proc. Intern. Conf. Low Radioactivity Measurements and Applications, pp. 471—474. Bratislava, 1977.
4. S. Boháta, I. Berecz, J. Tremmel and I. Hargittai, Proc. 7th Intern. Vac. Congr. and 3rd Intern. Conf. Solid Surfaces, pp. 193—196, Vienna, 1977.
5. G. Langer, I. Berecz and S. Bohäka, this Conference, p. 312.
6. To be published.

Acta Physica Academiae Scientiarum Hungaricae, ***Tomus 49 (1—3), pp. 293—299 (1980)***

INVESTIGATION OF THE GAS CONTENT OF GLASSES BY MEANS OF THE DYNAMIC EXTRACTION METHOD*

By

A. BRETH and R. DOBROZEMSKY

PHYSICS INSTITUTE, RESEARCH CENTER SEIBERSDORF, SGAE
A-1082 VIENNA, AUSTRIA

For the determination of the gas content of glasses, samples of approximately 50 mg are heated to 1200 °C and the released gases are measured with a quadrupole mass spectrometer. Problems were found to arise due to the evaporation of glass components and their high gettering efficiency. In spite of these problems gas analyses are possible under special conditions. We present a discussion of the measuring procedure and demonstrate two typical samples of gas extraction measurements.

1. Procedure

1. Dynamic extraction method

The amount of gas released from the heated sample is determined by the pressure vs time in a small extraction chamber, evacuated by a well-known and constant pumping speed (Figs. 1 and 2).

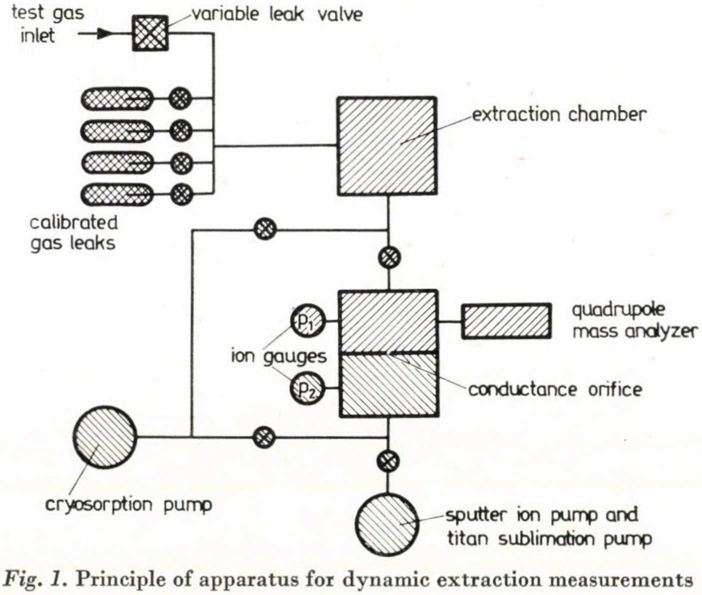

Fig. 1. Principle of apparatus for dynamic extraction measurements

---

* This work has been performed in cooperation with PHILIPS Gloeilampenfabrieken, Eindhoven, Holland (Divisions "Glastechnik" and "Natlab")

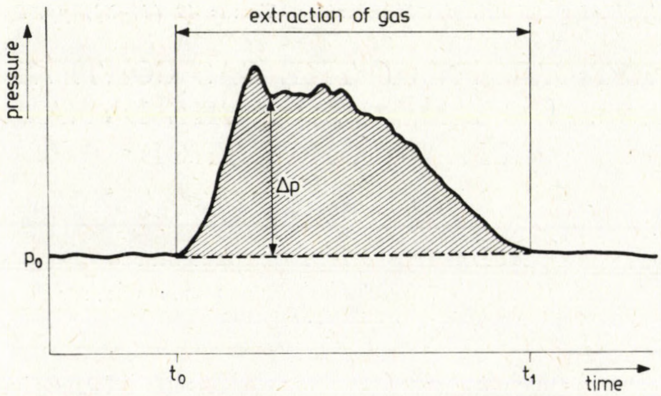

Fig. 2. Typical pressure vs time scan for a gas content measurement with the dynamic extraction method. The amount of gas released is calculated from the coloured area under the curve.

2. *Degassing of samples*

For degassing, a sample is transferred by a manipulator (Fig. 3) from the storage place onto a hot Pt-ribbon (Fig. 4). As the amount of gas released during heating up the ribbon often exceeds that of the sample, it is necessary to degas the ribbon well in advance and to keep it at the measuring tempera-

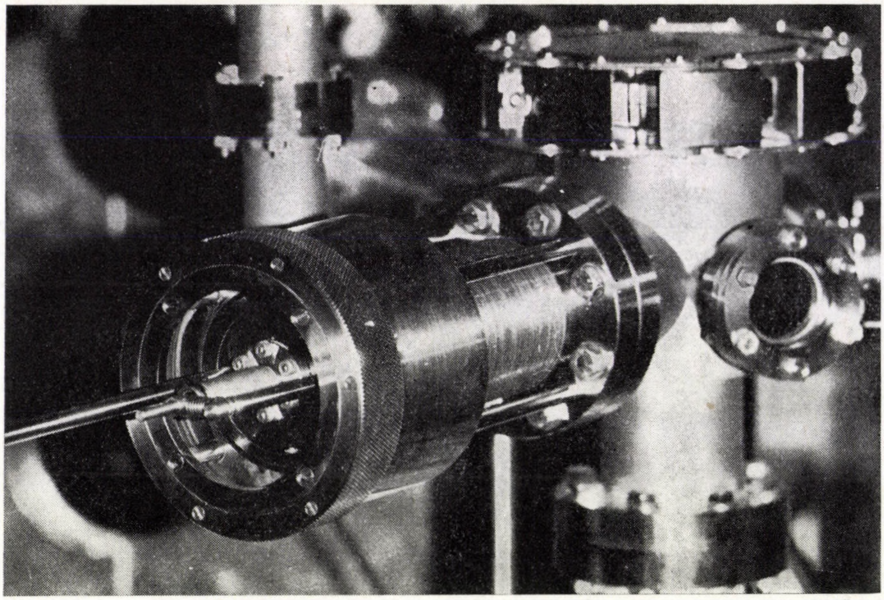

Fig. 3. View of the sample manipulator

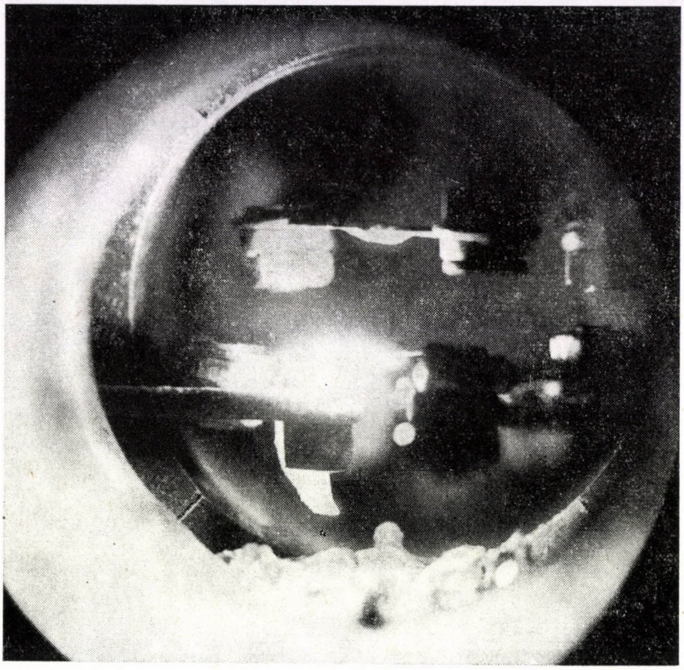

Fig. 4. View into the extraction chamber. A glass sample is just picked up and transferred to the heating filament.

ture until an essentially constant pressure is achieved. With the effective pumping speed applied (1.5 *l*/s for N_2) and with the ribbon at 1150 °C, the basic pressure is about 10^{-6} Torr.

2. Consideration of getter effects

Evaporated sample material, condensed on the wall of the extraction chamber (see Fig. 5), may cause selective pumping for some of the gases released during extraction. This effect is investigated by admitting a calibrated gas mixture. This calibration is not only done before and after extraction, but — in special cases — also during the measurement. Fig. 6 demonstrates the necessity for this procedure. A glass sample is heated by increasing stepwise the temperature of the Pt-ribbon. The influence of the melting and evaporating test material on admitted constant gas flows can clearly be seen.

Degassing glass samples, a considerable getter effect was observed for CO and CO_2. Thus, a large and often floating correction factor has to be applied, causing large errors in the results for these gases. On the other hand, N_2 and CH_4 are not affected by the glass getter and, therefore, can be

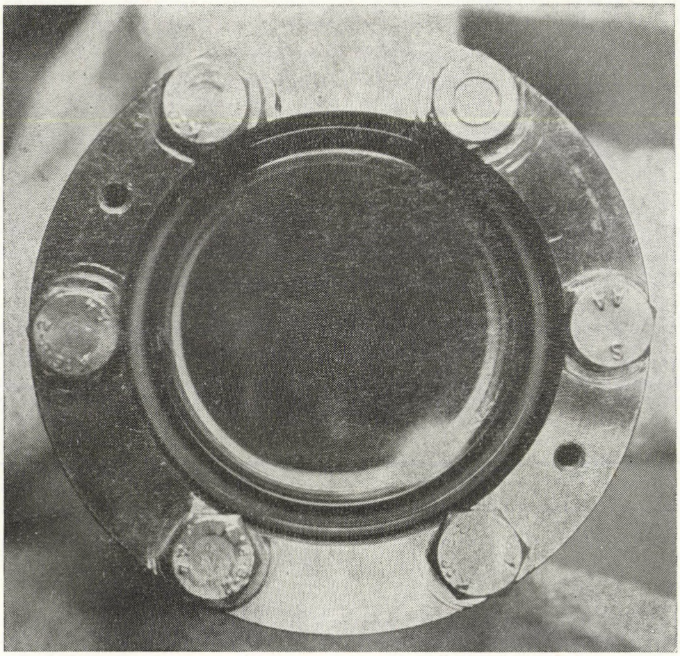

Fig. 5. **Condensate of test material on the viewing port (dendritic needles on the upper half)**

determined with more precision. The gases O_2 and H_2O, also of importance for glass technology, cannot be measured by this method, due to their strong adsorption on the chamber walls.

3. Typical results

The two glass samples discussed here (out of a series of several hundred measurements) had a mass of about 50 mg each. The degassing temperature was 1150 °C.

Gases under consideration:	CH_4, N_2, CO and CO_2
Observed mass numbers:	14, 15, 16, 28 and 44 (quadrupole, with peak multiplexing system).
Degassing time	30 to 60 s.

Sample 1:

Glass no. 576. Many large bubbles during extraction (Fig. 7). Two separated gas bursts are found, one dominated by masses 15 and 16, the other by masses 14 and 28.

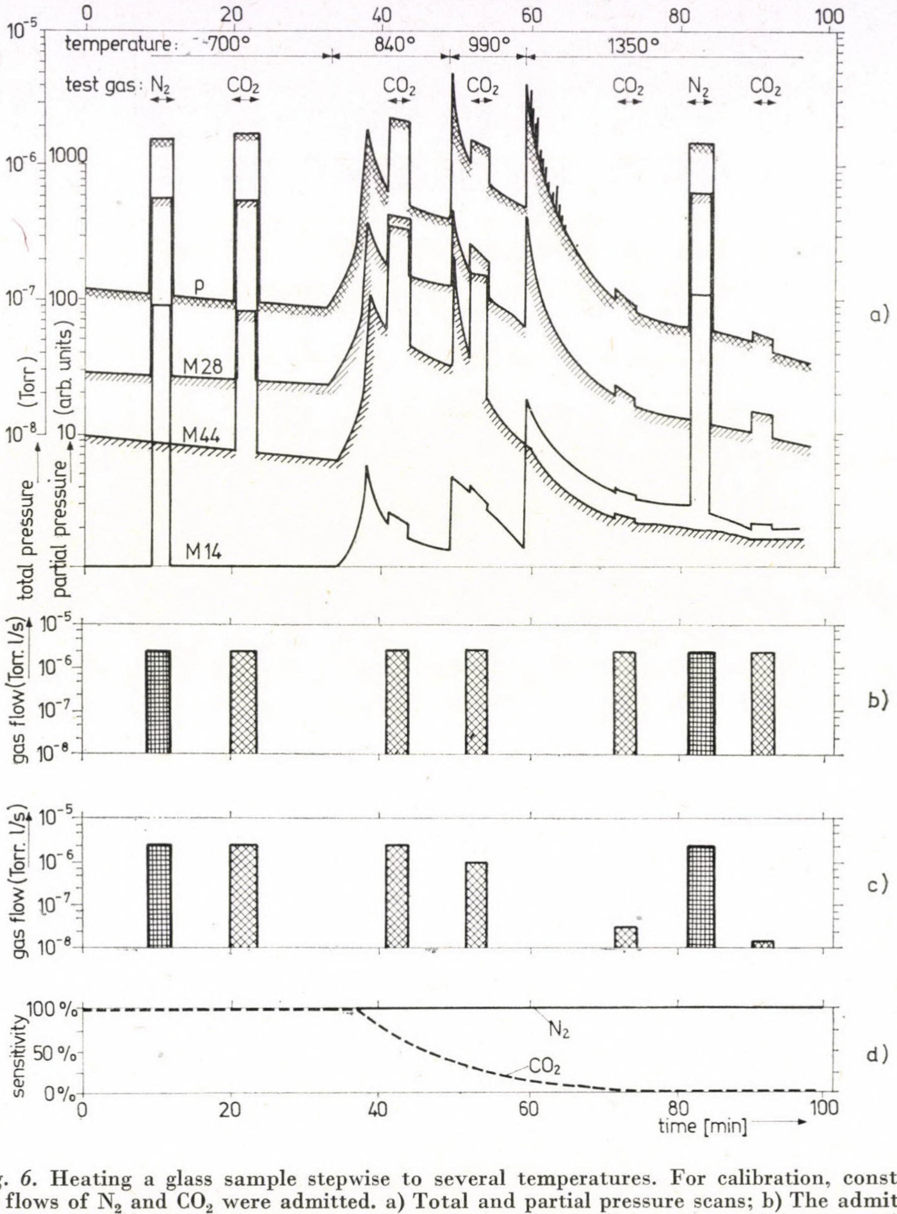

Fig. 6. Heating a glass sample stepwise to several temperatures. For calibration, constant gas flows of N_2 and CO_2 were admitted. a) Total and partial pressure scans; b) The admitted gas flows, as defined by the leak valve; c) The admitted gas flows, measured (no corrections applied); d) Calculated sensitivity for N_2 and CO_2

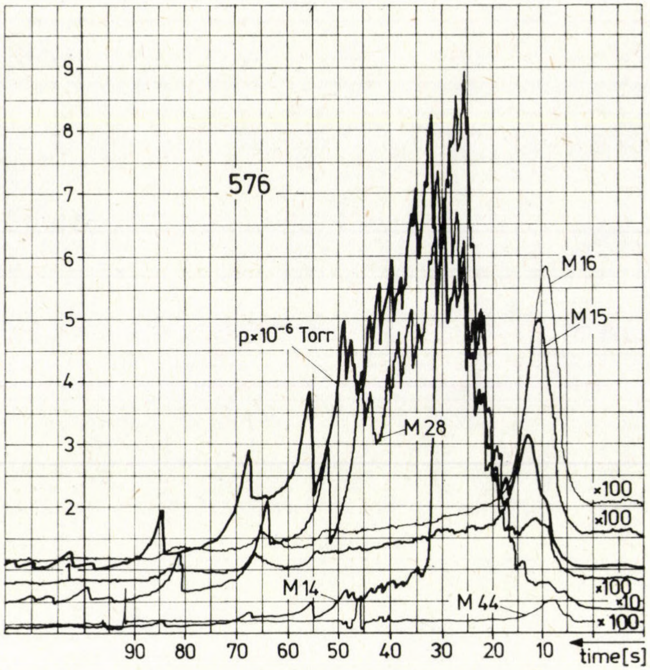

Fig. 7. **Gas extraction from glass no. 576**

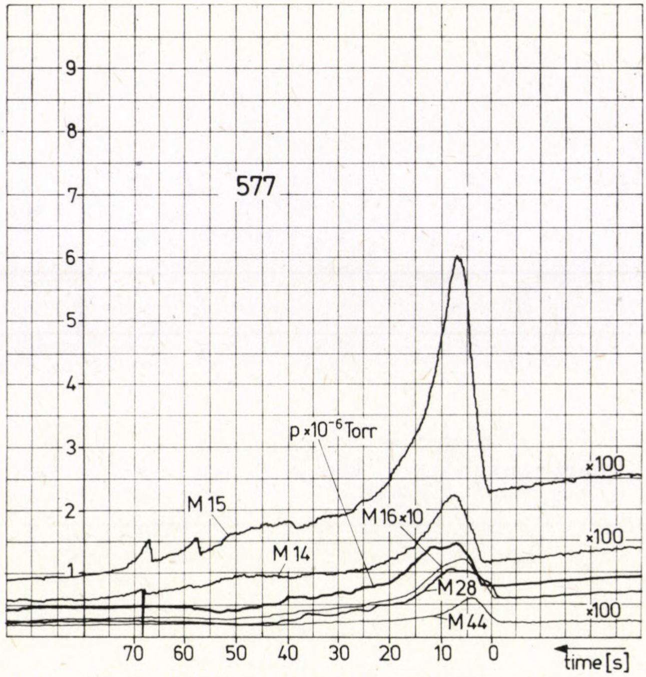

Fig. 8. **Gas extraction from glass no. 577**

Gas content:	7.5×10^{-3}	Torr l/g
Analysis of gases:	CH_4	3.7%
	N_2	91.9%
	CO	4.3%
	CO_2	0.1%

Sample 2:

Glass no. 577. No bubbles during extraction (Fig. 8)

Gas content:	2.6×10^{-3}	Torr l/g
Analysis of gases:	CH_4	7.8%
	N_2	$\leq$ 3.0%
	CO	$\geq$88.8%
	CO_2	0.4%

4. Conclusion

Due to the selective pumping of the oxygen-bearing gases (caused by the getter effect of hot glass samples) this method allows a good determination of even small amounts of N_2, although in the presence of large quantities of CO and CO_2. The amount of CO and CO_2 itself can, however, only be given within an error-range of a factor of 2 or 3.

Acta Physica Academiae Scientiarum Hungaricae, Tomus 49 (1—3), pp. 301—306 (1980)

SOME ASPECTS OF QUANTITATIVE GAS ANALYSIS BY QUADRUPOLE MASS SPECTROMETER

By

R. Dobrozemsky, B. Kraus and A. Breth

PHYSICS INSTITUTE, RESEARCH CENTER SEIBERSDORF, SGAE
A-1082 VIENNA, AUSTRIA

In spite of keeping conditions constant during various measurements, interpretations of gas-analytic mass spectra were often found to be difficult as, apparently, cracking patterns are not constant. This happens e.g. in case of variations of pressure during the measurement. Some possible effects (charge transfer processes in the high-pressure range, contributions from surface ions in the low-pressure range) have been studied and are discussed in the presentation.

1. Introduction

Interpretations of gas-analytic mass spectra are done by means of the cracking patterns. For this purpose, the cracking patterns of the gases to be analysed have to be determined (for the particular instrument used) by admitting pure gases before and after the analysis. Then, the measured spectra can be interpreted by unfolding via the cracking patterns. This has been done in our group for several years by a "least-squares-fit" program [1, 2]. To account for the experimental errors, different weights for the measured peaks as well as for the cracking patterns are used. In these calculations, especially if CO and CO_2 are in the system, often the accuracy obtained was unsatisfactory.

Our program for improving the accuracy of the data evaluation is presently to investigate the cracking patterns for a wide range of pressures, with special emphasis on the following two aspects:

(a) Deviation of cracking patterns at high pressure

Fig. 1 illustrates this effect for several simple cases. This Figure gives the relative abundances of the peaks at the given mass numbers in relation to the sum of all peaks from the respective gas (i. e., in case of N_2, the signal at mass number 14 divided by the sum of the signals at 14 and 28, after subtraction of the respective background signals). The upper limits of the pressure, for deviations of 10% from the values obtained at low pressure, were found to be in the lower 10^{-5} Torr range (for all gases considered here). Note that pure gases have been admitted and only ions of the admitted gases have been investigated. For pratical cases (i. e. mixtures of gases) a different behaviour may be possible.

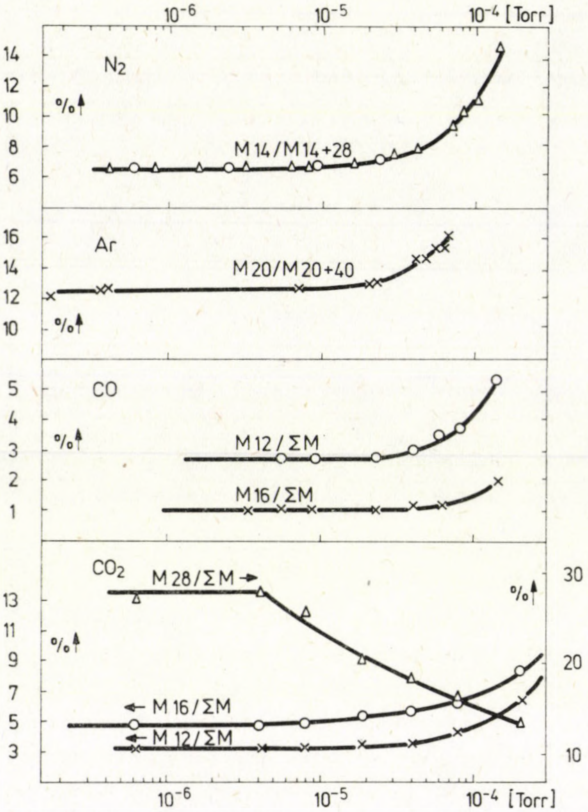

Fig. 1. Variation of cracking patterns with pressure

(b) The "background problem"

Fig. 2 gives pressure-time diagrams for typical cases of gas-analytical measurements. Curve (1), a constant flow of N_2 between marks (a) and (b), is rather simple to interpret (fast response and constant background). Curve (2) is a similar example, but with CO_2 admittance. Apparently, the background changes during this run. In case of a thermal desorption study — Curve (3) — generally a more complex diagram is obtained, and the "end" of the gas flow (b) cannot be determined exactly.

2. Special problems in quantitative gas analysis

Special difficulties arise if large amounts of CO_2 are in the system and if the pressure changes considerably during the measurement. Fig. 3 illustrates this by a simple measurement — the admittance of a pure CO_2-Ar mixture (the small Ar-content is used to check the sensitivity and transmission of the

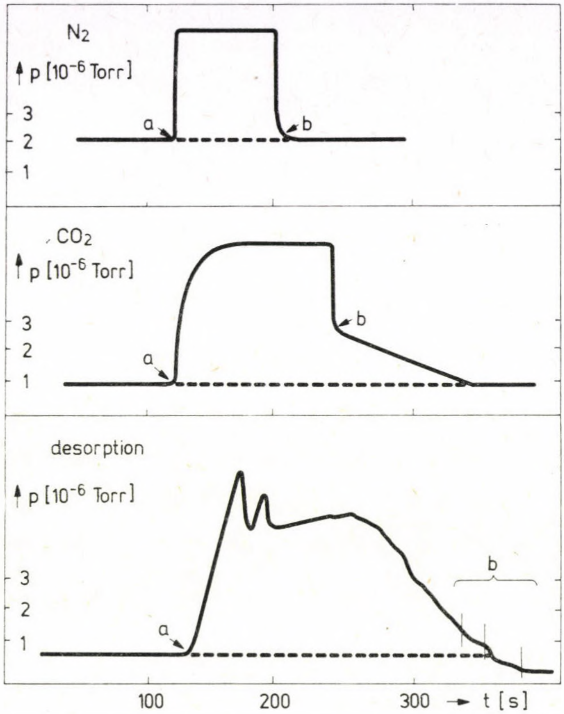

Fig. 2. Typical pressure-time diagrams of gas-analytical measurements (schematically)

mass spectrometer). The cracking patterns in the parts (2) and (13), as well as at point (12) are listed in this Figure — after correction for the respective background peaks at points (1) and (3), (12) and (14), etc. Besides the variations in the high pressure range, according to Section (a) above, there is an essential change in the signal at mass number 28 (CO^+): With the small flow rates at the beginning, the abundances are about 50%. After admitting larger amounts, this value decreases by about a factor of 2. The influence of the variations of the cracking patterns (as mentioned in Sections (a) and (b) above) on the results of gas-analytical measurements is described by the following samples (Table I).

Sample 1 is a synthetic spectrum constructed from the cracking patterns of the gases CH_4, N_2, CO and CO_2 at 5×10^{-7} Torr (25% of each). Consequently, the result of the calculation gives equal amounts with zero error.

Sample 2 is the same synthetic gas mixture, but with signals calculated for a pressure of 5×10^{-5} Torr (according to the deviations given in Fig. 1). Although the spectrum appears quite similar to the observer, the calculation (based on the "calibration" at low pressure) gives a "best fit" with considerable deviations and large errors for N_2 and CO.

Table I

Experimental results

Sample 1										
Mass spectrum	M 14	M 15	M 16	M 28	M 44	Result	CH_4	N_2	CO	CO_2
Peak height (mm)	21.61	48.35	73.76	177.34	54.82	Gas composition (%)	25.0	25.0	25.0	25.0
							±0.0	±0.0	±0.0	±0.0
Sample 2										
Mass spectrum	M 14	M 15	M 16	M 28	M 44	Result	CH_4	N_2	CO	CO_2
Peak height (mm)	27.50	48.35	87.94	155.08	54.82	Gas composition (%)	27.2	41.4	5.3	26.5
							±2.2	±17.1	±15.6	±0.7
Sample 3										
Mass spectrum	M 14	M 15	M 16	M 28	M 44	Result	CH_4	N_2	CO	CO_2
Peak height (mm)	0.40	0.00	7.66	46.99	100.00	Gas composition (%)	0.0	0.0	0.0	100.0
							±0.0	±0.0	±0.0	±0.0
Sample 4										
Mass spectrum	M 14	M 15	M 16	M 28	M 44	Result	CH_4	N_2	CO	CO_2
Peak height (mm)	0.40	0.00	7.44	24.80	100.00	Gas composition (%)	0.2	0.8	−36.5	135.5
							±0.8	±5.0	±4.6	±0.3
Sample 5										
Mass spectrum	M 14	M 15	M 16	M 28	M 44	Result	CH_4	N_2	CO	CO_2
Peak height (mm)	21.61	48.35	73.76	157.74	54.82	Gas composition (%)	26.8	26.9	19.5	26.8
							±0.2	±1.2	±1.1	±0.1
Sample 6										
Mass spectrum	M 14	M 15	M 16	M 28	M 44	Result	CH_4	N_2	CO	CO_2
Peak height (mm)	0.40	3.20	2.60	28.00	6.10	Gas composition (%)	9.6	4.2	63.3	22.9
							±6.2	±43.4	±39.6	±2.7

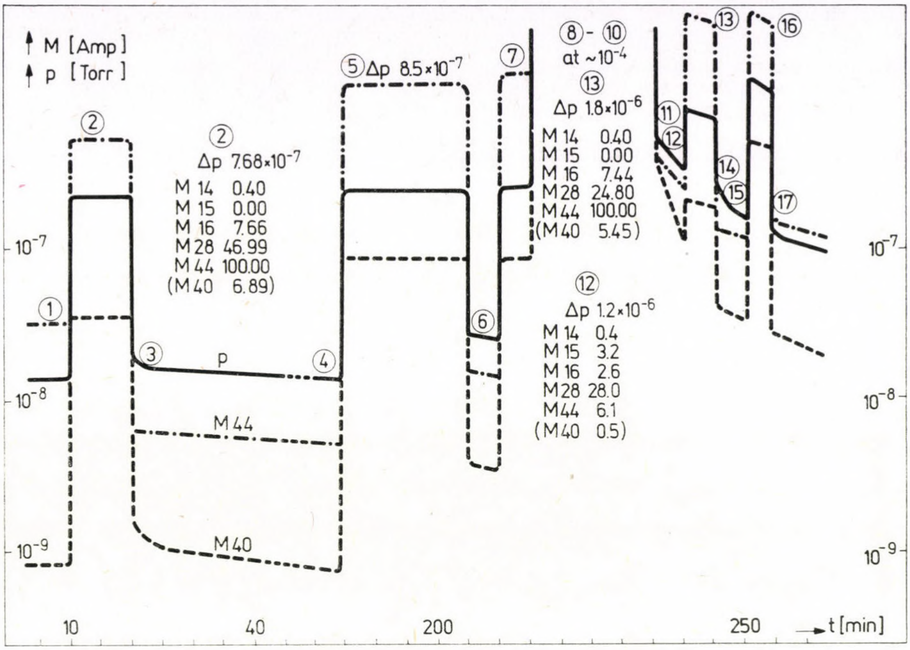

Fig. 3. **Admittance of a CO_2-Ar mixture into a baked uhv-system with 1 *l*/s effective pumping speed. Axial-beam ion source with 90 eV electron energy. The main cracking patterns are listed. From the 40/20 ratio a constant transmission of the spectrometer can be derived**

Sample 3 is the calculation for a pure CO_2-spectrum (data taken from part (2) in Fig. 3) — giving 100% CO_2 with zero error. The following samples illustrate the influence of surface effects:

Sample 4 shows what happens if this "calibration" is used to interpret a spectrum (13) with a 50% lower peak at mass number 28. Although it is the identical gas mixture, the calculation yields an almost senseless result: The error calculated for this "fit" is far too small with respect to the calculated (wrong!) amount of CO. The calculated result — 36% ± 4.6% deviates from the true value (0%) by more than 7 standard deviations.

Sample 5 shows the influence of this effect (50% change in the CO_2-signal at mass number 28) on the synthetic gas mixture of *Sample* 1.

Sample 6 gives the calculated gas content for the measured point (12) in Fig. 3. Again, large deviations from the true gas compositions are found.

3. Conclusion

Small deviations of the cracking patterns may cause large errors in the calculated results, especially if gas mixtures with interfering mass numbers are analysed. If the sample to be investigated is available in large quantities, and if the measurement can be repeated several times and in different pressure ranges, there is a chance to take the disturbing effects into consideration. In case of a less favourable situation (e. g. a desorption analysis as in Fig. 2c), special care has to be taken in order to obtain useful and reproducible results, and — generally — only a low precision will be achieved.

REFERENCES

1. R. Dobrozemsky und W. Färber, Vakuumtechnik, **20,** 231, 1971.
2. R. Dobrozemsky, J. Vac. Sci. Technol., **9,** 220, 1972.

Acta Physica Academiae Scientiarum Hungaricae, Tomus 49 (1—3), pp. 307—312 (1980)

DESIGN OF MEDICAL GAS ANALYSERS

By

G. Langer, I. Berecz and S. Bohátka

INSTITUTE OF NUCLEAR RESEARCH OF THE HUNGARIAN ACADEMY OF SCIENCES
ATOMKI, DEBRECEN, HUNGARY

Respiratory and blood gas analysers were constructed in the ATOMKI. The conditions for fast simultaneous determination of different gas components and some vacuum physical aspects of the design are reported. Examples of measurements are also shown, especially the recent analyses of blood gases ("in vivo" measurements) and of gases dissolved in industrial liquids.

The fact that mass spectrometers have become wide-spread has made their utilization possible in medical research as well as in medical diagnostics. The application of mass spectrometers is of major importance in the solution of analytical problems (respiration and blood gases) emerging in medical practice. With measuring methods previously used for this purpose only one component is measurable at a time, and measurements can be accomplished only over longer periods. A mass spectrometer having a suitable gas sampling unit is capable of measuring more than one gas simultaneously and continuously.

The requirements that mass spectrometer systems are to fulfil can be summed up as follows:

a. measuring rapid concentration changes;
b. simple construction; noiseless, automatic operation;
c. stable functioning for long periods.

Respiratory gas analysis

The ATOMKI have developed for the MEDICOR Works a quadrupole mass spectrometric medical gas analyser, meeting the requirements listed above. The equipment consists of three main parts (Fig. 1):

1. sampling unit consisting of a capillary (6), combined valve (7) and rotary pump (11). Auxiliary elements: Pirani gauge (8), pipe line (10);
2. quadrupole mass spectrometer (1) and electronics (3);
3. vacuum system (4; 5; 8; 9; 12; 13).

In the sampling unit (Fig. 2) the pressure of the air exhaled is reduced in two steps. A rotary pump sucks the gas of atmospheric pressure through a 1 m long capillary of 0.3 mm inside diameter. Thus, at the end of the capillary in the combined valve reduced pressure (some mbar) is obtained. In the next step a little part of the sample gas of a few mbar is let through a molecular leak into the high vacuum chamber of the quadrupole mass spectrometer. Gas consumption in this system is $\sim$ 25 cm^3/s.

It depends greatly on the sampling unit how rapid changes in the concentration of the gas sample can be measured with the device. The measuring speed of the system is characterized by the 90% response time. If, during sampling,

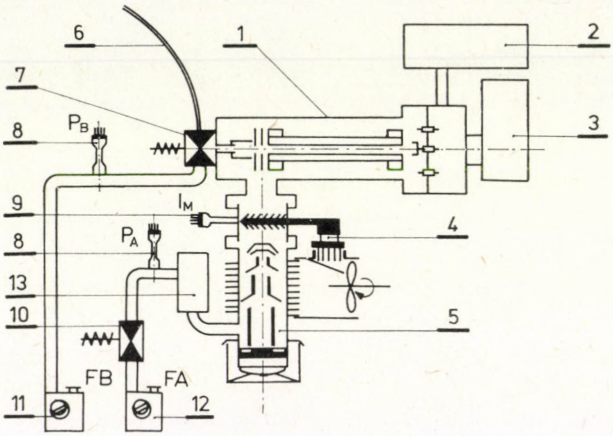

Fig. 1. **Schematic drawing of the respiration mass spectrometer. 1: quadrupole mass spectrometer: 2,3: electronics; 4: thermoelectric baffle: 5: diffusion pump; 6: capillary; 7: combined valve; 8: Pirani gauge; 9: high vacuum gauge; 11,12: rotary pumps; 13: buffer**

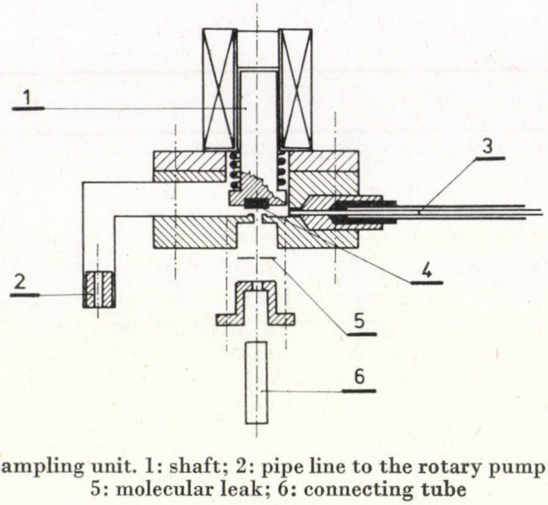

Fig. 2. **Respiration sampling unit. 1: shaft; 2: pipe line to the rotary pump; 3: capillary; 4: seal; 5: molecular leak; 6: connecting tube**

gas doses coming one after the other mix with one another, rapid changes in the gas sample get smoothed. At the first stage of pressure reduction, owing to the dimensions of the capillary and the pressure conditions, the gas flow is laminar, which excludes the possibility of mingling. In the second step, the molecular leak ensures that in the transition between laminar and molecular flow regions the composition of the gas mixture should suffer as slight a change as possible.

The response time of the system is considerably influenced by the dimensions of the dead space of the sampling valve. By reducing that to the minimum and letting the gas flow directly into the ion source, we attained a response time of 50—100 ms. The mass spectrometer we used was the smaller version of our NZ-850 type quadrupole [1], because the 4—50 a.m.u. mass range was fairly enough. With the help of a high capacity space charge ion source we attained a sensitivity of $7 \cdot 10^{-4}$ A/mbar, which made it possible to to use a Faraday cup.

A quadrupole mass pectrometer, in contrast to magnetic spectrometers, cannot measure more gas components simultaneously. Nevertheless, the time of switching in a quadrupole from one mass to another is extremely little (10—100 μs), so a quasi-simultaneous measurement of more than one gas can be easily accomplished. This means that the mass spectrometer, with the help of suitable electronic units, measures the different gas components periodically one after the other in rapid succession. In this way, even changes in 5 different components within 100 ms can surely be traced. This problem is discussed in detail in literature [2]. The mass spectrometer does not decisively influence the response time of the equipment.

In detecting small signals, due to the noise filtering applied in the signal processing unit, the response time of the equipment may be prolonged to a

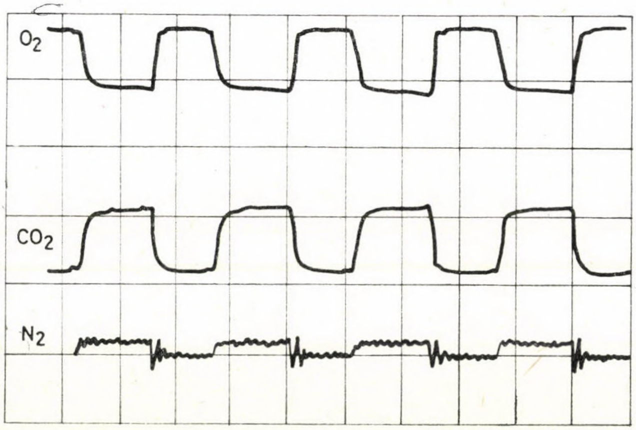

Fig. 3. Respiration curve of a healthy man [3]

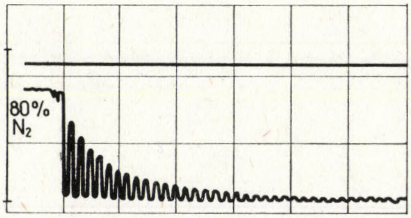

Fig. 4. Nitrogen wash-out curve [3]

considerable extent and may sometimes even exceed that of the sampling unit. The high vacuum necessary for the operation of the quadrupole mass spectrometer is provided by an air-cooled diffusion pump of 150 l/s pumping speed and a thermoelectric baffle. During the analysis the vacuum in the ion source is 10^{-5} mbar, the background is better than 1.10^{-7} mbar. The vacuum system is of all-automatic operation.

The equipment is capable of measuring 5 gases simultaneously with an extremely good — less than 100 msec — response time. The instrument continuously measures O_2, CO_2, N_2 and H_2O and in the 5th channel He, N_2O, N_2 or Ar can be detected alternatively. The signal processing unit of the equipment contains a circuitry capable of correcting changes in intensity resulting, for example, from changes in sensitivity of the ion source or from momentary blockings in the sampling capillary. As a result the equipment retains its calibration for a long time. A respiration curve of a healthy man taken with our respiration mass spectrometer is shown in Fig. 3. Fig. 4 shows wash-out curve of nitrogen.

Measuring blood gases

The wide-spread use of mass spectrometers has also made it possible to work out a measuring technique with the help of which alterations in the partial pressure of any gas dissolved in blood can be continuously tested without taking any blood samples. The block diagram of such a system is shown in Fig. 5. An important part of the equipment is the gas-permeable membrane. It is generally built on a metal tube (catheter) of special shape and placed directly into the blood stream. The dissolved gas molecules diffuse through the membrane in to the catheter. This set up joins the vacuum chamber of the spectrometer by a 1.5—2 m long flexible gas-tight tube in such a way that the gas molecules arriving through the tube should directly get to the ion source of the spectrometer.

The method described above facilitates a continuous, simultaneous and rapid analysis of any gas components dissolved in blood. The only limiting

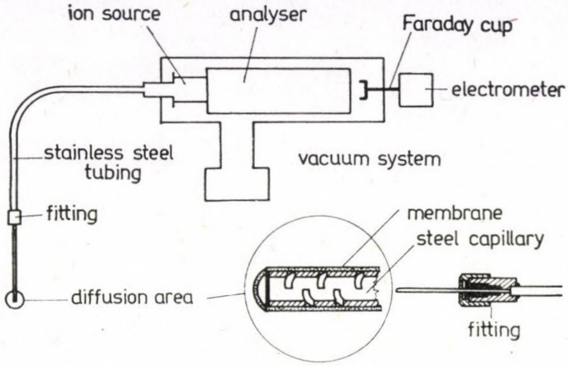

Fig. 5. Schematic drawing of the blood gas analyser

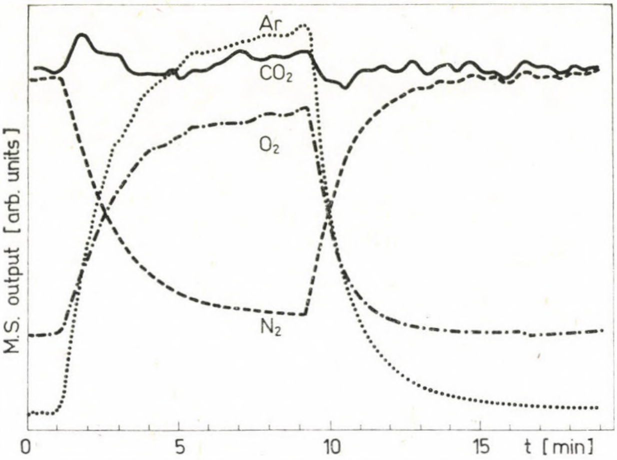

Fig. 6. Partial pressure change of gases dissolved in blood when O_2-Ar mixture is inhaled.

factor is the permeability of the membrane, since continuous sampling from the liquid is maintained by diffusion through the membrane. This diffusion process greatly influences the response time, stability and sensitivity of the measuring system. That is why choosing the material of the membrane properly is a point of importance.

On the basis of our measurements we found teflon and silicon rubber the most suitable for the purpose. Since the membrane is placed directly into the blood stream, it is important that it should be sterilized. Teflon and silicon rubber are also suitable from this point of view. We made the cannula from these two materials. The plastic tubes are pulled over the perforated metal capillary closed at one end. For vacuum sealing between the membrane and the capillary we took advantage of the elasticity of the plastic tubes. The thickness of the membranes used was 0.15 mm. Response time of the equipment for

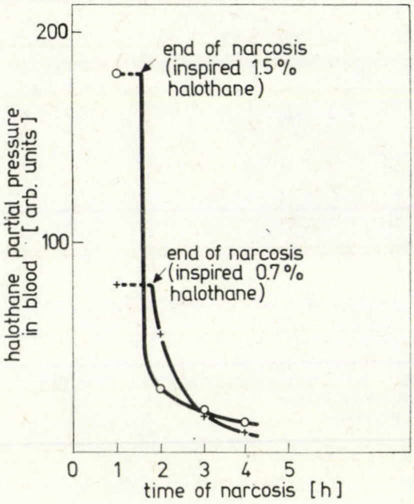

Fig. 7. Halothane depletion in blood after narcosis

silicon rubber was 15 s, for teflon 10 min. The vacuum system and the mass spectrometer are the same as applied for measuring respiration gases. For quantitative measurements we used a gas mixture of a known composition absorbed in a liquid to calibrate our device.

In an "in vivo" experiment with animals we measured the partial pressure changes of blood gases in the case of different gas mixtures inhaled (Fig. 6). Fig. 7 shows the depletion of narcotic gases from the blood, an "in vitro" measurement.

The experiments mentioned above make it clear that, with the help of a mass spectrometer, any gas dissolved in blood can be continuously tested.

REFERENCES

1. I. Berecz, S. Bohátka, J. Gál and A. Paál., ATOMKI Közl., **19**, 123, 1977 (in Hungarian).
2. I. Berecz, S. Bohátka and G. Langer, ATOMKI Közl., **18**, 585, 1976 (in Hungarian)
3. L. Murányi Medicor News **3**, 18, 1978.

Acta Physica Academiae Scientiarum Hungaricae, Tomus 49 (1—3), p. 313 (1980)

APPARENT CROSS SECTIONS FOR ELECTRON IMPACT PRODUCTION OF METASTABLE NOBLE GAS IONS

By

W. HOFER, P. VARGA and H. WINTER

INSTITUTE FOR GENERAL PHYSICS, TECHNICAL UNIVERSITY OF VIENNA, VIENNA, AUSTRIA*

Abstract

Quantitative determination of metastable fractions in noble gas ion beams was achieved via observation of potential electron emission due to slow ion impact on clean polycrystalline tungsten [1].

The ions were produced with an electron impact ion source under single collision conditions. With the knowledge of respective partial ionization cross sections [2] apparent cross sections for the production of singly and doubly charged metastable ions from Ar, Kr and Xe were determined. Results of the present work are compared with data obtained by other methods.

REFERENCES

1. P. VARGA and H. WINTER, Phys. Rev., A **18,** 2453, 1978.
2. K. STEPHAN, H. HELM and T. D. MÄRK, to be published (Ar, Kr);
   J. T. TATE and P. T. SMITH, Phys. Rev., **46,** 773, 1934 (Xe).

---

* Address: Institut für Allgemeine Physik der Technischen Universität Wien, 1040 Wien, Österreich

Acta Physica Academiae Scientiarum Hungaricae, Tomus 49 (1—3), p. 315 (1980)

POLARIZATION-FREE MEASUREMENTS OF VUV-RADIATION FROM ELECTRON IMPACT EXCITED ATOMIC PARTICLES

By

R. BLOCHBERGER, E. RILLE and H. WINTER

INSTITUTE FOR GENERAL PHYSICS, TECHNICAL UNIVERSITY OF VIENNA, VIENNA, AUSTRIA*

Abstract

Line radiation between 40 and 130 nm from rare gas ions and hydrogen molecules excited by electron impact was observed with a VUV-monochromator. Experimental errors due to emission of eventually polarized radiation were avoided by use of "double magic" arrangement.

Various emission cross sections were measured in dependence of electron impact energy, and were made absolute by comparison with published data.

With this procedure, at several wave lengths an absolute monochromator calibration could be obtained.

The results are discussed with reference to earlier work in this field.

---

*Address: Institut für Allgemeine Physik der Technischen Universität Wien, 1040 Wien, Österreich

AUTHORS' INDEX

Printed in Hungary

A kiadásért felel az Akadémiai Kiadó igazgatója. Műszaki szerkesztő: Botyánszky Pál
A kézirat a kiadóba érkezett: 1980. V. 16. — A kézirat nyomdába érkezett: 1980. V. 28.
Terjedelem: 28 (A/5) ív, 169 ábra (1 melléklet)

81.8381 Akadémiai Nyomda, Budapest — Felelős vezető: Bernát György

NOTES TO CONTRIBUTORS

I. PAPERS will be considered for publication in Acta Physica Hungarica, only if they have not previously been published or submitted for publication elsewhere. They may be written in English, French, German or Russian.

Papers should be submitted to

Prof. I. Kovács, Editor
Department of Atomic Physics, Technical University
1521 Budapest, Budafoki út 8, Hungary

Papers may be either articles with abstracts or short communications. Both should be as concise as possible, articles in general not exceeding 25 typed pages, short communications 8 typed pages.

II. MANUSCRIPTS

1. Papers should be submitted in three copies.

2. The text of papers must be of high stylistic standard, requiring minor corrections only.

3. Manuscripts should be typed in double spacing on good quality paper, with generous margins.

4. The name of the author(s) and of the institutes where the work was carried out should appear on the first page of the manuscript.

5. Particular care should be taken with mathematical expressions. The following should be clearly distinguished, e.g. by underlining in different colours: special founts (italics, script, bold type, Greek, Gothic, etc.); capital and small letters; subscripts and superscripts, e.g. x^2, x_3; small *l* and 1; zero and capital O; in expressions written by hand: *e* and *l*, *n* and *u*, *v* and *v*, etc.

6. References should be numbered serially and listed at the end of the paper in the following form: J. Ise and W. D. Fretter, Phys. Rev., *76*, 933, 1949.

For books, please give the initials and family name of the author(s), title, name of publisher, place and year of publication, e.g.: J. C. Slater, Quantum Theory of Atomic Structures, I. McGraw-Hill Book Company, Inc., New York, 1960.

References should be given in the text in the following forms: Heisenberg [5] or [5].

7. Captions to illustrations should be listed on a separate sheet, not inserted in the text.

8. As per lst January 1980 the use of SI units has been made compulsory for all publications issued in Hungary. Please note that in papers submitted to Acta Physica after that date all measures should be expressed in SI units.

III. ILLUSTRATIONS AND TABLES

1. Each paper should be accompanied by three sets of illustrations, one of which must be ready for the blockmaker. The other sets attached to the copies of the manuscript may be rough drawings in pencil or photocopies.

2. Illustrations must not be inserted in the text.

3. All illustrations should be identified in blue pencil by the author's name, abbreviated title of the paper and figure number.

4. Tables should be typed on separate pages and have captions describing their content. Clear wording of column heads is advisable. Tables should be numbered in Roman numerals. (I, II, III, etc.).

IV. RETURN OF MATERIAL

Owing to high postage costs, the Editorial Office cannot undertake to return *all* material not accepted for any reason for publication. Of papers to be revised (for not being in conformity with the above Notes or other reasons) only *one* copy will be returned. Material rejected for lack of space or on account of the Referees' opinion will not be returned to authors outside Europe.

Reviews of the Hungarian Academy of Sciences are obtainable at the following addresses:

AUSTRALIA
C.B.D. LIBRARY AND SUBSCRIPTION SERVICE,
Box 4886, G.P.O., *Sydney N.S.W.2001*
COSMOS BOOKSHOP, 145 Ackland Street,
St. Kilda (Melbourne), Victoria 3182

AUSTRIA
GLOBUS, Höchstädtplatz 3, *1200 Wien XX*

BELGIUM
OFFICE INTERNATIONAL DE LIBRAIRIE,
30 Avenue Marnix, *1050 Bruxelles*

LIBRAIRIE DU MONDE ENTIER, 162 Rue du Midi, *1000 Bruxelles*

BULGARIA
HEMUS, Bulvar Ruszki 6, *Sofia*

CANADA
PANNONIA BOOKS, P.O. Box 1017, Postal Station "B", *Toronto, Ontario M5T 2T8*

CHINA
CNPICOR, Periodical Department, P.O. Box 50, *Peking*

CZECHOSLOVAKIA
MAD'ARSKÁ KULTURA, Národní třida 22,
115 66 Praha
PNS DOVOZ TISKU, Vinohradská 46, *Praha 2*
PNS DOVOZ TLAČE, *Bratislava 2*

DENMARK
EJNAR MUNKSGAARD, Norregade 6,
1165 Copenhagen

FINLAND
AKATEEMINEN KIRJAKAUPPA, P.O. Box 128,
SF-00101 Helsinki 10

FRANCE
EUROPERIODIQUES S. A., 31 Avenue de Versailles, *78170 La Celle St.-Cloud*
LIBRAIRIE LAVOISIER, 11 rue Lavoisier,
75008 Paris
OFFICE INTERNATIONAL DE DOCUMENTATION ET LIBRAIRIE, 48 rue Gay-Lussac,
75240 Paris Cedex 05

GERMAN DEMOCRATIC REPUBLIC
HAUS DER UNGARISCHEN KULTUR,
Karl-Liebknecht-Strasse 9, *DDR-102 Berlin*
DEUTSCHE POST ZEITUNGSVERTRIEBSAMT,
Strasse der Pariser Kommüne 3—4, *DDR-104 Berlin*

GERMAN FEDERAL REPUBLIC
KUNST UND WISSEN ERICH BIEBER,
Postfach 46, *7000 Stuttgart 1*

GREAT BRITAIN
BLACKWELL'S PERIODICALS DIVISION,
Hythe Bridge Street, *Oxford OX1 2ET*
BUMPUS, HALDANE AND MAXWELL LTD.,
Cowper Works, *Olney, Bucks MK46 4BN*
COLLET'S HOLDINGS LTD., Denington Estate,
Wellingborough, Northants NN8 2QT
W.M. DAWSON AND SONS LTD., Cannon House,
Folkestone, Kent CT19 5EE
H. K. LEWIS AND CO., 136 Gower Street,
London WC1E 6BS

GREECE
KOSTARAKIS BROTHERS, International Booksellers, 2 Hippokratous Street, *Athens-143*

HOLLAND
MEULENHOFF-BRUNA B.V., Beulingstraat 2,
Amsterdam
MARTINUS NIJHOFF B.V., Lange Voorhout
9—11, *Den Haag*

SWETS SUBSCRIPTION SERVICE,
347b Heereweg, *Lisse*

INDIA
ALLIED PUBLISHING PRIVATE LTD.,
13/14 Asaf Ali Road, *New Delhi 110001*
150 B-6 Mount Road, *Madras 600002*
INTERNATIONAL BOOK HOUSE PVT. LTD.,
Madame Cama Road, *Bombay 400039*
THE STATE TRADING CORPORATION OF INDIA LTD., Books Import Division, Chandralok,
36 Janpath, *New Delhi 110001*

ITALY
EUGENIO CARLUCCI, P.O. Box 252, *70100 Bari*
INTERSCIENTIA, Via Mazzé 28, *10149 Torino*
LIBRERIA COMMISSIONARIA SANSONI,
Via Lamarmora 45, *50121 Firenze*
SANTO VANASIA, Via M. Macchi 58,
20124 Milano
D. E. A., Via Lima 28, *00198 Roma*

JAPAN
KINOKUNIYA BOOK-STORE CO. LTD., 17-7
Shinjuku-ku 3 chome, Shinjuku-ku, *Tokyo 160-91*
MARUZEN COMPANY LTD., Book Department,
P.O. Box 5050 Tokyo International, *Tokyo 100-31*
NAUKA LTD. IMPORT DEPARTMENT, 2-30-19
Minami Ikebukuro, Toshima-ku, *Tokyo 171*

KOREA
CHULPANMUL, *Phenjan*

NORWAY
TANUM-CAMMERMEYER,
Karl Johansgatan 41—43, *1000 Oslo*

POLAND
WĘGIERSKI INSTYTUT KULTURY,
Marszalkowska 80, *Warszawa*
CKP I W ul. Towarowa 28 *00-958 Warsaw*

ROMANIA
D. E. P., *Bucureşti*
ROMLIBRI, Str. Biserica Amzei 7, *Bucureşti*

SOVIET UNION
SOJUZPETCHATI — IMPORT, *Moscow*
and the post offices in each town
MEZHDUNARODNAYA KNIGA, *Moscow G-200*

SPAIN
DIAZ DE SANTOS, Lagasca 95, *Madrid 6*

SWEDEN
ALMQVIST AND WIKSELL, Gamla Brogatan 26,
101 20 Stockholm
GUMPERTS UNIVERSITETSBOKHANDEL AB,
Box 346, *401 25 Göteborg 1*

SWITZERLAND
KARGER LIBRI AG, Petersgraben 31, *4011 Basel*

USA
EBSCO SUBSCRIPTION SERVICES,
P.O. Box 1943, *Birmingham*, Alabama 35201
F. W. FAXON COMPANY, INC.,
15 Southwest Park, *Westwood*, Mass. 02090
THE MOORE-COTTRELL SUBSCRIPTION AGENCIES, *North Cohocton, N. Y. 14868*
READ-MORE PUBLICATIONS, INC.,
140 Cedar Street, *New York, N. Y. 10006*
STECHERT-MACMILLAN, INC.,
7250 Westfield Avenue, *Pennsauken* N. J. 08110

VIETNAM
XUNHASABA, 32, Hai Ba Trung, *Hanoi*

YUGOSLAVIA
JUGOSLAVENSKA KNJIGA, Terazije 27, *Beograd*
FORUM, Vojvode Mišića 1, *21000 Novi Sad*

Acta Phys. Hung. Tom. 49. No. 1—3. Budapest, 16. II. 1981
Index: 26.022
HU-ISSN 0001-6705

ACTA PHYSICA ACADEMIAE SCIENTIARUM HUNGARICAE

TOMUS XLIX FASCICULUS 4

AKADÉMIAI KIADÓ, BUDAPEST
1980

ACTA PHYS. HUNG. APAHAQ 49 (4) 319–438 (1980)

ACTA PHYSICA

ACADEMIAE SCIENTIARUM HUNGARICAE

SZERKESZTI

KOVÁCS ISTVÁN

Az *Acta Physica* angol, német, francia vagy orosz nyelven közöl értekezéseket. Évente két kötetben, kötetenként 4—4 füzetben jelenik meg. Kéziratok a szerkesztőség címére (1521 Budapest XI., Budafoki út 8.) küldendők.

Megrendelhető a belföld számára az Akadémiai Kiadónál (1363 Budapest Pf. 24. Bankszámla 215-11488), a külföld számára pedig a „Kultura" Külkereskedelmi Vállalatnál (1389 Budapest 62, P.O.B. 149. Bankszámla 217-10990) vagy annak külföldi képviseleteinél.

The *Acta Physica* publish paper on physics in English, German, French or Russian, in issues making up two volumes per year. Distributor: "Kultura" Foreign Trading Company (1389 Budapest 62, P. O. Box 149) or its representatives abroad.

Die *Acta Physica* veröffentlichen Abhandlungen aus dem Bereich der Physik in deutscher, englischer, französischer oder russischer Sprache, in Heften, die jährlich zwei Bände bilden.

Bestellbar bei »Kultura« Außenhandelsunternehmen (1389 Budapest 62, Postfach 149) oder seinen Auslandsvertretungen.

Les *Acta Physica* publient des travaux du domaine de la physique en français, anglais, allemand ou russe, en fascicules qui forment deux volumes par an.

On peut s'abonner à l'Entreprise du Commerce Extérieur «Kultura» (1389 Budapest 62, P.O.B. 149) ou chez représentants à l'étranger.

«*Acta Physica*» публикуют трактаты из области физических наук на русском, немецком, английском и французском языках.

«*Acta Physica*» выходят отдельными выпусками, составляющими два тома в год.

Заказы принимает предприятие по внешней торговле «Kultura» (1389 Budapest 62, P.O.B. 149) или его заграничные представительства.

ACTA PHYSICA

ACADEMIAE SCIENTIARUM HUNGARICAE

ADIUVANTIBUS

R. GÁSPÁR, K. NAGY, L. PÁL, A. SZALAY, I. TARJÁN

REDIGIT

I. KOVÁCS

TOMUS XLIX FASCICULUS 4

AKADÉMIAI KIADÓ, BUDAPEST

1980

ACTA PHYS. HUNG.

INDEX

GENERAL PHYSICS

NUCLEAR PHYSICS

ATOMIC AND MOLECULAR PHYSICS

PHYSICS OF CONDENSED MATTER

Acta Physica Academiae Scientiarum Hungaricae, Tomus 49 (4), pp. 319—323 (1980)

TRANSFERABILITY OF POTENTIAL ENERGY CONTRIBUTIONS FROM LOCALIZED MOLECULAR ORBITALS

By

E. KAPUY

QUANTUM THEORY GROUP, INSTITUTE OF PHYSICS, TECHNICAL UNIVERSITY
1521 BUDAPEST, HUNGARY

(Received 10. IV. 1980)

The transferability of effective potential energy contributions from localized molecular orbitals of some 10- and 18-electron systems is investigated. It is found that contributions from localized orbitals of a given type are very sensitive to the environment.

Introduction

One of the most intricate tasks of quantum chemistry is to interpret the empirical rules of chemistry. The transferability of certain molecular properties (bond energies, electric moments, etc.) can be considered as a long established fact. Theoretical justification would promote the rationalization of experimental results. The notion of transferability may be interpreted in several ways. One can investigate directly the localized molecular orbitals (LMO's) of related systems. Transferability would mean that the LMO's of one molecule can be used without alteration as LMO's of other related molecules. Plenty of calculations have shown, however, that the LMO's, even in closely related systems, are not transferable being not strictly localized in the regions they should describe (e.g. inner shells, lone pairs, bonding pairs) but "feel" the entire molecule [1—3, and references therein]. Another way to interpret transferability is through the use of the properties of the individual LMO's. In the latter case contributions from LMO's of the same type but in different environments are compared. In the present paper this interpretation is pursued and the transferability of the potential energy contributions from the individual LMO's are investigated.

Calculations

In a series of papers [2, 3] we have studied the following 10- and 18-electron compounds:

CH_4 CH_3CH_3 CH_3NH_2 CH_3OH

NH_3 NH_2NH_2 NH_2OH

H_2O HOOH

The Hartree—Fock—Roothaan equations had been solved by using large uniform Gaussian basis sets (13s, 7p/4s) contracted to [4s, 2p/2s]. The applied geometries can be found in [2]. The canonical orbitals were transformed into localized ones by using the EDMISTON—RUEDENBERG procedure [4].

The contribution to the nuclear-electron interaction energy from LMO φ_i is defined as follows

$$V_i = \langle \varphi_i | V | \varphi_i \rangle, \tag{1}$$

and in atomic units

$$V = \sum_a Z_a r_a^{-1}, \tag{2}$$

Table I

Values of V_i for localized orbitals

	Core C	Bond CH	—
CH_4	−36.4118	−5.86633	
CH_3CH_3	−38.7356	−7.82896	
CH_3NH_2 (1)	−38.9496	−7.95105	
(2)	—	−8.00461	
CH_3OH (1)	−38.1600	−8.11853	
(2)	—	−8.15473	
Mean value	−38.3142	7.65404	
St. dev. in%	2.89	10.54	
	Core N	Bond NH	Lone p. N
NH_3	−48.9635	−7.12579	− 7.6218
CH_3NH_2	−51.3362	−9.18730	− 9.8652
NH_2NH_2 (1)	−51.4906	−9.31684	−10.5445
(2)	—	−9.34605	—
NH_2OH	−51.6158	−9.47905	−10.1600
Mean value	−50.8515	−8.89101	− 9.4253
St. dev. in%	2.15	9.98	11.11
	Core O	Bond OH	Lone p. O
H_2O	−63.5106	−8.5832	− 9.4800
CH_3OH	−65.9491	−10.7681	−11.7877
NH_2OH	−66.0402	−10.9522	−11.9275
HOH (1)	−66.1243	−11.0876	−12.0598
(2)	—	—	−12.0656
Mean value	−65.4060	−10.3478	−11.4641
St. dev. in%	1.68	9.91	8.70

where Z_a is the atomic number of nucleus a, and r_a is the distance of the electron from nucleus a.

The values of V_i for the systems considered are listed in Table I. The mean values and the standard deviations for LMO's of a given type are also added.

Obviously the values of V_i are not transferable. In fact they tend to minus infinity when the size of the system (i.e. the number of the nuclei) is expanding beyond any limits.

The effect of distant nuclei on an electron in LMO φ_i is, however, partially screened by all the other electrons. Taking into account this screening we define the effective potential energy V_i^{eff} of an electron on LMO φ_i as follows

$$V_i^{\text{eff}} = V_i + \sum_j [2J_{ij} - K_{ij}] , \tag{3}$$

where J_{ij} is the Coulomb and K_{ij} is the exchange interaction energy of electrons on LMO's φ_i and φ_j, respectively.

The values of V_i^{eff}, in atomic units, are given in Table II, together with the mean values and the standard deviations for LMO's of a given type.

Results and discussion

It can be clearly seen from Table I that the transferability of quantities V_i is out of question. As was expected the values of V_i for LMO's of a given type decrease in algebraic sense with the size of the system. The presence of nuclei with larger atomic number in the vicinal group brings about a definite lowering of V_i. Except for the core orbitals the standard deviations are close to 10% or even larger.

Examining the values of V_i^{eff} in Table II we find similar trends. The screening effect of the other electrons increases V_i^{eff}, in algebraic sense, significantly above the corresponding V_i. The absolute values of V_i is much larger than those of V_i^{eff}, particularly for valence shell LMO's. Passing over to 18-electron compounds from the 10-electron ones in the values of V_i^{eff} a significant drop can be observed. (This lowering, however, is relatively smaller than that in the values of the corresponding V_i).

The V_i^{eff} appears to be still senstive to the character of the other heavy atom outside its main region. The larger the atomic number of the latter the lower is the value of the corresopnding V_i^{eff}. The above results show clearly that the other electrons cannot screen completely the effect of the distant nuclei. It is probable that in case of larger systems the screening would prove to be more pronounced particularly for the effect of nuclei far away from the central region of the corresponding φ_i.

Table II

Values of V_i^{eff} for localized orbitals

	Core C	Bond CH	—
CH_4	−27.7567	−1.54554	
CH_3CH_3	−28.6083	−1.88032	
CH_3NH_2 (1)	−28.6133	−1.91675	
(2)	—	−1.92597	
CH_3OH (1)	−28.6250	−1.96866	
(2)	—	−1.97136	
Mean value	−28.4008	−1.86810	
St. dev. in%	1.31	7.90	
	Core N	Bond NH	Lone p. N
NH_3	−38.4438	−1.99087	−2.03212
CH_3NH_2	−39.4822	−2.36935	−2.47525
NH_2NH_2 (1)	−39.5024	−2.40895	−2.53950
(2)	—	−2.41823	—
NH_2OH	−39.5656	−2.45044	−2.59000
Mean value	−39.2485	−2.32757	−2.40922
St. dev. in%	1.19	7.32	9.19
	Core O	Bond OH	Lone p. O
H_2O	−50.9617	−2.55696	−2.82469
CH_3OH	−52.1615	−2.99560	−3.29047
NH_2OH	−52.2238	−3.05340	−3.35691
HOOH (1)	−52.3044	−3.13535	−3.43322
(2)	—	—	−3.43630
Mean value	−51.8647	−2.93783	−3.26832
St. dev. in%	1.01	7.67	6.99

Many interesting characteristics of V_i^{eff} manifest themselves in the values listed in Table II. As was expected the magnitude of V_i^{eff} is uniquely related to the character of the heavy atom within its central region. The larger the atomic number of the latter, the lower is the corresponding value of V_i^{eff}. For LMO's connected to the same heavy atom obviously the V_i^{eff} of the core orbital has the lowest value. It is interesting to note, however, that the V_i^{eff} of the lone pair orbital is slightly lower than that of the bonding orbital in each case.

Due to the incomplete screening effect the transferability properties of the V_i^{eff} are not much better than those of the V_i. The standard deviations are relatively small for the core orbitals but appreciable for the valence shell orbitals and in case of the N lone pair orbital it exceeds 9%. Had we excluded all the 10-electron systems from the statistics we would have obtained standard deviations which are smaller by almost an order of magnitude. It means that the degree of transferability depends strongly on the size of the systems considered. LMO's of systems of similar size are transferable to a good approximation. This "size dependence" of the transferability of potential energy contributions is likely to decrease if we consider only larger systems.

The above findings differ considerably from those obtained for other properties. Investigating the kinetic energy contributions from LMO's of the same compounds we found that the standard deviations for core orbitals are always less than 0.1%, and for valence shell orbitals are always less than 2%. The study of the interaction energies (including exchange) has shown that the corresponding standard deviations never exceed the value of 4% [2]. For the first electric moments the standard deviations were always less than 2%. Only the case of the second electric moments was different: the standard deviations for the bonding orbitals were less than 4% but for the lone pair orbitals of O it exceeded the value of 10% [3].

It is very improbable that these deviations can be attributed to basis set deficiencies or to the experimental geometries we applied instead of some model ones. They rather indicate that the transferability properties of the individual quantities are not uniform, in the case of V_i^{eff} the effect of the first or even of the second neighbouring centres may be important.

The author gratefully acknowledges the help of Dr. C. KOZMUTZA and ZS. OZORÓCZY in the calculations.

REFERENCES

1. B. O'LEARY, B. J. DUKE and J. E. EILERS, Advan. Quant. Chem. **9**, 1, 1975.
2. E. KAPUY, C. KOZMUTZA, R. DAUDEL and M. E. STEPHENS, Theoret. Chim. Acta (Berl.) **53**, 147, 1975.
3. E. KAPUY, C. KOZMUTZA and R. DAUDEL, Theoret. Chim. Acta (Berl.) **56**, 259, 1980.
4. C. EDMISTON and K. RUEDENBERG, J. Chem. Phys., **43**A, 97, 1965.

Acta Physica Academiae Scientiarum Hungaricae, Tomus 49 (4), pp. 325—339 (1980)

INTERDEPENDENCE OF PROTON AFFINITY, GEOMETRY AND ELECTRON DENSITY CHANGES

By

C. KOZMUTZA and ZS. OZORÓCZY

QUANTUM THEORY GROUP, INSTITUTE OF PHYSICS, TECHNICAL UNIVERSITY
1521 BUDAPEST, HUNGARY

(Received 10. IV. 1980)

Some volume-like quantities derived from electric moments of localized charge distributions have been proposed. It is shown that they suitably characterize the main differences between bond and lone pair orbital densities for several molecules.

The geometry dependence study of the localized moments as well as that of the proton affinity of H_2O resulted in that the changes in the geometry parameters do not influence much these quantities. No close relationships were found, however, between the localized moment characteristics and the proton affinity of the H_2O molecule.

1. Introduction

As the simplest antisymmetric wavefunction of a closed-shell system, a single determinant of one-particle functions, is invariant under any unitary transformation, the transformation can be chosen to obtain localized orbitals. Several advantages of using localized orbitals justify the various attempts which have been made to describe localized molecular orbitals. In spite of the wide use of localization methods, no systematic investigation has yet been carried out on the influence of the geometry. The present paper is a study of the geometry dependence of the localized charge distributions of the molecules H_2O and NH_3 as well as that of the proton affinity of H_2O. The calculations were carried out by the use of basis sets of $(13s7p/4s]$ Gaussians contracted to $[4s2p/2s]$, and performed using the IMBOL-IV programme and the Edmiston—Ruedenberg localization procedure. The necessary one-electron properties were calculated using the POLYATOM-2 programme.

Isodensity contour maps are suitable for visualizing atomic and molecular orbitals [1]. Earlier investigations have shown that there is a significant difference between the contour plots of bond and lone pair localized orbital densities. The electron distribution of a bond pair orbital is elongated far away from the heavy (central atom) nucleus, while a lone pair orbital density is closer to the shperical symmetry. This is apparent from the localized orbitals of H_2O (Figs. 1 and 2): the contour corresponding to a density of 1.0 electron a_0^{-3} for instance, does not appear at all for the bond pair orbital, it is a rather dispersed distribution shared by two centres. From the contour plots it can also

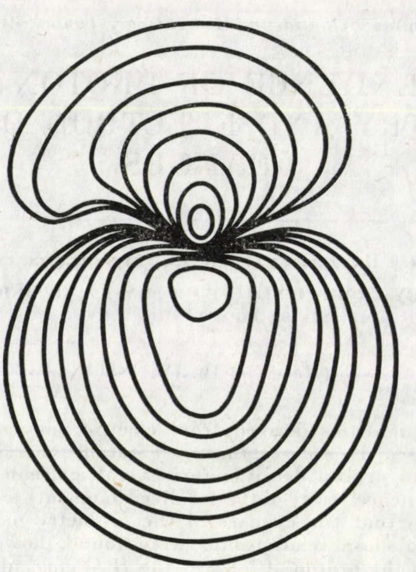

Fig. 1. Isodensity contour map for H_2O bond pair orbitals

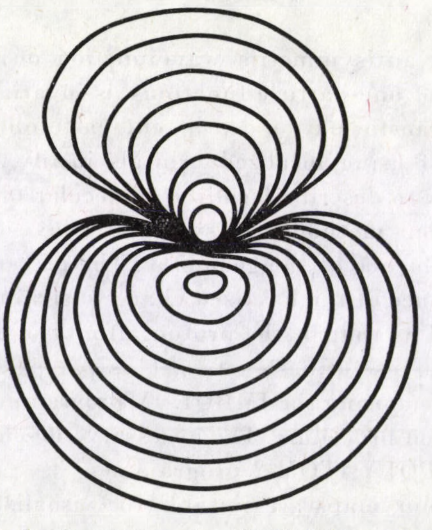

Fig. 2. Isodensity contour map for H_2O lone pair orbitals

be seen that the lone pair localized orbitals are rather distributed around the nucleus of the central atom and any electrophilic reagent from outside could approach "through" the lone pair orbital densities. Thus, it is expected that the lone pair orbitals play a role as nucleophilic reagent in chemical reactions.

A detailed analysis of the interdependence of the proton affinity and the electron density changes has shown that simple relations hold between the various moment characteristics of localized orbitals and the proton affinity. Linear relationships were found if the proton affinity was investigated versus the changes of some moment characteristics (as defined in [2]) of the given localized orbitals. In this paper we discuss whether similar relations hold if the characteristics of only the parent molecule are used: the H_2O molecule was chosen for this study. The interdependence will be investigated at different molecular geometries. We introduce, in addition, new measures for characterizing localized molecular orbital distributions.

2. Characterization of localized molecular orbitals

Before analyzing the interdependence of localized orbital moment characteristics and the geometry variation, the reliability of the characteristics chosen is to be investigated.

Four characteristics will now be studied which have not yet been discussed elsewhere. This is to be emphasized because some localized orbital characteristics have been investigated recently [2]. The quantities discussed here are "volume-like" measures in the sense that all of them characterize the spatial requirement of the given localized orbital distributions: they may be horizontal, vertical or effective spatial quantities. Their definitions are given as follows.

The quantity V_d is simply the ellipsoidal volume derived from the dispersion product, P_d (its definition is given in [2]):

$$V_d = \frac{4\pi}{3} P_d = \frac{4\pi}{3} (q_x \cdot q_y \cdot q_z) . \tag{1}$$

Here q_x, q_y and q_z, respectively are the square roots of the corresponding eigenvalues of the diagonalized second moment tensor for the given localized orbitals. The other ellipsoidal quantity, V_e, can be derived by using the first and second order localized moments:

$$V_e = \frac{2\pi}{3} \cdot (r_c + q_x) \cdot q_y \cdot q_z . \tag{2}$$

Here r_c is the centroid length for the given localized orbital density. The r_{eff} "vertical" quantity, is simply the sum of r_c and q_x:

$$r_{\text{eff}} = r_e + q_x . \tag{3}$$

The quantity V_{eff} corresponds to an effective spatial characteristic of localized orbital distribution: V_{eff} can be calculated by using the effective solid angle

Ω_{eff} (for definition see [2]) and r_{eff}:

$$V_{\mathrm{eff}} = \Omega_{\mathrm{eff}} \cdot r_{\mathrm{eff}} \,. \tag{4}$$

These quantities — if they reflect suitably the main differences between bond and lone pair orbitals for any system — may also be related to chemical reactivity. It is expected that these volume-like quantities may be in a simple relationship with the reactivity of some processes. More precisely it is, e.g. hoped that the quantities introduced here for lone pair orbital densities may be related to the proton affinity of the given system. This interdependence is to be investigated at different molecular geometries. The study of the protonation process for the H_2O molecule was chosen. First it is to be analyzed, whether the volume-like characteristics reflect the differences of bond and lone pair orbital densities in a good approximation.

For this reason we present the results obtained for the molecules HF, H_2O, NH_3 and CH_4, as well as for the atom Ne in Table I. The V_d, V_e, r_{eff} and V_{eff} quantities calculated are given in the Table for bond and lone pair charge distributions. The proton affinities (PA) are also shown: it is apparent that the larger the proton affinity the larger are all quantities determined for bond and lone pair orbital densities. The systematic variation of the characteristics suggests that they are suitable for reflecting the changes in the electron density of the system. It is important, on the other hand, to investigate, whether these quantities are transferable (in the sense as defined in [3]). In order to have a general view on their transferability property the quantities calculated

Table I

Characterization of localized orbitals for some neutral ten-electron systems

		V_d	V_e	r_{eff}	V_{eff}	PA
		a_0^3	a_0^3	a_0	sr · a_0	hartree
Ne	Lone	0.723	0.612	1.107	2.355	−0.0450
HF	Bond	1.337	1.290	1.724	2.040	−0.1693
	Lone	1.057	0.903	1.257	2.647	
H_2O	Bond	1.790	1.790	1.941	2.116	−0.2649
	Lone	1.614	1.385	1.445	4.038	
NH_3	Bond	2.369	2.369	2.175	2.189	−0.3613
	Lone	2.412	2.111	1.663	3.392	
CH_4	Bond	3.298	3.298	2.480	2.315	—

for some eighteen-electron systems are given in Table II. The quantities V_d are not tabulated, as they differ from the quantities P_d only in a constant factor and these latter have been given elsewhere [4]. From the results it can be seen that all quantities proposed here are transferable to a rather good approximation. The vertical requirements r_{eff} seem to be the most transferable quantities while the less transferable are the ellipsoidal volumes, V_e.

Table II

Characterization of localized orbitals for some neutral eighteen-electron systems

		V_e	r_{eff}	V_{eff}
		a_0^3	a_0	sr · a_0
CH bond in	CH_4	3.298	2.481	2.316
	C_2H_6	3.197	2.475	2.248
	CH_3NH_2	3.010	2.467	2.189
	CH_3OH	3.030	2.452	2.164
NH bond in	NH_3	2.369	2.175	2.189
	NH_2NH_2	2.291	2.155	2.135
	CH_3NH_2	2.365	2.173	2.180
	NH_2OH	2.223	2.141	2.100
OH bond in	H_2O	1.790	1.941	2.116
	H_2O_2	1.660	1.896	2.034
	CH_3OH	1.819	1.933	2.145
	NH_2OH	1.717	1.912	2.074
N lone in	H_2O	2.111	1.663	3.392
	H_2O_2	2.066	1.641	3.339
	CH_3OH	2.177	1.669	3.519
	NH_2OH	1.947	1.579	3.038
O lone in	H_2O	1.385	1.445	3.038
	H_2O_2	1.317	1.403	2.787
	CH_3OH	1.471	1.437	3.133
	NH_2OH	1.377	1.417	2.903

The conclusion could be drawn that the localized orbital moment characteristics as defined in (2), (3) and (4) suitably reflect the main differences between bond and lone pair charge densities and thus they are expected to be useful also in other theoretical investigations.

3. The effect of geometry variation on localized orbitals

The wavefunctions for H_2O and NH_3 were computed for a grid of nine different geometries around the respective equilibria (see, e.g. [2]). The geometries considered are given in Table III. For all H_2O and the non-planar NH_3 geometries unambiguous bond and lone pair orbitals were obtained. As a study of the proton affinity was also planned, the H_3O^+ molecule has also been

Table III

Geometries considered for molecules H_2O and NH_3

System	HO Bond length (bohr)	HOH Bond angle (degree)	HN Bond length (bohr)	HNH Bond angle (degree)
1.	1.559	89.52	1.662	91.69
2.	1.559	104.52	1.662	106.69
3.	1.559	119.52	1.662	120.00
4.	1.809	89.52	1.912	91.69
Exp.	1.809	104.52	1.912	106.69
5.	1.809	119.52	1.912	120.00
6.	2.059	89.52	2.162	91.69
7.	2.059	104.52	2.162	106.69
8.	2.059	119.52	2.162	120.00
Calc.	1.845	109.03	1.924	112.52

Table IV

Total energies obtained for molecules H_2O, H_3O^+ and NH_3 (in hartree)

System	H_2O	H_3O^+	NH_3
1.	−75.940040	−76.106694	−56.068979
2.	−75.959233	−76.180834	−56.112438
3.	−75.963412	−76.222290	−56.127419
4.	−75.998943	−76.224214	−56.144804
Exp.	−76.010814	−76.280258	−56.170648
5.	−76.008954	−76.307280	−56.169867
6.	−75.978955	−76.216280	−56.124140
7.	−75.985228	−76.257897	−56.135271
8.	−75.979079	−76.273215	−56.119540
Calc.	−76.012339	−76.312573	−56.173380

investigated at nine different geometries: the parameters were chosen as those used for H_2O. The total energies obtained for the molecules H_2O, H_3O^+ and NH_3, respectively, are given in Table IV (in atomic units). As the H_3O^+ geometry parameters are rather far from the experimental one [5] it is not surprising that the difference of the total energies obtained at the experimental equilibrium of H_2O and the interpolated minimum is the largest: the energy lowering is greater than 0.03 a.u.

4. Geometry dependence of some lower order localized moments

Before a study of the interdependence of the geometry variation, the proton affinity and the spatial moment characteristics, the geometry dependence investigation of the first and second order electric moments of localized orbitals is necessary. This is to be done because the quantities proposed in *E*2 are derived from these lower order localized moments.

The geometry dependence of H_2O and NH_3 localized orbital electric moments has been studied.

We have previously reported isodensity contour maps of the H_2O equilibrium bond and lone pair orbitals employed here (Figs. 1 and 2). Such plots of the lone and bond pair localized orbitals for an extensive series of hydride molecules (at the experimental equilibrium geometries, in a double-zeta basis) have been published as well. Throughout those examples, the spatial distribution of an X—H bond pair (X=C, N, O, F, Ne) is consistently larger elongated from the central nucleus towards the proton, while that of a lone pair is far closer to spherical symmetry of its principal lobe. Further bond pair densities are less "peaked" than those of lone pairs, as shown by the smaller area of the highest density contour (see Figures).

The first and second diagonal second moment elements for the molecules H_2O and NH_3 are given in Table V and Table VI, respectively. The changes in the bond moments are an order of magnitude greater than in the lone pair moments. Bond pair centroids are always found farther from the central nucleus than those of lone pairs. On bond extension, the lone pair distances decrease very slightly, while logically enough those of the bonds increase systematically.

The angles between the various orbital centroid vectors are given in Table VII for H_2O. At the respective minimum, they follow the VSEPR model equilibrium inequalities: bond/bond $<$ bond/lone $<$ lone/lone. But at geometries far from the equilibrium, the order may vary and even reverse. The bond/bond angle of centroids is consistently and significantly larger than the internuclear angle for geometries with smaller than the equilibrium value, and smaller for larger angles. The centroids remain slightly in the interior

Table V

First and second order electric moments calculated for H_2O (in a_0)

System		r_r	q_x	q_y	q_z
1.	Bond	0.890463	0.885147	0.625498	0.625002
	Lone	0.615115	0.832911	0.676193	0.676177
2.	Bond	0.892933	0.866856	0.625382	0.622815
	Lone	0.605212	0.845412	0.674596	0.672146
3.	Bond	0.885246	0.852382	0.628547	0.626652
	Lone	0.592058	0.860035	0.672333	0.668501
4.	Bond	0.979126	0.980290	0.667148	0.666951
	Lone	0.610152	0.833266	0.681046	0.677100
Exp.	Bond	0.977958	0.963384	0.666733	0.665248
	Lone	0.605252	0.839679	0.677397	0.675484
5.	Bond	0.965512	0.950694	0.670218	0.666951
	Lone	0.598190	0.848595	0.673501	0.673500
6.	Bond	1.074004	1.080973	0.704741	0.705541
	Lone	0.607744	0.829627	0.689162	0.678500
7.	Bond	1.070252	1.060044	0.705159	0.705130
	Lone	0.606068	0.830488	0.686793	0.676707
8.	Bond	1.054158	1.054197	0.710104	0.704635
	Lone	0.603246	0.834335	0.682229	0.674624
Calc.	Bond	0.988098	0.973397	0.672892	0.671562
	Lone	0.603616	0.839640	0.839640	0.677312

of the molecule at the experimental and computed equilibrium geometries. The angle between each internuclear axis and the corresponding x' (major dispersion) bond orbital axis is larger than the centroid vector deviations. As these two are consistently larger than the centroid vector—main axis deviation, it is interesting to see, whether they deviate in the same or in the opposite direction. The results have shown, that they are systematically in the opposite senses, to within a few degrees the bond densities are effectively parallel to, if slightly offset inside, the internuclear axes. As the results obtained are very similar to those obtained in [2], the values are not presented here in order not to make the paper too long.

Both bond and lone pair orbitals remain cylindrical, as shown by the q_y and q_z values which differ by less than 1% for all geometries for both mole-

Table VI

First and second order electric moments calculated for NH_3 (in a_0)

System		r_e	q_x	q_y	q_z
1.	Bond	1.043826	0.960777	0.707279	0.693927
	Lone	0.736760	0.918862	0.797285	0.797285
2.	Bond	1.045522	0.936842	0.699764	0.696928
	Lone	0.706881	0.964875	0.775107	0.775107
3.	Bond	1.052115	0.867588	0.714466	0.708146
	Lone	0.234567	1.246542	0.745589	0.745589
4.	Bond	1.151625	1.046315	0.750327	0.737083
	Lone	0.702691	0.947685	0.806288	0.806288
Exp.	Bond	1.147783	1.027597	0.742383	0.741231
	Lone	0.7128882	0.949693	0.778601	0.778601
5.	Bond	1.125248	0.982295	0.759880	0.754941
	Lone	0.380658	1.189440	0.758224	0.758224
6.	Bond	1.263340	1.133573	0.788264	0.775757
	Lone	0.661217	0.977613	0.824391	0.824391
7.	Bond	1.255606	1.119732	0.782391	0.780546
	Lone	0.711251	0.935013	0.788944	0.788944
8.	Bond	1.196128	1.091266	0.804766	0.798783
	Lone	0.477935	1.133765	0.772333	0.772333
Calc.	Bond	1.148473	1.014565	0.748890	0.747669
	Lone	0.602737	1.025648	0.768509	0.768509

cules. For the bond orbitals, bond angle increase results in monotonic decrease in q_x and nearly constant q_y. With bond length increase, both bond q_x and q_y and q_z increase. Lone pair dispersions show regular but much smaller changes, of the order of 2%. The one exception to this is the large increase in q_x for the NH_3 planar geometry (but this geometry can be considered as a rather extreme one).

5. Interdependence of the geometry variation and the proton affinity

It is well known that the gas phase basicity of a system A can be measured by its proton affinity:

$$A + H^+ \rightarrow AH^+.$$

Table VII

Angles calculated between the centroid of charge vectors for H_2O (in degrees)

System	Bond—Bond	Bond—Lone	Lone—Lone
1.	97.029	110.146	117.345
2.	104.174	109.626	113.729
3.	111.199	108.776	110.540
4.	95.823	109.124	121.480
Exp.	103.299	108.778	117.498
5.	110.675	108.078	113.869
6.	94.707	107.725	126.587
7.	102.631	107.602	122.130
8.	110.446	107.706	118.029
Calc.	105.346	108.467	116.963

The proton affinity PA is thus defined as the total energy difference of the protonated and the parent system:

$$PA \leq E(AH^+) - E(A). \tag{5}$$

The energy PA consists of electric and nuclear components (see, e.g. [6]):

$$PA = PA_e + PA_n ; \tag{6}$$

and while the $PA_e < 0$ and $PA_n > 0$ inequalities hold, the sign of the total PA is uncertain. Several calculations as well as experimental studies pointed out that PA is usually negative for neutral systems [5].

A systematic investigation on some ten-electron systems has shown that the first protonation is always exothermic while the multipole ones become endothermic [6].

No work has yet been reported, however, on the geometry dependence of the proton affinity and its components $E1$, $E2$ and E (nuclear). In this Section we give the results obtained for the protonation process investigated for H_2O. The $H_2O \rightarrow H_3O^+$ reaction was studied at nine different geometries.

The one-electron ($E1$) and two-electron ($E2$) components of the corresponding total energies are given in Table VIII. It is interesting to compare the results obtained for H_2O and those for H_3O^+. The changes in the one-electron components of total energy is monotonic increasing with increasing bond angle: the changes are about $0.04-0.07$ hartree by 15.0° for H_2O, but much larger, about $0.07-0.14$ hartree by 15.0° for H_3O^+. This difference could be seen especially at large bond distance (2.059 a.u. see in Table VIII). Similar

Table VIII

Energy components obtained for molecules H_2O and H_3O^+ at different geometries (in hartree)

System	H_2O		H_3O^+	
	*E*1	*E*2	*E*1	*E*2
1.	−125.57703	+38.918525	−132.36780	+39.500199
2.	−125.60337	+38.975573	−132.39967	+39.607638
3.	−125.64363	+39.046018	−132.43901	+39.708571
4.	−123.08127	+37.845172	−128.80525	+38.136495
Exp.	−123.11674	+37.911741	−128.87379	+38.277994
5.	−123.17411	+38.000587	−128.97093	+38.436870
6.	−121.04907	+36.954482	−125.98784	+37.080800
7.	−121.08689	+37.023824	−126.08553	+37.250249
8.	−121.15292	+37.121998	−126.23330	+37.460682

conclusion holds for the two-electron energy components: the variation of *E*2 with the bond angle changes is more sensitive for molecule H_3O^+ than that for H_2O. The greater sensitivity of H_3O^+ to these molecular geometry changes may be caused by different effects. First it is to be emphasized that the geometry parameters chosen (1.809 ± 0.25 a.u. and $104.52 \pm 15.0°$) are not too far from its equilibrium geometry (1.82 a.u. and 117°, see e.g. in [5]). Apart from this, it is expected that the electronic structure of H_3O^+ is more "contracted" than that of the molecule H_2O, therefore more sensitive to any changes in the molecular geometry.

Similar results were obtained for the bond length variation. The sensitivity of bond length of H_3O^+ resulted in the following: the changes in the *E*1 or *E*2 energy components for H_3O^+ are approximately twice as large as those for H_2O. The higher sensitivity of H_3O^+ may be due to its "concentrated" electronic cloud.

The contributions of the proton affinity — which can be derived from the results presented in Table VIII — at different geometries are given in Table IX. The components of *E*1, *E*2 and that of the nuclear energy are tabulated in order to investigate the sensitivity of each contribution to the geometry variation, separately. As to the values of one-electron energy changes, they are slightly increasing with increasing bond angles but they decrease if the bond length becomes larger (in absolute value). Similar results were obtained for the two-electron energy components. The nuclear energy contributions (see the values NP in Table IX) slightly decrease with increasing bond angle and they decrease with increasing bond lengths as well. The values of the sum of $\Delta E2$ and ΔNP for each case are also presented in Table IX. It is especially

Table IX

Contribution of the proton affinity (for $H_2O \rightarrow H_3O^+$) at different geometries (in hartree)

System	$\Delta E1$	$\Delta E2$	ΔNP	$\Delta(E2 + NP)$	Proton affinity PA
1.	−6.79077	+0.58167	+6.04244	+6.62411	−0.1667
2.	−6.79630	+0.63207	+5.94263	+.6.57470	−0.2216
3.	−6.79538	+0.66255	+5.87396	+6.53651	−0.2589
4.	−5.82398	+0.29132	+5.20738	+5.49870	−0.2253
Exp.	−5.75705	+0.36625	+5.12135	+5.48760	−0.2694
5.	−5.79682	+0.43628	+5.06221	+5.49849	−0.2983
6.	−4.93877	+0.12632	+4.57513	+4.70145	−0.2373
7.	−4.99864	+0.22642	+4.49954	+4.72596	−0.2727
8.	−5.08038	+0.33868	+4.44756	+4.78624	−0.2941

interesting that this sum is decreasing with increasing bond angle at small bond length ($R = 1.559$ a.u.). There it is interesting that the sum is increasing at large bond length ($R = 2.059$ a.u.). In addition, an "extremal point" also occurs, at the experimental geometry of H_2O: the value of $\Delta E2 + \Delta NP$ has a minimum if this quantity is investigated versus the variation of bond angle but at bond length fixed. The total proton affinity, however, does show systematic changes with the geometry variations. The *PA* is the larger (the more negative) the greater is the bond angle and/or the bond length. It is interesting, however, that there is seemingly a trend to have the largest *PA* (versus the bond length changes) at the equilibrium geometry (see, e.g. the *PA*'s obtained at geometries denoted by 3, 5 and 8, respectively in Table IX). It is also possible that there is a maximum value i.e. an absolute extremal at the whole potential surface grid near the equilibrium geometry.

This result, on the other hand, should be confirmed by calculations carried out using larger basis sets including also polarization function. This work should be extended to the investigation of other reactions, too. The only protonation process $H_2O \rightarrow H_3O^+$, which has been studied, does not allow to draw to general conclusion.

6. Localized moment characteristics related to the proton affinity

In this Section we return to the investigation of the localized moment characteristics. As has already been pointed out in Section 2, the volume quantities V_d, V_{eff} and V_e do characterize suitably the charge distribution of localized orbitals. It has already been shown as well that the proton affinity could be related to the first and second order electric moments of localized orbitals. Especially, the changes in the localized moments during protonation have been investigated and some regularities found. It was pointed out that the difference between the centroid lengths of bond pair orbitals of the protonated and that of lone pair orbitals of the parent systems is in a close relationship with the proton affinity [7]. Some other quantities have also been studied and similar results were found. It would be interesting to see, whether simple relationships can be found between the proton affinity and the moment characteristics of only the parent molecule. It is expected that if some quantities show these regularities, then they are the volume-like ones as defined in this paper. In order to avoid the influence of the geometry, this investigation is connected with a geometry dependence study as well. This is worth to implement as no systematic investigation has yet been reported whether and how the geometry variation influences the relationships between localized moment characteristics and the proton affinity.

Here some volume-like quantities determined for H_2O are investigated from the point of view of molecular reactivity. First the quantity V_d was studied. The values are given in Table X, in the first column. It is apparent that there is no close relationship between the changes in V_d of lone pair orbitals and the *PA* values at different geometries. Thus these results do not confirm those obtained in [7] for the first order electric moments. Similar conclusions hold for the V_e ellipsoidal volume and the effective bond length r_{eff} for lone pair orbitals: the first quantity is decreasing while the second one is slightly increasing (nearly constant, see points 6, 7 and 8, e.g.) with increasing bond angle at any fixed bond length, while the proton affinity becomes larger (more negative) with increasing bond angles. The quantity V_{eff} calculated for lone pair localized orbitals is changing very slightly with any changes in the molecular geometry, thus it could not be related in a simple way to the changes in the *PA* values either.

The characteristics calculated for bond pair orbitals are also presented in Table X. They are not much expected to play a role in the protonation process. As to their variation with the geometry changes, for the volume-like moment characteristics, the following regularity was found. The quantities V_d, V_e and r_{eff}, respectively do change in a similar way: all of them decrease with increasing bond angles, i.e. they change in the opposite direction to the proton affinities. The changes of these volume-like quantities are parallel to those of the proton affinity if they are investigated versus the variation of the bond length. It is interesting, on the other hand, that the V_{eff} quantities do show extremal values against the systematic changes in the bond angles for the bond pair localized orbitals. No such extrema were found, however, for the proton affinities.

Table X

Interdependence of some localized orbital characteristics and the proton affinity (for $H_2O \rightarrow H_3O^+$)

System		V_d	V_e	r_{eff}	V_{eff}	PA
		a_0^3	a_0^3	a_0	$sr \cdot a_0$	hartree
1.	Bond	1.449	1.449	1.776	2.026	−0.1667
	Lone	1.595	1.387	1.448	2.976	
2.	Bond	1.414	1.414	1.760	1.994	−0.2216
	Lone	1.606	1.378	1.451	3.022	
3.	Bond	1.407	1.406	1.738	2.011	−0.2589
	Lone	1.619	1.367	1.452	3.084	
4.	Bond	1.827	1.826	1.959	2.137	−0.2253
	Bone	1.610	1.394	1.443	3.008	
Exp.	Bond	1.790	1.790	1.941	2.116	−0.2694
	Lone	1.614	1.385	1.445	3.038	
5.	Bond	1.780	1.780	1.916	2.142	−0.2983
	Lone	1.612	1.375	1.447	3.054	
6.	Bond	2.255	2.247	2.155	2.224	−0.2373
	Lone	1.625	1.408	1.437	3.032	
7.	Bond	2.218	2.218	2.135	2.213	−0.2727
	Lone	1.617	1.398	1.437	3.029	
8.	Bond	2.210	2.210	2.108	2.247	−0.2941
	Lone	1.609	1.386	1.438	3.031	
Calc.	Bond	1.843	1.943	1.961	2.136	−0.2787
	Lone	1.616	1.383	1.443	3.308	

7. Conclusion

It was shown that the volume-like moment characteristics reflect the spatial extension for bond and lone pair localized charge distributions in a good approximation. It has been pointed out, that the geometry does not influence much the energy contributions in the neighbourhood of the equilibrium of nuclei. Some regularities, on the other hand, could be found.

As to the contributions $\Delta E1$, $\Delta E2$ and ΔNP, respectively, of the proton affinity for reaction $H_2O \rightarrow H_3O^+$, they change regularly with the changes of bond angle and/or distances. Only a few extremal values were found. The results confirm that the protonation process cannot be suitably treated without inclusion of polarization functions. The presence of polarization functions is of great importance in most quantum chemical calculations for molecules [8].

The investigation of the interdependence of the localized orbital characteristics proposed in this paper and the proton affinity has shown that the proton affinity of H_2O cannot be uniquely related to the spatial extension quantities of H_2O lone pair charge densities. This means that, unfortunately, there is not much hope to treat chemical reactions by the only study of the parent system. We intend to make further calculations in order to find close relationships between the localized moment characteristics and the proton affinity.

REFERENCES

1. A. C. Wahl, Science, **151,** 961, 1966.
2. E. Kapuy, C. Kozmutza and M. E. Stephens, Theoret. Chim. Acta (Berl.), **43,** 175, 1976.
3. E. Kapuy, C. Kozmutza, R. Daudel and M. E. Stephens, Theoret. Chim. Acta (Berl.), **53,** 147, 1979.
4. E. Kapuy, C. Kozmutza and R. Daudel, Transferability of Some Properties of Localized Molecular Orbitals II. Theoret. Chim. Acta (Berl.) **56,** 259, 1980.
5. A. C. Hopkinson, N. K. Holbrook, K. Yates and I. G. Csizmadia, J. Chem. Physics, **49,** 3596, 1968.
6. R. Daudel, C. Kozmutza and E. Kapuy, Chem. Physics Letters, **36,** 555, 1975.
7. C. Kozmutza, The Interdependence of Proton Affinity and Electron Density Changes, in Progress in Theoretical Organic Chemistry, Vol. 2., Elsevier, Amsterdam, 1977, pp. 537—544.
8. E. Kapuy and F. Török, Quantum Theory of Atoms and Molecules, Akadémiai Kiadó, Budapest, 1975.

Acta Physica Academiae Scientiarum Hungaricae, Tomus 49 (4), pp. 341–350 (1980)

NESTED HILBERT SPACES, COMPLEX CANONICAL TRANSFORMATIONS AND RESONANCES

By

B. GAZDY*

QUANTUM THEORY GROUP, INSTITUTE OF PHYSICS, TECHNICAL UNIVERSITY
1521 BUDAPEST, HUNGARY

(Received 10. IV. 1980 — Revised version 2. VI. 1980)

It has been shown that several techniques, applied to define a finite norm for Gamow states, can be deduced from a generalized description of quantum mechanics. The theory of nested Hilbert spaces realized through some specific complex canonical transformations is used in order to treat decaying states as generalized eigenstates of the Hamiltonian with complex eigenvalues.

1. Introduction

In quantum mechanics the Hilbert space framework is often found too restrictive. The need for extension is felt particularly in problems involving analytic continuation into unphysical sheets where one has to deal with functions that increase at infinity. This happens when we continue the S-matrix to the lower (or upper) half of the second Riemann level and reach a pole there. To this pole there corresponds a solution of purely out (in) going asymptotics (resonance solutions) to the Schrödinger equation which diverges exponentially at infinity. Therefore no eigenvector of the Hamiltonian, not even a state in the Hilbert space corresponds to this complex energy and wavefunction.

In quantum mechanics resonances can be properly described by a series of continuum eigenstates and eigenvalues, and in the vicinity of a narrow resonance the form of the scattering cross-section or of the scattering amplitude is usually given by a Lorentzian shape characterized by its position E and halfwidth Γ. The fact that the complex resonance eigenvalue $E - i1/2\,\Gamma$ contains both of these quantities, as well as that there is only one wavefunction corresponding to it, explains why physicists have not discarded these solutions as wrong ones.

The aim of this paper is to show that several earlier attempts to "regularize" the resonance wavefunctions can be considered as byproducts of a more effective theory of generalized eigenvectors.

---

* This work was completed at the International Centre for Theoretical Physics, Trieste, Italy.

The present work was strongly influenced by the papers of GROSSMANN [1] and WOLFF [2] and by the book of BOHM on rigged Hilbert space theory [3].

Section 2 contains the general mathematical tool of nested Hilbert spaces, the framework in which we are going to work. The possible realizations of nested Hilbert spaces by a set of complex canonical transformations are studied in Section 3. In Section 4 we briefly sketch two special transformations. In Section 5 several resonance definitions are given and connections between them are discussed. Finally, Section 6 contains some concluding remarks.

2. Generalized eigenvectors and eigenvalues in nested Hilbert spaces

Definition [1]: Let H_0 and H_1 be infinite dimensional separable Hilbert spaces. An inclusion of H_1 into H_0 is a linear mapping E_{01}, which

(a) is defined for every $f \in H_1$ and is continuous;

(b) has range dense in H_0;

(c) is one-to-one.

The inverse of E_{01} always exists and the adjoint of E_{01}, denoted by E_{10} and defined by

$$(\varphi, E_{01} f)_0 = (E_{10} \varphi, f)_1, \ \varphi \in H_0, \ f \in H_1,$$

is an inclusion of H_0 into H_1.

Definition: A nested Hilbert space (H_0, H_1, E_{01}) is a structure that consists of two Hilbert spaces H_0, H_1, an inclusion E_{01} of H_1 into H_0, and the adjoint inclusion E_{10} of H_0 into H_1.

One can identify every $f \in H_1$, with the linear functional $\varphi \to (f, \varphi)_1$ for all $\varphi \in H_1$, and correspondingly one has to identify $h \in H_0$ with the linear functional $\chi \to (E_{01} E_{10} h, \chi)_0 = (E_{10} h, E_{10} \chi)_1$ for all $\chi \in H_0$.

Consider the following operators

$$e_{10}(A) = E_{10} \, A E_{01} \tag{2.1}$$

and

$$j_{10}(A) = E_{01}^{-1} A E_{01}, \tag{2.2}$$

where A is any linear operator with domain and range contained in H_0. The domain of $e_{10}(A)$ is $E_{01}^{-1} D_A$, where D_A is the domain of A. The domain of $j_{10}(A)$ is the subset of $E_{01}^{-1} D_A$ consisting of vectors which are such that $A E_{01} f \in E_{01} H_1$.

Definition [1]: Let A be an operator in H_0 such that

(a) A is densely defined (the adjoint A^* exists)

(b) $j_{10}(A^*)$ is also densely defined (the adjoint $j_{10}(A^*)^*$ also exists), then the complex number z is said to be a generalized eigenvalue of A if there exists in H_1 a nonzero vector f such that

$$j_{10}(A^*)^* f = zf \,. \tag{2.3}$$

Notice that

$$j_{10}(A^*)^* \supset E_{10} A^{**} E_{10}^{-1} \supset E_{10} A E_{10}^{-1}$$

and if

$$Ag = zg, \; (g \in H_0, \; g \neq 0)$$

it implies

$$j_{10}(A^*)^* f = zf, \text{ with } f = E_{10}\, g \,.$$

States in quantum mechanics

Definition [1]:

(a) An admissible question is defined as an orthogonal projection operator in H_0 which is of the form

$$P = e_{01}(\mathcal{B}) = E_{01}\mathcal{B}E_{10},$$

where $\mathcal{B}$ is a bounded operator in H_1.

(b) A state is defined as an arbitrary nonzero vector in H_1.

(c) A normalizable (or physical) state is a nonzero element of the subset $E_{10}\, H_0 \subset H_1$. To every normalizable state $f = E_{10}\varphi$ $(\varphi \in H_0)$ corresponds to the unit vector $\varphi = ||\varphi||_0^{-1}$ in H_0.

(d) The wavefunction of a state $f \in H_1$ is defined as the linear functional which, to every $\chi \in H_1$ assigns the number $(f, \chi)_1$.

The statistical interpretation is given as follows:

(a) If a system is in the state $f \in H_1$, then the relative probability of a positive answer to the questions $P' = e_{01}(\mathcal{B}')$ and $P'' = e_{01}(\mathcal{B}'')$ is the ratio

$$(f, \mathcal{B}' f)_1 / (f, \mathcal{B}'' f)_1 \,.$$

(b) If the range of P is one-dimensional, and if the positive answer to the question P is observed, then the system is left in the normalizable state $E_{10}PH_0$.

An admissible question P of one-dimensional range is an operator of the form $Pg = (h, g)_0 h$, where $h \in E_{01}H_1$ and $||h||_0 = 1$. By (b), the complete measurement P leaves the system in the state $E_{10}h = E_{10}E_{01}f$, where $f \in H_1$. The wavefunction of this state is $\chi \to (E_{10}E_{01}f, \chi)_1 = (E_{01}f, E_{01}\chi)_0$.

Consider a system in the state of $f \in H_1$. Let $\varphi' \in H_1$ and $\varphi'' \in H_1$ be such that $||E_{01}\varphi'||_0 = ||E_{01}\varphi''||_0 = 1$. Then the relative probability of finding the system in the normalizable states $E_{10}E_{01}\varphi'$ and $E_{10}E_{01}\varphi''$ is the ratio $|(f, \varphi')_1|^2/ /|(f, \varphi'')_1|^2$. If it happens that $f = E_{10}h$, $(||h||_0 = 1)$ is a normalized state, the scalar product $(f, \varphi')_1$ becomes $(f, \varphi')_1 = (E_{10}h, \varphi')_1 = (h, E_{01}\varphi')_0$ in agreement with the usual interpretation.

3. Realization of the nested Hilbert spaces

Let H_0 be the radial part of the Hilbert space of quadratically integrable (and at least twice differentiable) functions defined over the n-dimensional real Euclidean space R^n, i.e.

$$H_0 = H_n^+ = L^2 r^{n-1}(R^+),$$

with the scalar product

$$(f, g)_0 = \int_0^\infty dr\, r^{n-1} f^*(r)\, g(r)\,. \tag{3.1}$$

The Schrödinger representation [4] of the operators $\hat{\mathbf{x}}^2$, $\hat{\mathbf{x}}\hat{\mathbf{p}}$ and $\hat{\mathbf{p}}^2$ is

$$(\hat{\mathbf{x}}^2 f)(r) = r^2 f(r)\,, \tag{3.2a}$$

$$(\hat{\mathbf{x}}\hat{\mathbf{p}}\, f)(r) = -\, ir \frac{d}{dr} f(r)\,, \tag{3.2b}$$

$$(\hat{\mathbf{p}}^2 f)\ (r) = -\left(\frac{d^2}{dr^2} + \frac{n-1}{r}\, \frac{d}{dr} - \frac{l(l+n-2)}{r^2}\right) f(r)\,, \tag{3.2c}$$

where $\hat{\mathbf{x}} = (\hat{x}_j)$, $\check{\mathbf{p}} = (\hat{p}_i)$, $j, i = 1, \ldots, n$, the usual n-dimensional space and momentum operators, respectively. The operators (3.2) are selfadjoint with respect to the scalar product (3.1).

In order to establish a relization for H_1, consider the following complex linear transformations between the quantum mechanical operators $\hat{\mathbf{x}}$ and $\hat{\mathbf{p}}$ [2]:

$$\begin{aligned} \hat{\eta} &= a\hat{\mathbf{x}} + b\hat{\mathbf{p}}\,, \\ \hat{\zeta} &= c\hat{\mathbf{x}} + d\hat{\mathbf{p}}\,, \end{aligned} \tag{3.3a}$$

with the unimodularity condition

$$ad - bc = 1\,, \tag{3.3b}$$

which ensures that (3.3a) is a canonical transformation in the sense that

$$[\hat{\mathbf{x}}, \hat{\mathbf{p}}] = i\,1 \Longleftrightarrow [\hat{\eta}, \hat{\zeta}] = i1\,, \tag{3.3c}$$

where, in general, a, b, c, and d are complex multiples of the unit matrix. Eqs. (3.3a, b) can be written in matrix form

$$Z \equiv \begin{pmatrix} \hat{\eta} \\ \hat{\zeta} \end{pmatrix} = \begin{pmatrix} a & b \\ c & d \end{pmatrix} \begin{pmatrix} \hat{\mathbf{x}} \\ \hat{\mathbf{p}} \end{pmatrix} \equiv MZ_0, \ \det(M) = 1\,,$$

i.e. $M \in SL(2, C)$. The corresponding adjoint operators are given by

$$Z^+ = \begin{pmatrix} \hat{\eta}^+ \\ \hat{\zeta}^+ \end{pmatrix} = M^* Z_0 = M^* M^{-1} Z = CZ\,,$$

where the conjugation matrix

$$C = \begin{pmatrix} u & iv \\ iw & u^* \end{pmatrix}$$

is such that $\det(C) = 1$, $CC^* = 1$, and

$$u = a^*d - b^*c \in C,$$

$$v = 2Im(b^*a), \ w = 2Im(c^*d) \in R$$

with

$$|u|^2 + vw = 1.$$

It can easily be seen that the angular properties, as given by the angular momentum operators, in any of the subspaces, remain invariant under (3.3a) since the unimodularity condition (3.3b) insures that

$$\hat{L}_{jk} = \hat{x}_j \hat{p}_k - \hat{x}_k \hat{p}_j = \hat{\eta}_j \hat{\zeta}_k - \hat{\eta}_k \hat{\zeta}_j\,.$$

Now we want to describe a family of Hilbert spaces $J^+_{nl(a,b,c,d)}$ (the indices a, b, c, d will be suppressed) for which a Schrödinger representation parallel to Eqs. (3.2) can be implemented for the new variables $\hat{\eta}^2$, $\hat{\eta}\hat{\zeta}$, $\hat{\zeta}^2$, namely

$$(\hat{\eta}^2 \tilde{f})(\varrho) = \varrho^2 \tilde{f}(\varrho)\,, \tag{3.4a}$$

$$(\hat{\eta}\zeta \tilde{f})(\varrho) = -i\varrho \frac{d}{d\varrho} \tilde{f}(\varrho), \tag{3.4b}$$

$$(\zeta^2 \tilde{f})(\varrho) = -\left(\frac{d^2}{d\varrho^2} + \frac{n-1}{\varrho}\frac{d}{d\varrho} - \frac{l(l+n-2)}{\varrho^2}\right)\tilde{f}(\varrho) \tag{3.4c}$$

on functions of the complex variable ϱ restricted to the region $C^+ \equiv \{\varrho \in C | \arg(\varrho) \in [-1/2\,\pi, 1/2\,\pi)\}$. In order that the total derivative with respect to a complex variable be well-defined, the functions $\tilde{f} \in J^+_{nl}$ will be analytic functions of ϱ and $\partial\tilde{f}(\varrho)/\partial\varrho^* = 0$. The measure for defining the scalar product in J^+_{nl},

$$(\tilde{f}, \tilde{g})_1 = \int_{C+} d\mu_{nl}(\varrho)\, \tilde{f}^*(\varrho)\, \tilde{g}(\varrho) \tag{3.5}$$

is of the form

$$d\mu_{ul}(\varrho) = \nu_{nl}(\varrho, \varrho^*)\, d\,\mathrm{Re}\, \varrho d\, \mathrm{Im}\, \varrho\,,$$

where the weight function $\nu_{nl}(\varrho, \varrho^*)$ will be found from the hermiticity properties of Eqs. (3.3), (3.4), and from the hermiticity of $\hat{\mathbf{x}}$ and $\hat{\mathbf{p}}$ [2]

$$\nu_{nl}(\varrho, \varrho^*) = \frac{2}{\pi v} \exp\left[\frac{1}{2v}(u\varrho^2 + u^*\varrho^{*2})\right](\varrho\varrho^*)^{1/2\,n}\, K_{\frac{1}{2}n+l-1}(\varrho\varrho^*/v)\,, \tag{3.6}$$

where K is the McDonald function.

Now we can define an inclusion E_{10} of $H_0 = H^+_{nl}$ into $H_1 = J^+_{nl}$ by

$$(E_{10}\tilde{f})(\varrho) \equiv \tilde{f}(\varrho) = \int_0^\infty = dr\, r^{n-1} A_{nl}(\varrho, r) f(r)\,. \tag{3.7a}$$

The adjoint of E_{10} is

$$(E_{10}\tilde{f})(r) \equiv f(r) = \int_{C+} d\mu_{nl}(\varrho)\, A^*_n(\varrho, r)\, \tilde{f}(\varrho)\,, \tag{3.7b}$$

where the transform kernel $A_n(\varrho, r)$ can be explicitly calculated by the requirements that if $\tilde{f}(\varrho)$ is the transform of $f(r)$ then $\varrho^2\tilde{f}(\varrho)$ be the transform of

$$\left[a^2 r^2 + 2iabr\partial_r - b^2\left(\partial_r^2 + \frac{n-1}{r}\partial_r - \frac{l(l+n-2)}{r^2}\right) + niab\right] f(r)\,,$$

since $\hat{\eta}^2 = a^2\hat{\mathbf{x}}^2 + 2ab\hat{\mathbf{x}}\hat{\mathbf{p}} + b^2\hat{\mathbf{p}}^2 - inab$, and similar conditions stem from $\hat{\eta}\hat{\zeta}$ and $\hat{\zeta}^2$ [2]:

$$A_{nl}(\varrho, r) = \frac{1}{b} e^{-i\frac{1}{2}\pi(\frac{1}{2}n+l)} \exp\left[(ar^2 + d\varrho^2)\frac{i}{2b}\right](\varrho r)^{1-\frac{1}{2}n} J_{\frac{1}{2}n+l-1}\left(\frac{\varrho r}{b}\right). \tag{3.8}$$

For our purposes it is sufficient to study the case when $b \to 0$, which implies $v \to 0$, $ad = 1$ and $-1/2 \arg(u) = \arg(a) = \vartheta = \arg(\varrho)$. Taking this limiting procedure we obtain that the integral (3.5) collapses over the line $R^+ e^{i\vartheta}$, i.e.

$$(\tilde{f},\tilde{g})_1=\int_{R+e^{i\vartheta}} d|\varrho||\varrho|^{n-1}\exp\,[-w|\varrho|^2/2]\,\tilde{f}(\varrho)^*\,\tilde{g}\,(\varrho), \tag{3.9}$$

and the kernel $A_n(\varrho, r)$ becomes

$$A_n(\varrho, r) = \varrho^{1-n}\, a^{\frac{1}{2}n-1}\, \delta(r - a^{-1}\,\varrho)\,\exp\,[(ic/2a)\,\varrho^2]\,. \tag{3.10}$$

4. Two one-parameter sub(semi)groups of SL(2,C)

Let us introduce the following notation:

$$\tilde{f}(r) = [U_\tau f](r) = \exp\,[i\tau G(r, d/dr)]\,f(r) = \int_{R+} dr'\,r'^{n-1}\,A_{nl(\tau)}(r, r')\,f(r')\,, \tag{4.1}$$

where τ labels the elements of a one-parameter subgroup (or subsemigroup) of $SL(2, C)$.

Example 1:

$$\tau_1\colon \begin{pmatrix} 1 & 0 \\ c & 1 \end{pmatrix} \Rightarrow U_{\tau_1} = \exp\left[ic\,\frac{1}{2}\,\hat{\mathbf{x}}^2\right] \tag{4.2}$$

with $c = c_r - i\varepsilon$, $\varepsilon \geq 0$. Eq. (4.2) defines a Hilbert space for which

$$(\tilde{f},\tilde{f})_1^1 = \int_0^\infty dr\, r^{n-1}\, e^{-\varepsilon r^2}\, |\tilde{f}(r)|^2\,. \tag{4.3}$$

U_{τ_1} leaves the Hamiltonian of the system invariant for arbitrary potentials.

Example 2:

$$\tau_2\colon \begin{pmatrix} \exp\,(i\vartheta) & 0 \\ 0 & \exp\,(-i\vartheta) \end{pmatrix} \Rightarrow U_{\tau_2} \equiv U(i\vartheta) = \exp\left[\frac{1}{2}\,\vartheta\,(\hat{\mathbf{x}}\hat{\mathbf{p}} + \hat{\mathbf{p}}\hat{\mathbf{x}})\right] \tag{4.4}$$

which is the inverse complex scale opreator, i.e.

$$(U_{\tau_2} f)\,(r) = \exp\left(-\frac{1}{2}\,ni\,\vartheta\right) f(re^{-i\vartheta})\,. \tag{4.4a}$$

Eq. (4.4a) defines a Hilbert space where the scalar product is given by

$$(\tilde{f}, \tilde{g})_1^2 = \int_0^\infty dr\, r^{n-1} \tilde{f}(re^{i\vartheta})^* \, \tilde{g}(re^{i\vartheta}) \,. \tag{4.5}$$

If the potential energy operator $\hat{V}$ is a multiplication by a function $V(z)$ restricted to the positive real axis, and $V(z) \to 0$ as $|z| \to \infty$ in some domain $|\arg(z)| \leq \alpha$, then if $\vartheta < \alpha$, we get

$$U(i\vartheta)\, \hat{H} U^{-1}(i\vartheta) = e^{-2i\vartheta}\, \hat{T} + \hat{V}(re^{i\vartheta}) \,, \tag{4.6}$$

where $\hat{T}$ is the usual kinetic-energy operator. Such a Hamiltonian is said to be dilatation analytic [5].

5. Resonance definitions

1. *Definition*: A complex resonance energy of a system with a given Hamiltonian $\hat{H}$ is given by the following eigenvalue problem in $H_1 = J^+_{nl(\tau_s)}$

$$\hat{H}(i\vartheta)\, \psi_r = \left(E - i\frac{1}{2}\Gamma\right)\psi_r, \quad 2\vartheta > \left|\arg\left(R - i\frac{1}{2}\Gamma\right)\right| , \tag{5.1}$$

where $\hat{H}(i\vartheta)$ is the rotated Hamiltonian.

Since $|\psi_r\rangle$ is a generalized eigenvector of $\hat{H}$ it is also a generalized eigenvector of $e^{-i\hat{H}t}$

$$e^{-i\hat{H}(i\vartheta)t}\, |\psi_r\rangle = e^{-iEt}\, e^{-\frac{1}{2}\Gamma t}\, |\psi_r\rangle \quad \text{for} \quad t > 0. \tag{5.2}$$

The adjoint equation is

$$\hat{H}^+(i\vartheta)\psi_r^+ = \left(E + i\frac{1}{2}\Gamma\right)\psi_r^+, \tag{5.3}$$

where $\hat{H}^+(i\vartheta) = \hat{H}(-i\vartheta)$ and $\psi_r^+ = \psi_r^*(r)$ in co-ordinate-space representation, so we have

$$e^{-i\hat{H}(-i\vartheta)t}\, |\psi_r\rangle^+ = e^{-iEt}\, e^{+\frac{1}{2}\Gamma t}\, |\psi_r\rangle^+ \quad \text{for } t < 0 \,. \tag{5.4}$$

We see from Eqs. (5.2), (5.4) that ψ_r (ψ_r^+) represents a decaying (capturing) state.

2. *Remark* 1: Simon [5] defines the resonance state vector as an element φ of $E_{01}H_1 \subset H_0$ for which $(E_{01}\varphi, \psi_r) \approx 1$.

Remark 2: It is common to define the resonance energy and wavefunction as the eigenvalue and eigensolution of the Schrödinger partial differential equation with purely outgoing-wave boundary conditions. The obtained resonance wavefunctions (Gamow functions) diverge exponentially for $r \to \infty$. Several techniques have been developed to define a finite norm for these functions. There is a common feature in all of these manipulations:

The "norm" is defined as the expectation value of the adjoint antiunitary time-reversal operator in a given state.

Berggren [6] showed that

$$\lim_{\varepsilon \to 0} (\hat{T}\tilde{f}_r, \tilde{f}_r)_1^1 < \infty\,, \tag{5.5}$$

where $\hat{T}$ is the time-reversal operator.

Romo [7] used analytic continuation technique in the complex energy plane which is equivalent to

$$(\hat{T}\tilde{f}_r, \tilde{f}_r)_1^2 < \infty\,, \tag{5.6}$$

as given by Eq. (4.5).

Gyarmati and **Vertse** [8] pointed out that these two methods give the same result, i.e.

$$\lim_{\varepsilon \to 0} (\hat{T}\tilde{f}_r, \tilde{f}_r)_1^1 = (\hat{T}\tilde{f}_r, \tilde{f}_r)_1^2\,.$$

It is very interesting that while $(\tilde{f}_r, \tilde{f}_r)_1^2 < \infty$, at the same time $\lim\limits_{\varepsilon \to 0} (\tilde{f}_r, \tilde{f}_r)_1^1 = \infty$.

6. Concluding remarks

We have shown by applying the nested Hilbert space formalism equipped with suitable realizations, i.e. the complex canonical transformations between two Hilbert spaces, resonances can be treated on equal footing with bound states. The advantage of this theory is that neither the selfadjointness of the Hamiltonian nor the underlying Hilbert space is distorted. The generalized resonance eigenvectors with complex eigenvalues of the essentially selfadjoint Hamiltonian operator defined on an everywhere dense subspace of the Hilert space $H_0 = L^2$ are elements of another Hilbert space with different scalar product.

The family of Hilbert spaces constructed by the help of complex canonical transformation, contains, as special cases, Hilbert spaces implicitly used by several authors before.

Here we note that when **Berggren** [6] extends the space L^2 by adding to it Gamow-state vectors and cumbersome complex continuum vectors, he fails to give the new space the structure of any normed or even scalar product space. This is because the Hilbert space defined by the scalar product (4.3) modified by the limit $\varepsilon \to 0$, does not contain Gamow functions.

Our choice of resonance definition is valid only for analytic potentials, but this is not a drawback, since most of the realistic potentials in physics are continuous or even analytic in some domain connected to the real axis, which is sufficient to include narrow resonances. The familiar square-well potential, however, is not "well-behaved" in the sense of our theory.

Acknowledgement

The author wishes to express his gratitude to the International Centre for Theoretical Physics for hospitality during writing this paper.

REFERENCES

1. A. **Grossmann**, J. Math. Phys., **5**, 1025, 1964.
2. K. B. **Wolff**, J. Math. Phys., **15**, 2102, 1974.
3. A. **Bohm**, The Rigged Hilbert Space and Quantum Mechanics. Springer, Berlin, 1978.
4. P. A. M. **Dirac**, The Principles of Quantum Mechanics, Clarendon Press, Oxford, 1958, 4th ed.
5. B. **Simon**, Ann. Math., **97**, 247, 1973.
6. T. **Berggren**, Nucl. Phys., A**109**, 265, 1968.
7. W. J. **Romo**, Nucl. Phys., A**116**, 617, 1968.
8. B. **Gyarmati** and T. **Vertse**, Nucl. Phys., A**160**, 523, 1971.

Acta Physica Academiae Scientiarum Hungaricae, Tomus 49 (4), pp. 351–360 (1980)

CRITICAL INVESTIGATION OF THE SECONDARY ION EMISSION OF PURE METALS USING THE PSEUDOATOM METHOD

By

J. ANTAL and S. KUGLER

DEPARTMENT OF PHYSICS, INSTITUTE OF PHYSICS, TECHNICAL UNIVERSITY
1521 BUDAPEST, HUNGARY

(Received 10. IV. 1980 — Revised version 10. VII. 1980)

The experimental data of secondary ion emission of 25 pure metals were compared to theoretical results calculated using the one dimensional pseudo-atom model. The ionization probabilities were computed at different input data varying within the published experimental limits. Agreement between theoretical and experimental values of the probability of secondary ion emission was mostly better than an order of magnitude for the metals investigated except for Zn, Ag and Sn.

The theoretical description of secondary ion emission from a target due to an energetic primary ion bombardment is rather difficult a problem. The sputtered particles are mostly neutral, only a very small amount of them being in ionized state. The ionization probability is very sensitive to target composition and surface condition varying in the order of 10^{-2}—10^{-6} range even for pure metals according to the experimental results.

The different theoretical models [1—6] take into account mostly only one possible physical mechanism and they are rather far from any realised experimental environment. Even under these circumstances they mostly give only some guesses for the order of magnitude and very few of them result in a closed expression which can be evaluated using experimental input data to specify the target materials.

The emission of secondary ions may be caused by different possible mechanisms depending on the energies of the secondary particles, target material, surface conditions and bombarding ions. In any case, it is a great challenge, even from the computational point of view, to obtain numerical results varying in four orders of magnitude from input data deviating for the different metals only in one order of magnitude. A second question is whether a theoretical model and the calculated results can be correlated to the experimental ones because of the rather different neglections, assumptions and possible experimental and numerical errors depending on circumstances and the method used.

In view of this very intricate situation we have investigated theoretical results for 25 pure metals calculated by a very simple one-dimensional model using the pseudo atom method [7]. This is a rather crude model of secondary ionic emission of positive ions, but in any case producing a simple formula without any fitting parameter, which is easy to evaluate and which can perhaps approximate the ionization probability in the low energy case.

The method applies the pseudo atom concept proposed by ZIMAN [8] for a moving ion in the bulk together with the screening produced by a many-body interaction of the valence electrons. The pseudoatom notion loses its meaning of course approching the surface region and the following part of the emission process cannot be described in this way. The perturbation in the Fermi sea disappears, however, and this will be approximated in calculating the reflection of the screening as a quasi particle due to the changing potential at the surface. The idea is rather similar to that proposed by JURETSCHKE [9] on the secondary electron emission for the reflection of the exchange hole existing only in the bulk.

Even this model is rather complicated for reliable evaluation using somewhat realistic physical circumstances. So for a first comparison and critical investigation as a further approximation a static step-potential model was used. In this case the reflection coefficient is [10]

$$R^{+}=\left(\frac{1-\beta}{1+\beta}\right)^{2}, \tag{1}$$

where

$$\beta=\frac{2E_i-\Phi}{E_F+2E_i\exp(-\lambda r_0)}, \tag{2}$$

while

$$\lambda=[4\pi e^2 N(E_F)]^{1/2}, \tag{3}$$

$$r_0=\left[\frac{3}{4\pi\varrho}\right]^{1/3}. \tag{4}$$

Here E_i is the ionization energy of the free atom, Φ is the work function, E_F is the Fermi energy, ϱ is the atomic density and $N(E_F)$ is the density of states of electrons at the Fermi level.

Using

$$k_1=\sqrt{2E_i-\Phi} \tag{5}$$

and

$$k_2=\sqrt{E_F+2E_i\exp(-\lambda r_0)} \tag{6}$$

(1) will be in the more usual form:

$$R^{+}=\left|\frac{k_1-k_2}{k_1+k_2}\right|^{2}. \tag{7}$$

One realises that R^+ can be very sensitive to input data because the experimental values of Φ can be found only with an uncertainty of $\pm 10-20\%$ and not every measured value E_F is known or even with a worse accuracy. Regarding the model used the E_F-s were calculated by the free electron theory using the atomic densities and valencies. These values may be significantly different from the actual Fermi levels of the metals investigated.

In Table I the input data collected from literature are shown. For work function three values are given. The most probable one Φ_0 and two factors T_{min} and T_{max} where

Table I

Experimental input data

Metal	Z	Valence [11]	ϱ_{atom} $10^{22}/\text{cm}^3$	E_i eV [11]	E_F, eV		Φ_0 eV	T_{max}	T_{min}
					calc (E_{FV})	meas (E_{FX})		%	
Be	4	2	12.35	9.32	14.35	—	4.45	82[13]	112[14]
Mg	12	2	4.30	7.644	7.10	8.10[12]	3.64[13]	92[13]	104[13]
Al	13	3	6.023	5.984	11.65	12.0[13]	4.27	97[13]	102[13]
Si	14	4	4.994	8.149	12.46	12.5[12]	4.8	83[13]	122[13]
Ti	22	3	5.663	6.83	11.18	6.5[17]	4.14	94[13]	107[15]
V	23	2	7.119	6.74	9.94	—	4.21	97[15]	106[13]
Cr	24	2	8.333	6.76	11.04	7.5[12]	4.54	96[13]	103[13]
Mn	24	2	7.935	7.432	10.69	—	3.97	95[13]	107[13]
Fe	26	2	8.496	7.896	11.19	10.0[12]	4.4	91[13]	109[15]
Co	27	2	9.025	7.86	11.60	9.1[17]	4.7	88[13]	109[15]
Ni	28	2	9.140	7.633	11.74	8.5[12]	4.83	90[13]	111[13]
Cu	29	1	8.467	7.724	7.03	9.0[12]	4.53	88[13]	111[13]
Zn	30	2	6.619	9.391	9.47	10.0[12]	4.29	96[13]	101[13]
Ge	32	4	4.417	7.88	11.48	—	4.88	90[13]	102[14]
Zr	40	4	4.295	6.84	11.26	—	4.0	96[13]	108[15]
Mo	42	3	6.417	7.10	12.16	6.8[12]	4.45	90[15]	107[15]
Pd	46	2	6.795	8.33	9.638	6.5[12]	4.96	93[13]	114[15]
Ag	47	1	5.894	7.574	5.504	7.5[13]	4.28	90[15]	105[16]
Sn	50	4	4.696	7.342	10.19	—	4.4	97[15]	116[16]
Sb	51	5	3.31	8.64	10.99	11	4.33	94[13]	106[13]
Ta	73	3	5.535	7.88	11.02	5.6[12]	4.20	88[13]	113[13]
W	74	2	6.308	7.98	9.17	6.8[12]	4.54	92[13]	113[13]
Pt	78	2	6.625	9.0	9.48	9.5[18]	5.5	84[13]	112[13]
Au	79	3	5.896	9.22	11.49	9.5[12]	4.7	97[13]	115[16]
Pb	82	4	3.297	7.415	9.45	—	4.14	93[12]	103[14]

$$\Phi_{\min} = \Phi_0 T_{\min} ,$$
$$\Phi_{\max} = \Phi_0 T_{\max}$$

are the extreme values of work function found in literature.

In Fig. 1 the typical dependence of k_1 and k_2 is given on Φ and E_F taking

$$\Phi = T\Phi_0 ,$$
$$E_F = TE_{F_0} ; \quad T_{\min} < T < T_{\max} .$$

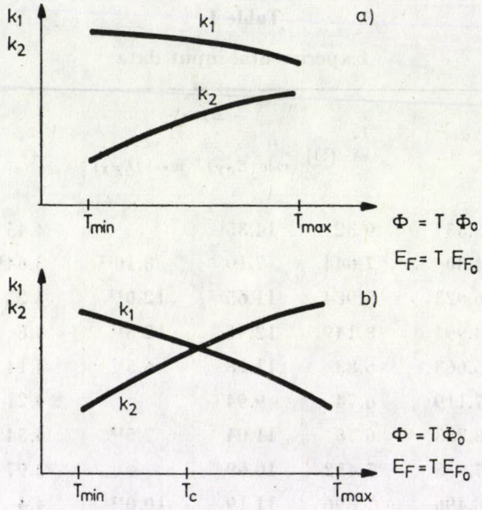

Fig. 1. Typical dependence of the wave vectors on work function and Fermi energy

In the case (a) R^+ varies continuously, between $R^+_{\min}$ and $R^+_{\max}$ depending on the actual value of T while in case (b) there is a T_c resulting in $R^+(T = T_c) = 0$. This possibility is inherently connected to the simple formula (7), providing also results of many orders of magnitude even in case of moderately changing input data. To find the capacities and limits of this simple model one has to investigate not only the actual results for some given, say "optimal" input values, but also the stability of the output against the existing uncertainties in input data.

For comparison sputtering and secondary ion yield were collected from literature for the above metals. Using relative mean values a reference ionization probability list was produced taking for Fe $R^+ = 3 \cdot 10^{-4}$. The data are shown in Table II. One has to note that this compilation of experimentally measured values under rather different experimental conditions provided only

Table II

Experimental data compiled from the literature

Metal	Z	Relative sputtering yield			Relative sputtering ion yield			Ionization probability K^+_{av}			
		S_{av}	S_{min}	S_{max}	K^+	K^+_{min}	K^+_{max}	$\gamma^+_{rel} = \frac{K^+_{av}}{S_{av}}$	γ^+_{min}	γ^+_{max}	$\gamma^+_{abs} \cdot 10^3$
			%			%			%		
Be	4	1.28	35[19]	165[20]	4.44	97[23]	103[20]	3.47	59	294	1.04
Mg	12	0.42	88[21]	107[22]	3.87	97[20]	103[24]	9.21	90	117	2.763
Al	13	0.74	68[21]	128[20]	3015 .	21[20]	249[23]	40.74	16	368	12.23
Si	14	0.45	96[20]	102[29]	1.59	52[23]	224[25]	3.53	51	234	1.059
Ti	22	0.76	32[22]	276[19]	10.25	16[24]	230[23]	13.49	6	729	4.044
V	23	0.59	71[21]	153[20]	9.65	52[20]	188[26]	16.36	34	263	4.908
Cr	24	0.79	47[21]	114[19]	7.06	58[20]	140[25]	8.94	51	298	2.682
Mn	25	1.06	100[20]		2.86	39[20]	160[26]	2.70	39	160	0.807
Fe	26	1	—		1	—		1	—		0.3
Co	27	1.16	88[20]	118[21]	0.6	91[23]	109[20]	0.52	76	123	0.155
Ni	28	1.42	77[20]	119[29]	0.73	64[26]	132[20]	0.51	54	171	0.153
Cu	29	2.91	40[20]	227[19]	0.43	60[23]	140[24]	0.15	27	353	0.045
Zn	30	6	100[21]		0.075	100[23]		0.013	100		0.0039
Ge	32	1.0	100[19]		2.09	92[23]	107[25]	2.09	93	107	0.627
Zr	40	0.57	67[20]	123[21]	2.02	52[25]	145[20]	3.54	43	217	1.062
Mo	42	0.95	64[20]	232[19]	10.04	61[23]	121[25]	10.57	26	189	3.171
Pd	46	2.01	61[19]	120[21]	0.25	88[23]	112[20]	01.2	68	185	0.036
Ag	47	4.26	44[20]	207[19]	0.07	71[24]	127[25]	0.016	35	288	0.0048
Sn	50	2.0	94[21]	106[21]	0.033	100[23]		0.017	94	107	0.0051
Sb	51	4.37	100[21]		0.078	100[23]		0.018	100		0.0054
Ta	73	0.56	61[20]	138[21]	0.46	39[25]	135[20]	0.82	28	222	0.246
W	74	0.8	59[20]	145[21]	1.68	64[23]	136[20]	2.1	44	232	0.63
Pt	78	1.8	44[20]	157[21]	0.32	91[20]	109[25]	0.18	58	249	0.054
Au	79	4.17	27[20]	201[19]	0.018	100[25]		0.0043	50	369	0.0012
Pb	82	5.28	86[21]	114[21]	0.069	100[25]		0.013	88	116	0.0039

a standard reference to facilitate comparison of calculated to measured values. (Unfortunately, we could not find a more reliable compilation of data in literature.)

Calculations were carried out for 25 pure metals using $T_{\min} \leq T \leq T_{\max}$, E_{FV} (calculated) and E_{FX} (experimental, if it was available). The results are shown in Table III and Figs. 2—3. In Table III γ^+ is the reference experimental value (taken from Table II). In the column headed by "Val" the valencies used are given and E signifies the value obtained using E_{FX}. In Figs. 2—3 the vertical

Table III/a

Results of calculations

Metal	$R^+ \cdot 10^3$	$\alpha = R^+/\gamma^+$			T		Val. Exp.	$T_{\min}$	$T_{\max}$
		$T_{\min}$	$T_{\max}$	$T = 1$	$\alpha = 0.1$	$\alpha = 10$			
Be	2.22	0.01	5.93	2.13	0.98	1.2	2	0.82	1.12
Mg	5.37	3.19	1.44	1.94	—	—	2	0.92	1.04
	2.66	1.93	0.61	0.96			E		
Al	16.28	1.12	1.48	1.33	—	—	3	0.97	1.02
	17.88	1.24	1.62	1.46	—	—	E		
Si	2.11	0.08	11.92	1.99	0.89	1.19	4	0.83	1.22
	2.17	0.07	12.07	2.05	0.89	1.18	E		
Ti	4.7	0.60	2.02	1.16	—	—	3	0.94	1.07
	1.17	0.64	0.05	0.29	1.05	—	E		
V	3.17	0.45	1.14	0.65	—	—	2	0.97	1.06
Cr	7.86	2.14	3.60	2.93	—	—	2	0.96	1.03
	0.31	0.01	0.26	0.12	1	—	E		
Mn	1.33	0.61	3.89	1.64	—	—	2	0.95	1.07
Fe	1.45	0.47	12.48	4.84	—	1.06	2	0.91	1.09
	0.295	0.23	5.89	0.98	0.92	—	E		
Co	2.98	2.13	42.37	19.21	—	0.95	2	0.88	1.09
	0.103	3.67	7.99	0.66	0.95 0.98 }	—	E		
Ni	4.88	9.75	69.72	31.92	—	0.9	2	0.9	1.11
	0.123	2.01	11.68	0.81	0.92 0.98 }	1.1	E		
Cu	1.09	90.68	0.50	24.12	—	1.05	1	0.88	1.11
	0.06	15.18	32.43	1.34	0.96 0.98	0.9 1.05 }	E		
Zn	2.76	1003	64.17	707.2	—	1.19	2	0.96	1.01
	1.84	722.3	416.7	4709	1.17	1.15	E		

Table III/b

Results of calculations

Metal	$R^+ \cdot 10^3$	$\alpha = R^+/\gamma^+$			T		Val. Exp.	$T_{\min}$	$T_{\max}$
		$T_{\min}$	$T_{\max}$	$T = 1$	$\alpha = 0.1$	$\alpha = 10$			
Ge	1.54	0.07	3.32	2.45	0.9	—	4	0.9	1.02
Zr	3.67	2.15	6.89	3.56	—	—	4	0.96	1.08
Mo	6.96 0.67	0.81 0.92	3.51 0.01	2.19 0.21	— 1.03	— —	3 E	0.9	1.07
Pd	0.0003 4.37	12.24 195.1	43.1 26.1	0.01 121.4	0.99 1.01 —	0.94 1.07 —	2 E	0.93	1.14
Ag	7.25 1.31	2480 840	1114 514	1510 272	— —	— 1.11	1 E	0.9	1.05
Sn	0.526	35.02	1027	103.1	0.93	0.91 0.95	4	0.97	1.16
Sb	0.300	230.3	0.01	55.51	—	1.03	5	0.94	1.06
Ta	0.424 9.57	0.95 64.27	13.54 18.52	1.72 38.89	0.91 0.95 —	0.88 1.1 —	3 E	0.88	1.13
W	0.060 3.49	1.49 1.008	1.30 1.06	0.1 5.54	1 1.06 —	— 0.92	2 E	0.92	1.13
Pt	0.306 1.32	76.41 122.53	11.87 0.49	5.66 24.53	1.05 1.07 1.12 1.14	0.98 1.14 1.05	2 E	0.84	1.15
Au	0.057 1.88	213.7 2201	940.5 14.27	47.34 1568	1.03 1.17	1.01 1.04 1.15 1.18	3 E	0.97	1.15
Pb	0.024	181.4	4.55	6.18	1.01 1.02	0.995	4	0.93	1.03

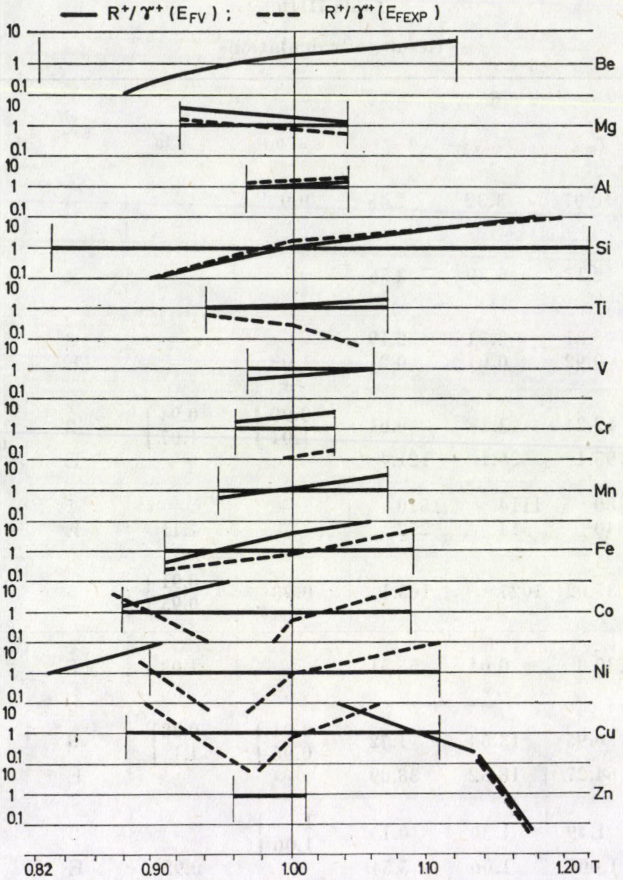

Fig. 2. **Experimental values of the secondary ionic probabilities**

lines give $T_{\min}$ and $T_{\max}$ limits. One observes that in the case of the following 13 metals; Be, Mg, Al, Si, Ti, V, Cr, Mn, Fe, Ge, Zr, Mo, Ta the results are completely stable in the given input range providing a very good agreement with experimental references. The second class of 9 metals: Co, Ni, Cu, Pd, Sb, W, Pt, Au and Pb give reliable agreement between the limits of input range but they have a T_c, too, when $R^+ = 0$, and are rather sensitive to correct input. There are 3 metals: Zn, Ag and Sn which cannot be described by the present model within the given input interval, in any case for Zn we could find only one measured secondary ion yield.

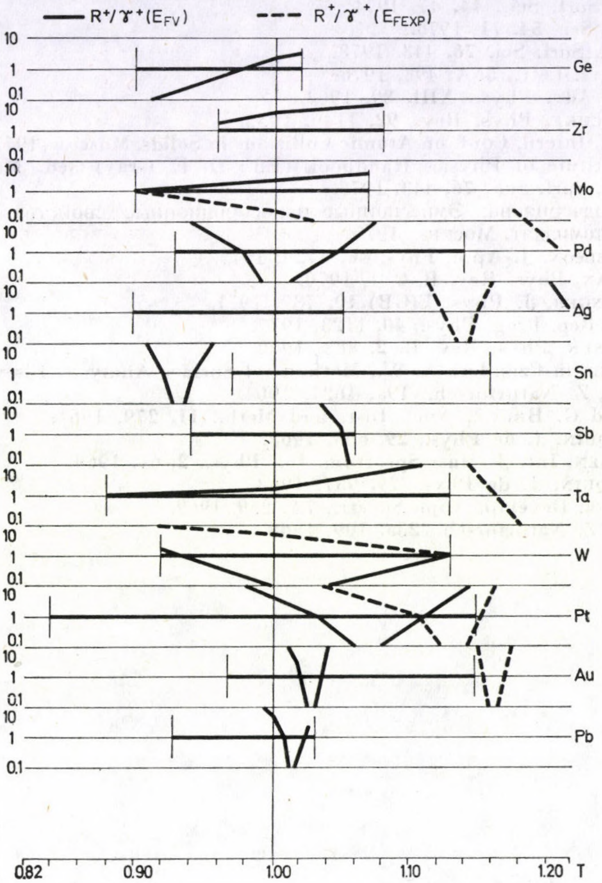

Fig. 3. Experimental values of the secondary ionic probabilities

The authors are completely aware of the very crude approximation of the surface condition using step potential, on the other hand, it seems to be remarkable that no fitting parameter was used in the above calculation. Further results using a more realistic potential will be published in the near future.

Acknowledgement

Our thanks are due to Mr. B. ZSIGMOND for the collection of experimental data from literature.

REFERENCES

1. P. JOYES, Conf. on Ion-Surface Interactions, Garching, 1972, Gordon and Breach, London, p. 139, 1973.
2. G. BLAISE, Conf. on Ion-Surface Interactions, Garching, 1972, Gordon and Breach, London, p. 147, 1973.
3. J. M. SCHROEER, T. N. RHODIN and R. C. BRADLEY, Surf. Sci., **34**, 571, 1973.

4. Z. **Sroubek**, Surf. Sci., **44**, 47, 1974.
5. M. **Cini**, Surf. Sci., **54**, 71, 1976.
6. H. G. **Prival**, Surf. Sci. **76**, 443, 1978.
7. J. **Antal**, Phys. Lett., **55**A, 493, 1976.
8. J. M. **Ziman**, Adv. Phys., **XIII**, 89, 1964.
9. H. J. **Juretschke**, Phys. Rev., **92**, 1140, 1953.
10. J. **Antal**, VII. Intern. Conf. on Atomic Collisions in Solids, Moscow, 1977 (Part II. p. 296).
11. American Institute of Physics Handbook (Ed.: D. E. Gray) 3ed. McGraw-Hill, 1972.
12. H. G. **Prival**, Surf. Sci., **76**, 443, 1978.
13. Фоменко—Подчерняева: Эмиссионные и абсорбционные свойства весчеств и материалов, Атомиздат, Москва, 1975.
14. H. B. **Michaelson**, J. Appl. Phys. **48**, 4729, 1977.
15. D. R. **Eastman**, Phys. Rev. B. **2**, 1, 1970.
16. J. **Barnes-Singer**, J. Phys. E(GB) **10**, 737, 1977.
17. R. C. **Young**, Rep. Prog. Phys., **40**, 1123, 1977.
18. O. K. **Andersen**, Phys. Rev. B. **2**, 883, 1970.
19. G. K. **Wehner**, in Czandera A. W., Methods of Surface Analysis, Elsevier, 1975.
20. H. E. **Beske**, Z. Naturforsch., **19**a, 1627, 1964.
21. O. **Almen** and G. **Bruce**, Nucl. Inst. and Meth., **11**, 279, 1961.
22. J. F. **Hennequin**, J. de Phys., **29**, 655, 1968.
23. C. A. **Andersen**, Int. J. Mass Spectrom. Ion Phys., **2**, 61, 1969.
24. J. F. **Hennequin**, J. de Phys., **29**, 957, 1968.
25. H. W. **Werner**, Develop. Appl. Spectr., **7A**, 239, 1969.
26. J. **Schelten**, Z. Naturforsch., **23**a, 109, 1968.

Acta Physica Academiae Scientiarum Hungaricae, Tomus 49 (4), pp. 361–369 (1980)

A SIMPLE MODEL FOR THE COMPUTATION OF ENERGY ACCOMMODATION COEFFICIENT

By

L. Füstöss

DEPARTMENT OF PHYSICS, INSTITUTE OF PHYSICS, TECHNICAL UNIVERSITY
1521 BUDAPEST, HUNGARY

(Received 10. IV. 1980. — Revised version 25. VIII. 1980)

The energy accommodation coefficient is often substituted by energy ratios defined arbitrarily because of the difficulties presented by the calculations. In order to account for the model developed for the computation of the energy accommodation coefficient this paper proves the necessity of applying the exact definition of this quantity. After a summary of the calculation methods relating the energy accommodation coefficient the model itself is presented with its limits and possibilities. The point of the model is the hard cube approximation with a constant potential characterizing the mean effect of the attractive forces of the surface atoms. To take into account the multiple collisions a simulation procedure is applied.

Introduction

The energy accommodation coefficient is an important quantity for the characterization of the interaction between the solid surface and the gas molecules. This quantity is very senstive to the purity of the surface and indicates the process of adsorption [1]. Formerly the momentum accommodation coefficient was considered as the characteristic of the gas-surface interaction through the formation of cosine distribution or specular reflection [2]. Recently the gas-surface interaction has been described by molecular beam data and the average behaviour of a gas-surface system has been represented by the energy accommodation coefficient [3]. The energy accommodation coefficient, however, is often substituted by energy ratios defined arbitrarily because of the difficulties inherent in the calculations.

In order to account for the model developed for the computation of the energy accommodation coefficient this paper proves the necessity of applying the exact definition of this quantity. After a summary of the calculation methods relating the energy accommodation coefficient the model itself is presented with its limits and possibilities.

Characterization of the surface in rarefied gas dynamics

According to the earliest approximation for the distribution of scattered molecules — introduced by Maxwell — the proportion α of the impinging molecules is scattered diffusely and the proportion $(1 - \tau)$ is reflected specularly. In the point given by the position vector $\mathbf{r}_s$ the adequate distribution function of molecules scattered from the surface with velocity $\mathbf{u}$ is

$$f(\mathbf{r}_s, \mathbf{u}) = (1-\tau)\, f(\mathbf{r}_s, \mathbf{v} - 2(\mathbf{u}\,\mathbf{n})\,\mathbf{n}) + \frac{\tau n_r}{u_0^3\, \pi^{3/2}} \exp\left(-u^2/u_0^2\right), \tag{1}$$

where $u_0^2 = 2kT_r/m$, $\mathbf{v}$ is the velocity of the incoming molecules, $\mathbf{n}$ is the unity vector of the surface normal, m is the mass of the gas molecule and k is the Boltzmann constant. n_r and T_r are parameters with dimensions of particle number density and temperature, respectively [4].

From the point of view of dynamics τ is the accommodation coefficient of the tangential component of momentum:

$$\tau = \frac{p_{i\tau} - p_{r\tau}}{p_{i\tau}}, \tag{2}$$

where

$$p_i = -m \int_{v_n<0} f_i\, \mathbf{v}_\tau (\mathbf{v}\,\mathbf{n})\, d\mathbf{v}$$

is the tangential momentum transferred to the surface by the molecules of distribution function f_i, and

$$p_r = m \int_{u_n>0} f_r\, \mathbf{u}_\tau (\mathbf{u}\,\mathbf{n})\, d\mathbf{u}$$

is the tangetial momentum transported from the surface by the molecules of distribution function f_r.

The gas molecules coming to the surface are characterized by Maxwell distribution of temperature T_i and have a mean energy E_i, while the gas molecules scattered from the surface have a mean energy E_r in accordance with the temperature T_r. If the gas is in thermal equilibrium with the surface of temperature T_s, then the gas molecules have the mean energy E_s. Using these quantities the energy accommodation coefficient is defined as

$$\alpha = \lim_{E_i \to E_s} \frac{E_i - E_r}{E_i - E_s}\,. \tag{3}$$

The equivalent formula for experiments is

$$\alpha = \lim_{T_i \to T_s} \frac{T_i - T_r}{T_i - T_s}\,. \tag{4}$$

Between the mean energy and the temperature there is a simple relation only if the Maxwell distribution is undistorted. The fulfilment of this condition must be checked for every experimental method. Theoretical models often define the energy accommodation coefficient instead of α in another way and investigate the characteristics of these arbitrary quantities [5]. Usually the condition $E_i \to E_s$ is omitted because of the limits of the theory.

It is easy to prove that supposing the accommodation coefficients to be independent of distribution function leads to contradiction. Using Eq. (1) the energy of molecules scattered from the surface can be expressed in the form

$$R_r = \int_{u_n>0} \frac{mu^2}{2} (\mathbf{un})\, f_r\, d\mathbf{u} = (1-\tau)\, E_i + \tau \frac{mn_r}{2\sqrt{\pi}} u_0^3 , \tag{5}$$

where

$$E_i = -\int_{v_n<0} \frac{mv^2}{2} (\mathbf{vn})\, f_i\, d\mathbf{v} \tag{6}$$

is the energy of the impinging molecules.

For a gas being in equilibrium with the surface the energy of the molecules is

$$E_s = (1-\tau)\, E_i + \tau \frac{mn_s}{2\sqrt{\pi}} u_{s0}^3 , \tag{7}$$

where $u_{s0}^2 = 2kT_s/m$. The number of molecules N_r, scattered from unit area in unit time is

$$N_r = \int_{u_n>0} (\mathbf{un})\, f_r\, d\mathbf{u} = (1-\tau) N_i + \frac{n_r}{2\sqrt{\pi}} u_0 , \tag{8}$$

where N_i is the number of incoming molecules in unit time to the same area:

$$N_i = -\int_{v_n<0} (\mathbf{vn})\, f_i\, d\mathbf{v} . \tag{9}$$

When the condition $T_r = T_s$ is satisfied, then

$$N_s = (1-\tau)\, N_i + \tau \frac{n_s}{2\sqrt{\pi}} u_{s0} . \tag{10}$$

As the numbers of incoming and scattered molecules are equal, the following equations are valid:

$$N_i = N_r = \frac{n_r}{2\sqrt{\pi}} u_0 \text{ or } N_i = N_s = \frac{n_s}{2\sqrt{\pi}} u_{s0} . \tag{11}$$

If the accommodation coefficients τ and α are known at a given surface temperature, the Eqs. (6)—(11) together with the definitions of α and τ allow us to calculate the values n_r, n_s and T_r.

The accommodation coefficients defined by Eqs. (2) and (3), however, are not independent of the distribution functions. Let us consider the conditions $\tau = 1$ and $\alpha = 1$ and let us investigate two molecular beams with molecules of velocities $\mathbf{v}_1$ and $\mathbf{v}_2$. If the number densities of molecules in the beams are small enough, then the presence of one of the beams does not disturb the other one, and the distribution function of the scattered molecules must be the sum of the two distribution functions. The distribution functions may be written in the common form

$$f_{rk} = \frac{2}{\pi} N_{ik} u_{k0}^{-2} \exp\left(-u^2/u_{k0}^2\right) \quad (k = 1, 2, 3) .$$

where $k = 1$ and $k = 2$ refer to the molecular beams of velocities $\mathbf{v}_1$ and $\mathbf{v}_2$, and $k = 2$ characterizes the simultaneous incidence of the beams. The equality $N_{i3} = N_{i1} + N_{i2}$ is evident and from Eq. (3) follows that

$$u_{k0}^2 = \frac{v_k^2}{2}(1 - \alpha) + \alpha u_{s0}^2, \qquad (k = 1, 2)$$

$$u_{30}^2 = \frac{N_{i1} v_1^2 + N_{i2} v_2^2}{2N_{i3}}(1 - \alpha) + \alpha u_{30}^2 .$$

Simple substitution shows that

$$f_{r3} \neq f_{r1} + f_{r2} .$$

Together with the definitions (2) and (3) the approximation in Eq. (1) is valid for scattered particles when the gas is in thermal equilibrium with the surface.

The accommodation coefficients τ and α play different roles in the characterization of a solid surface. τ is an important quantity in the rarefied gas dynamics, where for engineering materials τ is determined firstly by the roughness of the surface [6]. For microscopically smooth surfaces the tangential momentum accommodation characterizes the interaction between the gas molecules and the surface poorly. Only the values $\tau = 0$ and $\tau = 1$ give physically useful information, in other cases the knowledge of the angular distribution of scattered particles is required.

Theoretical models of the energy accommodation coefficient

The energy accommodation coefficient α summarizes the energy exchange processes which may occur when a solid surface is completely immersed in a still gas. The surface immersed in a still gas may be considered as representing the integrated effects of scattering of an infinite number of molecular beams coming from different directions with different energy. Each such beam will in general be scattered in a different way and will produce a different scattering pattern—however, the integrated pattern will be the same for all gas-surface systems in the case of thermal equilibrium [3].

Experiments in a still gas involve the sacrifice of most information on effects of directions and molecular speed. The experimental results are less sensitive and specific than those with molecular beams, but they provide data which represent the average behaviour of the gas-surface system. The experiments measuring the energy accommodation coefficients are relatively simple and the changes of values α of clean surfaces indicate the beginning and the process adsorption.

As the experiments are not made by molecular beams, the theory for the calculations of the energy accommodation coefficient must comply with specific requirements. It is hard to determine the interaction between an ideal solid surface and a monoenergetic molecular beam coming from a given direction. It is hopeless to get the energy accommodation coefficient by averaging the results of complicated calculations concerning the interaction between the molecular beams and the surface. The calculations can be made by averaging, but in this case the model for interaction must be oversimplified. Another possibility is to find some energy transfer process which represents the change of total energy suitably.

The tendency of the dependence of α on the mass ratio of the gas atom to the solid atom is correct in Baule's model, where the dynamics of two hard spheres are taken into account only. The cube models make it possible to calculate the energy accommodation coefficient as a function of the mass ratio and the temperatures. The hard cube model, however, is developed for calculating the angular distribution of scattered particles and in its present form this model gives only the relation between α and the mass ratio. The soft cube model contains adjustable parameters and cannot predict the equilibrium α values according to Eq. (4), but provides nonequilibrium α values when $T_i - T_s$ is sufficiently large. Comparison of soft cube model predictions with experimental data of the nonequilibrium energy accommodation coefficients gives good correlations [7].

At present the quantum theory of the energy accommodation coefficient is still unsatisfactory because it fails to produce agreement with experiment at low temperature, presumably due to the use of incorrect interaction potential models [3].

There are classical simulation models which can take into account a more realistic physical picture by using much computer time. A variety of sophisticated calculations of atomic trajectories near solid surfaces have been presented. The force is generally represented as an explicit sum of pairwise interaction between the gas atom and a set of oscillating atoms in the solid. The number of simultaneous differential equations which are to be solved becomes quite large. A large number of aiming points is required to obtain smooth distributions of scattering intensity and satisfactory statistical uncertainties — of the order of 10^4—$2 \cdot 10^4$. These trajectory calculations are suitable to obtain the relation between the scattering intensities and the gas atom — solid potential parameters [8]. It is hopeless, however, to determine the energy accommodation coefficient by these computations because of the required averaging.

In the lattice theory a real crystal is represented by a "lattice model" and interactions among atoms of a real crystal are represented by some lattice interatomic interaction law. The simplified lattice models have adjustable parameters and by suitably fitting these models a useful semiempirical formula can be obtained for the energy accommodation coefficient.

A simple model and the results

Except Baule's theory, classical and quantum calculations are lengthy and difficult. This paper suggests a simple simulation procedure for calculating the energy accommodation coefficient as a function of the mass ratio and the temperature.

In this model the solid is represented by a hard cube, i.e. the tangential velocity is unchanged during the collision. The solid atom has a velocity normal to the surface, in the directon of the positive z axis:

$$w = w' \cos(2\pi l), \tag{12}$$

where l is selected from random numbers distributed uniformly in the interval (0, 1). The velocity amplitude w' has a one-dimensional distribution

$$G(w')dw' = \frac{2}{\sqrt{\pi}\, w_0} \exp(-w'^2/w_0^2) dw', \tag{13}$$

with

$$w_0^2 = 2kT_s/M, \tag{14}$$

where T_s is the temperature of the solid and M is the mass of a solid atom.

The velocity magnitudes of the incoming gas molecules are given by the

$$F(v)dv = \frac{2v^3}{v_0^4} \exp(-v^2/v_0^2)\, dv \tag{15}$$

distribution function [9], and the direction is determined by the cosine distribution:

$$H(\vartheta)d\Omega = \frac{1}{\pi}\cos\vartheta d\Omega\,. \tag{16}$$

In Eq. (14)

$$v_0^2 = \frac{2kT_i}{m}\,,$$

where T_i is the temperature of the impinging molecules and m is the mass of the gas molecules.

The gas molecule near to the surface is accelerated by the potential $U =$ constant and hence the normal component v_n of the incoming molecular satisfies the equation

$$\frac{1}{2}mv_n^2 = \frac{1}{2}mv_i^2\cos^2\vartheta_i + U\,. \tag{17}$$

The potential U characterizes the mean effect of the attractive forces of the surface atoms.

The dynamics of the one dimensional collision between the gas molecule and the solid atom is very simple if after the collision the velocities of the gas molecule and of the solid are opposite. Applying the laws of the conservation of momentum and of energy the velocity of the gas molecule after collision is

$$u_n' = \frac{2w + (\mu - 1)v_n}{1 + \mu}\,, \tag{18}$$

where μ is the mass ratio: $\mu = m/M$.

In the other cases one must consider the possibility of a repeated collision. This requires the frequency of the vibration of solid atom $\nu = kT/h$, where h is Planck's constant. Knowing the velocities and the phase of the vibration by Eq. (12) it can be determined whether a further collision takes place. In the case of a further collision the velocity of the gas molecule after collision may be calculated by Eq. (18).

In both cases of simple and multiple collisions the molecule leaves the surface with a velocity u_n satisfying the following equation:

$$\frac{1}{2}mu_n^2 = \frac{1}{2}mu_n'^2 - U\,, \tag{19}$$

where u_n' is the velocity after the last collision.

To calculate α it is necessary to compute the mean energy of the N

scattered molecules:

$$E_r = \frac{1}{N} \sum_{j=1}^{N} \left(\frac{1}{2} mu_{nj}^2 + \frac{1}{2} mv_{ij}^2 \sin^2 \vartheta_{ij} \right) \tag{20}$$

and to check the validity of the relation

$$E_i = \frac{1}{N} \sum_{j=1}^{N} \frac{1}{2} mv_{ij}^2 = 2kT_i . \tag{21}$$

To determine the final velocity of each simulated molecule requires a simple calculation and the follow of 10 000 trajectories requires little computer time only. Unfortunately, in Eq. (3) the condition $E_i \to E_s$ demands the calculation of the energy difference $\Delta E = E_i - E_r$ at different energies E_i in the vicinity of the temperature $T_i = T_s$. For the determination of the value α $\Delta E/(E_i - E_s)$ must be extrapolated. So if we have an error of 1–2% in ΔE, the error of α calculated by the extrapolation may reach the 10–20%.

Fig. 1 shows the calculated energy accommodation coefficient for the Ne–W systems as a function of the temperature. The potential well depth U was chosen to be equal to the adsorption heat per molecule, $U = 3.5 \cdot 10^{-21}$ J [10]. The calculated values of α are larger than the experimental data [11]. This tendency is expectable because omitting the repulsive forces the energy accommodation is overestimated. Treating U as an adjustable parameter the results of computations would fit the experimental values better.

The deviation from the measurements is similar in Fig. 2, where the α vs T function is shown for the Ar–W system. Here $U = 16.8 \cdot 10^{-21}$ J [10], and the agreement with the experimental data is better. This better agreement shows that taking into account the multiple collision may be important since in the Ar–W system the multiple collisions are more frequent because of the larger mass ratio.

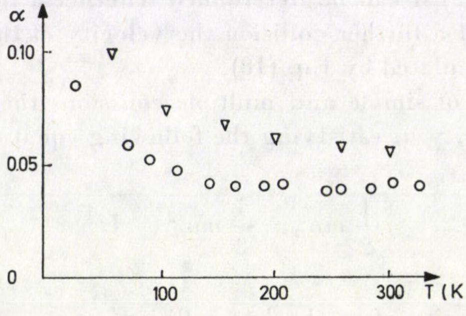

Fig. 1. Energy accommodation coefficients α at different temperatures T for Ne–W system ○ show the experimental data [7], the calculated values are denoted by ▽

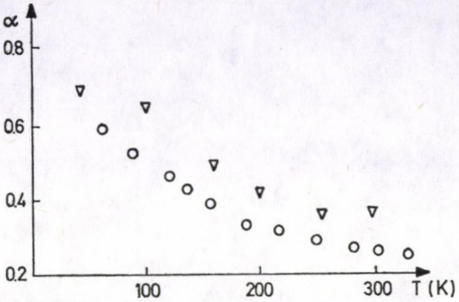

Fig. 2. Energy accommodation coefficients α at different temperatures T for Ar—W system ○ show the experimental data [7], the calculated values are denoted by ▽

The applied model is very simple and it seems suitable for analytical calculations. The assumptions are similar to those in the hard cube model except the multiple scattering and the potential well. The analytical treatment would allow of considering U as an adjustable parameter and of avoiding the summation of the errors at the extrapolation. Recently there have been attempts to apply the hard cube model with a potential well in order to calculate the energy accommodation coefficient [12], but the task remains to consider the multiple collisions in analytical calculations.

REFERENCES

1. H. Y. Wachman, Am. Rocket Soc. J., **32**, 2, 1962.
2. J. C. Maxwell, in "The Scientific Papers of James Clark Maxwell" Vol. 2, p. 706, Dover, New York, 1972.
3. F. O. Goodman and H. Y. Wachman, Dynamics of Gas-Surface Scattering, Chapter 10, Academic Press, New York, 1976.
4. M. N. Kogan, Dinamika razrezsonnovo gaza, Nauka, Moscow, 1967.
5. J. Lorenzen and L. M. Raff, J. Chem. Phys., **49**, 1165, 1968.
6. L. Füstöss, Sixth Czechoslovak Conference on Electronics and Vacuum Physics, p. 104, Bratislava, 1976.
7. R. M. Logan, Surface Science, **15**, 387, 1969.
8. J. D. McClure, J. Chem. Phys., **57**, 2810, 1972.
9. E. H. Kennard, Kinetic Theory of Gases, p. 63, McGraw-Hill, New York and London, 1938.
10. F. O. Goodman and H. Y. Wachman, J. Chem. Phys., **46**, 2376, 1967.
11. F. O. Goodman and H. Y. Wachman, Proc. Int. Sch. Phys. Enrico Fermi, Course LVIII, 491, 1974.
12. Ch. Steinbrüchel, Surface Science, **66**, 131, 1977.

Acta Physica Academiae Scientiarum Hungaricae, Tomus 49 (4), pp. 371–380 (1980)

THOMAS–FERMI POTENTIAL IN SHELL-CORRECTION CALCULATIONS

By

E. BALÁZS

DEPARTMENT OF PHYSICS, INSTITUTE OF PHYSICS, TECHNICAL UNIVERSITY
1521 BUDAPEST, HUNGARY

(Received 10. IV. 1980)

The possibility of the substitution of the shell-model potential in the shell-correction method by Thomas–Fermi potential is investigated. The preliminary results referring to the spherical nucleus ^{208}Pb show that after the re-adjustment of the applied effective two-nucleon interactions in the energy functional the Thomas–Fermi potential obtained as the variational derivative of the energy-functional can be used to calculate shell corrections.

1. Introduction

The shell-correction method proposed by STRUTINSKY [1] is a combination of two different phenomenological models, namely the shell model (SM) and the liquid drop model (LDM). According to this approach the binding energy of a deformed nucleus can be written as

$$E(A, \beta) = E^{\mathrm{LDM}}(A, \beta) + \delta E_1(U^{\mathrm{SM}}) + \delta E_2, \tag{1}$$

where A is the mass-number, β symbolizes certain parameters characterizing the deformation, E^{LDM} is the binding energy of the nucleus calculated within the framework of the LDM. The second term of the right hand side is the shell correction calculated in a given deformed SM potential,

$$\delta E_1(U^{\mathrm{SM}}) = \sum_{\nu} \varepsilon_\nu\,(U^{\mathrm{SM}}) - \Big(\sum_{\nu} \varepsilon_\nu\,(U^{\mathrm{SM}})\Big)_{av}. \tag{2}$$

Here ε_ν-s are the single particle energies calculated in the U^{SM} potential. The deformation parameters of the SM potential have to be consistent with those of the LDM. The averaging procedure for calculating the second term in (2) has little significance from the point of view of the present paper, hence the reader is referred to the literature (e.g. [1]). In Eq. (1) δE_2 is the second order correction term.

The shell-correction method has had considerable success in explaining many experimental data concerning nuclear ground state masses, deformations and especially for heavy nuclei fission barriers and isomers [2]. One has to emphasize that all these excellent results have been obtained with significantly less computational efforts than in the case of any microscopical approach.

It was shown by STRUTINSKY [3] and later by BRACK [4] for general case that the shell-correction method is theoretically founded on the basis of the Hartree—Fock (HF) theory. The so-called STRUTINSKY's energy theorem states that all the shell fluctuations of the total HF energy of the nucleus, both as a function of deformation (for fixed mass-number) and of mass-number (at given deformation) are contained in the sum of the occupied "shell model" energy levels (the first term of the right hand side of (2)). The numerical tests of this statement, however, had to be delayed up to recent time, as at that time no reliable HF calculations were available for heavy nuclei.

In the past few years the progress in the development of effective nucleon-nucleon interactions [5] and in HF technique [6] made it possible to perform numerical calculations concerning heavy deformed nuclei within the framework of the HF theory (e.g. [6]). Since that time hope has arisen to be able to treat the rather intricate fission process and the cheking of the shell-correction method on the basis of the microscopial HF approach. However, even if the mathematically simple Skyrme interactions are used, the HF calculation still requires a large amount of computing time. Nevertheless, a series of numerical tests has been carried out [7, 8] confirming the validity of the shell-correction method.

There is another possibility for the microscopical treatment of the physical properties of nuclei, too. If it is not the physical characteristics of the individual particles that are interesting but only the global features of the whole nucleus — the binding energy and the single particle distributions — one can apply the Thomas—Fermi (TF) approximation. TYAPIN [9] has justified the shell-correction method on the basis of the TF approximation. According to his considerations it can be verified that

$$E^{\mathrm{HF}} - E^{\mathrm{TF}} = \delta E_1(U^{\mathrm{SM}}), \tag{3}$$

where E^{HF} and E^{TF} are the binding energies of the deformed nucleus calculated in HF and TF approximation, respectively, and δE_1 is the shell-correction. This result enables us to formulate the shell-correction method according to the following procedure:

1. One determines the minimum of the energy-functional in TF approximation as described in [10]. This energy will be considered the smooth component of the binding energy.

2. Deriving from this energy functional the TF potential one has to solve using it the single particle Schrödinger equation. With the resulting single particle energies one can calculate the shell corrections according to STRUTINSKY's prescription.

This proposed procedure can be expressed in the following equation:

$$E - E^{\mathrm{TF}} = \delta E_1(U^{\mathrm{TF}}), \tag{4}$$

where $\delta E_1(U^{\mathrm{TF}})$ stands for the shell correction calculated using the single-particle energies obtained in the TF mean single-particle potential obtained as the variational derivative of the nuclear potential energy instead of the U^{SM} potential. Following the prescription of this procedure one arrives at a microscopical formulation of the shell-correction method.

The computational procedure becomes a bit more complicated because of the first microscopical — TF — approximation. However, the second microscopical approach — the substitution of the phenomenological SM potential by the TF one — does not mean any further complication. Hence, the proposed procedure fully conserves the simplicity of the shell-correction method as compared with the TF approach.

Our procedure is applicable, if

1. the TF binding energy reproduces the smooth behaviour of the experimental binding energies as well, as the LDM energy does;
2. the TF potential gives the right single-particle level densities in the vicinity of the Fermi energy.

In a previous paper [10] the first question has been investigated. The results indicate that the applied effective two-nucleon interactions have to be re-adjusted in order to get good deformation dependence on the binding energy.

In the present paper the problem concerning the TF potential is discussed. It is shown that the average TF single-particle potential is suitable to carry out shell-correction calculations. The case of spherical nucleus ^{208}Pb is investigated, the results of our calculations obtained using different effective two-nucleon interactions are compared with SM results.

2. The Thomas-Fermi potential

The energy-functional of a nucleus can be written in TF approximation as

$$\begin{aligned} E = \varkappa \int d\mathbf{r}\,[\varrho_n^{5/3} + \varrho_p^{5/3}] + \frac{\hbar^2}{72\,M}\int d\mathbf{r}\left[\frac{|\nabla\varrho_n|^2}{\varrho_n} + \frac{|\nabla\varrho_p|^2}{\varrho_p}\right] + \\ + E_{\mathrm{pot}}[\varrho_n, \varrho_p] + E_{\mathrm{Coul}}[\varrho_p] = E_{\mathrm{kin}} + E_{\mathrm{pot}} + E_{\mathrm{Coul}}, \end{aligned} \tag{5}$$

where $\varkappa = 119.6$ MeV fm^2 and M is the mass of a nucleon. At a given deformation the minimalization of this functional with the constraint of the mass-number conservation gives the binding energy of the nucleus in TF approximation.

Knowing the energy-functional (5) the single particle potential U is defined as a variational derivative of the total potential energy $E_{\mathrm{pot}}[\varrho_n, \varrho_n] + E_{\mathrm{Coul}}[\varrho_p]$:

$$U_\tau(\mathbf{r}) = \frac{\delta}{\delta \varrho_\tau} (E_{\mathrm{pot}}\,[\varrho_n, \varrho_p] + E_{\mathrm{Coul}}\,[\varrho]_p)\,, \tag{6}$$

where τ is the isotopic quantum number. The potential itself is a functional of the densities, hence the density distribution belonging to the energy minimum is to be used for the determination of the potential.

In the present paper the usual decomposition to two terms is used for the potential energy of the nuclear forces, i.e.:

$$E_{\mathrm{pot}}\,[\varrho_n, \varrho_p] = E_{\mathrm{NM}}\,[\varrho_n, \varrho_p] + E_{\mathrm{LR}}\,[\varrho_n, \varrho_p]\,, \tag{7}$$

where the terms E_{NM} and E_{LR} arise from the short-range and long-range components of nuclear forces, respectively (e.g. [11]).

In the local density approximation [11] E_{NM} can be written as

$$E_{\mathrm{NM}}\,[\varrho_n, \varrho_p] = \int d\mathbf{r}\, w\,(\varrho_n, \varrho_p)\,, \tag{8}$$

where the function w is fitted to nuclear matter calculations [12, 13]. The dependence of E_{LR} on the densities is as follows:

$$E_{\mathrm{LR}} = \frac{1}{2} \sum_{\tau\tau'} \int d\mathbf{r}_1\, d\mathbf{r}_2\, v_{\tau\tau'}(|\mathbf{r}_1 - \mathbf{r}_2|, \varrho)\, \varrho_\tau(\mathbf{r}_1)\, [\varrho_\tau(\mathbf{r}_2) - \varrho_{\tau'}(\mathbf{r}_1)]\,. \tag{9}$$

This energy term vanishes when the density is constant. The density dependent effective interaction $v_{\tau\tau'}$ is taken from [14].

The potential calculated according to [6] using the potential energies given in Eqs. (8) and (9) substitutes the SM potential in the single-particle Schrödinger equation,

$$\left[-\frac{\hbar^2}{2M} \Delta + U_\tau(\mathbf{r}, \beta) \right] \varphi_{\nu\tau}(\mathbf{r}, \beta) = \varepsilon_{\nu\tau}(\beta)\, \varphi_{\nu\tau}(\mathbf{r}, \beta), \tag{10}$$

where

$$U_\tau(\mathbf{r}, \beta) = U_\tau^{\mathrm{TF}}(\mathbf{r}, \beta) + U_\tau^{\mathrm{SO}}(\mathbf{r}, \beta) + \delta_{\tau 1} U_{\mathrm{Coul}}(\mathbf{r}, \beta) \tag{11}$$

is the sum of the mean single particle TF potential, of the spin-orbit potential and of the Coulomb potential.

The solution of (10) does not mean any difficulty. The procedure described in [15, 16] for the case of Woods—Saxon potential is used. The spin-orbit potential is approximated by the phenomenological expression

$$U_\tau^{\mathrm{SO}}(\mathbf{r}, \beta) = K \left(\frac{2}{3} \Delta\, \varrho_\tau + \frac{1}{3} \Delta\, \varrho_{\tau'} \right) [\mathbf{s} \cdot \mathbf{p}] \tag{12}$$

taken from [17]. K is a parameter to be fitted to the splitting of the single-particle levels; in the present calculation $K = 31.5$ MeV fm^2.

3. Results

In the TF energy calculations carried out according to [10] the nuclear density distributions are approximated with Fermi functions. The energy minimum of the spherical ^{208}Pb belongs to density distributions characterized by the parameters given in Table I.

Table I

Parameters of the Fermi functions approximating the density distributions of spherical ^{208}Pb in the energy minimum

	Radius (R_0)	Diffuseness (a)
Neutron	7.318 fm	0.541 fm
Proton	6.971 fm	0.467 fm

In the present calculation the potential energy was approximated in two slightly different ways: in case I the function w of Eq. (8) was taken from [12], in case II it was taken from [13].

In both cases the TF potentials were calculated according to (6). The parameters of these Woods—Saxon type potentials were determined by the least squares method. The results are shown in the fourth and fifth rows of Table II. In the first three rows the results of [18—20] are given.

As one can see, by comparison of the parameters of different potentials we are not able to decide unambiguously, which potential is suitable for our purposes. With the exception of the diffuseness parameters of case I all the other parameters obtained in our calculation are in the range of the parameters of the phenomenological potentials.

It is of greater significance to compare the single particle spectra calculated in the TF potential with those obtained using SM potential. According

Table II

Parameters of the Woods—Saxon potentials in the case of ^{208}Pb obtained from different calculations

	Neutron			Proton		
	R_0	a	V_0	R_0	a	V_0
[18]	7.52	0.67	−44.0	7.52	0.67	−58.0
[19]	7.98	0.70	−40.6	7.56	0.70	−58.7
[20]	7.36	0.66	−47.1	7.43	0.66	−60.1
I	7.71	0.82	−47.1	7.83	0.86	−61.8
II	7.69	0.63	−43.7	7.74	0.63	−57.6

to the shell-correction method the level density in the vicinity of the Fermi level is of crucial importance for the stability of nuclei.

In Fig. 1 the total single particle spectrum of case II is compared with the standard SM single particle spectrum. As it can be seen the spectrum ob-

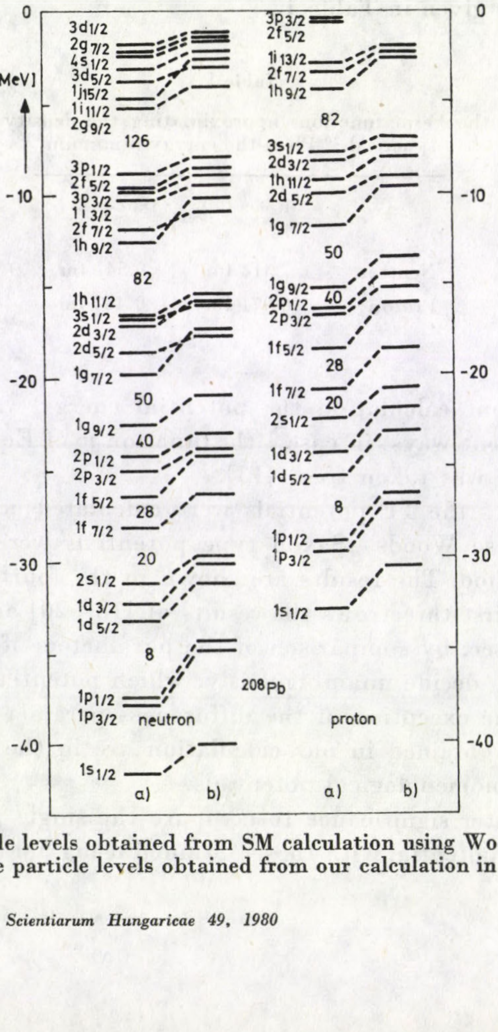

Fig. 1. (a) single particle levels obtained from SM calculation using Woods—Saxon potential; (b) single particle levels obtained from our calculation in case II

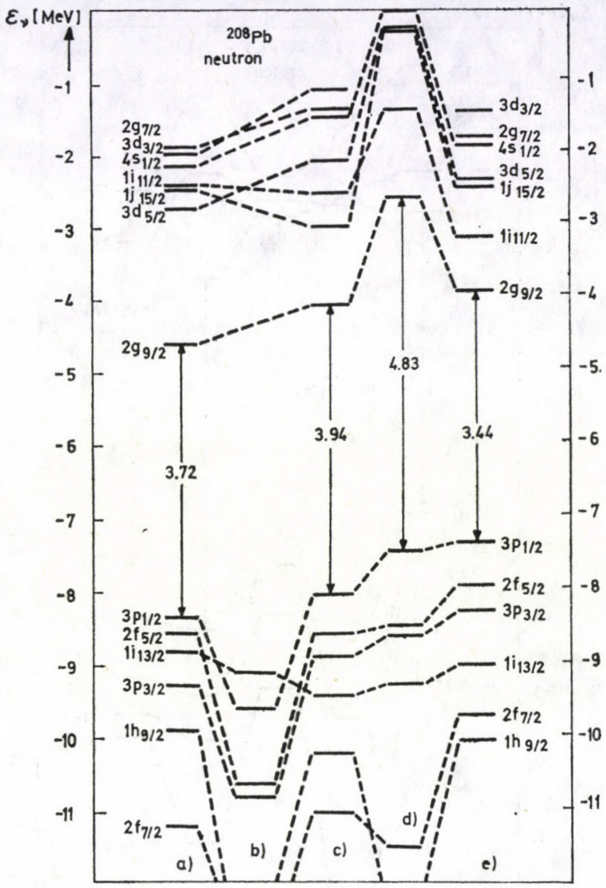

Fig. 2. The uppermost single particle levels of neutrons, (a) our calculation (case I); (b) results of the HF calculation [12]; (c) our calculation (case II); (d) results of the SM calculation [13]; (e) experimental values taken from [21]

tained from our calculations shows the most important characteristics of a SM single-particle spectrum. There is a well-defined shell structure and the level density is acceptable. However, the whole spectrum is shifted into the direction of higher energies. This fact indicates that neither the depth nor the radius of the potential have a correct value [20].

In some cases — as one can see in the Figure — there occurs a level order change in the spectrum (e.g. in the case of neutrons the levels $2d_{5/2}$ and $1g_{7/2}$ are changed). This fact indicates that neither the spin-orbit coupling is well fitted. It causes a less severe problem which can be corrected with the re-fitting of parameters K in Eq. (12). From the point of view of the shell-correction method anyway the order of the single particle levels in the deep energy region is not substantial. The correct level order is important, however,

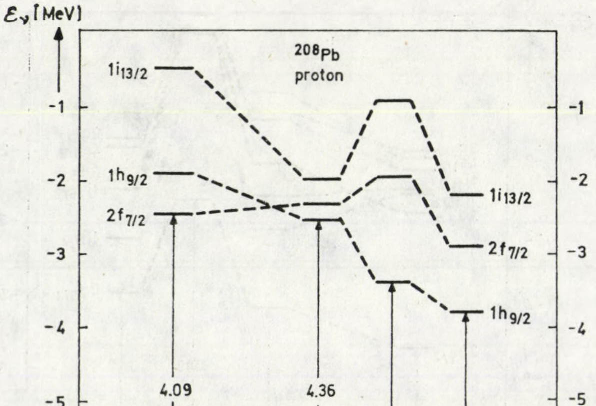

***Fig. 3.* The uppermost single particle levels of protons (a) our calculation (case I); (b) results of the HF calculation [12]; (c) our calculation (case II); (d) results of the SM calculation [13]; (e) experimental values taken from [21]**

in the vicinity of the Fermi level. The correct value of the energy gap is essential as well.

The crucial role of the uppermost levels and of the energy gap can easily be understood if one considers the effect of deformation on these levels. Deforming the nucleus the degeneration of the levels splits up, they will be mixed and the contribution of the uppermost levels to the total energy will not be compensated [1]. Hence the degeneracy of the topmost levels of a spherical nucleus may have great influence on the calculations of the deformation energy.

In Figs 2. and 3 the uppermost levels are compared with the results of SM calculations and with values obtained from experiments. In the same

Figures one can see the results of the HF [12] and SM [13] calculations which were carried out using the same function $w(\varrho_n, \varrho_p)$ as we did.

The Figures show that the experimental values of the single-particle levels are better approximated in case II. The results obtained in this case for the neutrons reproduce the level order quite well and the energy shift is less than 1 MeV. The only discrepancy is that the levels $1f_{7/2}$ and $1i_{11/2}$ are changed with the levels $1g_{9/2}$ and $1j_{15/2}$, respectively. The agreement in case I is less satisfactory. In addition to the above mentioned level changing some other levels are changed, too ($3d_{5/2}$, $3d_{3/2}$, $1i_{13/2}$).

For the protons, right level order was obtained in case II, however, the levels are higher about 1 MeV than the experimental ones. In case I another problem arises. The degeneracy of the uppermost level is high ($1h_{11/2}$). This result agrees with the result obtained from the HF calculation using the same $w(\varrho_n, \varrho_p)$ as in case I. This fact may cause troubles in calculations for deformed nuclei.

4. Summary

In spite of the above mentioned difficulties and slight discrepancies one can conclude that the obtained results are encouraging. Part of the anomalies of the investigated cases — the shifted energy spectrum — are due to the same problems as those arising in the TF energy calculations carried out with the effective two-nucleon interaction [12, 13] used in [10]. Hence it is hoped that using re-adjusted effective two-nucleon interactions not only the TF binding energy reproduces well the LDM results and its deformation dependence but the TF potentials derived from the correct energy functional will lead to correct results.

To get the right level order is a separate task. Its solution does not mean any difficulty, one has to fit the spin-orbit coupling. This is a common problem of all SM calculations, the solution is straightforward and well known [20].

After carrying out these corrections one can hope that our procedure proposed for the microscopical shell-correction method will be successful.

REFERENCES

1. V. M. Strutinsky, Nucl. Phys., **A95**, 320, 1967.
2. J. R. Nix, Ann. Rev. Nucl. Sci., **22**, 65, 1972.
3. M. Brack et al., Rev. Mod Phys., **44**, 320, 1972.
4. M. Brack, International School on Nuclear Physics, Predeal, Romania, 1974.
5. J. W. Negele, Second Intern. Workshop on Gross Properties of Nuclei and Nuclear Excitations, Hirschegg, Austria, 1974 (Techn. Hochschule Darmstadt, 1974).
6. J. W. Negele, Phys. Rev., **C1**, 1260, 1970.
7. M. Brack and P. Quentin, Workshop quoted in ref. 5.
8. M. Brack and P. Quentin, Phys. Lett., **56B**, 421, 1975 .
9. A. S. Tyapin, Yadernaya fizika, **11**, 98, 1970.

10. E. Balázs, Per. Polytechnica, **21,** 165, 1977.
11. K. A. Brueckner et al., Phys. Rev., **110,** 431, 1958.
12. G. Fái and J. Németh, Nucl. Phys., **A208,** 463, 1973.
13. R. J. Lombard, Ann. of Phys., **77,** 380, 1973.
14. D. W. L. Sprung, Nucl. Phys., **A168,** 273, 1973.
15. V. V. Pashkevich and V. M. Strutinsky, Sov. J. Nucl. Phys., **9,** 56, 1969.
16. J. Damgaard et al., Nucl. Phys., **A135,** 432, 1969.
17. R. S. Scheerbaum, Nucl. Phys., **A257,** 77, 1976.
18. J. Blomqvist and S. Wahlborn, Arkiv Fysik, **16,** 545, 1960.
19. E. Rost, Phys. Lett., **26B,** 184, 1968.
20. H. C. Pauli, Phys. Reports, **7C,** 35, 1973.
21. A. Bohr and B. R. Mottelson, Nuclear Structure, Vol. I. Benjamin Inc., Amsterdam, 1969.

Acta Physica Academiae Scientiarum Hungaricae, Tomus 49 (4), pp. 381—389 (1980)

ROTATIONAL ANALYSIS OF THE $^1\Phi - A^1\Delta$ AND $^1\Delta - A^1\Delta$ SYSTEMS OF ScF

By

E. A. SHENYAVSKAYA

INSTITUTE FOR HIGH TEMPERATURES, MOSCOW, USSR

and

I. PÉCZELI

DEPARTMENT OF ATOMIC PHYSICS, INSTITUTE OF PHYSICS, TECHNICAL UNIVERSITY
1521 BUDAPEST HUNGARY

(Received 10. IV. 1980)

Rotational analysis of the hitherto unknown $^1\Phi - A^1\Delta$ and $^1\Delta - A^1\Delta$ systems of ScF was carried out. The lower state of the transitions was identified with the first excited singlet state of the electron configuration $3d\delta\ 4s\sigma$.

Introduction

Scandium monofluoride is the simplest molecule containing the element with unfilled *d*-shell. That is why it was the subject of many experimental and theoretical investigations [1]—[10]. According to theoretical calculation [7] the ScF molecule has three low-lying states: $X^1\Sigma(4s\sigma)^2$, $a^3\Delta(3d\delta 4s\sigma)$ and $^1\Delta(3d\delta 4s\sigma)$. The electronic transitions which were observed in absorption involve both the $X^1\Sigma$ and $a^3\Delta$ states [3], [5]. The investigation of the spectrum of the matrix-isolated ScF molecule at a temperature of 4K [4] has shown that the ground state is $X^1\Delta$. The attempt to estimate the excitation energy of the $a^3\Delta$ state failed [10].

Till now there is no experimental information on the $A^1\Delta$ state. According to theoretical calculation [7] the excitation energy of the $A^1\Delta$ state is about 2600 cm^{-1}. This is why the contribution of the $A^1\Delta$ state to the partition function when calculating thermodynamic functions at high temperatures must be considerable.

This paper deals with two band systems involving the $A^1\Delta$ state $(3d\delta 4s\sigma)$ as a lower state of transitions: $^1\Delta - A^1\Delta$ and $^1\Phi - A^1\Delta$. The $^1\Delta - A^1\Delta$ bands have not been observed hitherto. The bands assigned as the $^1\Phi - A^1\Delta$ transition were previously supposed to belong to the $^3\pi - a^3\Delta$ transition [5].

Experimental

The spectrum of ScF was obtained in emission of a discharge in helium as carrier gas with traces of scandium trifluoride ($ScFl_3$). The discharge tube was described in [1].

The spectrum was photographed in experimental spectrograph SEM-1 equipped with a grating with 300 lines/mm, 200 mm long in XI order with a dispersion of about 0.04–0.05 nm/mm and a real resolving power not less than 450 000. The Fe lines excited in the hollow cathode lamp and taken without separation of orders provided a reference spectrum. The spectrum was measured using the IZA-2 comparator. The accuracy of measurements of unblended lines is estimated to be better than 0.02 cm^{-1}.

The spectra taken from the two transitions are shown in Figs. 1 and 2.

Rotational analysis

Many red-shaded bands are observed in the 540–590 nm region. Some of them can be unambiguously arranged to the known ($^1\Sigma - X^1\Sigma$) [2], [5] and ($^3\Delta - a^3\Delta$) [6] systems. In the present work the rotational analysis of the most intense bands at 544.47, 545.21, 567.77 and 570.81 nm was carried out.

Every $^1\Phi - A^1\Delta$ band has a very strong Q-head (0–0 band, at λ 544.47 nm and 1–1 band at λ 545.21 nm) and consists of three single branches R, Q and P. Wave numbers of band lines are given in Table I.

The rotational structure near the Q-heads is not resolved due to the small difference $B' - B''$. The first lines of P-branches are overlapped by strong lines of Q-branches. The lines of R-branches which follow from the Q-head to violet with intervals changing very little between neighbouring lines are traceable from the first lines. The intensity of R-lines decreases before the head formation.

The relative numbering was established by finding an agreement between combination differences $\Delta_1 F$: $R(J) - Q(J) = Q(J+1) - P(J+1)$ for the upper state and $R(J) - Q(J+1) = Q(J) - P(J+1)$ for the lower state. The absolute numbering was found graphically from the condition $\Delta_2 F(J) = 0$ at $J = -1/2$.

The rotational analysis permitted to determine the type of the transition with certainty. The strong Q-branch implies that $\Delta\Lambda = \pm 1$. The lines of the R-branch are noticeably stronger than those of the P-branch indicating that $\Delta\Lambda = +1$. The absence of the doubling of branch lines and the absence of the combination defect up to highest values of J eliminate from the consideration the states with $\Lambda = 0.1$. The first line $R(2)$ which is clearly seen in the 0–0 band has shown that $\Lambda'' = 2$. From the above it follows that the bands belong to the $^1\Phi - {}^1\Delta$ transition.

Both the 0–0 and 1–1 bands reveal very strong perturbations. In the 0–0 band at $J' \geq 73$ and in the 1–1 band at $J' \geq 45$ the intensity of lines decreases sharply and the lines of branches deviate from the regular courses. At the positions of the exrapolated $Q(78)$ and $Q(96)$ lines in the 0–0 and 1–1 bands respectively there seem to be violet degraded heads on the spectrograms taken with low dispersion.

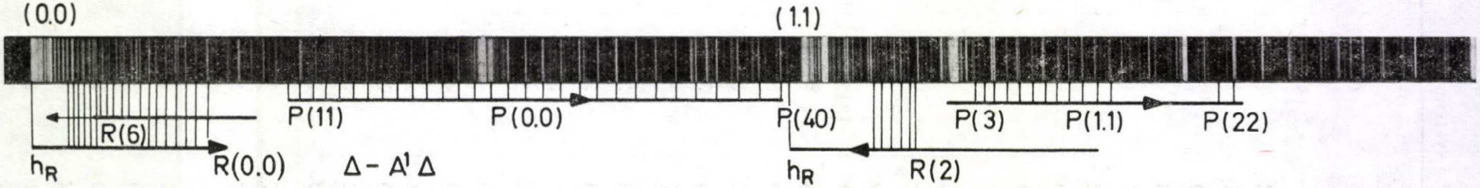

Fig. 1. $^1\Delta$ — A$^1\Delta$ system (0.0) (1.1)

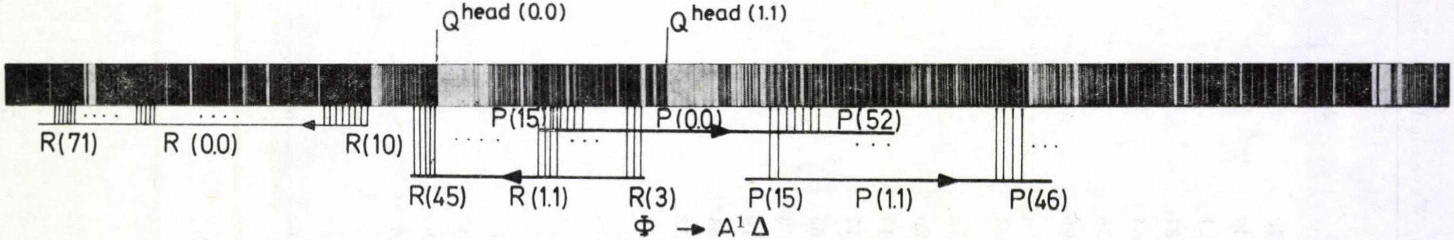

Fig. 2. $^1\Phi$ — A$^1\Delta$ system (0.0) (1.1)

Table I
Wavenumbers of band lines of the $^1\Delta - A^1\Delta$ system

J	0—0			1—1		
	R	Q	P	R	Q	P
2	18363.78					
3	65.49			18339.12		
4	65.21			39.95		
5	65.87			40.69		
6	66.64			41.38		
7	67.36			42.05		
8	68.06			42.72		
9	68.65			43.40		18329.79
10	69.43		18354.25	44.09		29.04
11	70.13			44.75		28.22
12	70.80		52.79*	45.39		27.48
13	71.49		51.96	46.05		26.72
14	72.17		51.08	46.69		25.84**
15	72.85		50.47	47.33	18335.91	25.16
16	73.53		49.65	47.96	35.82	24.33
17	74.19		48.86	48.60	35.75	23.58
18	74.84**		48.11	49.27	35.68	22.74
19	75.53		47.33	49.86	35.56	21.95
20	76.20		46.55	50.47	35.43	21.08
21	76.85		45.76	51.08	35.33	20.27
22	77.51		44.98	51.70	35.24	19.47
23	78.18		44.20	52.29	35.10	18.64
24	78.82	18360.78	43.40	52.86	34.98	17.82
25	79.47		42.57	53.48	34.84	16.96
26	80.09	60.62	41.85	54.06	34.72	16.12
27	80.67**	60.51	40.99	54.57	34.58	15.29
28	81.38	60.46	40.19	55.20	34.45	14.41
29	81.01	60.37	39.40	55.72	34.29	13.56
30	82.64	60.27	38.58	46.30	34.13	12.69
31	83.25	60.16	37.79	56.87	33.97	11.80
32	83.89	60.04	36.95	57.47	33.79	10.95
33	84.49	59.98	36.12	57.97	33.63	10.04
34	85.12	59.86	35.33	58.44	33.44	09.14
35	85.72	59.75	34.45	59.00	33.27	08.27
36	86.32	59.64	33.63	59.50	33.09	07.35
37	86.91	59.50	32.82	60.04	32.88	06.42
38	87.50	59.40	32.03	60.51	32.66	05.50
39	88.11	59.26	31.10	61.01	32.47	04.61
40	88.69	59.16	3.030	61.57	32.36	03.65

Table I (continued)

J	0—0			1—1		
	R	Q	P	R	Q	P
41	89.27	59.00	29.41	62.02	32.03	02.77
42	89.84	58.87	28.61	62.54	31.82	01.85
43	90.42	58.73	27.76	63.06	31.61	00.88
44	91.00	58.58	26.90	63.56	31.40	18299.99
45	91.57	58.44	26.10			99.07
46	92.12	58.29	25.16			
47	92.67	58.10	24.33			
48	93.22	57.97	23.44			
49	93.77	57.85	22.56			
50	94.31	57.64	21.70			
51	94.84	57.47	20.83			
52	95.37	57.30	19.95			
53	95.89	57.11	19.05			
54	96.41	56.91	18.14			
55	96.93	56.72	17.26			
56	97.44	5.653	16.35			
57	97.94	56.30	15.43			
58	98.43	56.14	14.53			
59	98.93	55.92	13.62			
60	99.42	55.72	12.69			
61	99.91	55.49	11.80			
62	18400.26	55.27	10.85			
63	00.85	55.03	0.90			
64	01.33	54.80	08.94			
65	01.78	54.57	08.07			
66	02.25	54.33	07.11			
67	02.70	54.06	06.14			
68	03.14	53.82	05.23			
69	03.59	53.58	04.26			
70	04.01	53.31	03.32			
71	04.46	53.06	02.34			
72	04.87	52.79*	01.38			
73	05.33	52.52	00.45			
75		52.29	18299.47			
75			98.49			

* The lines overlapped by other band lines are marked by one asterisk.
** The badly blended lines are marked by two asterisks.

Table II

Wavenumbers of band lines of the $^1\Phi - A^1\Delta$ system

J	0—0		1—1	
	R	*P*	*R*	*P*
2			17505.79	
3		17560.78	06.32	17501.45
4	17566.34	60.03	06.90	00.73
5	66.90	59.17	07.58	17499.97**
6	67.47	58.27	08.14	99.02
7	68.01	57.52**	08.56	98.13
8	68.51	56.59*	09.12	97.21
9	69.03	55.65*	09.55	96.29
10	69.50	54.68	09.98	95.47
11	69.95	53.77	10.46*	17494.47
12	70.38	52.78	10.85*	93.47
13	70.77	51.78	11.23*	92.39
14	71.16	50.75	11.59*	91.38
15	71.49	49.68	11.94*	90.28
16	71.79*	48.64	12.26*	89.23
17	72.10*	47.52	12.55^{al}	88.13
18	72.45*	46.40	12.78*	86.99
19	72.67*	45.25	12.99*	85.95**
20	72.90*	44.09	13.25*	84.68
21	73.13*	42.90	13.44*	83.47
22	73.30*	41.69	13.63*	82.25
23	73.48*	40.46	13.78*	81.00
24	73.62*	39.20	13.91*	79.73
25	73.76*	37.92	13.91*	78.44
26	73.82*	36.62	14.01*	77.11
27	73.98^{h**}	35.29	14.10^{h}	75.78
28	73.98^{h}	33.91	14.10^{h}	74.40
29	73.98^{h}	32.56	14.10^{h}	73.02
30	73.98^{h}	31.15	14.10^{h}	71.61
31	73.98^{h}	29.74	14.01*	70.18
32	73.98^{h}	28.29	13.91*	68.69
33	73.82*	26.82	13.78*	67.22
34	73.76*	25.33	13.78*	65.69
35	73.62*	23.82	13.63*	64.13
36	73.48*	22.29	13.44*	52.59

Table II (continued)

J	0—0		1—1	
	R	P	R	P
37	73.30*	20.70	13.25*	60.99
38	73.13*	19.12	12.99*	59.47
39	72.90*	17.52	12.78*	57.83
40	72.67*	15.89	12.55*	56.17
41	72.45*	14.23	12.26*	
42	72.10*	12.55	11.94*	
43	71.79*	10.85		
44	71.43	09.12		
45	71.06	07.38		
46	70.66	05.61		
47	70.25	03.82		
48	69.80	01.99		
49	69.34	00.15		
50	68.85	17498.28		
51	68.33	96.39		
52	67.79	94.47		
53	67.22	92.53		
54	66.62	90.55		
55	66.02	88.57		
56	65.35	86.57		
57	64.65	84.52		
58	64.09[p]	82,45		
59	63.31	80.33		
60	62.55	78,36[p]		
61	61.78	76.16		
62	60.96	73,97		
63	60.15	71,79		
64	59.31	69,57		
65	58.43	67.36		
66	57.52*	65.23**		
67	56.59*	62.79		
86	55.65*	60.53		
69	54.68*	58.19		
70	53.65	55.83		

* The lines overlapped by other band lines are marked by one asterisk.
** The badly blended lines are marked by two asterisks.
[h] The lines forming the band head are marked by "h".
[p] — perturbed
al — atomic line

The 568.87 and 570.81 nm bands assigned to the 0—0 and 1—1 bands, respectively, of the $^1\Delta - A^1\Delta$ transition consist of two single branches R and P. Wavenumbers of band lines are given in Table II. The numbering was established by finding an agreement between $\Delta F''(J)$ values of the 0—0 and 1—1 bands of two systems analyzed. The rotational structure corresponds to the transition with $\Delta\Lambda = 0$. The assignment of bands to the $^1\Delta - A^1\Delta$ transition is based on the fact that the two systems have the lower state in common. Table II shows that in this case some of first lines of transition have been measured, too. The $R(58)$ and $P(60)$ lines are shifted from the regular courses of branches, so the $J' = 59$ level is perturbed. Molecular constants have been calculated by least-squares technique using the following equations:

$$\Delta_2 F = 4\,B\left(J + \frac{1}{2}\right) - 8D\left(J + \frac{1}{2}\right)^2, \tag{1}$$

$$R(J-1) + P(J) = 2\nu_2 + 2\,(B' - B'')\,J^2 - 2(D' - D')\,J^2\,(J+1)^2. \tag{2}$$

Table III

Molecular constant of ScF

Assignment	ν_0	B'	$D'\ 10^7$	B''	$D''\ 10^7$
'φ — 'Δ 0—0	18361.64 (1)	0.36200 (4)	4.96 (6)	0.36347 (4)	4.53 (6)
'φ — 'Δ 1—1	18336.46 (1)	0.3583 (2)	3.4 (9)	0.3607 (2)	2.7 (8)
'Δ — 'Δ 0—0	17563.02 (1)	0.35201 (4)	4.14 (6)	0.36359 (4)	4.70 (6)
'Δ — 'Δ 1—1	17503.70 (1)	0.3485 (2)	1.8 (14)	0.3607 (2)	2.7 (7)

The figures in parentheses are the accuracy in the last digit which corresponds to two standard derivations.

In Table III the molecular constants B'' and D'' have been obtained from Eq. (1), the constants B' and D' have been calculated using these B'' and D'' values and the appropriate differences $B' - B''$ and $D' - D''$, determined with much better accuracy from Eq. (2) than from the corresponding combination differences. The band origins of the $^1\Phi - A^1\Delta$ system calculated using Eq. (2) are equal within the error limit of measurements to the wavenumbers of measured Q-heads.

Discussion

The rotational analysis of the 544.47 and 545.21 nm band has shown that the lower state of transition is not the $a^3\Delta$ state as was supposed in [5]. The rotational constants in the lower state differ substantially from those of the $a^3\Delta$ state [3], [5]. The intensity distribution in this group of bands is reasonable for a diagonal group of a singlet system, but cannot be explained if these bands are components of triplet transition. Moreover if in the 544.4 nm group of bands one more very weak band can be measured, it is easy to measure five bands with gradually decreasing intensity in the diagonal group of $^1\Delta$ — — $A^1\Delta$ system.

The rotational structure of the 544.47 and 545.21 nm bands is identical. In case of the assignment of these bands $\Pi_2 - {}^3\Delta_3$ and $^3\Pi_1 - {}^3\Delta_2$, as was suggested in [5], Π-doubling of lines should be expected in the 545.21 nm band. The Q-head of the 546.0 nm band is single but in the case of triplet transition it should be doubled due to large Λ-doubling in the $^3\Pi_0$-component.

The 544.47 and 545.21 nm bands were obtained in absorption in [5]. Apparently, this was the reason for the erroneous assumption that the lower state must be the $a^3\Delta$ state. On the other hand, this fact permits to conclude that the lower $^1\Delta$ state is the first excited singlet state of scandium monofluoride of configuration $3d\delta\ 4s\sigma$.

Acknowledgement

The authors are grateful to Prof. I. Kovács and Prof. L. Gurivch for many informative discussions.

REFERENCES

1. А. В. Гурвич, Е. А. Шенявская, Оптика и спектр., **14**, 307, 1963.
2. R. F. Barrow, W. J. M. Gissane, R. C. Bargy, G. V. M. Rose and P. A. Ross, Proc. Phys. Soc., **83**, 889, 1964.
3. R. F. Barrow and W. J. M. Gissane, Proc. Phys. Soc., **84**, 615, 1964.
4. D. McLeod and W. Weltner, J. Phys. Chem., **70**, 3293, 1966.
5. R. F. Barrow, M. W. Bastin, D. L. G. Moore and C. J. Pott, Nature, **215**, 1072, 1967.
6. Е. А. Шенявская, А. А. Мальцев, Л. В. Гурвич, Вестник Моск. Ун-та, Химия, № **4**, 104, 1967.
7. K. D. Carlson and C. Moser, J. Chem. Phys., **46**, 35, 1967.
8. R. F. Barrow and L. G. Pedersen, J. Phys. B, **4**, L-11-L-12, 1971.
9. P. R. Scott and W. G. Richards, Chem. Phys. Lett., **28**, 101, 1974.
10. L. Brewer and D. W. Green, High Temp. Sci., **1**, 26, 1969.

Acta Physica Academiae Scientiarum Hungaricae, Tomus 49 (4), pp. 391–398 (1980)

THE INFLUENCE OF AGGREGATES ON THE CRITICAL YIELD STRESS OF NaCl : M²⁺ CRYSTALS

By

J. Sárközi and P. Kálmán

DEPARTMENT OF EXPERIMENTAL PHYSICS, INSTITUTE OF PHYSICS, TECHNICAL UNIVERSITY
1521 BUDAPEST, HUNGARY

(Received 10. IV. 1980)

The connection between the structure of aggregates and the critical yield stress of NaCl : M^{2+} crystals was investigated. The fast and slow cooling of samples produces critical yield stress — impurity concentration functions of different forms. The fast cooling of samples doped with Sr^{2+} and Ca^{2+} produces dimers and the slow cooling results in greater aggregates. For the other impurities (Mg, Mn, Cd, Pb, Ba) not even the fast cooling produces dimers and the critical yield stress increment is due to greater aggregates for both cooling rates.

Introduction

In alkali halide crystals doped with divalent impurities the cation vacancies and the divalent impurities form pairs, so-called dipoles [1]. The elastic interaction between moving dislocations and dipoles considerably influences the critical yield stress of the crystal above 1At-ppm impurity concentration [2]. In heavily doped crystals the dipoles form dipole groups (aggregates) after appropriate heat treatment. The presence of aggregates also increases the critical yield stress of the crystal. The aggregation process is generally investigated with the aid of thermal depolarisation and dielectric loss measurements [3, 4, 5, 6, 7]. In investigations of aggregation kinetics it was found by Dryden and his co-workers [8] that an aggregate contains three or more dipoles except in cases where the aggregate is built up of Sr^{2+} or Ca^{2+} impurities. The thermal depolarisation [6] and the dielectric loss [7, 8] measurements indicate that the aggregates which are formed from the above mentioned impurities contain only two dipoles. This type of aggregate is called dimer.

The purpose of our work is to investigate the dimer formation and disappearence measuring the critical yield stress of differently doped crystals. The crystals were grown under special circumstances, thus the quantities of OH^- ion groups and other anion impurities are negligibly small as compared to the divalent impurity content [9]. This fact is very important because the unwanted anion impurities, especially the OH^- ion groups, can react with the cation impurities making the evaluation of the effect of the divalent impurity on the critical yield stress unreliable.

Experimental results

The critical yield stress was measured at room temperature with the aid of an Instron instrument after heat treatment of the crystal. The experiments were carried out with specially grown OH^- free NaCl crystals. The samples were doped with Mg, Mn, Cd, Sr, Ca, Pb and Ba so that each sample contained only one kind of cation impurity. The impurity concentration varied in the range of 1—1000 ppm. Furthermore we had at our disposal a specially pure NaCl crystal in which the concentrations of the different divalent impurities remained under 0.2 ppm. The OH^- free pure crystal and the samples doped with different impurities had been grown by the Research Group for Crystal Physics of the Hungarian Academy of Sciences [9]. The heat treatments, the annealing and quenching of the crystals were carried out in a furnace of low heat capacity filled with inert gas atmosphere.

As a first step the cooling rate (v) dependence of the critical yield stress was determined for differently doped samples cooled from 600 °C to room temperature. The cooling rates applied in our experiments always remained under the critical value at which stresses and plastic deformations occur in the samples, consequently the dislocation density remained unchanged all the time. Thus the changes in the critical yield stress caused by quenching can be brought into unambiguous connection with the change of state of the cation impurities. It was found that below 100 ppm impurity concentration the critical yield stress τ measured at room temperature did not show any cooling rate dependence which appeared only above the 100 ppm limit. Let τ and τ_0 be the critical yield stresses of the doped and the pure crystals, respectively, and τ_A the impurity sensitive part of the critical yield stress. The function $\tau_A(v)$ has the same character in the case of different kinds of impurities and at different impurity concentrations as well, therefore to illustrate the form of τ_A we give one example only (Fig. 1), which shows the $\tau_A(v)$ function of the sample containing 700 ppm Sr^{2+}. τ_A hardly increases with the cooling rate in the low cooling rate range but at a certain value, which depends weakly on the impurity concentration τ_A becomes rapidly increasing, then above another value of the cooling rate it remains again insensitive to the cooling rate variation (See Fig. 1). The existence of three sections in $\tau_A(v)$ with obviously different characters suggests that a moving dislocation is obstructed by two different mechanisms caused by aggregates of different types due to quenching with different rates. Presumably, τ_A is essentially determined by one type of obstructing centres at low rates and by the other type of centres at high rates. In the mean cooling rate range τ_A results from the competition between the different obstructing effects.

In the second step the dependence of the critical yield stress on the impurity concentration (C) was investigated. The $\tau_A(C)$ function was determined

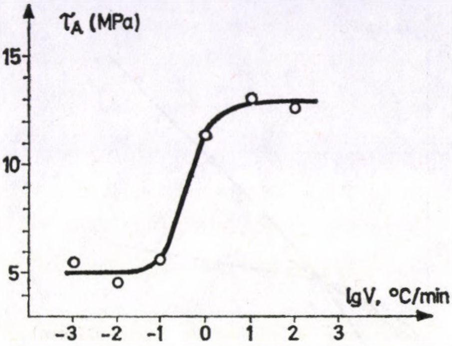

Fig. 1. The cooling rate dependence of the critical yield stress in a sample doped with 700 ppm Sr^{2+}

in the case of each impurity mentioned above at two fixed cooling rates v_1, v_2 corresponding to the low and to the high cooling rate ranges. It was found that $\tau_A(C)$ had different shapes at low and high cooling rates. This fact agrees with the above assumption that $\tau_A(C)$ is caused by different interaction mechanisms between the dislocation and the various types of aggregates produced at low and high cooling rates. In other words this means that at slow and fast cooling different types of obstacles originate from the dipoles. The character of $\tau_A(C)$ depends on the type of the impurity too.

To demonstrate the above assertions some of the measured $\tau_A(C)$ functions are given in Figs. 2a, 2b and 3a, 3b. The curves 1, 2 in Fig. 2a are the $\tau_A(C)$ functions corresponding to the fast and slow quenching ($v_1 = 10$ °C/min and $v_2 = 0.1$ °C/min) in $NaCl : Sr^{2+}$, respectively. Both curves are given as the function of $\sqrt{C}$ in Fig. 2b, too. The Ca impurity produces $\tau_A(C)$ similar to the curves plotted in Figs. 2a, 2b. For the remaining impurities (Mn, Mg, Cd, Pb, Ba) the $\tau_A(C)$ functions have identical forms, therefore it is sufficient to plot, for instance, the $\tau_A(C)$ of the $NaCl : Pb^{2+}$ systems shown in Figs. 3a, 3b where the numbering is the same as before.

At last the samples of high τ_A, which were obtained at high cooling rate and have the curves 1 in Figs. 2 and 3, were annealed at various annealing temperatures for different annealing times. We always wanted to measure the critical yield stress at room temperature, therefore the samples were quenched from the constant annealing temperature T_a ($100\ °C < T_a < 150\ °C$) to room temperature and so in all probability, the aggregate form corresponding to the annealing temperature and time was frozen in our samples.

The kinetic curves (Figs. 4a and 4b) show the alterations of the frozen aggregates in $NaCl : Sr^{2+}$ and $NaCl : Pb^{2+}$ systems. They describe the critical yield stress vs annealing time. We give the results of the annealing measurements carried out for samples of 700 ppm Sr^{2+} and 750 ppm Pb^{2+} impu-

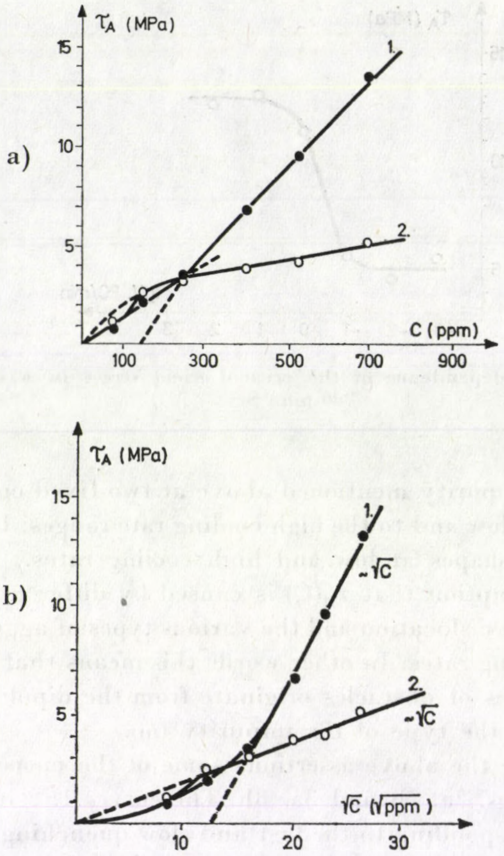

Figs. 2a, b. **The impurity concentration dependence of the critical yield stress for Sr^{2+} with fast (curve 1) and slow (curve 2) cooling**

rity contents (Figs. 4a and 4b, respectively). Similar curves were obtained measuring samples of other impurity contents.

Discussion

Theoretically, at constant temperature the critical yield stress is due to the elastic interactions between moving dislocations and aggregates containing Z dipoles [10]. Correspondingly, τ_A is given by the following formula

$$\tau_A = P\sqrt{\alpha C_Z}\,, \tag{1}$$

where P and α are appropriate constants [10] and C_Z is the aggregate concentration, which can be expressed in terms of the divalent impurity concentration C. According to DRYDEN and his co-workers [8] the crystals contain aggre-

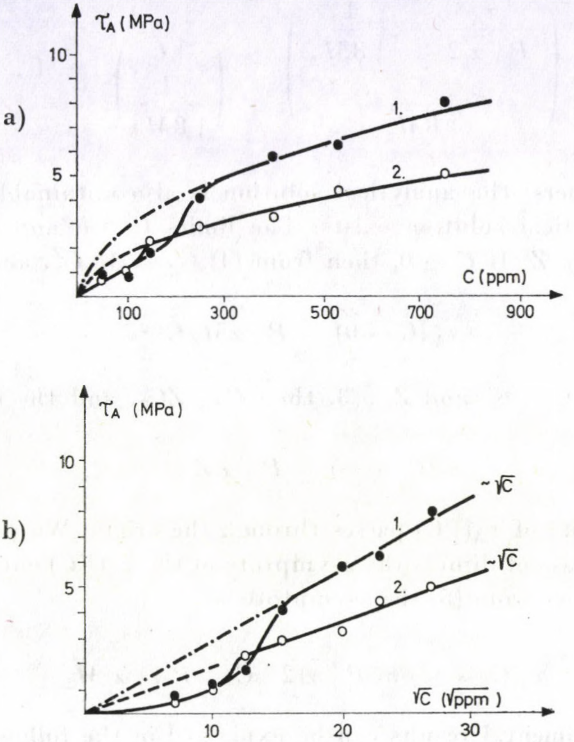

Figs. 3a, b. **The impurity concentration dependence of the critical yield stress for the Pb^{2+} with fast (1) and slow cooling (2)**

gates, made up of a definite number of dipoles (Z), with concentration C_Z and also dipoles with concentration C_D. Owing to the law of mass action the following relation is valid between concentrations C_Z and C_D

$$C_Z = M_Z C_D^Z, \tag{2}$$

where M_Z is the constant in the law of mass action. The total concentration of the divalent impurity is

$$C = C_D + ZC_Z\,. \tag{3}$$

Hence and from (3):

$$C = (C_Z/M_Z)^{1/Z} + ZC_Z\,. \tag{4}$$

Using the Eqs. (1) and (4) one can get τ_A as the function of the impurity concentration. In the case of dimers ($Z = 2$) the $\tau_A(\sqrt{C})$ function is a hyperbola:

$$\left(\frac{\dfrac{\tau_A}{P\sqrt{\alpha/2}}+\dfrac{1}{\sqrt{8M_2}}}{\dfrac{1}{\sqrt{8M_2}}}\right)^2-\left(\frac{\sqrt{C}}{\dfrac{1}{\sqrt{8M_2}}}\right)^2=1\,. \tag{5}$$

For $Z = 3$ (trimers) the analytical solution is also obtainable but for cases $Z > 3$ no analytical solution exists. The limits $C \to 0$ and $C \to \infty$ can be discussed for any Z. If $C \to 0$, then from (4) $C_Z = M_Z C^Z$, and the asymptotical τ_A reads

$$\tau_A\,(C \to 0) = P\sqrt{\alpha M_Z}\,C^{Z/2}.$$

Furthermore if $C \to \infty$ and $Z \geq 3$, then $C = ZC_Z$, and the equation of the asymptote is

$$\tau_A(C \to \infty) = P\sqrt{\alpha/Z}\sqrt{C}\,.$$

i.e. the asymptote of $\tau_A(\sqrt{C})$ passes through the origin. We can see from Eq. (5) that in the case of dimers the asymptote of the $\tau_A(\sqrt{C})$ curve has non zero axial sections since from (5) the asymptote is

$$\tau_A(C \to \infty) = P\sqrt{\alpha/2}\sqrt{C} - P/4\sqrt{\alpha/M_2}\,.$$

Our experimental results can be explained in the following manner. In Fig. 2b the asymptote of curve 1 does not pass through the origin and this refers to dimers. The asymptote of curve 2 in Fig. 2b and simultaneously the asymptote of curves 1 and 2 in Fig. 3b pass through the origin, i.e. in these cases $Z \geq 3$. The fact that the asymptote of curve 1 relates to Eq. (5) does not mean that the curve follows Eq. (5) throughout. Indeed, τ_A is proportional to the impurity concentration at low concentrations for all the impurities as can be seen from Figs. 2a and 3a. Theoretically it can be assumed [10] that in these cases τ_A is determined by the Snoek effect of single dipoles. At not too low concentrations the critical yield stress increment of samples doped with Sr and Ca is caused by dimers after fast cooling and by aggregates containing three or more dipoles after slow cooling. The Mn, Mg, Pb, Cd and Ba increase the critical yield stress after fast cooling more strongly than after slow cooling and in both cases the occurring aggregates contain three or more dipoles. Presumably, the fast cooling brings about aggregates, which are smaller and are dispersed more densely than the aggregates produced by slow cooling. From our experimental results we can give those points of curves $\tau_A(C)$ at which the effect of a given dipole association stops or at which the effect of another one starts. For instance, the τ_A of fastly cooled samples containing more than 250 ppm Sr^{2+} are determined by dimers but below this concentration single dipoles are responsible for τ_A. Similarly the τ_A of the slowly cooled samples doped above 100 ppm Sr^{2+} are determined by aggregates consisting of three or more dipoles.

The kinetic curves can be explained as follows. If that portion of the critical yield stress which depends on the number of a certain kind of obstacles decreases during annealing, then this means also the decrease of the number of the given aggregate, e.g. the decrease of τ_A in Fig. 4a denotes the decrease of the dimer number. Thus with the aid of annealing of the crystal we can pass over from curve 1 in Fig. 2a to curve 2. According to theory, this fact indicates the dissociation of dimers and the association of larger aggregates. We can also pass over from curve 1 in Figs. 3 to curve 2 as it is proved by the graphs of annealing in Fig. 4b. This observation may be interpreted by step-by-step dissociation of small aggregates and the simultaneous building up of larger ones.

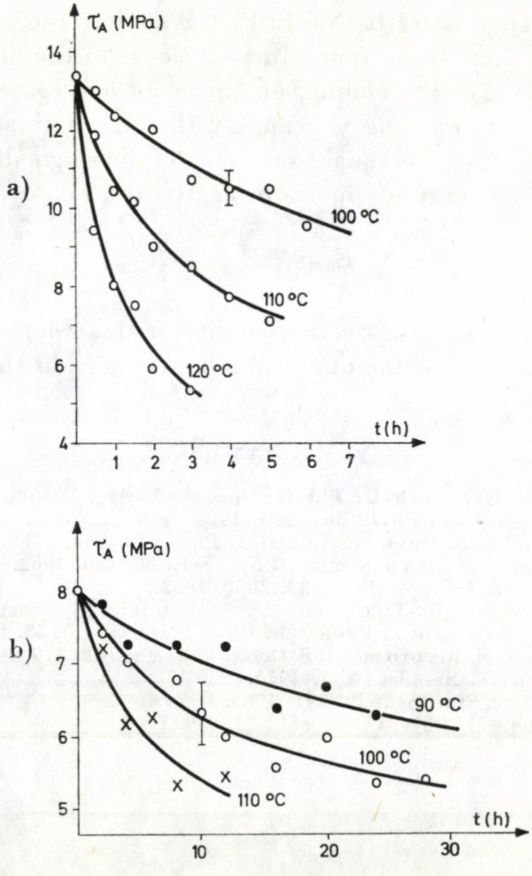

Figs. 4a, b. **The kinetic curves, i.e. the critical yield stress vs annealing time of samples doped with Sr^{2+} (a), Pb^{2+} (b)**

The order of kinetics and the binding energy of disappearing dipole groups can be determined from the kinetic curves (Figs. 4a, b). The numerical evaluation of the graphs confirms the above described annealing mechanism. Each curve in Figs. 4a, 4b has an exponential time dependence. It means that the kinetics is of first order in all cases. The activation energies obtained from the curves are 1.66 eV and 1.40 eV in NaCl : Sr^{2+} and NaCl : Ca^{2+} systems, respectively. The known theoretical calculation for binding energies of different dipole groups (dimers, trimers) has been made in point charge approximation [11] and it has yielded 0.4 eV for the binding energy between the two dipoles in dimers. The diffusion energy of dipoles is 1 eV for Sr, and 0.92 eV for Ca. In the case of Ca the sum of the binding energy and the dipole diffusion energy equals the activation energy obtained (see above) but in the case of Sr deviation arises. One possible reason for this is probably the type of the impurity upon which the dimer binding energy depends. Thus the calculation for the binding energy cannot be satisfactory in point charge approximation. The kinetics is of first order in NaCl : Pb^{2+} systems, too, where the activation energy ($E_{\mathrm{act}} = 1.08$ eV) is approximately equal to the dipole diffusion energy ($E_{\mathrm{diff}} = 1.0$ eV), i.e. the binding of dipoles in aggregates larger than dimers is very weak. Summarizing we can say that the activation energy obtained from the kinetic curves is equal to the sum of the single dipole diffusion energy and the binding energy of dipoles in aggregates, i.e.

$$E_{\mathrm{act}} = E_{\mathrm{diff}} + E_{\mathrm{bind}} \, .$$

We should like to investigate the validity of this relation with the aid of an atomistic calculation of the dimer binding energies in the near future.

REFERENCES

1. A. B. LIDIARD, Handbuch der Physik, Springer Verlag, Berlin, **20,** p. 246, 1957.
2. J. J. GILMAN, J. Appl. Phys., **36,** 3195, 1965.
3. J. S. COOK and J. S. DRYDEN, Austral J. Phys., **13,** 960, 1960.
4. J. S. COOK and J. S. DRYDEN, Proc. Phys. Soc., **80,** 479, 1962.
5. W. G. JOHNSTON, J. Appl. Phys., **33,** 2050, 1962.
6. P. W. M. AH MEE HOR-JACOBS and K. S. MOODIE, Phys. Stat. Sol. (a), **38,** 293, 1976.
7. M. DUBIEL, G. BERG and F. FRÖHLICH, Phys. Stat. Sol. (a), **55,** 153, 1979.
8. J. S. DRYDEN, S. MARIMOTO and J. S. COOK, Phil. Mag., **12,** 379, 1965.
9. R. VOSZKA, Fizikai Szemle, **20,** 1, 1970.
10. W. FRANK, Phys. Stat. Sol., **29,** 391, 1968.
11. J. H. CRAWFORD, J. Phys. Chem. Sol., **31,** 339, 1970.

Acta Physica Academiae Scientiarum Hungaricae, Tomus 49 (4), pp. 399–405 (1980)

STUDIES ON POINT DEFECT STRUCTURES OF NaCl : Mn⁺⁺ AND NaCl : Sr⁺⁺ SINGLE CRYSTAL SYSTEMS

By

J. SÁRKÖZI, K. ORBÁN, P. KÁLMÁN and A. TÓTH

DEPARTMENT OF EXPERIMENTAL PHYSICS, INSTITUTE OF PHYSICS, TECHNICAL UNIVERSITY
1521 BUDAPEST, HUNGARY

(Received 10. IV. 1980)

The temperature-dependent impurity distribution of NaCl : Sr^{++} and the NaCl : Mn^{++} systems was studied by using the measuring methods of microhardness, flow stress, conductivity and the gold decoration method. The results show that with increasing quenching temperature the measured values of mechanical and electrical characteristics increase monotonously up to a point characterized by the impurity. This is in accordance with our decoration studies; the impurities dissolve gradually into the lattice with increasing temperature. In the NaCl : Sr^{++} system there are needle-like precipitates whereas the NaCl : Mn^{++} system produces rectangular parallelepipedons. The size of these formations decreases with increasing quenching temperature.

Introduction

It is particularly important to know the point defect structure of real crystals at different temperatures when one studies properties depending on impurities. The majority of the experimental methods are indirect, e.g. the measurement of conductivity [1] and density [2, 3], however, there are direct methods as well, e.g. the electron microscopic decoration which allows the topographic study of separate formations developed by impurities [4]. This method is based on the fact that the defects of the crystal surface formed by impurity ions, vacancies or some combinations of them are favourable for the crystallization of the decorating gold particles. In our work we applied the indirect methods of microhardness, ionic conductivity and the above mentioned direct method of decoration.

Experimental methods

The modification of the point defect structure was carried out by quenching the crystals from different temperatures. We supposed that by this method the impurity distribution formed at the quenching temperature is in good approximation preserved at room temperature. The samples were cooled at a constant rate (100 °C/min) from different annealing temperatures in the evaporating equipment at a pressure of 1 Pa to room temperature and first gold, afterwards carbon was evaporated onto the crystal surface. The gold particles nucleated according to the structure of the crystal surface on the produced thin carbon film which was taken off from the surface and studied in the electron microscope.

The other part of the identical samples was quenched to room temperature at the above mentioned rate and pressure in a furnace of small heat capacity. On the furnace-quenched samples Vickers-hardness measurements with a load of $4 \cdot 10^{-2}$ N and flow stress measurements were carried out at room temperature. The purpose of the former was to obtain knowledge of the surface hardening effect of the impurity distribution changes and of the latter to study the bulk effects. Simultaneously the conductivity of the samples was measured as well.

We used in our measurements specially grown [5], extremely pure (impurity contents are less than 10^{-7} mol/mol) crystals and OH^- free crystals doped with divalent ions (Mn^{++}, Sr^{++}). The Sr^{++} and Mn^{++} impurity concentration was about $0.5 \cdot 10^{-3}$ mol/mol.

The impurity distribution was modified by tempering the crystals for hours together at temperatures higher than 100 °C. The temperature-dependent impurity precipitation does not vary after the necessary developing time with further annealing. The gold decoration method was used for making the precipitates visible. The size of our samples was $3 \times 3 \times 6$ mm.

In the course of annealing and quenching (with appropriately chosen quenching rate) the samples were not deformed plastically, so the dislocation density remained constant, thus their role in the variation of microhardness, conductivity and flow stress due to the heat treatment was considered negligible.

Experimental results, conclusions

The changes of microhardness ($H(T_q)$), flow stress ($\tau(T_l)$) and conductivity ($\sigma(T_q)$) due to quenching in the case of NaCl : Sr^{++} system are illustrated in Figs. 1a, 1b, 1c and 2 (curve 1). The NaCl : Mn^{++} system produced similar curves. Apparently, there are no marked differences in the character of the three curves for neither of the two systems. Only the concrete values and the saturation quenching temperatures differ. The places of breaks in the curves of Fig. 2, i.e. the joining parts of the association and precipitation controlled conductivity correspond to the saturation temperatures (in the case of NaCl : Sr^{++} 350 °C, at NaCl : Mn^{++} 300 °C). The fact that the measured small load microhardness and flow stress values vary similarly with temperature proves that the point defect formations on the surface and within the crystal do not differ from each other. This means that the information obtained by the decoration method for the surface is valid for the whole bulk

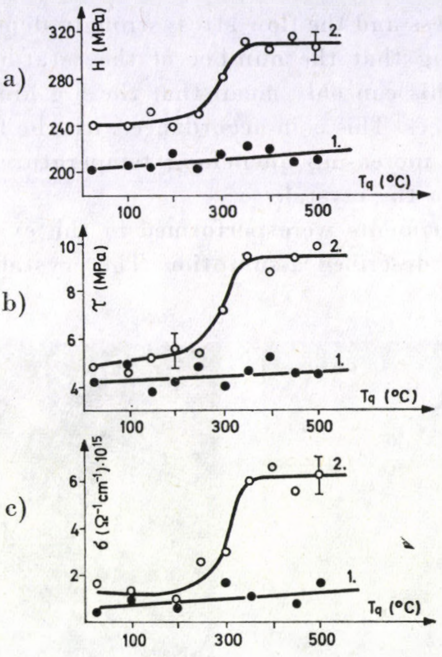

***Fig. 1.* The variation of microhardness, flow stress and conductivity as function of the quenching temperature. Curves 1 — pure NaCl, curves 2 — NaCl : Sr⁺⁺ system**

material. The mechanical and the electrical properties of the pure crystal (Figs. 1a, 1b, 1c, curves 1) are independent of the quenching temperature. This is in accordance with our assumption that the changes of the measured quantities are tightly connected with the changes in the state of the impurity.

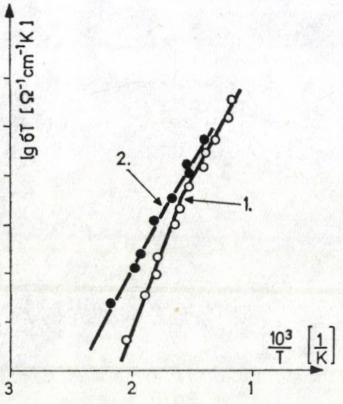

***Fig. 2.* lg σT — T curves of the NaCl : Sr⁺⁺ (curve 1) and of the NaCl : Mn⁺⁺ (curve 2) systems**

The microhardness and the flow stress strongly depend on the annealing temperature suggesting that the number of the retarding centres increases with increasing T_q. This can only mean that the big hindering centres go to small but efficient pieces. This is in accordance with the fact that the conductivity increases with increasing quenching temperature, i.e. the impurities dissolve gradually into the crystal.

Quenching experiments were performed in the evaporation equipment for testing the above described assumption. The crystals were tempered for

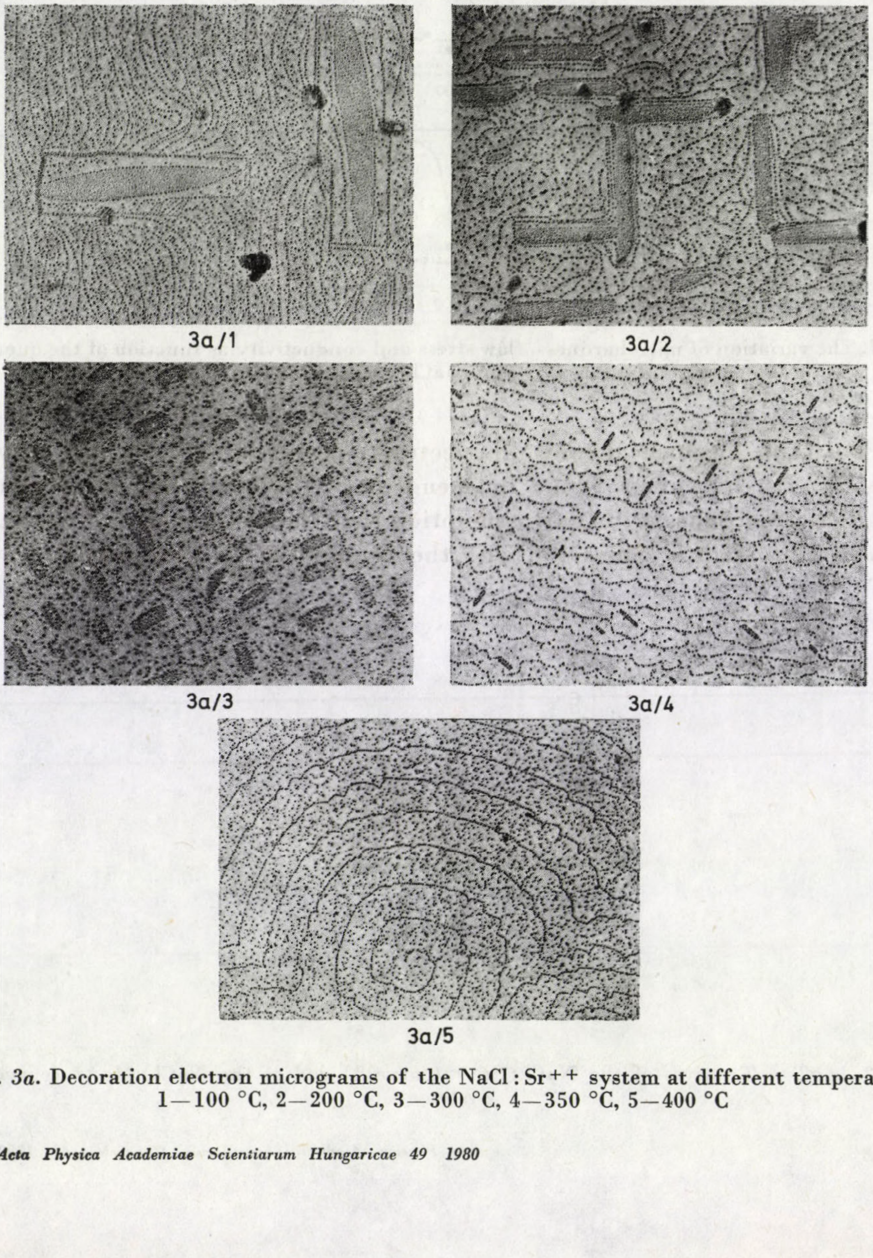

3a/1 3a/2

3a/3 3a/4

3a/5

Fig. 3a. Decoration electron micrograms of the NaCl : Sr^{++} system at different temperatures 1—100 °C, 2—200 °C, 3—300 °C, 4—350 °C, 5—400 °C

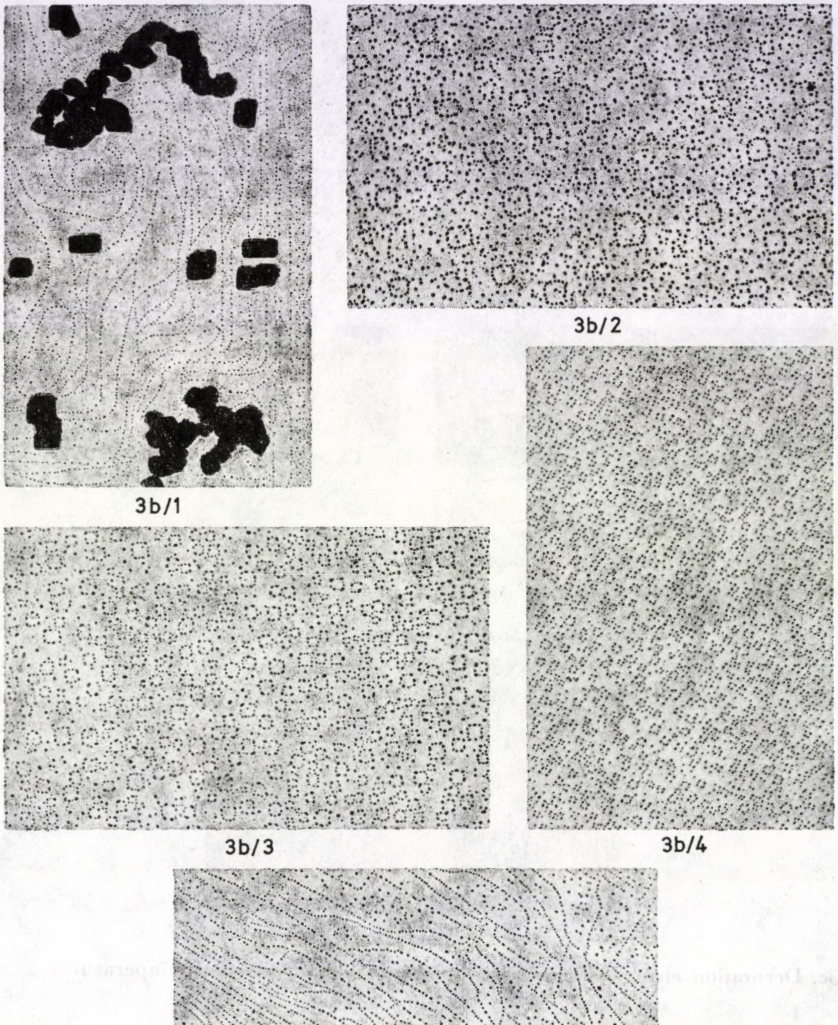

3b/1

3b/2

3b/3

3b/4

3b/5

Fig. 3b. Decoration electron micrograms of the NaCl:Mn^{++} system at different temperatures: 1—100 °C, 2—200 °C, 3—300 °C, 4—350 °C, 5—400 °C

hours, then cooled to room temperature, afterwards gold and carbon was evaporated on their thermally demolished surface. The carbon layer with the gold particles, distributed according to the surface structure, was separated from the crystal and was studied in the electron microscope.

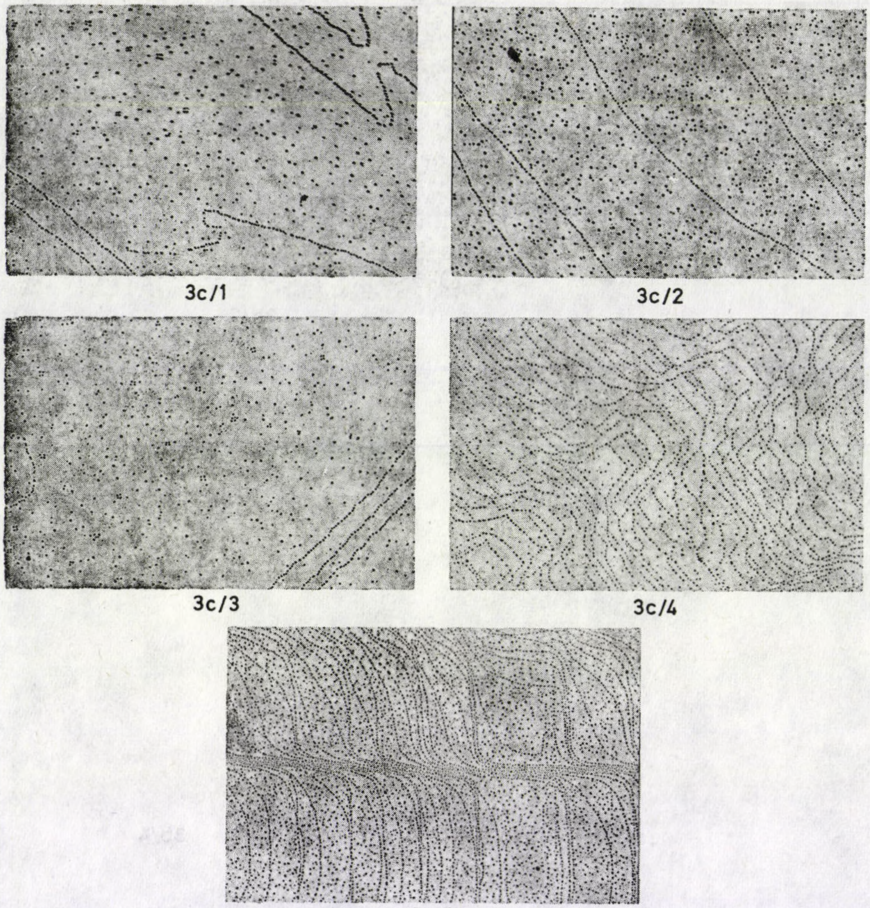

3c/1 3c/2 3c/3 3c/4 3c/5

Fig. 3c. Decoration electron micrograms of pure NaCl at different temperatures: 1—100 °C, 2—200 °C, 3—300 °C, 4—350 °C, 5—400 °C

The results are shown in Fig. 3 for different quenching temperatures (100 °C, 200 °C, 300 °C, 350 °C, 400 °C) and for the two kinds of impurities (Fig. 3a NaCl : Sr^{++}, Fig. 3b NaCl : Mn^{++}). The photographs prove the gradual dissolution of the impurity with increasing temperature. The size of precipitates is smaller and smaller with higher temperature and at 350 °C (NaCl : Mn^{++}) and 300 °C (NaCl : Sr^{++}) respectively they vanish by dissolving into the lattice. Using the extremely pure crystal we could not observe any oriented formations on the surface (Fig. 3c). The precipitated particles are different for the two impurities studied. The precipitation of Sr^{++} appears as needle-like formations in the $< 110 >$ direction. In the case of Mn^{++} rectangular parallelepipedons are formed with edges in the $< 100 >$ direction. The length of the needles is 1—10 μm and the length of the parallelepipedons is approx. 0.1 — 1 μm. The revealed shapes and sizes agree with the results of other technics [6]. According to the latter paper there is a second phase ($SrCl_2$) in the NaCl lattice. In the case of Mn^{++} the presence of the so-called Suzuki phase ($6NaCl : MnCl_2$) in the NaCl single crystal [7] is proved. Our experiments seem to prove the existence of this phase in the $NaCl : Mn^{2+}$ system.

The surface replica method used by us provides limited information as compared e.g. to the X-ray diffraction procedure. In spite of this, the decoration method is a simple but useful way to reveal the impurity precipitation and to follow the process of changing the shape of precipitates caused by heat treatment.

REFERENCES

1. S. Kupca, M. Hartmanova and G. Vlasák, Czechosl. J. Phys., **B19**, 789, 1969.
2. G. A. Andrejev, Fiz. Tverd. Tela **7**, 183, 1965.
3. M. Debes and F. Fröhlich, Crystal Lattice Defects, **2**, 55, 1961.
4. G. I. Distler, V. Lebedeva, V. V. Moskvin, E. I. Kortukova, Kristallografiya, **15**, 1049, 1970.
5. R. Voszka, I. Tarján, L. Berkes and J. Krajsovszky, Kristall und Technik, **1**, 423, 1966.
6. M. I. Abajev and M. I. Kornfeld, Fiz. Tverd. Tela, **7**, 2809, 1965.
7. R. P. Harrison and C. W. Newey, Phil. Mag., **17**, 525, 1968.

temperatures. The [illegible] shape and size agree with the results of other methods [illegible]. According to the latter paper there is an ordered phase [illegible] in the [illegible] lattices in the case of [illegible] the presence of the so-called [illegible] parts [illegible] and [illegible] in the [illegible] crystal [illegible] phase. Our experiments seem to prove the existence of this phase in the [illegible] state [illegible]. The [illegible] method used [illegible] gives more information as compared e.g. to the X-ray diffraction procedure. In spite of this, the [illegible] method is a simple but useful way to reveal the [illegible] precipitation and to follow the [illegible] of changes the shape of precipitates caused by heat treatment.

REFERENCES

1. [illegible] and G. [illegible], [illegible] Phys. [illegible]
2. G. [illegible], Phys. Stat. [illegible]
3. M. [illegible] and [illegible], Crystal Lattice Defects, 1, 1969.
4. [illegible], Kristallografiya, 13, 109, [illegible]
5. [illegible]
6. M. [illegible] and [illegible], [illegible], 7, 209, [illegible]
7. R. [illegible] and C. W. [illegible], Phil. Mag., [illegible], 1965.

Acta Physica Academiae Scientiarum Hungaricae, Tomus 49 (4), pp. 407–414 (1980)

ATOMIC DISPLACEMENTS CAUSED BY DIVALENT IMPURITY-VACANCY PAIRS IN NaCl

By

P. KÁLMÁN, T. KESZTHELYI, A. TÓTH and J. SÁRKÖZI
DEPARTMENT OF EXPERIMENTAL PHYSICS, INSTITUTE OF PHYSICS, TECHNICAL UNIVERSITY
1521 BUDAPEST, HUNGARY

(Received 10. IV. 1980. — Revised version 11. IX. 1980)

The binding energies of divalent impurity ions and positive ion vacancies situated at the distance of next nearest neighbours and the atomic displacements around this type of lattice imperfections have been computed in NaCl crystals using the semiclassical Born—Mayer model of ionic solids. The procedure followed in calculating the binding energies of complexes containing Be, Mg, Ca, Sr, Ba, Zn, Cd, Hg and Pb was based on the method developed by REITZ and GAMMEL. The calculations were carried out with and without the inclusion of the Van der Waals interaction. The numerical results show that in agreement with the experimental data, the binding energy increases with the ionic radius of the impurity.

Introduction

In the alkali halides doped with divalent impurities there exist impurity — vacancy pairs, I—V dipoles. Their existence is of great importance in interpreting most of the crystal data e.g. the results of conductivity and diffusion measurements [1], therefore dissociation energies and the lattice distortion around certain I—V dipoles containing Ca^{2+}, Sr^{2+} and Cd^{2+} had been computed in an atomistic model [2, 3] on the ground of the MOTT—LITTLETON theory [4]. The purpose of our paper is to investigate theoretically the lattice distortion effect and the ground state binding energy of dipoles for every divalent impurity of practical importance.

The calculation method is the following. The displacement and the induced dipole moments of the nearest neighbours of a single impurity and an impurity — vacancy dipole were computed solving systems of nonlinear equations numerically. The two equations of the systems describe the statical force balance and the polarization of the nearest neighbours of the defect. The I—V dipole binding energy calculation is based on the method of REITZ and GAMMEL [2] i.e. the work necessary to remove a sodium ion from the closest vicinity of the divalent impurity to infinity was calculated and subtracted from the work necessary to create a single positive ion vacancy in the prefect lattice.

Interionic potentials

The potentials of the different types of interactions between the ions are as follows. The repulsion between two ions is due to the overlap of their electron clouds. Different kinds of repulsive potentials are available [5, 6]. We use the

Born—Mayer exponential formula [7] since the electron density on the periphery of the ions decreases exponentially and so it can be expected that the overlap potential may also be described by an exponentially decreasing function of the increasing interionic distance. The Born—Mayer repulsive potential is

$$\Phi = a_{ij}\, b \exp\left[(r_i + r_j - r)/\varrho\right], \tag{1}$$

where r_i, r_j are the corresponding ionic radii, r is the interionic distance, b and ϱ are parameters characteristic of the two ions. The constant a_{ij} is the Pauling factor

$$a_{ij} = 1 + z_i/n_i + z_j/n_j\,, \tag{2}$$

where z_i, z_j and n_i, n_j are the valencies and numbers of outer electrons in ions i and j. We use the ionic radii given by GOLDSCHMIDT [8]. Theoretically for fixed b the quantity ϱ is characteristic of the interacting ion pair. An attempt was made by TOSI and FUMI [9] to determine a set of repulsive parameters and ionic radii on the ground of the Born—Mayer theory of the crystal. We cannot use their results because the calculation was made only for the alkali and halide ions (alkali halide crystals) but for the alkali earth ions such calculation does not exist. Thus we use an average b and ϱ as was done by many of the authors [1, 2, 3] in the past ($b = 0.1429$ eV, $\varrho = 0.0345$ nm).

The potential of the Van der Waals interaction between the ions i, j is

$$\Psi = -c_{ij}/r^6 - d_{ij}/r^8\,, \tag{3}$$

where the coefficients c_{ij}, d_{ij} are [8]

$$c_{ij} = (3/2)\, h\alpha_i\, \alpha_j\, \nu_i\, \nu_j/(\nu_i + \nu_j)\,, \tag{4}$$

$$d_{ij} = c_{ij}(\alpha_i\, \nu_i + \alpha_j\, \nu_j)\, 2\pi/(\alpha_f\, c)\,. \tag{5}$$

c is the velocity of light and α_f is the fine structure constant. The quantities α_i, α_j are the electronic polarizabilities of the ions i, j and ν_i, ν_j are the frequency limits in their discrete spectra. The formulae (4) and (5) are valid only in the case of free ions. For crystals more accurate values of c_{ij} and d_{ij} may be derived from optical absorption data of the crystal. The Van der Waals coefficients of alkali halides were determined by MAYER [10] in this manner. In the case of alkali earth halides we have no c_{ij} and d_{ij} values based on optical absorption data therefore in this calculation we use formulae (4) and (5) for all the ions. However for the sake of better accuracy instead of the frequency limits of the free Na^+ and Cl^- ions we use the frequencies determined with the aid of (4) and (5) from the accurate c_{ij} and d_{ij} data of the NaCl crystal given by MAYER [10]. BOSWARVA [11] has given the corresponding ν_i values of ions Mg^{2+}, Ca^{2+},Sr^{2+} and Ba^{2+}. In the case of these alkali earth ions, the ν_i values of BOSWARVA and for the other types of divalent impurities the free ion frequency limits are used [12].

The electrical potential produced by a point charge q and a point like electric dipole moment μ is as usual

$$U = q/r + \boldsymbol{\mu}\mathbf{r}/r^3, \tag{6}$$

where $\mathbf{r}$ is a vector from the charge to a distant point and r is its absolute value.

Description of calculation

The ions in the lattice interact with each other as described above and each ion is in equilibrium at a lattice site of the perfect crystal. In the vicinity of defects the equilibrium is disturbed, the lattice becomes deformed and the distortion of the lattice may be characterized by ionic displacements from the original positions and for charged defects also by electronic dipole moments induced on the neighbouring ions.

For the determination of the displacements and dipole moments caused by charged point defects the cyrstal is usually divided into two regions [13]. Region I includes the defect and a certain number of surrounding ions, in our case the nearest neighbours. The displacements and dipole moments of the ions in region I are calculated simultaneously. In region II, which surrounds region I, the continuum theory is used.

The calculation has two steps. First the distortion and the dipole moments caused by a single impurity at (000) are computed in region I which contains the six nearest neighbours of the foreign ion (the ions 2, 3, 4, 5, 8 and 9 in Fig. 1). It follows from the symmetry of the NaCl lattice that the magnitudes of the displacement and induced dipole moment vectors of the ions 2, 3, 4, 5, 8 and 9 are equal. Thus we can use two independent variables, the absolute value of the displacements and that of the dipole moments, ξ and μ respectively. The outward displacement and dipole moment are $\xi = x_{++} \cdot r_0$ and $\mu = m_{++} \cdot er_0$ respectively, where r_0 is the anion — cation distance and e is the charge of the electron. The equations determining m_{++} and x_{++} are

$$F_e + F_r + F_{VW} = 0\,, \tag{7}$$

$$F_e - m_{++} e^2 r_0/\alpha_2 = 0\,, \tag{8}$$

where F_e, F_r and F_{VW} depending on m_{++} and x_{++} are the resultants of the electrostatic, repulsive and Van der Waals forces and α_2 is the electronic polarizability of the Cl^- ion. (The detailed formulae of F_e and F_r are given in

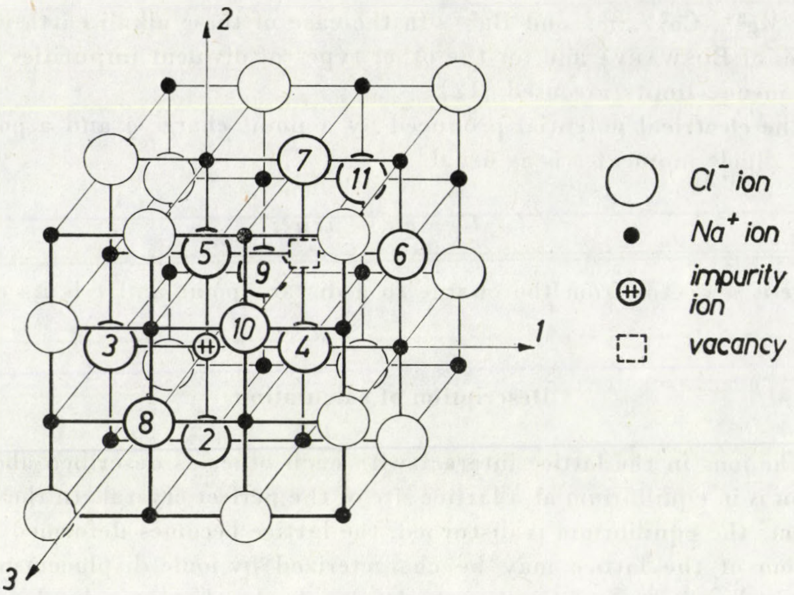

Fig. 1. The frame of reference and the ion numeration used in calculations

[1] p. 271–272). The F_{VW} contains the short range attraction between the displaced (100) ion and its twelve nearest neighbour chlorine ions. The interactions of ion (100) with the impurity and the oppositely placed sodium ion are included in F_{VW} too. The system of nonlinear equations (7) and (8) is solved numerically.

In the continuum region (region II) the charge of the defect induces dipole moments on the distant positive and negative ions due to electron and displacement polarizations. The induced dipole moments of Na^+ and Cl^- are respectively

$$\mu_+ = M'_+ e r_0^3/r^2, \tag{9}$$

$$\mu_- = M'_- e r_0^3/r^2, \tag{10}$$

where

$$M'_+ = \frac{1}{4\pi}\left(1-\frac{1}{\varkappa}\right)\frac{\alpha+\alpha_1}{1/2(\alpha_1+\alpha_2)+\alpha}, \tag{11}$$

$$M'_- = \frac{1}{4\pi}\left(1-\frac{1}{\varkappa}\right)\frac{\alpha+\alpha_2}{1/2(\alpha_1+\alpha_2)+\alpha'}. \tag{12}$$

α_1 and α_2 are the electronic polarizabilities of the positive and negative ions, $\varkappa$ and α are the static dielectric constant and the displacement polarizability of the crystal [1]. The induced dipole moments in region II act upon the ions in region I. This effect is also included in the electrostatic force F_e [1]. Using the solution of (7) and (8) the potential U_1 is computed at the lattice point (110), i.e. at the place of the sodium ion which will be removed. (See Fig. 1.)

The second step is to find distortion around the dipole. For the sake of simplicity it was assumed that each defect in the pair (the vacancy and the impurity) produces its own distortion and the resultant is built up by superposition of the individual distortions. The polarization of region II is neglected in this case because the I—V dipole is neutral. Thus the system of equations (7) and (8) is solved with $M'_+ = M'_- = 0$ in the cases of single impurity and single vacancy too. The absolute values of the displacement and the dipole moment vectors of the ions surrounding the impurity (2, 3, 4, 5, 8 and 9 in Fig. 1.) are denoted by x_D, m_D and the corresponding quantities of the ions surrounding the vacancy (4, 5, 6, 7, 9 and 11 in Fig. 1.) are denoted by x_V, m_V. The distortion of the I—V dipole is constructed from the displacements x_D, x_V in the following manner. The displacements of the two chlorine ions are the vector sums of the displacements x_D and x_V. The displacements of the ions 2, 3, 8 and 9 are x_D and the displacements of the ions 5, 7, 10 and 11 are x_V only. The dipole moments are calculated similarly. Using the above explained distortion the potential U_2 at point (110) is computed.

The potentials U_1, U_2 have three terms: the electrostatic, the repulsive and the Van der Waals ones. The electrical term in U_1 and U_2 has parts due to the displacements and induced dipole moments of the nearest neighbours and the polarization in region II, in U_2 the last term referred to is calculated so that the induced dipole moment μ_i at a lattice point i is computed from the expressions $\mu_i = \alpha_i \mathbf{E}_i$ [2] and the potentials of the induced dipoles are added. The summation was carried out over ions nearer to the point (110) than $4r_0$. The impurity is polarized by the vacancy and the potential caused by this dipole moment is included in U_2, too. The repulsive and attractive potentials at the point (110) produced by the ions in the above mentioned region are calculated and included in U_1 and U_2. The work W necessary to remove the sodium ion from the point (110) to infinity is [2]

$$W = (U_1 + U_2)/2. \tag{13}$$

The binding energy of the complex is obtained if W is subtracted from the work V necessary to form a single positive ion vacancy at a distant point in the lattice.

Results and discussion

The numerical solution of the system of equations and the calculation of the binding energies were performed on a Siemens 4004 computer. We give two sets of results obtained with and without the inclusion of the Van der Waals interaction, in Tables I, II and III where the notation is the same as before.

Table I

Displacement, induced electric dipole moment and W results without Van der Waals interaction. r_0 is the ionic radius in 0.1 nm

Ion	r_0	x^{I}_{++}	x^{I}_{D}	m^{I}_{++}	m^{I}_{D}	W (eV)
Be	0.34	−.01163	−0.1242	0.0833	0.0945	4.521
Mg	0.78	−0.0990	−0.1071	0.0869	0.0985	4.480
Ca	1.06	−0.0663	−0.0743	0.0932	0.1055	4.387
Sr	1.27	−0.0302	−0.0380	0.0991	0.1121	4.274
Ba	1.43	+0.0029	−0.0045	0.1038	0.1175	4.150
Zn	0.83	−0.0986	−0.1067	0.0870	0.0986	4.478
Cd	1.03	−0.0768	−0.0849	0.0913	0.1032	4.398
Hg	1.12	−0.0641	−0.0721	0.0936	0.1059	4.360
Pb	1.32	+0.0177	+0.0105	0.1056	0.1196	4.026

Table II

Displacement, induced electric dipole moment and W results with Van der Waals interaction. The electronic polarizabilities μ of the different ions are given in 10^{-3} nm³ units.

Ion	x^{II}_{++}	x^{II}_{D}	m^{II}_{++}	m^{II}_{D}	W (eV)	α [15]
Be		no solution				0.008
Mg	−0.1092	−0.1176	0.0848	0.0961	4.512	0.094
Ca	−0.0791	−0.0877	0.0908	0.1027	4.432	0.472
Sr	−0.0424	−0.0510	0.0972	0.1099	4.323	0.865
Ba	−0.0098	−0.0182	0.1021	0.1154	4.209	1.560
Zn		no solution				0.286
Cd	−0.1200	−0.1283	0.0825	0.0935	4.518	1.080
Hg	−0.1060	−0.1147	0.0855	0.0968	4.484	1.250
Pb		no solution				4.320

The solutions x_V and m_V belonging to the vacancy are $x_V = 0.0837$, $m_V = -0.0863$ in the simpler calculation (calculation I) and $x_V = 0.0981$, in $m_V = -0.0814$ in the calculation with Van der Waals forces (calculation II). (The suffixes I or II in Tables I, II and III refer to calculation I or calculation II.) W denotes the work necessary to create a positive ion vacancy at a next nearest neighbouring point of the impurity. For the work V necessary to create a vacancy at a distant point in the lattice we use the value of SCHOLZ [14] which is $V = 4.64$ eV in NaCl. The dipole binding enegies ($E_d = V - W$)

Table III

The calculated and the measured dipole binding energies in eV units

Ion	E_d^{I} (eV)	E_d^{II} (eV)	E_{theor} (eV)	$E_{d,\mathrm{exp}}$ (eV)			
	This calculation		[3]	[16]	[17]		[18]
Be	0.12	—	—	—	—		—
Mg	0.16	0.13	—	0.30	—		—
Ca	0.25	0.21	0.38	0.30	0.31	0.30	0.67
Sr	0.37	0.32	0.45	0.45	0.55		—
Ba	0.49	0.43	—	0.55	—		0.76
Zn	0.16	—	—	—	—		0.48
Cd	0.24	0.12	0.38	—	0.34		0.40
Hg	0.28	0.15	—	—	—		—
Pb	0.61	—	—	0.5	—	0.47	0.41

obtained in both cases (E_d^{I} and E_d^{II}) are listed in Table III where the results of a previous calculation (E_{theor}) and experiments ($E_{d,\mathrm{exp}}$) are also given for comparison. The ionic radii are shown in Table I. For the divalent ion polarizabilities we have adopted the data of PAULING [15] and the values are listed in Table II.

The displacement and dipole moment results of the calculation without Van der Waals interaction (listed in Table I) agree with those of [3] for Ca^{2+} and Sr^{2+}, but deviation appears for Cd^{2+} which arises for the following reason. The correct value of the Pauling factor (see Eq. (2)) is $1-1/8+2/18 = 0.9861$ instead of 1.125 used in [2] and [3] because the Cd^{2+} ion has 18 electrons in its outer shell.

The numerical results in Tables I, II and III show that the induced dipole moments m_{++} and m_D furthermore the binding energies E_d^{I}, E_d^{II} increase but the displacements x_{++} and x_D decrease with increasing ionic radius in a given column of the periodical system of elements.

The difference between our binding energies and those of [3] originates from the fact that in our binding energy calculation we took larger surroundings of the defect as was done in [3].

Our binding energies are smaller than the observed ones as it can be seen in Table III. One possible reason for this deviation is the fixing of the vacancy and the impurity at their lattice points. It is highly probable that the impurity is displaced toward the vacancy, thus the calculated impurity — vacancy binding energy may become greater. Therefore it is planned to extend the distortion and the binding energy calculations permitting the motion and polarization of the divalent ion and of all the nearest neighbours of the defect.

REFERENCES

1. A. B. Lidiard, Handbuch der Physik, **20**, Springer Verlag, Berlin p. 246, 1957.
2. J. R. Reitz and J. L. Gammel, J. Chem. Phys., **19**, 894, 1951.
3. F. Bassani and F. G. Fumi, Nuovo Cimento, **11**, 274, 1954.
4. N. F. Mott and M. J. Littleton, Trans. Farad. Soc., **34**, 485, 1938.
5. L. Pauling, The Nature of the Chemical Bond, Cornell, New York, 1960.
6. M. Born and K. Huang, Dynamical Theory of Crystal Lattices, Clarendon, Oxford, 1954.
7. M. Born and J. Mayer, Z. Phys., **75**, 1, 1932.
8. F. Seitz, The Modern Theory of Solids, McGraw-Hill, New York—London, 1940.
9. M. P. Tosi and F. G. Fumi, J. Phys. Chem. Solids, **25**, 45, 1964.
10. J. E. Mayer, J. Chem. Phys., **1**, 270, 1933.
11. I. M. Boswarva, Phys. Rev., **B1**, 1698, 1970.
12. C. E. Moore, Atomic Energy Levels, Vol. 1—2—3, Circular of the National Bureau of Standards 467, Washington, 1949—1952—1955.
13. I. M. Boswarva and A. B. Lidiard, Phil. Mag., **16**, 805, 1967.
14. A. H. Scholz, Phys. Stat. Sol., **25**, 285, 1968.
15. L. Pauling, Proc. Roy. Soc., **A114**, 181, 1927.
16. J. Sárközi, The Effect of the State and Quantity of Impurities on the Hardening of NaCl Single Crystals, Thesis 1975.
17. R. G. Fuller, Point Defects in Solids, Vol. **1**, p. 103, (Edited by J. H. Crawford, Jr. and L. M. Slifkin) Plenum, New York—London, 1972.
18. P. Süptitz and J. Teltow, Phys. Stat. Sol., **23**, 9, 1967.

Acta Physica Academiae Scientiarum Hungaricae, Tomus 49 (4), pp. 415—422 (1980)

KINETIC MODEL FOR VACANCY TRANSPORT CAUSED BY MOVING DISLOCATIONS IN IONIC CRYSTALS

By

A. Tóth, T. Keszthelyi and J. Sárközi

DEPARTMENT OF EXPERIMENTAL PHYSICS, INSTITUTE OF PHYSICS, TECHNICAL UNIVERSITY
1521 BUDAPEST, HUNGARY

(Received 10. IV. 1980 — Revised version 23. VII. 1980)

A simplified kinetic model for the calculation of vacancy transport caused by moving dislocations is developed. The basic principle of the model is that the transport process is carried out by the diffusion of vacancies in the potential field of the moving dislocations. The numerical results obtained in ionic crystals agree well with the experimental results at room temperature, but at higher temperatures there is significant discrepancy between the theory and experiment. The estimations show that this discrepancy can be attributed to the unjustified neglects made during the evaluation of the measurements.

Introduction

The plastic properties of materials have been investigated for several decades. These investigations have shown that the plastic deformation of crystalline materials occurs primarily by the movement of dislocations, consequently the knowledge of elementary processes taking place during the motion of dislocations is very important for the understanding of the plastic properties of materials. One of these processes is the interaction between dislocations and point defects, which can in many cases have an essential effect on the plastic behaviour of crystals [1, 2] The fact that in certain types of crystals — among others ionic crystals — the defects can carry a net electric charge, makes it possible to investigate the movement and interactions of defects. In these crystals the movement of charged defects in the course of plastic deformation results in a macroscopic transport of electric charges, and can give rise to observable electric effects. The analysis of such effects gives new information on the elementary defect interactions [3].

One of the oldest effects of this kind discovered by Stepanov [4] is that in ionic crystals subjected to inhomogeneous plastic deformation, electric potential differences appear between different points of the crystal (Stepanov effect). Since the discovery of the effect many research workers have dealt with the problem. The results were summarized by Whitworth in a detailed review [3]. In spite of the very large amount of work done in this field the theoretical treatment of the effect is missing up to the present.

The aim of this paper is to explain the **Stepanov** effect by means of a simple theoretical model. The experimental results obtained in the latest years threw light on some important characteristics of the effect and this is what made it possible to work out this model. Earlier it had been already assumed that the phenomenon was related to the fact that dislocations generated in the course of the plastic deformation carry electric charge, that they acquire sweeping up some charged point defects of the crystal. Nowadays it is well known that in NaCl type crystals these point defects are cation vacancies [3], and that the amount of carried vacancies depends on the velocity of the dislocations [5]. This velocity dependence has an essential characteristic. Namely, there exists a critical velocity above which the vacancy contcentration on the moving dislocations decreases considerably. The critical velocity varies with the reciprocal temperature according to an exponential law. These results suggest that the vacancy transport is realized by means of a diffusive motion of cation vacancies.

Basic principles of the model

As a starting point of the model we assume that the vacancies diffuse under the influence of the stress field of the dislocation. In this case the vacancy transport, in principle, may be calculated by solving the appropriate diffusion equation, taking into account the moving potential field of the dislocation. This equation is, however, very difficult to solve and only its approximate solutions are known [6, 7]. In the model described here the diffusion of vacancies is considered as a succession of atomic jumps [7], but this method is used in a simplified form.

Since the dislocation — vacancy interaction decreases rapidly with the distance between them, it is assumed that a dislocation interacts only with the vacancies situated in its core region.

For the frequency of atomic jumps (ν) the well known expression of the rate theory [8] is used:

$$\nu = p \cdot \nu_0 \cdot \exp\{-U/k \cdot T\}. \tag{1}$$

Here ν_0 is the vibration frequency of an atom including the entropy term, U is the activation energy for the jump, p is the geometrical factor. The jump frequency for a vacancy moving towards the dislocation (ν') is different from that in the opposite direction (ν''), because the presence of the mechanical and electric fields of the dislocation modifies the potential energy (Fig. 1). With the notation of Fig. 1 these frequencies can be written:

$$\nu' = p \cdot \nu_0 \cdot \exp\{-(U_m - \Delta U/2)/k \cdot T\}, \tag{2a}$$

$$\nu'' = p \cdot \nu_0 \cdot \exp\{-(U_m + \Delta U/2)/k \cdot T\}. \tag{2b}$$

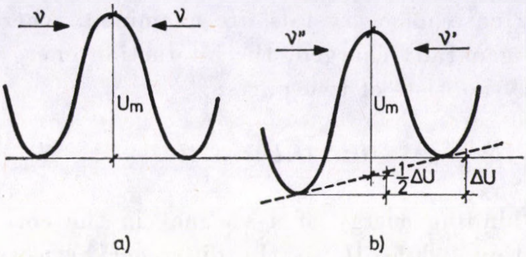

Fig. 1. Potential energy curves explaining the calculation of the jumping rate

The vacancy concentration in the core of the dislocation (f) is calculated by considering the jumps shown in Fig. 2. Then the rate of vacancy concentration change in the core (Φ) may be given [7] under the assumptions used as:

$$\Phi(f) = \frac{df}{dt} = 4 \cdot \nu' \cdot n_v \cdot (1 - f) - 4 \cdot \nu'' \cdot f \cdot (1 - n_v) + \frac{v}{s} \cdot (n_v - f), \qquad (3)$$

where s is the distance between the dislocation and one of the nearest cation sites, n_v is the concentration of free cation vacancies in the crystal and t is

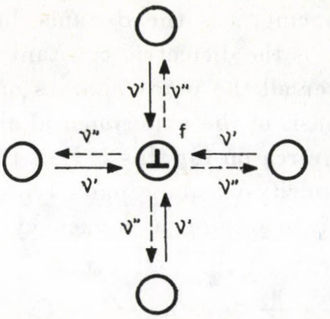

Fig. 2. Vacancy jumps taken into account in the model

the time. The last term in (3) gives the concentration change resulting from the motion of the dislocation.

The concentration of free cation vacancies (n_v) is calculated on the basis of the association theory [9], and is given by the equation:

$$\frac{c - n_v}{n_v^2} = z \cdot \exp\{-S_a/k\} \cdot \exp\{U_a/kT\}. \qquad (4)$$

Herce c is the concentration of divalent cation impurity, U_a and S_a are the binding energy and entropy, respectively, z is the geometrical factor.

Since in our case ionic crystals are examined, where the dislocations and vacancies are generally charged, the interaction energy ΔU of a dislocation and a vacancy consists of two parts:

$$\Delta U = \Delta U_b + \Delta U_e. \tag{5}$$

Here ΔU_b is the binding energy of a vacancy in the core of an otherwise uncharged dislocation, while ΔU_e is the difference between the electrostatic energies of a vacancy in the core and on a site nearest to the core. Considering the charge of the dislocation as a row of point charges all equal to either e and spaced uniformly [10] this latter energy is:

$$\Delta U_e = \frac{2 \cdot e^2}{4 \cdot \pi \cdot \varepsilon \cdot \varepsilon_0} \cdot \sum_i \left(\frac{1}{\sqrt{s^2 + (i+1/2)^2 \cdot d^2}} - \frac{1}{(i+1/2) \cdot d} \right). \tag{6}$$

Here d is the spacing of the point charges, which can be expressed in terms of the unknown concentration f as:

$$d = \frac{2 \cdot a}{f}. \tag{7}$$

a is the cation-anion spacing, s is the distance between the dislocation and the nearest cation site, ε is the dielectric constant of the crystal. The summation should be taken over all the point charges on the dislocation.

However, on the basis of the experimental observations [11] the Eq. (3) should be completed. The reason for this is that the dislocation can sweep up vacancies also from impurity-vacancy pairs lying near the slip plane. This process should be taken into account as a vacancy source, which may be given by the term:

$$\frac{v}{s} \cdot n_p \cdot w_c \cdot (1 - f). \tag{8}$$

Here n_p is the concentration of the impurity-vacancy pairs, w_c is the probability of the break-up of an impurity-vacancy pair by a moving dislocation. Completed with this term Eq. (3) reads:

$$\begin{aligned} \Phi(f) = 4 \cdot \nu' \cdot n_v \cdot (1 - f) - 4 \cdot \nu'' \cdot f \cdot (1 - n_v) + \\ + \frac{v}{s} \cdot (n_v - f) + \frac{v}{s} \cdot n_p \cdot w_c \cdot (1 - f). \end{aligned} \tag{9}$$

The solution of Eq. (9) is complicated by the fact that in general the interaction energy ΔU depends on the concentration f. The approximate solution shows, however, that the vacancy concentration on the dislocation becomes stationary in a very short time, and this means that only the stationary equation

$$\Phi(f) = 0 \tag{10}$$

should be solved. This can be carried out by using a simple iteration method.

Results and discussion

Using the model described above numerical calculations were carried out for some cases, which had been studied experimentally as well.

As a first example LiF crystals doped with Mg^{2+} ions were investigated, because this is the only system for which experimental results are available concerning the dislocation velocity dependence of the charge (i.e. the vacancy concentration) formed round a moving edge dislocation [5]. The unknown binding energy ΔU_b was determined by fitting the theoretical curve to the experimental points obtained at room temperature. The value $\Delta U_b = 0.46$ eV obtained in this way is in agreement with expectations [12]. The activation energy for migration of cation vacancies (U_m) was assumed to be 0.6 eV [5]. The other data used were: $w_c = 1$ [11, 13], $\nu_0 = 2.9 \cdot 10^{14}\ \mathrm{s}^{-1}$ [14], $U_a = 0.4$ eV [15], $c = 6 \cdot 10^{-5}$ (fitting).

Fig. 3 shows the vacancy concentration on an edge dislocation (f) as a function of the dislocation velocity (v). The solid curves are calculated from Eq. (10), the broken curves represent experimental results [5]. As it can be seen, the model is in good agreement with the experiment at room temperature, but at higher temperature only the upper and lower saturation limits and the critical velocities agree with the experimental results.

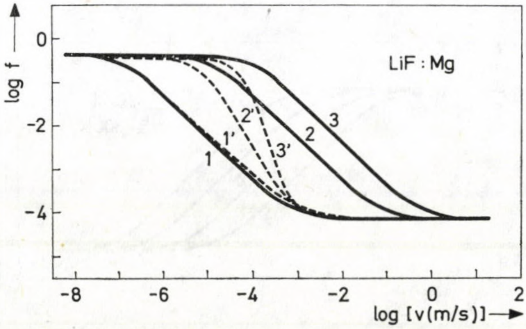

Fig. 3. Dislocation velocity (v) dependence of the vacancy concentration (f) on an edge dislocation in the LiF : Mg^{2+} system at different temperatures. The solid curves are calculated from Eq. (10), the broken curves represent experimental results [5]. The temperatures are: *1,1'* : 293 K, *2,2'* : 373 K, *3,3'* : 423 K

In Figs. 4 and 5 similar theoretical curves are shown as in Fig. 3, but for NaCl crystals at room temperature. The different curves represent results with different concentrations of Ca^{2+} impurity (Fig. 4) and with different divalent cations having different association energy at the same concentrations (Fig. 5). In these cases the following data were used: $\nu_0 = 2.8 \cdot 10^{13}$ s^{-1}, $U_m = 0.65$ eV, $U_a = 0.31$ eV [16], $\Delta U_b = 0.5$ eV [12], $w_c = 1$ [11, 13].

Since experimental data obtained at room temperature in NaCl crystals correspond to constant dislocation velocity, but to different free cation vacancy concentrations [17], in Fig. 6 the vacancy concentration on the dislocation (f) is plotted against the vacancy concentration in the bulk (n_v) at room temperature and with different dislocation velocities. The calculated f vs n_v graphs (solid lines) are straight lines in the velocity range of 10^{-4}—10^{-6} m/s. The experimental results [17] yield also a linear relationship between f and n_v (broken line), although the dislocation velocity is not known in these experi-

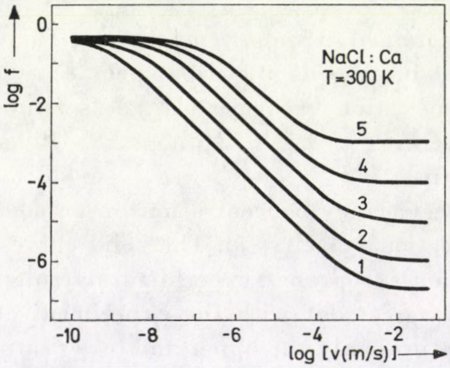

Fig. 4. Calculated $\log f$ vs $\log v$ curves for NaCl : Ca^{2+} system at room temperature with different Ca^{2+} concentrations: *1* : $2 \cdot 10^{-7}$, *2* : 10^{-6}, *3* : 10^{-5}, *4* : 10^{-4}, *5* : 10^{-3} mol/mol

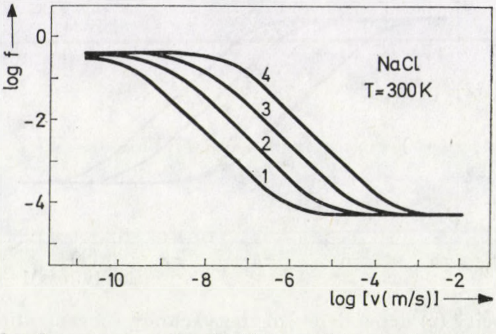

Fig. 5. Calculated $\log f$ vs $\log v$ curves for NaCl crystals containing divalent cation impurities with different association energies (U_a). The U_a values are: *1* : 0.6 eV, *2* : 0.5 eV, *3* : 0.4 eV, *4* : 0.3 eV. The impurity concentration is $5 \cdot 10^{-5}$ mol/mol, the temperature: $T = 300$ K

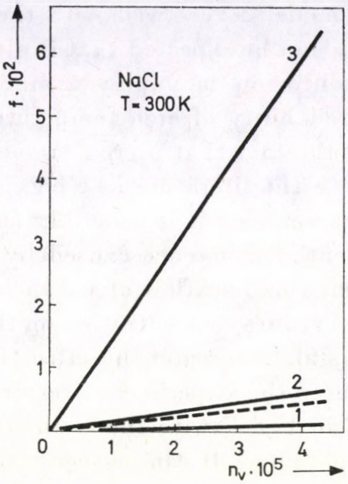

Fig. 6. Vacancy concentration on the dislocation (f) vs vacancy concentration in the bulk (n_v) for NaCl crystals at room temperature. Solid lines are calculated, broken line represents experimental results [17]. The velocities used: *1* : 10^{-4} m/s, *2* : 10^{-5} m/s, *3* : 10^{-6} m/s

ments. On the basis of Fig. 6, however, we may conclude that the average velocity of dislocations should be in the range of 10^{-5}—10^{-4} m/s. Such a conclusion seems to be very reasonable.

The temperature (T) dependence of the vacancy concentration on the dislocation (f) is shown in Fig. 7 As it can be seen, the theoretical curve (1) deviates significantly from the experimental [18] one (2). It should be noted that the experimental values are lower than the theoretical ones just as in the case of the LiF : Mg^{2+} system (Fig. 3).

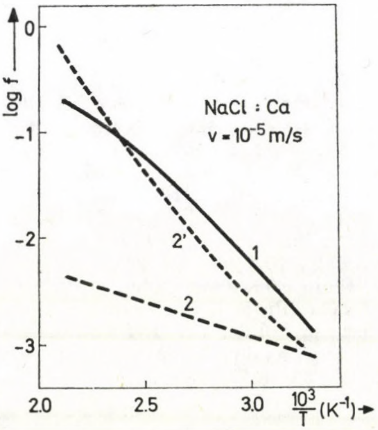

Fig. 7. Temperature (T) dependence of the vacancy concentration on the dislocation (f) in NaCl : 10^{-5} mol/mol Ca^{2+} system at $v = 10^{-5}$ m/s. *1:* calculated results, *2:* experimental results [18], *2':* corrected experimental results

Since the diffusion model agrees well with the experimental results at room temperature, it would not be expected that it gives worse results at higher temperatures, where diffusion may play a more important role. Consequently, the problem of reliability of high temperature measurements arises, which is justified also by the fact that a great amount of contradictory high temperature results exist in the literature (see e.g. isoelectric point [3]).

Evaluating the measurements it is generally accepted that the vacancy transport due to the potential difference caused by the moving dislocations can be neglected. However, this backflow of vacancies may result in lowering the measured value of the vacancy concentration on the dislocation. The higher the conductivity of the crystal, the greater this effect, i.e. the higher the measuring temperature, the greater the experimental error. After the correction of the experimental curve 2 in Fig. 7 with the estimated value of this vacancy backflow, the curve 2′ is obtained. It can be seen that this effect can give rise to gross errors in measurements. The deviation of the corrected curve (2′) from the calculated results (1) is considerably lower than that of the uncorrected one (2). Similar estimations may also be made, in principle, in the case of the LiF : Mg^{2+} system, but for this a better knowledge of experimental details [5] would be required.

Finally, it must be noted, that in the model used here an essential simplifying assumption was made. Namely, the diffusion of the vacancies was taken into account only in the closest vicinity of the dislocation. The development of an improved model is in progress.

REFERENCES

1. A. H. Cottrell, Dislocations and Plastic Flow in Crystals, Oxford, 1953.
2. F. R. N. Nabarro, Phil. Mag., **35**, 613, 1977.
3. R. W. Whitworth, Adv. Phys., **24**, 203, 1975.
4. A. V. Stepanov, Z. Phys., **81**, 560, 1933.
5. V. I. Alshits, M. V. Galustashvili and I. M. Paperno, Kristallografiya, **20**, 1113, 1975.
6. A. H. Cottrell and M. A. Jaswon, Proc. Roy. Soc., **A 199**, 104, 1949.
7. H. Yoshinaga and S. Morozumi, Phil. Mag., **23**, 1367, 1971.
8. H. R. Glyde, Rev. Mod. Phys., **39**, 373, 1967.
9. A. B. Lidiard, Handbuch der Physik, Vol. **20**, Springer-Verlag, Berlin 1957.
10. R. W. Whitworth, Phil. Mag., **17**, 1207, 1968.
11. A. Huddart and R. W. Whitworth, Phil. Mag., **27**, 107, 1973.
12. F. Bassani and R. Thomson, Phys. Rev., **102**, 1264, 1956.
13. R. W. Whitworth, Phil. Mag., **15**, 305, 1967.
14. H. Haven, Recueil Trav. Chim., **69**, 1471, 1950.
15. T. G. Stoebe and P. L. Pratt, Proc. Brit. Ceram. Soc., **9**, 181, 1967.
16. R. G. Fuller, Point Defects in Solids, Vol. **1**, Plenum Press, New York, 1972.
17. A. Tóth and J. Sárközi, J. de Physique, **C7**, 604, 1976.
18. A. Tóth, Phys. Stat. Sol. (a), **33**, K47, 1976.

Acta Physica Academiae Scientiarum Hungaricae, Tomus 49 (4), pp. 423–428 (1980)

SUBHARMONIC RESONANCES IN KDP ELECTROOPTICAL LIGHT SHUTTERS

By

J. S. Bakos and Zs. Sörlei

CENTRAL RESEARCH INSTITUTE FOR PHYSICS, 1525 BUDAPEST 114, P.O.B. 49, HUNGARY

Cs. Kuti and S. Szikora

DEPARTMENT OF EXPERIMENTAL PHYSICS, INSTITUTE OF PHYSICS, TECHNICAL UNIVERSITY
1521 BUDAPEST, HUNGARY

(Received 10. IV. 1980 — Revised version 15. IX. 1980)

Acoustic resonance vibration generated by the inverse piezoelectric effect was investigated in longitudinal KDP electrooptic light shutters driven by a series of high voltage pulses. Although the repetition rate of the driving pulses was far below the mechanical frequencies of the modulator crystals significant resonances were observed.

1. Acoustic resonances in KDP type crystals

KDP type electrooptical crystals are strongly piezoelectric. Acoustic processes, induced by the inverse piezoelectric effect, can greatly affect the operation of electrooptical light modulators made of KDP type crystals. Characteristic examples of disturbing influence of the acoustic processes are resonances observed in periodically driven electrooptic modulators.

An electric field applied to a linear electrooptic crystal induces elastic deformations of the crystal by the inverse piezoelectric effect. The elastic deformations are generated at the surface of the crystals where the elastic forces are not compensated. The elastic deformations propagate inside the crystal as acoustic waves. In longitudinal KDP modulators with rectangularly shaped modulator crystals (Fig. 1) the sources of the acoustic waves are at the lateral faces perpendicular to the x and y crystallographic axis [1]. The

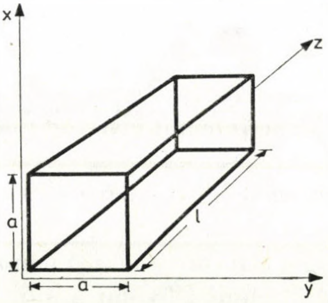

Fig. 1. KDP longitudinal modulator crystal

waves generated at the surface are plane transverse waves propagating along the x and y directions with shear components in the y and x directions, respectively. The waves propagate across the crystal. Arriving at the opposite side the acoustic waves are reflected back into the crystal and propagate in the opposite direction [2]. In the case of continuous generation of acoustic waves by using a.c. driving potential, at frequencies equal to the mechanical resonance frequencies of the modulator crystal acoustic standing waves are developed by wave superposition. Similarly, resonances can take place driving the modulators which are used as light shutters by a series of high voltage pulses of subharmonic repetition rate if the driving potential contains large enough Fourier components at the fundamental or at the harmonic frequencies of the crystal.

The acoustic processes, especially the resonances, can greatly affect the transmission of the KDP electrooptic modulators. The acoustic resonances are usually investigated by measurement of the frequency transfer function of the electrooptic modulators [3, 4]. Careful theoretical treatment and experimental investigation of acoustic resonance processes in longitudinal KDP modulator crystals, driven by radio-frequency voltages, was given by STEPHANY [5]. STEPHANY chose a simple but demonstrative way of experimental investigation. He photographed the transmission distribution across the full aperture of the modulator crystal placed between crossed polarizers. KUZOKOVA and NILOV investigated the acoustic resonances developed in KDP and DKDP electrooptic light shutters driven by a periodic series of high voltage pulses [6]. They applied an interferometric method. The interferograms were photographed by a fast ciné camera.

The authors of papers [3—6] found the resonances at driving frequencies equal to the fundamental or the overtone mechanical frequency of the modulator crystals. We drove our longitudinal KDP modulators by a series of high voltage pulses at a repetition rate far below the fundamental frequency of the modulator crystal and we observed significant resonance vibrations of the crystal. The measured frequencies of the resonance vibrations developed by subharmonic driving are equal to the fundamental frequency or the frequency of the overtones.

2. Experimental investigations

An experimental arrangement similar to that used by STEPHANY [5] was applied (Fig. 2).

The experiments were performed on a 15 mm × 15 mm × 25 mm KDP crystal (Fig. 1) grown and machined by our group. The crystal was mounted in a plexi-glass sample holder; copper plate electrode with 14 mm diameter,

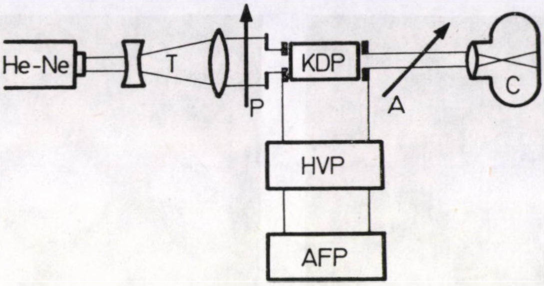

Fig. 2. Experimental arrangement

circular openings were pressed against the polished end-faces of the crystal by springs. The beam of a 3 mW He—Ne laser was expanded about ten times in diameter by a Galilean telescope (T). The crystal was placed in the collimated laser beam between crossed polarizers (A, P). The modulator was driven by the 12 kV pulses of the high voltage pulse (HVP) generator triggered by a master (AFP) generator. The AFP generator was tuned in the 0.01 kHz—10 kHz range to get the standing wave transmission distribution characterizing the resonances. The camera (C) was foused on the exit face of the crystal and took time averaged transmission pictures. The frequency of the resonance vibrations could be checked by a photodiode (PD) connected to a frequency meter (FM). The photodiode was placed in the axis of the arrangement. To be able to compare the resonances developed in the case of subharmonic driving with the resonance generated by a.c. driving potential, we used a radio-frequency generator (RFG).

With driving frequencies under 1 kHz we could hardly observe resonances. In the case of subharmonic driving the resonances observed in the 1 kHz—2.5 kHz frequency range were better developed than those found at lower frequencies, but they were also not well defined. Above 2.5 kHz but under 10 kHz (upper limit of the HVP generator) the resonances could be observed almost continuously by changing the repetition rate.

It tended to be difficult to tune to the resonances and the resonance transmission distribution was stable only for a short time but it was enough for photographing purposes. We were unable to observe the fundamental resonance of the crystal and some of the harmonics such as the third and fourth (indexed by $m = 7$ and 9 according to STEPHANY [5]). The first harmonic and specially the second one numbered by 3 and 5 were developed in many cases tuning across the audio-frequency range available (Fig. 3). A mixed transmission distribution of two or several coexisting resonances was observed in some cases (Fig. 4). For well defined resonances the internal structure of the transmission distribution was developed as a consequence of the high resonance amplitude (Fig. 5).

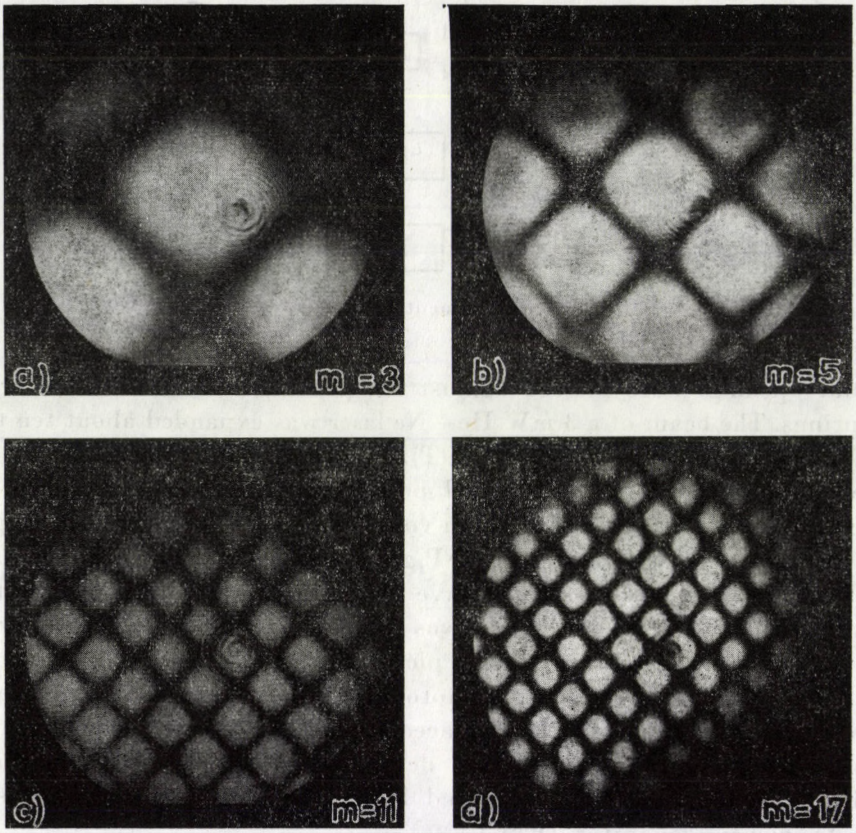

Fig. 3. **Resonances developed by subharmonic driving.**
a. $m = 3$; b. $m = 5$; c. $m = 11$; d. $m = 17$

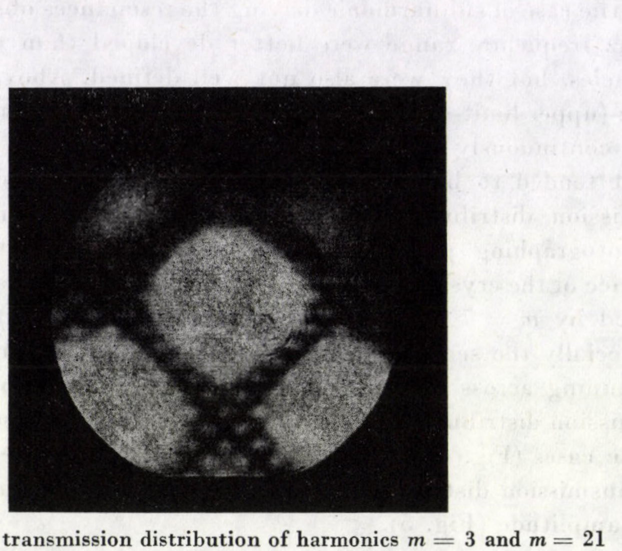

Fig. 4. **Mixed transmission distribution of harmonics $m = 3$ and $m = 21$**

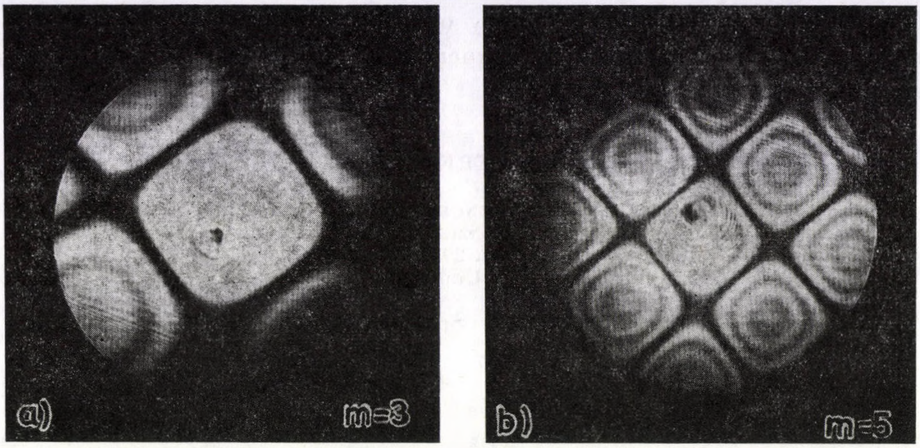

Fig. 5. Internal structure of the transmission distributions. a. $m = 3$; b. $m = 5$

On comparing the resonance transmission pictures of subharmonic driving with that of the radio-frequency driving we found good agreement for some well developed resonances in spite of the significant difference of the time dependence of the driving potentials. Varying the amplitude of the radio-frequency driving we got congruency between the resonance transmission distributions obtained by using radio-frequency and subharmonic driving and could roughly estimate the resonance component of the subharmonic driving.

The frequency of the resonance vibrations of subharmonic driving was measured and good agreement was found with the resonance frequency measured in the case of radio-frequency driving and with the frequency values calculated in STEPHANY's approximation. The velocity of the shear waves was calculated and it agreed well with the corrected value [7] of the velocity of the acoustic transient pulses in KDP modulators investigated earlier [2].

3. Conclusions

Well defined resonances can be developed in longitudinal KDP modulators driven by a series of high voltage pulses at subhamonic frequencies. The effect can be explained by the Fourier spectrum of the series of high voltage pulses of subharmonic frequency. If the subharmonic resonances are compared with the resonances developed by the a.c. driving the resonance frequency component of the Fourier series of driving pulses can be estimated. With longitudinal KDP modulators used as light shutters driven by a series of high voltage pulses the possibility of acoustic resonances must be taken into account even if the driving frequency is far below the mechanical resonance of the modulator crystal.

REFERENCES

1. H. Veeser, U. Bogner and W. Eisenmenger, Phys. Stat. Sol. (a), **37**, 161, 1976.
2. J. S. Bakos, Zs. Sörlei, Cs. Kuti and S. Szikora, Appl. Phys., **19**, 59, 1979.
3. F. Hoff and B. Stadnik, Electr. Lett., **2**, 293, 1966.
4. S. F. Broveev, A. I. Snakov and A. A. Ugodenko, PTE, No **3**, 181, 1972.
5. F. J. Stephany, JOSA, **55**, 136, 1965.
6. T. A. Kuzovkova and E. V. Nilov, Opt. i Spectr., **42**, 687, 1977.
7. J. S. Bakos et al. to be published.

Acta Physica Academiae Scientiarum Hungaricae, Tomus 49 (4), pp. 429—433 (1980)

GROWTH OF ALPHA-IODIC ACID CRYSTALS FROM AQUEOUS SOLUTION

By

L. Vannay

DEPARTMENT OF EXPERIMENTAL PHYSICS, INSTITUTE OF PHYSICS, TECHNICAL UNIVERSITY
1521 BUDAPEST, HUNGARY

and

E. Hartmann

RESEARCH LABORATORY FOR CRYSTAL PHYSICS OF THE HUNGARIAN ACADEMY OF SCIENCES
1502 BUDAPEST, HUNGARY

(Received 10. IV. 1980)

An evaporating method to grow large, good quality alpha-iodic acid (HIO_3) single crystals from their aqueous solutions under controlled circumstances is described. The crystals obtained with this method proved to be suitable for acousto-optical purposes.

1. Introduction

Alpha-iodic acid crystals $(HIO)_3$ are of some interest because of their electrooptical, acoustooptical and non-linear optical properties [1, 2, 3]. The crystals belong to the $D_2^4 - P2_12_12_1$ space group [4], their density is $4.63 \cdot 10^3$ kg/m³, they cleave well along the $\{011\}$ planes, they are colourless and transparent in the 0.3—1.0 μm range [5] and double axial.

The outstanding importance of the alpha-iodic acid crystals is due to their acousto-optical properties.

The factor of merit (M_2) of alpha-iodic acid as related to quartz glass for longitudinal acoustic waves in the [001] direction and light waves of $\lambda = 0.63$ μm propagating in the [010] direction and polarized in the [100] direction amounts to 55.2 [2]. At the same time the acoustic attenuation is rather low: 2.5 $dB \cdot m^{-1}$ for longitudinal acoustic waves of the frequency of 500 MHz. For comparison in case of longitudinal acoustic waves the factor of merit as related to quartz glass is 22.8 for TeO_2 crystals, 23.7 for $PbMoO_4$, 6.99 for $LiNbO_3$, 2.78 for ADP and 1.91 for KDP crystals [2, 3, 6]. The acoustic attenuation of the alpha-iodic acid crystals is better than the attenuation of TeO_2 or $PbMoO_4$ [3]. With regard to $LiNbO_3$ a further advantage is the absence of optical damage even in case of considerable light intensity [2, 5].

Near to the melting point (110 °C) the crystals begin to decompose and releasing water transform into I_2O_5 (iodic-acidanhydrid). At the same time HIO_3 dissolves readily in water. According to Kaye and Laby [7] 100 g water dissolves 286 g at 0 °C and 472 g HIO_3 at 80 °C. Accordingly, it is quite obvious that the best and simplest way of obtaining large single crystals should be to grow them from aqueous solutions. Though the earlier papers refer to this method of growth [1, 2, 5, 8, 9], with the exception of one paper, no details of the growth technology are given.

Parker and **Pinnel** [9] grew 60 g single crystals with the evaporation method. The rate of evaporation has been regulated by the temperatue of growth, and the number and size of the openings through which the water vapour evaporated. The seed crystals were fastened to $5-12\times10^{-3}$ cm thick gold or platinum filaments. The use of thicker filaments resulted in crack formation. In their experiments cracks were induced also by the mixing of the solution because of the oscillating motion of the filaments used to fasten the seeds.

In what follows we wish to present an evaporating method to grow alpha-iodic acid crystals without the use of filaments, which enabled a more precise change of the rate of evaporation. With this method it became possible to avoid crack formation due to mixing, and grow larger crystals than with the method referred to in [9].

2. Experimental method and results

(a) *Growth equipment*

The growth equipment consisted basically of a double wall thermostat. The inner working space where the actual growth took place, was a 210 mm high glass vessel with a diameter of 130 mm. The vessel was enclosed in a thermostating water jacket (the diameter and height of the outer vessel were approximately 300 mm). The water content of the jacket was intensively mixed with a centrifugal pump, and the water temperature was kept constant with a contact-thermometer thermoregulator.

In order to minimize the temperature fluctuations due to switching on and off the heating current a low heat capacity heater was used; the heater output has been experimentally optimalized with a thyristor controlled regulator device. Thus the temperature fluctuation of the thermostating water could be kept below 0.05 °C.

The growth vessel was covered with a conical teflon lid. Since the lid is in contact with the open air its temperature is lower than the vapour above the solution. As a result of this temperature gradient the water vapor became continually condensed on the lid. The condensate trickled down the conical shape and was collected in a small pot from which it was periodically extracted.

The solution was mixed with teflon shovels moving in alternating, periodically changing, directions [10]. The scheme of the equipment is presented in Fig. 1.

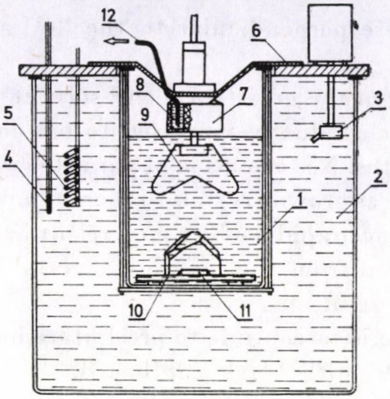

Fig. 1. The scheme of the growth equipment. 1. Working space; 2. Thermostating water jacket; 3. Centrifugal pump; 4. Contact thermometer; 5. Heater; 6. Lid; 7. Collecting pot; 8. Condensate; 9. Teflon mixing shovel; 10. Seed holder; 11. Seed crystal and growing crystal; 12. Solvent eduction pipe

(b) *Growth process*

The experiments were carried out in an air conditioned environment at a constant temperature of 24 °C, the solution temperature was 40 °C. At lower solution temperature (35 °C) the rate of condensation proved to be unsatisfactory, a growth temperature higher than 40 °C on the other hand gave rise to difficulties when pulling out the as grown crystals from the growth vessel.

As quality basic material Merck "zur Analyse" HIO_3 was used.

The material quantity as calculated from supersaturation data published in the literature was not enough. With these quantities the first experiments resulted in the dissolution of the seed crystals. For this reason in the subsequent experiments while keeping the solution at constant temperature the supersaturation was obtained by adding the HIO_3 to the solution till the necessary supersaturation has been obtained. The saturated solution was then decanted, heated, filtered and poured at a temperature of approximately 45 °C on the seed crystals already deposited in the growing vessel whose temperature was 40 °C.

The seed was glued on a teflon plate put on the bottom of the vessel. Since the solution density is rather high the teflon plate would have floated on the surface. In order to avoid this also the teflon plate was glued to the bottom of the vessel. The seed crystal as well as the teflon holder were fixed in position with silica-rubber glue (Rhone-poulenc-chimie fine "CAF 4" rhodosil silicones were used). The size of the seed crystals was approximately $20 \times 20 \times 4$ mm, two of the surfaces were parallel with the (110) i.e. $(1\bar{1}0)$ planes and the other two surfaces were perpendicular to the "c" axis (notation according to [9]).

At the beginning of the growth 1.5 cm^3 solvent was extracted each day. This quantity has been gradually increased to 6.0 cm^3 per day. One growth period lasted four months. No formation of parasite crystals has been observed.

The cooling of the as grown crystals to room temperature should be carried out rather carefully, since rapid cooling may result in cracking. It is advisable to draw off the solution from the as grown crystal and let the crystal cool down slowly in the vessel itself.

Since the solution is susceptible to precipitate iodine by light, the growth equipment was covered with black cardboard.

(c) *Results*

With the method described crystals weighing 1300 g were grown. The length of the sides of the rhombus perpendicular to the "c" axis was 76 mm. The size of the crystal in the direction of the "c" axis amounted to 65 mm.

The average daily rate of growth in the direction of the "a", "b" and "c" axis was 0.3, 0.35 and 0.54 mm, respectively.

The as grown crystals were free of defects or inclusions. The photograph of an as grown crystal is shown in Fig. 2.

From the as grown crystals workable acoustooptical units could be made.

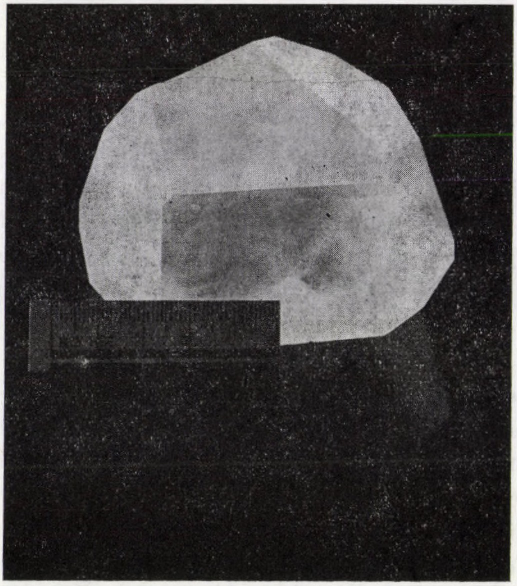

Fig. 2. The photograph of an as grown HIO_3 crystal

REFERENCES

1. E. N. Volkova, V. A. Dianova, A. L. Zuev, A. N. Izrailenko, A. S. Lipatov, V. N. Parigin, L. N. Raskovich and L. E. Chirkov, Kristallografiya, **16**, 346, 1971.
2. D. A. Pinnow and R. W. Dixon, Appl. Phys. Letters. **13**, 156, 1968.
3. "Tablici fizicheskih velichin" (Ed. I. K. Kikoin) Atomizdat, Moscow, 1976.
4. R. W. G. Wyckoff, Crystal Structures, Vol. II., p. 387, Interscience Publishers, New York, 1964.
5. S. K. Kurtz, T. T. Perry and J. G. Bergman, J. Appl. Phys. Lettres, **12**, 186, 1968.
6. "Physical Acoustics" Vol. **7**, p. 352, W. P. Mason and R. N. Thurston (ed.) Academic Press, New York, 1970.
7. G. W. Kaye and T. H. Laby, Tables of Physical and Chemical Constants, Longmans Green and Co, London, 1958.
8. The Art and Science of Growing Crystals, O. J. Gilman (ed), John Wiley, New York, 1963, p. 194.
9. S. G. Parker and J. E. Pinnel, J. Crystal Growth, **12**, 277, 1972.
10. L. Vannay, Kristall und Technik, **14** (7) K 38–41, 1979.

Acta Physica Academiae Scientiarum Hungaricae, Tomus 49 (4), pp. 435—438 (1980)

COMMUNICATIO BREVIS

THE INTERACTION OF DISLOCATIONS WITH IMPURITY VACANCY DIPOLES IN NaCl CRYSTALS

By

T. KESZTHELYI, P. KÁLMÁN, A. TÓTH and J. SÁRKÖZI
DEPARTMENT OF EXPERIMENTAL PHYSICS, INSTITUTE OF PHYSICS, TECHNICAL UNIVERSITY,
1521 BUDAPEST, HUNGARY

(Received 10. IV. 1980 — Revised version 18. IX. 1980)

It is a long established fact that divalent impurity ions considerably increase the yield stress of alkali halide crystals [1]. The effect is generally attributed to the presence of complexes made up of the divalent impurity ions and the vacancies attracted to them by their electric charge surplus (I—V dipoles). **FLEISCHER** [2] calculated the yield stress increment $\Delta\tau$ of alkali halide crystals from the interaction of dislocations with I—V dipoles treating them as tetragonal defects. These defects are characterized by the so-called tetragonality, i.e. the difference between the longitudinal and transverse strain of the distortion. Comparing experimental results with **FLEISCHER**'s formulae a number of authors (e.g. [1—3]) gave tetragonality values for I—V dipoles. But since there is no independent information on the tetragonality based on the strain field of the defect, its value is essentially a floating parameter in the theory [1]. This paper is intended to be an attempt to evaluate $\Delta\tau$ caused by I—V dipoles using the atomic displacement field around them and avoiding the use of the notion of tetragonality.

For the sake of simplicity the vacancy and the impurity ion are taken as dilatation centres and their strain fields are summed up to give the strain of the I—V dipole. The strengths δ of the dilatation centres are computed from the atomic displacements of their nearest neighbour ions in the way suggested by **BASSANI** and **THOMSON** [4]:

$$\delta^{++} = \frac{\xi^{++} + M'}{2r_0}, \quad \delta_V = \frac{\xi_V - M'}{2r_0}.$$

Here ξ and M' denote the displacements and the polarization displacements of the nearest neighbour ions of the centres (r_0 is the lattice parameter). Suffixes $++$ and V refer to the impurity ion and the vacancy, respectively. For ξ and M' we use the values evaluated in [5] on the basis of the Born—Mayer theory of ionic solids. The values δ obtained are listed in Table I for several cations.

Table I

Strength of dilatation centres associated with impurity ions and vacancy

	Mg	Ca	Sr	Pb	Ba	Vacancy
$\delta^{++}=$	-0.0311	-0.0147	0.0035	0.0277	0.0202	$\delta_V=0.0194$

It is known from the literature [1, 2] that the vexed question whether edge or screw dislocations are responsible for the measured increment in yield stress is far from being resolved. In our model we assume that the yield stress increment $\Delta\tau$ results from the interaction of the dipoles with edge dislocations.

Making use of the formula given by BILBY [6] according to which the interaction energy between a dilatation centre of strength δ at the origin and a dislocation parallel to the axis z at the point x, y is

$$E_{\text{int}} = -4\mu b \delta r_0^3 \frac{x}{x^2+y^2},$$

for the dipole-dislocation interaction energy we obtain:

$$E_{\text{int}} = -4\mu b r_0^3 \left[\frac{\delta^{++} y}{x^2+y^2} + \frac{\delta_V (y-\varepsilon_y)}{(x-\varepsilon_x)^2+(y-\varepsilon_y)^2}\right]. \tag{1}$$

Here μ is the shear modulus, r_0 is the lattice parameter and b is the Burgers vector. The impurity ion is placed at the origin and the vacancy at the point ε_x, ε_y (see Fig. 1).

The yield stress increment $\Delta\tau$ can be calculated by means of the Friedel relationship [7]:

$$\Delta\tau = \frac{F_{\max}^{3/2}\, c_p^{1/2}}{(2T)^{1/2}\, b}, \tag{2}$$

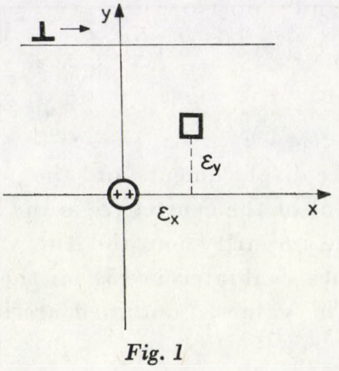

Fig. 1

where c_p is the concentration of the obstacles in the slip plane, $F_{\max}$ is the maximum of the force the dislocation must overcome as it passes an obstacle and T is the line tension of the dislocation.

The force has been derived from (1):

$$F_x = -\frac{\partial E_{\text{int}}}{\partial x}$$

and the maxima of F have been computed by numerically solving the equation:

$$\frac{\partial F_x}{\partial x} = 0 \, .$$

We have regarded only the nearest possible (110) planes to the dipoles as the interaction rapidly decreases with increasing distance. In NaCl a dipole can have 12 geometrically different orientations which, considering the two possible slip planes and the physically equivalent orientations with the same coordinate ε_z, give 8 different situations. From these we have chosen the case to which the largest $F_{\max}$ belongs. For 5 different impurity ions Table II contains these $F_{\max}$ values together with the corresponding slip plane and dipole orientation coordinates. In applying Eq. (2) c_p is computed by means of the simple association theory [8] with divalent impurity concentration of 10^{-5} mol/mol.

Table II

Maxima of force acting on the dislocations and the corresponding yield stress increments

	Mg	Ca	Sr	Pb	Ba	
$F_{\max}$	30.1	19.9	14.9	23.7	18.2	$\cdot\, 10^{-11} N$
y	$\frac{1}{\sqrt{2}}$	$\frac{1}{\sqrt{2}}$	$\sqrt{2}$	$-\frac{1}{\sqrt{2}}$	$-\frac{1}{\sqrt{2}}$	$\cdot\, r_0$
ε_x	$\sqrt{2}$	$\sqrt{2}$	$\frac{1}{\sqrt{2}}$	$\frac{1}{\sqrt{2}}$	$\frac{1}{\sqrt{2}}$	
ε_y	0	0	$\frac{1}{\sqrt{2}}$	$\frac{1}{\sqrt{2}}$	$\frac{1}{\sqrt{2}}$	
ΔT_{exp}	0.15	0.15	0.55	0.3	0.03	$\cdot\, 10^6 \frac{\text{N}}{\text{m}^2}$
ΔT	0.31	0.17	0.2	0.37	0.25	

The values $\Delta\tau$ obtained are valid at 0 K and in order to make them comparable with data measured at room temperature, they have been corrected in the way given in [1]. The computed and measured [9] values of $\Delta\tau$ are also listed in Table II.

As it is seen from Table II a calculation for $\Delta\tau$ based on the interaction between I—V dipoles and edge dislocations without using the concept of tetragonality can lead to reasonable results. The model described above needs of course further refinement to reflect the physical reality more accurately. The dipole ought to be described with more realistic strain field taking into account among others the off-centre displacement of the impurity ion, too. In addition, the Snoek effect may also shift $\Delta\tau$ considerably. Elaboration of an improved model is in progress.

REFERENCES

1. T. E. Mitchell and A. H. Heuer, Mat. Sci. Eng., **28**, 81, 1977.
2. R. L. Fleischer, J. Appl. Phys., **33**, 3504, 1962.
3. W. Frank, Phys. Stat. Sol., **29**, 391, 1968.
4. F. Bassani and R. Thomson, Phys. Rev., **102**, 1264, 1956.
5. P. Kálmán, T. Keszthelyi, A. Tóth and J. Sárközi, Acta Phys. Hung., **49**, 407, 1980.
6. B. A. Bilby, Proc. Phys. Aoc., **A63**, 191, 1950.
7. J. Friedel, Les Dislocations, Gauthier-Villars, Paris, 1956, p. 205.
8. A. B. Lidiard, Handbuch der Physik, Band XX., Springer Verlag, Berlin, 1957.
9. J. Sárközi, A. Tóth and T. Keszthelyi, Periodica Polytechnica, Mech. Eng., **21**, 235, 1977.

Printed in Hungary

A kiadásért felel az Akadémiai Kiadó igazgatója. Műszaki szerkesztő: Botyánszky Pál
A kézirat a kiadóba érkezett: 1980. X. 10. — A kézirat nyomdába érkezett: 1980. X. 15. — Terjedelem: 10,75 (A/5) ív, 39 ábra

---

81.8841 Akadémiai Nyomda, Budapest — Felelős vezető: Bernát György

NOTES TO CONTRIBUTORS

I. PAPERS will be considered for publication in Acta Physica Hungarica, only if they have not previously been published or submitted for publication elsewhere. They may be written in English, French, German or Russian.

Papers should be submitted to

Prof. I. Kovács, Editor
Department of Atomic Physics, Technical University
1521 Budapest, Budafoki út 8, Hungary

Papers may be either articles with abstracts or short communications. Both should be as concise as possible, articles in general not exceeding 25 typed pages, short communications 8 typed pages.

II. MANUSCRIPTS

1. Papers should be submitted in three copies.

2. The text of papers must be of high stylistic standard, requiring minor corrections only.

3. Manuscripts should be typed in double spacing on good quality paper, with generous margins.

4. The name of the author(s) and of the institutes where the work was carried out should appear on the first page of the manuscript.

5. Particular care should be taken with mathematical expressions. The following should be clearly distinguished, e.g. by underlining in different colours: special founts (italics, script, bold type, Greek, Gothic, etc.); capital and small letters; subscripts and superscripts, e.g. x^2, x_3; small l and 1; zero and capital O; in expressions written by hand: e and l, n and u, ν and v, etc.

6. References should be numbered serially and listed at the end of the paper in the following form: J. Ise and W. D. Fretter, Phys. Rev., *76*, 933, 1949.

For books, please give the initials and family name of the author(s), title, name of publisher, place and year of publication, e.g.: J. C. Slater, Quantum Theory of Atomic Structures, I. McGraw-Hill Book Company, Inc., New York, 1960.

References should be given in the text in the following forms: Heisenberg [5] or [5].

7. Captions to illustrations should be listed on a separate sheet, not inserted in the text.

8. As per Ist January 1980 the use of SI units has been made compulsory for all publications issued in Hungary. Please note that in papers submitted to Acta Physica after that date all measures should be expressed in SI units.

III. ILLUSTRATIONS AND TABLES

1. Each paper should be accompanied by three sets of illustrations, one of which must be ready for the blockmaker. The other sets attached to the copies of the manuscript may be rough drawings in pencil or photocopies.

2. Illustrations must not be inserted in the text.

3. All illustrations should be identified in blue pencil by the author's name, abbreviated title of the paper and figure number.

4. Tables should be typed on separate pages and have captions describing their content. Clear wording of column heads is advisable. Tables should be numbered in Roman numerals. (I, II, III, etc.).

IV. RETURN OF MATERIAL

Owing to high postage costs, the Editorial Office cannot undertake to return *all* material not accepted for any reason for publication. Of papers to be revised (for not being in conformity with the above Notes or other reasons) only *one* copy will be returned. Material rejected for lack of space or on account of the Referees' opinion will not be returned to authors outside Europe.

Reviews of the Hungarian Academy of Sciences are obtainable at the following addresses:

AUSTRALIA
C.B.D. LIBRARY AND SUBSCRIPTION SERVICE. Box 4886, G.P.O., *Sydney N.S.W. 2001*
COSMOS BOOKSHOP, 145 Ackland Street, *St. Kilda (Melbourne), Victoria 3182*

AUSTRIA
GLOBUS, Höchstädtplatz 3, *1200 Wien XX*

BELGIUM
OFFICE INTERNATIONAL DE LIBRAIRIE, 30 Avenue Marnix, *1050 Bruxelles*
LIBRARIE DU MONDE ENTIER, 162 Rue du Midi, *1000 Bruxelles*

BULGARIA
HEMUS, Bulvar Ruski 6, *Sofia*

CANADA
PANNONIA BOOKS, P.O. Box 1017, Postal Station "B", *Toronto, Ontario M5T 2T8*

CHINA
CNPICOR, Periodical Department, P.O. Box 50, *Peking*

CZECHOSLOVAKIA
MAD'ARSKÁ KULTURA, Národni třida 22, *115 66 Praha*
PNS DOVOZ TISKU, Vinohradská 46, *Praha 2*
PNS DOVOZ TLAČE, *Bratislava 2*

DENMARK
EJNAR MUNKSGAARD, Norregade 6, *1165 Copenhagen*

FINLAND
AKATEEMINEN KIRJAKAUPPA, P.O. Box 128, *SF-00101 Helsinki 10*

FRANCE
EUROPERIODIQUES S.A., 31 Avenue de Versailles, *78170 La Celle St. Cloud*
LIBRAIRIE LAVOISIER, 11 rue Lavoisier, *75008 Paris*
OFFICE INTERNATIONAL DE DOCUMENTATION ET LIBRAIRIE, 48 rue Gay-Lussac, *75240 Paris Cedex 05*

GERMAN DEMOCRATIC REPUBLIC
HAUS DER UNGARISCHEN KULTUR, Karl-Liebknecht-Strasse 9, *DDR-102 Berlin*
DEUTSCHE POST ZEITUNGSVERTRIEBSAMT, Strasse der Pariser Kommüne 3—4, *DDR-104 Berlin*

GERMAN FEDERAL REPUBLIC
KUNST UND WISSEN ERICH BIEBER, Postfach 46, *7000 Stuttgart 1*

GREAT BRITAIN
BLACKWELL'S PERIODICALS DIVISION, Hythe Bridge Street, *Oxford OX1 2EU*
BUMPUS, HALDANE AND MAXWELL LTD., Cowper Works, *Olney, Bucks MK46 4BN*
COLLET'S HOLDINGS LTD., Denington Estate, *Wellingborough, Northants MN8 2QT*
W,M. DAWSON AND SONS LTD., Cannon House, *Folkestone, Kent CT19 5EE*
H. K. LEWIS AND CO., 136 Gower Street, *London WC1E 6BS*

GREECE
KOSTARAKIS BROTHERS, International Booksellers, 2 Hippokratous Street, *Athens-143*

HOLLAND
MEULENHOFF-BRUNA B.V., Beulingstraat 2, *Amsterdam*
MARTINUS NIJHOFF B.V., Lange Voorhout 9—11, *Den Haag*
SWETS SUBSCRIPTION SERVICE 347b Heereewg, *Lisse*

INDIA
ALLIED PUBLISHING PRIVATE LTD., 13/14 Asaf Ali Road, *New Delhi 110001*
150 B-6 Mount Road, *Madras 600002*
INTERNATIONAL BOOK HOUSE PVT. LTD., Madame Cama Road, *Bombay 400039*
THE STATE TRADING CORPORATION OF INDIA LTD., Books Import Division, Chandralok, 36 Janpath, *New Delhi 110001*

ITALV
EUGENIO CARLUCCI, P.O. Box 252, *70100 Bari*
INTERSCIENTIA, Via Mazzé 28, *10149 Torino*
LIBRERIA COMMISSIONARIA SANSONI, Via Lamarmora 45, *50121 Firenze*
SANTO VANASIA, Via M. Macchi 58, *20124 Milano*
D. E. A., Via Lima 28, *00198 Roma*

JAPAN
KINOKUNIYA BOOK-STORE CO. LTD., 17-7 Shinjuku-ku 3 chome. Shinjuku-ku, *Tokyo 160-91*
MARUZEN COMPANY LTD., Book Department, P.O. Box 5050 Tokyo International, *Tokyo 100-31*
NAUKA LTD. IMPORT DEPARTMENT, 2-30-19 Minami Ikebukuro, Toshima-ku, *Tokyo 171*

KOREA
CHULPANMUL, *Phenjan*

NORWAV
TANUM-CAMMERMEYER, Karl Johansgatan 41—43, *1000 Oslo*

POLAND
WĘGIERSKI INSTYTUT KULTURY, Marszalkowska 80, *Warszawa*
CKP I W ul. Towarowa 28 *00-958 Warszawa*

ROMANIA
D. E. P., *Bucureşti*
ROMLIBRI, Str. Biserica Amzei 7, *Bucureşti*

SOVIET UNION
SOJUZPETCHATJ — IMPORT, *Moscow*
and the post offices in each town
MEZHDUNARODNAYA KNIGA, *Moscow G-200*

SPAIN
DIAZ DE SANTOS, Lagasca 95, *Madrid 6*

SWEDEN
ALMQVIST AND WIKSELL, Gamla Brogatan 26, *S-101 20 Stockholm*
GUMPERTS UNIVERSITETSBOKHANDEL AB, Box 346, *401 25 Göteborg 1*

SWITZERLAND
KARGER LIBRI AG, Petersgraben 31, *4011 Basel*

USA
EBSCO SUBSCRIPTION SERVICES, P.O. Box 1943, *Birmingham, Alabama 35201*
F. W. FAXON COMPANY, INC., 15 Southwest Park, *Westwood, Mass. 02090*
THE MOORE-COTTRELL SUBSCRIPTION AGENCIES, *North Cohocton, N. Y. 14868*
READ-MORE PUBLICATIONS, INC., 140 Cedar Street, *New York, N. Y. 10006*
STECHERT-MACMILLAN, INC., 7250 Westfield Avenue, *Pennsauken N. J. 08110*

VIETNAM
XUNHASABA, 42, Hai Ba Trung, *Hanoi*

YUGOSLAVIA
JUGOSLAVENSKA KNJIGA, Terazije 27, *Beograd*
FORUM, Vojvode Mišića 1, *21000 Novi Sad*

Index: 26.022
Acta Phys. Hung. Tom. 49. No. 4. Budapest, 15. IV. 1981
HU-ISSN 0001-6705